OPTICAL SCIENCES

Pierre Jaeglé

Coherent Sources of XUV Radiation

Soft X-Ray Lasers and High-Order Harmonic Generation

Springer

Springer Series in
OPTICAL SCIENCES 106

Founded by H.K.V. Lotsch

Springer Series in
OPTICAL SCIENCES

The Springer Series in Optical Sciences, under the leadership of Editor-in-Chief *William T. Rhodes*, Georgia Institute of Technology, USA, and Georgia Tech Lorraine, France, provides an expanding selection of research monographs in all major areas of optics: lasers and quantum optics, ultrafast phenomena, optical spectroscopy techniques, optoelectronics, quantum information, information optics, applied laser technology, industrial applications, and other topics of contemporary interest.

With this broad coverage of topics, the series is of use to all research scientists and engineers who need up-to-date reference books.

The editors encourage prospective authors to correspond with them in advance of submitting a manuscript. Submission of manuscripts should be made to the Editor-in-Chief or one of the Editors. See also http://www.springer.de/phys/books/optical_science/

Pierre Jaeglé

Coherent Sources of XUV Radiation

Soft X-Ray Lasers and High-Order Harmonic Generation

With 332 Illustrations

Springer

Pierre Jaeglé
Directeur de Recherche Emérite au Centre National de la Recherche Scientifique
X-Ray Matter Interaction Laboratory (LIXAM)
Université Paris-Sud
91405 Orsay
France

Library of Congress Control Number: 2005934933

ISBN 10: 0-387-23007-6
ISBN 13: 978-0387-23007-8

Printed on acid-free paper.

Printed in the United States of America. (TB/EB)

9 8 7 6 5 4 3 2 1

springeronline.com

To Rachel

Acknowledgments

I am grateful to my colleagues Clary Möller and Pierre Dhez for their help in the preparation of this book. The dynamism of the X-Ray Laser Research Group of LIXAM has provided great encouragement in the completion of this work.

Contents

Part I. Introduction to Coherent Extreme-Ultraviolet and Soft X-Ray Sources

1. Short Survey of XUV Emission Mechanisms and Sources

The radiation range of photon energy comprised between, let us say, 20 eV and 600 eV is known by the names of extreme ultraviolet, soft X-ray or XUV radiation. This fluctuating designation reflects the various origins of a radiation pattern which, in other respects, exhibits singular optical properties marking it off from far-ultraviolet, on one side, and X-rays, on the other. The penetration length of XUV radiation is very small in almost all materials—generally less than 1 μm. There is practically no reflection on optical surfaces under normal incidence and, in addition, wavelength is too large to make use of Bragg reflection on natural crystals. These peculiarities made the development of instrumentation for XUV studies more difficult than for others spectral fields, a fact which has been prejudicial to the advance of XUV research. During the last decades important progress, especially in XUV optics, became possible with the help of synchrotron radiation sources.

As illustrated in Figure 1.1, the energy of the transitions occurring between two upper electronic shells of atoms, remains of a constant order of magnitude as the atomic number increases. For instance, the L_{II}–K transition of boron ($Z = 5$), the M_I–L_{II} transition of silicon ($Z = 14$), the N_I–M_{II} transition of zinc ($Z = 30$), the O_I–N_{II} transition of tin ($Z = 50$), all have an energy of the order of 100 eV, which corresponds to a wavelength of ∼12 nm. Therefore B atoms ionized in K-shell, Si atoms ionized in L-shell, Zn atoms ionized in M-shell, and so on, will be sources of soft X-ray emission (see for instance [1]).

One can ask the question whether this process can provide excitation densities such that population inversions might appear between lower and upper levels. This would open the way to neutral atom photo-pumped XUV lasers. But attempts at implementing X-ray photo-pumping have not yet succeeded since a very large X-ray flux is necessary to pump the lasing material, while the small aperture of XUV optics makes it difficult to concentrate the flux on the target.

XUV radiation is also emitted by electron transitions between the optical levels of multicharged ions. The word "optical" refers to the empty levels above the ground state, that is to say the levels otherwise involved in the visible or

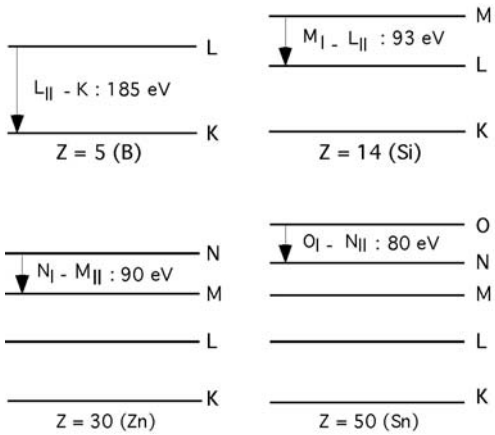

Fig. 1.1. Simplified atomic level diagrams that show soft X-ray transitions.

near ultraviolet spectra of neutral atoms. Multicharged ions are obtained by removing external bound electrons from atoms. Let us consider, for instance, the lithium atom ($Z = 3$), then the singly charged beryllium ion, the doubly charged boron ion, and the triply charged carbon ion. All the members of this so-called lithium-like isoelectronic sequence have the same number of bound electrons as lithium itself. Their optical spectra are very similar but they are shifted to higher energy region as the ion charge increases. It results from this that multicharged ions will form a huge reserve of XUV and X-ray emitters.

Except for the case of ion beams in particle accelerators, multicharged ions are mainly found in the fourth state of the matter known as "plasma." In a plasma, the negative electrons removed from each atom make up a gas—or a sea—of free electrons, which surrounds the positive ions and so ensures the plasma global neutrality. The simultaneous presence of free electrons and ions gives rise to a dense ion excitation, which generates line and continuous emission spectra [2–4].

Temperature and density are the important parameters that characterize a macroscopic plasma state. Temperature governs the mean ionization degree, from which follows the rough spectral structure and its energy range. Density has a strong effect on the balance between collisional and radiative processes, on the one hand, and on photon propagation through the plasma, on the other hand. Roughly speaking, the plasma temperature necessary for achieving XUV emission extends from 100 eV ($\sim 10^6$ K) to 1 keV ($\sim 10^7$ K). In laboratory plasmas, the electron density lies between 10^{10} cm^{-3} and 10^{23} cm^{-3}, except in the extreme case of plasmas confined under thermonuclear fusion conditions.

Near the low-density limit of this domain, the photon mean free path exceeds widely the plasma chamber size. The observed spectrum then directly

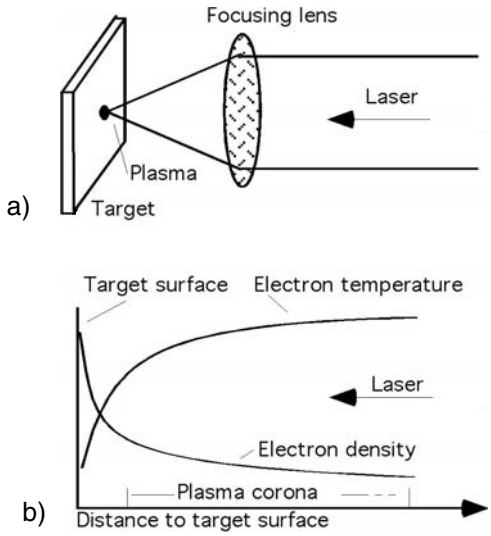

Fig. 1.2. (a) Dense hot plasma produced by laser pulse; (b) diagram showing the opposite variations of plasma density and plasma temperature.

displays the excitation of individual atoms or ions. For a propagation path length of about 1 cm the spectrum is significantly modified by reabsorption or stimulated emission at densities exceeding 10^{18} cm^{-3}. As we will see later, the densities suitable for XUV lasers lie between 10^{18} cm^{-3} and 10^{21} cm^{-3} approximately.

XUV plasma sources are commonly achieved by producing highly ionized atoms, either by triggering electric gas discharges or by focusing pulsed laser beam onto solid targets. To reach high discharge currents, very short electric pulses are required. This leads to the use of coaxial circuits of low impedance. The electrode geometry is chosen in order to optimize the directionality of the electron flow. A self-induced magnetic field then may appear, generating plasma confinement and electron density increase. These days, systems with coaxial capillary discharge [5] arouse a large interest.

Figure 1.2 summarizes the principle of hot-dense plasma production by focusing a powerful pulsed laser beam onto the surface of a solid material. The main energy-transfer process between laser light and plasma consists in the inverse-bremsstrahlung of free electrons crossing the multicharged ion electric field [6]. The plasma's hydrodynamic expansion causes density to decrease from a high value near the target surface to much smaller values far away from it.

Figure 1.2b displays this general feature in the bottom curve. Owing to the electron density gradient, the laser beam absorption varies with the target distance. Now let us recall that radiation cannot propagate if the plasma

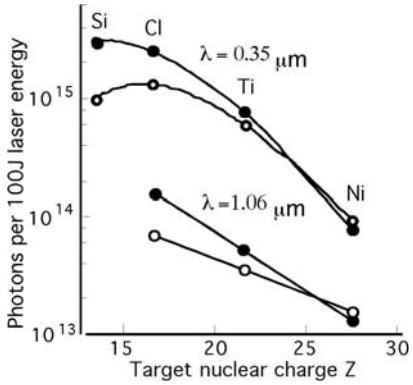

Fig. 1.3. Efficiency of XUV emission for the resonance line of He-like ions for two laser irradiation parameters: white circles, $E = 175$ J, $\tau = 800$ ps, $\Phi = 10^{15}$ W/cm^2; black circles, $E = 40$ J, $\tau = 500$ ps, $\Phi = 5 \times 10^{14}$ W/cm^2.

frequency becomes larger than the radiation frequency. Since the plasma frequency increases as the density to the square, the beam propagation ends reaching a density zone where it cannot penetrate more deeply into the plasma. For near-infrared and visible lasers this occurs at densities about two orders of magnitude smaller than solid state density. This explains the temperature curve of Figure 1.2b which falls at large density, near the target. The lower density region, which is directly heated by the laser, is known as the "subcritical" region, or plasma corona. The gradient lengths of density and temperature depend on pulse duration. In Figure 1.2b, the length scale along the horizontal axis is of a few microns for picosecond pulses, but of tens or hundreds of microns for nanosecond pulses. Considering these features, XUV spectra will depend, to a large rate, on the distance of the emitting region and the target surface. The corona is the plasma region of interest for X-ray lasers.

Other emission parameters are target composition, total laser deposited energy, and wavelength of the focused laser beam. As an example, Figure 1.3 displays the efficiency of the $1s^2-1s2p$ line emission of helium-like ions versus the emitter nuclear charge, Z, for two laser wavelengths commonly used to heat the plasma [7]. General features of the conversion of laser light into soft X-rays can be found in [8, 9].

There are other important sources of XUV radiation, which are not usually referred to the standard atomic spectroscopy. This the case of high-order harmonic generation, which will be treated in Part III of this book. For synchrotron radiation, undulators and transition radiation the reader may refer to [10]. A wide view on general XUV radiation physics and optics specific to the XUV range may be found in [11] and [12]. As regards the base of optical coherence theory, which will be referred to in the next chapters, it is exhaustively treated in [13].

1.1 Radiation Transfer Through Matter, Opacity, and Gain

Except for the case of a small emitting volume of dilute matter, the shape of the spectral lines emitted by atoms and ions results from the properties of individual emitter properties together with reabsorption and scattering by the particles. This is exemplified in Figure 1.4, which shows the experimentally observed profiles of the 2p–3s lines of neon-like aluminium coming from the under-dense region of a laser-produced plasma, compared to the same lines observed in the dense plasma region [14]. It can be established that the broadening of the lines is due to reabsorption in the central hot dense plasma region while their split-like line shape is due to reabsorption in the external colder plasma shell. Thus the understanding of line spectra calls for radiation-transfer calculations in which, as we will see, the atomic level populations are important parameters. Moreover, since radiation amplification requires population inversion to occur between the upper and lower levels of some transition, X-ray laser physics has to resort, in some respects, to radiation transfer calculation.

The study of radiative transfer offers a very wide field to theoretical investigation and numerical calculation [15–19]. However, we will restrict ourselves to a simplified treatment, which proved nevertheless appropriate for many

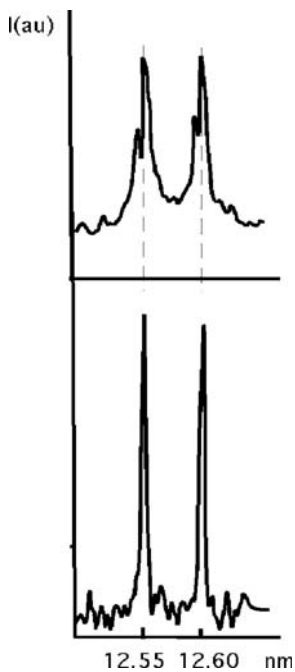

Fig. 1.4. Example of spectral line shape modifications produced by radiation transfer in a laser-produced plasma.

practical investigations. More sophisticated developments, about specific topics like radiation polarization and optical coherence, will appear further.

We shall thus make the following assumptions:

(a) As we deal with media, where excited level and ion species population balances are essentially controlled by electron–ion collisions and not by radiation, radiative transfer calculations can be performed on the radiation intensity rather than on the electromagnetic field amplitude. We may then use the standard atomic emission and absorption coefficients, known as Einstein's coefficients. Let us mention that, for very large volume of dilute gas, this choice may be inappropriate, owing to radiation–particle interaction affecting the line profiles via the partial frequency redistribution process [20–24]. We must also keep in mind that intensity calculation may be inaccurate at the very large intensity of laser close to the saturation regime. At large amplification level, it becomes necessary to calculate the electromagnetic field amplitude step-by-step, coupling it to particle response. This will be done in Section 6.3 devoted to X-ray laser coherence. Moreover, owing to a strong phase relation between the emitters, a simple intensity calculation is not appropriate to investigate high-order harmonic propagation (Section 11.2).
(b) Frequency redistribution is assumed to be complete. This means that, when an atom is excited and then de-excited by successively absorbing and emitting a photon, there is no relation between the frequencies of the two processes, within the line-width frequency domain. For such a relation to exist, the atom should "remember" the frequency involved in the absorption at the time of the following emission. But perturbations by electron collisions result in blotting out this memory. Thus, incomplete frequency redistribution will result from the first process taking place after the photo-absorption event, either radiative decay or collision with another particle. In the first case, a redistribution relation will modify the emission line profile compared to the absorption profile. In the second case, both profiles are identical.

One sees that the role of frequency redistribution is necessarily negligible in a medium where atomic levels are mainly populated by electron collisions. This is certainly the case in plasmas where the electronic populations are in thermal equilibrium, that is to say satisfying Boltzman's law. When this plasma state is not completed by black-body radiation equilibrium, it is known as Local Thermodynamic Equilibrium (LTE plasma).
(c) As our purpose is not to investigate the part of radiation in the emitting material energy balance, frequency integration will be performed over a small frequency interval around the line center.

1.2 Transfer Equation, Absorption, and Gain

Let us first consider plan–parallel volume of ionized gas in which a radiation beam at frequency ν covers the distance l, as schematically represented in

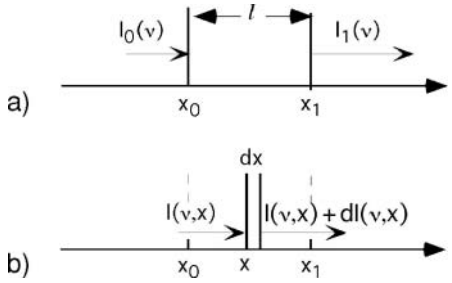

Fig. 1.5. Diagram illustrating step-by-step radiation transfer calculation in a non-homogeneous medium.

Figure 1.5a. The elementary problem of radiative transfer calculation consists in calculating the intensity $I_1(\nu)$ at the exit of the gas column as a function of the intensity $I_0(\nu)$ at the entrance. The differential equation, that accounts for a very small intensity change over a very short propagation distance, is built phenomenologically by considering an elementary gas shell of thickness dz, which changes the incoming intensity $I(\nu, z)$ by an amount $dI(\nu, z)$ at position z along the axis, as shown in Figure 1.5b. The value of dz is chosen small enough to make the density and temperature variations negligible within the interval dz. Let $j(\nu, z)$ and $k(\nu, z)$ be respectively the emissivity and absorption (or opacity) function of the source medium. The variable $j(\nu, z)\ dz$ represents the positive thin layer contribution to the incoming intensity $I(\nu, z)$, whereas $k(\nu, z)\ dz$ is the radiation part absorbed in the layer. We can thus write

$$\frac{dI\,(\nu, z)}{dz} = j\,(\nu, z) - k\,(\nu, z)\,I\,(\nu, z) \tag{1.1}$$

Assuming a homogenous source medium, j and k are constant along the propagation path. Integrating equation (1.1) we then obtain the outgoing intensity as a function of j, k, and l:

$$I_1\,(\nu) = \frac{j\,(\nu)}{k\,(\nu)}\left(1 - e^{-k(\nu).l}\right) + I_0 e^{-k(\nu)l} \tag{1.2}$$

if $k\,(\nu)$ is positive (absorbing medium). If $k\,(\nu)$ is negative we replace it by the gain coefficient $g\,(\nu) = -k\,(\nu)$ and we write in a similar way

$$\frac{dI\,(\nu, z)}{dz} = j\,(\nu, z) + g\,(\nu, z)\,I\,(\nu, z) \tag{1.3}$$

$$I_1\,(\nu) = \frac{j\,(\nu)}{g\,(\nu)}\left(e^{g(\nu)l} - 1\right) + I_0 e^{g(\nu)l} \tag{1.4}$$

In the case of a so-called "optically thin" medium, $k\,(\nu)\,l$ [or $g\,(\nu)\,l$] is very small and equation (1.2), as well as equation (1.4) reduce to:

$$I_1\,(\nu) = j\,(\nu)\,l + I_0 \tag{1.5}$$

Transfer equation integration in nonhomogeneous media of various geometrical properties is an important chapter of radiative transfer theory (see for instance [11]. Here we will only mention that, if j and k are functions of z, equation (1.2) may be used for intensity numerical integration. Let us write it in the form

$$I_{n+1}(\nu) = \frac{j_{n+1}(\nu)}{k_{n+1}(\nu)}\left(1 - e^{-k_{n+1}(\nu)d}\right) + I_n e^{-k_n(\nu).d} \tag{1.6}$$

where d is the thickness of each of the N thin layers of constant emissivity and absorption coefficient, n is the layer index number. For a propagation length $l = Nd$, the integrated intensity is merely

$$I(\nu) = \sum_{1}^{N} I_n(\nu) \tag{1.7}$$

Equation (1.1) gives us the opportunity to recall two usual definitions. The first one refers to the ratio

$$S = \frac{j(\nu)}{k(\nu)} \tag{1.8}$$

i.e., the "source function" and the second, to the quantity

$$\tau = -k(\nu)\, l \tag{1.9}$$

which is known as the "optical depth" of the source medium. Substituting S and τ in transfer equation (1.1) gives

$$\frac{dI}{d\tau} = I - S \tag{1.10}$$

In a similar way, for an amplifier, we can write

$$S = \frac{j(\nu)}{g(\nu)} \tag{1.11}$$

$$G = g(\nu)\, l \tag{1.12}$$

where G is the gain length product, often merely labeled "gain-length." The transfer equation is then

$$\frac{dI}{dG} = I + S \tag{1.13}$$

The previous expressions left aside the actual emission or absorption processes. We will now introduce the specific form of j and k, corresponding to spectral lines emitted by discrete transitions.

Let us consider a radiative transition of frequency ν between two atomic levels, 1 and 2, as shown in Figure 1.6. The factors to be taken into consideration in the radiation intensity calculation are the quantum line strength, $s_{1,2}$, the level populations, N_1 and N_2, the levels statistical weights, $g_1$and g_2,

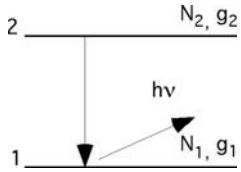

Fig. 1.6. Spontaneous radiative transition between discrete levels: N_1 and N_2 are the level population densities; $g_1$and g_2 the statistical weights of the levels 1 and 2, respectively; $h\nu$ is the photon energy.

and the profile function, $\Phi(\upsilon)$. Einstein's coefficient of spontaneous emission from level 2 to level 1 is then defined by the relation

$$A_{2,1} = \frac{1}{g_2} \frac{8\pi^3 \nu^3}{3hc^3} s_{1,2} \tag{1.14}$$

In the same way, Einstein's absorption coefficient from level 1 to level 2 reads

$$B_{1,2} = \frac{1}{g_1} \frac{\pi^2}{3h^2} s_{1,2} \tag{1.15}$$

As for stimulated emission, we have

$$B_{2,1} = \frac{1}{g_2} \frac{\pi^2}{3h^2} s_{1,2} \tag{1.16}$$

In terms of Einstein's coefficients, the emissivity $j(\nu)$, the absorption $k(\nu)$, and the gain coefficient $g(\nu)$ are now respectively

$$j(\nu) = \frac{h\nu}{4\pi} A_{2,1} N_2 \Phi(\nu) \tag{1.17}$$

$$k(\nu) = \frac{h\nu}{c} g_1 B_{1,2} \left(\frac{N_1}{g_1} - \frac{N_2}{g_2} \right) \Phi(\nu) \tag{1.18}$$

$$g(\nu) = \frac{h\nu}{c} g_2 B_{2,1} \left(\frac{N_2}{g_2} - \frac{N_1}{g_1} \right) \Phi(\nu) \tag{1.19}$$

Let us set

$$\Delta N = \frac{N_2}{g_2} - \frac{N_1}{g_1} \tag{1.20}$$

where ΔN represents the number of atoms with inverted level population densities per volume units. ΔN is called population inversion density. The gain coefficient given by equation (1.19) may be directly measured in a perfectly homogeneous medium only. For amplifying media having density and temperature gradients 1.19 defines the so-called *local* gain, that can be obtained by calculation in each point of the plasma. The gain experimentally

measured is an average over the varying local gain. Moreover, the large intensity achieved in long amplifying media tends to reduce the population inversion, ΔN. Then the gain coefficient decreases and the laser is said to saturate. To distinguish the gain coefficient, that does not depend on laser intensity, from the decreasing gain observed at saturation, the first of them is usually called *small-signal gain.*

It is not a patent fact that one and the same profile function $\Phi(\nu)$ must be chosen for both emission and absorption processes. In fact this choice is no more than the direct consequence of the complete photon frequency redistribution assumption, which has been mentioned previously. From equations (1.17) and (1.18) one immediately obtains the source function for a spectral line in the form

$$S = \frac{2h\nu^3}{c^2} \frac{g_1 N_2}{g_2 N_{1-} g_1 N_2} \tag{1.21}$$

for an absorber and

$$S = \frac{2h\nu^3}{c^2} \frac{g_1 N_2}{g_1 N_{2-} g_2 N_1} \tag{1.22}$$

for an amplifier where population inversion occurs between levels N_1 and N_2.

It is worthwhile noticing that the source function given by equations (1.21) or (1.22) depends only on upper and lower level populations but not on oscillator strength and profile function. One can also observe that, if N_1 and N_2 satisfy Boltzman's equilibrium relation, viz.

$$\frac{N_2}{N_1} = \frac{g_2}{g_1} e^{-\frac{h\nu}{kT_e}} \tag{1.23}$$

where T_e is the electron temperature, S reduces to the well-known Plank function:

$$S = \frac{2h\nu^3}{c^2} \frac{1}{e^{\frac{h\nu}{kT_e}} - 1} \tag{1.24}$$

To complete this set of basic properties, let us now assume that the radiation intensity results from the superposition of several contributions due, for instance, to line wings and to possible continuous recombination spectra. Summing the various contributions provides a source function of the form:

$$S = \frac{j_1(\nu) + j_2(\nu) + j_3(\nu) + \cdots}{k_1(\nu) + k_1(\nu) + k_1(\nu) + \cdots} \tag{1.25}$$

Returning to equations (1.2) or (1.4) we see that, except for the case of an optically thin medium, the contributions of several transitions to the total intensity are not additive. This fact has to be considered in interpreting experimental results, that involve continuous background at line wavelengths.

1.3 Profile Functions

As regards the profile function appearing in relations (1.17), (1.18), (1.19) let us first remark that, considering the transition probability at frequency ν, $A_{21}(\nu)$, and the total transition probability, A_{21}, we can write

$$A_{21}(\nu) = A_{21}\Phi(\nu) \tag{1.26}$$

which shows that $\Phi(\nu)$ must obey the normalization condition:

$$\int_{-\infty}^{+\infty} \Phi(\nu)\, d\nu = 1 \tag{1.27}$$

In calculations, that do not require the exact line profile, a usual approximation consists in substituting a rectangular profile of width $\Delta\nu$ and height $\Phi_{\text{rect}} = 1/\Delta\nu$, where Φ_{rect} is the mean value of $\Phi(\nu)$ in an interval $\left[-\frac{\Delta\nu}{2}, +\frac{\Delta\nu}{2}\right]$. Then the expression of $g(\nu)$ given by equation (1.19) is replaced by

$$g = \frac{h\nu}{c} g_2 B_{2,1} \left(\frac{N_2}{g_2} - \frac{N_1}{g_1}\right) \frac{1}{\Delta\nu} \tag{1.28}$$

In the general case the profile must be chosen in order to fit the properties of the emitting medium. For instance, a high temperature results in an increase of the mean particle velocity. Therefore the emission lines are broadened by random Doppler wavelength shift. Calculation shows that the broadening due to a Maxwellian distribution of emitter velocity yields a Gaussian line shape:

$$\Phi_{\text{D}}(\nu) = \frac{1}{\Delta\nu_{\text{D}}\sqrt{\pi}} \exp\left[-\left(\frac{\nu - \nu_0}{\Delta\nu_{\text{D}}}\right)^2\right] \tag{1.29}$$

where the Doppler width $\Delta\nu_{\text{D}}$ reads (see for instance, [23])

$$\Delta\nu_{\text{D}} = \nu_0 \sqrt{\frac{2kT_{\text{i}}}{m_{\text{A}}c^2}} \tag{1.30}$$

In this expression T_{i} is the ion temperature, m_{A}, the atomic mass.

On the other hand, large densities increase the perturbation of atomic potentials, which induce collisional and Stark broadening. Collisional profiles are well represented by a Lorentzian curve:

$$\Phi_{\text{L}}(\nu) = \frac{1}{2\pi} \frac{\Delta\nu_{\text{L}}}{(\Delta\nu_{\text{L}}/2)^2 + (\nu - \nu_0)^2} \tag{1.31}$$

In the frame of the so-called impact approximation, the electronic density, n_{e}, and the electronic temperature, T_{e}, can be directly introduced in the profile function by way of the proportionality relation:

$$\Delta\nu_{\text{L}} \propto n_{\text{e}}^2 T_{\text{e}}^{-1/2} \tag{1.32}$$

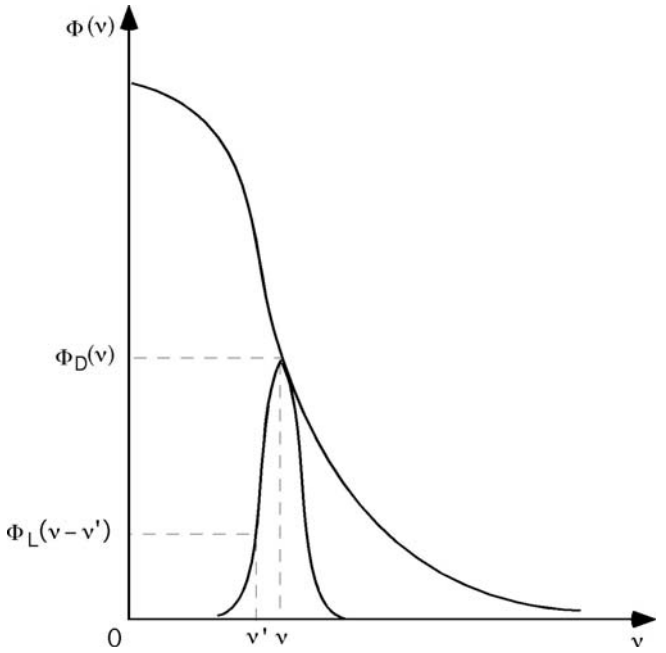

Fig. 1.7. Doppler profile $[\Phi_{\mathrm{D}}(\nu)]$ and Lorentz profile $[\Phi_{\mathrm{L}}(\nu-\nu')]$ whose convolution generates a Voigt profile that fits a larger class of line broadening processes than each profile separately.

In these expressions $\Delta\nu_{\mathrm{L}}$ is the line full-width-at-half-maximum (FWHM), defined by $\Phi\left(\nu_0 \mp \frac{\Delta\nu_{\mathrm{L}}}{2}\right) = \frac{1}{2}\Phi(\nu_0)$. A simple calculation shows it is not the case of $\Delta\nu_{\mathrm{D}}$ in expression (1.29). For Doppler profiles indeed we have

$$\Delta\nu_{\mathrm{FWHM}} = \frac{\Delta\nu_{\mathrm{D}}}{2\sqrt{\ln 2}} \cong 0.60\Delta\nu_{\mathrm{D}} \tag{1.33}$$

A pure Doppler or Lorenz profile will occur only if one of the broadening factors, temperature or density, prevails strongly over the other. If neither of them can be neglected, a more realistic profile may be calculated by the convolution (see Fig. 1.7):

$$\Phi_{\mathrm{V}}(\nu') = \int_{-\infty}^{+\infty} \Phi_{\mathrm{D}}(\nu)\,\Phi_{\mathrm{L}}(\nu-\nu')\,d\nu \tag{1.34}$$

which is currently accepted as a Voigt profile

1.4 Line Narrowing

The previous expressions refer to local line shapes. Now substituting equations (1.17), (1.18), and (1.19) into equations (1.2) and (1.4) shows that, except for

an optically thin medium, the line profile is not conserved by integrating the transfer equation. As a matter of fact light propagation modifies the line profiles. It is well known, for instance, that the line width is an increasing function of the length traveled through an absorbing medium. On the contrary, amplification has a narrowing effect on line widths. This may be easily shown at the large gain limit.

Let us choose, for instance, a local profile controlled by the particle thermal motion. Without loss of generality we can set $\nu_0 = 0$ in equation (1.29). The local profile reads then

$$\Phi_{\mathrm{D}}(\Delta\nu) = \frac{1}{\Delta\nu_{\mathrm{D}}\sqrt{\pi}} \exp\left[-\left(\frac{\nu}{\Delta\nu_{\mathrm{D}}}\right)^2\right] \tag{1.35}$$

We are looking for the relation between $\Delta\nu_{\mathrm{FWHM}}$, and the gain factor—or gain-length product—gl involved in the source emission according to equation (1.4). $\Delta\nu$ is defined by

$$I(\Delta\nu_{\mathrm{FWHM}}/2) = \frac{1}{2} I(0) \tag{1.36}$$

Combining this relation with equation (1.4) allows us to write

$$\exp\left[g_0 l \ \exp\left[-\left(\frac{\Delta\nu_{\mathrm{l}}}{\Delta\nu_{\mathrm{D}}}\right)^2\right]\right] - 1 = \frac{1}{2}\left[\exp g_0 l - 1\right] \tag{1.37}$$

where $\Delta\nu_l$ is the FWHM after amplification over the distance l. At the limit of large $g_0 l$ values one may use the development $\exp\left(-x^2\right) = 1 - x^2 + \cdots + O$ in the left-hand side and the fact that $\mathrm{e}^{g_{0l}} \gg 1$. A short calculation then yields:

$$\frac{\Delta\nu_{\mathrm{l}}}{\Delta\nu_{\mathrm{D}}} \cong \sqrt{\frac{\ln 2}{g_0 l}} \tag{1.38}$$

Replacing $\Delta\nu_{\mathrm{D}}$ by its value deduced from relation (1.33) we obtain the narrowing rate at large gain factor:

$$\Delta\nu_{\mathrm{l}} \cong \Delta\nu_{\mathrm{l}=0} \frac{2\ln 2}{\sqrt{g_0 l}} \tag{1.39}$$

Figure 1.8 displays curves of line narrowing versus gain, calculated by using the above approximations or by exact numerical integration [25]. Similar results are obtained for a Lorentzian profile.

A consequence of the line narrowing is that the total intensity of the spectral line varies as a function of the length l in a more complex way than simply suggested by the exponential factor of equation (1.4). The instrumental width being generally larger than the line width $\Delta\nu_{\mathrm{l}}$, the quantity returned by laser experiments is generally close to the total line intensity defined by

$$I_T = \int_{-\infty}^{+\infty} I(\nu)\, d\nu \tag{1.40}$$

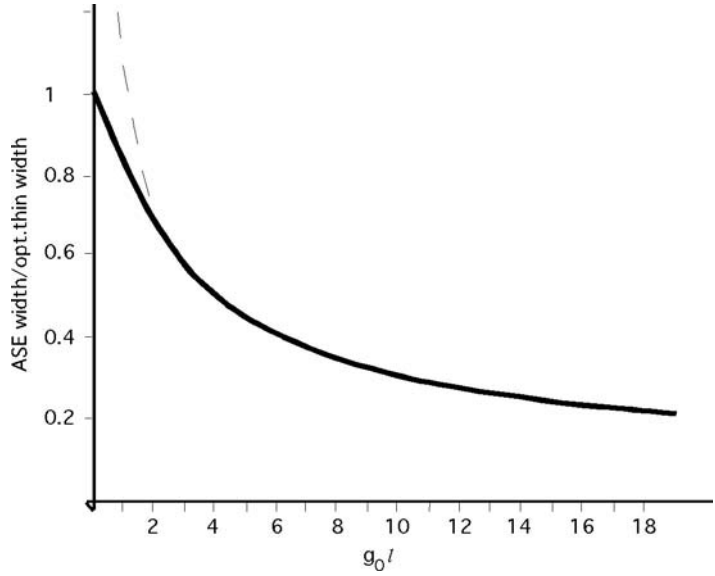

Fig. 1.8. Line narrowing as a function of the gain factor $g_0 l$, for a Doppler local profile. Continuous line: result of exact numerical integration; dashed line: narrowing factor approximated at $1/\sqrt{g_0 l}$.

By substituting $I(\nu)$ given by equation (1.4), with $I_0 = 0$, into the previous expression, we obtain

$$I_T = \frac{j_0}{g_0} \int_{-\infty}^{+\infty} \left(e^{g_0 \Phi(\nu) l} - 1 \right) d\nu \tag{1.41}$$

In most cases this integral cannot be calculated analytically. The same approximation as above for the case of large gain–length products leads to the relation

$$I_T = \sqrt{\pi} \Delta\nu_{\mathrm{D}} \frac{j_0}{g_0} \frac{e^{g_0 l}}{\sqrt{g_0 l}} \tag{1.42}$$

which shows that the total intensity increase is smaller than the increase in the line center. This fact must be taken into account in experimental gain measurements. A more general approximation, which matches the limits $g_0 l \to 0$ and $g_0 l \to \infty$, has been proposed by Lindford *et al.* [26]. It leads to the relation

$$I_T = \sqrt{\pi} \Delta\nu_{\mathrm{D}} \frac{j_0}{g_0} \frac{\left(e^{g_0 l} - 1\right)^{3/2}}{\sqrt{g_0 l \times e^{g_0 l}}} \tag{1.43}$$

One sees I_T to be reduced by the same factor, $\sqrt{g_0 l}$, as the line width [cf. equation (1.39)]. Lindford's relation is in current use in the treatment of gain experimental data.

1.5 Atomic Level Population Densities

The functions involved in radiative transfer calculations—viz. emissivity, $j(\nu)$, opacity, $k(\nu)$, and gain, $g(\nu)$—presented above in equations (1.17), (1.18), and (1.19), all include atomic level populations, which should be evaluated. A specific aspect of coherent XUV emission is to call upon nonequilibrium populations at the very center of investigations. As a consequence, Boltzman's' law (1.23) cannot be used to reach the actual values of electron level populations, neither can the corresponding Saha equation (see for instance [27])

$$\frac{n_{\mathrm{e}} N_{Z+1}}{N_z} = \frac{2(g_0)_{Z+1}}{(g_0)_Z} \left(\frac{2\pi m_{\mathrm{e}} K T_{\mathrm{e}}}{h^2}\right) \exp\left(\frac{-I_Z}{K T_{\mathrm{e}}}\right) \tag{1.44}$$

—where N_Z, $(g_0)_Z$ (conversely $Z+1$) are the density and the ground state of the ion of charge Z (conversely $Z+1$), m_{e} is the electron mass and I_Z the ionization energy—be used for ion populations. It is necessary to calculate each discrete level population by solving an equation system which involves the contributions of a number of radiative and collisional transitions.

Figure 1.9 shows the simplified scheme of a set of levels, $\ldots i, j$,e populations must be calculated. The variables i and j denote two successive excited levels of the set. Z and $Z+1$, represent the ground levels of ions of charge Z and $Z+1$, respectively. They are also the ionization limits of ions $Z-1$ and Z. An ionizing electron collision with an electron of the i-level followed by the radiative transition from the j-level toward the vacancy just created

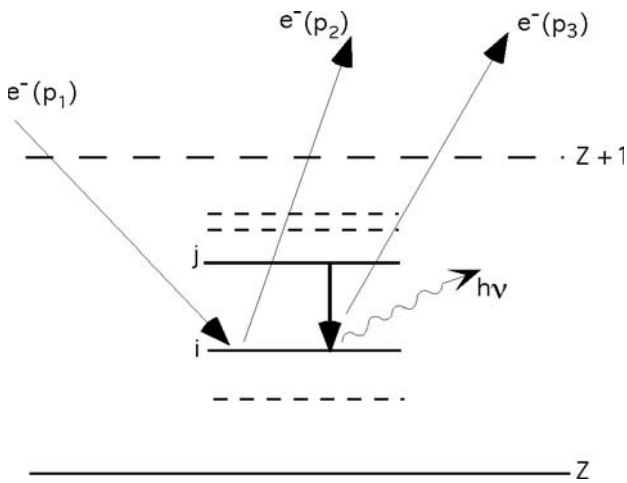

Fig. 1.9. Typical example of processes involved in population rate equations. An ionizing electron of momentum p_1 collides with a multicharged ion in which it creates a vacancy at level i. The electron goes away with momentum $p_2 < p_1$ while the electron ejected from the level i moves off with momentum p_3. The vacancy is filled by radiative transition from level l. Other nonrepresented processes follow.

in the i-level is represented as an example. Let N_i be the population of the i-level at a given instant t, N_j the j-level population, A_{ji} the radiative transition probability from j to i, $\langle \sigma_{ki} v \rangle$ the collisional transition cross-section from k to i, averaged over the free electrons velocity distribution, respectively $\langle \sigma_I v \rangle$, the ionization cross-section of the i-level and $I(\nu_{ri})$, the radiation intensity at frequency ν_{ri} due to the $r \to i$ transition. Owing to the very short electron thermalization time, the electron velocity distribution can be considered as Maxwellian when the temperature variation time exceeds ∼1 ps, as will be the case here. Let n_e be the free electron density. Ionizing collisions will contribute a negative population $-n_\mathrm{e} N_i \langle \sigma_I v \rangle dt$ to the i-level, whereas the radiative transitions from the j-level and other upper levels contribute a positive population $+\sum_{j>i} N_j A_{ji} dt$. Similar notations can be extended to more processes as photo-recombination, photoexcitation and photoabsorption, three-body recombination. We finally may write the i -level population rate, $\frac{dN_i}{dt}$, as

$$\begin{aligned}\frac{dN_i}{dt} = &\sum_{j>i} N_j A_{ji} - N_i \sum_{l<i} A_{il} + n_\mathrm{e} \sum_k N_k \langle \sigma_{ki} v \rangle \\ &- n_\mathrm{e} N_i \sum_m \langle \sigma_{im} v \rangle + n_\mathrm{e} N_{z+1} \left\langle \sigma^{\text{photorecomb.}} v \right\rangle - n_\mathrm{e} N_i \langle \sigma_I v \rangle \\ &+ \sum_{r<i} \frac{4\pi N_r I(\nu_{ri}) B_{ri}}{c} - N_i \sum_{q>i} \frac{4\pi I(\nu_{iq}) B_{iq}}{c} + \cdots \end{aligned} \tag{1.45}$$

and a similar equation may be written for each level of the set. Moreover, one can often use the quasi-static approximation that assumes level populations to vary slowly with respect to atomic relaxation times. It makes then sense to consider time intervals, dt, small enough for the whole population balance to obey equations

$$\begin{aligned}\frac{dN_1}{dt} &= 0 \\ \cdots &= 0 \\ \frac{dN_i}{dt} &= 0 \\ \frac{dN_j}{dt} &= 0 \\ \cdots &= 0 \end{aligned} \tag{1.46}$$

We get a system of linear equations whose solutions are the quasi-steady state (QSS) populations of the atomic levels.

The transition probabilities involved in the coefficients of this system can be obtained by using the standard methods of atomic physics calculation. However, the terms representing radiative processes, in the above equations, include the intensities of a number of spectral lines, like $I(\nu_{ri})_{r<i}$, $I(\nu_{iq})_{q>i}$.

Each of them satisfies a transfer equation of the form

$$\frac{dI\left(\nu_{lm}\right)}{dx} = j\left(\nu_{lm}\right) - k\left(\nu_{lm}\right) I\left(\nu_{lm}\right) \tag{1.47}$$

As a result, when radiation takes a significant part in level populations, a second system, formed of differential equations similar to equation (1.47) must be solved. More exactly, since $j\left(\nu_{lm}\right)$ and $k\left(\nu_{lm}\right)$ are functions of N_l and N_m, what we have to solve two coupled equation systems. Let us mention that, as this may be a heavy calculation, the so-called "escape factor" approximation has been developed to reduce the coupled systems to a single one [28–30]. The principle of this approximation consists in replacing the Einstein coefficient of spontaneous emission by a "corrected" coefficient, which includes a roughly estimated absorption term. To illustrate the method let us consider simply the radiative transitions from the m to the l level. We can write

$$\frac{dN_l}{dt} = N_m A_{m\,l} - \frac{4\pi}{c} I\left(\nu_{m\,l}\right)\left(N_l B_{lm} + N_m B_{m\,l}\right) \tag{1.48}$$

By using the relations between $A_{m\,l}$, B_{lm}, and $B_{m\,l}$ derived from equations (1.14), (1.15), and (1.16) this equation takes the form

$$\frac{dN_l}{dt} = N_m A_{m\,l}\left(1 - \frac{c^2}{2h\nu^3}\left(1 - \frac{g_m}{g_l}\frac{N_l}{N_m}\right) I\left(\nu_{lm}\right)\right) \tag{1.49}$$

and can be written

$$\frac{dN_l}{dt} = N_m A_{m\,l} G_{m\,l} \tag{1.50}$$

the escape factor being defined as

$$G_{m\,l} = \left(1 - \frac{c^2}{2h\nu^3}\left(1 - \frac{g_m}{g_l}\frac{N_l}{N_m}\right) I\left(\nu_{lm}\right)\right) \tag{1.51}$$

The presence of the unknown quantity $I\left(\nu_{lm}\right)$ as a parameter in this expression shows that the escape factor value can by no means be reached by "ab initio" calculations. One has to turn to the macroscopic source characteristics, as well as to experimental observations, to obtain a relevant estimation of the escape factor.

1.6 Source Brightness and Number of Photons per Mode

Let $\overline{I(\nu)}$ be the mean value, over the frequency interval $\Delta\nu$ of intensities supplied by integrating the radiation transfer equation (1.1). The quantity $\overline{I(\nu)}\Delta\nu$ is the power radiated per surface unit, within solid angle unit, say a number of watts/m^2/steradian. This quantity may be reached in spectroscopy experiments, $\Delta\nu$ being then an experimental band width. It is necessary to know the quantum efficiency of the detector and the reflection coefficient of the optics.

As for $I(\nu)$, it thus has a dimension of the form Joule/m^2/steradian, though a number of watts per surface unit emitted by a laser is often called the intensity of this laser. Experimentalists, who cannot make use of the restricted-to-visible-light photometric MKSA units, often characterize the emerging radiation in terms of source brightness $B(\nu)$, namely the power, $P(\nu)$, radiated per surface unit, per solid angle unit, per frequency interval unit, or, in MKSA units, watt/m^2/sr/Hz:

$$B\left(\nu\right) = \frac{P\left(\nu\right)_{\text{watts}}}{\Delta S_{\text{m}^2} \Delta \Omega_{\text{sr}} \Delta \nu_{\text{Hz}}} \tag{1.52}$$

One immediately sees that, from the dimensional point of view, the intensity $I\left(\nu\right)$ used in the transfer equations (1.2) and (1.4) and the brightness $B\left(\nu\right)$ are identical.

It is worth concluding about the general properties of radiation transfer, by showing the relationship between brightness and another quantity, the number of photons per mode, which introduces a pinch of coherent optics into radiation intensity definitions. At this point, the word "mode" should not be understood here as referring to a strict field-mode definition, which would require, for instance, a definite complete set of modes. We only consider the elementary physical cells within which it makes sense to speak of coherent radiation.

To this end, Figure 1.10 exemplifies three relevant coherence parameters, δs, $\delta\theta$, and δt, for Young's interference experiment in Figure 1.10a, and similarly for near-field diffraction by a screen edge crossing the beam in Figure 1.10b. Within the incident quasi-monochromatic beam of wavelength λ, we consider two paths separated from each other by a small angle $\delta\theta$, and starting from two source points separated by a small interval δs. After diffraction, the paths intersect at point P. The distances traveled from the source to point P differ by a small interval δL, corresponding to a time interval $\delta t = \delta L/c$. A fourth parameter, the spectral band-width $\delta\nu$, yields a phase mismatch at point P between radiations of frequency ν and $\nu \mp \delta\nu$. The values of δs, $\delta\theta$, δt, and $\delta\nu$, determine the occurrence of Young's fringes, in Figure 1.10a, as well as Fresnel's fringes, in Figure 1.10b. Experiments show that the space condition

$$\delta s \delta\theta \lesssim \lambda \tag{1.53}$$

and the time condition

$$\delta\nu \delta t \lesssim 1 \tag{1.54}$$

must be fulfilled for fringes to appear near P.

Let $\delta S \simeq (\delta s)^2$ and $\delta\Omega \simeq (\delta\theta)^2$ be respectively the area of the source and the solid angle of the beam. By squaring equation (1.53), the spatial coherence condition reads

$$\delta S \delta\Omega \lesssim \lambda^2 \tag{1.55}$$

In other words the radiation field is coherent within the limits fixed by values of δS, $\delta\Omega$, δt, and $\delta\nu$ such that the previous criteria are satisfied. Let us

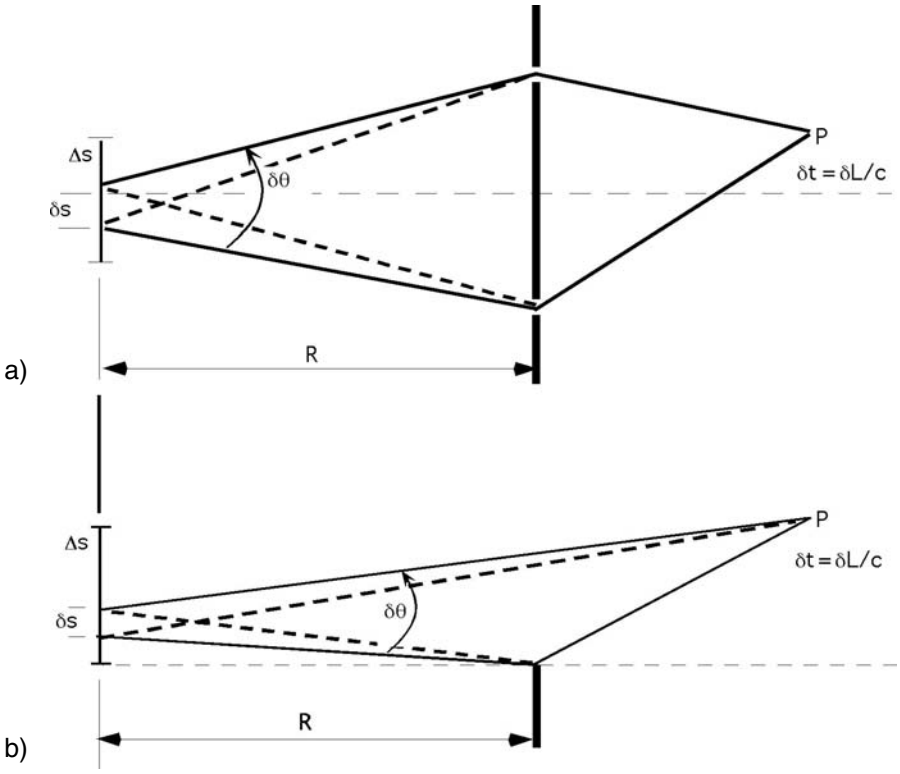

Fig. 1.10. Young slit (a) and Fresnel's diffraction experiment (b).

assume the surface of the real incoherent source to be $\Delta S \geqq \delta S$ and the source divergence, $\Delta\Omega \geqq \delta\Omega$. From equation (1.55), the quantity $\Delta S \Delta\Omega$ can be divided in $\Delta S \Delta\Omega/\lambda^2$ elementary spatial cells able to supply spatially coherent radiation (see [12] p. 150 *et seq*). In the same way, the emission of total duration $\Delta t \geqq \delta t$ and band-width $\Delta\nu \geqq \delta\nu$ can be divided in $\Delta t \Delta\nu$ elementary temporal steps during which radiation remains temporally coherent. In view of interference experiments making use of incoherent sources, the question arises of how many photons are available in each of these elementary configurations, that we are calling "modes." From relations (1.54) and (1.55) the total number of spatio-temporal modes is

$$N_{\text{modes}} = \frac{\Delta S \Delta\Omega}{\lambda^2} \Delta\nu \Delta t \tag{1.56}$$

Let us now consider the total energy, E, emitted by the source during the time interval Δt. The mean number of photons per mode is merely

$$N_{\text{ph/mode}} = \frac{E}{h\nu} \frac{\lambda^2}{\Delta S \Delta\Omega \Delta\nu \Delta t} \tag{1.57}$$

By comparing the above equation with equation (1.52) we see that

$$N_{\mathrm{ph/modes}} = \frac{c^2}{h\nu^3} B(\nu) \tag{1.58}$$

Let us remark that this equation can be rewritten in terms of atomic spontaneous emission and absorption coefficient since, for a spectral line emitted between levels 2 and 1, substituting equations (1.14) and (1.15) in equation (1.58) leads to

$$N_{\mathrm{ph/modes}} = \frac{8\pi}{c} \frac{g_1}{g_2} \frac{B_{12}}{A_{21}} B(\nu) \tag{1.59}$$

These expressions show the narrow relationship existing between the brightness, $B(\nu)$, of an incoherent source and the coherent radiation that this source is capable of supplying an interferometric experiment.

Applied to usual isotropic sources, equation (1.58) shows the number of photons per mode to be generally less than one. For instance an isotropic XUV source of 10^{-6} m^2 emissive surface and 1000 W power, within 0.1 nm bandwidth in the 10 nm wavelength region, yields about 10^{-3} photons per mode. However, contemporary synchrotrons, though by no means being coherent sources, yield up to 10^{6-7} XUV photons per mode [10]. In this case the intense, narrowly focused electron beam, as well as the strong emission directivity along the tangent to the electron orbit raises the radiation brightness to a very large value. Interference experiments applied to XUV refraction index measurements have thus been successfully performed by using synchrotron radiation [31]. Time-resolved interferential investigation of fast physical processes need a still larger number of photons per mode, which requires sources of larger coherence, such as XUV lasers and high harmonics generated from infrared or visible lasers.

2. XUV Optics

Before presenting an overview of coherent XUV sources, we must remember the peculiarities that made it difficult, in the past, to extend the visible and UV optical know-how to XUV wavelengths. As we briefly stated at the very outset of these introductory chapters, XUV optical properties of condensed matter are to absorb most of the radiation along less than $\sim$1 μm length and to offer an extremely poor reflectance, viz. $\lesssim 10^{-4}$, at near normal incidence. Below we will recall the basis of the optical constant theory and its application to the XUV radiation. Thanks to the many investigations carried out with the help of synchrotron radiation, the development of multilayered optical components, which will be described a little further, considerably reduces the effect of the discouraging characteristics of XUV radiation.

2.1 XUV Optical Constants

The global response of matter to the penetration of an electromagnetic field is summarized in its complex refractive index. From this index, refraction and reflection at the interfaces, as well as absorption within the medium, can be calculated. Many books explain how the refractive index can be deduced from the scattering of radiation by molecules, atoms, and electrons (see for instance [32–35]). As regards XUV radiation, a clear presentation of the subject can be found in Chapters 2 and 3 of [11]. Here we shall just introduce the prominent features of the XUV optical properties of matter, without detailed calculation.

The refractive index n of a material is usually defined as the square root of the dielectric constant, ϵ, i.e.,

$$n = \sqrt{\epsilon} \tag{2.1}$$

In the range of XUV frequencies, oscillations of bound electrons in the attractive field of atomic nuclei provide the main contribution to the dielectric constant of solid and gaseous materials. In hot dense plasmas this part is played

by free-electron collective oscillations, due to the density-dependent restoring force which follows from electron density disturbances. In both cases the nuclei are too slow to significantly contribute to the material response. According to the semiclassical model, the equation of motion for bound electrons of resonance frequency ω_k may be written as

$$m\frac{d^2x}{dt^2} + m\gamma_k\frac{dx}{dt} + m\omega_k^2 x = -eE \tag{2.2}$$

where $E = E_0 e^{-i\omega t}$ is the oscillating electric field of the propagating electromagnetic wave, m is the electron mass, and γ_k a damping factor. Solving this equation shows that electrons oscillate with the same frequency as the incident electric field but with a frequency-dependent amplitude, x_k, given by

$$x_k = \frac{e}{m}\frac{E}{\omega^2 - \omega_k^2 + i\gamma_k\omega} \tag{2.3}$$

Let g_k be the occupation number of the kth atomic shell and n_A the atom density number. The polarization of the medium, $P = n_\mathrm{A} e \sum_k x_k$, is then:

$$P = E\frac{e^2 n_\mathrm{A}}{m}\sum_k \frac{g_k}{\omega^2 - \omega_k^2 + i\gamma_k\omega} \tag{2.4}$$

and the dielectric constant, $\epsilon = 1 - P/E\epsilon_0$, reads

$$\epsilon = 1 - \frac{e^2 n_\mathrm{A}}{m\epsilon_0}\sum_k \frac{g_k}{\omega^2 - \omega_k^2 + i\gamma_k\omega} \tag{2.5}$$

It may be easily verified that, at XUV frequencies, the second term of equation (2.5) is much less than unity. Hence the complex refractive index, $n = \sqrt{\epsilon}$, takes the form

$$n(\omega) = 1 - \frac{1}{2}\frac{e^2 n_\mathrm{A}}{m\epsilon_0}\sum_k \frac{g_k}{\omega^2 - \omega_k^2 + i\gamma_k\omega} \tag{2.6}$$

Separation of $n(\omega)$ into real and imaginary parts (Chap. IX in [33]) leads to equation

$$n(\omega) = 1 - \delta + i\beta \tag{2.7}$$

with

$$\delta = \frac{1}{2}\frac{e^2 n_\mathrm{A}}{m\epsilon_0}\sum_k \frac{g_k\left(\omega^2 - \omega_k^2\right)}{\left(\omega^2 - \omega_k^2\right)^2 + \gamma_k^2\omega^2} \tag{2.8}$$

and

$$\beta = -\frac{1}{2}\frac{e^2 n_\mathrm{A}}{m\epsilon_0}\sum_k \frac{g_k\gamma_k\omega}{\left(\omega^2 - \omega_k^2\right)^2 + \gamma_k^2\omega^2} \tag{2.9}$$

The behavior of β and δ near resonances is as shown in Figure 2.1 Moreover Figure 2.2 displays the example of silica for photon energy comprised

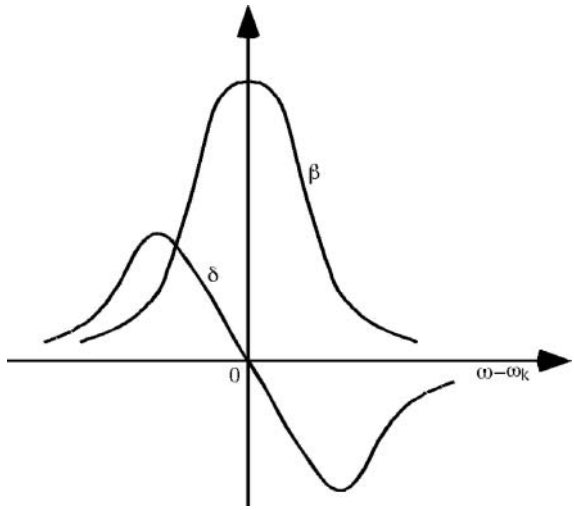

Fig. 2.1. Variation of the real and imaginary parts of the refractive index, $n = 1 - \delta - i\beta$, near a resonance frequence ω_k.

between 30 eV and 1000 eV. The jumps near 100 eV and 550 eV correspond to the 1s resonance of oxygen and to the 2p resonance of silicon, respectively.

Equation (2.6) can also be derived from atomic scattering theory in a way that gives a deeper understanding of the role of atomic properties in XUV wave propagation. A detailed presentation of this approach is out of our scope. However, a highly acknowledged tabulation of atomic scattering factors has been published by Henke, Gullikson, and Davis for all elements

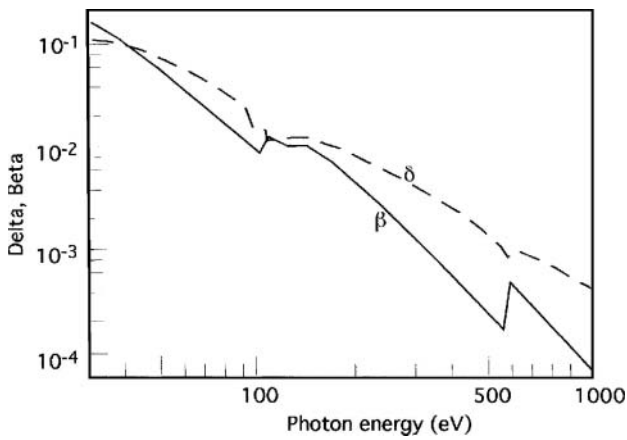

Fig. 2.2. Variation of the real (δ) and imaginary (β) parts of the refractive index of silica in a wide XUV energy range (data from Ref. [35]).

in an extended range of XUV wavelengths [36]. To make these tables easy to use let us recall that the complex scattering factor of interest for XUV propagation, $f = f_1 + if_2$, can be written as

$$f = \sum_k \frac{g_k \omega^2}{\omega^2 - \omega_k^2 + i\gamma_k \omega} \tag{2.10}$$

where the g_k's are now the quantum mechanical oscillator strength, whereas, in the semiclassical model, they were integers such that $\sum_k g_k$ equaled the total number of bound electrons surrounding the nucleus. Equation (2.6) can be thus rewritten:

$$n(\omega) = 1 - \frac{1}{2\omega^2} \frac{e^2 n_\mathrm{A}}{m\epsilon_0} (f_1(\omega) + if_2(\omega)) \tag{2.11}$$

Substituting the value of the classical electron radius, $r_\mathrm{e} = e^2/4\pi m\epsilon_0 c^2$, and $\lambda = 2\pi c/\omega$ in this expression yields

$$n(\omega) = 1 - \frac{1}{2\pi} r_\mathrm{e} n_\mathrm{A} \lambda^2 (f_1(\omega) + if_2(\omega)) \tag{2.12}$$

and we see that the previously defined δ and β real numbers are given by

$$\delta = \frac{1}{2\pi} r_\mathrm{e} n_\mathrm{A} \lambda^2 f_1(\omega) \tag{2.13}$$

and

$$\beta = \frac{1}{2\pi} r_\mathrm{e} n_\mathrm{A} \lambda^2 f_2(\omega) \tag{2.14}$$

Let us now briefly consider the case of hot plasmas which, as we already know, play an important part in XUV radiation sources. Hot plasmas consist of multicharged ions and free electrons that have been ejected from neutral atoms by strong thermal agitation. Plasmas are globally neutral though each particle is submitted to the microfield of neighboring particles. If all atoms are fully ionized, there are no more bound electrons effecting oscillations near resonance frequencies. However, any local disturbance of the free electron gas induces a local change of the mean electron density and the occurrence of a restoring force which increases with the electron density. The propagation of this density disturbance results in longitudinal plasma waves of frequency:

$$\omega_\mathrm{p} = \left(\frac{e^2 n_\mathrm{e}}{m\epsilon_0} \right)^{1/2} \tag{2.15}$$

or

$$\omega_\mathrm{p} = 5.65 \times 10^4 n_\mathrm{e}^{1/2}$$

where n_e is in cm^{-3} unit.

Dispersion of transverse electromagnetic waves occurs according to the relation

$$\omega^2 = \omega_\mathrm{p}^2 + k^2 c^2 \tag{2.16}$$

where ω is the frequency and $\overrightarrow{k}$ is the wave vector such that $|k| = 2\pi/\lambda$. The dispersion relation (2.16) has real solutions only for waves of frequency $\omega > \omega_{\mathrm{p}}$, which then have the phase velocity

$$v_{\Phi} = \omega/k \tag{2.17}$$

Therefore electromagnetic waves of frequency less than ω_{p} cannot propagate. Using the familiar refractive index definition, $n = c/v_{\Phi}$, with relations (2.17) and (2.15) leads to the following expression of plasma refractive index:

$$n = \left(1 - \frac{\omega_{\mathrm{p}}^2}{\omega^2}\right)^{1/2} \tag{2.18}$$

In nonhomogeneous plasmas, equation (2.15) shows ω_{p} to vary as the electron density square root. When electromagnetic radiation of frequency ω reaches a plasma density layer such that $\omega_{\mathrm{p}} = \omega$, the radiation is reflected away, toward less dense regions. From equation (2.15) one obtains this limiting density

$$n_{\mathrm{c}} = \frac{m\epsilon_0\omega^2}{e^2} \tag{2.19}$$

where n_{c} is called the critical density for the radiation of frequency ω, or

$$n_{\mathrm{c}} = 1.1 \times 10^{21}\lambda^{-2} \ (n_{\mathrm{c}} \text{ in cm}^{-3} \ \text{ for } \lambda \text{ in } \mu\text{m}) \tag{2.20}$$

More generally, the spatial variations of refractive index give rise to light path curvature. Figure 2.3 illustrates this fact by showing the qualitative

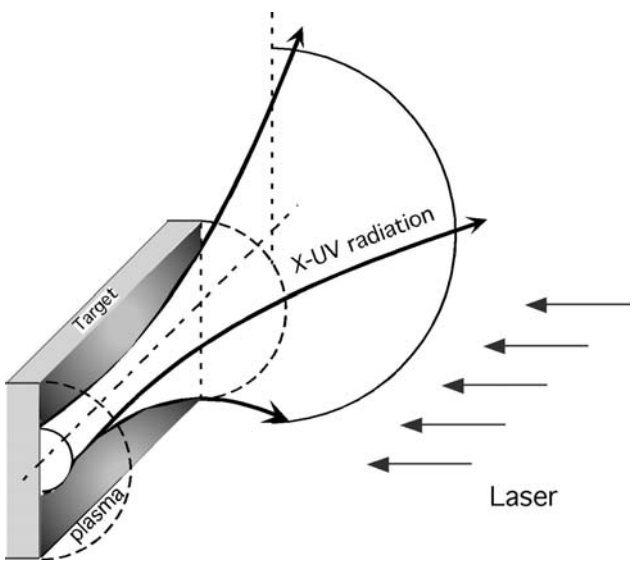

Fig. 2.3. XUV radiation path curvature due to density gradients between target and vacuum within a cylindrical plasma.

features of XUV radiation pencils in an elongated plasma produced by a laser impact onto a solid plane target. Let $\overrightarrow{\Delta n}$ be the gradient of the plasma refractive index and $\vec{N}$ the unit vector normal to a given trajectory. The light path curvature radius of the trajectory to this point is given by [34]

$$\frac{1}{R} = \vec{N} \cdot \frac{\overrightarrow{\Delta n}}{n} \tag{2.21}$$

If we also assume that $\overrightarrow{\Delta n}$ is normal to the trajectory tangent, equation (2.21) shows that $|R|$, the absolute value of R, is given by

$$\frac{1}{|R|} = \frac{1}{n}\frac{dn}{dx} \tag{2.22}$$

where x is the space coordinate in the $\overrightarrow{\Delta n}$ direction. From equations (2.15), (2.18), and (2.19) one may now give the refractive index the new form:

$$n = \sqrt{1 - \frac{n_\mathrm{e}}{n_\mathrm{c}}} \tag{2.23}$$

Hence, assuming that $n_\mathrm{e} \ll n_\mathrm{c}$, we readily obtain

$$\frac{1}{|R|} = \frac{1}{2n_\mathrm{c}}\frac{dn_\mathrm{e}}{dx} \tag{2.24}$$

By substituting the classical electron radius $r_\mathrm{e} = e^2/4\pi m\varepsilon_0 c^2$ and $\lambda = 2\pi c/\omega$ in equation (2.19), equation (2.24) becomes

$$\frac{1}{|R|} = \frac{r_\mathrm{e}\lambda^2}{2\pi}\frac{dn_\mathrm{e}}{dx} \tag{2.25}$$

If we call δx the distance along which n_e decreases by a factor of 10, so that $\delta n_\mathrm{e} \simeq 0.9 n_\mathrm{e}$, relation (2.25) gives

$$|R| \simeq \frac{6.98}{r_\mathrm{e}}\frac{\delta x}{n_\mathrm{e}\lambda^2} \tag{2.26}$$

or

$$|R|_\mathrm{cm} \simeq 2.5 \times 10^{23}\frac{\delta x_{(\mu\mathrm{m})}}{n_{\mathrm{e}(\mathrm{cm}^{-3})}\lambda^2_{(\mathrm{nm})}} \tag{2.27}$$

If we consider for instance an XUV amplifying plasma with $n_\mathrm{e} = 5 \times 10^{20}$ cm^{-3}, $\delta x = 50$ μm, $\lambda = 15$ nm, the curvature radius is ∼111 cm, which leads to a divergence angle of about 9 mrad after a 1 cm long path in plasma.

2.2 Absorption, Reflection, and Refraction of XUV Radiation

For the sake of simplicity let us consider a plane wave described by relation

$$E = E_0 e^{-i(\omega t - kr)} \tag{2.28}$$

where $\omega = 2\pi\nu = 2\pi/T$ and $k = 2\pi/\lambda$, with ν and λ being, respectively, the frequency and the wavelength of radiation. For practical applications, let us recall that wavelength and frequency satisfy the numerical relation

$$\lambda\,(\mathrm{nm}) \times h\nu\,(\mathrm{eV}) = 1239.9 \tag{2.29}$$

In a medium of refractive index $n\,(\omega)$ the phase velocity dispersion of the wave reads

$$v_\phi = \frac{c}{n\,(\omega)} = \frac{\omega}{k} \tag{2.30}$$

Introducing $n\,(\omega)$ given by equation (2.7) in this equation gives

$$k = \frac{\omega}{c}\,(1 - \delta + i\beta) \tag{2.31}$$

We can then rewrite equation (2.28) in the form

$$E = E_0 e^{-(2\pi\beta/\lambda)r} \mathrm{e}^{-i[\omega(t-r/c)+(2\pi\delta/\lambda)r]} \tag{2.32}$$

which shows the refraction index imaginary part, β, to introduce wave amplitude attenuation, when the real part, δ, introduces a phase shift in wave propagation. By squaring the field amplitude (2.32) we obtain the intensity drop

$$I = I_0 e^{-(4\pi\beta/\lambda)r} \tag{2.33}$$

which shows that the usual linear absorption coefficient of the medium, μ_l,may be deduced from β by the relation

$$\mu_\mathrm{l} = \frac{4\pi\beta}{\lambda} \tag{2.34}$$

To illustrate the role of this formula, let us go back to Figure 2.2 which displays the β values of silica. For a photon energy of about 100 eV, viz. $\sim$12 nm wavelength, we see that $\beta \simeq 10^{-2}$. From equation (2.34) radiation intensity is attenuated by factor $1/e$ for a covered distance $1/\mu_\mathrm{l} \simeq 95$ nm, that is to say about 8 wavelengths.

The general properties of XUV reflection are determined by the fact that the refractive index of materials, n, is very close to but slightly less than unity. The small difference between n and 1 makes the reflectance at interfaces between vacuum and materials very small too.

At the same time, as illustrated by the sketches of Figure 2.4, the fact that this difference is negative turns the refracted beam upwards, to separation surface, instead of turning it downwards, to the normal to the separation surface, as usual in visible optics. The consequence is that an XUV beam flowing in vacuum may undergo total reflection at the vacuum-to-matter interface. In other words, total reflection is an "external" process in XUV region, whereas it is an "internal" process elsewhere. However, it requires a large incidence angle onto the surface, as we will see below. This is why XUV experimentation originated a special kind of optical devices that makes use of grazing incidence on reflecting surfaces. It is an important fact that the considerable advance

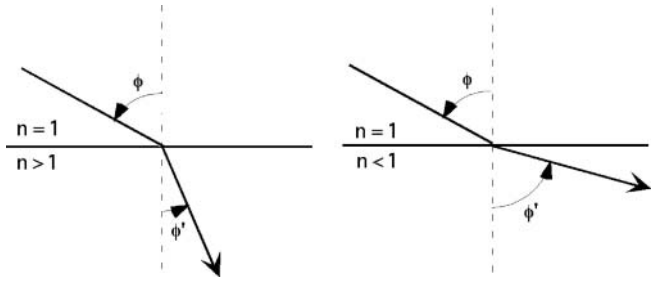

Fig. 2.4. Refraction at interface between vacuum ($n = 1$) and material ($n > 1$ or < 1). For XUV radiation $n < 1$ implies $\Phi' > \phi$. Thus total reflection occurs from vacuum to material, contrary to reflection of visible light.

in the art of making interferential mirrors, including normal incidence mirrors, results from progress in the knowledge of XUV optical constants, made these last two decades. This has indeed changed the prospect for using XUV radiation in science and technology.

The reflectance for perpendicular and parallel polarizations, given by Fresnel's formula, and written here in terms of the glancing angles, $\theta = \pi/2 - \phi$ and $\theta' = \pi/2 - \phi'$ (see Fig. 2.5), instead of the incidence and reflection angles ϕ and ϕ', are

$$R_{\mathrm{s}} = \left(\frac{\sin\theta - n\sin\theta'}{\sin\theta + n\sin\theta'} \right)^2 \tag{2.35}$$

and

$$R_{\mathrm{p}} = \left(\frac{n\sin\theta - \sin\theta'}{n\sin\theta + \sin\theta'} \right)^2 \tag{2.36}$$

with

$$\cos\theta = n\cos\theta' \tag{2.37}$$

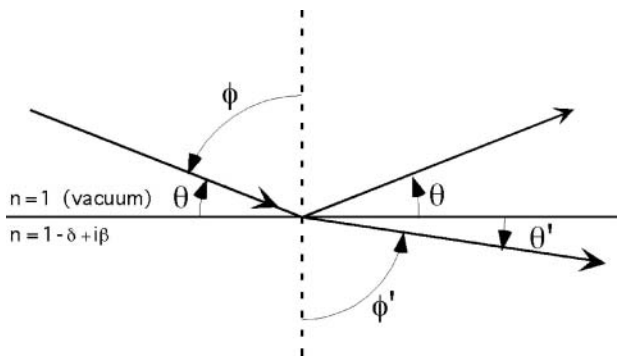

Fig. 2.5. Glancing incidence angle (θ) and glancing refraction angle (θ').

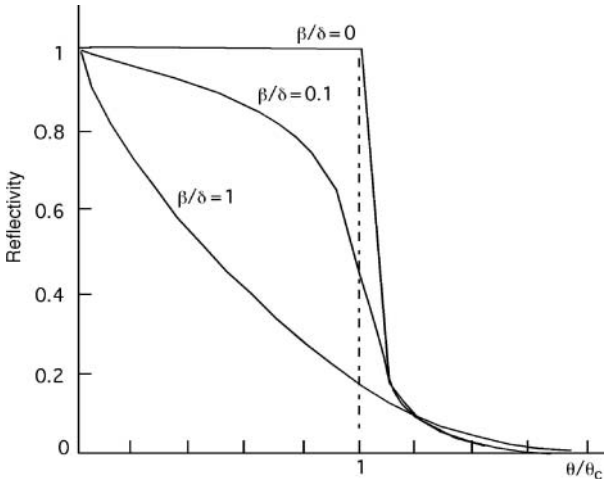

Fig. 2.6. Reflectivity versus glancing incidence angle for various values of β/δ (data from Ref. [35]).

As usual, R_s denotes the reflectance for an electric field vector perpendicular to the incidence plane, R_p denoting the same coefficient for fields vector parallel to the incidence plane.

External total reflection occurs when

$$\theta' = 0 \tag{2.38}$$

that is to say, from equations (2.37) and (2.7)

$$\cos\theta = 1 - \delta \tag{2.39}$$

where we temporarily assumed $\beta = 0$, as in a fully transparent medium. For small δ's, the glancing angle at which total reflection will start, i.e. the "critical" angle denoted by θ_c, will be

$$\theta_\mathrm{c} = \sqrt{2\delta} \tag{2.40}$$

Figure 2.6 shows reflectivity versus glancing angle following Parrat's calculation [37], for four values of β/δ. The upper dashed curve corresponds to $\beta = 0$, for which total reflection is achieved for all θ's $\leqq \theta_\mathrm{c}$. One sees that for a lossy medium, viz. $\beta \neq 0$, reflectance also strongly increases for small θ's, but does not completely reach total reflection.

Detailed study of refracted wave propagation for $\theta < \theta_\mathrm{c}$ in lossy media has been performed by Attwood [11] (Chapter 3). This study leads to equations giving the radiation penetration depth, z, into the lossy medium under conditions which would yield total reflection in a transparent medium. In particular

$$z_0 \simeq \frac{\lambda}{2\sqrt{2}}\pi\delta^{1/2} \quad (\theta \ll \theta_\mathrm{c}) \tag{2.41}$$

Table 2.1. Penetration depth Z of 12.4 nm wavelength radiation in silica and gold for normal, critical, and strongly subcritical incidence

	SiO^2 ($\theta_c \simeq 10°$)		Au ($\theta_c \simeq 23°$)	
θ	z/λ	z	z/λ	z
$\pi/2$	8.84	109 nm	2.65	32.9 nm
θ_c	1.68	20.8 nm	0.92	11.4 nm
$\ll\theta_c$	0.13	1.6 nm	0.31	3.8 nm

and

$$z_c \simeq \frac{\lambda}{2\pi\beta^{1/2}} \quad (\theta = \theta_c) \tag{2.42}$$

Moreover, the time-averaged power per unit area crossing the interface is found proportional to the small angle, ϑ', of the refracted wave with the interface, which is given by

$$\vartheta'^2 = \frac{\sqrt{(\theta^2 - 2\delta)^2 + 4\beta^2} + (\theta^2 - 2\delta)}{2} \tag{2.43}$$

These relations are of importance, not only for a full understanding of XUV reflection properties, but also for estimating the possible damages which may be caused to optical interfaces by intense XUV sources.

To illustrate the scale of wave penetration under various conditions, Table 2.1 allows us to compare the penetration depths obtained for photons of 100 eV energy ($\lambda = 12.4$ nm) in silica ($\delta = 0.014$, $\beta = 0.009$) and in gold ($\delta = 0.08$, $\beta = 0.03$) by using equations (2.34) (normal incidence), (2.42) (critical incidence), and (2.41) (extreme grazing incidence).

This comparison between silica and gold, chosen for the well-separated positions of their components in the periodic table, as well as for their practical importance in XUV optics, may be extended to their reflectivities. Figures 2.7 and 2.8 display the spectral reflection curves from 30 eV to 600 eV, for $\theta = 5°$ ($< \theta_c$) in Figure 2.7 and for $\theta = \theta_c$ in Figure 2.8. These curves are a good illustration of the behavior of XUV reflectivity discussed in the previous paragraph. In particular, in both cases one sees the reflectivity cutoff near 100 eV at the critical angle $\sim 10°$ for silica and $\backsim 23°$ for Au.

It is easy to see, from equations (2.36) and (2.35), that grazing incidence reflection hardly polarizes XUV radiation. As a matter of fact, when θ' cancels, both R_s and R_p tend to unity. Besides, seeing that normal reflection is extremely weak, it may seem unreal to discuss polarization in this case. Let us mention that calculation shows R_p/R_s also tend toward unity, when $\theta \to \pi/2$. One can then ask what about Brewster's angle? The maximum polarization degree is reached when $R_p = 0$, viz. from equation (2.36)

$$\sin\theta' = n \sin\theta \tag{2.44}$$

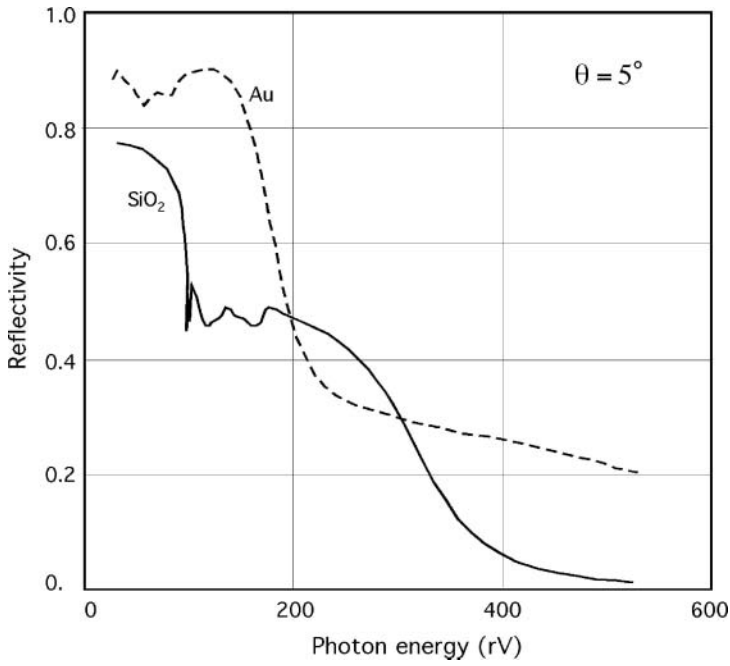

Fig. 2.7. Reflectivity of silica and gold versus photon energy for the same glancing angle smaller, in both cases, than the critical angle [35].

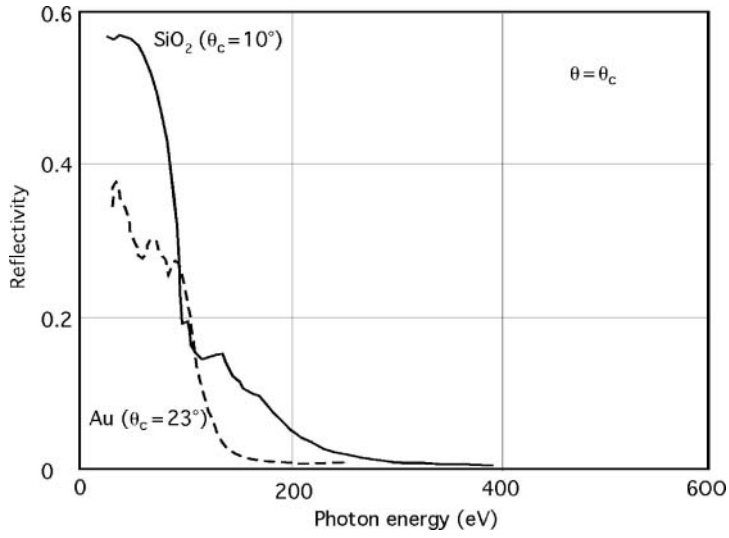

Fig. 2.8. Reflectivity of silica and gold versus photon energy for the critical incidence angle of each material [35].

By combining this relation with equation (2.37) we obtain the new equation

$$n^2 \sin^2\theta + \frac{1}{n^2}\cos^2\theta = 1 \tag{2.45}$$

which leads to

$$\sin^2\theta = \frac{1}{1+n^2} \tag{2.46}$$

Since the refractive index, n, is close to 1, Brewster's angle is approximately given by

$$\sin\theta_{\mathrm{B}} \simeq \frac{1}{\sqrt{2}} \tag{2.47}$$

viz.

$$\theta_{\mathrm{B}} \simeq 45^\circ \tag{2.48}$$

As shown previously, the 45°-incidence reflectance at a single interface is much too small to be useful to build polarizers. But due to the fact that the magnitude of θ_{B} does not depend much on the nature of the material, multilayer mirrors can provide high linear polarization of intense beams reflected near 45°-incidence.

2.3 Grazing Incidence Optics

For a long time, reflection under grazing incidence had been the only way to drive radiation propagation in XUV experimental devices. The advent of interferential multilayer mirrors deeply changed the capability—as well as the design—of XUV optical components. However, grazing incidence techniques retain an important part in contemporary experiments, especially as a large band width can be investigated with one and the same device, whereas multilayer reflectors are narrow-band systems. In fact both types of components are used together in many sophisticated arrangements of today.

Grazing incidence reflection onto plane mirrors does not present any peculiarity except that the size of the mirror in the incidence direction has to be increased by factor $\sim 1/\sin\theta$, as compared to normal reflection with identical cross-section. Near 10 nm wavelengths the glancing angle can be about 5°, which leads to a lengthening factor about 10. At shorter wavelengths, with glancing angles of 1° or less, the lengthening factor becomes larger than 50, which may lead to technical issues. Moreover mirror's polishing must be of especially high quality in order to reduce XUV radiation scattering on the surface ruggedness.

The peculiarity of grazing incidence optics mainly lies in the exceptionally strong astigmatism of spherical reflectors. This is schematically illustrated in Figure 2.9, which represents a spherical mirror M of curvature center C, with the incident light coming from the source point A, under the glancing angle θ. As is well known, the beam will not converge toward some well-defined image

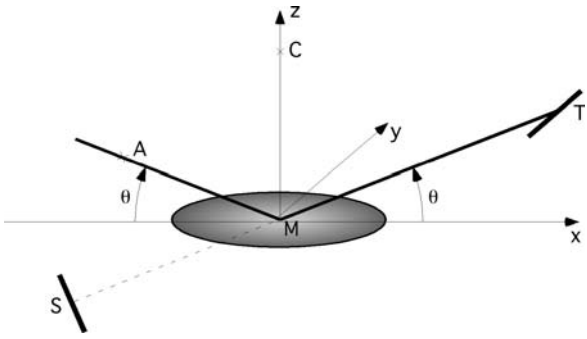

Fig. 2.9. Grazing incidence astigmatism of concave mirror; the reflected beam is supported by two small straight lines, one of them, S, being generally virtual as shown in the figure.

point after reflection, but it rests on two "astigmatism focal lines," S, in the incidence plane, and T perpendicular to this plane. Let us choose the origin of the distances at the mirror center, M, and call S (resp. T) the point of intersection of the focal line S (resp. T) and the central reflected ray. The positive direction being the direction of light, the positions of S and T are calculated from the next expressions respectively:

$$\frac{1}{MS} = \frac{1}{MA} + \frac{2\sin\theta}{R} \tag{2.49}$$

$$\frac{1}{MT} = \frac{1}{MA} + \frac{2}{R\sin\theta} \tag{2.50}$$

where R is the radius of the mirror. The conditions for the focal lines to be real, namely to lie in the image space, are obviously $MS > 0$ and $MT > 0$. From equations (2.49) and (2.50) one can see that S is real if

$$|MA| > \frac{R}{2\sin\theta} \tag{2.51}$$

and T is real if

$$|MA| > \frac{R\sin\theta}{2} \tag{2.52}$$

Since θ is a small angle, the first of these two conditions is fulfilled only for remote sources. Therefore, for grazing incidence experimental arrangements, one generally gets to use the tangential focal line T to yield radiation concentration into a "focal" spot.

To achieve better focalization, one may replace the spherical mirror by a toroidal one, so as to adjust MS and MT by using two different curvature radii in equations (2.49) and (2.50) [38]. One immediately see that the points S and T will merge when the ratio of radii takes the value $\sin^2\theta$. However, it is clear that this is practicable only if the glancing angle is not too small.

In many applications of XUV optics, it is found convenient that A, the point source, and its "image" T be symmetrical with respect to the normal

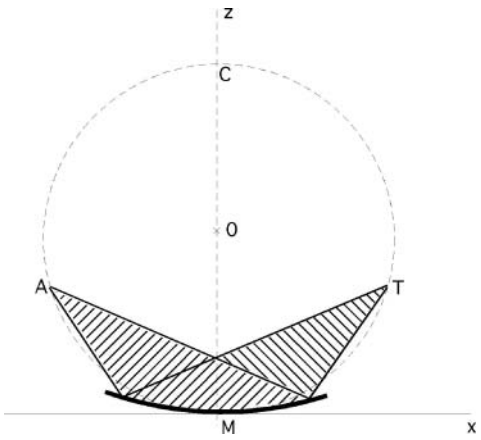

Fig. 2.10. Rowland circle of concave mirror; C is the curvature center of the mirror. The diameter of the Rowland circle equals the radius of the mirror.

to the mirror. If we substitute $MT = -MA$ in equation (2.50), we obtain $|MA| = R\sin\theta$. This means that the required symmetry does exist for a set of points A, which forms a circle of radius $R/2$, tangent at M to the mirror. This circle, represented in Figure 2.10, is known as the Rowland circle of the spherical mirror. Besides, as we all know, the image of a source located at the curvature center of a mirror (point C in Fig. 2.10) is perfectly stigmatic.

Something of this property holds for all the points of the Rowland circle, though the less so as the source moves away from the center C. Under grazing incidence, the Rowland circle remains the location of source points which minimizes optical aberrations. This property and the practical advantages of a simple geometry explains that the Rowland circle mountings have been largely used in XUV spectroscopic devices, before holographic diffraction gratings appeared with their completely new capabilities. A sketch of a grazing incidence Rowland spectrograph that makes use of a spherical grating under grazing incidence is shown in Figure 2.11. Spectral lines are focalized along the Rowland circle, the spectral dispersion being easily calculated from the familiar grating equation written here under the convenient form

$$\cos\theta - \cos\theta' = N\frac{\lambda}{a} \tag{2.53}$$

where N is the interference order, a the period of the grating, and λ the wavelength.

2.4 Multilayer Mirrors

In visible optics it is usual to use interferences produced within thin layers to increase reflectance or transmittance at the interface between two media. The

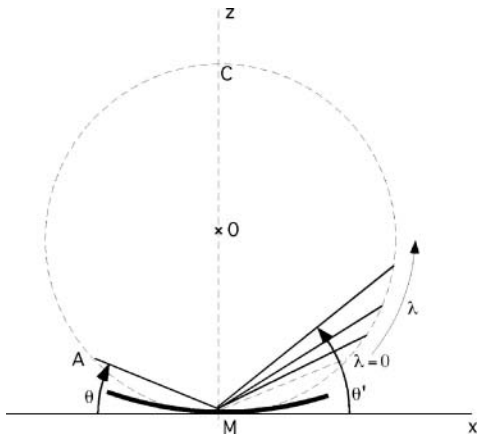

Fig. 2.11. Principle of grazing incidence Rowland spectrograph for XUV radiation.

first attempts to extend this method to far UV and XUV radiation, mainly in connection with the development of synchrotron radiation experiments, date from the seventies [39–42].

The principle of constructive interference achieved by coating a surface with a thin layer is illustrated in Figure 2.12. The thin layer 1, of thickness d, deposited on the substrate 2, causes two waves to be reflected from a single incident wave coming from vacuum 0. As the real part of the refractive index is very close to 1 for XUV wavelengths, refraction does not appear in the figure

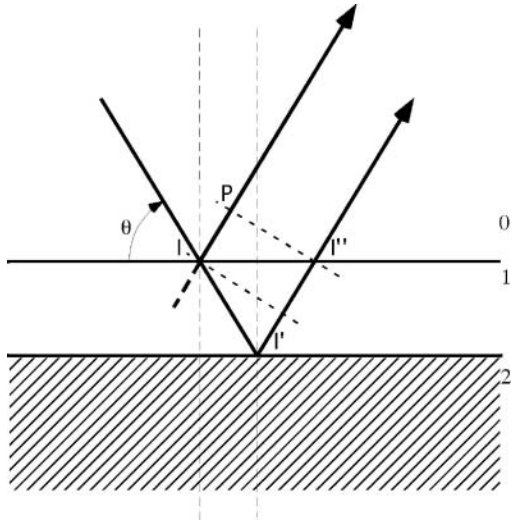

Fig. 2.12. Constructive interference obtained by coating a surface with a thin layer of thickness d.

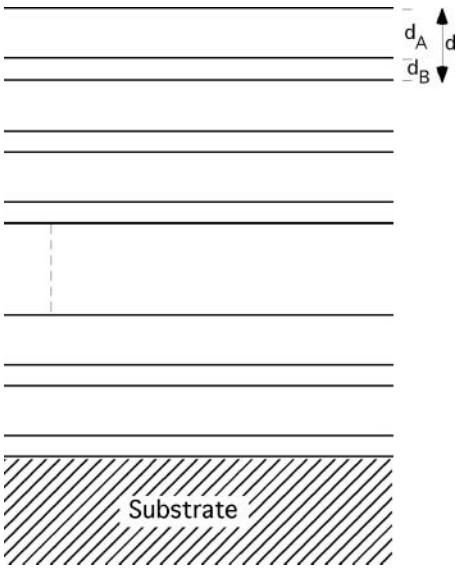

Fig. 2.13. Periodic thin layer structure where weakly and strongly absorbing layers, of thickness d_{A} and d_{B} respectively, succeed to each other.

at the 0–1 separation. Let us call I and I' the incidence points on each side of the thin layer. The path difference $II' + I'I'' - IP$ between the reflected waves is readily calculated to be $2d \sin\theta$. Moreover, we know that constructive interferences between the waves appear when the path difference is a multiple of the wavelength, λ, viz. when:

$$m\lambda \simeq 2d \sin\theta \tag{2.54}$$

with $m = 1, 2, 3, \ldots$ Therefore, at normal incidence and for $m = 1$, the maximum reflectance occurs for a layer thickness of $d = \lambda/2$.

However, owing to the very small amplitude reflected when $\theta > \theta_{\mathrm{c}}$ [see equation (2.40)], a single thin layer cannot provide a large XUV reflectance in near normal incidence. To improve the efficiency of constructive interferences, one turns to periodic thin layer structures, such as shown in Figure 2.13. At normal incidence, with $d \simeq \lambda/2$, the multilayer structure reflects as many interfering waves as the number of periods allows, thus considerably increasing the reflectance of the mirror. Each period consists of two films, one of small, the other of large, absorbing coefficient. Figure 2.13 represents the thin film stack, d_{A} (respectively, d_{B}) being the thickness of the weakly (respectively, strongly) absorbing material.

The way in which reflectivity depends on the number of periods is shown in Figure 2.14, for several values of d_{B}, from Spiller's data [39]. One sees the ratio $d_{\mathrm{B}}/d_{\mathrm{A}}$ to be an important parameter of multilayer efficiency (see also [41]). The larger the period number, the thinner the absorbing layers need to be. Otherwise the improvement of reflectivity is counterbalanced by the increase

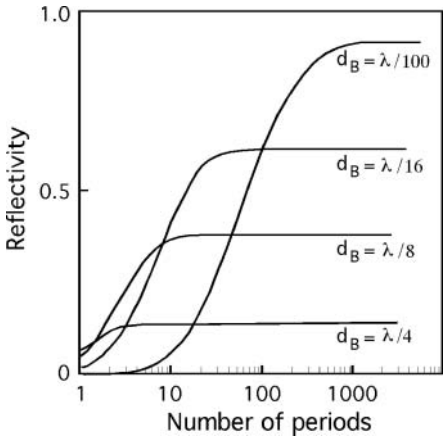

Fig. 2.14. Reflectivity as a function of the number of multilayer periods for various absorbing layer thicknesses (data from Spiller [36]).

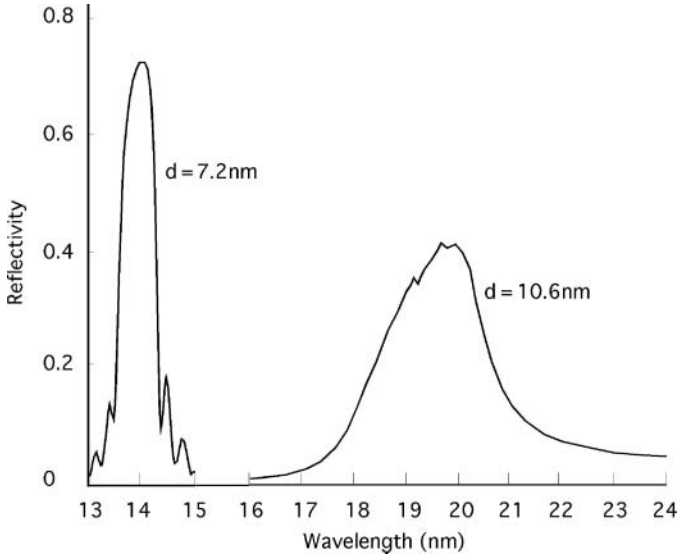

Fig. 2.15. Forty-period Si/Mo mirror reflectivity for two values of the period (data from Ref. [35]). It is worthy to observe that reflectivity is maximum at a wavelength close to twice the period d.

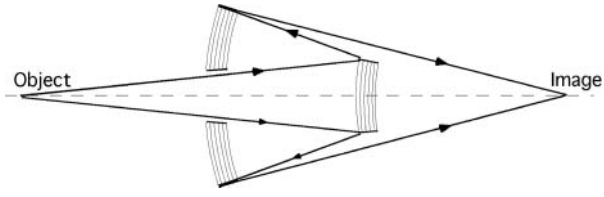

Fig. 2.16. Multilayer Schwartzschild objective used for XUV microscopy.

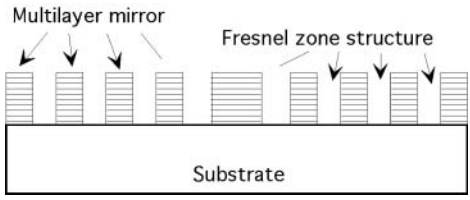

Fig. 2.17. Principle of a Bragg–Fresnel lens that combines the properties of multilayer structures with those of diffractive zone-plates.

of absorption. As a matter of fact one can observe in Figure 2.14 that, except for small period numbers, the lessening of d_B yields important reflectance enhancement. That is why multilayer mirrors are made in such a way that the area of each absorbing layer is occupied by one node of the standing waves. The remarkable efficiency obtained with the help of multilayer structures is illustrated in Figure 2.15, which shows the reflectivity expected from 40-period Si/Mo mirrors with $d = 7.2$ nm at $\lambda \simeq 14$ nm and $d = 10.6$ nm at $\lambda \simeq 20$ nm (data from [36]).

Many applications of XUV radiation resort to multilayer mirrors [43]. Filters, polarizers, microscopes, telescopes, XUV laser cavities are typical developments that were made possible thanks to them. As an example, Figure 2.16 displays the diagram of a Schwartzschild objective used for XUV microscopy [44]. Moreover, combination of multilayer mirror properties with diffractive zone-plate structures brought about further progress in XUV optics (see, e.g. [45]). As an illustration of this technique, Figure 2.17 schematically represents the cross-section of a Bragg–Fresnel lens that may be carved in a multilayer mirror either by masking selected zones of the substrate in the course of the coating process, or by etching the complementary portions of the mirror after multilayered deposition. Such three-dimensional optical components have proved to supply a large gain of resolution in imaging techniques.

3. Coherent XUV Radiation Beams

Coherence and incoherence are two opposite characterizations of the properties of propagating radiation. Propagation by itself introduces coherence in the radiation field since it implies spatio-temporal phase relations,which are at the very origin of field correlation from a point to another one. On the other hand, the very large number of independent microscopic emission sources and the lack of absolutely monochromatic emission cause coherence never to be complete. Nevertheless complete incoherence would mean field without propagation, which would be a nonsense generally speaking. As a matter of fact, it can be shown that the light field vanishes if the degree of coherence is assumed to cancel [46].

The radiation field is thus doomed to be like a sea where strong swash and regular rollers compete for shaking ships and seamen. However one knows how to form streams of coherent field into this choppy sea. This can be done simply by reducing the size of a noncorrelated emitters source surface, but much more efficiently by correlating emitters by the means of atomic stimulated emission or by laser collective excitation. Lasers generally comprise a resonant cavity that considerably increases the beam coherence but, for reasons which will be presented further, this has not been the case of XUV lasers so far. To help understanding the high degree of coherence nevertheless achieved with these lasers, it is worth briefly recalling the principles of radiation coherence. Furthermore we shall see another way open up to coherent XUV production, that is the generation of high harmonics of visible laser light (HHG).

3.1 Interferences and Degree of Coherence

The experimental evidence of correlation between fields at points separated in the space rests in the possibility of observing interferences between these fields. For instance, the well-known Young's slits test the coherence at two points of a beam emitted by an incoherent source. The principle of the experimental arrangement is recalled in Figure 3.1. The source extends on

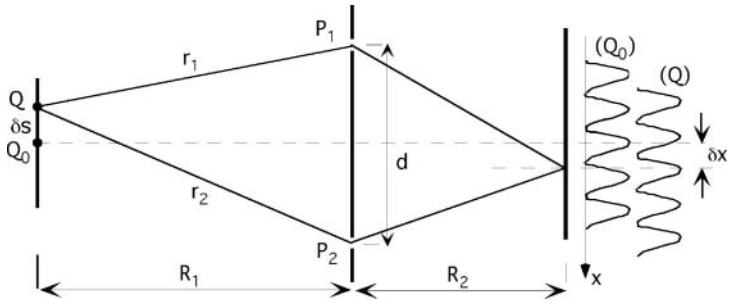

Fig. 3.1. Young's slit interferences.

a small surface around the point Q_0 on the optic axis. Two slits, P_1 and P_2, separated by a distance d, are made through a stop perpendicular to the axis. Let R_1be the distance from Q_0 to the stop, R_2, the distance from the stop to the imaging screen. Let Q be a point of the light source at a distance δs from Q_0 and let us consider the fringe system on the screen given by quasimonochromatic light, of mean wavelength λ, emitted from this point. We assume $d \ll R_2$ and $\delta x \ll R_2$. Calculation shows that, when δs varies from zero to its actual value, the fringes shift on the screen by [46]

$$\delta x \simeq \frac{R_2}{R_1}\delta s \tag{3.1}$$

If we assume the points of the source to emit independently from each other, the overlap of the corresponding fields reduces to intensity addition since there is no established phase relation between them. A uniform distribution of pinpoint sources between Q and Q_0 being assumed, the width of the fringes increases with the source size δs, lowering the contrast of the system consequently as a result. The fringe system remains observable, though with reduced contrast, as long as δx remains smaller than the fringe separation, which requires.

$$\delta s \leqslant \lambda \frac{R1}{2d} \tag{3.2}$$

This illustrates the general fact, already mentioned in Section 1.6, that partial coherence may be observed in fields coming from incoherent sources. The reason is that the field phases are involved in amplitude additions only through the differences they acquire by following different paths between source and detector. No defined phase can be attributed to the wave trains emitted by the source, but field propagation, which mixes in each point phase and amplitude of fields coming from different points, introduces coherence in the resulting field. As an example, let us consider again the waves, emitted at points Q and Q_0 and their overlap at points P_1 and P_2 of Figure 3.1. The field cross-correlation at these points may appear in the form of a fringe pattern on the

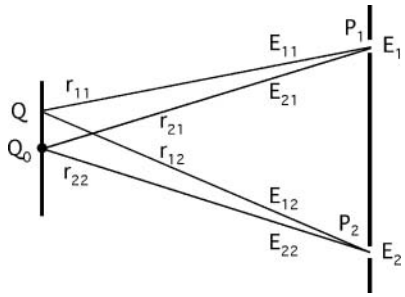

Fig. 3.2. Fluctuations of radiation emitted from Q_0 propagate toward P_1 and P_2. Fluctuations from the independent source Q also propagate to P_1 and P_2. Both sets of fluctuations are finally present in the fields $E_1 = E_{11} + E_{21}$ and $E_2 = E_{12} + E_{22}$. That is why correlations appear between E_1 and E_2 as it is shown by the production of interference fringes.

screen. Four paths, represented in Figure 3.2, are to be taken into consideration: r_{11} and r_{12} from Q to P_1 and P_2, r_{21} and r_{22} from Q_0 to P_1 and P_2. Let E_{11}, E_{21} and E_{12}, E_{22} be the corresponding fields at P_1 and P_2 (see [47], Chapter 4). The fluctuations of the waves emerging from the two non-correlated source points will reproduce in each of the resulting fields, E_1, E_2, at points P_1 and P_2. Hence, except for a phase factor due to the small path length differences, $r_{11} - r_{21}$ and $r_{12} - r_{22}$, we will have:

$$E_1 = E_{11} + E_{21} \tag{3.3}$$

and

$$E_2 = E_{12} + E_{22} \tag{3.4}$$

Therefore, the sums E_1 and E_2 will give similar wave trains at P_1 and P_2, although the constituent wave trains, E_{11} and E_{21}, on one side, E_{12} and E_{22}, on the other, may be of completely different forms. That is why correlations may appear, as a result of propagation, between the fields E_1 and E_2.

Young's slit interferences particularly refer to the spatial coherence of a radiation field. However we just saw that the role of propagation in field coherence prompts us to consider wave trains in the region where beams overlap. The length associated with a wave train of bandwidth $\Delta\nu$ is $l_c \sim c/\Delta\nu$, to which is associated a correlation time

$$\tau = l_c/c \tag{3.5}$$

Wave trains propagating in the same direction will interfere only if the time interval between them is shorter than the correlation time τ. The length of the wave train refers to the second aspect of coherence, namely, the temporal coherence of the field. Since $\tau = 1/\Delta\nu$, the more monochromatic the radiation, the more coherent the radiation field will be. A completely monochromatic

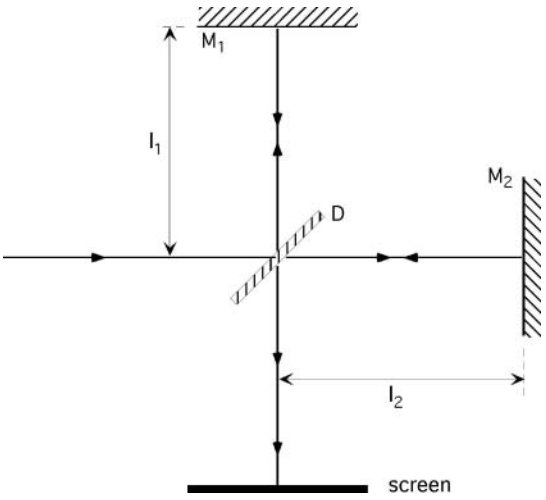

Fig. 3.3. Michelson interferometer. If the incoming radiation is temporally coherent the outgoing beam is uniform on the screen but varies periodically by shifting M_2 owing to the phase difference $\Delta\phi = 4\pi(l_1 - l_2)/\lambda$.

radiation would have an infinite wave train length and would therefore be temporally monomode.

Temporal coherence is directly displayed by the interference pattern produced by Michelson's interferometer (Fig. 3.3). In this experimental arrangement a beam splitter separates the incoming beam into two parts, each of which is reflected by a normal incidence mirror. One of the mirrors (M_2 in Fig. 3.3) can be shifted along the beam. One observes the result of the superposition of the two beams after a second pass through the beam splitter. The path difference, $\Delta l = 2(l_1 - l_2)$, between the beams being obviously constant along the beam diameter, no spatial dephasing occurs to yield fringes. Therefore, if the screen is perpendicular to the beam axis, the intensity at its surface is uniform, but varies periodically when shifting M_2, because of the time delay $\Delta t = 2\Delta l/c$ (and the corresponding phase difference $\Delta\phi = 2\pi c\Delta t/\lambda$) introduced between the beams. Alternatively, one can also directly observe fringes by slightly tilting the screen.

Whatever the more prominent character—spatial or temporal—of coherence, the fringe contrast (or visibility)

$$K = \frac{I_{\max} - I_{\min}}{I_{\max} + I_{\min}} \tag{3.6}$$

where $I_{\max}$ and $I_{\min}$ are the intensities at fringe top and bottom, K is the measure of the degree of coherence.

A simple example may illustrate this relation. Let us consider the abstract case of a harmonic wave arriving at a stop provided with two pinholes P_1 and

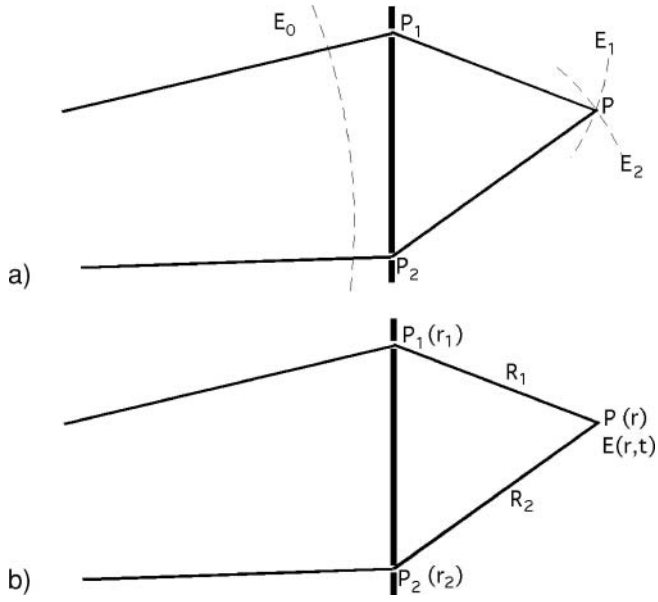

Fig. 3.4. Calculation of fringe contrast: (a) simple case of an incoming spherical harmonic wave, (b) diagram for a general calculation.

P_2 (Fig. 3.4a). Let

$$E_1 = E_0 \exp i\,[2\pi\nu t - \phi_1] \tag{3.7}$$

$$E_2 = E_0 \exp i\,[2\pi\nu t - \phi_2] \tag{3.8}$$

be the fields reaching P, from P_1 and P_2, respectively. The field and the intensity at P will be

$$E_P = E_1 + E_2 \tag{3.9}$$

$$I_P = E_P E_P^* \tag{3.10}$$

and one readily finds that

$$I_P = 2I_0(1 + \cos(\phi_1 - \phi_2)) \tag{3.11}$$

where

$$I_0 = E_0^* E_0 \tag{3.12}$$

Equation (3.11) shows that $I_{\min} = 0$ for $\phi_1 - \phi_2 = (2k+1)\pi/2$. The contrast, given by relation (3.6), is then $K = 1$, which is not surprising since the field checked at points P_1 and P_2 is completely coherent by the very fact that it was assumed to be a harmonic wave.

More generally, let us assume the field, at point P, of vectorial coordinate $\mathbf{r}$, to be represented by a complex signal $E(\mathbf{r}, t)$, sum of fields coming from

points of coordinates r_1 and r_2 (Fig. 3.4b), viz.

$$E(\mathbf{r},t) = E(\mathbf{r}_1, t-t_1) + E(\mathbf{r}_2, t-t_2) \tag{3.13}$$

where

$$t_1 = R_1/c, \quad t_2 = R_2/c \tag{3.14}$$

In equations (3.14), R_1 (respectively R_2) is the distance between the points P_1 (respectively P_2). The instantaneous intensity at P is

$$I(\mathbf{r},t) = E^*(r,t)\,E(r,t) \tag{3.15}$$

and the time-averaged intensity may be written under the form [47]

$$\begin{aligned}\langle I(\mathbf{r},t)\rangle_t = {} & \langle I_1(\mathbf{r},t)\rangle_t + \langle I_2(\mathbf{r},t)\rangle_t \\ & + 2\left[\langle I_1(\mathbf{r},t)\rangle_t\right]^{1/2}\left[\langle I_2(\mathbf{r},t)\rangle_t\right]^{1/2}\mathrm{Re}\left[\gamma(\mathbf{r}_1,\mathbf{r}_2,\tau)\right]\end{aligned} \tag{3.16}$$

where

$$\tau = t_1 - t_2 \tag{3.17}$$

The function $\gamma(\mathbf{r}_1,\mathbf{r}_2,\tau)$, usually known as the *complex degree of coherence*, is the normalized form of the *mutual coherence function*

$$\Gamma(\mathbf{r}_1,\mathbf{r}_2,t) = \langle E^*(\mathbf{r}_1,t)\,E(r_2,t+\tau)\rangle_t \tag{3.18}$$

namely

$$\begin{aligned}\gamma(\mathbf{r}_1,\mathbf{r}_2,\tau) &= \frac{\Gamma(\mathbf{r}_1,\mathbf{r}_2,\tau)}{\left[\Gamma(\mathbf{r}_1,\mathbf{r}_1,0)\right]^{1/2}\left[\Gamma(\mathbf{r}_2,\mathbf{r}_2,0)\right]^{1/2}} \\ &\equiv \frac{\Gamma(\mathbf{r}_1,\mathbf{r}_2,\tau)}{\left[\langle I_1(\mathbf{r}_1,0)\rangle\right]^{1/2}\left[\langle I_2(\mathbf{r}_2,0)\rangle\right]^{1/2}}\end{aligned} \tag{3.19}$$

In spatial coherence calculations, it may be useful to also consider the equal-time correlation function, or *mutual intensity*

$$J(\mathbf{r}_1,\mathbf{r}_2)_t \equiv \Gamma(\mathbf{r}_1,\mathbf{r}_2,0) = \langle E_1^*(\mathbf{r}_1,t)\,E(r_2,t)\rangle \tag{3.20}$$

that represents the correlation of the field oscillations at the points $P(r_1)$ and $P(r_2)$. The complex degree of coherence is then

$$j(r_1,r_2)_t \equiv \gamma(\mathbf{r}_1,\mathbf{r}_2,0)_t = \frac{J(\mathbf{r}_1,\mathbf{r}_2)_t}{\left[J(\mathbf{r}_1,\mathbf{r}_1)_t\right]^{1/2}\left[J(\mathbf{r}_2,\mathbf{r}_2)_t\right]^{1/2}} \tag{3.21}$$

There is a close relation between the module of the complex degree of coherence and the fringe contrast K defined by equation (3.6). It is shown in [47] (par. 4.3) that, after substituting equations (3.17) and (3.14) in the expression of γ, this relation reduces to

$$K = \left|\gamma\left[\mathbf{r}_1,\mathbf{r}_2,(R_1-R_2)/c\right]\right| \tag{3.22}$$

within a good approximation, when the intensities of the two beams at point P are equal. Let us notice finally that, if we assume $\langle I_1(\mathbf{r},t)\rangle = \langle I_2(\mathbf{r},t)\rangle = I_0$,

equation (3.16) becomes

$$I(\mathbf{r}) = 2I_0(\mathbf{r})\left(1 + \mathrm{Re}\left[\gamma(\mathbf{r}_1, \mathbf{r}_2, \tau)\right]\right) \tag{3.23}$$

where we see the real part of the complex degree of coherence to replace the term $\cos(\phi_1 - \phi_2)$ of equation (3.11).

As we mentioned above in connection with Young's slit experiment, field coherence such as expressed in the last term of equation (3.16), is a propagation effect. The theoretical study of correlation propagation leads to the very important van Cittert–Zernike theorem , which gives the general expression of coherence distribution, around a given point, of a beam emitted from an incoherent source. This theorem states that the (equal-time) complex degree of coherence is equal to the amplitude of the diffraction pattern around this point, of an aperture of the same size as the light source. This statement implies that $R_1 \simeq R_2$ so that the time interval τ defined by equations (3.17) and (3.14) may be neglected. The equal-time complex degree of coherence

$$j(\mathbf{r}_1, \mathbf{r}_2) \equiv \gamma(\mathbf{r}_1, \mathbf{r}_2, 0) \tag{3.24}$$

then replaces the complex degree of coherence $\gamma(\mathbf{r}_1, \mathbf{r}_2, \tau)$ defined by relation (3.19) in calculations.

Figure 3.5 shows the main components used in the $j(\mathbf{r}_1, \mathbf{r}_2)$ calculation. Let us consider a couple of source points $S_1(\mathbf{r}'_1)$and $S_2(\mathbf{r}'_2)$, in the source area (σ). The vectors $\mathbf{r}'_1$ and $\mathbf{r}'_2$ are vectorial coordinates of S_1 and S_2. Intensities at $P_1(\mathbf{r}_1)$ and $P_2(\mathbf{r}_2)$ are calculated for each couple S_1, S_2, via equation (3.16). All contributions are then summed, giving the total intensities in P_1 and P_2. Figure 3.5 displays, for one direction, the pattern of a coherence degree distribution, $j(\mathbf{r}_1, \mathbf{r}_2)$, which might be obtained around P_1.

If we consider a uniform circular source of radius a, then $j(\mathbf{r}_1, \mathbf{r}_2)$ takes a simple symmetric form. Let points P_1 and P_2 be at a large distance r from the source and symmetrically placed with respect to the normal at the center of the source area. Let d_{12} be the distance between P_1 and P_2. The degree of

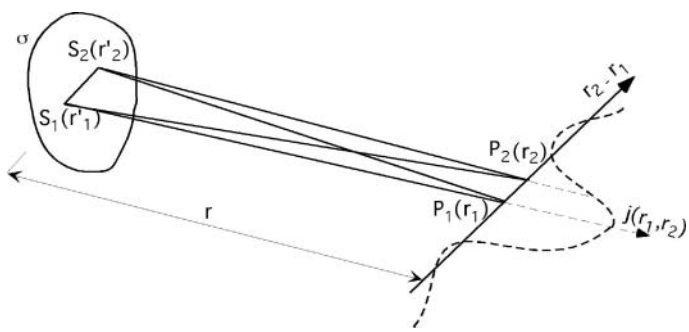

Fig. 3.5. This diagram illustrates the coherence of propagation predicted by the van Cittert–Zernike theorem. $j(r_1, r_2)$ is the distribution of coherence degree around a given point P_1, of the light beam emitted from the incoherent source, σ.

coherence then reads [47]

$$j\left(\mathbf{r}_1, \mathbf{r}_2\right) = \frac{2J(w)}{w} \tag{3.25}$$

where $J_1\left(w\right)$ is the first order Bessel function and w is given by

$$w = \frac{2\pi}{\lambda}\frac{ad_{12}}{r} \tag{3.26}$$

In the case of an elongated rectangular source, we have

$$j\left(\mathbf{r}_1, \mathbf{r}_2\right) = \frac{\sin w}{w} \tag{3.27}$$

In both cases it is easy to see that $j\left(\mathbf{r}_1, \mathbf{r}_2\right)$ decreases by a factor $\sim 16\%$ when w goes from 0 to 1. This is the reason why $w = 1$ has been chosen in order to fix the spatial coherence length to the conventional value

$$L_c = \frac{\lambda}{2\pi}\frac{r}{a} \tag{3.28}$$

via equation (3.26). This relation shows the coherence length to grow proportionally to the distance to the source, which is an important characteristic of spatial coherence. Let us mention that comparing equation (3.28) with the order of magnitude relation (1.55) would correspond to a fringe contrast about 0.60 instead of the 0.84 value used here above.

3.2 Modes of Free Radiation Field

In optics the widely shared notion of mode refers to narrow frequency bands and peculiar spatial distribution pattern of light, both fixed by the constraints due to resonant cavity and wave guiding. Modes exist for any vibrational system known in physics. However when we are dealing with incoherent or partially coherent sources, not with lasers, in order to produce radiation beams of large degree of coherence, the notion of mode needs to be somewhat enlarged.

This is illustrated, for instance, by the fact that, in Section 1.6, it made sense, at least qualitatively, to speak of modes even when the usual space constraints were absent. This was because we only considered the elementary conditions necessary to obtain coherence at two separated points of a field emerging from a globally incoherent source (see for instance Fig. 3.2). One condition was that the emitting points were all inside an area δS and the pair of sample points inside another area δA, such that $\delta S \delta A / R^2 \lesssim \lambda^2$, R being the distance from the source to δA (see Fig. 3.6). A second condition, that referred to temporal coherence, was the band width $\delta\nu$ and the desired correlation time δt to be such that $\delta\nu\delta t \lesssim 1$. A field domain defined by δS, $\delta A/R^2$ (or $\delta\Omega$), $\delta\nu$, δt was what we called "mode."

Now a large set of such modes may fill the space between the source and the receiving surface. The "grid" formed on this surface by a set of elements

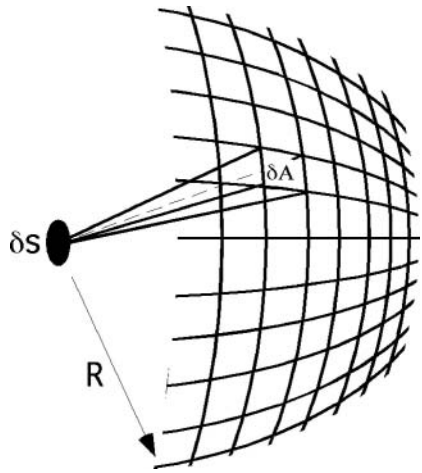

Fig. 3.6. Definition of spatial modes by the coherence condition $\delta s \delta A / R^2 \leq \lambda^2$.

similar to δA can be arbitrarily translated in directions perpendicular to light propagation direction. In this sense the modes are not strictly localized in space. However, the fact that they define coherent field zones is clearly demonstrated by the fringe patterns that may be observed through pinholes bored inside each of the coherence area, δA. Let us also mention that the smaller the number of modes occupied by photons, the larger the global coherence of the source will be. Moreover the size of the coherent area δA increases proportionally to R^2.

To rigorously establish a coherent-mode representation of fields in the free space it is necessary to refer to the space–frequency domain rather than the space–time domain.[1] In the space–frequency domain, the averaged radiation intensity, $\langle I(\mathbf{r}, t)\rangle_t$, used in equations (3.16)–(3.23), is replaced by the spectral density $S(\mathbf{r}, \nu)$, which is the field self-correlation function at a point $\mathbf{r}$ of the space–frequency domain.

$S(\mathbf{r}, \nu)$ may be introduced in the following way. Let us consider the Fourier transform of the mutual coherence function (3.18):

$$W(\mathbf{r}_1, \mathbf{r}_2, \nu) = \int_{-\infty}^{\infty} \Gamma(\mathbf{r}_1, \mathbf{r}_2, \tau)\, e^{2\pi i \nu \tau} d\tau \tag{3.29}$$

The left-hand side of this expression, $W(\mathbf{r}_1, \mathbf{r}_2, \nu)$, is the so-called cross-spectral density function. Function $S(\mathbf{r}, \nu)$ has the same relation with the cross-spectral density function $W(\mathbf{r}_1, \mathbf{r}_2, \nu)$ as intensity $I(\mathbf{r}, \tau)$ with the mutual-coherence function $\Gamma(\mathbf{r}_1, \mathbf{r}_2, \tau)$ when $\mathbf{r}_1$ and $\mathbf{r}_2$ coincide [cf. equation

[1] This paragraph is a summary of the detailed presentation to be found in Sections 4.5 and 5.5 of *Optical Coherence and Quantum Optics* by L. Mandel and E. Wolf, Cambridge University Press, 1995.

(3.19)], viz.

$$S(\mathbf{r},\nu) = W(\mathbf{r},\nu) \tag{3.30}$$

The important fact is that $S(\mathbf{r},\nu)$ obeys an equation analogous to equation (3.16), that is

$$\begin{aligned} S(\mathbf{r},\nu) &= S^{(1)}(\mathbf{r},\nu) + S^{(2)}(\mathbf{r},\nu) \\ &\quad + \left[S^{(1)}(\mathbf{r},\nu)\right]^{1/2}\left[S^{(2)}(\mathbf{r},\nu)\right]^{1/2} \mathrm{Re}\left[\mu(\mathbf{r}_1,\mathbf{r}_2,\nu)\,\mathrm{e}^{-2\pi\mathrm{i}\nu(\mathrm{R}_1-\mathrm{R}_2)/\mathrm{c}}\right] \end{aligned} \tag{3.31}$$

where $\mu(\mathbf{r}_1,\mathbf{r}_2,\tau)$ is the spectral degree of coherence, at frequency ν, defined by

$$\mu(\mathbf{r}_1,\mathbf{r}_2,\nu) = \frac{W(\mathbf{r}_1,\mathbf{r}_2,\nu)}{\left[W(\mathbf{r}_1,\mathbf{r}_1,\nu)\right]^{1/2}\left[W(\mathbf{r}_2,\mathbf{r}_2,\nu)\right]^{1/2}}$$

or

$$\mu(\mathbf{r}_1,\mathbf{r}_2,\nu) = \frac{W(\mathbf{r}_1,\mathbf{r}_2,\nu)}{\left[S(\mathbf{r}_1,\nu)\right]^{1/2}\left[S(\mathbf{r}_2,\nu)\right]^{1/2}} \tag{3.32}$$

in the same manner as the complex degree of coherence $\gamma(\mathbf{r}_1,\mathbf{r}_2,\tau)$ was defined by equation (3.19) in the space–time domain. Now it is shown (cf. [47], 4.7.1) that $W(\mathbf{r}_1,\mathbf{r}_2,\nu)$ can be expressed in the form

$$W(\mathbf{r}_1,\mathbf{r}_2,\nu) = \sum_n \alpha_n(\nu)\,\psi_n^*(\mathbf{r}_1,\nu)\,\psi_n(\mathbf{r}_2,\nu) \tag{3.33}$$

where the functions $\psi_n(\mathbf{r},\nu)$ form an orthonormal set of eigenfunctions of the integral equation

$$\int_D W(\mathbf{r}_1,\mathbf{r}_2,\nu)\psi_n(\mathbf{r}_1,\nu)\,d^3r_1 = \alpha_n(\nu)\,\psi_n(\mathbf{r}_2,\nu) \tag{3.34}$$

Equation (3.33) may be rewritten as

$$W(\mathbf{r}_1,\mathbf{r}_2,\nu) = \sum_n \alpha_n(\nu)\,W^n(\mathbf{r}_1,\mathbf{r}_2,\nu) \tag{3.35}$$

where

$$W^n(\mathbf{r}_1,\mathbf{r}_2,\nu) = \psi_n^*(\mathbf{r}_1,\nu)\,\psi_n(\mathbf{r}_2,\nu) \tag{3.36}$$

Further examination shows that, for each n, the cross-spectral density function, $W^n(\mathbf{r}_1,\mathbf{r}_2,\nu)$, represents a fully coherent field in the space–frequency domain. Moreover $W^n(\mathbf{r}_1,\mathbf{r}_2,\nu)$ satisfies the Fourier transform of the propagation equation of the mutual coherence function $\Gamma(\mathbf{r}_1,\mathbf{r}_2,\tau)$. That is why $W^n(\mathbf{r}_1,\mathbf{r}_2,\nu)$ is regarded as a mode of the field. We see that the expansion (3.35) therefore represents the cross-spectral density function as a superposition of modes $W^n(\mathbf{r}_1,\mathbf{r}_2,\nu)$.

We will now consider a partially coherent plane source, the spectral degree of coherence of which, $\mu(\mathbf{r}_1, \mathbf{r}_2, \nu)$, depends on $\mathbf{r}_1$and $\mathbf{r}_2$ only through the difference $\delta\mathbf{r} = \mathbf{r}_2 - \mathbf{r}_1$, viz.

$$\mu(\mathbf{r}_1, \mathbf{r}_2, \nu) = g(\delta\mathbf{r}, \nu) \tag{3.37}$$

and similarly a cross-spectral function $W(\mathbf{r}_1, \mathbf{r}_2, \nu)$

$$W(\mathbf{r}_1, \mathbf{r}_2, \nu) = [S(\mathbf{r}_1, \nu)]^{1/2} [S(\mathbf{r}_2, \nu)]^{1/2} g(\delta\mathbf{r}, \nu) \tag{3.38}$$

In a one-dimensional source model of Gaussian type, the spatial distribution of the spectral density $S(x, \nu)$ and the spectral degree of coherence $g(\delta x, \nu)$ are of the form

$$S(x, \nu) = A^2(\nu) e^{-x^2/2\sigma_s^2(\nu)} \tag{3.39}$$

$$g(\delta x, \nu) = e^{-\delta x^2/2\sigma_g^2(\nu)} \tag{3.40}$$

The parameter

$$q(\nu) = \frac{\sigma_g(\nu)}{\sigma_s(\nu)} \tag{3.41}$$

is considered as the measure of the global degree of spatial coherence of this type of source.

The expansion (3.35) may be rewritten

$$W(\mathbf{r}_1, \mathbf{r}_2, \nu) = \sum_n \beta_n(\nu) \Phi_n^*(x_1, \nu) \Phi_n(x_2, \nu) \tag{3.42}$$

By substituting the expression of the cross-spectral density (3.42) in equation (3.34) one obtains the new form of the integral equation

$$\int_{-\infty}^{+\infty} W(x_1, x_2, \nu) \Phi_n(x_1, \nu)\, dx_1 = \beta_n(\nu) \Phi_n(x_2, \nu) \tag{3.43}$$

After calculation the eigenfunctions and the eigenvalues of equation (3.43) are found to be of the form

$$\Phi_n(x, \upsilon) = \left(\frac{2c}{\pi}\right)^{1/4} \frac{1}{(2^n n!)^{1/2}} H_n\left[x(2c)^{1/2}\right] e^{-cx^2} \tag{3.44}$$

$$\beta_n(\nu) = A^2 \left(\frac{\pi}{a+b+c}\right)^{1/2} \left(\frac{b}{a+b+c}\right)^n \tag{3.45}$$

where $H_n(x)$ are the Hermit polynomials, and

$$a(\nu) = \frac{1}{4\sigma_s^2(\nu)}, b(\nu) = \frac{1}{2\sigma_g^2(\nu)},\ c(\nu) = \left[a^2(\nu) + 2a(\nu) b(\nu)\right]^{1/2} \tag{3.46}$$

Figure 3.7 displays examples of the behavior of the ratio β_n/β_0 for selected values of the global degree of coherence, $q(\nu)$, defined above [cf. Eq. (3.41)]. One sees the modes of high order strongly increase when the coherence decreases.

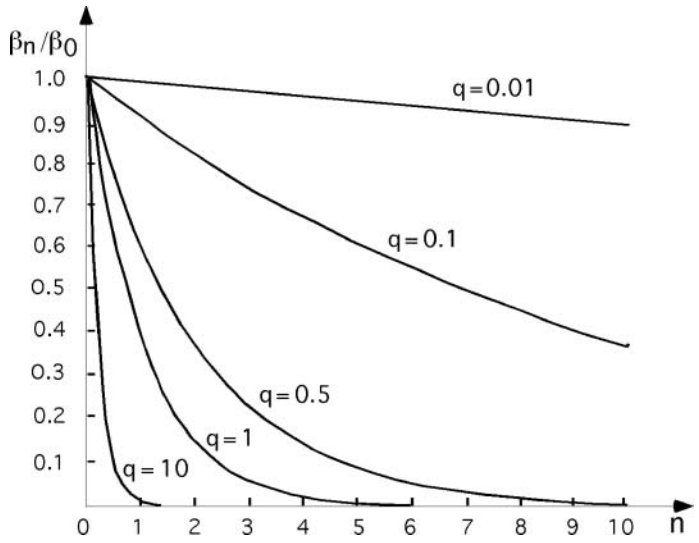

Fig. 3.7. Contribution β_n to the field of each separated mode as a function of the mode number n, for several values of the total degree of coherence q, of a partially coherent Gaussian beam. For $q = 10$ the beam is practically monomode.

In other words, the smaller the spatial coherence, the larger the number of modes necessary to represent the spatial correlations of the field.

3.3 Three Ways of Producing Coherent XUV Radiation Beams

The development of XUV optics during these last years points to three different ways of producing coherent XUV beams, suitable for coherent optics experiment: monochromatized synchrotron radiation, X-ray lasers (XRL), and generation of high order harmonics from infrared or visible lasers (HHG) [48, 49].

In the case of synchrotron radiation, there is no phase relation between the waves born of the electron bunch . Nevertheless, coherence appears as a result of radiation propagation (cf. Section 3.1) from the synchrotron electrons to the input of the XUV optical device. This effect is more significant for synchrotron than for many other usual sources because the synchrotron emission is strongly anisotropic. The temporal and the spatial coherences are optimized by adjusting the widths of entrance and exit slits respectively until achieving well-contrasted fringes. Figure 3.8 shows interferograms obtained in the region of the carbon K-edge, near 44-nm wavelength [48]. In this figure the change of the interferometric pattern for wavelengths crossing the K-edge is a direct illustration of the behavior of the index refractive part, δ, which was shown in Figure 2.1 (Section 2.1).

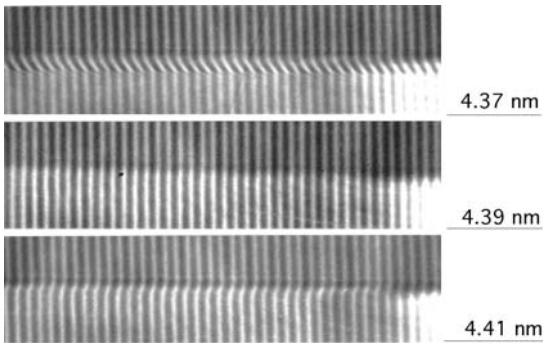

Fig. 3.8. Interferograms obtained in the region of the carbon K-edge, near 44-nm wavelength, with synchrotron radiation. The change of the interferometric pattern crossing the K-edge is a direct illustration of the behavior of the index refractive part, δ (cf. Fig. 2.1) (Ref. [48]).

In X-ray (or XUV) lasers the amplifying medium is a hot, short-pulse, plasma of cylindrical shape. Here too propagation coherence has a large part in the production of coherent beams since up to now these lasers latter have been working without cavity, viz. in the regime of amplification of spontaneous emission (ASE). ASE means that any spontaneously emitted photon may give rise to stimulated emission from another excited atom. A rough estimate of the spatial mode number that can appear in this way in a cylindrical amplifying plasma can be obtained as follows. Figure 3.9 represents a plasma cylinder of section $\Delta S = \pi D^2/4$ and length L. Let us consider a small part $\Delta S'$ of the left end of the plasma column. From relation (1.56) the order of magnitude of the spatial mode number for photons coming from $\Delta S'$ is given by

$$N \sim \frac{\Delta S' \Delta \Omega}{\lambda^2} \tag{3.47}$$

Substituting $\Delta S/L^2 = \Delta\Omega$ in this relation we obtain

$$N \sim \frac{\Delta S' \Delta S}{\lambda^2 L^2} \tag{3.48}$$

Extending $\Delta S'$ to the whole surface ΔS of the cylinder cross-section, the total number of spatial modes for a cylindrical plasma of diameter $D = 2a$ is found

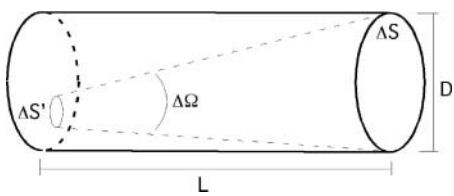

Fig. 3.9. Estimation of the spatial mode number in the emission of a cylindrical amplifying plasma (see text).

to be approximately

$$N \sim \left(\frac{\Delta S}{\lambda L}\right)^2 = \left(\frac{\pi a^2}{\lambda L}\right)^2 \tag{3.49}$$

Remembering the familiar definition of the Fresnel number

$$F \equiv \frac{2\pi a^2}{\lambda L} \tag{3.50}$$

we see that

$$N \simeq \frac{F^2}{4} \tag{3.51}$$

From equation (3.49) one may infer that an XUV laser of wavelength $\lambda = 20$ nm, produced from a plasma column of 2 cm length and 20 μm diameter would be spatially monomode. Such conditions might be approached in the future. A present the amplifying column is nearer 50 μm wide, which corresponds to about 40 spatial modes. However, in the next part of this book, we will see that a radial density gradient within the plasma provides a mode selection that reduces this number. In addition, double-pass of the XUV laser beam through the plasma, achieved with the help of a "half-cavity" mirror, as well as the use of two or more successive plasmas also increase the beam coherence.

As regards XRL temporal coherence let us mention that the laser line width, $\Delta\lambda$, which results mainly from thermal Doppler broadening at the temperature of a few 10^6K [cf. Eqs. (1.29) and (1.30)], is such that

$$\frac{\Delta\lambda}{\lambda} \simeq 10^{-4} \tag{3.52}$$

By using the temporal coherence condition 1.54 with $\lambda = c/\nu$, $\Delta\nu/\nu = \Delta\lambda/\lambda$, we readily find that the longitudinal coherence length

$$l_{\text{coh}} = c\Delta t \tag{3.53}$$

is of the order of $10^4\lambda$, that is more than sufficient for interferometric experiments.

In contrast with the two previous sources of coherent XUV radiation, the generation of high harmonics, schematically illustrated in Figure 3.10, introduces coherence in the emission mechanism itself because all the atomic dipoles of the emitting medium are excited by one and the same laser field.

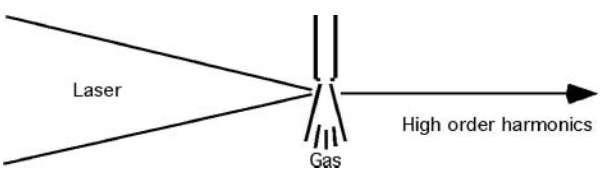

Fig. 3.10. Principle of experimental high harmonic generation.

That is why spatially monomode emission may be observed. However, the coherent addition of the radiation fields of the nonlinear atomic dipoles depends not only on the complex nonlinear atomic behavior, but also on the macroscopic properties of the medium. Further on we will see that the so-called "phase matching" of the XUV radiation obtained by HHG is strongly dependent on the laser focusing conditions, as well as on the free electron density of the medium. As for l_{coh}, it is found in the range $10^2\lambda$–$10^3\lambda$.

XUV lasers and HHG will be the subjects of the next two parts of this book. A number of practical applications of coherent XUV radiation, either already in use, or sometimes in project will be described in the last part.

References

1. B.K. Agarwal, *X-Ray Spectroscopy*, Springer Verlag, Berlin, Series in Optical Sciences, 1979.
2. H.R. Griem, *Plasma Spectrosopy*, McGraw-Hill, New York, 1964.
3. I.I. Sobelman, *Atomic Spectra and Radiative Transitions*, Springer-Verlag, Berlin, Series in Chemical Physics, 1979.
4. G. Bekefi, *Radiation Processes in Plasmas*, Willey, New York, 1966.
5. J.J. Rocca, O.D. Cortazar, B. Szapiro, R. Floyd, F.G. Tomasel, Phys. Rev. E, **47** (1993) 1229.
6. C.E. Max, Physics of the coronal plasma in laser fusion target, in *Laser Plasma Interaction*, Les Houches session XXXIV, edited by R. Balian and J.C. Adam, North-Holland, Amsterdam, 1982.
7. B. Yaakoby, P. Bourke, Y. Conturie, J. Delettrez, J.M. Forsyth, R.D. Frankel, L.M. Goldman, R.L. McCrory, W. Seka, J.M. Soures, Optics Commun., **38** (1981) 196.
8. P. Alaterre, H. Pépin, R. Fabbro, B. Faral, Phys. Rev. A, **34** (1986) 4184.
9. R. Sigel, K. Eidman, F. Lavarenne, R.F. Schmalz, Phys. Fluids B, **2** (1990) 199–207 and 208–217.
10. P. Rullhusen, X. Artru, P. Dhez, *Novel Radiation Sources Using Relativistic Electrons*, Word Scientific, Singapore, 1998.
11. D. Attwood, *Soft X-Rays and Extreme Ultraviolet Radiation*, Cambridge University Press, Cambridge, UK, 1999D.
12. J.A. Samson, D.L. Ederer (editors), Vacuum ultraviolet spectroscopy, in *Experimental Methods in the Physical Sciences*, volume 31, Academic Press, New York 1998.
13. L. Mandel, E. Wolf, *Optical Coherence and Quantum Optics*, Cambridge University Press, Cambridge, UK, 1995
14. P. Jaeglé, A. Carillon, G. Jamelot, C. Wehenkel, A. Sureau, H. Guennou, J. Phys. (France), **41**(C-3) (1980) 191.
15. S. Chandrasekhar, *Radiative Transfer*, Dover, New York, 1964.
16. D. Mihalas, *Stellar Atmospheres*, W.H. Freeman, San Francisco, 1978.
17. W. Kalkofen (editors), *Methods in Radiative Transfer Calculations*, Cambridge University Press, Cambridge, UK 1984.
18. C.J. Canon, *The Transfer of Spectral Line Radiation*, Cambridge University Press, Cambridge, UK 1985.

19. J.E Beckman, L. Crivellari (editors), *Progress in Stellar Spectral Line Formation*, NATO ASI Series C, Vol. 152, D. Reidel, Dordrecht, 1984.
20. P. Heinzel, I. Hubeny, J. Quant. Spectrosc. Radiat. Transfer., **27** (1982) 1.
21. I. Hubeny, J. Quant. Spectrosc. Radiat. Transfer., **27** (1982) 593.
22. K. Burnett, Phys. Rep., **118** (1985) 339.
23. L. Klein, B. Talin, V.P. Kaftandjian, R. Stam, *Spectral Line Shapes*, Vol. 3, ed. by F. Rostas, Walker De Gruyter, Berlin, 1985.
24. C.J. Canon, *The Transfer of Spectral Line Radiation*, Cambridge University Press, Cambridge, UK 1985, p. 14
25. B. Rus, Thèses, Université Paris-XI , no. 3549, 1995.
26. G.L. Lindford, E.R. Peressini, W.R. Sooy, M.L. Spaeth, Appl. Optics, **13** (1974) 379.
27. E.H. Kennard, *Kinetic Theory of Gases*, McGraw-Hill, New York, 1938.
28. T. Holstein, Phys. Rev., **72** (1947) 1212; Phys. Rev., **83** (1951) 1159.
29. H.W. Drawin, F. Emard, Plasma Phys., **13** (1973) 143.
30. F.E. Irons, **22** (1979) 1–20, 21–36, 37–44; S. Quant. Spectrosc. Radiat. Transfer., **24** (1980) 119–132.
31. D. Joyeux, F. Polack, D. Phalippou, Rev. Sci. Intrum., **70** (1999) 2921.
32. A.H. Compton, S.K. Allison, *X-Rays in Theory and Practice*, Van Nostrand, New York, 1935.
33. J.C. Slater, N.H. Frank, *Electromagnetism*, McGraw-Hill, New York, 1947.
34. L.D. Landau, E.M. Lifchitz, *Electrodynamics of Continuous Media*, Addison-Wesley, New York, 1960.
35. E.M. Gullikson, Optical Properties of Materials, Chapter 13, in *Vacuum Ultraviolet Spectroqscopy*, edited by J.A.R. Samson, D.L. Ederer, Academic Press, New York, 1998.
36. B.L. Henke, E.M. Gullikson, J.C. Davis, Atomic Nucl. Data Tables, **54** (1993) 181–342 (http://www-cxro.lbl.gov/optical_constants/intro.html).
37. L.G. Parrat, Phys. Rev., **95** (1954) 359.
38. P. Jaeglé, A. Carillon, G. Jamelot, C. Wehenkel, J. Phys. Lett., **40** (1979) L-551.
39. E. Spiller, Appl. Phys. Lett., **20** (1972) 365; Appl. Optics, **15** (1976) 2333.
40. R.P. Haeblich, C. Kunz, Optics Commun., **17** (1976) 287.
41. A.V. Vinogradov, B.Ya. Zeldovich, Appl. Optics, **16** (1977) 89.
42. J.H. Underwood, T.W. Barbie Jr., Appl. Optics, **20** (1981) 3027.
43. P. Dhez, SPIE Proc., **733** (1986) 308.
44. J.P. Chauvineau, J.P. Marioge, F. Bridou, et al., SPIE Proc., **733** (1986) 301.
45. A.I. Erko, V.V. Aristov, B. Vidal, *Diffraction in X-Ray Optics*, Institute of Physics Publishing, Bristol, 1996.
46. See, for instance, W. Lauterborn, T. Kurz, M. Wiesenfeldt, *Coherent Optics* (Chapter 4), Springer, Berlin 1993.
47. L. Mandel, E. Wolf, *Optical Coherence and Quantum Optics*, Cambridge University Press, Cambridge, UK, 1995.
48. D. Joyeux, P. Jaeglé, A. L'Huillier, Doing Coherent Optics with Soft X-ray Sources, in *Trends in Optics*, ed. by A. Consortini, Academic Press, New York 1996.
49. J. Svatos, D. Joyeux, D. Phalippou, F. Polack, Opt. Lett., **18** (1993) 1367.

Part II. State of the Art and Prospect of X-Ray Lasers

4. Beginnings

The first order-of-magnitude estimate of an X-ray laser pumping scheme appeared in 1967, in the paper entitled "Some Approaches to Vacuum UV and X-ray Lasers" by M.A. Dugay and P.M. Rentzepis [1]. The authors examined the possibility of creating population inversions in the XUV energy range by photo-ionizing neutral atoms in such a way that the created ions present an inner shell vacancy. A large number of ions, simultaneously prepared in a time interval shorter than the vacancy lifetime, would offer the population inversion necessary to generate a laser action. This pumping scheme was illustrated by order-of-magnitude calculations for a sodium vapor tube and for a solid copper rod, from which laser emission could be expected at 37.2 nm and 0.154 nm, respectively.

According to this study, pumping such lasers was a "formidable problem." Seeing the very short vacancy lifetimes and the energy required from the pump photons, the characteristics of the primary X-ray source seemed quite unrealistic, all the more since optical means for concentrating pumping radiation on the X-ray amplifier did not exist at all. As a matter of fact the difficulties inherent to optical pumping of very short wavelength lasers are still not completely solved today. In conclusion, the authors suggested to use a traveling wave technique in order to reduce the necessary pumping energy.

4.1 Experiments

The first experimental investigation of a possible XUV laser emission was reported by Jaeglé et al. in 1971 [2]. At the beginning was the aluminium spectrum of a laser-produced plasma (see also [3]) showing a strong intensity anomaly of the neon-like lines. This anomaly affected the group of the $2p^5 4d\ ^1P_1^0, ^3D_1^0, ^3P_1^0$–$2p^6\ ^1S_0$ lines. As shown in Figure 4.1a, the $^3P_1^0$ line exhibits a large intensity while the $^1P_1^0$ and $^3D_1^0$ lines vanishes. This result is inconsistent with the spectrum usually observed, which shows intense $^1P_1^{03}$ and D_1^0 lines at 11.65 nm and 11.69 nm and a very weak $^3P_1$ line at 11.74 nm, in agreement

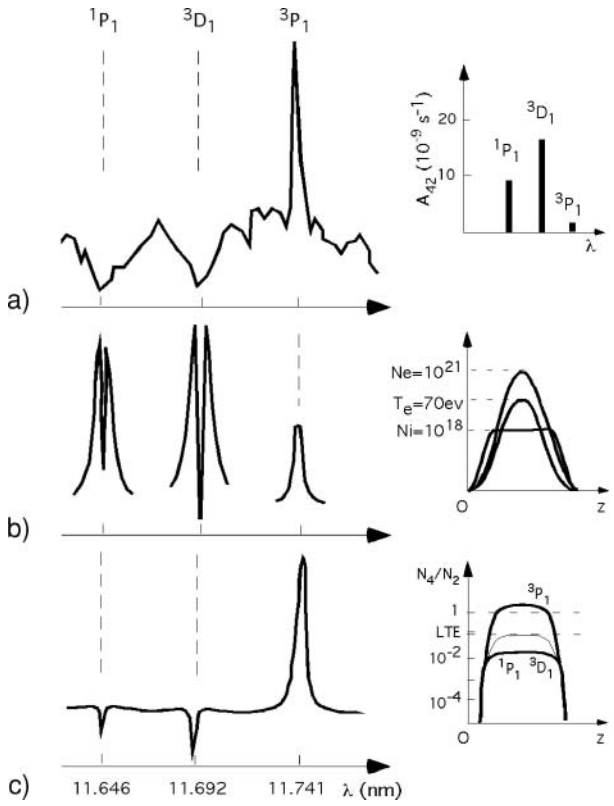

Fig. 4.1. Intensity anomalies in the neon-like aluminium ($2p^5 4d–2p^6$ lines) for a laser-produced plasma. (a) Experimentally observed spectrum compared to the transition probabilities shown in inset. (b) Spectrum simulated for the LTE plasma model displayed in inset. The splitting of the intense lines is an effect of the reabsorption of the radiation emitted in the center through the cooler peripheral shell of the plasma. (c) Spectrum calculated with the same N_i, N_e, T_e values as in (b) but with level populations departing from LTE according to the spatial distributions displayed in inset. The spectrum calculated in this way is very similar to the experimental spectrum.

with the calculated transition probabilities represented in inset. This anomaly occurred in a narrow plasma region, not far away from the target surface. At larger distances, corresponding to lower densities, the spectrum retrieved the usual pattern.

The measurement of the spectral absorption of the plasma in the same wavelength region, with the help of a method previously described by Carillon et al. [4], showed absorption rates in good agreement with the corresponding transition probabilities. A possible modification of transition probabilities by the dense plasma was thus dismissed. Remembering now equations (1.17),

(1.18), and (1.19) (Section 1.2) one can see that such results clearly raised the question of the electron population distribution between the three upper levels $^1P_1^0, ^3D_1^0, ^3P_1^0$.

It was suggested that instead of being in thermal equilibrium with the neighboring levels, the $^3P_1^0$ level population was strongly enhanced by dielectronic recombination of Al^{4+} ions with free plasma electrons, more precisely the processes,

$$Al^{4+}(2s^2 2p^5\ ^2P^0) + e^- \rightarrow Al^{3+}(2s2p^6 np\, ^3P^0)$$
$$Al^{3+}(2s2p^6 np\ ^3P^0) + e^- \rightarrow Al^{3+}(2s^2 2p^5 n'd\, ^3P^0) + e^-$$

where $2s2p^6 np\ ^3P^0$ is an autoionizing level, were invoked as candidates for yielding a population inversion between the $2p^5 3d\ ^3P^0$–$2p^6\ ^1S^0$ neon-like levels [5].

In opposition to this interpretation it has been asserted that the spectral feature of Figure 4.1a simply resulted from line–radiation reabsorption in a cold plasma region [6]. No definite radiation-transfer calculation of line intensities was made in support of this conclusion. However, cooler reabsorbing shells do indeed exist around the plasma zone directly heated by the driving laser. These shells are mainly characterized by decreasing density and temperature as one moves away from the center of the plasma.

A model of such a plasma is shown in inset in Figure 4.1b [7]. Assuming populations in local thermodynamic equilibrium (LTE), the spectrum radiated by this plasma can be numerically calculated by using equations (1.6), (1.7) and the line profile functions described in Section 1.3. $N_\mathrm{i}, N_\mathrm{e}, T_\mathrm{e}$ are the ion density, the electron density, and the electron temperature, respectively. The radiation is observed in the direction Oz. Figure 4.1b shows the intensities and the shape of the spectral lines corresponding to the LTE model. It obviously does not account for the experimental spectrum shown in Figure 4.1a. In fact it is necessary to resort to non-LTE populations, including a possible population inversion for the $4d\ ^3P_1^0$ level, to reproduce the main features of the experimental spectrum, as shown in Figure 4.1c, where N_4 and N_2 are the population densities of the levels $n = 4$ and $n = 2$, respectively.

A further attempt to measure gain at 11.74 nm, premature given the very limited experimental facilities at that time, led to clearly exaggerated gain values in spite of the care taken in processing the data [8]. Nevertheless a first stone has been laid on the way to laser–plasma amplifiers that would lead to the first X-ray lasers. As a matter of fact, a quantitative estimation showed that, a that time, a powerful mode-locked laser was the only source able to supply a plasma with the necessary pump energy [9]. At the same time Vinogradov and Sobelman [10] published a first review of laser–plasma processes, such as plasma recombination and charge exchange between charged particles, which were of interest for the production of population inversions.

Since direct gain measurements were practically out of reach of experimentalists, further experimental investigations proceeded to look for population

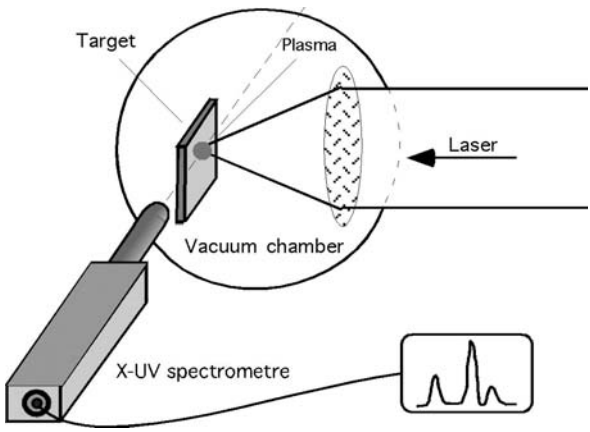

Fig. 4.2. Principle of an experimental arrangement for spectral investigations of a laser-produced plasma.

inversions by inferring the population densities from quantitative spectroscopic studies. The principle of the experimental setup used in these experiments is schematically shown in Figure 4.2. The energy necessary to produce the plasma was supplied by Nd-lasers of 1.06 μm wavelength and ∼1 ns pulse duration. By using this technique, evidence was obtained of the population inversion between the levels 2 and 3 of hydrogenic carbon ions. The wavelength of the corresponding transition is 18.2 nm [11–13]. Time-resolution of the line intensity measurements [13] allowed the authors to show that the population inversion occurred 800 ps after the target irradiation and about 550 μm away from the target. This clearly established the role of plasma recombination in the production of the population inversion.

Similarly population inversion had been observed between the 4d and 3d levels of lithium-like aluminium, the corresponding line lying at 15.4 nm [14]. For the first time, parameters like the density number of Al^{10+}-ion, the electron temperature and the ratio of the inverted populations N^{4d}/N^{3d}, had been scrutinized at several distances from the target (Fig. 4.3).

The first attempt to investigate possible lasing lines by using an elongated plasma took place in 1977 [15]. It aimed at increasing the observable gain thanks to the long plasma size in one direction. In addition the authors initiated the method which consists in sending two successive laser pulses onto the target, the first one to generate the plasma, the second, much shorter, to produce additional heating of the plasma electrons. A Cl^{6+} line at 5.82 nm, absent from a single-pulse plasma emission, appeared in the long size direction, only when the short pulse was used. The pulse separation was of 1.6 ns. Since electron heating was found efficient in enhancing the line intensity, it is clear that collisional excitation rather than plasma recombination was relevant to explain the observed spectral anomaly. This double-pulse method

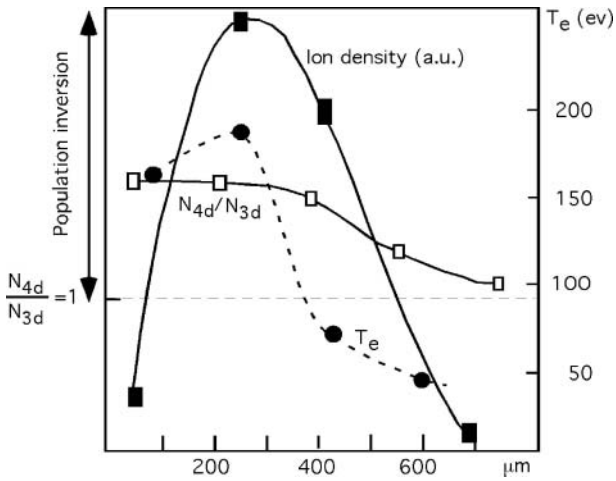

Fig. 4.3. Experimental study of the 4d to 3d population ratio of lithium-like aluminium in a laser-produced plasma; 4d to 3d population inversion is observed up to 600 μm from the target surface; ion density and electronic temperature are displayed against the distance to target [14].

was to meet a great success many years later and we shall describe it in detail in Sections 7.3 and 7.4 of this book. To this group of pioneering works belongs the study of population inversion between the levels 3 and 4 of Al^{11+} ions produced from a target specially designed to accelerate the cooling of the plasma and so increase the efficiency of its recombination [16].[1]

The first direct demonstration of the non-linear increase of an XUV spectral line—namely the 5f-3d line of lithium-like aluminium at 10:56 *nm* wavelenth—as a function of the length of a plasma column, was obtained on year 1981. It showed a gain coefficient g a 1 cm^{-1} (see Section 8.1.2) [314, 344]. This result opened a long series of progresses on the way of XUV lasers.

4.2 Pumping Mechanisms

The novelty of XUV laser pumping processes consisted, from the earliest experiments, in the fact that population inversions can appear in hot laser-produced plasmas, used as amplifiers, without the help of external photon or electron pumping beams. To clarify the conditions of population inversion

[1] A paper entitled "Experimental Evidence of an X-Ray Laser" [J.G. Kepros, et al., Proc. Natl. Acad. Sci. USA, **69** (1972) 1744] attracted a worldwide attention. However it has been promptly shown that it was not X-rays that produce the photographic black spots observed when irradiating a thin layer of gelatine containing $CuSo_4$ in solution [T.A. Boster, Appl. Optics, **12** (1973) 433].

emergence, theoretical research had to start with the study of the complex medium consisting of a fast-evolving, dense collection of multicharged ions and free electrons. This stimulated the development of plasma modeling and the calculation of radiative and collisional atomic cross-sections to be introduced in population rate equations (cf. Section 1.2).

As early as 1974, E.Ya. Kononov and K.N. Koshelev [17] performed level population calculations for a fast expanding aluminium plasma, as is expected to be a laser-produced plasma. The plasma was supposed to consist mainly of Li-like (Al^{10+}) and He-like (Al^{11+}) ions at the initial temperature of 150 eV. The authors show that when the plasma is cooling down rapidly with an electron temperature T_e being reduced by factor 2 in $\sim$1 ns for instance, population inversion can be expected between the levels $n = 4$ and $n = 3$ of lithium-like aluminium ions. They emphasized the part of radiative emission, in addition to the expansion and recombination mechanisms, in lowering the plasma temperature.

Two years later, for the first time G.J. Pert combines a model of hydrodynamic plasma expansion with the collisional–radiative calculation of level populations in the case of hydrogen-like ions produced from a carbon fiber [18]. This calculation shows several stages to occur in the evolution of the C^{5+} level populations according to the relative importances of line reabsorption, radiative cascades, and collisional electron recombination. The gain is calculated in the axial direction of the fiber. Results are illustrated in Figure 4.4 which shows the gain expected for the Balmer-α line, that is to say due to the 3- to 2-level population inversion. The important feature of the curve displayed in the figure is the gain peak appearing 250 ps after the beginning of plasma expansion.

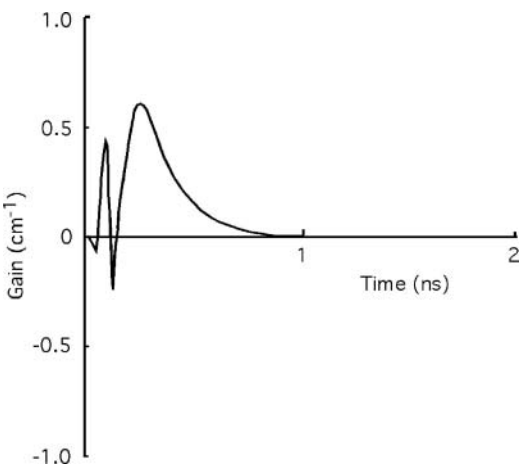

Fig. 4.4. Gain calculated for the Balmer-α line of hydrogenic ions of carbon, at 18.2 nm. The gain peak occurs 250 ps after the beginning of the plasma expansion. The oscillations which appear during the first 100 ps are an effect due to the initial conditions of calculation [18].

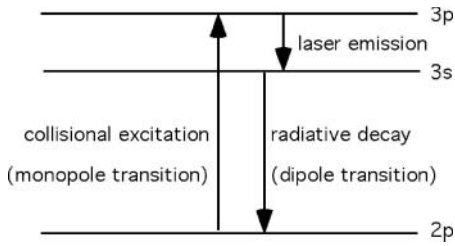

Fig. 4.5. Simplified diagram of the 3s–3p population inversion pumping scheme.

During the same period R.C. Elton opened another way to soft X-ray lasers by investigating the conditions necessary to extend ion lasers, operating in the visible or near-ultraviolet spectrum, to the vacuum ultraviolet region [19]. Previously Moltchanov had pointed out a possible extension of the $\mathrm{p}^{k-1}(n+1)\mathrm{p}-\ n\mathrm{p}^{k-1}(n+1)\mathrm{s}$ population inversion mechanism in ions of $n\mathrm{p}^k$ ground state, to high Z elements in order to reach the far ultraviolet region [20]. Elton's' analysis also refers to laser transitions between two states having the same principal quantum number, $n = 3$. A very simplified diagram of the pumping scheme considered for these lasers is displayed in Figure 4.5. The transition rate from the 2p ground state to the upper 3p level is proportional to the electron density, n_e. The radiative decay from the 3p to the 2p level is forbidden ($l = 1 \rightarrow l = 1$ transition). The radiative decay from 3s to 2p level is very rapid (resonance line). Such a combination of transition probabilities may induce population inversion between the 3p and the 3s levels, provided that the electron density and temperature have suitable values. This is the principle of a collisional pumping method that takes advantage of the plasma's free electrons instead of resorting to a beam of external electrons.

Calculations were performed for carbon-like ions from neon up to molybdenum, with lasing wavelengths ranging from 230 nm to 30 nm. Given how few atomic data related to highly charged ions were available at that time, most wavelengths and oscillator strengths had to be extrapolated from those of lower Z ions. To test the laser efficiency the author chose to calculate the minimum length L_min of the plasma fiber, necessary to supply a fixed value of the gain factor, also named gain–length product, gL_min, where g is the gain coefficient given by equation (1.19).

Calculations were done, first assuming that both ions and electrons were at the same temperature, taken as a fixed fraction of the next lower ion (boron-like) ionization potential, then arbitrarily assuming that $T_\mathrm{e} = 10T_\mathrm{i}$. The results displayed in Figure 4.6 refer to an amplified emission $I = e^{gL_\mathrm{min}}$, where the gain factor is taken equal to 5. The upper curve, for $T_\mathrm{e} = T_\mathrm{i}$, shows that the length required to achieve this gain is of several tens of centimeters, which does not seem realistic. However the second curve, corresponding to the case of strongly enhanced electron temperature, points much more realistic lengths of a few centimeters. Another result was the calculation of the maximum electronic density n_e, beyond which the collisional mixing between the populations

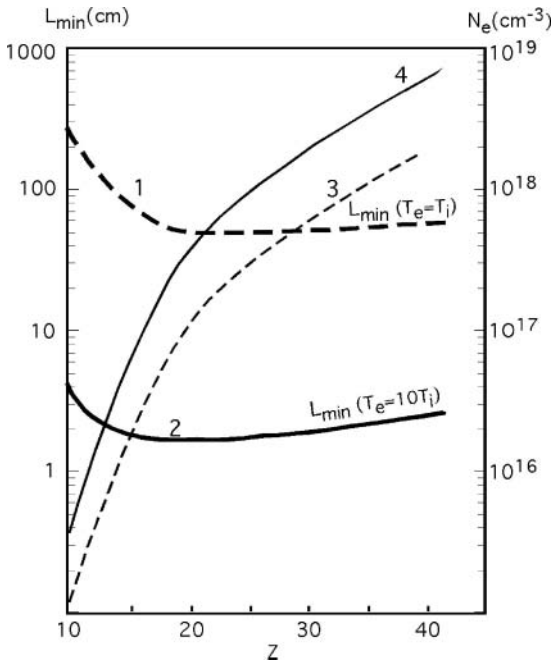

Fig. 4.6. Theoretical investigation of collisional pumping efficiency [19]. The test value of the gain factor, gL, is arbitrarily fixed at 5. The curves 1 and 2 give the minimum plasma length $L_{\min}$, necessary to reach this value, for two electron temperatures. One sees that $L_{\min}$, given by the curves 1 and 2, decreases by a factor $\sim$50, when T_e is increased by a factor 10 at constant ion temperature T_i. Curves 3 and 4 represent the maximum electron densities that are consistent with a nonvanishing gain, when the collisional mixing of the level populations is considered. One sees that the increase of electron temperature allows for the increase of the electron density.

of the two levels of the lasing transition completely destroys the population inversion. In the extreme ultraviolet range, i.e. for $Z \geqq 25$, the predicted upper density limit is between 10^{18} and 10^{19} electrons per cubic centimeter.

It is clear that a steady-state plasma would offer to electron temperature no chance to exceed the ion temperature by factor of 10. Nevertheless, owing to the large difference between the thermalization times of ions and electrons, in short pulsed plasmas as we shall see, electrons are heated much faster than ions. This leads during a short while to temperature discrepancies sufficient for achieving an efficient lasing action.

Moreover A.V. Vinogradov [21] demonstrated that neon-like ions were especially liable to produce large gains by collisional pumping. His calculation showed that a gain of 10–100 cm^{-1} could be expected from a neon-like calcium plasma of 10^{19}–10^{20} cm^{-3} density and 100–200 eV temperature, even without a large excess of electron temperature. The advantages of neon-like ions

have been then sighted in other ions whose the fundamental state is a closed electronic shell, as in the case of nickel-like ions. Other contributions to this first stage on the way to XUV-lasers included recombination and collisional pumping (cf. for instance [22–25]), as well as other schemes like charge exchange mechanisms ([26–28]) or autoioniziation [29].

The conceptual framework, that would lead to the first very bright X-ray lasers 10 years later, was now set. For many years, linearly focused laser-produced plasmas became the main matter of research about the pumping of multicharged ions. Since recombination pumping did not require as much energy as other schemes, it had been developed early in many laboratories. Therefore it played an important role in the technical progress of XUV laser investigations. As for collisional pumping it had to wait for much more powerful driving lasers. When such lasers became available in the frame of research programs on plasma inertial confinement for thermonuclear fusion, collisional pumping quickly succeeded in providing large gain X-ray lasers [30] and in producing the first saturated emission of such lasers [31].

5. General Features of X-Ray Lasers

The principle of producing a thin column—or a "fiber"—of dense hot expanding plasma is presented in Figure 5.1. The beam of a pulsed laser is linearly focused in vacuum onto a solid target surface with the help of a cylindrical optical system. Neodymium glass-lasers are currently used at the wavelength of the first ($\lambda = 1.05\,\mu\text{m}$), the second ($\lambda = 0.53\,\mu\text{m}$), or the third harmonic ($\lambda = 0.35\,\mu\text{m}$). The XUV laser beam is emitted along the axis of the plasma fiber, perpendicularly to the axis of the drive (or pump) laser. In this chapter we will summarize the methods which have been developed to produce plasma columns as well as to characterize the lasing emission. Details regarding each pumping scheme, collisional excitation or plasma recombination, will be presented in further sections. Let us start with the physics of laser-produced plasmas.

5.1 Survey of Laser-Produced Plasma Physics

5.1.1 Main Parameters Related to Plasma Expansion

The transfer of energy from the laser beam to the plasma takes place mainly via electron heating due to electron–photon collisions in the ion electric field, i.e. the inverse bremsstrahlung process (see for instance [32]). In this process free electrons oscillations are excited by the laser and converted into thermal motion by electron–electron collisions. According to [33] the inverse bremsstrahlung absorption coefficient can be calculated from the following equation:

$$\kappa_{\text{ib}} \simeq 3.4 \frac{\left(n_{\text{e}}/n_{\text{c}}\right)^2 Z \ln \Lambda}{\sqrt{1 - n_{\text{e}}/n_{\text{c}}}\lambda^2_{[\mu\text{m}]} \left(kT_{\text{e}}\right)^{3/2}_{[\text{KeV}]}} \tag{5.1}$$

where n_{c} is the critical density previously defined in Section 2.2, λ the wavelength of the laser, Z the mean ion charge, and $\ln \Lambda$ the Coulomb logarithm for inverse bremsstrahlung. In the plasma corona, where the plasma frequency is

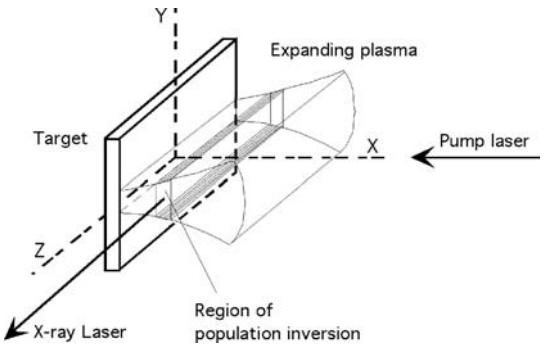

Fig. 5.1. Production of a plasma column by cylindrical focusing of a pump-laser beam onto a solid target surface.

smaller than the laser light frequency, ω, the Coulomb parameter Λ is given by

$$\Lambda = \frac{v_{\mathrm{T}}}{p_{\min}\omega}$$

v_{T} being the thermal velocity of the electrons and $p_{\min}$ the minimum impact parameter of electron–ion collisions. To calculate the Coulomb logarithm, Hughes [32] proposed to use the relation $\ln\Lambda \simeq 31 - \ln(n_{\mathrm{e(cm^{-3})}}^{1/2} T_{\mathrm{e(KeV)}}^{-1})$ (1 KeV corresponds to a temperature of 1.1605×10^7 K). Numerical simulations show that 80–90% of the laser energy is absorbed by inverse bremsstrahlung [34].

Let us recall that an electromagnetic radiation does not propagate within the plasma if the frequency becomes equal to or larger than the plasma frequency. Therefore propagation stops at a cut-off fixed by the critical density, n_{c}, given by [see Eqs. (2.19) and (2.20)]

$$n_{\mathrm{c}} \simeq \frac{1.1 \times 10^{21}}{\lambda_{[\mu\mathrm{m}]}^2} \left[\mathrm{cm}^{-3}\right]$$

One sees that, for Nd-laser radiation ($\lambda \simeq 1.06$ μm), n_{c} is about 10^{21} cm^{-3}. It follows from the expression of n_{c} and from equations (2.15) and (2.18) that the plasma refractive index at a point of electron density, n_{e}, takes the value

$$n = \left(1 - \frac{n_{\mathrm{e}}}{n_{\mathrm{c}}}\right)^{1/2} \tag{5.2}$$

Figure 5.2 shows the main regions of a laser-produced plasma. The critical surface in the plasma is the limit of laser propagation. Beyond the critical surface, plasma heating is only due to electron thermal conduction and possibly by short wavelength radiations coming from the subcritical region. The subcritical plasma region is called plasma *corona*. Plasma corona is the region where, not far from the critical surface, the temperature is maximum. Population inversions giving rise to soft X-ray laser emission occur in the corona.

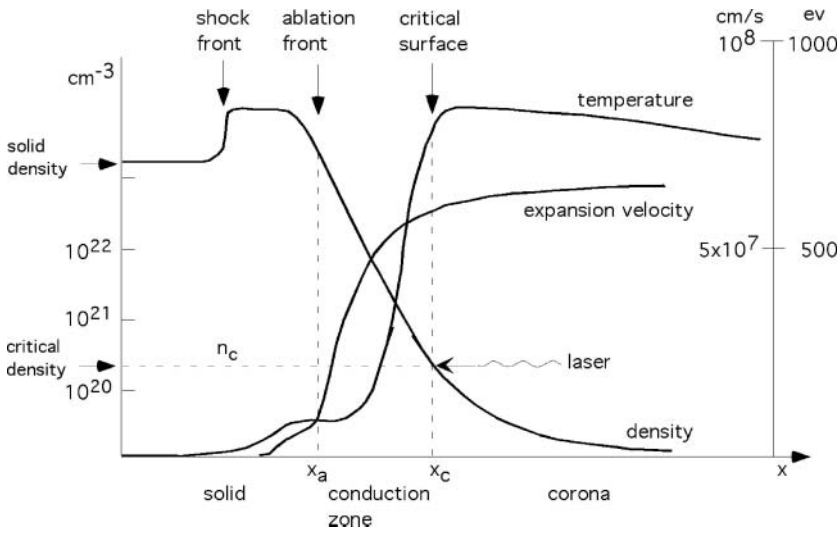

Fig. 5.2. Schematic distribution of the plasma regions from the hot corona, heated by the laser, to the cold solid target material.

As long as the plasma is heated by the laser, electron heating and thermal electron conduction compensate the losses due to plasma expansion and to radiative losses. The plasma is then approximately isothermal and its expansion can be described using the self-similarity relations involving the coordinates x and t in the form of their ratio x/t only [35, 36]. In this case the density distribution reads

$$n_\mathrm{e} = n_\mathrm{c} \exp\left(-\frac{x - x_\mathrm{c}}{c_\mathrm{s} t}\right) \tag{5.3}$$

where c_s is the velocity of sound

$$c_\mathrm{s} = \left(\frac{ZkT_\mathrm{e}}{m_i}\right)^{1/2} \tag{5.4}$$

The expansion velocity is given by

$$v = c_\mathrm{s} + \frac{x - x_\mathrm{c}}{\mathrm{t}} \tag{5.5}$$

Another important parameter is the density gradient scale length

$$L = n_\mathrm{e} / \left(\frac{\partial n_\mathrm{e}}{\partial x}\right) \tag{5.6}$$

where n_e is the electron density at a given point of the plasma. If the density profile were linear, L would be the length along which the density decreased from n_e to 0. By substituting equation (5.3) into equation (5.6) L takes the

form

$$L = c_s t = (ZkT_e m_i)^{1/2} t \tag{5.7}$$

This equation shows the gradient steepness to decrease proportionally to the elapsed time.

As regards the corona temperature during the laser pulse, it can be estimated with the help of equation

$$T_e \simeq 1.1 \times 10^{-5} \left(Z I_L t \ln \Lambda\right)^{1/3} \left(\frac{Z+1}{A}\right)^{1/6} \tag{5.8}$$

where Z is the mean ion charge, I_L the laser intensity in W/m^2, t the time in ns, and A the atomic number of the material. In this case the model does not resort to self-similarity. Laser irradiation is assumed to start at $t = 0$ and remain constant.

In the conduction zone, which is not heated by the laser light (cf. Fig. 5.2), numerical simulation fittings lead to the following expressions of temperature, density, and expansion velocity [36].

$$T_e(x) \simeq T_c \left(\frac{x - x_a}{\Delta_s}\right)^{2/5} \tag{5.9}$$

$$n_e(x) \simeq n_c \left(\frac{\Delta_s}{x - x_a}\right)^{3/5} \tag{5.10}$$

$$v(x) \simeq c_s \left(\frac{x - x_a}{\Delta_s}\right)^{3/5} \tag{5.11}$$

where Δ_s is the length of the conduction zone, given in the same model by

$$\Delta_s \simeq 0.6 c_s t \tag{5.12}$$

In these expressions x_a is the position of the high density limit of the conduction zone, viz. the ablation surface position (see Fig. 5.2), T_c is the electron temperature at the critical surface, and n_c the critical density.

5.1.2 Atomic Physics in the Plasma Corona

Within a thermodynamic-equilibrium plasma any microscopic process altering the energy of atomic electrons is statistically balanced by the inverse process, a fact known as the "principle of detailed balance." In this case it is not necessary to know photon–atom or electron–atom interaction cross-sections to calculate the level populations which obey well-known statistical laws. In addition, the electron and ion temperatures are identical. The population ratio of two excited levels, i and j, of statistical weights g_i and g_j, separated by the energy interval E_{ij} (see Fig. 5.3) is given by the familiar Boltzman's relation (1.23)

$$\frac{N_i}{N_j} = \frac{g_i}{g_j} \exp \frac{E_{ij}}{kT} \tag{5.13}$$

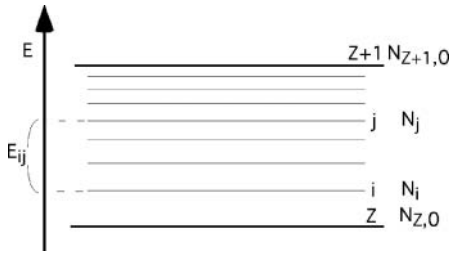

Fig. 5.3. Diagram showing the notations used to represent the excited levels of an ion of charge Z^+.

The ion balance is fixed by the ratio of the ground level populations of ions of successive charges, given by Saha's equation

$$\frac{N_{Z-1,0}}{N_{Z,0}} = \frac{1}{2}\frac{g_{Z-1,0}}{g_{Z,0}} n_\mathrm{e} \left(\frac{h^2}{2\pi m_\mathrm{e} kT}\right)^{3/2} \exp \frac{I_z}{kT} \tag{5.14}$$

with

$$n_\mathrm{e} = \sum_{1}^{Z_\mathrm{max}} Z N_Z \tag{5.15}$$

I_z is the ionization potential of the Z-ion, n_e the electron density, m_e the electron mass, T the plasma temperature, and N_Z the total density of ions of charge Z.

Now plasma corona is neither in thermodynamic equilibrium, since part of the radiation escapes, nor in local thermodynamic equilibrium, which also satisfies the above relations, since the electron density is not sufficient for collisions to balance the radiative de-excitation of deep inner levels, separated from each other by large energy gaps. Therefore it is not possible to deduce all the level populations from equilibrium relations. However the populations of the high-lying levels are submitted to a strong collisional mixing and can thus be considered in thermal equilibrium with the free electrons at the temperature T_e, according to equation (5.13). Moreover, the energy gap between each of these levels and the $Z + 1$ ion ground level is small and the thermal motion of the free electrons provides recombination and ionization at a rate which also makes up equilibrium at this spot. As for the populations of intermediate levels, they have to be calculated from radiative and collisional atomic cross-sections. One commonly use the collisional-radiative model (CRM) [37], illustrated in Figure 5.4, that represents the "thermal band," consisting of a large number of high-lying levels, above deeper intermediate levels. For these last one assumes the difference between ionization and recombination rates to be negligible compared to excitation or de-excitation by free electron collisions as well as radiative decay rates. Hence the corresponding set of population rate

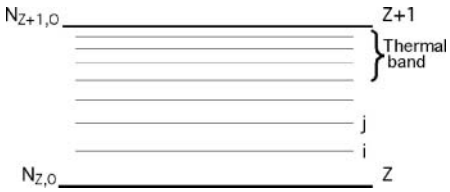

Fig. 5.4. Model of the thermal band: For the higher excited levels, populations are assumed to be in thermal equilibrium and they obey Boltzman's statistic. For all other levels the populations are calculated by solving the rate equations.

equations may be written as

$$\frac{dN_i}{dt} = \sum_{j>i} N_j A_{ji} + n_e \sum_{j\neq i} N_j < \sigma_{ji} v > -N_i \left[\sum_{j<i} A_{ij} + n_e \sum_{j\neq i} < \sigma_{ij} v > \right] \tag{5.16}$$

where $< \sigma_{ji} v >$ is the cross-section of collisional transitions from level j to level i, averaged over the Maxwellian electron velocity distribution. Moreover Saha relation (5.14) may be modified as follows:

$$\frac{N_{Z-1,0}}{N_{Z,0}} = \delta \frac{1}{2} \frac{g_{Z-1,0}}{g_{Z,0}} n_e \left(\frac{h^2}{2\pi m_e kT} \right)^{3/2} \exp \frac{I_z}{kT} \tag{5.17}$$

where δ is an adjustable parameter that can be fixed from the results of the hydrodynamical code describing the plasma state (see for instance [38]. Equations (5.15), (5.16), and (5.17) form the frame of the time-dependent radiative collisional model. If population variations can be considered as slow as compared to the atomic relaxation times, one can replace the dN_i/dt's by 0 in equation (5.16). Then the populations are simply obtained by solving a system of linear equations which defines the quasi-steady-state (QSS) model.

This summary does not aim at replacing the structured body of computational simulations involving hydrodynamics and atomic physics that is essential to accurate investigations about lasing in specific conditions. It should just help the reader to have a general view of the plasma properties involved in X-ray laser experiments.

5.2 X-Ray Laser Configurations

5.2.1 X-Ray Lasers Pumped by Lasers

As we have already seen (Fig. 5.1), the main components of an X-ray laser are the target, the pump (or driving) infrared or visible laser, and a cylindrical focusing optics. For years, lasers dedicated to plasma inertial confinement research were the only ones able to supply the power required to pump XUV

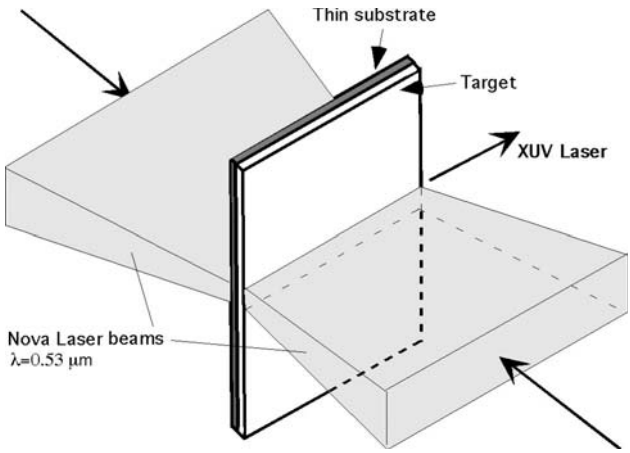

Fig. 5.5. X-ray laser exploding foil configuration (Laser NOVA, LLNL, USA).

lasers. They were pulsed Neodymium-glass lasers emitting radiation pulses of very high energy at 1.6 μm. This wavelength could be doubled or tripled by nonlinear conversion in crystal.

Their characteristics, such as beam size, number of available beams, pulse duration, repetition rate, pumping radiation wavelength, although shaped to the requirements of confinement physics, dictated the general features of XUV laser configurations. It is a fact, for instance, that the pump laser has the largest part in the global size of XUV laser setups: its structure fixes the number and the size of beams to be focused onto the target and therefore the main characteristics of the focusing optics. Beyond the example of the simple one-beam configuration of Figure 5.1, Figures 5.5–5.9 will present a set of typical configurations developed in the vicinity of different large laser

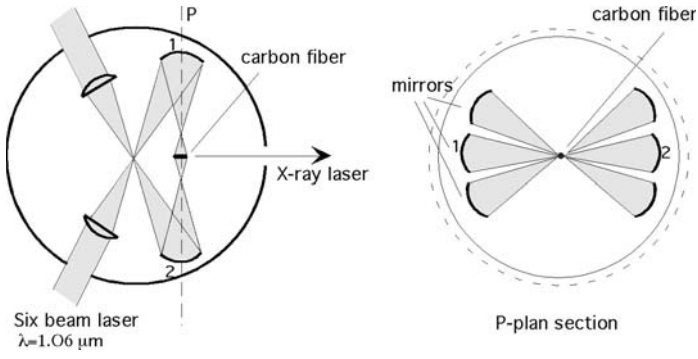

Fig. 5.6. Six beams configuration providing a symmetric irradiation of a carbon-fiber target (Laser Vulcan, RAL, UK).

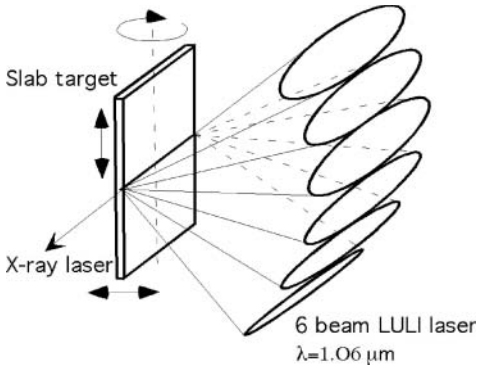

Fig. 5.7. Six beams configuration allowing for fast changes of the focused impact spot by driven translation of the slab target (LULI, France).

facilities and with various choices of target illumination schemes. The reader should remember that laser–plasma interaction takes place in vacuum chambers, which will not be represented in the figures.

Figure 5.5 exhibits the exploding foil configuration scheme which has been used successfully for years at Lawrence Livermore National Laboratory (USA)[39, 40]. The use of two opposite beams aims to increase the energy that can be deposited on the target surface. This reduces the random illumination nonuniformities which can affect each beam separately and produces plasma density smoother than by using one-side illumination. Considering the transverse size of the Nova laser beams ($\Phi \gtrapprox 70$ cm), an opposite beam configuration also results in a relatively compact target–laser interaction area.

Two irradiation geometries are possible, either opposite beams irradiating the same target area, as shown in Figure 5.5, or slightly deflecting one beam in the horizontal plane in order to increase the plasma fiber length. Opposite beams configuration obviously requires the use of a thin foil target, which will be burnt-through by the laser impact during the hot plasma formation. The plasma length can vary from ∼1 mm to ∼20 mm. The thickness of the thin target layer is of the order of 100 nm. The pump-laser pulse-length is ∼450 ps with a minimum time interval between successive shots of 1 hr. The

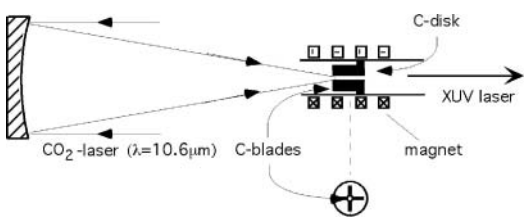

Fig. 5.8. Axial configuration with magnetic confinement of a carbon plasma (Princeton University).

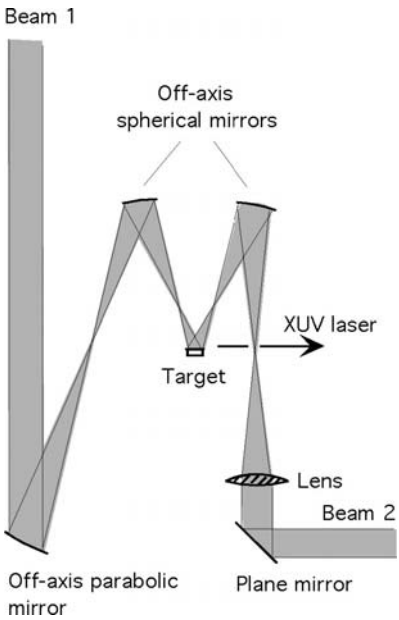

Fig. 5.9. In the configuration represented in the figure, a delayed shorter (beam 2) pulse heats the plasma produced by a longer pulse (beam 1); phase variation across the beam 2 generates a traveling wave which provides transient pumping.

typical incident intensity at 0.53 μm wavelength is about $5 \times 10^{13}\,\mathrm{W/cm^2}$. This system allowed the first demonstration of high XUV gain at 20.63 nm and 20.96 nm in Se neon-like ions [40]. A similar configuration has been used at Centre d'Etudes de Limeil-Valenton (France) with the laser Phebus [41].

Figure 5.6 displays the quite different target illumination scheme developed at Rutherford Appleton Laboratory (G.B.). The Vulcan laser of R.A.L includes six beams of ∼10 cm diameter, each of them delivering up to ∼250 J per pulse. The pulse length can vary from 50 ps to more than 1 ns. The focusing scheme makes use of the astigmatism of tilted mirrors. Each beam is primarily focused near the diffraction limit with an aspheric lens. Then each beam is reflected by a tilted mirror, which focuses it along a perfectly straight line in the incidence plane [42]. Lenses and mirrors are disposed in such a way that the six focal lines are superposed. The line focus length can be modified by changing the mirror tilt angle. One sees that this system is suitable for symmetrical irradiation of thin fibers of lasing material. With small modifications it can also be used with slab targets.

At L.U.L.I. (France) the Nd-glass laser uses six beams of 9 cm diameter. For 600 ps pulses the total output is about 500 J per pulse. As shown in Figure 5.7, six beams are focused onto one and the same side of a slab target [43]. The beams enter the target chamber with 18° angular separation. Focusing

is obtained thanks to a combination of spherical and cylindrical lenses. This configuration keeps the target back room free, which allows for the implementation of a system able to quickly position a fresh portion of a slab target between successive laser shots.

The configuration of Figure 5.8 is an exception to the common use of transverse focusing of Nd-glass lasers. A CO_2 laser beam ($\lambda = 10.6$ μm) is here axially focused onto a solid or gaseous target by a 2.84 m focal length NaCl lens [44]. A solenoidal magnet surrounds the target chamber in order to confine the plasma with a magnetic field up to 90 kG. This arrangement has been specifically designed to investigate laser emissions following the fast recombination of rapidly cooling plasmas.

One of the most recent developments of XUV laser pumping techniques is presented in Figure 5.9 [45]. This configuration includes two beams with the same tilted focusing mirrors as those of Figure 5.6. However the role of the beams is now different. Only one beam, on the right of Figure 5.6, is used to produce the plasma with a long pulse of 280 ps duration. The left beam carries a short 1.3 ps pulse, which serves to heat the plasma very rapidly. As the heating pulse is much shorter than the radiation propagation along the plasma fiber (∼30 ps), the heating efficiency is strongly optimized when a phase difference is introduced, across the beam, creating a traveling wave with a velocity nearly that of light. Production of population inversion and XUV beam transit may therefore be synchronized for the benefit of amplification in each point of the plasma. The physics involved in this transient collisional–excitation pumping scheme (TCE), which considerably reduces the necessary pump energy, shall be presented in Section 7.4.

5.2.2 Multiple Target Systems

Two factors limit the maximum length of targets. One is the fact that the plasma density gradient, which is perpendicular to target surface (see Fig. 5.2), generates a refraction index gradient in the same direction. Hence the XUV laser beam is bent toward vacuum and is finally carried away from the amplifying zone. In the case of slab targets, according to the various shot parameters, this results in a propagation length limited to 1–2 cm. The second limiting factor is the fact that any lengthening of the target increase implies an equivalent increase of pump energy, in order to keep the heating intensity constant along the plasma line.

For nanosecond pulses the minimum energy necessary to achieve collisional pumping is of the order of 500 J/cm and goes up to several kJ/cm for high Z elements. Considering the potential of Nd-glass lasers, this means that the target length should generally remain below ∼2 cm. This limit may be short to reach the saturation of XUV laser emission. To overcome these limits one designs configurations that combine several targets.

Figure 5.10 displays the diagram of the refraction-compensating double target system [46, 47]. It aims to couple the plasma output of the first plasma into the second plasma. The distances d and d' and possibly a small angle θ

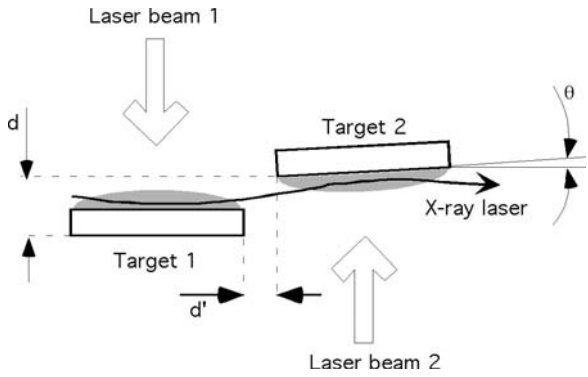

Fig. 5.10. Refraction-compensating double target system.

between the targets must be carefully adjusted in order to optimize plasma coupling. Furthermore owing to the time of XUV beam propagation from target 1 to target 2, the laser beam 2 must be delayed by a few tens of picoseconds with respect to the laser beam 1.

Instead of using two successive targets one can achieve two successive passes on one and the same targets by reflecting the XUV laser radiation with a multilayer mirror, as shown in Figure 5.11 [48]. The distance between the end of the target to the mirror must be less than $\sim$10 mm in order that the reflected beam reach the plasma before the amplification duration is terminated. This system works only in the case of "long" pumping pulses, let us say $\gtrsim$0.5 ns, for which it considerably increase gain length and spatial coherence of XUV emission, without increase of pump energy (see Sections 7.2.2 and 7.3.2).

A further development consists in making an oscillator–amplifier system by coupling either two single targets [49] or two double targets as shown in Figure 5.12 [50, 51]. The radiation of the oscillator is transferred to the amplifier by a concave mirror which conjugates the exit of the oscillator with the entrance of the amplifier. The fringe pattern of wires crossing the beam at the exit of the system shows the fringe visibility to be largely enhanced when the amplifier is brought into use.

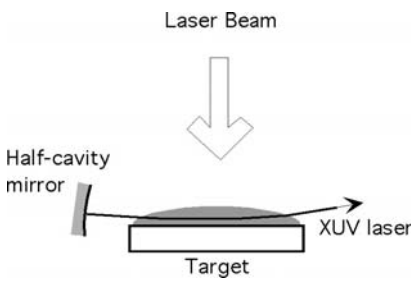

Fig. 5.11. Half-cavity configuration.

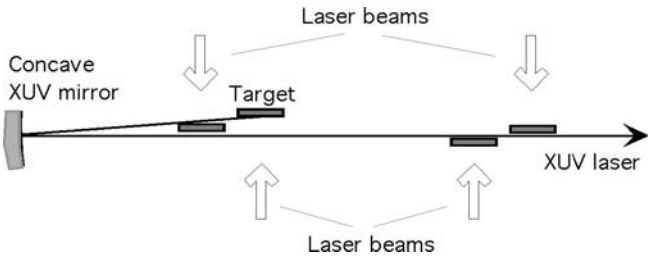

Fig. 5.12. Coupling of two double-targets.

Refraction may also be offset by using a curved target as shown in Figure 5.13. Considering for instance an exponential electron-density profile from target to vacuum, the plasma may then behave as a wave guide for the XUV laser beam. As a matter of fact, experiments show that a concave target increases the intensity and reduces the divergence of the beam [52].

5.2.3 Optics for the Production of Line Focused Plasmas

The simplest technique to obtain a line focus consists in using a cylindrical lens with either a spherical lens, or a second cylindrical lens, as shown in Figure 5.14. In this figure, only the horizontal focal line is represented for each system. However, one could also use the nonrepresented vertical focal line situated at a somewhat larger distance from the lenses. In the case displayed in Figure 5.14a, the focal line length may be varied by changing the cylindrical lens. For a pair of cylindrical lenses (Fig. 5.14b), the length may be varied by changing the distance between the lenses. When their distance has been modified, the lenses must be refocused. The intensity at any point of the line focus is the integral of the intensity along a vertical chord of the circular beam cross-section. Therefore a weak point of these systems is that the focused intensity varies, from one side to the other one, as does the corresponding chord length

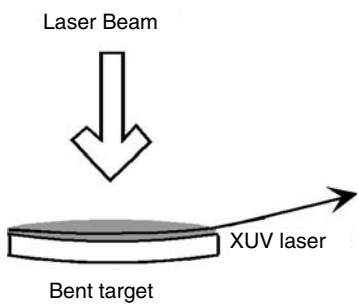

Fig. 5.13. Concave target used to maintain the amplified beam in the high-gain region of the plasma.

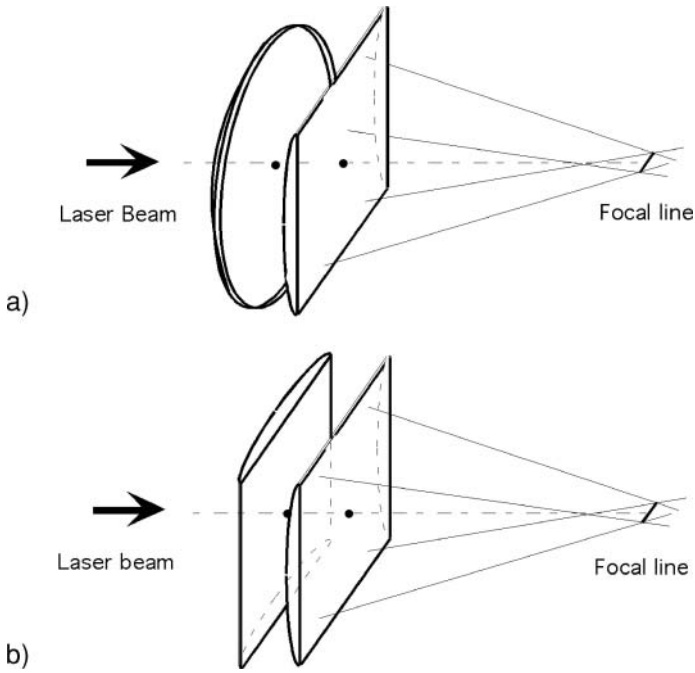

Fig. 5.14. Lens combinations used to produce linear plasmas.

across the beam. Hence the irradiation has a maximum at the center of the line and drops to zero at the ends. Furthermore the transverse nonuniformities of the beam are reproduced along the line.

Line focus lighting uniformity may be largely improved by using segmented optical elements such as shown in Figures 5.15 and 5.17. The segmented wedge array (Fig. 5.15) consists of a cylindrical lens and an array of wedges each of which displaces the beam so that the resulting set of line foci come to be superimposed to each other [53]. This results in averaging the unequal contributions of each wedge and, to some extent, the local beam nonuniformities.

The line focus length l, obviously equals the wedge width. Thus it is necessary to change the wedge array when one wants to change l. For a beam of diameter D, the maximum number of segments is $N = D/l$. Figure 5.16 displays calculated intensities assuming a uniform circular beam and various numbers of wedges. One sees that 10 wedges ensure an almost constant irradiation along a line focus of length 1.

In the lens array system the optical wedges are replaced by identical cylindrical lenses [54]. Figure 5.17 (from Ref. [55]) shows the diverging cylindrical lenses that stretch the point focus of the spherical lens along a linear segment. As above, the resulting line foci merge into one another thus forming the line focus of the system. For a spherical lens of given focal length, the parameter that fixes the length of the line focus is now the cylindrical lens optical

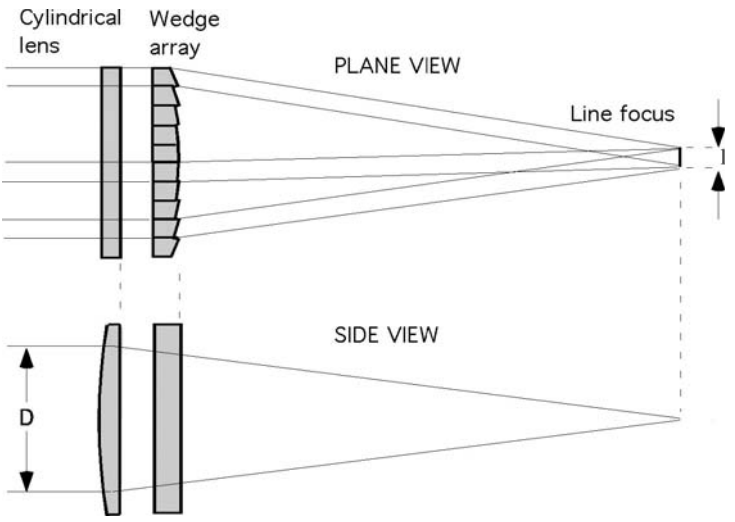

Fig. 5.15. Combination of cylindrical lens and wedge array used to produce linear plasmas. The length of the line focus l, equals the wedge width. For N wedges a line focus of length l is obtained with a beam of diameter $D = Nl$.

aperture A. Let w and F_{cyl} be the width and the focal length of the lenses. The relevant parameter then reads $A = w/F_{\mathrm{cyl}}$ and the length of the line focus is $l \sim AF_{\mathrm{sph}}$, i.e. $l \sim w \times F_{\mathrm{sph}}/F_{\mathrm{cyl}}$, where F_{sph} is the spherical lens focal length. Therefore the line focus length does not depend on the beam diameter and it can be changed by simply choosing another spherical lens. Moreover the number of cylindrical lenses has no theoretical upper limit.

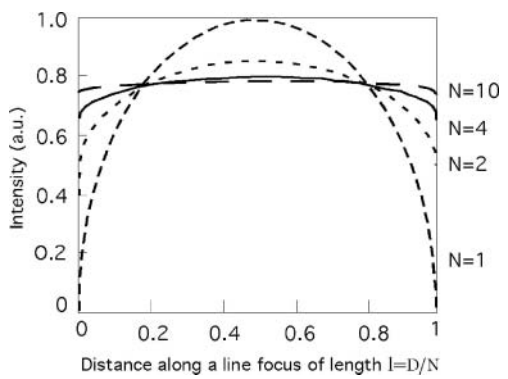

Fig. 5.16. Intensity along the line focus for several values of the number of wedges (the intensity of the incident beam is constant within the limits of the beam diameter D). One sees that an excellent uniformity could be obtained using wedges of width $D/10$.

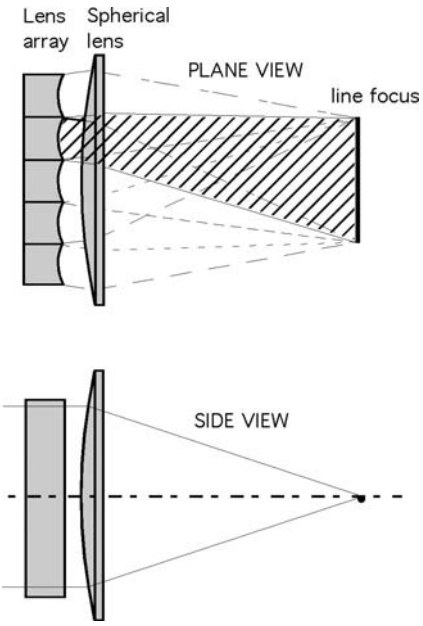

Fig. 5.17. Combination of cylindrical lens array and spherical lens. The spherical lens makes the line foci coming from each cylindrical lens to merge into one another and to form the line focus of the system.

5.2.4 Capillary-Discharge XUV Laser

The fast-discharge excitation of hot plasmas produced in capillary, proposed and demonstrated by J.J. Rocca, represents to this day the only exception to the configurations based on driving lasers. An example of the calculated properties of a plasma produced in capillary is displayed in Figure 5.18 (Ref. [56a]. The circuit characteristics are a capacity of 0.15 nf charged to 700 kV, with an inductance of 0.1 nF. The discharge is assumed to be produced in vacuum, in polyethylene capillaries 2 cm in length and 100 μm in diameter. The hydrogenic carbon plasma is produced by atoms extracted from the capillary wall and then heated by the discharge current. The power pulse duration is of 12 ns. Calculation predicts that, when the current pulse decreases, the fast cooling of the plasmas generates population inversions between the levels of the C^{5+}-ions, similarly to what occurs during the adiabatic expansion of laser produced plasmas (cf. Section 4.2). Figure 5.18 shows the resulting peak of gain to appear about 12 ns after the outset of the discharge.

It is important to observe that electron heating is somewhat faster than ion heating during the pulse increase. These circumstances favor the population of highly excited ion levels.These populations, larger than equilibrium values, nearly reach population inversions. However, the characteristics of the discharge shown in Figure 5.18 do not quite suffice this goal. That is why

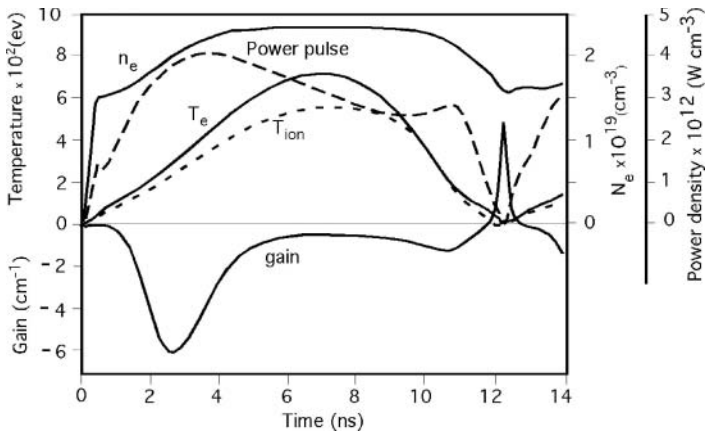

Fig. 5.18. Calculation of capillary discharge parameters, which shows gain to be produced by the C^{5+} ions extracted from the capillary wall. The gain peak occurs 12 ns after discharge outset, i.e. during the plasma cooling (Ref. [56a]).

vacuum discharge is replaced by gas discharge with the result that the plasma can be separated from the capillary wall (Ref. [56b]). The pinch effect due to the self-generated magnetic field increases the electron density and reduces the heat losses due to electron conduction towards the wall. The discharge is stabilized by gas pre-ionization. These techniques prove very efficiently to pump neon-like argon, whose main XUV lasing line is at a wavelength of 46.9 nm [57].

The principle of the fast-discharge arrangement is illustrated by Figure 5.19 [58]. The typical size of the plastic capillary used for large gain production is 12 cm in length and 4 mm diameter. The amplitude of the current pulses is a few kA. The XUV laser emission duration is of several ns. The energy per XUV pulse is one order of magnitude less than with using ns-laser pumped XUV lasers but the repetition rate is 2–3 orders of magnitude larger. Moreover the XUV beam emitted by this laser proves to exhibit a very large coherence. However, the present limit of capillary discharge lasers lies in the difficulty to extend them to new wavelengths. Details on the achievements realized with these lasers are presented in Section 7.5.

5.2.5 XUV Laser Cavity Issues

From the beginning, designing laser cavities has been considered as a difficult challenge [59–61]. Before the advent of multilayer mirrors, the only reflection techniques were grazing incidence mirrors and Bragg reflection. A number of successive reflections were then necessary to close the radiation path, especially when using grazing incidence mirrors. This would lead to large radiation losses and propagation times larger than plasma amplification duration.

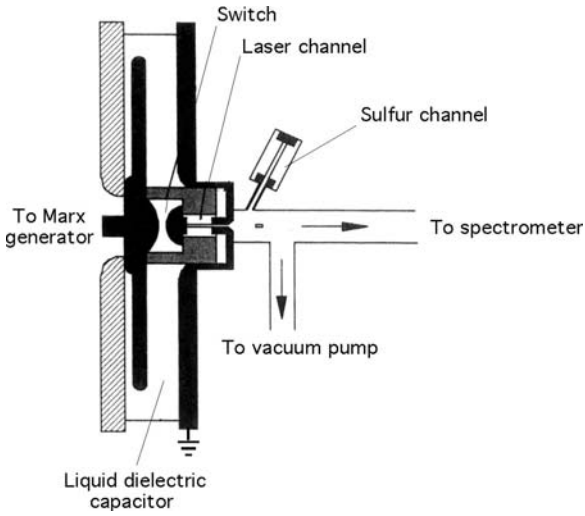

Fig. 5.19. Principle of fast capillary discharge arrangement (from Ref. [56b]).

Multilayer mirrors brought about a very important progress in XUV optics by restoring near normal incidence reflection in optical components (see for instance [62]). The fact that the reflection coefficient of multilayers (15–70% according to the wavelength) remains much weaker than usual visible coefficients is much less of a problem than grazing incidence inadequacy.

The efficiency of multilayer mirrors in XUV laser techniques is illustrated by the early result shown in Figure 5.20 [63]. The 10.57-nm line of Li-like alumnium has been found amplified with a gain coefficient $\sim$0.8 cm^{-1} in a 20-mm long plasma fiber. The bottom curve in Figure 5.20 shows the experimental line profile at the exit of the plasma fiber. As for the top curve, it shows the numerically simulated intensity enhancement of the line after reflection on a mirror of 15% reflection coefficient and a second pass through the plasma, as shown in Figure 5.21. Notwithstanding the relatively small reflection coefficient, one sees that the multilayer mirror increases the line intensity by a factor $\sim$1.8.

An elementary calculation of this type of effect can be made from equation (1.4), which is now rewritten as follows:

$$I = S\left(e^{gl} - 1\right) + I_0 e^{gl} \tag{5.18}$$

where l is the plasma length and g the gain coefficient. Let I_{single} and I_{double} be respectively the single- or double-pass intensity, and R the reflection coefficient of the mirror. The intensity of the radiation reaching the mirror is obviously

$$I_{\text{single}} = S\left(e^{gl} - 1\right)$$

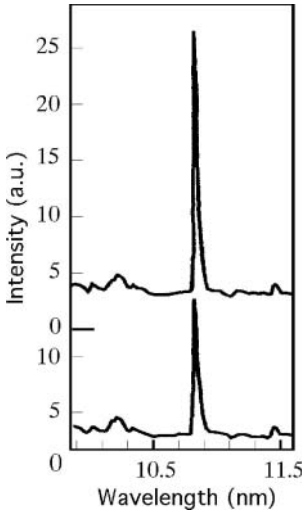

Fig. 5.20. Bottom curve, 10.5-nm wavelength line of Li-like aluminium, amplified in a 20-mm long plasma with gain coefficient of 0.8 cm^{-1}. Upper curve, numerical simulation of the line intensity enhancement after reflection on a mirror of 15% reflection coefficient and a second pass through the plasma (see Fig. 5.21).

Hence the external intensity I_0 (see Fig. 5.21) of equation (5.18) reads

$$I_0 = R.S\left(e^{gl} - 1\right)$$

and the total emerging intensity

$$I_{\text{double}} = S\left(e^{gl} - 1\right)\left(1 + Re^{gl}\right) \tag{5.19}$$

For $R \gtrsim 0.05$ and $gl \gtrsim 5$ this expression may be written in the form

$$I_{\text{double}} \simeq Se^{(2gl + \ln R)} \tag{5.20}$$

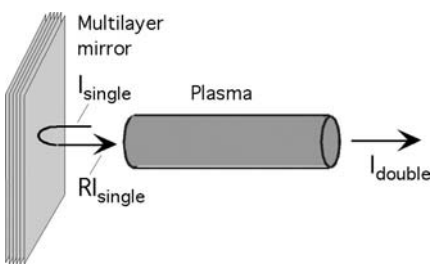

Fig. 5.21. Amplification by double pass in the plasma fiber. I_{single} points the single pass intensity. R is the mirror reflection coefficient. Reflection on the mirror returns the intensity RI_{single} to the plasma. I_{double} is the intensity which results from the second pass.

which allows us to define the effective gain × length product

$$(gl)_{\text{eff}} \simeq 2gl + \ln R \tag{5.21}$$

Even for small signal gain ($gl \simeq 3$) and a weak reflection coefficient ($R \simeq 0.05$) the increase in intensity, $I_{\text{double}}/I_{\text{single}} = 1 + \text{Re}^{\text{gl}}$, is about factor of 2, which is easily measurable. Thus a multilayer mirror may be used as a simple tool for diagnosing small plasma laser emission. For large gain ($gl \gtrsim 8$) intensity increases by more than 100 and the laser emission rapidly comes to saturation [48, 64]. We shall see in Section 6.3 that the spatial coherence of the radiation is also strongly enhanced. That is why the double-pass arrangement provided by one multilayer mirror is often referred to by the name of "half-cavity." Let us mention that half-cavity works in capillary discharge lasers as well [65].

The above treatment does not account for all experimental details. We assumed, for instance, the gain coefficient to be the same for the forward and the return propagation of the X-ray laser beam through the plasma. Since the plasma is pulsed, the gain coefficient generally varies during the light propagation. Let g_{f} and g_{r} respectively label the "forward" and the "return" gain coefficients. For plasma lasing durations shorter than ∼60 ps, the round trip propagation generally takes to much time for the plasma to retain any amplifying efficiency ($g_{\text{r}} \to 0$). Moreover, owing to beam divergence, as well as to a possible curvature of the mirror, R should be replaced by an effective reflection coefficient,

$$R_{\text{eff}} = RC_{\text{g}} \tag{5.22}$$

where C_{g} is the geometric coupling efficiency depending on the curvature radius, the source size and the mirror-to-plasma distance. Equation (5.21) then becomes

$$(gl)_{\text{eff}} \simeq (g_{\text{f}} + g_{\text{r}})\, l + \ln R_{\text{eff}} \tag{5.23}$$

Finally, in the nearly saturated regime, the simple intensity calculation of the mirror reflection coefficient is no longer relevant and it is necessary to resort to the amplitude of the radiation field.

Let us mention that in practical applications, given the short plasma lasing duration, the half-cavity mirror must be set at distance less than ∼1 cm from the plasma. At such a short distance the laser–plasma interaction damages the mirror, either by ion projection or by intense radiation scattering. A shield with a small aperture, placed between plasma and mirror, limits the damaged area to a narrow spot of the order of 1 mm^2. Mechanical devices are used to move the mirror in order to set a clean surface in position after each laser shot.

The only physical impediment to the implementation of complete cavities remains the wrong ratio between multiple radiation passes and laser emission durations. In the case of nanosecond pumping pulses and 1-cm long plasma fibers, for instance, one has to compare the time necessary to one pass through

the cavity, $t \sim 33$ ps, to the 50–100 ps plasma lasing duration. Those conditions roughly correspond to the requirement of the double-pass technique, but not to a complete cavity as it has been confirmed by comparing double- and triple-pass intensities of neon-like selenium lasing lines [66]. Using shorter pumping pulses gives shorter lasing duration, the gain coefficient being possibly enhanced. One could, for instance, consider a 2-mm long plasma fiber with a gain coefficient of about 20 cm^{-1}, and a 3-mm long cavity in which the one-pass duration is 9 ps. Then, providing that plasma lasing action lasts ~40 ps, an efficient quadruple-pass amplification could be achieved.

5.3 Diagnostics of X-Ray Laser Media

Information about plasma parameters such as ion and electron temperatures, electronic density, ionization balance are of first importance to understand and to exploit the mechanisms that are able to drive population inversions. In principle most of this information can be deduced from plasma radiation, especially from X-rays and XUV radiation. K-shell and L-shell spectra of elements, analyzed by using the QSS model, are generally well adapted to the requirements of temperature and density diagnostics. In addition line broadening by Stark and Doppler effects is also information source on density and temperature. In amplifier plasmas, parameter values vary as a function of space and time. Therefore X-ray imaging and X-ray spectroscopy are the specific tools of laser plasma diagnostics. In the next paragraphs we shall illustrate this fact by examples that are mostly typical of situations encountered in collisionally pumped lasers.

5.3.1 Plasma Imaging

A simple means of obtaining X-ray images of extended sources is the well-known pinhole camera equipped with filters which are selected according to the radiation band of interest. One can choose to look at line or continuous radiation, or both, according to the desired diagnostic. For instance, the temperature generally varies along the line focus owing to the nonuniformities of the light distribution in the pump–laser beam and to the characteristics of focusing optics. Comparing plasma images in several radiation bands of the continuous spectrum provides information about electron temperature.

The elongated shape of the amplifier plasma requires the pinhole technique to be adapted in order that magnification be much larger in transverse direction than along the longitudinal axis. This is done by replacing the pinhole by two crossed slits as shown in Figure 5.22 [67]. An example of intensity distribution measured along a 1-cm line of copper plasma with the help of such a double-slit camera is displayed in Figure 5.23 [68]. The plasma line was produced by a cylindrical lens array focusing a 100 ps–1.5 J laser beam onto the target (see Section 5.2.3). The strong modulation observed at both ends are

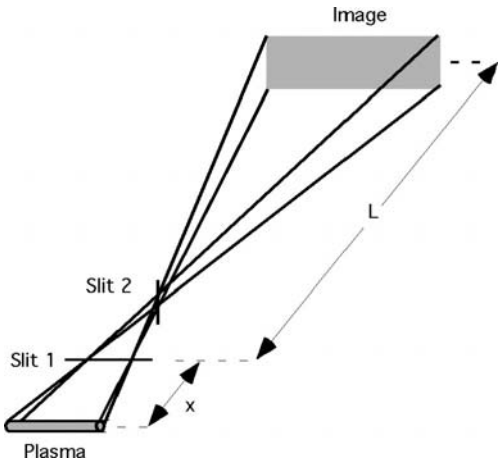

Fig. 5.22. Principle of a crossed-slits pinhole camera for elongated plasma imaging.

attributed to Fresnel diffraction by the edges of each of the cylindrical lenses. The transverse measurement showed a less than 50-μm wide plasma.

A number of devices, that combines pinhole and crystal spectrometry, can be proposed to produce monochromatic plasma images. Johann geometry, based on Bragg's reflection of a cylindrical bent crystal, becomes suitable for monochromatic X-ray imaging when a pinhole is placed on the Rowland circle and a 2D-detector near the crystal, as shown in Figure 5.24 [69].

Figure 5.25 exhibits an example of plasma electron-density determination performed by using this technique [70]. Two monochromatic, 2D spatially resolved images of an aluminium line-focused plasma have been recorded on the same laser shot with two different spectrometers. The detection windows are 0.774–0.779 nm and 0.778–0.783 nm respectively, what corresponds to the He_α

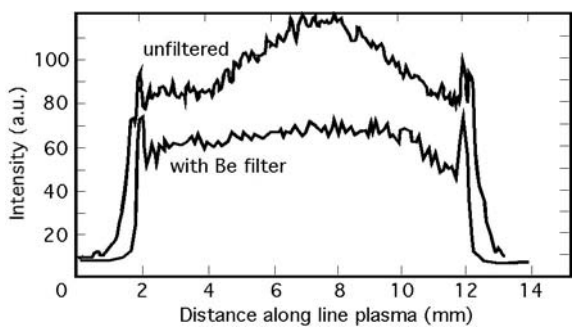

Fig. 5.23. Intensity distribution along a copper plasma fiber measured with the double slit camera. The laser intensity is 3.10^{12} W/cm^2, the pulse duration, 100 ps. The thickness of the beryllium filter is 14 μm.

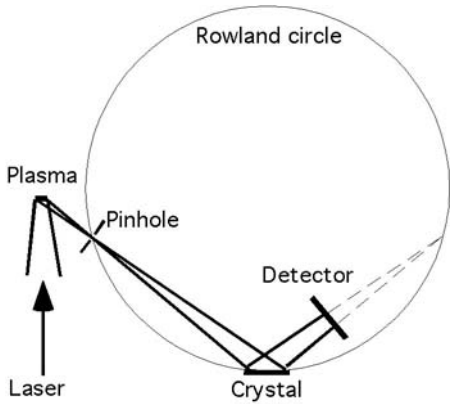

Fig. 5.24. Bent crystal lighted from a pinhole placed on the Rowland circle to obtain monochromatic X-ray images of a plasma fiber.

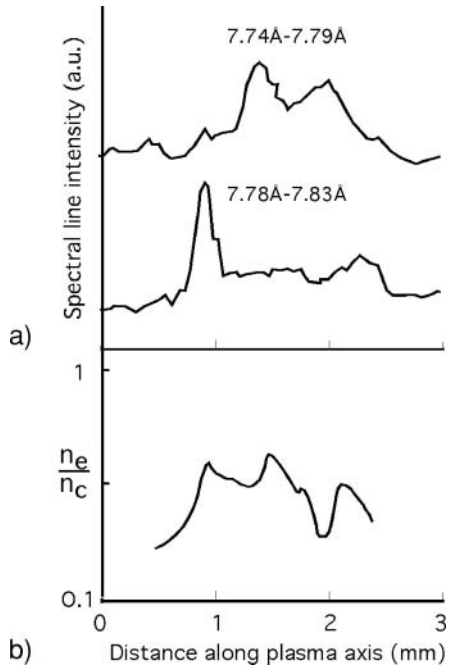

Fig. 5.25. (a) Traces obtained at two wavelengths for the same laser shot, from images of the plasma fiber provided by two spectrometers arranged as shown in Fig. 5.24. (b) Distribution of the (normalized) electron density deduced from the data supplied by the curves of Fig. 5.24a.

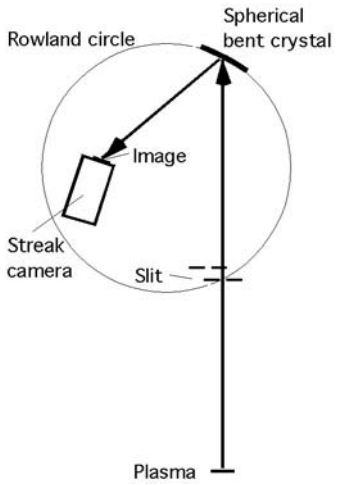

Fig. 5.26. Imaging spectrometer according to Ref. [71]. The wavelength of the monochromatic image can be changed by moving the crystal.

resonance line ($1s^2$–$1s2p^1P_1$), on one hand, and to the He_α intercombination line ($1s^2$–$1s2p^3P_1$), on the other hand. From these data one infers the map of the resonance-to-intercombination line-intensity ratio at each point along the plasma axis. The map is interpreted in terms of plasma electron density—and corresponding plasma ionization—with the help of a QSS–CRM code [cf. Eqs. (5.15)–(5.17)] that calculates the excited level populations from rate equations. The bottom curve in Figure 5.2 shows a time-integrated, 1D distribution curve of the electron density, normalized to the critical density n_c (Eq. 2.19). The critical density is about 10^{21} cm^{-3} for the Nd-glass laser radiation used to produce the plasma in this experiment. The observed nonuniformity of the density is admittedly correlated to local laser intensity fluctuations, a greater density corresponding to a higher intensity.

Instead of pinhole-formed images, one can obtain monochromatic focused images by using a spherical bent crystal as analyzer. Figure 5.26 displays the scheme of an experimental setup that uses a spherically bent quartz of 888.8 mm curvature radius, in the $(1, 0, 0)$ reflection with $2d = 0.85096$ nm [71]. The image of an aluminium line-focused plasma, placed at 1450 mm from the target, is projected onto the photocathode of a streak camera in order to achieve spectral, spatial, and temporal resolution on one and the same laser shot. Choosing the 0.77566 nm wavelength of the He_α resonance line of aluminium fixes the value of the Bragg angle at 65.716°. It is necessary to move the crystal as shown on the figure to change the wavelength. Figure 5.27 illustrates the results one can achieve by this technique. It shows the temporal history of the Al He_α resonance emission from a 20 mm long line-focus plasma produced by a ∼50 J, 600 ps laser pulse. The corresponding

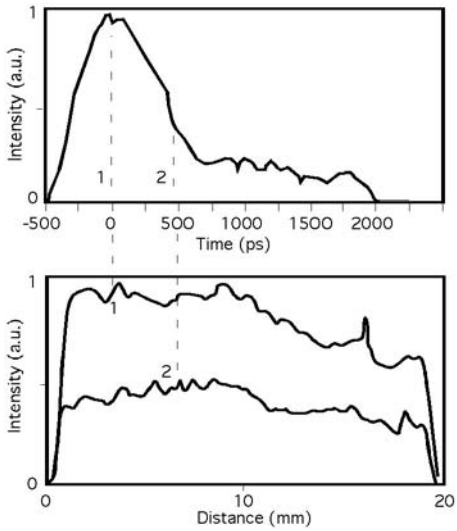

Fig. 5.27. Temporal history and spatial distribution of the He_α-line of aluminium emitted from a plasma fiber of 20-mm in length obtained thanks to the spectrometer setup represented in Fig. 5.26. The dashed vertical lines points the instants corresponding to each one of the spatial curves.

spatial profiles at two different times are also displayed at the bottom of the figure.

5.3.2 Temperature and Density Diagnostics

Electron densities are commonly measured by standard interferometry techniques which exploit the relation between plasma refraction index and electronic density [see Eq. (5.2)]. The upper-limit of the density which can be observed by this method is fixed by the propagation cut-off at the critical density n_c, which is of the order of 10^{21} free electrons per cubic centimeter when using visible light. Beyond this limit UV and XUV radiation should be used. One can also employ the noncoherent radiation method that consists in measuring the fringes created by Moiré deflectometry using two almost parallel Ronchi rulings [72, 73].

X-ray spectroscopy is one of the most efficient tools of ionization balance, temperature, and density diagnostic. An obvious feature of relations between experiments and calculation models is the fact that computed spectra are as necessary to interpret the observed spectral line intensities in terms of plasma parameters as experimental spectral data are essential to check and validate the calculation models. Thereby plasma diagnostics make use continually of well-characterized experiments to test and improve the models, on one hand,

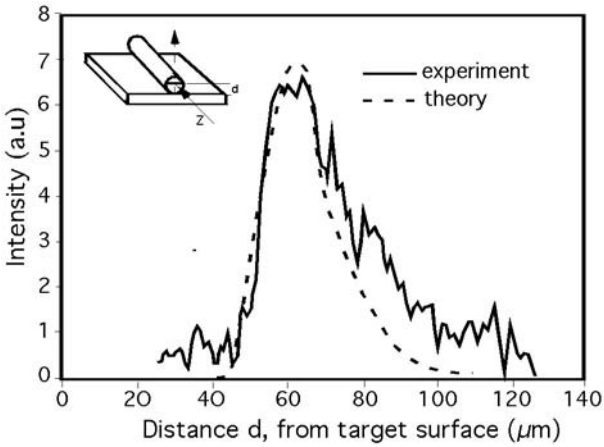

Fig. 5.28. Measured and computed emission profile of Ge as a function of the distance to the target. The observation axis is parallel to the plasma fiber at a variable distance *d*, from the target, as shown in the inset. This experiment aims to improve the line opacity model used to estimate the ion balance in the plasma.

and of validated models to obtain quantitative plasma parameter values from spectroscopic experimental data, on the other hand.

Let us start with the example of experiments designed to test the atomic physics coupled to a hydrodynamic code, known as EHYBRID [74]. The idea is to introduce in the code, the resonant emissions of neon-like and fluor-like ions of germanium, whose balance plays an important role in collisionally pumped lasers. This can be done by investigating the role of the resonant line opacities [75]. The germanium spectrum of a plasma fiber is thus observed between 0.7 nm and 1.05 nm using a curved KAP crystal spectrometer. The detector is a CCD camera protected from visible light by a 25 μm thick Be filter. A pinhole camera monitors the spatial variations of the integrated resonant emission versus the distance from the target. Comparison of experimental and theoretical spectra shows the relative intensities of the lines to be very sensitive to the opacity model introduced in the QSS calculation (cf. Section 5.2.1) performed by EHYBRID. Finally, as shown Figure 5.28, one can obtain a good agreement between observed and computed germanium transverse emission profile as a function of the distance to the target.

Here is now an example of the inverse process. The goal is to measure electronic density and temperature of a 2.2-cm long selenium X-ray laser plasma as a function of time, during the nanosecond pulse of the driving laser [76]. To begin with, a QSS collisional–radiative model is built to calculate the intensities and the line ratios of the neon-like resonance lines and of their dielectronic satellites. A simplified scheme of the model, which includes more than 200 levels, is shown in Figure 5.29. Collisional rates are calculated assuming

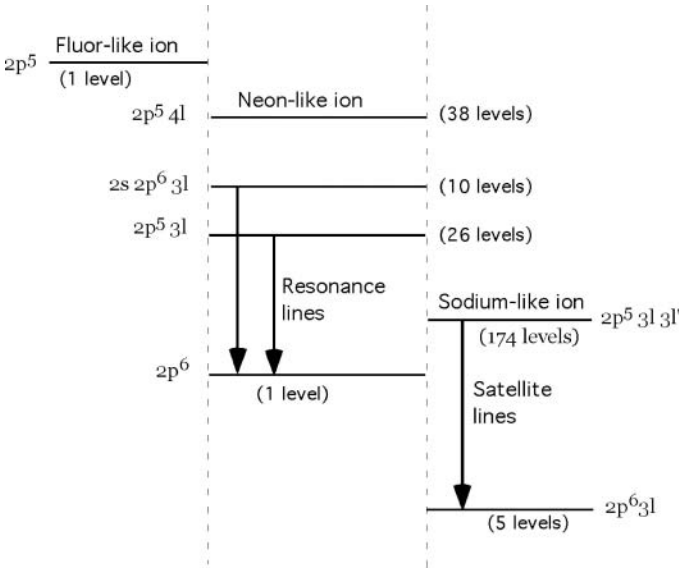

Fig. 5.29. Simplified diagram of a 200-level model used to calculate the intensities of the selenium Ne-like resonance lines and their satellites.

a Maxwellian distribution of free electrons. Collisional ionization, three-body recombination and radiative recombination are taken into account. Opacities are treated with the escape-probability approximation.

The experimental arrangement includes a concave crystal spectrometer equipped with a streak-camera which records time-resolved spectra. Only a few mm portion of the plasma column can be seen from the spectrograph. An example of results, shown in Figure 5.30, exhibits the spectrum emitted 550 ps after the X-ray emission outset. The diagnostic is then completed for

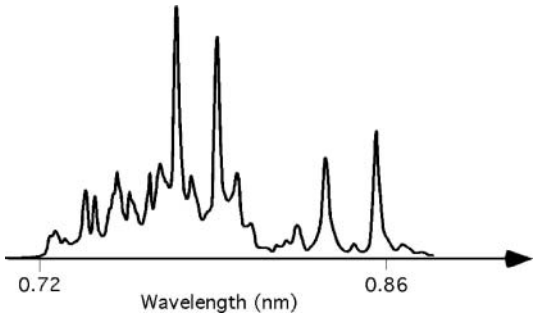

Fig. 5.30. Example of a time-resolved spectrum of the selenium Ne-like ions, experimentally observed in the wavelength region of the resonance lines, 550 ps after the laser pulse outset.

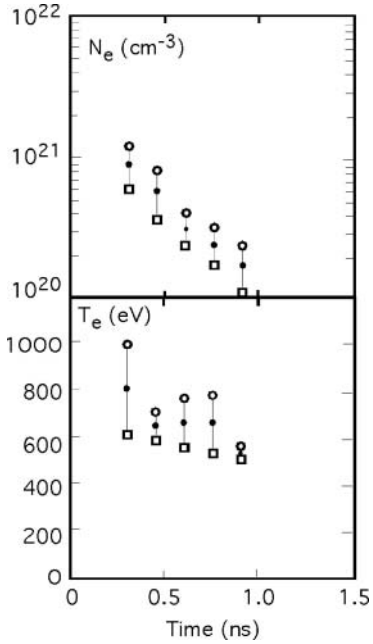

Fig. 5.31. Electron density and temperatures estimated as a function of time from the line ratios measured in the experimental spectra. Circles and squares point the ratios obtained involving or not the line pedestals.

a pair of n_e and T_e by minimizing the differences between experimental and calculated line ratios. The results are displayed in Figure 5.31. The lines being superimposed on a wide pedestal (see Figure 5.30), the zero level is successively chosen at the zero of X-ray intensity (circles) and at the intensity where the line emerge from the pedestal (squares). The distance between circles and squares represents the uncertainty of the values obtained with the help of the model.

Temperature profiles can also be measured by analyzing the K-shell emission spectra produced by a low-Z tracer material put in an XUV laser target of high Z. For the experiment reported on this subject in paper Ref. [77]. the target of the exploding foil X-ray laser (see Fig. 5.5) was an yttrium foil with a thin carbon overcoat and a plastic substrate. An Al strip provided the tracer material (Fig. 5.32).

The aluminium spectrum was recorded with a streaked flat field spectrometer, viz. a grazing incidence spectrograph provided with a variable-step grating especially calculated to form the XUV image spectrum on a flat surface, like the photocathode of a streak camera. The XUV laser gain was simultaneously measured with a second grazing incidence spectrometer. Figure 5.33 shows the example of temperature versus time for two shots for which the pump

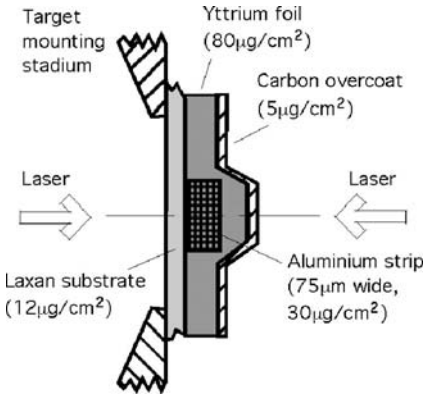

Fig. 5.32. Yttrium exploding foil target.

intensities on target were 1.1×10^{14} Wcm^{-2} and 1.3×10^{14} Wcm^{-2}, respectively. The upper curve is the result of a theoretical simulation performed with the bidimensional hydrodynamical code LASNEX. An advantage of using tracers such as aluminium is that the same experimental and theoretical analysis material can be used, with some caution, for a wide set of lasing elements, let us say from iron to zirconium in the case of Ne-like lasers.

Another way of investigating the plasma state is to turn to X-ray absorption spectroscopy. The technique of "point projection absorption spec-

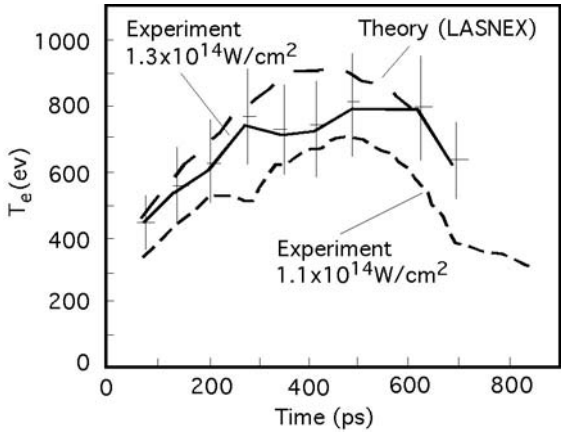

Fig. 5.33. Electron temperature as a function of time. Short dashed line: temperatures obtained with 1.1×10^{14} W/cm^2 focused energy. Continuous line: temperatures obtained with 1.3×10^{14} W/cm^2 focused energy. Long dashed line: temperatures calculated using the numerical code LASNEX. The vertical thin lines are the error bars.

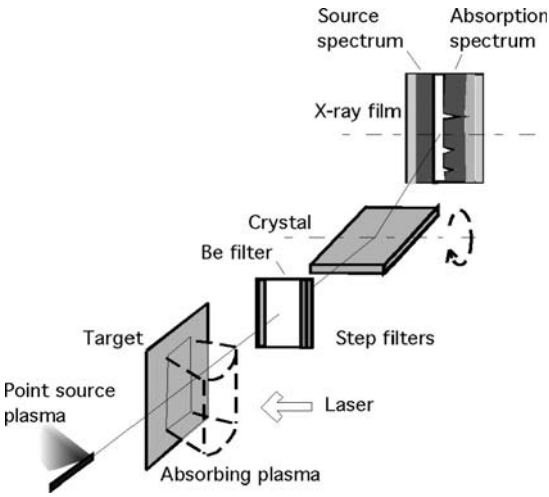

Fig. 5.34. Experimental arrangement providing spectrally, spatially and temporally resolved data on the plasma soft X-ray absorption.

troscopy," whose principle is displayed in Figure 5.34 [78], provides spatially and temporally resolved spectroscopic information. A point source (∼30-μm diameter spot) is produced by focusing the radiation of two 80-ps beams of the Vulcan laser (Rutherford Appleton Laboratory) onto uranium-coated copper wire. The probe radiation emitted from this point travels on both sides of a thin foil (or wire) target. The absorbed spectrum may therefore be compared to the source spectrum, once a plasma has been produced by laser impact on the target. The beams are configurated so that the expanding plasma can be backlighted up to times as long as 1.5 ns after the initial pulse. One obtains a set of single time frames which provide space-resolved data on the time-dependent plasma state.

Besides it has been shown that the absorption spectrum of unresolved 2p–3d lines of complex atoms of medium-Z materials can be used for diagnosing temperatures [79]. Calculation of the absorption spectra makes use of a statistical simulation of individual lines in the framework of the unresolved, spin–orbit–split transition array formalism [80]. This atomic calculation is used as postprocessor to a hydrodynamical code. The absorption spectra can be then predicted as a function of space, time, and temperature.

A very different approach of electron temperature determination consists in observing the Thomson scattering, by the plasma, of a laser-beam probe, more precisely its scattering by plasma acoustic waves (see for instance [32]. When a probe radiation of wavelength λ is scattered by acoustic waves of frequency ω_{ia}, the scattered spectrum exhibits, on each side of the central wavelength, λ, two Gaussian peaks separated by $\Delta\lambda$, such that $\omega_{\mathrm{ia}} = \Delta\lambda\, c_{\mathrm{s}}$. Now, as we have previously seen, the sound speed, c_{s}, depends directly on the

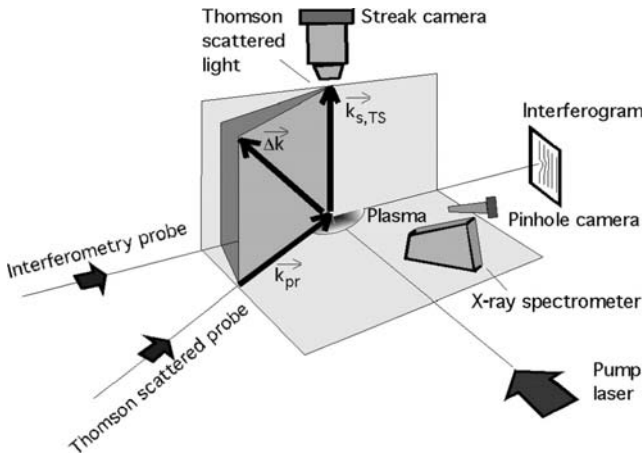

Fig. 5.35. Determination of the plasma electron temperature using the Thomson scattering of a probe beam by the plasma acoustic waves. Additional interferometric measurements give data on the electronic density.

electron temperature T_e [Eq. (5.4)]. The diagram of the experimental setup for measuring the Thomson scattering spectrum is shown in Figure 5.35 [81]. The line focus is imaged by an X-ray pinhole camera and the ionization conditions may be observed with an X-ray spectrometer. In addition interferometric measurements of the plasma give information on the electron density spatial distribution. A theoretical fit of experimental data involving parameters like temperatures, drift velocities of electrons and ions, and electron density leads to estimate T_e with about 15% accuracy.

6. Propagation of XUV Laser Beams

With the exception of using half-cavities, the only bounds to XUV laser beam propagation are those set by the gain coefficient distribution and the refraction effects within the amplifying plasma. There is no mode selection by means of the optical cavity as in most lasers. Therefore once population inversion is achieved, brightness and coherence of the laser are mostly dependent on the conditions of propagation in the plasma.

Being produced from solid targets, and expanding freely in vacuum, XUV laser plasmas always exhibit strong density gradients, especially in the direction perpendicular to laser axis. Refraction through the free electron density gradient causes ray curvature of amplified radiation [cf. Eq. (2.21)–(2.24)]. At a glance it looks like a pure mischief since it increases the beam divergence and, in the case of slab targets, it deflects the beam away from the geometric X-ray laser axis (cf. Fig. 2.3). It is a fact that, for steep gradients causing large curvature, most of the radiation can emerge from the amplifying channel before the plasma end, which reduces, or even completely prevents, laser action (the reader may find a review of works on angular divergence and spatial coherence of X-ray laser radiation in Ref. [82]).

However after more thorough investigations, the contribution of refraction to laser coherence through the selection of modes will prove more significant. This is illustrated in Figure 6.1 by the result from a pioneering XUV laser coherence investigation by R.A. London [83,84]. Calculation of the transverse coherence length L_c by a modal method (see Section 6.3) was performed for two XUV laser plasma transverse profiles. One, where gain coefficient and electronic density are spatially constant in the plasma, is represented by dashed lines in the left frame of Figure 6.1, and is obviously not a refractive profile. The second, represented by a solid line, assumes the electronic density and the gain coefficient to vary as $\sec h^2(x/a)$, where x/a is the transverse coordinate normalized to the FWHM a of the plasma profile. This profile clearly models a refractive plasma. The right frame of the figure shows the complex degree of spatial coherence γ at the plasma end [cf. Eq. (3.19)]. One immediately sees that the coherence length is found to be much larger in the case of the

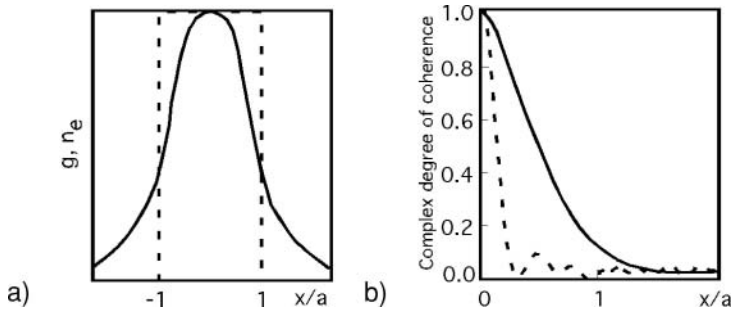

Fig. 6.1. Effect of the plasma profile on the coherence of amplified beam. Gain and electronic density are supposed to have the same spatial profiles, of width a (FWHM). Two types of profiles are represented in (a); the corresponding degrees of coherence are plotted in (b). One sees the bell-shaped profile (continuous line) to considerably increase the coherence with respect to the flat profile (dashed line).

refractive than the nonrefractive plasma profile. This result strongly supports the assumption that *refraction reduces the number of modes*. In fact, as we will see, the XUV laser beam propagation is under the control of three parameters that represent the effect of refraction, of gain, and of mode–number geometrical limit.

Considering this very important influence of refraction effects on X-ray laser quality, experimental methods have been developed to investigate the angular distribution of laser intensity. To this end one generally chooses flat-field grating spectrometers, the principle of which is shown in Figure 6.2. Unlike the standard Rowland circle system (cf. Section 2.3), the variable groove-spacing holographic grating implemented in the new system focuses the spectrum on a plane surface. Figure 6.3 gives an example of time-resolved angular distribution investigation of the XUV beam by coupling a streak-camera to the flat-field spectrometer output [85].

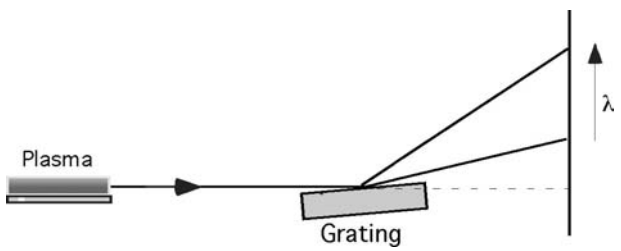

Fig. 6.2. Principle of a setup using a flat field grating. XUV radiation is focused on a flat surface unlike spherical concave gratings which focus along their Rowland circle.

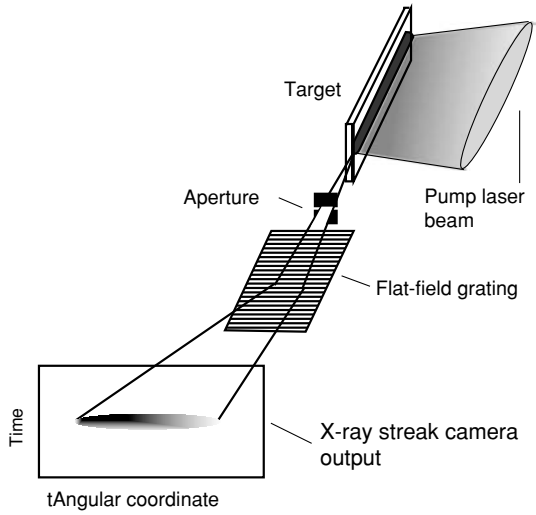

Fig. 6.3. Diagram of an experimental arrangement used to obtain the time-resolved angular distribution of X-ray laser emission (Ref. [85]).

6.1 Beam Refraction

Experimental verification of beam refraction is straightforward in the case of single slab target lasers shown in Figure 6.4. The deflection angle, θ, can be as large as $\sim$15 mrad and the divergence, ϕ, is generally between 3 and 6 mrad. Direct measurement of θ and ϕ can readily be obtained by placing XUV-sensitive CCD detectors at 1–2 m distance from the target. From travel through symmetrically produced plasmas, like exploding foil (cf. Fig. 5.5) or tin fiber configurations (cf. Fig. 5.6), one does not expect deflection but divergence only.

As for the trajectories through double target systems or in half-cavities (cf. Fig. 5.11) they have a more complex behavior. This is illustrated in Figure 6.5 for the case of double target [86]. Trajectories here strongly depend on the

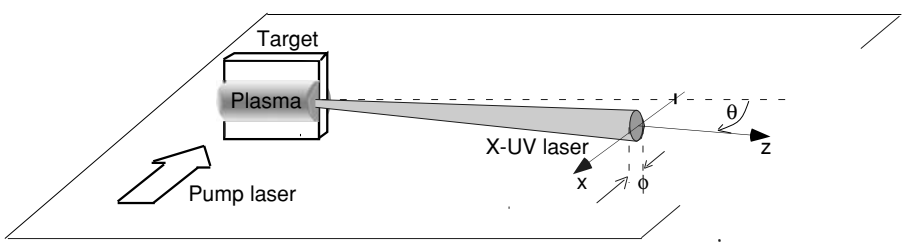

Fig. 6.4. XUV laser beam deflection and divergences due to refraction within the plasma.

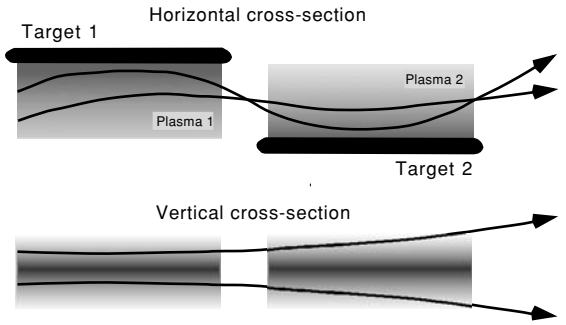

Fig. 6.5. Characteristic features of optical trajectories in a double target configuration.

adjustment of the two targets relatively to each other. The same holds for the adjustment of the mirror near the end of the target in the double-pass system. Models have thus been developed in order not only to understand the physics of propagation but also to optimize the various laser configurations.

In X-ray trajectory computation codes, the plasma variables may be defined on a rectangular grid. As regards the refractive index either it is assumed constant within the cells [87], the total path being calculated as the sum of all the linear segments forming the trajectory, or it is the index gradient which is assumed constant in each cell and the total path is then a sequence of parabolic arcs between the cell faces [88, 89]. However the analytical calculation of trajectories has the advantage of giving a general view of propagation physics, so it will be our starting point.

The general equation of ray propagation in a medium of continuously varying refraction index n reads [90, 91]

$$\frac{d}{ds}\left(n\frac{d\mathbf{r}}{ds}\right) = \nabla n \tag{6.1}$$

where $\mathbf{r}$ is the vector position and ds is the differential path length. Let us consider an amplifier plasma elongated in the OZ-direction with the target in the YZ-plane (Fig. 6.6). If we assume a uniform density along the line focus axis, equation (6.1) becomes

$$\frac{d}{ds}\left(n\left(x,y\right)\frac{d\mathbf{r}}{ds}\right) = \nabla n\left(x,y\right) \tag{6.2}$$

Moreover, since the typical length of the refraction index gradient is usually much shorter in the expansion direction, OX, than in the transverse direction, OY, one can adopt a planar geometry in which the ray equation reduces to

$$\frac{d}{ds}\left(n\left(x\right)\frac{d\mathbf{r}}{ds}\right) = \frac{dn(x)}{dx} \tag{6.3}$$

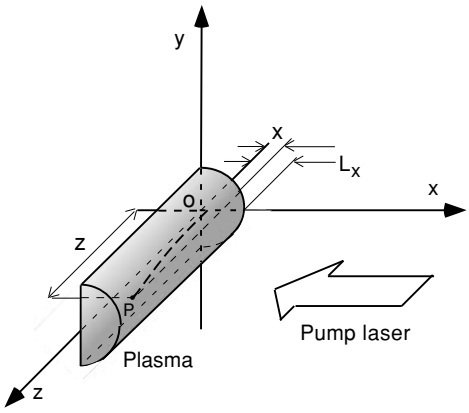

Fig. 6.6. The figure shows a trajectory in the XZ plane (thick dashed line). The profile of electron density is assumed to be parabolic and to vanish at $x = L_x$. With this assumption, the trajectory equation may be obtained by analytical calculation (see text).

Then, by introducing a parabolic electron density profile, viz.

$$n_{\mathrm{e}}(x) = n_0 \left[1 - \left(\frac{x}{L_x}\right)^2\right] \tag{6.4}$$

where n_0 is the electron density along the plasma axis and $2L_x$ the transverse plasma dimension, in the refraction index equation (5.2) one can obtain an analytical expression that describe the XUV trajectories.

n_{c} being the critical density given by equation (2.20), let us define

$$\phi_{\mathrm{r}} = \left(\frac{n_0}{n_{\mathrm{c}}}\right)^{1/2}, \qquad L_{\mathrm{r}} = \frac{L_x}{\phi_{\mathrm{r}}}$$

Let P be a point of the trajectory, of coordinates x, z. From Ref. [91] the trajectory equation takes the form

$$x = A \exp\left(\frac{z}{L_{\mathrm{r}}}\right) + B \exp\left(-\frac{z}{L_{\mathrm{r}}}\right) \tag{6.5}$$

where

$$A = \left[\frac{1}{2}\left(\frac{x_{\mathrm{b}}}{L_x} + \frac{\varphi_{\mathrm{b}}}{\varphi_{\mathrm{r}}}\right) \exp\left(\frac{-z_{\mathrm{b}}}{L_{\mathrm{r}}}\right)\right] L_{\mathrm{r}}$$

and

$$B = \left[\frac{1}{2}\left(\frac{x_{\mathrm{b}}}{L_x} - \frac{\varphi_{\mathrm{b}}}{\varphi_{\mathrm{r}}}\right) \exp\left(\frac{z_{\mathrm{b}}}{L_{\mathrm{r}}}\right)\right] L_{\mathrm{r}}$$

x_{b}, φ_{b}, and z_{b} are boundaries conditions applied at the exit coordinates of the rays, viz. at the plasma bottom end in Fig. 6.6. Calculation shows that

significant bending of trajectories appears for a length L_z such that $L_z > L_\mathrm{r}$, for what reason L_r is called "refraction length." Taking into account the above definitions of L_r and ϕ_r, this condition can be written as a relation between longitudinal and transverse plasma dimensions

$$L_z > \left(\frac{n_\mathrm{c}}{n_0}\right)^{1/2} L_x \tag{6.6}$$

Referring to equation (2.19) one can see that, for XUV radiation, the critical electron density lies usually in the interval

$$10^{23}\ \mathrm{cm}^{-3} \lesssim n_\mathrm{c} \lesssim 10^{24}\ \mathrm{cm}^{-3} \tag{6.7}$$

It follows that, for $n_0 = 5 \times 10^{20}$ cm^{-3}, the magnitude of $(n_\mathrm{c}/n_0)^{1/2}$ is between $\sim$15 and $\sim$45. For plasma width of 100 μm, the refraction length L_r will thus have values between 1.5 mm and 4.5 mm.

For both families of trajectories shown in Figure 6.7 the plasma length has been chosen such that $L_z = 3L_\mathrm{r}$. Seeing the definition of the boundary conditions, each family is defined by a fixed value of the exit angle φ_b. This figure therefore illustrates the parametric behavior of typical trajectories rather than realistic maps of the radiation flux. However, according to the "light inverse return principle," the graphics may also be read from left to right. One sees that rays emitted near the central axis of the plasma and propagating at small angle with respect to this axis does not tend to leave the central plasma region quickly. This results in a high intensity region, limited by the dotted curves,

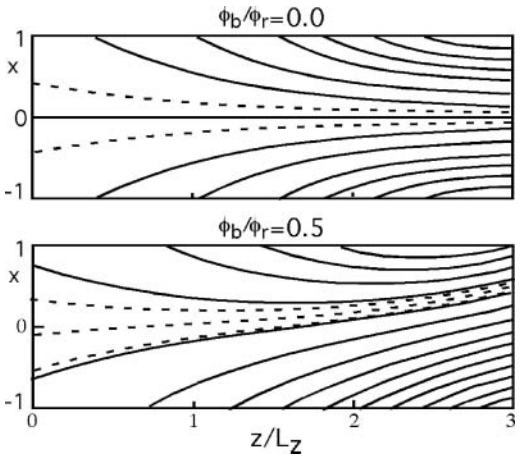

Fig. 6.7. Each trajectory family represented in the figure corresponds to a constant exit angle ϕ_b (Ref. [91]). If the curves are read in the opposite direction (from left to right) ϕ_b is to be interpreted as the entrance angle. The dotted curves limit high intensity regions resulting from the smaller deflection of the rays travelling near the central axis.

surrounding the plasma central axis in Figure 6.7. Moreover, on the left of the figure, these limits do suggest that the beam divergence grows owing to refraction during radiation transfer.

To calculate the angle-dependent emergent flux one has to integrate radiation transfer equations (Section 1.2). Introducing the refraction index $n(s)$ in equation (1.1), it becomes

$$n(s)^2 \frac{d}{ds}\left(\frac{I}{n(s)^2}\right) = j - kI$$

By substituting the gain coefficient g for $-k$, the transfer equation reads

$$n(s)^2 \frac{d}{ds}\left(\frac{I}{n(s)^2}\right) = j + gI \tag{6.8}$$

and replacing j/g by the source function S [see Eq. (1.8)] leads to

$$\frac{d}{dG}\left(\frac{I}{n(s)^2}\right) = \frac{S+I}{n(s)^2} \tag{6.9}$$

where $dG = gds$ is an infinitesimal variation of the gain–length factor

$$G = \int_{z_0}^{z_b} g(s)ds \tag{6.10}$$

along the ray. $S/n(s)^2$ is assumed to remain constant since both S and $n(s)^2$ vary slowly with respect to G and I. Then, the solution of equation (6.9) can be written

$$I(G) = S\left(e^G - 1\right) \tag{6.11}$$

For a parabolic gain profile, using the ray path given by equation (6.5), one finds (cf. [90])

$$\begin{aligned} G = {} & g_0(z_b - z_0)(1 - 2AB) \\ & -\frac{A^2}{2}\left[\exp\left(2\frac{z_b}{L_r}\right) - \exp\left(2\frac{z_0}{L_r}\right)\right] \\ & -\frac{B^2}{2}\left[\exp\left(-2\frac{z_b}{L_r}\right) - \exp\left(-2\frac{z_0}{L_r}\right)\right] \end{aligned} \tag{6.12}$$

where the dependance of G on x_b and ϕ_b is enclosed in A and B. The variable g_0 is the maximum gain at $x = 0$.

For a given plasma column length, each ray depends on the two parameters x_b and ϕ_b. The emergent flux in direction ϕ_b at distance D from the plasma is given by

$$F(\phi_b) = \frac{2L_y}{D}\int I(x_b, \phi_b)\cos\phi_b dx_b \tag{6.13}$$

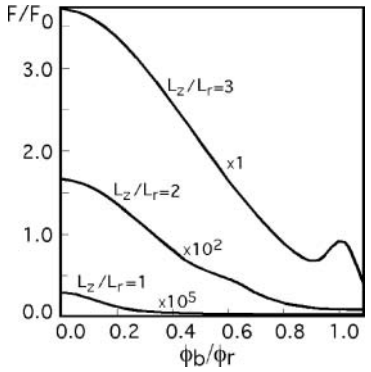

Fig. 6.8. Angular distribution of X-ray laser flux, calculated as a function of the plasma fiber length L_z, L_r is the refraction length, ϕ_b the exit angle.

Figure 6.8 shows calculated angular laser-beam pattern for three plasma lengths. The fluxes are normalized by the value of

$$F_0 = 4\frac{L_\mathrm{x}L_\mathrm{y}}{D^2}S$$

To bring the three curves together, the F/F_0 scale has been increased by factor 10^2 for $L_z/L_\mathrm{r} = 2$ and 10^5 for $L_z/L_\mathrm{r} = 3$. The central part of the on-axis peak is due to the rays flying near axis, where the gain is high and refraction slight. The smaller off-axis peak seen at $\phi_\mathrm{b} = \phi_\mathrm{r}$ for large plasma lengths is due to the rays that emerge from the sides of the plasma, at $x_\mathrm{b} \sim L_x$.

One thus sees that an analytical treatment of plasma refraction reveals general features of the XUV laser beam propagation but it needs approximations such as the introduction of parabolic, or squared, electron density profiles and of gain coefficients in the ray equation. The variety of target arrangements, that we observed in XUV laser configurations, in irradiation by single or multiple pulses, by pulse and prepulse, requires calculation tools able to treat realistic density and gain distributions for each specific experimental XUV laser. So hydrodynamics computational code will process laser–matter interaction and compute the time–space dependance of plasma mean ionization, ion temperature, electron temperature, and free electron density. A detailed atomic physics code will use the relevant data coming from this first calculation stage to calculate the ionization balance and population inversions. The results are then addressed to a propagation ray-tracing code which simulates experiments. This rather complex computational organization is clearly summarized in Figure 6.9 [92].

Figure 6.10 shows a 3D-trajectory S, the calculation of which requires the 3D ray equations to be integrated [93]. The refraction index has the form

$$n(x,y) = \left(1 - \frac{n_\mathrm{e}(x,y)}{n_\mathrm{c}}\right)^{1/2} \approx 1$$

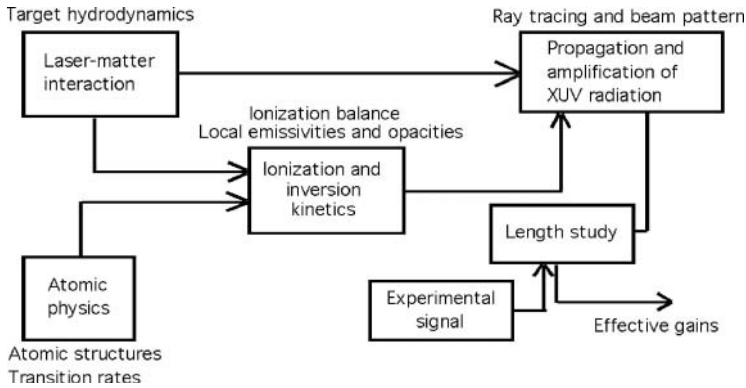

Fig. 6.9. Diagram of the X-ray gain computation organization.

As in the above analytical treatment, trajectories are calculated backwards starting from the emerging point (x, y) and direction (θ_x, θ_y). Since θ is small, the path length $s \approx z$. The ray equations take the simplified form

$$\frac{d}{dz}(x, y) = (\theta_x, \theta_y)$$
$$\frac{d}{dz}(\theta_x, \theta_y) = \left(\frac{\partial n(x, y)}{\partial x}, \frac{\partial n(x, y)}{\partial y}\right) \tag{6.14}$$

The next calculation steps, which give the gain–length factor G and the emergent flux I, use the same equations as before [Eqs. (6.10) and (6.11)] but do not make *ad hoc* assumption about electron density profile. It is obtained from a numerical simulation using a 2D hydrodynamics code. Since the radiation transit time in long plasmas is of the order of 100 ps or more, whereas large temperature and density variations can occur in much shorter time, the finite speed of X-ray propagation is included in the gain–length calculation. The name given to this radiation transport code is CASER.

Figure 6.11 displays a set of trajectories (projected onto the xOz plan) of rays emerging at a specific time (−40 ps before the peak of the driving laser pulse) and at one spatial point ($x = 0$, $y = 450$ μm, $z = 0$). The transfer equation is solved for a number of frequencies ν, within the line profile. The

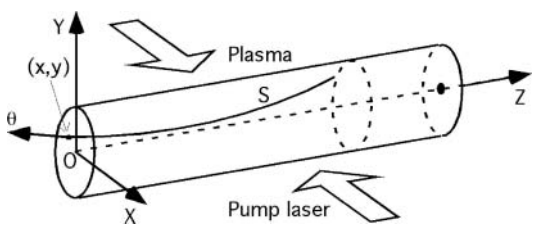

Fig. 6.10. Sketch of 3D-trajectory in the amplifying plasma.

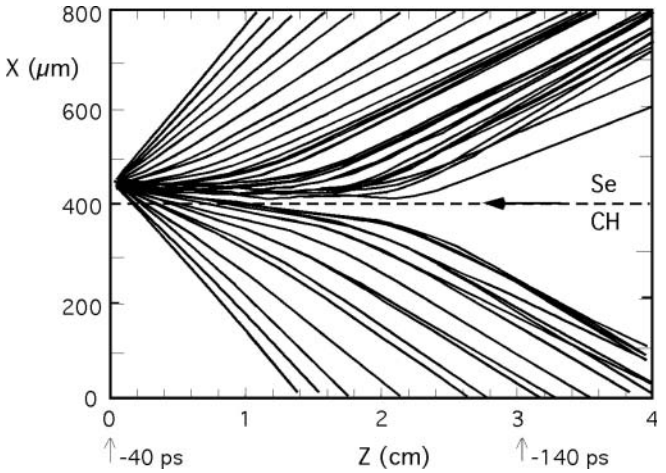

Fig. 6.11. Projection of 3D-trajectories calculated for an exploding foil target on the xOz plane. Calculation includes the finite speed of X-ray propagation. in the plasma (Ref. [93]). Rays propagate from the right- to the left-hand side as indicated by the arrow.

initial conditions are those of the exploding-foil XUV laser configuration (cf. Fig. 5.5, Section 5.2.1) with a 750-Å selenium layer on 1500-Å formvar irradiated from both sides in the OX direction with a 4-cm long line focus (see for instance [30]). The separation surface between the lasing material and the formvar support is defined to be $X = 400$ μm. The pump laser pulse duration is ∼500 ps. The figure shows all the trajectories selected for their significant contribution to the integrated flux

$$F = \int I\left((x, y, \vartheta_x, \vartheta_y, \nu, t)\, dxdyd\vartheta_x d\vartheta_y d\nu dt \right. \tag{6.15}$$

with the exception of values ϑ_y greater than 4 mrad which are omitted for clarity. One can see that the bulk of the gain comes from rays emerging from the right-hand side of the figure with a small positive ϑ_x. Another noticeable feature is that, within the ∼130 ps time interval considered in the calculation, no ray could be selected emitted from points close to the central plasma axis.

Comparison of experimental and CASER-calculated results relative to radiation angular distribution shows the calculated divergence to be ∼13 mrad compared to ∼10 mrad from experimental measurements. Moreover the calculated deflection from the OZ axis is found to be rather small, viz. ∼5 mrad, as expected from the symmetric irradiation used in the exploding foil configuration. In this configuration a flat density plateau is expected to occur near the exploded foil, at the beginning of the plasma expansion. However the symmetry is not perfect as one of the laser beams has to cross the formvar support before reaching the lasing material foil. Thus calculation predicts a

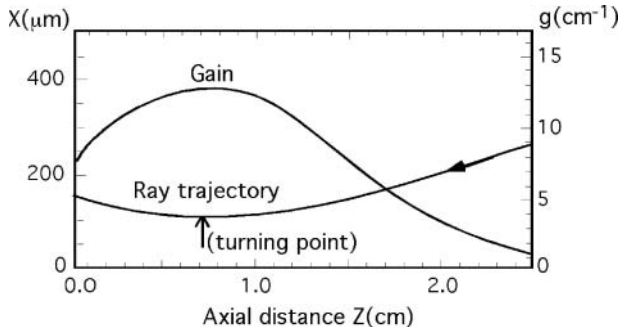

Fig. 6.12. Ray trajectory and corresponding gain coefficient curve in a Ne-like plasma fiber produced from an one-side irradiated Ge-slab target.

few mrad deflection. In fact experimental measurements return a significantly larger ∼10 mrad value.

The same computational code has been used [94], with a view to compare refraction in exploding foil arrangement and in one-side irradiated slab-target configurations (cf. Fig. 5.1, Section 5.2.1). Since there cannot be any density plateau in the second case, one expects a stronger deflection from the plasma column axis. Calculations are performed for the 23.6 nm wavelength lasing line of Ne-like germanium ions emitted from a thick target. A sample X-ray trajectory is shown in Figure 6.12 with the corresponding gain coefficient curve. One can see that the maximum refraction (turning point in Fig. 6.12) occurs in the zone of maximum gain. Figure 6.13 shows measured (black line) and calculated (circles) angular distributions to be in close agreement for the beam divergence. However a discrepancy between calculated and measured deflection appears since the simulated distribution curve has been shifted

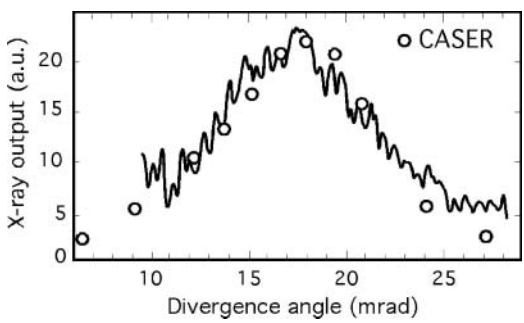

Fig. 6.13. Measured (curve) and calculated (circles) angular distribution of the amplified radiation of a plasma fiber, similar to that of Figure 6.12 Divergences are in good agreement. However the calculated curve has been shifted by 5 mrad to the measured. This shows that calculation did not account accurately for the total deflection of the beam.

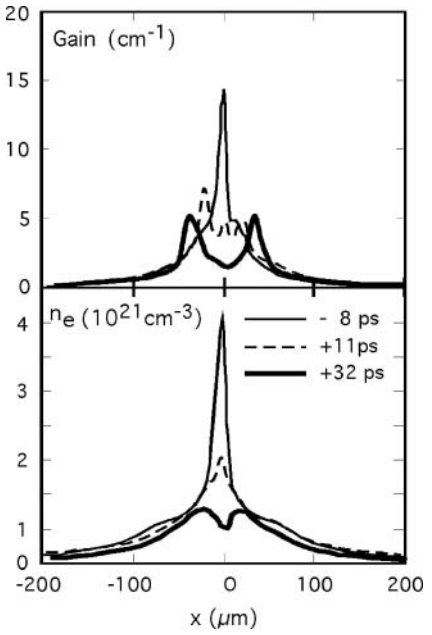

Fig. 6.14. Calculated transverse electron density profile and corresponding gain for a plasma fiber produced by exploding foil technique. The figure shows the rapid change of the profiles with time, whose origin had been placed at the peack of the laser pulse (Ref. [95]).

along the angular axis by ∼5 mrad toward the axis to obtain the fit to the experimental results. This shows that some inaccuracy of plasma parameters persists in numerical simulations.

The complexity and the rapidity of the processes controlling the local gain and local trajectory bending makes it difficult to deduce the amplifier plasma properties from elementary models only. This may be noticed in the curves of Figure 6.14 which show the calculated variations of electron density and gain coefficient in the central zone of a silver plasma produced by the exploding foil technique [95]. The central part of the curves can be seen to change very quickly. It shows anything looking like the sometimes expected density plateau. The same holds for the gain curves, whose initial sharp peak then develops a two-lobe pattern ∼20 ps after the top of the laser peak. Moreover there is no simple relation between these profiles and the resulting intensity distributions displayed in Figure 6.15, where one sees a large lobe arising at 8 ps before laser peak, at an angle of ∼15 mrad from the axis on the formvar foil side. As a matter of fact, experimental investigation of the 9.9 nm and 100 nm Ne-like silver lasing lines showed the radiation time-integrated angular distribution to be shifted toward the formvar side by 6–7 mrad [96]. For similar reasons, although the joint parts of refraction and gain

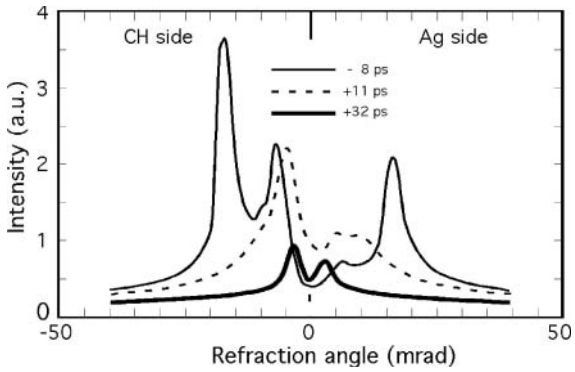

Fig. 6.15. Transverse intensity distributions calculated at the same times as in Figure 6.14.

in intensity angular distribution are clearly established, achieving an XUV laser following the gain-guided beam model (see for instance [97]) would need a control of plasma parameters which is beyond the present capabilities of laser plasma production. However very important progress in propagation control in collisionally pumped lasers was made with the discovery of the density gradients being strongly relaxed when a small prepulse was shot at the target before the main pumping pulse [98]. This technique will be described in Section 7.3.

6.2 From Small-Signal Gain to Saturation

Lasers without cavity are commonly called *amplified spontaneous emission (ASE) lasers*. The physics of this class of lasers is summarized in equations (1.4), (1.19), and (1.20) that show photons spontaneously emitted near one amplifier end to be amplified before reaching the opposite end. Those equations, merely adapted by introducing a z-dependence of the gain coefficient g, were successfully used in the refraction theory of the above section.

As long as spontaneous emission outweighs stimulated emission, the beam itself has no significant action on the decay rate of the upper level. Then the increase of the laser output does not affect the value of g. Therefore, in the previous examples of refracted–amplified radiation paths, the quasi-steady-state populations of upper and lower levels of the lasing transition were obtained by solving the relevant system of population equations at every moment of the plasma life (1.46), (1.45). This describes the principle of the so-called small-signal gain laser operation, characterized by the radiation output growing exponentially on length, according to equation (1.4).

When the gain–length factor, gl, increases more and more, the stimulated emission rate becomes sufficient to significantly lower the upper level

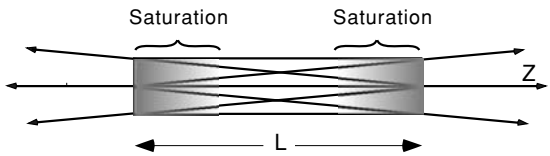

Fig. 6.16. Illustration of saturation occuring first near the ends of the plasma column.

population. Consequently population inversion and gain coefficient are also found to decrease. The laser is then said to approach saturated operation which implies gain limits. Saturation first occurs near the ends of the plasma column, where gl is the largest, as shown in Figure 6.16.

We have seen in Section 3.3 that, for ASE amplifiers, a close relation exists between plasma length and number of spatial modes. From the order of magnitude equation (3.49), it is obvious that achieving large coherence requires the use of plasmas as long as possible or, in other words, lasers operating at saturation. Therefore it is worth carefully studying the transition from ASE to saturated laser. The reader may resort to a number of publications, for instance [99–103], that may help him to perfect his knowledge of the subject.

Figure 6.17 displays an atomic level diagram reduced for simplicity to the two laser levels, 2 and 1, of statistical weights g_1 and g_2. In what follows we shall use many definitions given in Section 1. As compared with the processes included in population equation (1.45), this diagram does neglect ionizing transitions. Let us recall that terms of the form $n_e\langle\sigma_{ij}v\rangle$ represent the rates of collisional transitions in a plasma of electron density n_e. Since the upper-level population density, N_2, is assumed to be larger than the population N_1 of the lower level, the diagram obviously includes the stimulated emission between

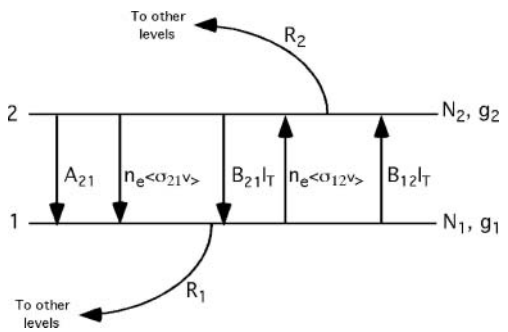

Fig. 6.17. This diagram shows the transition probabilites which are used to calculate the X-ray laser intensity saturation for the emission from level 2 to level 1. I_T is the total intensity integrated over the laser line width. R_1 and R_2 gather the decay rates of levels 1 and 2, respectively, to the nonrepresented levels. Other notations are usual.

levels 2 and 1. The collisional and radiative decay rates of levels 1 and 2 to all other nonrepresented levels are gathered under labels R_1 and R_2 respectively. Let $\Phi(\nu)$ be the optically thin profile function of the laser line, with $\nu = 0$ at the line center (cf. Section 1.3.), normalized so that $\int_{-\infty}^{+\infty} \Phi(\nu)\, d\nu = 1$, and I_{T} the total intensity

$$I_{\mathrm{T}} = \int_{-\infty}^{+\infty} I(\nu)\, \Phi(\nu)\, d\nu \tag{6.16}$$

We assume levels 1 and 2 to be populated at total constant rates

$$\frac{dN_1}{dt} \equiv \Gamma_1 = cst$$
$$\frac{dN_2}{dt} \equiv \Gamma_2 = cst$$

Those transition rates, depending on beam intensity, are stimulated emission, $B_{21} I_{\mathrm{T}}$, and photoabsorption, $B_{12} I_{\mathrm{T}}$. Then, the system of rate equations (1.45) reads

$$\begin{aligned}
\Gamma_1 &= -N_1 \left(R_1 + n_{\mathrm{e}} < \sigma_{12} v > + B_{12} I_{\mathrm{T}}\right) \\
&\quad + N_2 \left(A_{21} + n_{\mathrm{e}} < \sigma_{21} v > + B_{21} I_{\mathrm{T}}\right) \\
\Gamma_2 &= N_1 \left(n_{\mathrm{e}} < \sigma_{12} v > + B_{12} I_{\mathrm{T}}\right) \\
&\quad - N_2 \left(R_2 + A_{21} + n_{\mathrm{e}} < \sigma_{21} v > + B_{21} I_{\mathrm{T}}\right)
\end{aligned} \tag{6.17}$$

where the $\langle \sigma v \rangle$ factors are the collision cross-sections averaged over the Maxwellian electron distribution. By extracting N_1 and N_2 the population inversion is found to be given by the relation

$$\frac{N_2}{g_2} - \frac{N_1}{g_1} = \frac{A}{B + C I_{\mathrm{T}}} \tag{6.18}$$

where

$$A = \Gamma_2 R_1 / g_2 - \Gamma_1 R_2 / g_1 + (\Gamma_1 + \Gamma_2) \left(n_{\mathrm{e}} \langle \sigma_{12} v \rangle / g_2 - \left(A_{21} + n_{\mathrm{e}} \langle \sigma_{21} v \rangle\right) / g_1\right)$$
$$B = R_1 R_2 + R_1 \left(A_{21} + n_{\mathrm{e}} \langle \sigma_{21} v \rangle\right) + R_2 n_{\mathrm{e}} \langle \sigma_{12} v \rangle$$
$$C = R_2 B_{12} + R_1 B_{21}$$

From equation (6.18) we can see that, when the intensity increases from 0 to I_{T}, the population inversion ΔN decreases from A/B to $A/(B + C I_{\mathrm{T}})$. Thus the initial population inversion is reduced by factor of 2 once the intensity reaches a value

$$I_{\mathrm{s}} = B/C \tag{6.19}$$

It is usual to call I_{s}, given by [101],

$$I_{\mathrm{s}} = \frac{R_1 R_2 + R_1 \left(A_{21} + n_{\mathrm{e}} \langle \sigma_{21} v \rangle\right) + R_2 n_{\mathrm{e}} \langle \sigma_{12} v \rangle}{R_2 B_{12} + R_1 B_{21}} \tag{6.20}$$

the *saturation intensity* of the laser. Let us mention that, for the Ne-like and Ni-like ion collisionally excited lasers, experiments and calculations show that the saturation intensity, I_s, occurs generally when the gain–length product, gl, is about 16. On substituting equation (6.18) in equation (1.28) the gain coefficient reads

$$g = \frac{h\nu}{c} g_2 B_{21} \frac{A}{B + CI_T} \frac{1}{\Delta\nu} \tag{6.21}$$

where $\Delta\nu$ is the line width. Substituting I_s to B/C in the second member of this equation we obtain the gain coefficient, g_s, for the saturated laser

$$g_s = \frac{h\nu}{c} g_2 B_{21} \frac{A/B}{1 + I_T/I_s} \frac{1}{\Delta\nu}$$

The ratio of gain near saturation to small-signal gain ($I \simeq 0,\ \nu = 0$) is given by

$$\frac{g_s}{g} = \frac{1}{1 + I_T/I_s} \tag{6.22}$$

It is usual to substitute the stimulated emission cross-section

$$\sigma_{sti} \equiv \frac{g}{\Delta N} = \frac{h\nu}{c} \frac{1}{\Delta\nu} B_{21} = \frac{1}{8\pi} \frac{1}{\Delta\nu} \lambda^2 A_{21} \tag{6.23}$$

where ΔN is the population inversion density $g_2 \left(\frac{N_2}{g_2} - \frac{N_1}{g_1} \right)$ in equation (6.20). Then I_s reads

$$I_s = \frac{h\nu}{c} \frac{1}{\sigma_{sti} \tau_r} \tag{6.24}$$

where

$$\tau_r = \frac{1}{g_1} \frac{g_2 R_{2+} g_1 R_1}{R_1 R_2 + R_1 \left(A_{21} + n_e \langle \sigma_{21} v \rangle \right) + R_2 n_e \langle \sigma_{12} v \rangle} \tag{6.25}$$

is called *recovery time* of the population inversion.

With regard to the performance of a particular laser scheme, the small-signal gain coefficient, g, and the saturation intensity, I_s, are crucial factors since the saturation intensity is the limit of the available output power while a large gain–length product value is the condition for achieving beam of small Fresnel number. However previous equations show a conflicting dependence of stimulated emission cross-section on saturation intensity and gain [102]. Large I_s implies recovery time τ_r short, which in turn implies $\Delta\nu$ large owing to the large collisional broadening in this case. But $\Delta\nu$ large implies g small [cf. for instance Eq. (6.21)]. The necessary compromise between gain and saturation intensity will introduce significant differences between the laser characteristics for high- or low- plasma density operation.

It has been rightly observed that in the basic differential equation [cf. Eq. (1.3)]

$$\frac{dI}{dz} = j + gI$$

not only the gain g but also the emissivity j are affected by the depletion of the upper level of the lasing transition [cf. Eq. (1.17)] [101]. The reduction ratio of j is found to be

$$\frac{j_\mathrm{s}}{j} = \frac{1 + I_\mathrm{T}/I'_\mathrm{s}}{1 + I_\mathrm{T}/I_\mathrm{s}} \tag{6.26}$$

where

$$I'_\mathrm{s} = \frac{R_1 R_2 + R_1 \left(A_{21} + n_\mathrm{e} \langle \sigma_{21} v \rangle\right) + R_2 n_\mathrm{e} \langle \sigma_{12} v \rangle}{R_2 B_{12} + \left(g_2 N_1^0 / g_1 N_2^0\right) R_1 B_{21}}$$

N_1^0 and N_2^0 are the small-signal gain populations, i.e. populations nondepleted by saturation. We notice that the condition $N_2/g_2 > N_1/g_1$, i.e. population inversion, implies the other condition

$$I'_\mathrm{s} > I_\mathrm{s}$$

Moreover for very large N_2 (or very small N_1) we have

$$I'_\mathrm{s}/I_\mathrm{s} \simeq 1 + \frac{g_1 R_1}{g_2 R_2} \tag{6.27}$$

Thus for lasers in which the total depopulation rate to other levels is much larger for the lower than for the higher laser level, which is an understandable condition of efficient lasing, we can assume

$$I'_\mathrm{s} \gg I_\mathrm{s} \tag{6.28}$$

Then equation (6.26) reduces to

$$\frac{j_\mathrm{s}}{j} \simeq \frac{g_\mathrm{s}}{g} = \frac{1}{1 + I_\mathrm{T}/I_\mathrm{s}} \tag{6.29}$$

Besides, the general radiative transfer equation (1.3), modified by saturation, may be written

$$\frac{dI(\nu)}{dz} = j_\mathrm{s}(\nu) + g_\mathrm{s}(\nu) I(\nu) \tag{6.30}$$

Let us consider for simplicity the case of rectangular profiles of constant width for g and j and I. We can replace $g_\mathrm{s}(\nu), j_\mathrm{s}(\nu)$ by the values of g_s and j_s averaged over the linewidth and similarly $I(\nu)$ by $I = I_\mathrm{T}/\Delta\nu$. By using equation (6.29) we obtain the transfer equation

$$\frac{dI}{dz} = \frac{j + gI}{1 + I/I_\mathrm{s}} \tag{6.31}$$

that holds for the total output of unidirectional amplifier. Integrating this leads to

$$I + (I_\mathrm{s} - S) \ln \left(1 + \frac{I}{S}\right) = g I_\mathrm{s} z \tag{6.32}$$

where $S = j/g$ is the usual small-signal source function previously introduced by equations (1.11) and (1.22). Let us set

$$I_n = \frac{I}{I_\mathrm{s}}, \qquad s = \frac{S}{I_\mathrm{s}} \tag{6.33}$$

where I_n is the intensity normalized by its saturation value and s the saturation parameter. Equation (6.32) now reads

$$I_n + (1 - s) \ln \left(1 + \frac{I_n}{s}\right) = gz \tag{6.34}$$

Figure 6.18 shows plots of I_n versus the gain–length factor gz for four values of the saturation parameter. Save for the case of no gain ($s = 1$) the

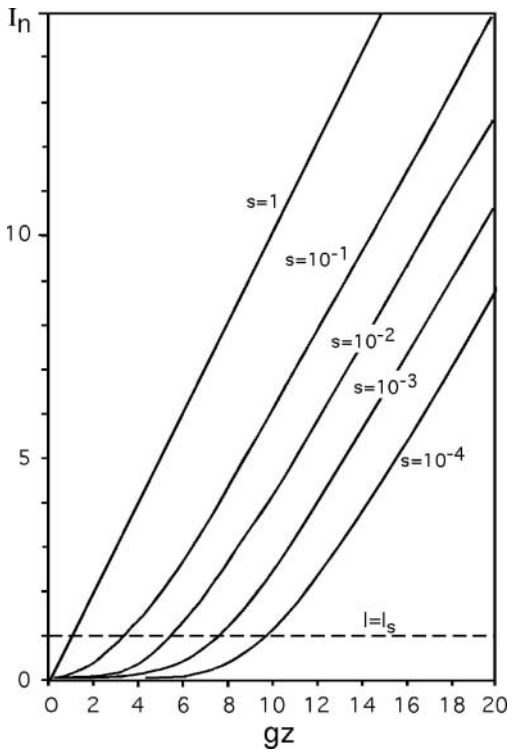

Fig. 6.18. Intensity I_n, as a function of the gain–length factor gz, for various values of the saturation parameter. I_n is the intensity normalized by the saturation value.

increase of intensity is strongly nonlinear before saturation ($I_n \leq 1$). For

$$\frac{S}{I_\mathrm{s}} \ll \frac{I}{I_\mathrm{s}} \ll 1$$

Equation (6.32) reduces to

$$\ln\left(1+\frac{I}{S}\right) \simeq gz$$

whose solution leads to the familiar exponential increase rule $I = S\,(e^{gz}-1)$. Let us mention that, in order to find a simple relation between the gain–length G_s achievable at saturation and the main parameters of the laser emission, one may assume that, until I reaches I_s, most of I comes from the exponentially growing beam, viz. $I_\mathrm{s} \simeq Se^{G_\mathrm{s}}$. Then using equation (6.24) for I_s one obtains

$$G_\mathrm{s} \simeq \ln\left(\frac{1}{2}\frac{\lambda^4}{c\Delta\lambda}\frac{N_2}{g\tau_R}\right) \tag{6.35}$$

where g is the small-signal gain. λ, $\Delta\lambda$, and g are generally known from experiments; the upper level population N_2 and the recovery time τ_r are to be estimated by calculation. Above saturation, due to the slow variation of the second term in the first member of equation (6.32), the curves progressively approximates straight lines. For XUV lasers, this behavior has been experimentally observed for the first time in 1991, with germanium [104, 105] and selenium [106] Ne-like lasers.

In the case of bidirectional propagation (see Fig. 6.16), the equations of forward and backward intensities, integrated over the line width, take the form

$$\frac{dI_+}{dz} = \frac{j+gI_+}{1+\overline{I}/I_\mathrm{s}} \tag{6.36}$$

$$\frac{dI_-}{dz} = \frac{j+gI_-}{1+\overline{I}/I_\mathrm{s}}$$

$$\overline{I} = I_+ + I_- \tag{6.37}$$

where j and g are emissivity and gain coefficient at line center, in the small-signal gain region. This system has analytical solutions that show a general behavior similar to that of the unidirectional amplifier, except for some changes in laser output before saturation [100, 101].

Another issue of the saturation problem concerns the line profiles. Let us first consider the case of homogeneous narrowing (or broadening) where the shape of the emission line profile is not affected by the beam, as it is the case of the Lorentzian profiles of discrete spontaneously emitted lines or of electron-collision broadened lines. In Section 1.4 we showed, without any consideration of saturation, that the width of an homogeneous Gaussian is reduced by factor of $\sqrt{gl}$ by propagating in an amplifier of length l. This can be simply understood as an effect of the gain being larger at line center than

in the wings. We show below that similar narrowing occurs for various line profiles, up to saturation.

As above, $\Phi(\nu)$ is the normalized emission line profile (cf. Eqs. (1.17) and (1.19)). Following this, we define the line center ratio $F(\nu)$ by the relation $F(\nu) = \Phi(\nu)/\Phi(0)$ such that $F(0) = 1$. Let

$$G(\nu) = \int g(\nu)\, dz \tag{6.38}$$

be the integrated gain–length factor of the amplifier. $G(0)$ being the gain–length at the line center, we can write

$$G(\nu) = G(0)\, F(\nu)$$

We now write the transfer equation in the form of equation (1.13), viz.

$$\frac{dI(\nu)}{dG(\nu)} = S + I(\nu) \tag{6.39}$$

where S is the line source function. We have shown in Section 1.3 that, for an isolated line, the emission and gain (or absorption) profiles are identical, from which it results that the source function $S = j(\nu)/g(\nu)$ does not depend on ν. Then the intensity (1.4) at the exit of the amplifier reads

$$I(\nu) = S\left(e^{G(\nu)} - 1\right) \tag{6.40}$$

Therefore the line center ratio of the amplified line profile $f(\nu)$ may be written as

$$f(\nu) = \frac{e^{G(0)F(\nu)} - 1}{e^{G(0)} - 1}$$

For large gain–length factors the line emission concentrates near the line center and the profile function $F(\nu)$ may be replaced by the development

$$F(\nu) = 1 - F_2\nu^2 + F_4\nu^4 - F_6\nu^6 + \cdots \tag{6.41}$$

which implies a symmetric profile. For sufficiently large gain–lengths, the form of the line may be represented by

$$f(\nu) \approx e^{-G(0)F_2\nu^2} \tag{6.42}$$

that is to say a Gaussian profile with half-width

$$\Delta\nu = [G(0)\, F_2]^{-1/2} \tag{6.43}$$

which shows that the linewidth decreases as $G(0)^{-1/2}$ even at saturation. This behavior is illustrated by the dashed curves of Figure 6.19 for the Lorentzian (a) and Gaussian (b) homogeneous profiles. Examples of exact line-widths calculations performed by G.J. Pert [101] for various values of the saturation parameter s, defined by equation (6.33), are plotted as continuous lines in the same figure.

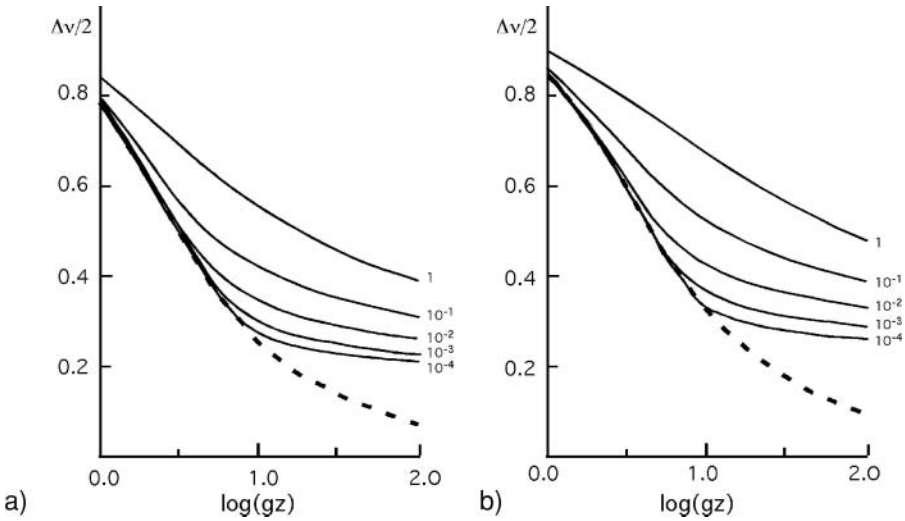

Fig. 6.19. Laser line half-width, as a function of the gain–length factor gz for a set of values of the saturation parameter s (see Fig. 6.18); (a) homogeneous Lorentzian profile, (b) homogeneous Gaussian profile (data from Ref. [101]).

The physics underlying the building of inhomogeneous profiles is much more complex. The assumption of complete frequency-redistribution (cf. Section 1.1), used for the radiation transfer calculations presented so far, cannot be directly extended. Let us imagine a low-density, high-temperature plasma. Each particle emits a homogeneous spectral line, which is shifted by Doppler effect. The summation of the individual components due to a collection of emitters with a thermal (Maxwellian) velocity distribution generates a Gaussian local profile (cf. Section 1.3). At low density, the homogeneous components remain mutually independent in the sense that an individual velocity change affects a single emitter only and a one-to-one relation exists between velocities before and after the event. The global Gaussian profile is then said to be inhomogeneous. In this case one cannot use equation (6.16) nor the ensuing equations that contain the total intensity I_{T}. In this case calculation predicts that *line rebroadening* should occur beyond saturation.

However, at larger density, the width of the single homogeneous components is collisionally increased, possibly up to or beyond the width of the global profile. Hence the random collisional shift combines with the velocity-change shift and the deterministic relation between initial and final velocity disappears. This strong collisional frequency-redistribution process is the condition for the global profile to homogenize. Many Gaussian profiles encountered in laser pumped X-ray lasers are of this kind. The fact is that no rebroadening has been found for the 20.6-nm lasing line of the Ne-like selenium X-ray laser though measurements were performed with an extremely high-resolution spectrometer [107].

6.3 Coherence Building

Unlike gain saturation, coherence is a radiation phase property which requires amplitude rather than intensity of the field [83, 107–121]. Therefore the starting point here is the Maxwell wave equation

$$\nabla^2 E - \frac{1}{c^2}\frac{\partial^2 E}{\partial t^2} = \frac{4\pi}{c^2}\frac{\partial^2 P}{\partial t^2} - \frac{\omega_p^2}{c^2}E \tag{6.44}$$

where $\nabla^2 E$ is the Laplacian of the electric field, E. The right-hand side of this equation contains two contributions, respectively due to stimulated and to spontaneous emission. The first term is proportional to the population inversion density and to the field amplitude E. The second term, that includes the electron plasma frequency ω_{p} [cf. Eq. (2.15)] represents the interaction of the field with the plasma free electrons. It introduces the refraction of the beam in the wave equation.

It stands to reason that, as long as we consider monochromatic waves, the temporal coherence is assumed to be complete. For XUV lasers with no longitudinal mode selection by means of a cavity, the question of temporal coherence amounts that one of the intrinsic laser linewidth $\Delta\nu$, namely the small-signal linewidth. The coherence time is then $t_{\mathrm{c}} \sim 1/\Delta\nu$. The longitudinal coherence length defined as $l_{\mathrm{c}} = ct_{\mathrm{c}} = \lambda^2/\Delta\lambda$ is of the order of $10^4\lambda$. Using the fact that the coherence time is actually 10^4 orders of magnitude larger than the wave period and that the beam is nearly parallel (see geometry in Fig. 6.20), we may, in equation (6.44), replace E, by the slowly varying paraxial envelope $\check{E}(\mathbf{r})$ with

$$E(\mathbf{r},t) = \mathrm{Re}\left[\check{E}_+(\mathbf{r})\, e^{i(\omega t - kz)} + \check{E}_-(\mathbf{r})\, e^{-i(\omega t + kz)}\right]$$

where $\check{E}_+, \check{E}_-$ are waves propagating in opposite directions and $\omega = 2\pi\nu$. Then $\check{E}_y$ satisfies the paraxial wave equation (see, e.g. [115])

$$\left[2i\frac{\partial}{\partial z} + \frac{1}{k}\frac{\partial^2}{\partial x^2} - h(x) + ig(x)\right]\check{E}_y(x,z) = -4\pi P_{sp}(x,z) \tag{6.45}$$

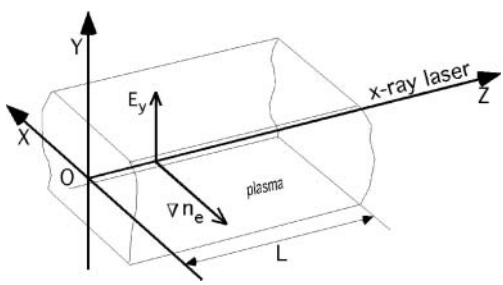

Fig. 6.20. Diagram of the geometry used to investigate the building of the coherence.

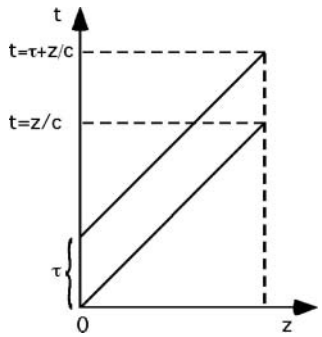

Fig. 6.21. Definition of the local time variable t.

where

$$k = 2\pi/\lambda$$
$$h\,(x) = \omega_p^2/kc^2$$

and the gain $g\,(x)$ is proportional to population inversion, $P_{sp}\,(x, z)$ is the source term due to atomic spontaneous polarization. As shown in Figure 6.20, the transverse gradients are parallel to Ox axis.

Several methods have been developed to obtain analytical or numerical solutions of the paraxial equation with a view to calculate the equal time correlation function of the electric field [cf. equation (3.20)]

$$J(x_1, x_2, 0) = \langle \check{E}^*(x_1, t)\check{E}(x_2, t)\rangle$$

which, by changing the time variable to a local time variable (see Fig. 6.21), i.e. $t \to t - z/c$, may be written as

$$J(x_1, x_2)_z = \langle E^*(x_1, z)E(x_2, z)\rangle \tag{6.46}$$

whereas the complex degree of coherence reads

$$j(x_1, x_2)_z = \frac{J(x_1, x_2)_z}{[I(x_1, z)]^{1/2}[I(x_2, z)]^{1/2}} \tag{6.47}$$

where I labels the intensities at points of coordinates x_1, z and x_2, z. The solution of the paraxial equation for $\check{E}_y(t)$, (6.45) can be then expressed in terms the Green's function (see, e.g. [115]) as

$$\check{E}(x, z) = \int\int G(x, z; x_0, z_0)P_{sp}(x_0, z_0)dx_0dz_0$$

with the initial condition

$$G\,(x, z_0; x_0, z_0) = \delta\,(x - x_0)$$

and where $G(x, z; x_0, z_0)$ must satisfy equation (6.45) without the source term $-4\pi P_{sp}(x, z)$. For practical calculations one assumes that electron density and gain are constant along the amplifier axis.

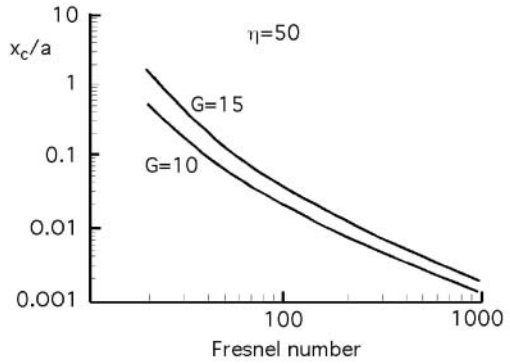

Fig. 6.22. Transverse coherence length as a function of Fresnel number for two values of the gain–length factor G; a is the half-width of the laser beam; η is the density (or refraction) parameter.

Examples of results are shown in Figures 6.22 and 6.23 [115]. Figure 6.22 displays the variation of the spatial coherence length x_c, normalized to the characteristic laser half-width a, as a function of Fresnel number, $F = 2\pi a^2/\lambda L$, gain–length factor, G, and the density (or refraction) parameter η which may be written as

$$\eta = 5.65 \times 10^{-20} \frac{n_{e_0\{\mathrm{cm}^{-3}\}} \lambda_{\{\mathrm{nm}\}}}{g_{0\{\mathrm{cm}^{-1}\}}} \tag{6.48}$$

where n_{e_0}, g_0 are the maximum electronic density and the peak gain both situated at $x = 0$. Calculations are performed for parabolic profiles of density and gain. The curves of Figure 6.22 represent the transverse coherence length near the amplifier exit versus the density parameter, according to the

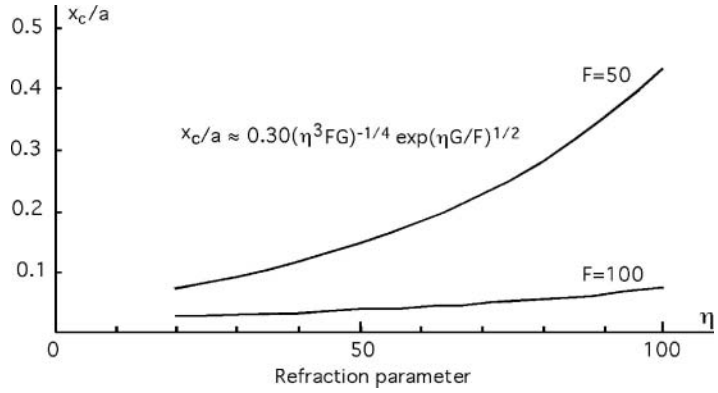

Fig. 6.23. Transverse coherence length as a function of the density (or refraction) parameter for a gain–length factor $G = 15$ and for two values of the Fresnel number.

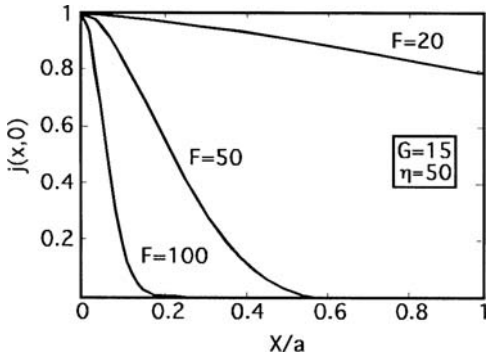

Fig. 6.24. Degree of coherence versus the distance to beam axis for three values of the Fresnel number.

scaling relation

$$\frac{x_{\mathrm{c}}}{a} \approx 0.30 \left(\eta^3 FG\right)^{-1/4} \exp\left(\eta G/F\right)^{1/2}$$

This relation is found to hold when the normalized length, L/a, of the amplifier exceeds a lower limit about $\sim 10^2$ for a 10-nm wavelength for instance. In this equation the coherence length, x_{c}, is defined according to the conventional criterion that requires the degree of coherence to be greater than 0.84 between two points separated by the length x_{c} [cf. Eqs. (3.26)–(3.28)]. The reader should remember that the Fresnel number F characterizes the X-ray laser geometry and that the refraction parameter η introduces the defocusing effect of refraction in calculations.

Figure 6.23 shows the relation between the coherence length and the Fresnel number which is fixed by the geometry of the amplifying medium and the laser wavelength. These curves very clearly illustrate the part of refraction, together with gain–length factor and Fresnel number, in the building of XUV lasers coherence. As for Figure 6.24, it displays the variation of the degree of coherence $j\left(x,0\right)_L$ at the exit end of the laser versus the (normalized) distance x to the central axis, for various Fresnel numbers. Briefly stated, these calculations show that the defocusing refraction causes exponential growth of the coherence length with the amplifier length.

Another approach of coherence building consists in looking for a modal type solution of equation (6.45) [110–112]. We mentioned in Section 3.2. that this should be done in the space–frequency domain rather than in the usual space–time domain. However, although it fails to produce a complete set of orthogonal functions as the base of the field description, the more familiar and easier to understand space–time description is generally used. Therefore one looks for solutions of equation (6.45) that could be written as

$$\check{E}_{\omega}(x;z) = \sum_{n} c_n\left(z\right) u_n\left(x\right) \tag{6.49}$$

Carrying equation (6.49) into equation (6.45) leads to a transverse mode equation

$$\left\{ \frac{\partial^2}{\partial x^2} - F_{ef} \left[\eta h \left(x \right) - i g \left(x \right) \right] \right\} u_n \left(x \right) = - \check{E}_n u_n \left(x \right) \tag{6.50}$$

and a longitudinal transfer equation

$$\sum_n \left[u_n \left(x \right) \frac{\partial c_n(z)}{\partial z} - \frac{i}{2} \check{E}_n c_n \left(z \right) u_n \left(x \right) \right] = - i P_{sp} \tag{6.51}$$

where $\check{E}_n$ is the field eigenvalue. x and z are dimensionless variables obtained by the rescaling to $x \rightarrow x/a,\ z \rightarrow zka^2$. In the same way $P_{sp} \rightarrow P_{sp}/2\pi \left(ka \right)^2$. As above, a is the amplifier transverse scale length. Moreover $h \rightarrow h/h_0,\ g \rightarrow g/g_0$ are normalized transverse profiles, $F_{ef} = kg_0a^2$ is an effective Fresnel number, $\eta = h_0/g_0$ is the density (or refraction) parameter defined by equation (6.48). The electric-field correlation function writes

$$\left\langle \check{E}_\omega \left(\mathbf{r}_1 \right) \check{E}^*_\omega \left(\mathbf{r}_2 \right) \right\rangle = \sum_{n,m} \left\langle c_n \left(z \right) c^*_m \left(z \right) \right\rangle u_n \left(x_1 \right) u^*_m \left(x_2 \right) \tag{6.52}$$

We do not intend to go now into the rather complex procedure that, for unbounded geometry, leads from the solutions of equations (6.50) and (6.51) to results of physical significance. We just mention that the mode spectrum is found to include both discrete (or bound) and continuous (or free) modes. This is illustrated by Figure 6.25 which shows the discrete and continuous spectra of field eigenvalues in the complex E plane for the special case of square density and gain profiles [112b]. However individual modes are mathematical entities

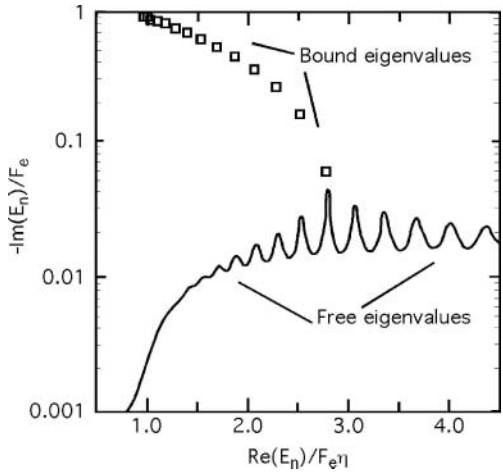

Fig. 6.25. Spectrum of discrete (or bound) and continuous (or free) modes of the X-ray laser field obtained in the case of square profiles of plasma density and gain (from Ref. [112b]).

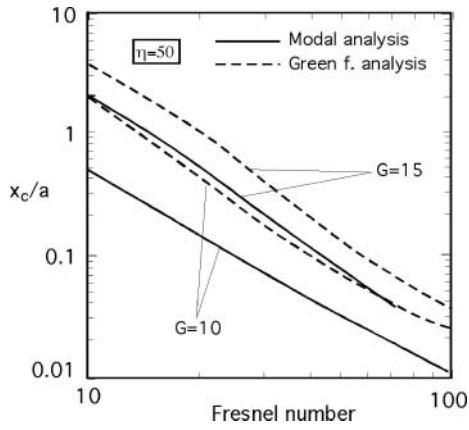

Fig. 6.26. Coherence length versus Fresnel number for two values of gain factor, in the case of $\mathrm{sech}^2(x)$ profiles. Continuous lines represent the results of the modal analysis. For comparison, dashed lines show the results of the Green function analysis.

which are not directly connected to the field intensity distribution. Instead the relevant electric intensity, $I\,(x,z)$), at each point should be obtained by summing the contributions of all modes at this point. Failing to do so gives rise to unphysical features such as "excess noise" (see e.g. [111]) and strong resonances between continuous and discrete modes, at large distances from the central axis of the gain region.

As an example of coherence parameter study by modal analysis is given by Figure 6.26 which shows coherence length as a function of Fresnel number, for two values of the gain–length factor, for a $\mathrm{sech}^2\,(x)$ profile. The reader will remember that $\mathrm{sech}(x) = 1/\cosh\,(x) = 2/\,(e^x + e^{-x})$. For comparison the results supplied by the Green function method for the same profile are also plotted in the figure. Results are within factor of 2 for gain factor of 15, though the agreement is somewhat less for smaller gain–length.

More important than numerical accuracy of the calculated parameters is the contribution that the coherence building theory makes to the general understanding of the role of the various experimental parameters in XUV laser operation. As a last example, let us again consider the effect of beam refraction on laser performances. We have seen above that refractive defocusing, combined with large gain–length factors, strongly increases beam coherence (cf. Fig. 6.23). However it is clear that, at the same time, refractive defocusing reduces the laser output by bending a good part of the rays out of the amplifying zone. The important quantity is the *coherent power* that can be defined as the power passing through a coherence area A_c (note that for an axially symmetric propagation, A_c is of the order of $\pi x_c^2/4$). Therefore one should compare the coherent power obtained for different values of the refraction parameter η.

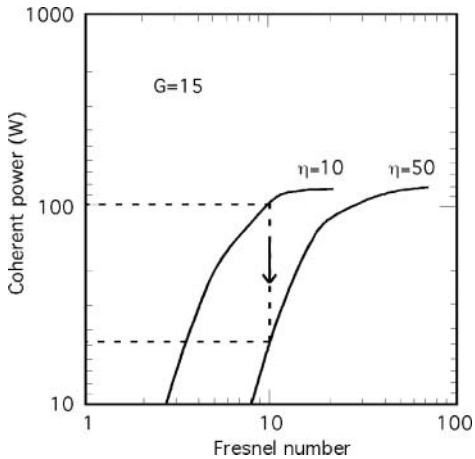

Fig. 6.27. Coherent power versus Fresnel number for two values of the refraction parameter η. Refractive defocusing reduces the coherent power although it was shown increasing the coherence length in Figure 6.23.

Figure 6.27 gives an example of such a comparison performed in the case of a Ni-like plasma of Ta [111]. One sees that, for a given amplifier geometry (viz. a fixed Fresnel number), refraction increase (from $\eta = 10$ to $\eta = 50$ in the figure) may strongly reduce the coherent power. Therefore refraction optimization in amplifying plasmas is a key problem for XUV lasers. We shall see in Section 7.3 how preforming the plasma, by irradiating the target with a low intensity prepulse a few nanosecond before the pump pulse, greatly helps to solve this problem.

However interesting and useful the analytical methods involve some limitations in the description of the amplification process. For instance they do not include gain saturation. Neither could detailed quantum atomic properties of the emitters be introduced in the description. Moreover plasma properties are assumed to be constant in time, as well as along the plasma column, and standard mathematical functions account only roughly for the transverse profiles. More refined models are required to reproduce the time-dependent building of coherence with an accurate description of refraction and saturation. It is possible to build such advanced models by combining the Maxwell wave equation and the Bloch equations which set the time-dependence of the atomic system density matrix [116–120].

For these models the electric field, E, is calculated as above by using the Maxwell equation. The other stages of calculation involve (a) the determination of the polarization vector, $P(x, y; z; t)$ included in equation (6.44), by using the density operator, ρ, of the quantum system; (b) the calculation of the time-dependent populations, ρ_i, by means of the Bloch equation including the perturbed Hamiltonian, H; the unperturbed atomic potential is labeled H_{A}. Thus, in addition to the electric wave equation (6.45), the basic equations

used in Maxwell–Bloch models are the equation which gives the polarization vector P from the atomic electric dipole d

$$P = Tr\,(\rho, d) \tag{6.53}$$

and the Bloch equation

$$i\hbar \frac{\partial \rho}{\partial t} = [H, \rho] \tag{6.54}$$

where

$$H = H_A - d.E \tag{6.55}$$

Equations (6.44) (or 6.45), (6.53), and (6.54) form a coupled system to be generally solved with the help of numerical codes.

This system describes the space–time-dependent interaction between atoms and laser field. Hence solutions will naturally account for the occurrence of gain saturation and therefore for the saturation effects on the coherence of the amplified radiation (see [119] and [120]). A hydrodynamical code provides free electron and ion density distribution data. Furthermore population rate equations are implemented in order to account for spontaneous radiative decay, collisional transitions, ionization, and recombination. The Maxwell–Bloch analysis is incorporated into the rate equations so that population coupling, due for instance to a common lower level of two lasing transitions, are involved in the description of the process. Furthermore the atomic level degeneracy may be taken into account in deriving the Maxwell–Bloch equations [120]. This enables a much more detailed investigation of saturation, which may be of interest when studying problems such as XUV laser polarization.

The efficiency of Maxwell–Bloch models is illustrated by Figures 6.28, 6.29, and 6.30, relative to the 21.2 nm lasing line of a zinc Ne-like plasma [121]. In this example, the model is applied to the propagation through a double-pass system, which involves a half-cavity whose principle is recalled in Figure 6.28. The plasma length is $L = 2$ cm. The distance from the mirror to the left plasma exit is 9 mm, which corresponds to a round-trip transit time of 54 ps. A small shift of the mirror in the Ox direction changes the collimation angle. This angle cancels out when the mirror is centered on the OZ axis. Calculations have been made for a 7 mrad angle, close to the experimental value that offsets the XUV beam refraction in the plasma.

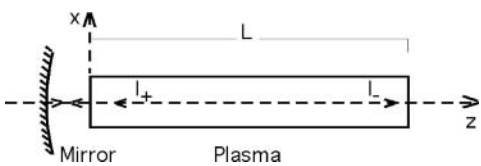

Fig. 6.28. Bidirectional propagation in half-cavity.

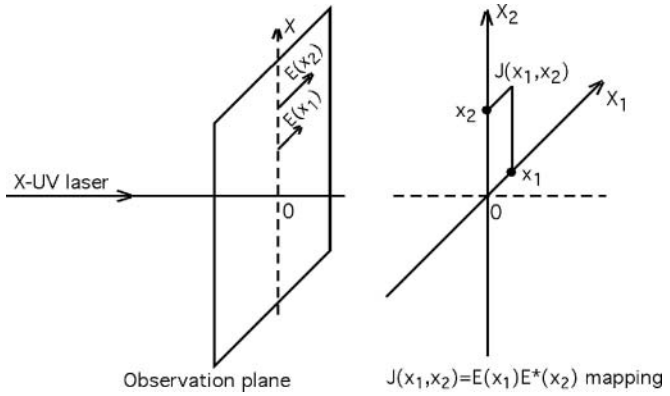

Fig. 6.29. Diagram showing the principle of mapping the mutual intensity $J(x_1, x_2) = E(x_1) \times E^*(x_2)$, along the Ox axis.

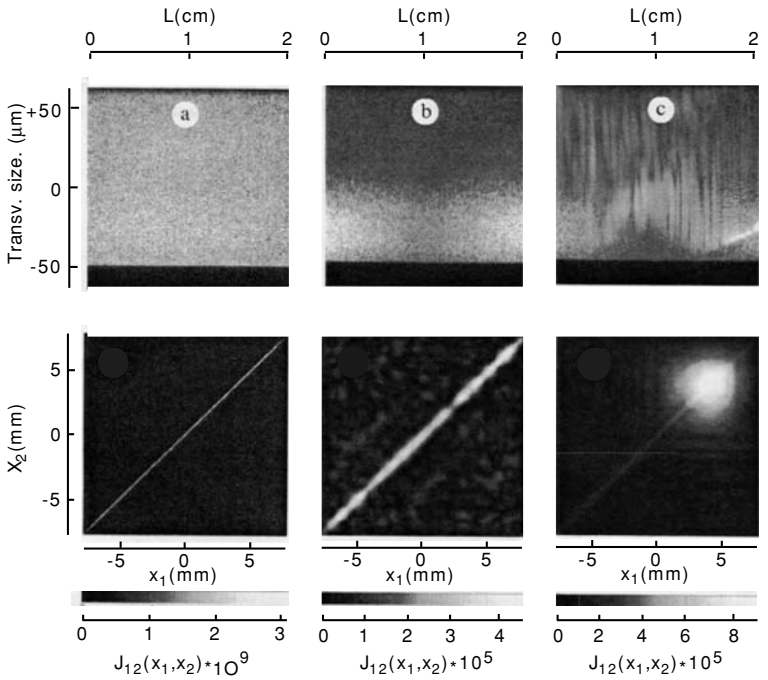

Fig. 6.30. Coherence building in double-pass system (Ref. [121]). L is the distance along the propagation axis in the plasma fiber; x_1 and x_2 are the transverse distances defined in Figure 6.30. Above: XUV intensity distribution in the 2-cm long, 100-μm wide plasma fiber; (a) $t = 50$ ps, (b) $t = 200$ ps, (c) $t = 300$ ps. Below: corresponding maps of the mutual intensity $J(x_1, x_2)$, in the observation plane. Note that the intensity scale increases by 4 orders of magnitude from 50 ps to 200 ps. The intense spot near the right upper corner, in frame (c), reveals the high level of coherence which is reached at this moment. The shift of the highly coherent zone away from beam center ($x_1 = x_2 = 0$) is due to refraction.

The mutual intensity, $J(x_1, x_2) = \check{E}(x_1) \times \check{E}^*(x_2)$, is calculated in every point of the observation plane, 50 cm far away from the exit end of the plasma, as shown in Figure 6.29. The upper part of the figure shows the XUV intensity distribution in the 2-cm in length, 100-μm in width plasma fiber at times 50 ps (a), 200 ps (b), and 300 ps (c). The Jx_1, x_2 maps corresponding to the same times are plotted in the lower part of the figure. Let us notice that the intensity scale is increased by 4 orders of magnitude from 50 ps to 200 ps. The high coherence that appears at 300 ps is shown by the very brigthing spot near the right upper corner in frame (c). The shift away from the beam center of this strongly coherent zone results from refraction.

6.4 Coherence Measurements

6.4.1 Coherence Characterization

Temporal coherence determination needs accurate measurements of line widths but the spectral resolution of usual XUV spectrometers is generally not sufficient for this task, mainly due to the rather low spatial resolution of electronic detectors. It is necessary to call for very large devices, able to enhance the spectral dispersion so that line width becomes significantly larger than the detector pixel size. The line widths, $\Delta\lambda$, found for the lasing lines of selenium and germanium X-ray lasers are of the order of $10^{-4}\lambda$, which is consistent with the assumption that the profiles are dominated by thermal Doppler broadening [122, 123]. From equation (3.53), the longitudinal coherence length is thus about $10^4\lambda$, viz. about 100–500 μm for this type of lasers.

Spatial coherence is observed by means of interferograms or of Fresnel diffraction patterns produced in an observation plane at a given distance from the end of the plasma. The transverse coherence length is deduced from the size of the interferogram region where the fringe contrast is higher than a threshold value, often fixed at 0.84 (cf. Section 3.1). If measurements are performed with a view of using the XUV laser for practical applications only, this result is generally adequate. However, if the point is to improve the knowledge of coherence building in the lasing plasma, it is necessary to include coherence propagation in the treatment of the experimental results. An elementary characterization of the source can be obtained by using the van Cittert–Zernike theorem (cf. Section 3.1) which, under the assumption of *complete incoherence* of the source, defines a relation between the source intensity distribution and the degree of coherence observed in a remote plane. The simplest expression of this theorem is the coherence area A_c, at distance z from a circular uniform quasi-monochromatic incoherent source of radius a, viz. [124]

$$A_c = \frac{\lambda^2 z^2}{\pi a^2} \tag{6.56}$$

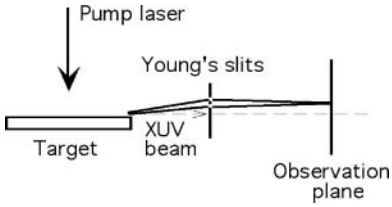

Fig. 6.31. Spatial coherence measurement with a Young's slits arrangement.

as we have previously seen [Eq. (3.28)]. One generally deduces the "equivalent" radius a from the measured diameter of A_c. More advanced coherence investigations have to resort to models including some state of coherence of the source, like the Gaussian–Schell models for instance, in which both intensity and coherence obey a Gaussian distribution [125].

6.4.2 Interferometric Methods

6.4.2.1 Young's Slits

Figure 6.31 recalls the principle of Young's slits method. The measurement consists in determining the separating distance between the two slits that achieves a fair fringe contrast, e.g. ∼0.84. This cannot be achieved with a single laser shot using and a simple pair of fixed slits.

Therefore many variants of Young's slit system have been thought out in order to improve its capability of providing more information from single shots. It is for instance possible to apply the technique of coded apertures to the diffracting structure in order to carry out an uniformly redundant slit array [126]. In this type of structure each separating distance between pairs of slits occurs a constant number of times, which is expected to optimize the signal-to-noise ratio relatively to random slit separation. This has been realized for one of the first experiments aiming at measuring XUV laser coherence [127, 128]. To illustrate the results of this method, Figure 6.32 displays the intensity distribution obtained, beyond the slit array, from the selenium laser radiation ($\lambda \simeq 20.6$ nm and 21 nm), on a screen set perpendicularly to the beam. The array consists of 27 slits. The observed distribution (lower curve) is compared with the curve calculated under the assumption of full coherence (upper curve). It is obvious that the laser exhibits partial coherence. Numerical calculation of the cross-correlation function, which uses the theory of partially coherent diffraction by apertures [129], affords quantitative estimation of coherence from such diffraction patterns.

Figure 6.33 now shows an example of dispersive slit array, which carries out several simultaneous measurements in a single shot [130, 131]. Dispersion is generated by sets of transverse bars of periodicity 2.5 μm or 4 μm in order to separate the diffracted fringe patterns of each slit pair on the detection plane. This design is used to make coherence measurements, with a single laser shot,

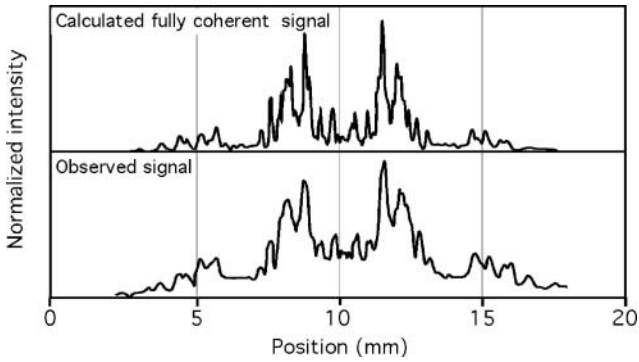

Fig. 6.32. Below, fringe pattern obtained from the selenium X-ray laser ($\lambda \simeq$ 20.6 nm and 21 nm) with a slit array which includes 27 slits (from Ref. [128]). Above: fringe pattern calculated assuming a full coherent signal.

across the angular distribution of the output from a mirror-coupled injector–amplifier system.

If the laser used in the experiment has sufficiently high pulse energy, pinholes can be used instead of slits to form the diffracting mask (see for instance [123]). A good example is given in Figure 6.34 which displays interferograms obtained with two pinholes separated by 200 μm and positioned at a distance of 40 cm from the laser exit [132]. The laser that produces these interferograms, at the wavelength of 46.9 nm, is the capillary-discharge argon laser described briefly in Section 5.2.4 and with details in Section 7.5. The fringe visibility is of 0.05 for the 18-cm long capillary, 0.33 for the 27-cm long plasma and increases up to 0.8 for the 36-cm long capillary. These results

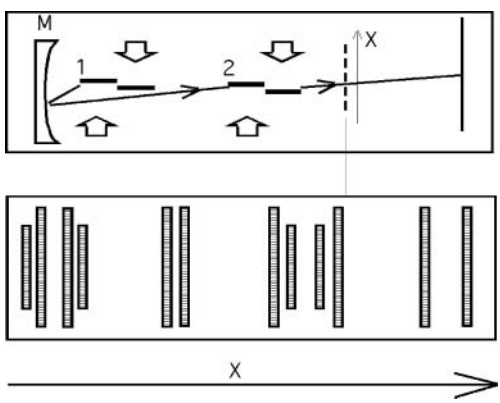

Fig. 6.33. Slit array providing vertical dispersion of the fringe patterns of slit pairs in order to separate them when coherence measurements are performed with a single X-ray laser shot.

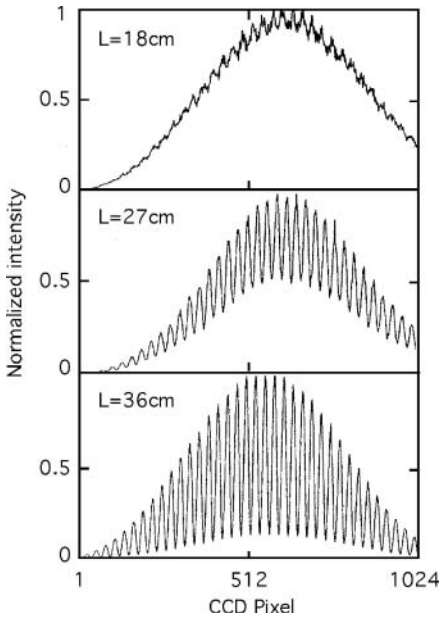

Fig. 6.34. Interference patterns produced by diffraction of the capillary-discharge laser beam ($\lambda = 46.9$ μm) through two pinholes separated by distance of 200 μm (Ref. [131]). The increase of the laser length L results in the enhancement of the spatial coherence. This observation clearly illustrates the reduction of the mode number by refractive defocusing.

illustrate remarkably well the part played by the refractive defocusing, which increases with the amplifier length, in the coherence of the soft X-ray laser.

6.4.2.2 Wave Front Division Interferometer

Let us recall that there are two different ways of dividing a radiation beam into two beams. One can use an interferential separating multilayer system, which shares the field amplitude into two separated beams, at each point of the incident beam section. This is the principle of Michelson interferometers for instance.

The second method consists in splitting the radiation wave-front by using a double mirror system. This is illustrated in Figure 6.35 which shows the principle of the so-called Fresnel bi-mirror interferometer that consists of two silica mirror arranged as a "ridged roof" with an angle between the mirrors of π–ε, where ε is of a few milliradians. Each mirror reflects half of the beam, so that the two half-beams cross and overlap along their propagation path [133]. With this arrangement the coherence of the X-ray laser beam is revealed by the vertical fringes that appear in the beam overlapping zone [134]. The coherence length at a given distance from the laser exit is inferred from the width of the fringe pattern observed at this distance with the interferometer.

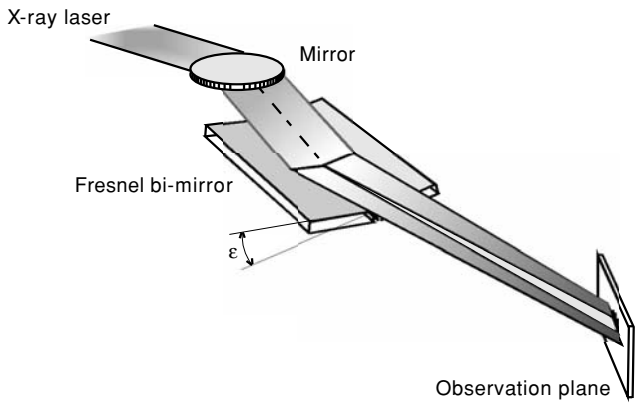

Fig. 6.35. Fresnel bi-mirror interferometer. The bi-mirror separates the incoming beam into two beams which then recombine generating interference fringes.

6.4.3 Diffractometry

Figure 6.36 displays the well-known near-field diffraction pattern produced by a screen edge illuminated by a coherent source (Fresnel diffraction). While the fringe visibility (3.6) is constant over all the field in the case of full coherence, it decreases with the distance to the geometrical shadow in the case where illumination is spatially coherent. To define the coherence length L_c, we use the principle of the equivalent incoherent source that gives the same diffraction pattern as the real partially coherent source and we express the fringe visibility as if the fringe system was produced by Young slits. It is convenient to represent the remote source by a Gaussian angular intensity distribution,

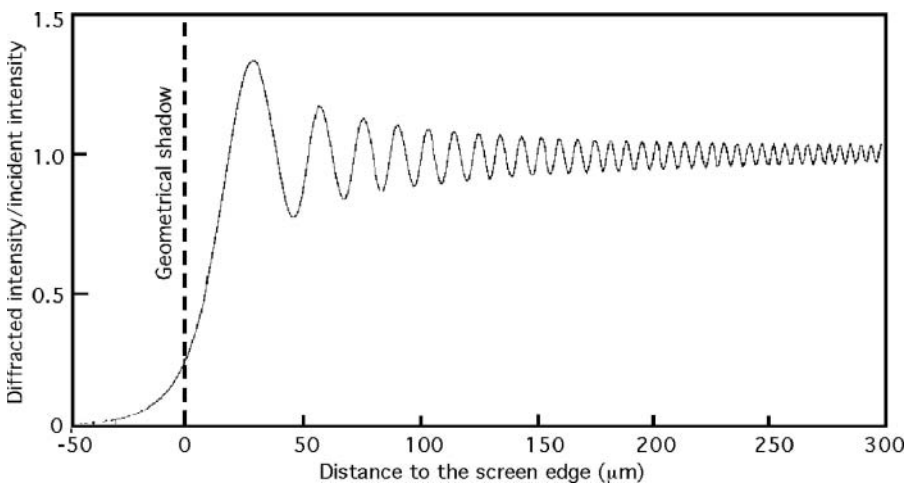

Fig. 6.36. Fresnel diffraction pattern produced by a screen edge illuminated by a coherent source.

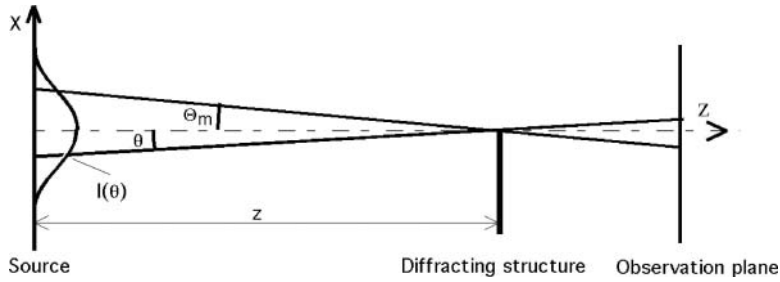

Fig. 6.37. Diagram illustrating the production of Fresnel diffraction from a Gaussian radiation source.

as shown in Figure 6.37 [135]. Let

$$I(\theta) = A \exp\left(-\frac{\theta^2}{\Theta_m^2} \ln 2\right) \tag{6.57}$$

be the angular intensity distribution, where Θ_m is the Gaussian angular half-width at half-intensity. From the van Cittert–Zernike theorem (cf. Section 3.1), the visibility of the Young-slits fringes for this source is found to be

$$K = \exp\left(-\frac{\pi^2 \Theta_m^2 \Delta x^2}{\ln 2 \ \lambda^2}\right) \tag{6.58}$$

where Δx is the separating distance of the slits and λ is the wavelength. The coherence length is then defined as

$$L_{\mathrm{c}} = \Delta x_{(K=\text{well chosen value})} \tag{6.59}$$

For the standard value, $K = 0.88$, corresponding to Gaussian sources, one obtains

$$L_{\mathrm{c}} \simeq 0.1 \frac{\lambda}{\Theta_m}$$

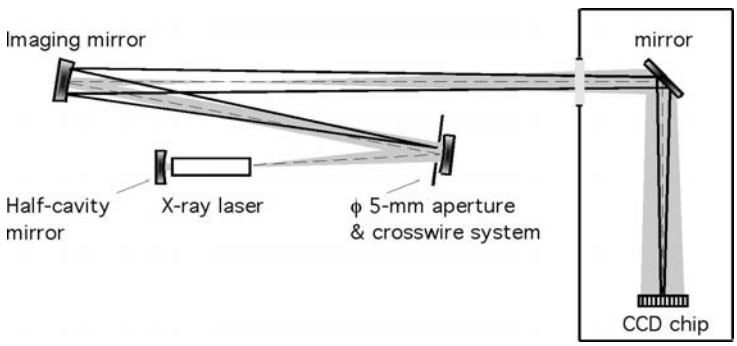

Fig. 6.38. Experimental arrangement with circular aperture and cross wires for the measurement of X-ray laser spatial coherence.

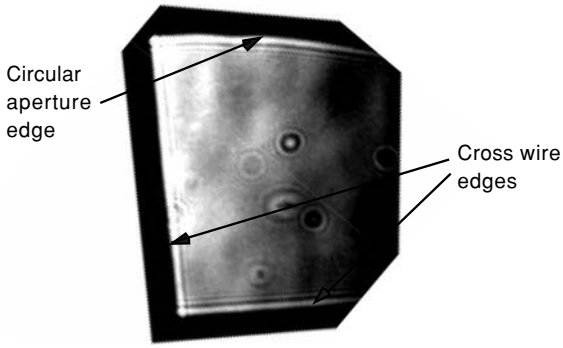

Fig. 6.39. Near field image of Fresnel fringes produced by cross wires and by a circular aperture edge obtained with the experimental arrangement shown in Figure 6.38. Diffraction patterns due to small debris likely projected from the lasant to the mirror surface are also visible.

and for a value of K agreeing with most experimental requirements, e.g. $K = 0.5$

$$L_c \simeq 0.22 \frac{\lambda}{\Theta_m}$$

The value of the adjustable parameter Θ_m is obtained by fitting the calculated fringe pattern to the experimentally observed screen-edge pattern.

This method of characterizing the coherence of XUV sources has been used is several experiments [51, 136, 137]. The example of Figure 6.38 shows the diagram of an experimental setup, in which the Fresnel diffraction pattern of a circular aperture and crosswires, positioned at about 50 cm from the laser exit, is recorded by a CCD camera [136]. The diameter of the wires is sufficient to neglect the interaction between the two sides. Thus wires give the same fringe system as the aperture edge. Figure 6.39 shows Fresnel fringes, which are visible along each of the edges. From this image the coherence length, at 0.88 -visibility, was estimated at $\sim$77 μm near the border of the beam, while it was $\sim$20 μm at the center.

7. Saturated XUV Lasers

At present all lasers, that achieve very large brightness XUV at saturated emission, are collisionally pumped lasers. Their principle, Section 4.2, rests in the production by the plasma free electrons of population inversions between multicharged ion excited levels. This requires plasma densities generally a little larger than 10^{20} particles per cubic centimeter and temperatures of a few hundreds eV. Let us recall that the temperature associated to 1 eV is approximately 1.16×10^4 K.

It is clear that only powerful energy sources, such as shortly pulsed infrared lasers, can produce—or "pump" as they say—plasmas capable of laser action. Pump lasers are neodymium-doped glass lasers whose fundamental radiation wavelength is close to 1.06 μm. The second harmonic, at 0.53 μm, is also frequently used. A shorter wavelength means deeper penetration through the plasma and population inversions produced at higher density, but a greater refraction effect on the propagation of the amplified XUV radiation.

The ion species currently used as emitters belong to the neon-like and the nickel-like series and, to a lesser extent, to the palladium-like series. The ground levels of these ions are respectively $2p^6$, $3d^{10}$ and $4d^{10}$, i.e. they consist of many electron closed shells. The presence of complete outer shells makes the populations of these ion species relatively stable in the plasma. Moreover the collisional-excitation rate of the ground levels is larger than for other species. If density and temperature are sufficient, ion–electron collisions yield large excitation rates from the ground level to higher states. Moreover some of the excited states cannot decay radiatively back to the ground state. This is the case for the $2p^53p$ Ne-like states, the $3d^94d$ Ni-like states and the $4d^95d$ Pd-like states, since the associated decay transitions do not allow level parity change. However the radiative decay from these states is allowed toward the $2p^53s$, $3d^94p$ and $4d^95p$ levels respectively, while these levels empty very quickly to the ground level.

This is the basis for the appearance of population inversions leading to laser lines between the 3p and 3s levels (Ne-like ions), the 4d and 4p levels (Ni-like ions), and the 5d and 5p levels (Pd-like ion), however appropriate

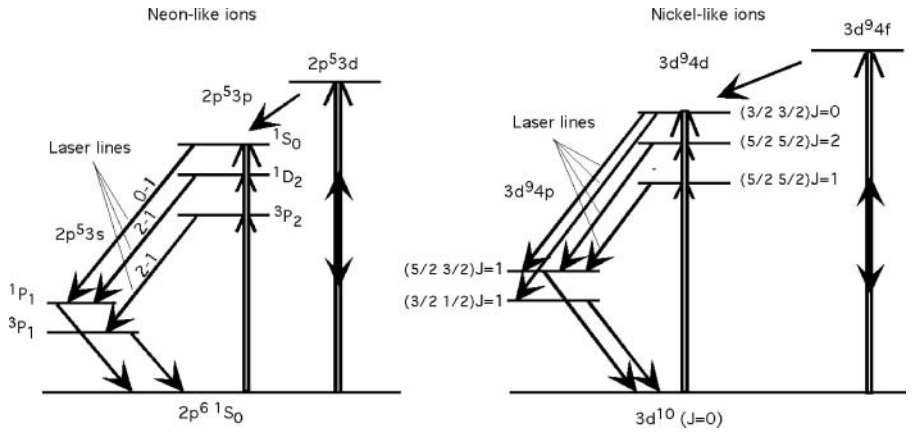

Fig. 7.1. Simplified Grotrian diagram of Ne-like and Ni-like ions. The main laser lines only are represented.

are atomic rates and plasma parameters. The main radiative and collisional transitions of interest for this pumping scheme are displayed in Figure 7.1, which shows the simplified Grotrian diagrams of neon-like and nickel-like ion. The diagrams also point out the contribution of higher levels, respectively 3d and 4f, to the upper-level populations of the lasing transitions. Only the lines, that are expected to show large gain, are represented.

The magnitude of the laser-line wavelengths can be seen in Figure 7.2 for both ion series . The stars point out elements for which saturated lasers have effectively been demonstrated and are used, for several of them, as sources for laser applications. A systematic estimate of Ne-like ion wavelengths from S^{6+} to Xe^{44+} can be found in [138]. Experimental evidence of Ne-like or Ni-like

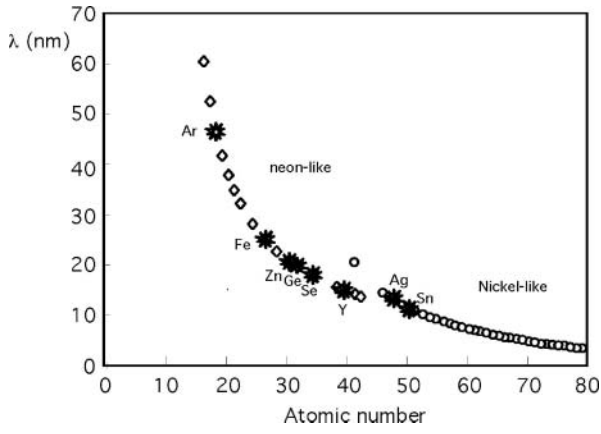

Fig. 7.2. Main XUV laser line wavelengths versus the atomic number of the lasant. Stars points laser lines which have been studied in great detail.

plasma lasing has also been given for a few elements heavier than those shown in the figure (see for instance, [139, 140]).

7.1 Gain Predictions for the Collisional-Excitation Pumping Scheme

The first difficulty in modeling the collisional-excitation lasing scheme is the complex level structure of the highly ionized neon-like and nickel-like ions. Accurate modeling requires a large number of levels to be included in steady-states equations. Extensive calculations of atomic data are necessary in order to have reliable values of energies, radiative transitions probability, and collisional rates. Data can be found for a wide range of atomic numbers in Refs. [141–150], for instance, for neon-like ions and in Refs. [151–154] for nickel-like ions.

Level populations are calculated by solving a QSS equation system of type (1.45), (1.46). In Ref. [142] the QSS system consists of 27 coupled equations that include radiative and collisional-excitation and de-excitation, viz.

$$N_{0<i\leq 27}\left[\sum_{h<i}A_{ih}+n_{\mathrm{e}}\left(\sum_{j>i}\langle\sigma_{ji}v\rangle+\sum_{h<i}\langle\sigma_{ih}v\rangle\right)\right]$$
$$=\sum_{j>i}N_jA_{ji}+n_{\mathrm{e}}\left(\sum_{j>i}N_j\langle\sigma_{ji}v\rangle+\sum_{h<i}N_h\langle\sigma_{ih}v\rangle\right) \tag{7.1}$$

where n_{e} is the electron density. It is worth mentioning that, for Ne-like ions, the optimum value of electron density in a neon-like XUV laser may be estimated by the scaling relation (see Ref. [60], p. 107)

$$(n_{\mathrm{e}})_{\mathrm{opt}}=4\times 10^{15}\,(Z-9)^{3.75}\,\mathrm{cm}^{-3} \tag{7.2}$$

where Z is the atomic number of the lasing element.

The averaged collisional-excitation cross-sections $\langle\sigma v\rangle$ are calculated as a function of the electron temperature, which is defined as a fraction of the ionization potential of each neon-like ion. The maximum abundance of neon-like ions is expected to occur for an electron temperature near 1/2 the ionization potential. The system is solved for a group of electronic densities, n_{e}. The solutions are represented in the form of reduced fractional populations $N_i'=\frac{1}{g_i}\frac{N_i}{N_I}$, where N_I is the total density of neon-like ions. Figure 7.3 shows the example of results obtained for the laser upper levels of neon-like iron and germanium. Spectroscopic notations are the same as in Figure 7.1. The populations are presented as functions of electron density at temperature equal to 1/2 the ionization potential.

It is patent that, for both elements, the population inversion between levels 3p $^1S_0$ and 3s ($^1P_1$, $^3P_1$) is much larger than those between levels 3p $^3P_2$ and 3s $^3P_1$or between levels 3p $^1D_2$ and 3p $^1P_1$. This is a constant fact in the neon-like series, which is due to the strong collisional coupling between

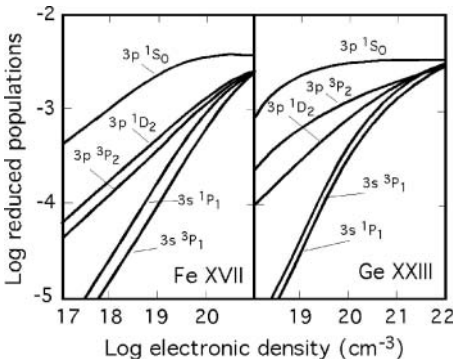

Fig. 7.3. Level populations of Ne-like and Ni-like ions referred to the density number of these ions as a function of the electron density (data from Ref. [142]). The corresponding lasing lines are represented in Figure 7.1. This diagram shows populations inversions to decrease at larger electron density owing to collisional mixing between levels.

the ground state $2\,s^2 2p^6$, $J = 0$, and the $2\,s^2 2p_{1/2} 2p^4_{3/2}\, 3p_{1/2}$, $J = 0$ state. Therefore the gain calculated for the $2p^5 3p\ ^1S_0 \rightarrow 2p^5 3s\ ^1P_1$ line, shortly called the $J = 0$ to 1 or $J = 0{-}1$ line, is *systematically larger* than that for the two other lines, i.e. the $J = 2$–1 lines pointed to in Figure 7.1. The gain calculated for the $J = 0$–1 line is plotted in Figure 7.4 as a function of the

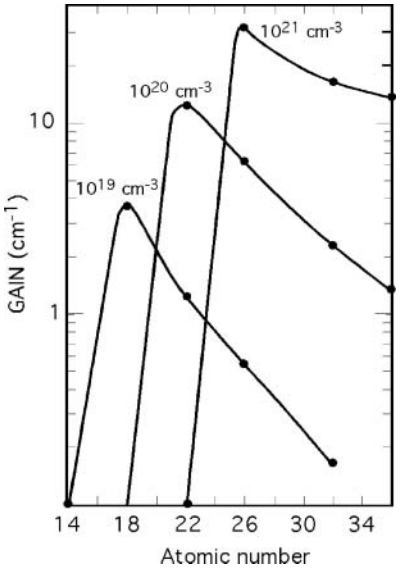

Fig. 7.4. Gain coefficient of the Ne-like $J = 0{-}1$ line calculated as a function of the atomic number for three electron densities. The electron temperature is defined one-half the ionization potential (data from Ref. [142]).

target element atomic number for three electron densities. Predicted gains for the $J = 2$–1 lines may be found in Ref. [148] which, in addition, discusses the role of dielectronic recombination from fluor-like ions in population inversions. It is also shown [155] that including the $3d$ levels in the QSS system (Figure 7.1) is an important factor of calculation accuracy improvement. Moreover the $J = 0$–1 gain depends mainly on the $2p^6$–$2p^5 3p$ monopole transition rate, while the feed of the $J = 2{-}1$ gain involves a larger contribution of $2p^6$–$2p^5 3d$ collisional and radiative excitations followed by 3d–3p cascades.

Simple scaling laws can be established for gain coefficients, as a function of the plasma electron density, and the laser wavelength [156]. Let Z_i be the lasing ion charge. Given the definition (1.28) of gain coefficient, results of hydrodynamical simulations lead to scaling relation

$$g \propto \frac{n_e \lambda}{Z_i}$$

for lines dominated by Doppler profile. Moreover, one considers $\lambda \propto Z_i^{-1}$ and $\lambda \propto Z_i^{-2}$ scalings for the $J = 0{-}1$ and $J = 2$–1 lines, respectively. Scale relations can thus be written as

$$\begin{aligned} g &\propto n_e \lambda^2 \quad \text{for} \quad J = 0{-}1 \text{ lines} \\ g &\propto n_e \lambda^{3/2} \quad \text{for} \quad J = 0{-}2 \text{ lines} \end{aligned} \tag{7.3}$$

Both relations show that lasing at shorter wavelength requires higher density plasma to keep the same gain, especially for the $J = 0{-}1$ lines. Therefore the plasma refraction effects on X-ray laser operation should be expected to increase at short wavelengths.

Concerning the Ni-like ions, gain calculations have been done for elements of high atomic numbers, like Eu, Ta, W, in order to specify the characteristics a soft X-ray laser at wavelengths near the carbon K-edge, i.e. the upper limit of the "water window," which offers many possibilities of biological applications [157–159]. Moreover atomic data and population inversion kinetics have been calculated extensively for elements whose atomic numbers range from 36 to 92 [153]. The 3d–4d transition energy, required to pump Ni-like X-ray laser (see Fig. 7.1), and the value of the electronic temperature T_e, which maximizes the Ni-like ion abundance, obtained from a collisional radiative equilibrium model, are represented in Figure 7.5.

A crucial point of collisionally pumped laser physics lies in the relation between the intensity of driving lasers and the wavelengths of lasing lines. Scaling laws involving plasma parameters, target material and pump–laser characteristics have been derived from self-similar plasma models from which analytical solutions of hydrodynamical equations can be obtained [160,161]. It shows the plasma temperature, T_e, to vary approximately as $I_{\text{pump}}^{1/3}$ in the case of Ne-like ions. Moreover optimal gain calculations, reported in [148] give the temperatures at which one expects the maximum gain to occur for the lasing lines of a set of elements between $Z = 20$ (calcium) and $Z = 56$ (barium). One

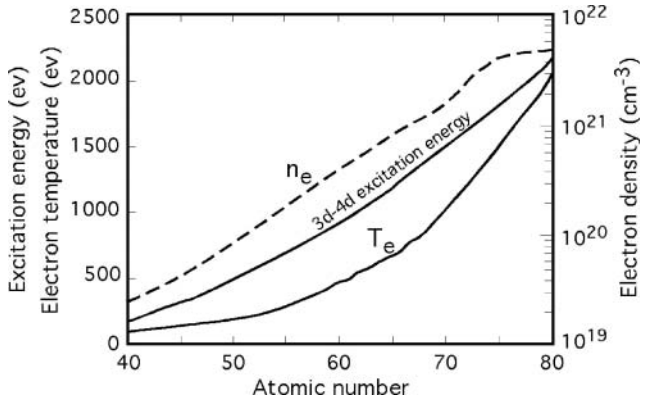

Fig. 7.5. Electron density and electron temperature providing optimal 4d–3d population inversion in Ni-like ions versus the atomic number of the lasant (data from Ref. [153]).

can infer from these data that the pump intensity necessary to produce a laser line of wavelength λ varies according to the magnitude order relation

$$I_{\text{pump}} \propto \lambda^{-\gamma} \tag{7.4}$$

where γ may be estimated at

$$\gamma \simeq 4$$

Therefore, with the simplest of pumping dynamics, namely a single pump–laser pulse focused onto the lasing material, any progress toward shorter laser wavelengths will require a huge increase of pump intensity. For instance, reducing the wavelength from 20 nm, a value commonly achieved for years, to 4 nm, viz. a wavelength lying in the "water-window," would call for an increase of pump intensity by a factor larger than 3000. On the other hand, lasers in the 50-nm wavelength range could work with small inexpensive pulsed lasers, supplying only a few Joules in nanosecond pulses.

A way to reduce the amount of pump energy, especially when lasing at short wavelengths, consists in separating the electron heating process from the plasma production. Figure 7.6 shows that the energy necessary to excite the lasing upper level of Ge-like ions is 1.4 times larger than the Na-like to Ne-like ion ionization energy. Therefore when the electron temperature is optimum with respect to neon-like abundance, it is too low to provide an optimum excitation rate. Moreover the temperature maximum, which coincides in time with the maximum of the pulse [cf. relation (5.8)], occurs later than the maximum of neon-like density, which decreases through plasma expansion after a rapid initial rise due to the high target density (see for instance [88]).

These characteristics are illustrated in Figure 7.7a where the Ne-like abundance curve originates from experiments [162]. It is obvious that a single

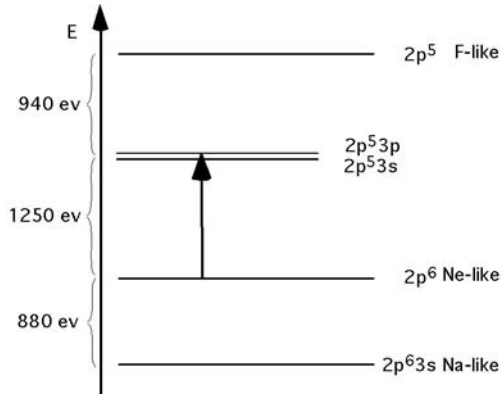

Fig. 7.6. This diagram shows, in the case of Ne-like germanium, the energies involved in the production of $2p^5 3p$–$2p^5 3s$ population inversion. The $J = 0$ to $J-1$ lasing transition emits photons of ∼63 eV. The ionization energy required to produce Ne-like from Na-like ions is ∼880 eV while the excitation energy of the $2p^5 3p$ level is ∼1250 eV.

nanosecond pulse cannot lead to optimum pumping conditions since part of the energy is lost keeping the plasma hot, while the number of potential emitters is vanishing. However, as shown in Figure 7.7b this loss may be prevented by using two pulses: a nanosecond one, of relatively low intensity, is optimized to produce Ne-like (or Ni-like) ions and it is followed by an intense short pulse, allotted to electron heating only. Pumping efficiency is optimized thanks to an adjustable delay between the two pulses. The reliability of this so-called transient pumping method has been experimentally demonstrated for the first

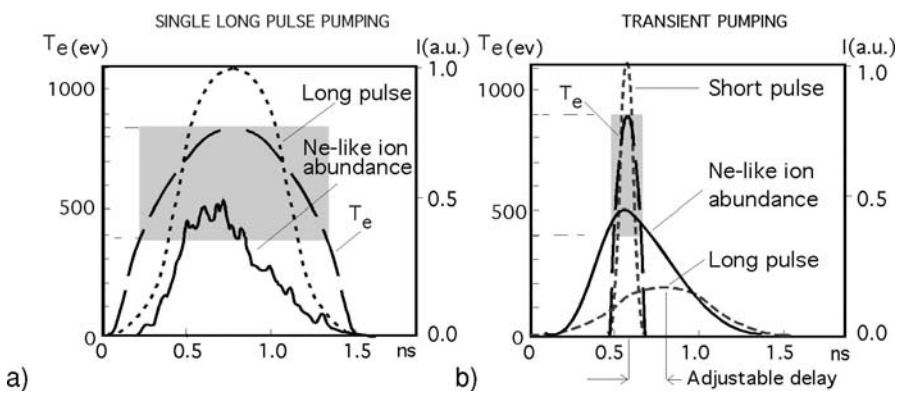

Fig. 7.7. Temporal characteristics of pumping by single long pulse (a) compared to pumping by short pulse following long pulse (b). Short dashed line: intensity I of the pump laser; long dashed line: electron temperature ($\propto I^{1/3}$); continuous line: Ne-like ion abundance. Grey areas represent the regions where pumping is effective.

time by P.V. Nickles et al. [163,164]. Then the development of ultrashort pulse lasers led to use traveling waves to deposit the energy of pump pulse along the line focus (see Section 7.4).

We shall also see that an additional pulse of low intensity, preceding the main pulse, both having the same duration, proves to be essential to the emission of some of the intense laser lines. The role of this prepulse is to improve laser propagation by smoothing the plasma density gradients, which results in a laser gain–length factor increase.

Below we present the characteristics of typical examples of collisionally pumped XUV lasers which will be sorted according to their pumping dynamics.

7.2 Single Pump-Pulse of Nanosecond Duration

7.2.1 Ne-Like Selenium Laser

Considered as the most promising element, selenium ($Z = 34$) has been chosen as the emitter material for the soft X-ray laser that used collisional-excitation pumping for the first time [39]. For this element, three laser lines were expected at wavelengths of 18.24 nm ($J = 0-1$), 20.63 nm ($J = 2-1$), and 20.96 nm ($J = 2-1$). Experiments were performed at the Novet laser-target irradiation facility (LLNL, USA) using the principle of exploding-foil target described in Section 5.2.1. Two frequency-doubled arms of the NOVA laser ($\lambda = 0.532$ μm) were used to produce the lasing selenium plasma. The experimental arrangement is schematically shown in Figure 7.8 [40]. XUV spectrometers and detectors are positioned on the two axial directions and

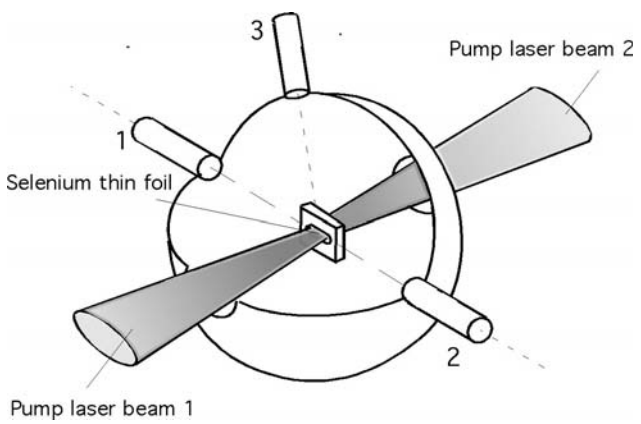

Fig. 7.8. Exploding foil Ne-like selenium laser, 1 and 2 are on axis spectrometers. Laser lines are measured with spectrometers 1 and 2 and spectrometer 3 verifies that these lines are missing off axis.

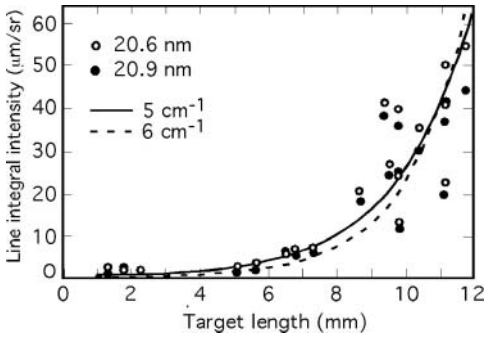

Fig. 7.9. Nonlinear increase of the $J = 2$ to $J = 1$ lines of Ne-like selenium demonstrating a 5–6 cm^{-1} gain coefficient for both lines (Ref. [40]).

at 77° off-axis. The off-axis spectrometer contributes to laser action identification as laser lines are visible on axis only, not in any other direction.

The target is composed of a 75-nm layer of Se deposited on one side of a 150-nm thick Formvar substrate. The selenium foil is illuminated by the second harmonic of the driving laser light, at wavelength of 0.532 μm. The two line foci, obtained with the help of combinations of ∼80-cm diameter cylindrical and spherical lenses, are 1.12 cm × 200 μm dimensioned. The nominal pulse duration is of 450 ps. The typical incident intensity is of 5×10^{13} $\mathrm{W/cm}^2$, which requires more than 1 KJ energy per pulse and per beam at the fundamental wavelength of the laser. Ion temperature in the hot plasma is of ∼400 eV. The XUV laser power output is estimated at 1 MW with duration of 200 ps. The beam divergence is about 8 mrad [165]. The gain coefficient g is obtained by fitting the simplified Lindford form of the growth curve (1.42)

$$I_{\mathrm{T}} \propto l^{-1/2} e^{gl} \tag{7.5}$$

where g is the adjustable parameter, on the total line intensity I_{T}, measured as a function of the plasma-line length l. The results for the $J = 2{-}1$ lines appear in Figure 7.9, for two test values of g. The curves clearly show the nonlinear intensity increase of both lines with the plasma length.

Calculated and observed gains are displayed in Table 7.1 for the three selenium laser lines predicted by calculation. For the 2–1 lines the observed gain agrees with theoretical predictions. The surprise obviously comes from

Table 7.1. Predicted and observed gain for the main lasing lines of neon-like selenium

Transition	λ(nm)	Predicted gain	Observed gain
$J = 2$ to 1	20.96	∼4 cm^{-1}	5.5 cm^{-1}
$J = 2$ to 1	20.63	∼4 cm^{-1}	5.5 cm^{-1}
$J = 0$ to 1	18.24	∼10 cm^{-1}	<1 cm^{-1}

the $J = 0-1$ line exhibiting no gain at all, while calculation allotted to this line the largest gain coefficient. This disagreement, which recurred for all similar lasers using other lasant material, became the source of theoretical investigations based on more sophisticated physics, especially with regard to atomic physics, than at the time of first calculations. However no conclusive explanation of the observed discrepancy could be found in this way. Then the discrepancy has been found less pronounced when slab targets rather than exploding foils were used to produce the plasma [166]. Experimental occasions finally showed that a small pulse sent before main pulse fully restores the large gain predicted for the 0–1 line (see Section 7.3).

Selenium laser made possible the first measurements of ASE–laser line profiles in the XUV wavelength region [106]. Therefore it was now possible to compare the observed behavior of the line profile when gain–length increases, with the theoretical predictions performed for homogeneous and nonhomogeneous profiles.

The continuous curve in Figure 7.10 represents the calculated line width (Full Width at Half Maximum) for homogeneous profiles as a function of target length. The gain coefficient is assumed to be $\sim 6\ \mathrm{cm}^{-1}$. The figure shows a fast line narrowing for small gain–lengths ($gl \lesssim 12$) and then a nearly constant line width at large gain–lengths. Contrasting with this result, calculations for nonhomogeneous profiles predicted a line rebroadening for large gain–lengths, i.e. $gl \gtrsim 12$ in the present case (cf. Section 6.3).

Experimental measurements have been performed using an experimental arrangement which includes high-resolution XUV spectrometers and a streak camera with a narrow (35 μm) slit. Convolution of both instrumental functions leads to a total resolution power ($\lambda/\Delta\lambda$) of 14,000 and 17,000 for the two different spectrometers used in this experiments. In Figure 7.10 triangles represent the raw data and black circles the reduced (deconvolved) data. The fact that they do not reveal any line rebroadening shows that the profile is dominated by homogeneous contribution. By extrapolating them to $l = 0$, one can infer an intrinsic line-width of 50 ∓ 10 mÅ, from the reduced data.

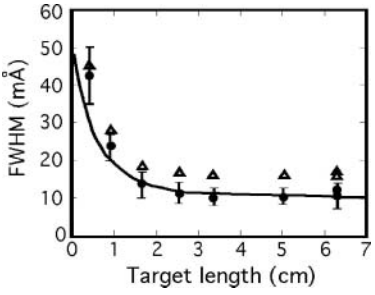

Fig. 7.10. Width of the soft X-ray laser line versus plasma length; triangles: experimental raw data; black circles: deconvolved data; continuous line: calculated widths.

7.2.2 Ne-Like Ge Laser (Saturation, Coherence, Polarization)

7.2.2.1 First Experimental Observations

From selenium ($Z = 34$) to germanium ($Z = 32$) the lasing line wavelengths increase by about 10%. Therefore, from relation (7.4), the pump energy is expected to be lessened by factor $\sim 0.9^5 \simeq 0.6$ and a larger number of laser facilities may contribute to gain coefficient, angular distribution and other X-ray laser characteristics determination.

First measurements using a thick slab target of germanium, instead of an exploding foil, and the fundamental 1.06-μm wavelength of a 350–480 J Nd–glass laser, showed gain for five Ge^{22+} 3p–3s lines [167, 168]. The pulse duration was of 2 ns. A combination of cylindrical–spherical lenses produced a line focus of 200 μm in width and 18 mm in length. The target irradiance was about 6×10^{12} W/cm^2.

Two previously observed $J = 2{-}1$ lines in Ge ($\lambda = 23.22$ nm and $\lambda = 23.63$ nm) and a new $J = 2{-}1$ line ($\lambda = 28.78$ nm) showed gain about 4 cm^{-1}. The corresponding transitions can be seen in the Grotrian diagram in Figure 7.11. A new laser line, corresponding to a $J = 0$–1 transition, appeared at $\lambda = 19.61$ nm with gain of 3.1 cm^{-1}. It is worth noticing that this value was well below theoretical prediction. Another laser line, identified as due to transition between two core-excited levels ($2s2p^6 3s{-}2s2p^6 3d$), was observed at 19.90 nm with gain coefficient of 2.5 cm^{-1} [169]. At nearly the same time, a work performed in conditions very similar to those used for selenium with the exploding foil technique, obtained gain for three $J = 2{-}1$ lines but failed to observe gain for the $J = 0{-}1$ one [170].

Given the large difference between the slopes of the density gradient produced by thin foil two-side illumination and 0.53–μm wavelength pump, on the one hand, and by single side illumination of a plane thick target and 1.06–μm wavelength pump, on the other hand, these results confirmed that refraction as a part in the gain obtained for each line. Though the method able to control such effects was not still known, the germanium laser, with the two $J = 2{-}1$ lines at 23.22 and 23.63 nm, quickly became an important tool of XUV laser physics, especially to improve the beam characterization, to study new target designs and to investigate laser saturation, coherence, and polarization of the beam.

7.2.2.2 Calculations

Extensive calculations about the germanium plasma laser have been carried out by P.B. Holden et al. [88] and D. Benredjem et al. [171]. As an example the averaged plasma charge Z, calculated in a large domain of electron density and temperature, is shown in Figure 7.12 [88]. Furthermore, the gain coefficients for the 19.6 nm, 19.9 nm, 23.2 nm, and 23.6 nm in the same domain of parameters were obtained with the help of steady-state calculations including 124 excited levels and the dielectronic recombination

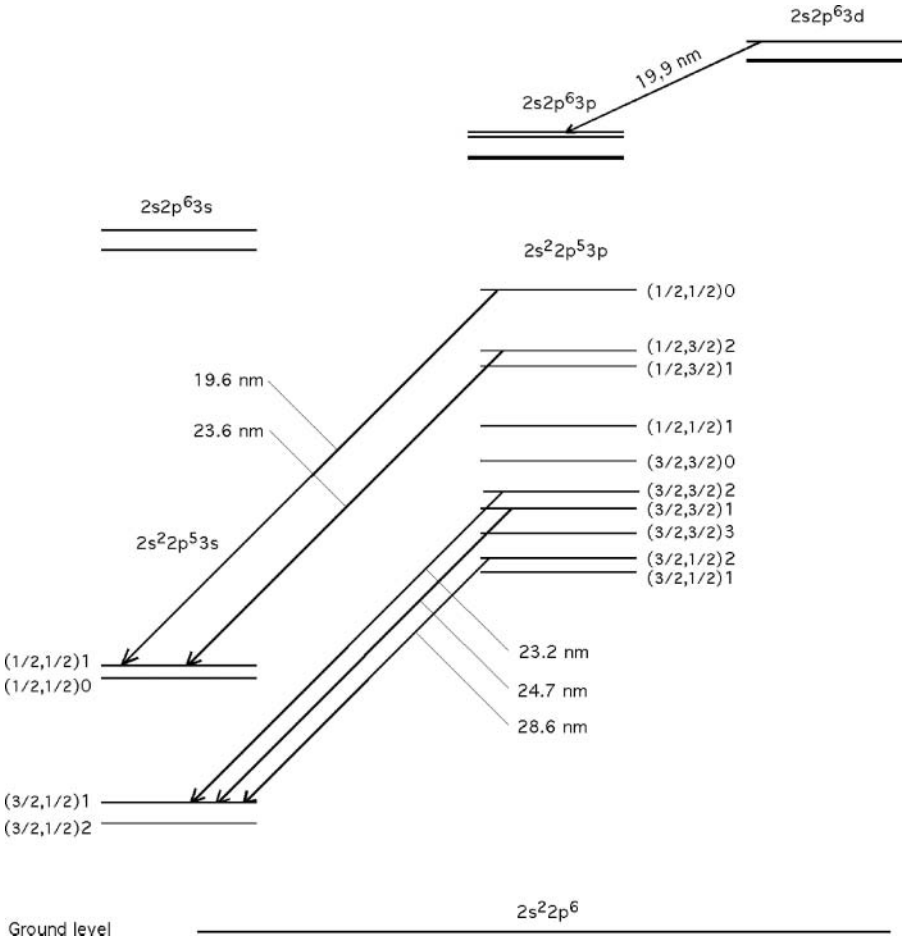

Fig. 7.11. Grotrian diagram of Ne-like ions of germanium.

from the lowest excited levels of F-like ions. This is illustrated in Figure 7.13, which shows the predicted gains for the 19.6 nm and 23.2 nm lines. It is worth noting that Figure 7.11 shows Ge^{22+} neon-like ions to dominate plasma at temperature below 500 eV while, according to the results of Figure 7.12, large gains require temperatures above 700 eV. This clearly confirms that one cannot achieve optimum ionization and temperature conditions for gain within the plasma dynamics produced by a single pump pulse.

In connection with the line width problem (cf. Section 7.2.1), it is found that the broadening by electron collision is such that the ratio between the Lorenz homogeneous component and the Doppler inhomogeneous component is approximately $\sqrt{800/T_\mathrm{i}}$, where T_i is the ion temperature in eV. More recently the frequency redistribution produced by electron collisions has been

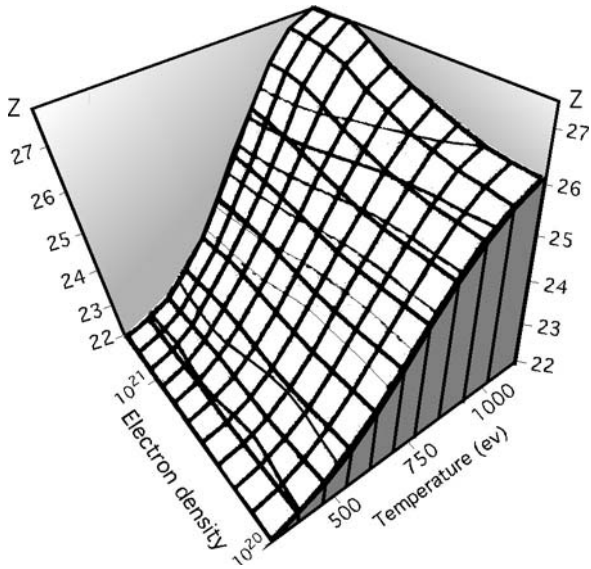

Fig. 7.12. Plasma averaged charge as a function of electron density and temperature (Ref. [88]).

introduced in the calculation of the radiative transfer for the laser line. It has been found to have a small effect on XUV laser emission intensity [171, 172].

7.2.2.3 Experimental Beam Characterization

Unsaturated emission. Figure 7.14 shows laser lines of germanium at 19.6 nm, 23.2 nm and 23.6 nm recorded for two lengths of the plasma line, with a flat

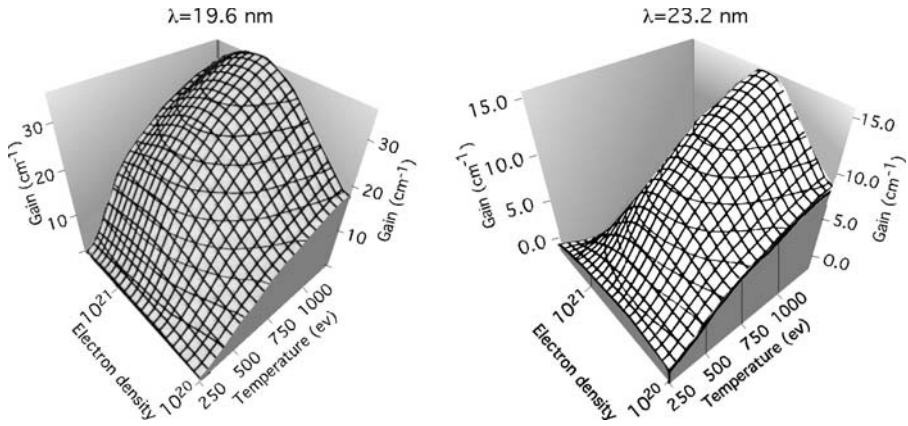

Fig. 7.13. Gain coefficient of two laser lines of Ne-like germanium calculated as a function of electron density and temperature (Ref. [88]).

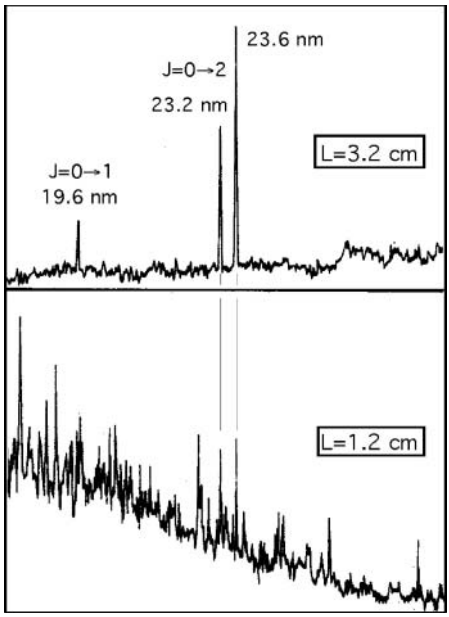

Fig. 7.14. Experimental spectra of Ne-like germanium for two lengths of the plasma fiber. The measured gain coefficient is 3.8 cm^{-1} for the 23.6-nm line.

field grating of resolving power $\lambda/\delta\lambda \simeq 350-500$ [173]. The laser configuration used in this experiment is similar to the one represented in Figure 5.6 (Section 5.2.1) but reduced to three laser beams only. The lengths of the three line foci are 1.2 cm. They are in-line positioned to increase plasma length up to 3.2 cm. The incident intensity is 2.5×10^{13} W/cm^2 with a line-focus of width $\sim$200 μm. The pulse duration is of 0.5 ns at FWHM. The spectra correspond to plasma lengths of 1.2 and 3.2 cm, respectively. The emergence of laser lines when the plasma becomes long is patent. From the output measurement with increasing length, one finds gain coefficients of 3.8 cm^{-1} at 23.6 nm and 2.7 cm^{-1} at 23.2 nm. Therefore the maximum gain–length is about 12.

The angular distribution of the X-ray laser beam is deduced from the line intensity variation in the horizontal plane, perpendicularly to the target, as schematically shown in Figure 7.15. Ψ, the angle between the target plane

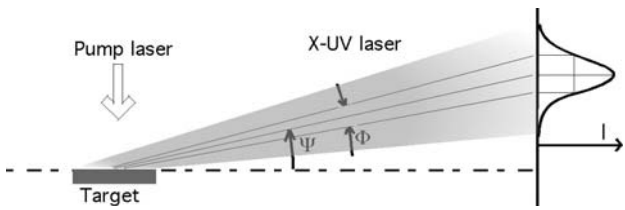

Fig. 7.15. Deflection Ψ, and horizontal divergence Φ, of soft X-ray laser.

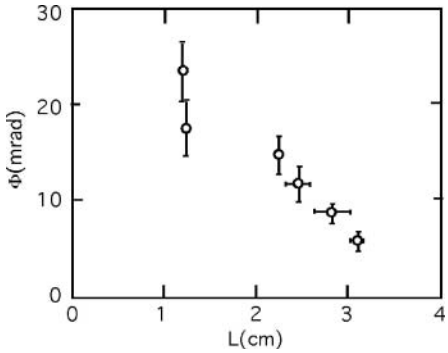

Fig. 7.16. Divergence of the soft X-ray laser beam versus plasma length.

and the measured beam axis, is a global measure of the deflection due to refraction through the plasma. The value of Ψ is found to be 7 ∓ 2 mrad. Φ, the horizontal half-width of the angular distribution defined by the FWHM of the far field intensity pattern, is the divergence of the soft X-ray laser. Figure 7.16 shows the divergence Φ to decrease from $\sim$20 mrad to $\sim$5 mrad when the target length increases from 1.2 cm to 3.2 cm.

A streak camera with a CsI photocathode, coupled to spectrometer, gives information about the time–evolution of the gain. The time resolution is typically 50 ps. Figure 7.17 shows the XUV laser emission to last as long as the incident laser pulse itself in the present experiment.

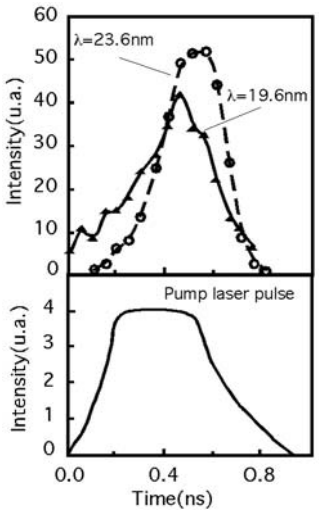

Fig. 7.17. Temporal variation of laser intensity. Top: intensity variation of the 23.6- and 19.6-nm lines with time; bottom: intensity variation of the pump beam with time.

Table 7.2. Time-integrated gain coefficients of Ne-like germanium lines obtained with 1 ns pump pulse (Ref. [175]); GL is the gain–length factor

λ(nm)	L(cm)	G(cm^{-1})	GL
19.6	4.0	2.67	10.7
23.2	4.0	3.66	14.6
23.6	4.0	3.66	14.6
24.7	3.4	2.57	8.7
28.6v	3.4	3.52	12.0

Similar results have been obtained with the system of double target coupling (see Fig. 5.10, Section 5.2.2) with which one can minimize refraction effects without increasing plasma length [174, 175]. From the work described in [175], measurement of gain for five lines, with a pump–laser irradiance of 1.2×10^{13} W/cm^2, gives the results presented in Table 7.2.

Saturated emission. Increase of the amplifier plasma length to achieve laser saturation is limited by the pump power available in each experiment. Moreover counterbalancing refraction over long radiation flights requires complex target configurations. However, half-cavities increase the effective gain–length [see Eq. (5.21)] with the same energy as for a single-pass of laser radiation. Furthermore, with a proper adjustment of the mirror, the trajectories of the direct and the reflected beam intermingle so that refraction as nearly the same effect on the two passes.

This technique, applied to the 23.6-nm wavelength line of germanium, has given the first unequivocal demonstration of the saturation of an XUV laser [31, 48]. The experimental arrangement, shown in Figure 7.18 is based on the double-plasma configuration. In addition, it uses the half-cavity mirror that will implement the double-pass through double plasma. The distance from targets to mirror must be shorter than a maximum $d_{\max}$, which is of the order of $c \times \tau_{\mathrm{XRL}}/2$, where τ_{XRL} is the amplified XUV emission duration. For the results presented below d was $\sim$2 cm and the curvature radius of the concave mirror was 13 cm. A shield protects the mirror from ion impacts and

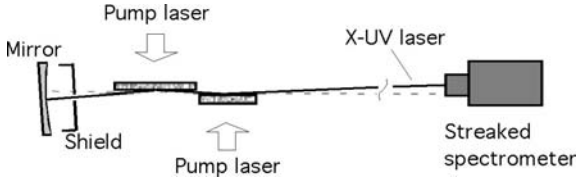

Fig. 7.18. Double-target and half-cavity system used to demonstrate germanium laser saturation at the wavelength of 23.6 nm.

target debris, except on a $\sim 1-\text{mm}^2$ surface that is used to reflect the beam. This surface is changed after each shot. Target lengths are 22 mm and 14 mm.

The reflectivity of the mirror measured at 23.6 nm is ∼28%. However the radiation that initiates the second pass does not involve all the reflected radiation but only the portion that will reach the narrow amplifying zone of the plasma. This portion varies with the divergence of the beam, the curvature radius of the mirror, and the size of the amplifying zone. In practice it can be evaluated from the intensity increase obtained by adding the mirror with a plasma length short enough to maintain the laser in the unsaturated regime. In the present case, the typical increase was of a factor 30 for the 22-mm long plasma. The effective feedback from the mirror was then about 2%. Furthermore, the small-signal gain is measured to be 3.8 cm^{-1}. Thus, for plasma lengths $l \gtrsim 15$ mm, the effective gain–length (5.21) was given by

$$gl_{\text{eff}} \simeq 7.6 \times l_{\text{cm}} - 3.9$$

Figure 7.19 shows the exponential increase of the time-integrated intensity for effective values of gl less than ∼14. Then the saturated emission behavior starts and it is observed for values of gl_{eff} up to ∼22. The maximum source brightness is estimated at $\sim 1.3 \times 10^{14}$ W/cm^2/sterad in 0.01% band width.

Coherence. The coherence of the 23.6-nm laser emission has been investigated using the injector–amplifier system described in Section 5.2.2 (see Fig. 5.12) [51]. Reference wires of 150-μm diameter were placed in the X-ray mirror alignment. Coherence was estimated from the fringe visibility in the far field pattern (Fraunhofer diffraction) of wires. As an example, Figure 7.20 displays

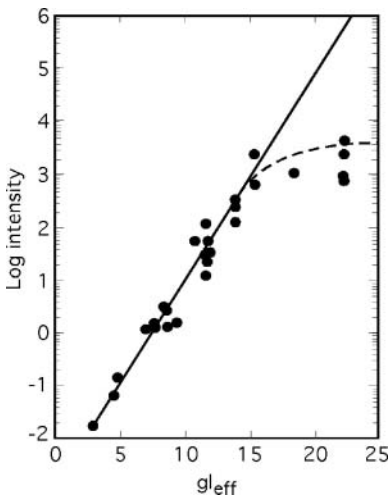

Fig. 7.19. Exponential intensity growing and saturation behavior for gain–length factors ≳15.

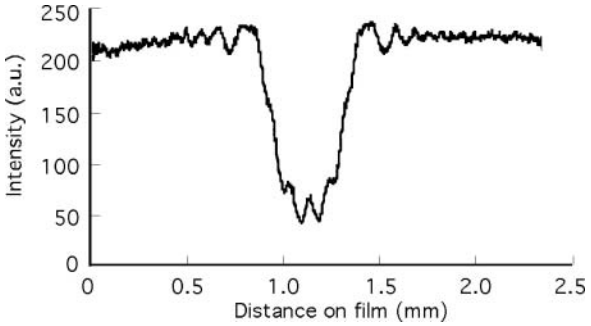

Fig. 7.20. X-ray laser intensity distribution obtained in the shadow of a 180-μm diameter cross-wire (Ref. [51]).

the intensity distribution observed in the geometrical shadow of one of the wires. Coherence changes with laser saturation were observed by first using the injector only, then the injector plus one or two amplifiers. Fringe visibility was measured for several shots and various amplifier combination. The results are presented in Figure 7.21 which exhibits three groups of data, i.e. without amplifier and with one or two amplifiers. Different symbols are used for near-field and far-field data. One can see that fringe visibility increases when the laser tends to saturation. Moreover, as a consequence of coherence propagation, the visibility is larger in the far-field than in the near field. It is also observed that the visibility varies along the wires, indicating that the coherence is not constant on all parts of the beam.

Polarization. A typical X-ray laser pulse consists of several thousand of wave trains, each with a definite polarization state. These polarization states are

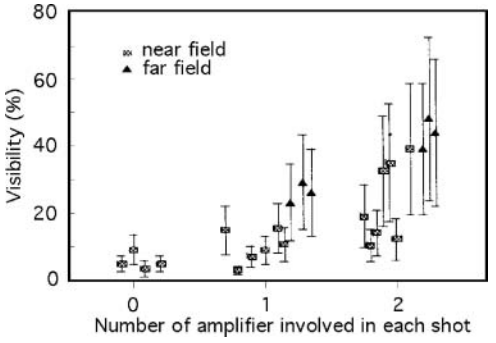

Fig. 7.21. Fringe visibility measured in the near field and in the far field without amplifier (emission of the injector only) and with one or two amplifiers. Coherence increases with the number of amplifiers, viz. when the soft X-ray laser tends to saturation.

mutually uncorrelated so long as laser is unsaturated and degree of coherence continues weak. In this case the laser output will appear unpolarized. However several plasma processes can generate polarization of the laser line radiation. It is known for instance that the anisotropy of the free electron velocity distribution can lead to anisotropic excitation processes, which results in polarized emission lines [176–178]. Another example is a group of radiative transitions sharing a common level, where radiation field does not lead systematically to random populations between all the quantum states involved in each excited level [179, 180].

An important issue concerns the way in which amplification could modify the polarization state of an initially polarized beam. In other words, if we polarize an ASE beam before injecting it in the amplifier, will this beam suffer a change of its polarization state due to amplification? One could imagine that collisions experienced by the emitting ions of the amplifier change their dipole moment orientations randomly, which would pull down the initial degree of polarization. In other respects magnetic fields, which appear spontaneously in the plasma, could produce Faraday's rotation of the X-ray beam electric vector, thereby modifying the polarization state.

Moreover one has to consider the contribution of the unpolarized ASE amplifier radiation to the total output. The principle of the injection of a polarized beam into an amplifier plasma is illustrated in Figure 7.22 which shows a polarizer placed between injector and amplifier. Owing to beam divergence and polarizer geometrical properties, the input into the injector is reduced by a coupling factor C as compared to the injector output. Due to the injector beam divergence and to the narrow amplifying fiber, the coupling factor C is a small number. Furthermore, for XUV radiation, polarizers are mirrors used under Brewster angle. Let R be the reflection coefficient of the mirror. The injector intensity reaching the amplifier is finally reduced by a factor RC.

Let $g_i l_i$ be the gain–length of the injector, $g_a l_a$, the gain–length of the amplifier, $S_i = j_i/g_i$ and $S_a = j_a/g_a$, their respective source functions. The gls are assumed to be $\gtrsim 3$ in order that $\exp(gl) \gg 1$. From the radiative transfer equations of Section 1.2 one readily obtains the expression of the injector–amplifier system output which reads

$$I(\nu)^{\text{out}} \simeq S_a e^{g_a l_a} + RCS_i e^{(g_i l_i + g_a l_a)}$$

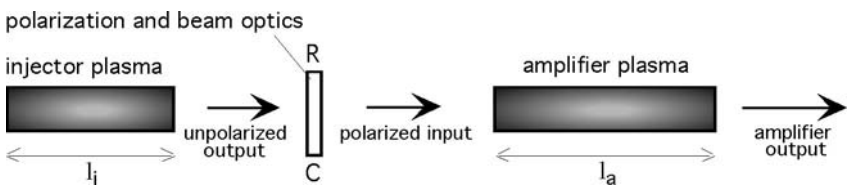

Fig. 7.22. Principle of the polarized XUV beam amplification by an amplifier plasma. C is the injector–amplifier coupling coefficient. R is the reflection coefficient of the not-represented mirror used as polarizer at Brewster's incidence angle.

where $I(\nu)^{\text{out}}$ is the intensity at frequency ν. The total intensity may be obtained by using the simplified form of the Lindford approximation (1.42), from which we have

$$I_T^{\text{out}} \simeq \sqrt{\pi}\Delta\nu \left[S_a \frac{e^{g_a l_a}}{\sqrt{g_a l_a}} + RCS_i \frac{e^{(g_i l_i + g_a l_a)}}{\sqrt{g_i l_i + g_a l_a}} \right] \tag{7.6}$$

where the line is assumed to have an homogeneous Doppler profile. When the injector radiation is polarized, the first term of this equation is the unpolarized component of the total output. Let us notice that the sources functions S_a and S_i, which depend on the population ratio of the upper and lower levels of the laser, will generally have similar values. The degree of polarization, defined as

$$D_{\text{p}} = \frac{I_{\text{p}}}{I_{\text{p}} + I_{\text{u}}} \tag{7.7}$$

where I_{p} and I_{u} are the intensities of the polarized and the unpolarized waves, will thus be determined by the respective magnitudes of the two exponential terms of equation (7.6).

Therefore, it is worth experimentally investigating the polarization state of the ASE emission of XUV lasers. A propitious circumstance to develop polarization studies is the fact that Brewster's angle at these wavelengths is near 45°. Thus multilayer mirrors used at 45° angle of incidence are generally good polarizers. Compared to normal incidence mirrors, only a few pairs of layers are necessary to reach high reflection coefficients. However it is necessary to minimize the surface roughness in order to reduce *p*-reflectivity and so to achieve the highest possible extinction ratio between *s* and *p* components. The polarizers used by B. Rus et al., in Ref. [135] using the radiation of the Ne-like germanium laser, were coated onto silica substrates with an rms surface roughness of less than 0.1 nm. Three pairs of Mo:Si layers were produced by ion-beam sputtering. A reflectance of ∼24% was achieved for s-polarized light (electric vector parallel to the polarizer surface). Calculation of the s- to p-reflectance ratio suggested the p-reflectance to be of ∼3.25%.

The experimental polarization arrangement is shown with its analyzers in Figure 7.23. The injector is made of two successive germanium targets, each of them of 22 mm in length. Two polarizers, called analyzer 1 and analyzer 2, are used as analyzers for the p- and s-polarization directions, respectively. Figure 7.23a shows the injector and the concave mirror which focuses the XUV laser beam to a point located beyond injector, near the location designed for the amplifier. The normal to the concave mirror is at a small angle to the beam, so that the mirror works as focusing optics but not as double-pass system, i.e. not as half-cavity. A spatial fiducial, consisting of three crossed 150-μm diameter wires is positioned in the beam. Gain coefficients were found to be 3.5 cm^{-1} for the injector and 3 cm^{-1} for the amplifier.

The first part of the experiment aimed to control that the time-integrated radiation of the injector at 23.6-nm was not polarized. The amplifier was thus removed away from the beam path. The results showed the footprint images

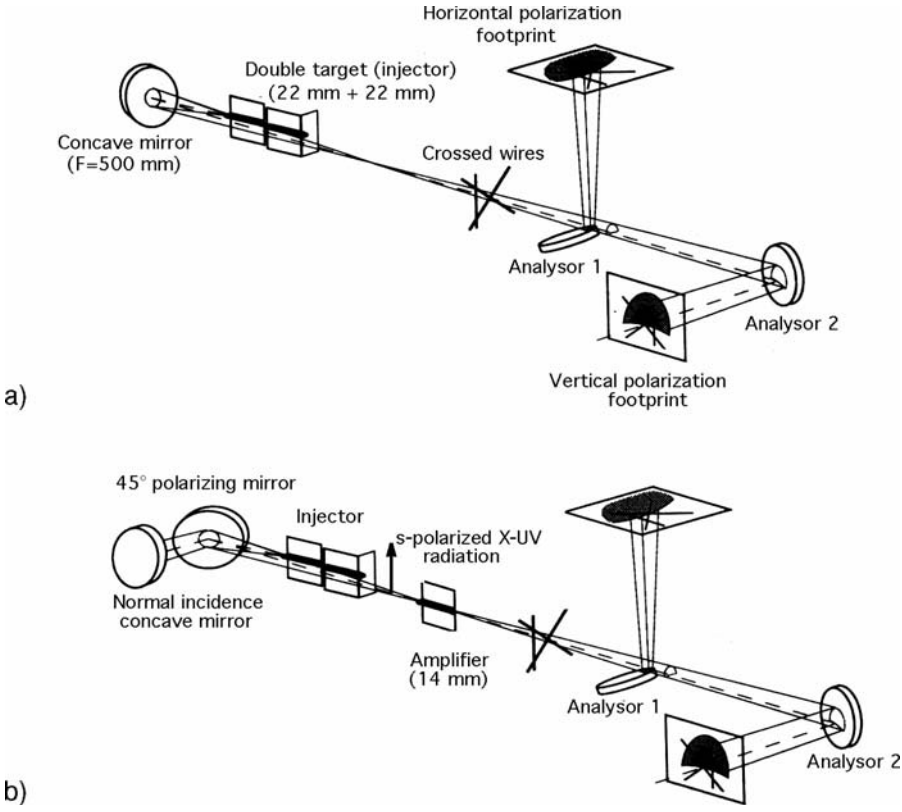

Fig. 7.23. (a) Arrangement used to control the absence of polarization in the injector emission. (b) Arrangement used to produce a *s*-polarized beam and to measure a possible change of polarization in the amplifier plasma.

of the injector output in each of the crossed polarizers arms to have similar signal strength, which confirmed the absence of polarization of the injector beam within the experimental accuracy estimated at ∼5%.

During the second part of the experiment the injector radiation was polarized by a near 45° incidence polarizing mirror as shown in Figure 7.23b. The 14 mm in length amplifier was positioned on the beam axis, its entrance end being at short distance from the focus of the injected beam. Amplifier was shot ≈7.55 ns after injector in order to synchronize the injected beam with the phase of the amplifier gain.

Recording the footprint shown in Figure 7.24a analyzer 1 was removed from the beam path so that only the s-polarized component of the whole beam contributes to the image which shows the high quality of the beam profile. On the other hand, a typical result with both analyzers in position is shown in Figure 7.24b. To show the whole beam in a single image, the

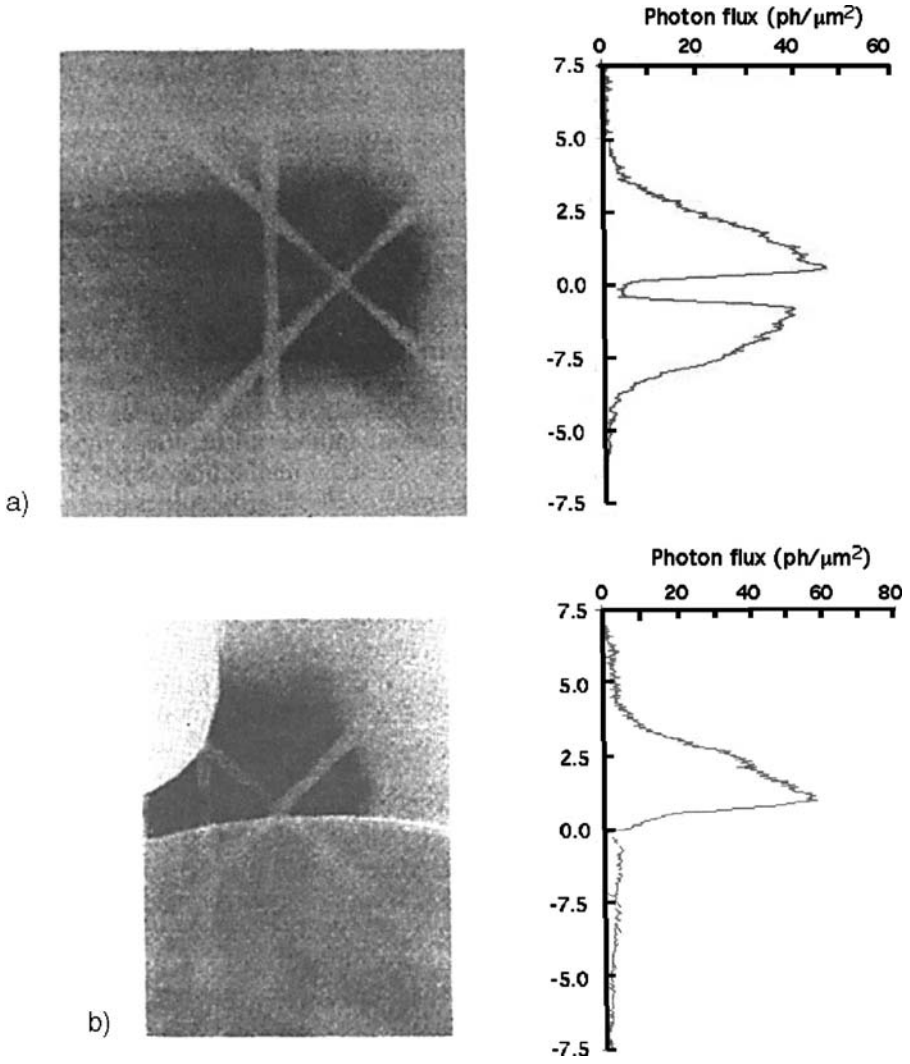

Fig. 7.24. (a) Footprint of the s-polarized beam after passage through the amplifier. (b) Comparaison of *s*- and *p*-polarized signals after passage through the amplifier showing that almost all the intensity is carried by the *s*-polarized signal.

two footprints produced by a single shot have been reassembled with the help of the spatial fiducial. The top and the bottom half-parts of the image correspond to the s- and to the p-polarization, respectively. On the right-hand part of the figure, densitometer traces show that there is virtually no p-polarized signal. Quantitative analysis of image intensities, averaged over all shots, gives $D_{\mathrm{p}} \simeq 0.98$, which is essentially the value of the polarization

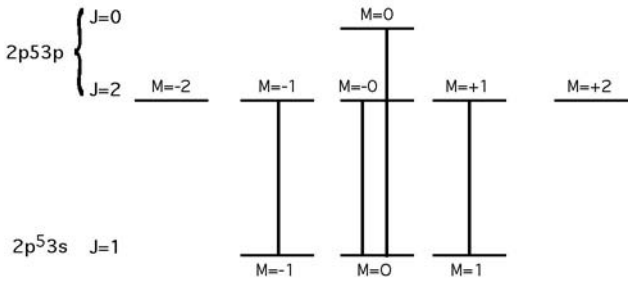

Fig. 7.25. Diagram of the linearly polarized transitions between the $2J + 1$ quantum states of $J = 0$, 1, 2 levels.

degree of the injected beam. The experiment thus shows that amplification by plasma did not depolarize the initially polarized beam.

For the gain–lengths achieved in this experiment and an RC factor of $\sim 7 \times 10^{-4}$, which accounts for the effective transmission of the X-ray optical elements, the first term in the right member of equation (7.6) is three orders of magnitude smaller than the second term. Therefore, the ASE emission of the amplifier cannot significantly modify the beam polarization. Moreover a careful examination of polarization effect due to plasma self-generated magnetic fields through Faraday's rotation, leads to the conclusion that this effect is negligible (see [135]).

A more complex effect may result from the distribution of a given atomic level population, let say $2p^5 3p$ $J = 2$, between the $2J + 1$ magnetic quantum states that constitute this level. Figure 7.25 shows the diagram of transitions that induce linear polarization of the $J = 0{-}1$ and $J = 2{-}1$ Ne-like emission lines. In most cases, magnetic states are degenerate and respond as a whole to excitation by radiation field. However, magnetics fields can appear in plasma removing the degeneracy. In this case separated population equations must be solved for each sublevel.

This magnetic effect has been numerically investigated for a representative value of the magnetic field generated in a collisionally pumped germanium plasma, viz. $B \approx 10T$, in Refs. [179,180], which use Maxwell–Bloch approach (cf. Section 6.3). This study shows that ignoring the collisional population redistribution leads to significant population differences between sublevels. However, if calculation includes the intersublevel transitions due to electron–ion collisions, the population differences practically disappear. Therefore calculation predicts that, when a linearly polarized beam is injected into plasma, the degree of polarization remains very close to unity, which is confirmed by the experimental observation reported above.

It is thus relatively easy to produce intense linearly polarized XUV sources by using laser techniques. Saturated lasers of very large gain–length factor are not required to this end.

7.2.3 Ne-Like Yttrium Laser

Yttrium laser is the third typical example of first generation X-ray lasers. It presents two notable characteristics. The total output measured at 15.5-nm wavelength has been found ∼7 mJ with a peak power of 32 MW, for a total irradiation intensity of 1.5×10^{14} W/cm^2 and a pulse duration of 500 ps [181]. These remarkably high values make this laser a potential attractive tool for applications.

Furthermore a single lasing line dominates the laser output while Ne-like lasers usually showed two $J = 2-1$ laser lines. This peculiarity, which may be of interest in practical applications, has been a headache for X-ray laser physicists. They knew that the wavelengths of the $J = 0-1$ line and of the shortest wavelength $J = 2-1$ line of Ne-like yttrium were nearly identical and that these lines could not be resolved with ordinary techniques [165]. However, the difficulty arose from the fact that gain coefficient was found to be smaller, viz. 5.3 cm^{-1}, for the intense line at 15.5 nm, than for the much weaker line, at 15.7 nm, which exhibited a 6.4 cm^{-1} gain value. Figure 7.26 illustrates this anomaly.

To explain this strange peculiarity of yttrium laser, it was necessary to investigate in details the effects of the $J = 2-1$ and $J = 0-1$ line overlapping. We summarize hereafter the main steps of the interpretation proposed by P.B. Holden et al. [182].

(a) Overlapping of two lasing lines may strongly enhance the intensity of the composite line because, at each frequency of the line profile, the intensity grows up exponentially versus the sum of the two gain–length products, i.e. in the present case $(g(\nu)_{J=2-1} + g(\nu)_{J=0-1}) \times l$. Therefore, it is likely that the anomalously large intensity ratio of the two observed lines is due to the overlapping of the $J = 0-1$ line with the 15.5 nm, $J = 2-1$ line.
(b) However this by no means explains that the measured gain coefficient at 15.5 nm remains smaller than the one measured at 15.7 nm. Here it is important to keep in mind that measured gain coefficients are more or less

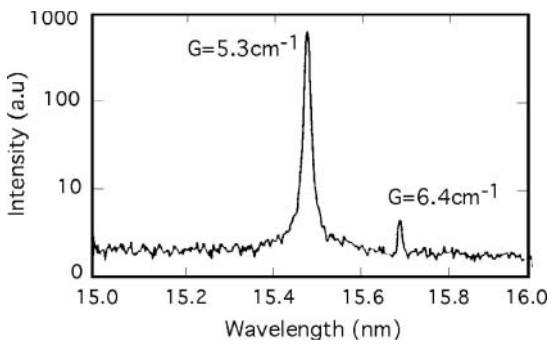

Fig. 7.26. Experimentally observed lasing lines of Ne-like yttrium.

space–time averaged and hence differ from the local instantaneous values obtained by calculation. Since line profiles are narrowed by propagation in plasma (see Sections 1.3 and 1.4), their overlapping progressively reduces so that the two components finally separate. This should lower the apparent gain, that is the gain averaged over the photon propagation time.
(c) However it is found that, for the very small line separation considered in the present case ($0 < \delta\lambda < 50$ mÅ), a line narrowing scaling such as $\Delta\nu \propto 1/\sqrt{gl}$ [Eq. (1.39)] has an almost negligible effect on line coupling. Thus, one is led to consider other line narrowing mechanisms which should be induced by the varying plasma conditions. As a matter of fact, hydrodynamic calculation shows plasma expansion to cause a significant reduction of electron density (n_e), accompanied by a fall of ion temperature (T_i), during the propagation of the amplified beam. The beam propagates across a gradient of refractive index and emerges from the gain region in plasma shells where electron densities and ion temperatures are less than on axis. The calculated variation of plasma parameters so experienced by the beam as a function of the distance traveled through a 3-cm length plasma is displayed in Figure 7.27. The plasma peak density corresponds to free electron density $n_e \sim 7 \times 10^{20}$ cm^{-3}. The remarkable result of this analysis is that the total line width reduction is sufficient to significantly reduce the coupling of the lines and to actually reduce their global effective gain coefficient.

Besides, the intensities of the 15.5 nm and 15.7 nm lines, calculated as a function of the plasma length using this model, are shown in Figure 7.28. One sees that the line intensity ratio increases very rapidly over a propagation length of ∼1 cm and then is stabilized at a value close to 10^2. This result

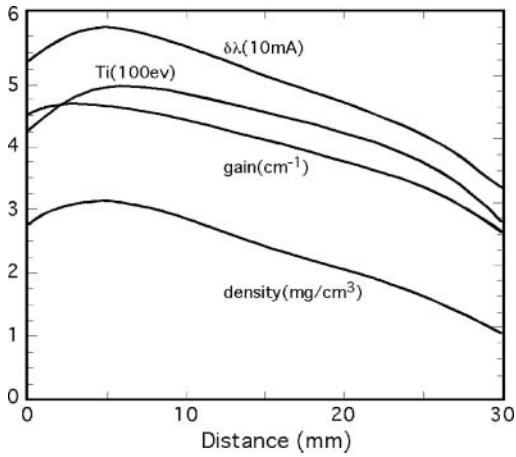

Fig. 7.27. Plasma parameter variation experienced by a laser beam propagating in a plasma of 3-cm in length (Ref. [182]). Unities are defined in brackets and correspond to the separation of two successive main steps on the vertical axis.

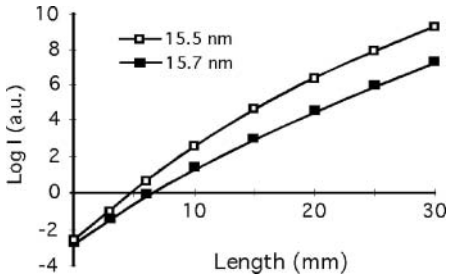

Fig. 7.28. Intensities of the 15.5 nm and 15.7 nm lines of the Ne-like yttrium laser calculated as a function of plasma length.

explains that far high intensities may be obtained for the 15.5-nm line than expected from apparent gain coefficients. These lasts, calculated from the 9 cm^{-1} and 7 cm^{-1} obtained, on axis, for these two lines respectively are found equal to $\sim$5.5 cm^{-1} for both lines. The observed contradiction between the ratios of gain coefficients, on the one hand, and of line intensities, on the other hand, is thus the result of the opposite effects overlapping and narrowing of the two lines.

7.2.4 Ne-Like Silver Laser

The shortest wavelength of laser lines emitted from neon-like ions are due to the neon-like silver laser [183]. The used technique was exploding foil with 6×10^4 W/cm^2 irradiance focused on target. The gain coefficients for the two main $J = 2-1$ lines were 9.4 ∓ 1.5 cm^{-1} and $6.4^{+2.0}_{-1.5}$ for the 9.94-nm and 10.04-nm wavelength lines respectively. Gain was observed for three other lines including the $J = 0-1$ line at 8.16 nm. These results confirmed the validity of the collisional pumping scheme applied to neon-like ions of high Z elements. However the very high pumping energy necessary to achieve laser action with targets of high Z element restricts the practical use of such lasers and further extension of the single pump-pulse neon-like scheme to shorter wavelengths.

7.2.5 Ni-Like Ion Lasers

Lasers using nickel-like ions and operating in the single long-pulse regime must be mentioned here because one expects wavelengths shorter from them than from those obtained with neon-like ions [139, 157, 184–187]. Let us recall that the level diagram corresponding to Ni-like lasing lines is displayed in Figure 7.1. The reader will find the measured wavelengths of the $J = 0-1$, 4d–4p lines of nickel-like Nd ($Z = 60$), Sm ($Z = 62$), Gd ($Z = 64$), Dy ($Z = 66$), Ho ($Z = 67$), Yb ($Z = 70$), Hf ($Z = 72$), and Ta ($Z = 73$) in Ref. [140].

Table 7.3 displays the gain coefficients which have been measured for the $(3/2, 3/2)J = 0-(3/2, 1/2)J = 1$ lines of europium, tantalum, and tungsten.

Table 7.3. Gain coefficient measured for the J = 0−1 lines of Ni-like ions of Eu ($Z = 63$), Ta ($Z = 73$), and W ($Z = 74$); for gold ($Z = 79$), the laser line has been observed but gain has not been measured

Ion	λ(nm)	Gain(cm^{-1})
Eu^{35+}	6.583	∼1
Ta^{45+}	4.483	2.3
W^{46+}	4.319	2.6
Au^{51+}	3.560	—

A gain–length product of 7 has been obtained for tungsten with a target irradiance of 3.1×10^{14} W/cm^2. A lasing line has been observed and its wavelength measured in the Ni-like spectrum of Au. It is worth noting that the wavelengths of tantalum and tungsten laser lines lie in the "water window," namely between the K-edges of carbon and oxygen. Lasers at such wavelengths are considered especially interesting for biological applications. However, due to the lack of a sufficient pump power, Ni-like lasers pumped by single long pulses did not achieve emission saturation till now. We shall see that, with the development of prepulse and transient pumping techniques, nickel-like lasers began to progress with big strides.

7.3 Pumping with Prepulses

The first generation of XUV lasers required a very large pump energy, which unavoidably reduced the field of their applications. In particular the most intense predicted laser line ($J = 0-1$) of Ne-like ions was missing, a fact which remained misunderstood notwithstanding big theoretical efforts.

Considerable progress occurred from the first observation of intense $J = 0-1$ neon-like lines using elements like Ti [188] and Ti, Cr, Fe [98], for experiments where the main laser pulse, which drives the highly ionized plasma, was preceded by a low-intensity prepulse as shown in Figure 7.29. Figure 7.30 illustrates this observation. In this case, a 6-J, 600-ps FWHM prepulse precedes the 1100-J, 600-ps main pulse by 7 ns. One sees that, for the three

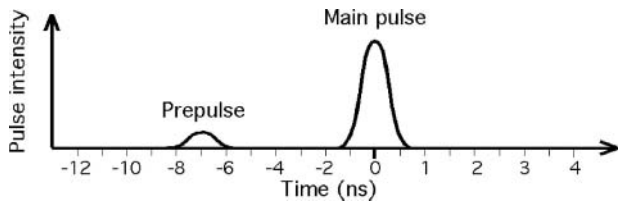

Fig. 7.29. Principle of pumping with prepulse; prepulse generates a low-temperature plasma which expands before the main pulse arrival.

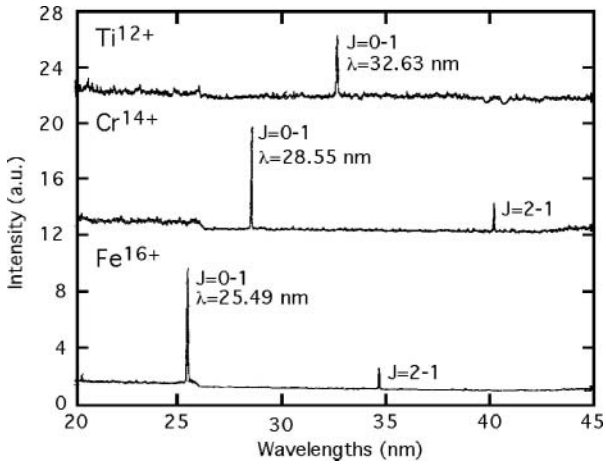

Fig. 7.30. Intense $J = 0-1$ lines of Ne-like ions obtained thanks to the prepulse pump technique.

elements, the spectrum is dominated by the $J = 0-1$ lines. Gain coefficients were estimated at 2.6 cm^{-1} for Ti at 32.6 nm as for Cr at 28.6 nm.

7.3.1 General Characteristics of Prepulse Influence on Pumping

Computer simulations, described in [98], show some aspects of the role played by prepulses. It is patent from Figure 7.31a that prepulse reduces the steepness of the plasma density gradient. Consequently the curvature of the laser beam trajectory is reduced as well, which enhances the length traveled in the narrow gain region of the plasma. Moreover the radiation of the main-pulse laser penetrates more deeply within the relaxed preplasma than it could do in the immediately dense plasma created by the single-pulse scheme. As shown in Figure 5.5b, this increases the size of the gain region and contributes to elongate the profitable propagation length.

In the general conditions of the experiment illustrated by the results displayed in Figure 7.30, it is estimated that, when prepulse is used, a laser photon travels 5.4 cm before reaching the limit of the gain region while, without prepulse, it would travel 1.4 cm only before to be refracted out. This explains that, in the single pulse scheme, $J = 0-1$ lines do not achieve the high gain–lengths predicted by calculation of *local* gain coefficients. Regarding the $J = 2-1$ lines, the gain region is situated at lower densities. This makes them to be less subject to the gain–length decrease caused by strong refraction in the steep density profile. This interpretation of the paradoxical behavior of $J = 0-1$ lines, encountered in the single pump–pulse system, is consistent with results obtained by using curved targets, whose the shape

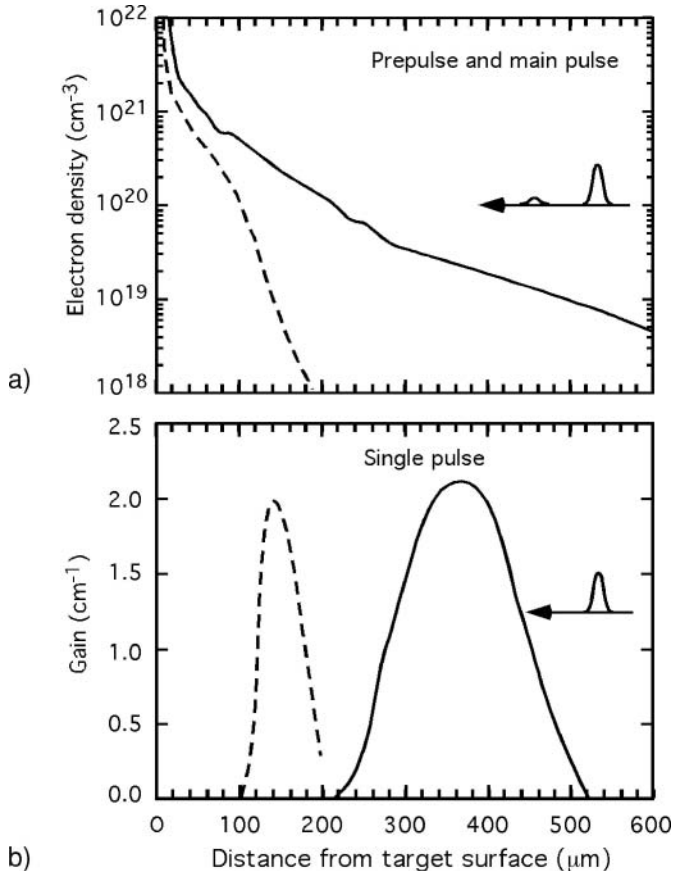

Fig. 7.31. Electron density and gain coefficient distribution (a) with and (b) without prepulse (from Ref. [98]).

partially counterbalances the refraction effect (cf. Fig. 2.19 and Ref. [52], see also [189–191]).

An interesting question appears about the relationship between efficiency and intensity of prepulse. The prepulse intensity is usually characterized by the fraction of the total intensity used to generate the prepulse, e.g. ∼5.5% in the above experiment which was performed with a 6 J prepulse compared with the 1100 total available energy. One observes that $J = 0-1$ line enhancement can be obtained for a wide range of prepulse intensity. This has been first shown in the case of the 19.6-nm line of germanium [192, 193].

Very low prepulses (0.02%) proved to enhance the line intensity by a factor of the order of 9, while a higher prepulse (1.2%) led to an enhancement factor about 7. For both prepulse intensities the temporal width of the X-ray laser emission profile was much shorter than the driving pulse width (∼120 ps and

∼100 ps FWHM respectively to be compared to 700 ps for the main pulse. The laser emission peaked during the rise-time of the main pulse.

Moreover the line peaked at 9 mrad off axis, without prepulse, but the deflection was reduced to 4 mrad with the low prepulse. This gives a direct evidence of the prepulse effect consisting in the decrease of refraction through the gain zone of the plasma. In fact, computational modeling exhibits three effects from prepulse: (a) an enhanced absorption of the main pulse energy during earlier time of plasma expansion, (b) an increase of the gain zone volume, and (c) a relaxation of electron density gradients.

Furthermore, to understand the physics of the pumping schemes that use prepulses, we should consider not only the modifications generated in the lasing hot plasma, but also the conditions of the cold "preplasma" production itself. Given the low energy involved in preplasma, it is necessary to take into account the coupling between this cold plasma and the solid material of the target. Properties such as target density, electron conductivity, melting point, latent fusion, and latent vaporization heats, etc. should be considered for explaining the variations of prepulse efficiency, which may be related to the target material. Surface oxidation and polishing quality also may more or less modify preplasma parameters [194, 195].

The characteristics of the prepulse effect on nickel ($Z = 28$), copper ($Z = 29$), and zinc ($Z = 30$) targets, for delays varying from 2 ns to 4.5 ns between prepulse and main pulse, have been investigated in several works. For instance, time-integrated KeV spectroscopy of lasing plasma showed that the lateral size of the Ne-like plasma region increases roughly logarithmically with prepulse intensity [196,197]. Plasma size increase was also observed in expansion direction, perpendicularly to the target. This effect is likely connected with a lowering of density gradient in this direction, though the spatial resolution of the experimental setup was not sufficient to give a direct evidence of the fact. A remarkable observation was the plasma exhibiting a much larger size increase for zinc than for the two other elements. Moreover the Ne-like ground state density was found to increase with prepulse by 3%, for nickel, 10% for copper, and 20% for Zn. Such properties correlate very likely with the exceptionally large gain-coefficient sensitivity of zinc plasma to the prepulse level.

Detailed simulations, including the equations of state-of-solid materials, have been performed to estimate the effect of level and delay of prepulses on the gradient scale-length and the lateral size of the plasma, viz. the parameters that control the laser beam refraction and the maximum of the gain–length [198]. Let C be the prepulse contrast, i.e. the ratio of prepulse to main pulse energy, L, the electronic density gradient scale-length [cf. Eq. (5.6)] in the expansion direction, $2R$, the maximum lateral width of the Ne-like plasma region, as shown in Figure 7.32. Tables 7.4 and 7.5 display the values of $2R$ and L obtained for a zinc target. One see calculation to clearly confirm the prepulse effect consisting in the increase of the plasma width and the smoothing of the density gradient. The effect is much less pronounced in the case of a short delay (2 ns), likely because the pre-plasma is not yet completely relaxed. However,

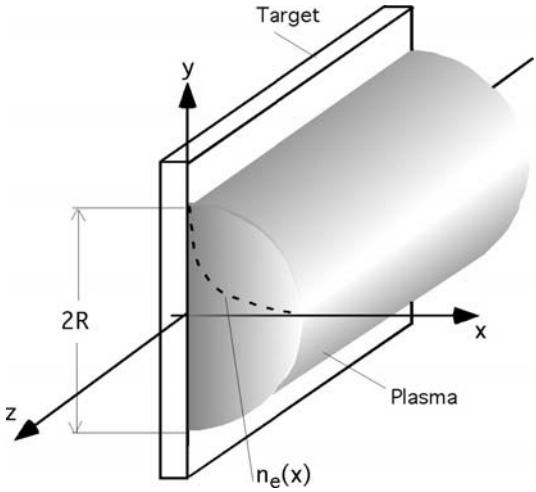

Fig. 7.32. Electron-density distribution and lateral size R of plasma fiber. R and the gradient–length of the density distribution L, calculated for a set of contrasts and delays of the prepulse, are shown in Tables 7.4 and 7.5.

it must be mentioned these simulations not to predict significant differences between gradient-lengths for zinc, copper, and nickel.

Figure 7.33 displays the measured factors of ASE enhancement of $J = 0{-}1$ line intensity versus the prepulse fraction for Zn, Cu, and Ni [199]. The enhancement factor is defined as the ratio of the time-integrated signal of the

Table 7.4. Gradient scale-length L of electronic density as a function of the prepulse contrast and the prepulse-to-main pulse delay. 0 and 1 contrast values refer to no-prepulse and double-pulse, respectively.

	$L(\mu m)$					
Contrast	0	10^{-4}	10^{-3}	10^{-2}	10^{-1}	1
$t_d = 7$ ns			212	438	966	
$t_d = 4.5$ ns	134	133	145	308	659	1205
$t_d = 2$ ns			117	161	344	631

Table 7.5. Lateral size R of zinc Ne-like plasma as a function of the prepulse contrast and the delay between prepulse and main pulse

	$2R(\mu m)$					
Contrast	0	10^{-4}	10^{-3}	10^{-2}	10^{-1}	1
$t_d = 7$ ns			309	757	2322	
$t_d = 4.5$ ns	301	304	305	522	1517	3117
$t_d = 2$ ns			309	346	727	1471

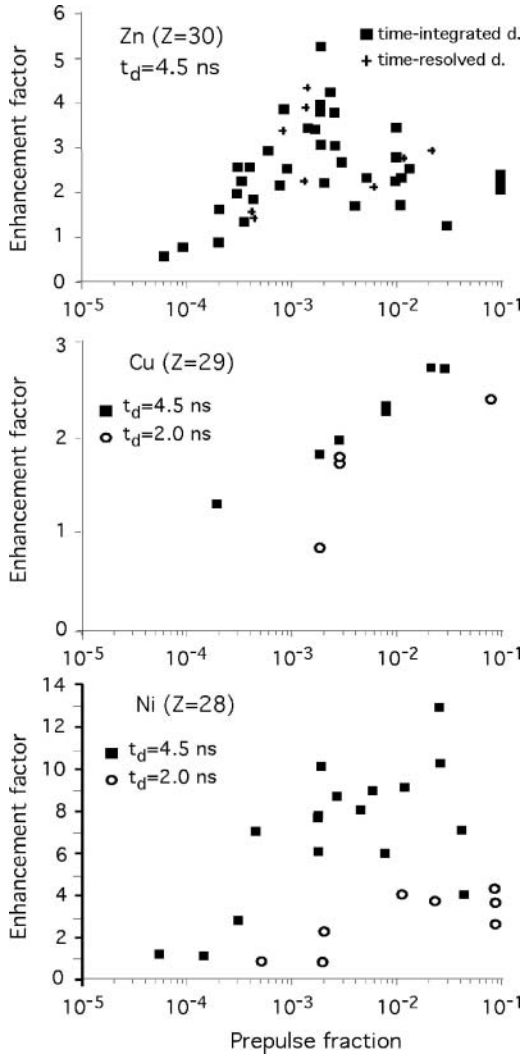

Fig. 7.33. Enhancement factor of the $J = 0-1$ Ne-like laser line of Zn, Cu, and Ni as a function of prepulse contrast (data from Ref. [199]). The variable t_d is the time delay from prepulse to main pulse.

$J = 0-1$ laser line with prepulse to the corresponding signal without prepulse. Prepulse contrast was monitored at fractional levels between 10^{-5} and 10^{-1} using photodiode-based detectors. A Gaussian main pulse of 800-ps FWHM irradiated the 20-mm long slab target with an averaged intensity $\sim 10^{13}$ W/cm^2. The main pulse was preceded by a similarly shaped prepulse whose intensity on target ranged from $\sim 10^8$ to $\sim 10^{12}$ W/cm^2.

An outstanding characteristic of these results is the sensitivity to prepulse action to be far smaller for copper than for zinc and nickel. For a 10^{-3} prepulse

Table 7.6. Enhancement factor, EF, of the $J = 0-1$ line for a 0.001 pulse, thermal conductivity, TC, and melting point of Cu, Zn, and Ni

Element	EF	TC (W cm^{-1} K^{-1})	t_{m}(°C)
Cu	1.6	4.01	1085
Zn	3.5	1.16	420
Ni	5.6	0.91	1455

contrast, Table 7.6 shows that the enhancement factor is roughly of 1.6 for Cu, 3.5 for Zn, 5.6 for Ni. It is interesting to write thermal conductivities at laboratory temperature near enhancement factors in Table 7.6. One sees the smallest enhancement factor, the one of copper, to correspond to the largest thermal conductivity. This suggests that fast heat dissipation within the target would reduce the number of ionized atoms produced by prepulse.

In the case of zinc laser, a second important result is the ASE enhancement factor to exhibit an optimum prepulse value with a prepulse contrast of $\approx 2 \times 10^{-3}$, which corresponds to intensity about 2.10^{10} W/cm^2, for a delay of 4.5 ns. The gain coefficient measured with these prepulse characteristics is of 3 ∓ 0.5 cm^{-1}. Beyond the optimum, the enhancement factor seems to continuously decrease until the prepulse fraction reaches 10^{-1}. It is very likely that this result is out of the scope of usual models plasma based on plasma hydrodynamics and population rate equations. To understanding it one should rather refer to the largely unexplored interaction between the radiation of the small prepulse, the solid target material and the generated plasma. Let us mention that, for a 2-ns prepulse delay, the enhancement factor (not represented in Fig. 7.33 for Zn), is reduced by factor 1.5–2 compared to the 4-ns case and exhibits a monotonic increase with prepulse contrast.

To learn more about the characteristics of prepulse-produced plasmas it is worth investigating them directly in low temperature line-plasmas produced in conditions equivalent to those of the prepulses for X-ray lasers. B. Rus et al. used an interferometric probing method to determine the map of electron density in plasma cross-section, perpendicularly to the line plasma axis [200]. Line plasmas, of 100 μm width, were generated by near Gaussian 400-ps FWHM pulses supplied by an iodine laser at 1.315-μm wavelength. The 438-nm probe beam was a separated fraction of the iodine laser output, frequency tripled in DKDP crystals. The beam was sent, via a delay line, down the axis of the plasma. Interferograms were recorded using delays of 4 ns and 10 ns, i.e. at times where the action of the laser pulse on target was terminated. Fringe shifts are proportional to the difference between the optical path length of a ray passing through the plasma and the optical path length, at the same point, of a reference ray propagating in free space. This difference reads

$$\phi\,(x,y) = \frac{2\pi}{\lambda} l \left[1 - \left(1 - \frac{n_{\mathrm{e}}(x,y)}{n_{\mathrm{c}}} \right)^{1/2} \right] \simeq \frac{\pi}{\lambda} \frac{n_{\mathrm{e}}\,(x,y)}{n_{\mathrm{c}}} l \tag{7.8}$$

where λ is the wavelength of the probe beam, l the plasma length, n_{e} the

electron density, n_c the critical electron density ($n_c \simeq \frac{1.1\times10^{21}}{\lambda^2_{[\mu m]}}[\mathrm{cm}^{-3}]$), x, y the coordinates in the cross-section plane.

Examples of interferograms achieved with zinc and copper targets are shown in Figure 7.34. Densities up to more than 10^{18} cm^{-3} are observed. One can see the large differences between zinc and copper plasmas for both pulse energies of 10^{10} and 10^{11} W/cm^2, which correspond to 5×10^{-4} and 5×10^{-3} prepulse contrasts. The density patterns which can be deduced from these interferograms are essentially the same as would encounter the main pulse of an X-ray laser for similar time delays.

At low irradiance (10^{10} W/cm^2), Zn and Cu plasmas are localized near target surface and laterally limited to the 100-μm width of the laser line focus. However, one sees zinc plasma to be much more dense and more spreadout than copper plasma. These features are likely to be assigned to the especially low melting (see Table 7.6) and boiling temperatures of zinc, which turns into plasma faster than copper. The difference, which thereby appear between of Zn and Cu behavior during the first nanoseconds, may explain that the enhancement factor achieved for weak prepulses, with a 4.5-ns delay, was found larger for Zn than for Cu.

At larger irradiance (10^{11} W/cm^2) interferograms show evidence of "nozzle-like" plasma profiles, with a density dip in the center, and strongly localized symmetrical density flanks in the case of copper. Such qualitative changes cannot be induced by the simple free expansion of an already existing plasma. It rather suggests that an additional plasma, generated during the

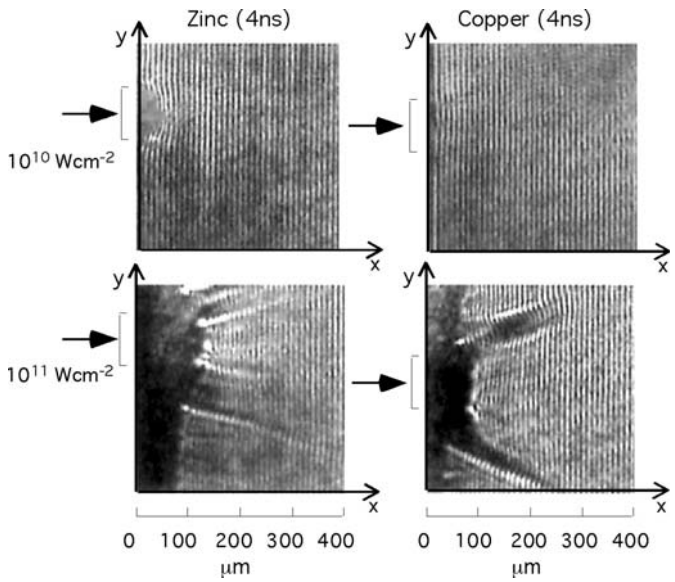

Fig. 7.34. Interferograms of low-temperature plasmas produced by pulses of intensities similar to those of the prepulses involved in X-ray laser pumping. The wavelength of the probe beam is of 438 nm.

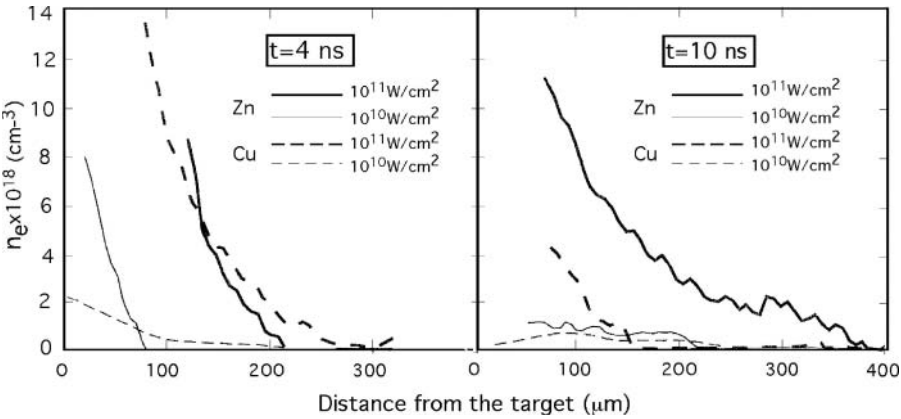

Fig. 7.35. Electron-density distribution in Zn and Cu plasmas produced by low-intensity prepulses. Large differences appear between Zn and Cu distributions. In particular, for a 10^{10}-W/cm^2 prepulse, electron density increases higher and faster for Zn than for Cu.

period of interferogram recording, is expelled obliquely with respect to the target surface. In [200] a possible mechanisms for this process, based on the thermodynamical properties of the metal–plasma system, is proposed.

Another important difference between Zn– and Cu–plasma evolutions appears in Figure 7.35, which displays the electron density gradients corresponding to the center of the laser focus (shown by the arrows in Fig. 7.34), for low and high irradiance. The prominent fact is the collapse of the density gradient of the Zn–plasma (thin continuous lines), that occurs between 4 ns and 10 ns for higher irradiance, while only a slight gradient relaxation (thick continuous line) appears for lower irradiance. This result is consistent with the observation of the enhancement factor decrease beyond an optimum intensity of $\sim 2 \times 10^{10}$ W/cm^2, as shown in the Zn-diagram of Fig. 7.33. Initial conditions of Zn–plasma creation appear to be quickly spoiled when prepulse intensity increases from 10^{10} to 10^{11} W/cm^2.

7.3.2 Prepulsed Ne-Like Zinc Laser

Amplification of the $J = 0-1$ and $J = 2-1$ line radiation of Ne-like zinc, at 21.2 nm, 26.2 nm and 26.7 nm, respectively, was first observed using single pump-pulses, as in the case of the lasers described in the previous section [201]. The gain coefficients were 2.3 cm^{-1} for the $J = 0-1$ line and 2.0 cm^{-1} for the two $J = 2-1$ lines. However, strong lasing of the $J = 0-1$ line, expected from theoretical predictions for most elements but never observed with single pulses, has been obtained for the first time by producing a zinc plasma with the help of small prepulses before the main pump pulse [202–205]. Laser saturation at 21.2 nm was achieved by double-passing the XUV beam through the plasma.

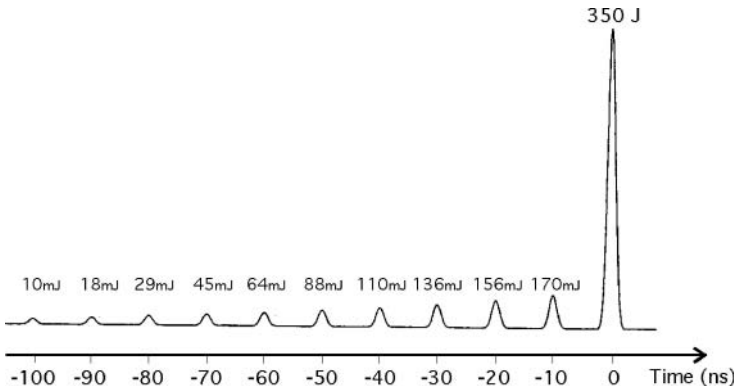

Fig. 7.36. Small prepulse train preceding the main pulse, which proved to be very efficient to pump the $J = 0-1$ line of Ne-like zinc laser.

The experimental arrangement used for the zinc laser includes the 6 beams configuration previously illustrated in Figure 5.7. Energies typically 430 J at 1.06-μm wavelength are available, in near Gaussian ∼600-ps FWHM pulses, at the output of the pump laser. The six line foci are superimposed upon one another giving rise to a ∼150-μm wide resulting spot. The net irradiance is typically $\sim 1.4 \times 10^{13}$ W/cm^2. The main pulse is accompanied by a train of small pulses separated by 10 ns as shown in Figure 7.36. The train is a remnant from the mode-locked oscillator, which is incompletely isolated by operating one Pockels cell in the chain with an attenuation factor $\sim 10^{-3}$ only. The last prepulse preceding the main pulse delivers 170 mJ on the target and produces an irradiance $\sim 7 \times 10^9$ W/cm^2. A scheme of the basic arrangement of the target and the diagnostics is shown in Figure 7.37. A zinc laser using

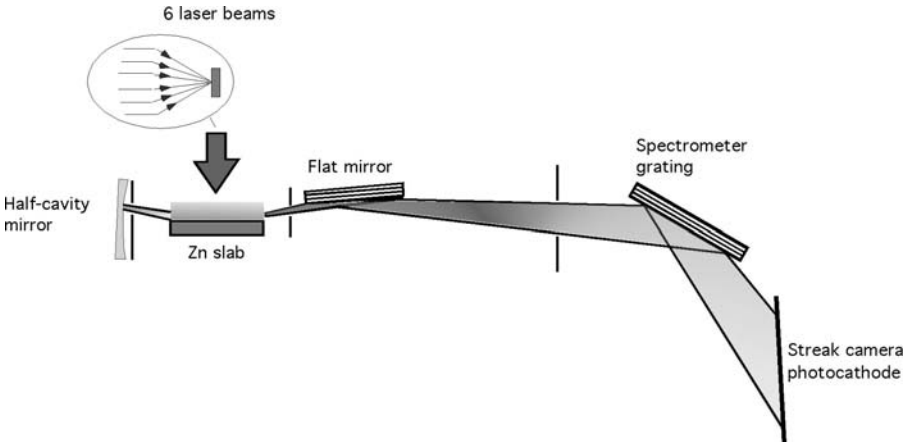

Fig. 7.37. Principle of the experimental arrangement used for the Ne-like zinc laser.

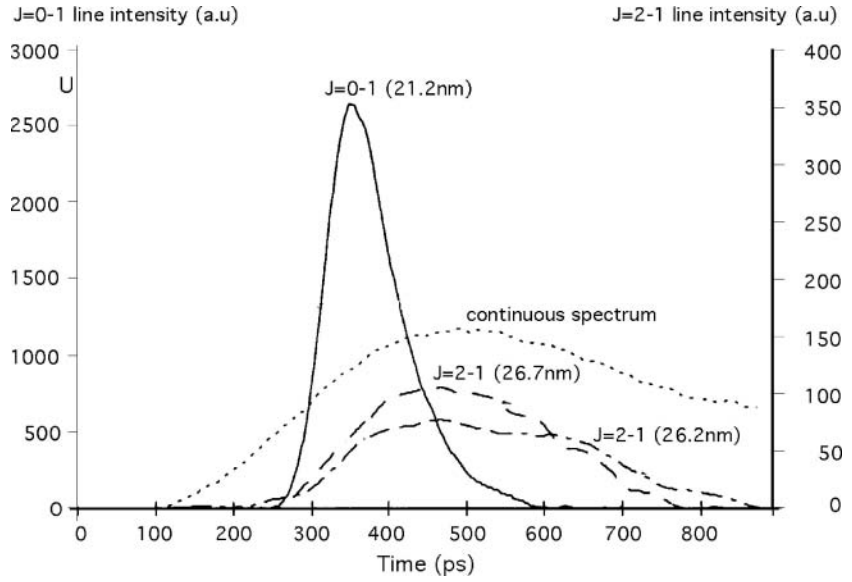

Fig. 7.38. Time history of the three main laser lines of Zn-laser. The differences observed between the $J = 0-1$ and the two $J = 2-1$ lines, as regards the position of peak intensity and the lasing duration, indicate that population inversions are not driven by the same processes for the three lines.

the same general techniques, except for the pump which is a single beam iodine laser at 1.315-μm wavelength, operates at the Prague Asterix Laser System [206].

Single-pass measurements showed gain coefficients $\sim$5.0 cm^{-1} on the $J = 0-1$ line, $\sim$2.3 and $\sim$2.6 cm^{-1} on the $J = 2-1$ lines, which were almost insensitive to the presence of prepulses. As shown in Figure 7.38, the laser emission of the $J = 0-1$ line, on the one hand, and the $J = 2-1$ lines, on the other hand, have very different time histories. The $J = 0-1$ line peaks 100 ∓ 50 ps before the $J = 2-1$ lines that roughly follow the evolution of the continuum plasma emission, the peak of which is expected to occur near the peak of the main pulse. Moreover the FWHM duration is $\sim$100 ps for the $J = 0-1$ line in contrast with $\sim$300 ps for the two $J = 2-1$ lines. This indicates the $J = 0-1$ inversion to be predominantly driven by processes other than the $J = 2-1$ inversions. As a matter of fact, calculations assign the dominant contribution to the $J = 0$ level-population to direct 2p–3p monopole excitations produced by electron collisions, while 3d–3p cascades have a larger part in the $J = 2$ level population (cf. Fig. 7.1).

A consequence of this difference between the populating mechanisms is that the $J = 0-1$ line and the $J = 2-1$ lines come from different plasma regions. This can be experimentally confirmed by the characteristics of the near field ASE pattern, investigated for instance with the help of a stainless

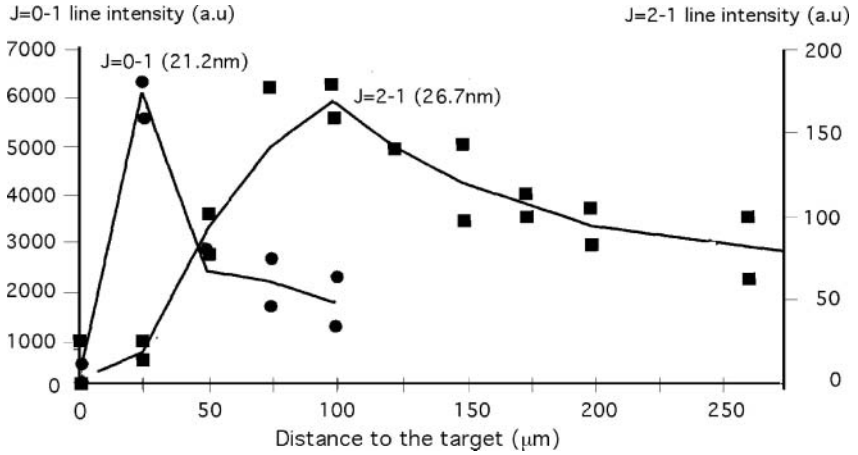

Fig. 7.39. Intensity as a function of the distance of the beam axis to the Zn-target surface for two laser lines. The role of electron collisions populating the $J = 0$ upper level explains that the $J = 0{-}1$ line is emitted from a region of high electron density, close to the target.

cut edge placed near the plasma end. Figure 7.39 shows the 21.2 nm emission to essentially emerge from a narrow 35-μm wide region peaking ∼30 μm from the target surface, whereas the 26.7-nm line is emitted over a 200-μm broad zone with its maximum ∼100 μm from the target.

Angular distributions, which involve refraction and divergence of the beams, are also different. This is exemplified by the far field patterns corresponding to the instant of the maximum intensity of each line, displayed in Figure 7.40. In the case of the 21.2-nm line, the beam is found to be very

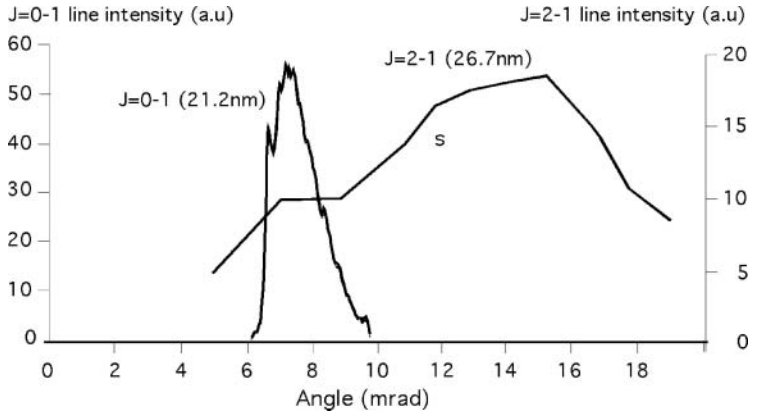

Fig. 7.40. Angular distribution of laser emission for the same two lines as in Figure 7.39. The $J = 0{-}1$ is highly collimated compared with its companion.

narrow, with a 2.8 ∓ 0.5 mrad divergence and a refraction angle ∼7.2 mrad. For the 26.7-nm line, the divergence is much larger (∼11 mrad) and the refraction angle peaks ∼15 mrad. Ray tracing simulations account for the general features of these observations by assuming a relaxed electron density profile characterized by a scale length of about 125 μm, which is 2–3 times larger than values occurring in a single-pulse-driven plasma produced with the same target irradiance [207].

To achieve laser saturation at 21.2 nm, a large increase of the $J = 0-1$ line intensity can be obtained by double passing the XUV beam through the plasma. To this end a Mo:Si multilayer concave mirror produces the half-cavity (cf. Fig. 7.37). The mirror is aligned to return the emission appearing 7.2 mrad away from the axis. To use it many times, it is protected from target debris by a shield with a hole 1 mm in diameter to pass the X-ray laser beam. The mirror is shifted by ∼2 mm between two successive shots. Its normal incidence reflectivity is ∼30% and the geometric coupling efficiency C_g [see Eq. (5.22)] is estimated $\sim 6.8 \times 10^{-2}$ and $\sim 9.8 \times 10^{-2}$ when the mirror is placed at 9 mm and 6 mm from the plasma end, respectively [205]. The intensity enhancement brought by the mirror is typically ∼60 at the distance of 9 mm and ∼80 at the distance of 6 mm. The ratio of these two values roughly equals the ratio of the corresponding geometric coupling efficiencies.

Figure 7.41 displays an example of the 21.2-nm intensity increase as a function of plasma length. The half-cavity was used to provide XUV beam double-passing with effective path lengths larger than 1.5 cm [cf. Eq. (5.21)]. The results are compared to the unsaturated exponential intensity growth (straight solid line) and to a calculated curve involving the emission saturation (thin continuous line) introduced according to the method described in Section 6.2.

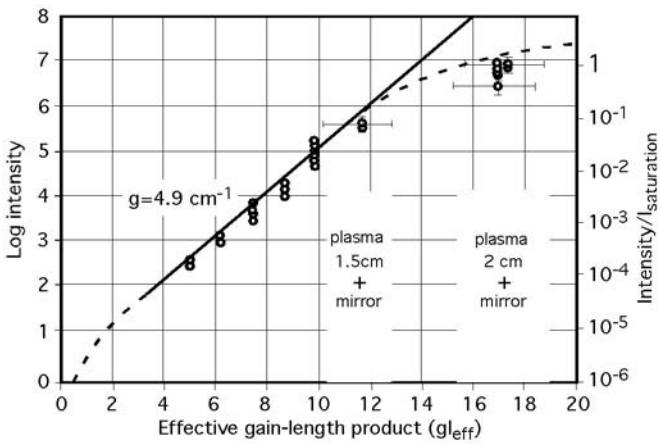

Fig. 7.41. Emission intensity of the $J = 0-1$ line of the Zn-laser as a function of the gain–length factor. The curve shows the outset of laser saturation for a gain–length ∼16.

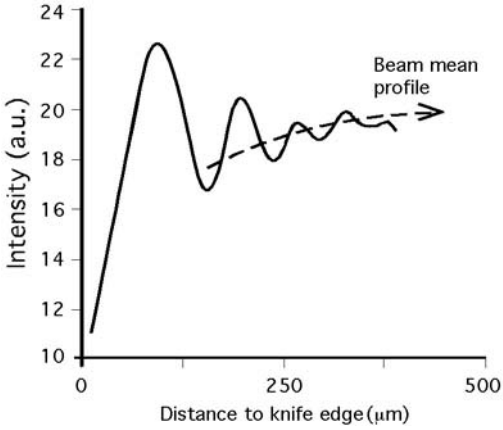

Fig. 7.42. Measurement of the spatial coherence of the zinc X-ray laser, at 21.2-nm wavelength, using the Fresnel fringes of a knife edge placed across the laser beam.

The temporal evolution of the half-cavity X-ray laser pulse is found to be similar to that observed in the single-pass case but with a slightly reduced duration FWHM of ∼80 ps. The estimation of the total time-integrated output of the laser is ∼1 mJ, i.e. $\sim 10^{14}$ photons at 21.2 nm. The corresponding peak power is ∼12 MW. With a bandwidth emission $\sim 10^{-4}$, the zinc laser brightness amounts to $\sim 7 \times 10^{15}$ Wcm^{-2} sterad^{-1}.

Fresnel fringes, present at the edge of a knife edge shadow (Fig. 7.42), show the transverse coherence length to be ∼50 μm at 50-cm distance from the plasma end [208]. Taking into account the propagation of the mutual coherence, a ∼300-μm diameter region of a test material may be investigated with the help of an interferometer located 3 m from the X-ray laser.

7.3.3 Prepulsed Ne-Like Germanium Laser

As we showed in Section 7.2.2, saturated emission of the $J = 2-1$ lines at 23.2- and 23.6-nm wavelength has been achieved with single pulse pumping, whereas this technique failed to give the large intensity expected for the $J = 0-1$ line at 19.6 nm. It is also to be mentioned that a systematic study of the intensity variation of the three lines with 0–56 mm plasma lengths, with the help of a four-target system, has shown that saturation starts at ∼45 mm for the $J = 2-1$ lines, while the $J = 0-1$ line increase remains exponential over the full interval [209].

Now the comparison between enhancements of the $J = 0-1$ line output provided by curved targets (cf. Fig. 5.13), designed to overcome the refraction problem, and by the prepulse technique, gives clear indication of the advantage of the latter. For instance, with a 600-J, 450-ps main pulse focused on a 150 μm × 3 cm target area, a 15% prepulse does increase the 19.6-nm line

output by a factor near 500, whereas a 10-mrad/cm target curvature provides an enhancement factor of 10 only compared to the case of a flat target [210].

Different combinations of main pulses and prepulses have been investigated and quantitatively compared [202]. The results are summarized in Figure 7.43. The prepulses are of the order of the percent level (1–5%). The time-averaged output for each configuration is normalized to the long pulse

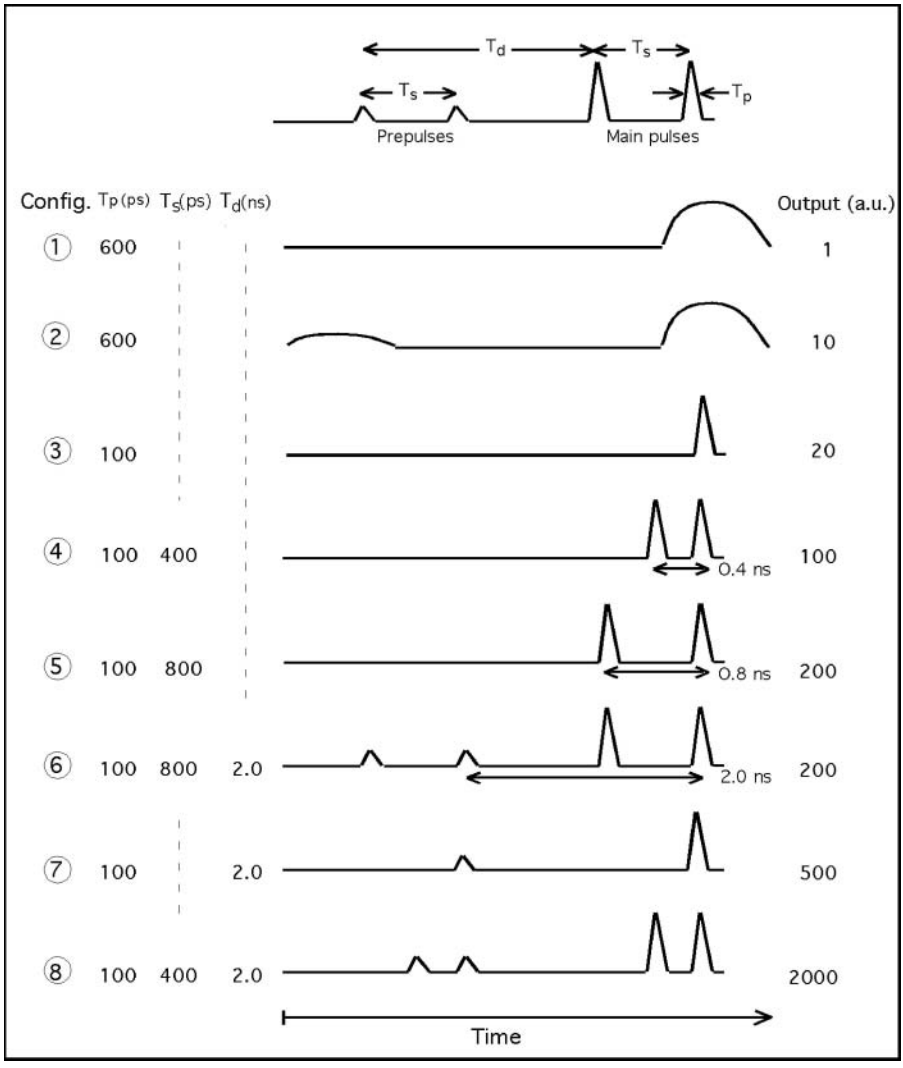

Fig. 7.43. Germanium laser output in arbitrary units for a set of combinations of pulses and prepulses. T_p: pulse duration (ps); T_s: pulse separation (ps); T_d: pulse delay (Ref. [210]).

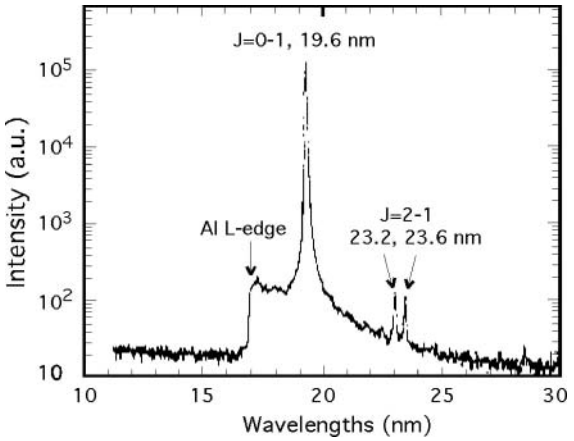

Fig. 7.44. Germanium laser lines obtained with a combination of two prepulses and two main pulses (No. 8 in Fig. 7.43). The prepulse contrast is 10–30%. The intensity of the $J = 0-1$ line is three orders of magnitude higher than that of other lasing lines (data from Ref. [210]).

case (configuration no. 1). One sees a double main pulse or, in other words, a 100% prepulse (configurations no. 4 and 5) to enhance the $J = 0-1$ output by one order of magnitude in comparison to the single pulse (configuration no. 3).

However, 1% prepulses preceding the main pulses by 2 ns have a much larger effect (configurations no. 7 and 8). In the case of double pulse + double prepulse, that leads by far to the largest enhancement (configuration no. 8), the temporal structure of the XUV laser pulse should be investigated in details to understand the part of each pulse in the measured output. It is worth mentioning that multiple short pulses have also been used to pump Ne-like selenium [211] and yttrium lasers [212].

Saturation of the germanium $J = 0-1$ line has been obtained by using a configuration similar to that of no. 8 in Figure 7.43, but with 10%–30% instead of 1–5% prepulse, preceding the 150-J, 75-ps main pulse by 2.2 ns. The double target system of Figure 5.10 was used. Figure 7.44 shows the $J = 0-1$ line dominating the spectrum with an intensity which is three orders of magnitude larger than for the two $J = 2-1$ lines [213]. The total output is estimated to be ∼0.9 mJ, with a peak power ∼22 MW. The laser brightness is of the same order of magnitude as in the case of the zinc laser, previously described. Furthermore, compared with the $J = 2-1$ lines, the $J = 0-1$ line shows a significantly better spatial coherence [131].

7.3.4 Ne-Like Lasers with Low Z Elements

From selenium ($Z = 34$) to chlorine ($Z = 17$), which is one of the lowest Z elements accessible to the Ne-like pumping scheme, the $J = 0-1$ line

Table 7.7. Neon-like lasing data for low Z elements (data from Refs. [218, 219])

Ions	$\lambda(nm)$	Prepulse level	g (cm^{-1})
Ge^{22+}	19.6	1.5%	3.7
Ga^{21+}	20.4	15%	4.3
Zn^{20+}	21.2	1.5%	4.5
Cu^{19+}	22.1	1.5%	4.3
Ni^{18+}	23.1	1.5%	4.3
Fe^{16+}	25.5	1.5%	4.1
Mn^{15+}	26.9	15%	4.3
Cr^{14+}	28.5	15%	3.9
V^{13+}	30.4	15%	4.4
Ti^{12+}	32.6	15%	3.0
Sc^{11+}	35.2	15%	3.8
Ca^{10+}	38.3	15%	3.8
K^{9+}	42.1	15%	3.4
Cl^{7+}	52.9	15%	2.5

wavelength increases from 18.2 nm up to 52.9 nm. Therefore the introduction of the prepulse technique opens the way to efficient X-ray lasers in the 20-nm to 50-nm wavelength range, which do not require very large laser facilities to produce an efficient pump beam [cf. the order-of-magnitude relation (7.4)]. As an example, lasing at 28.5 nm in a chromium plasma has been achieved with a gain coefficient of 2.2 cm^{-1} by using 500-ps driving pulses of 90 J energy only and a 0.7% prepulse [214]. This in turn led to a deeper understanding of the prepulse effect.

Detailed information about lasing in low-Z elements can be found in Ref. [211, 212, 215–224]. The results are illustrated in Table 7.7, which displays data referring to the usual $J = 0{-}1$ line. This line corresponds to transitions between the $^1S_0$ term of the $2p^53p$ configuration and the $^1P_1$ term of the $2p^53s$ configuration (cf. Fig. 7.1). However, lasing of a second $J = 0{-}1$ line, corresponding to transitions to the $^3P_1$ term instead of the singlet one, may also be observed [223]. Its gain coefficient is generally smaller than that of the first line, with the exception of the case of vanadium for which the gain is about 5 cm^{-1}. Let us note that the wavelengths of these two lines differing by 4.3 nm only, the design of a monochromatic laser for applications could meet with some difficulties in this particular case.

Table 7.7 displays the data of a systematic study of the relevance of small or large prepulse using for achieving high $J = 0{-}1$ gain. One sees that, with the exception of gallium, the prepulse level is one order-of-magnitude larger from manganese to chlorine than for the heavier elements of the upper part of the table. Figure 7.45, from Ref. [218] displays the intensity change observed for the $J = 0{-}1$ line of titanium, iron, and nickel, when the prepulse intensity is changed from 1.5% to 15% of that of the main pulse. One can see that using

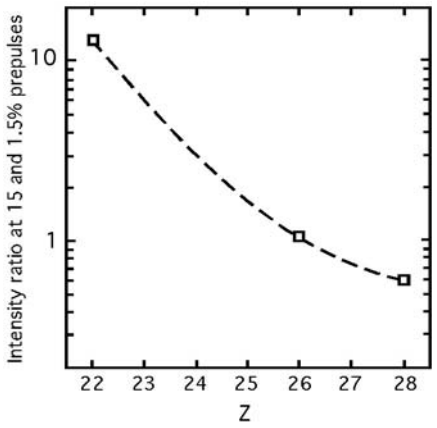

Fig. 7.45. Change of the $J = 0{-}1$ line intensity obtained by changing the prepulse contrast from 1.5% to 15% for Ni ($Z = 28$), Fe ($Z = 26$), and Ti ($Z = 22$).

the same prepulse contrast for all elements would reduce the laser intensity for the lower Z elements. Thus, for these lasts it can be suggested to reduce the intensity ratio between pulse and prepulse. However, an unexplained exception amongst the heavier elements is observed for gallium (Table 7.7) and might be connected with the difficulty of achieving a well-defined target surface state for this element whose melting point is of 30° only [216]. Other irregularities due to physico-chemical target properties could appear in future.

Keeping in mind the relationship between the value of the optimal electronic density for neon-like ion lasers [Eq. (7.2)], viz.

$$(n_{\mathrm{e}})_{\mathrm{opt}} = 4 \times 10^{15} \, (Z - 9)^{3.75} \, \mathrm{cm}^{-3}$$

the density of the lasing region is expected to grow from 6.0×10^{19} cm^{-3}, for titanium, up to 2.5×10^{21} cm^{-3}, for nickel. Thus the optimal lasing plasma zone should come closer to the target surface with higher Z. However, increasing the prepulse intensity reduces the stiffness of the electron density gradient, what will shift the optimal zone farther away from the target. Let us represent the distance between the target and the laser intensity peak as shown in Figure 7.46. Then Figure 7.47 gives the laser peak position against the atomic number under two prepulse conditions. One sees the distance to the target to decrease as Z increases and, at the same time, this distance to turn to an obviously larger one for larger prepulses.

Moreover, the plasma temperature will be somewhat lower as the prepulse increases because the amount of produced plasma also increases, while the heating energy supplied by the main pulse remains unchanged. Now the threshold temperature for neon-like lasing is estimated to scale as $(Z - 9)^{3.5}$ [156]. Equating the threshold temperature to that of the prepulsed plasma will thus lead to a Z-scaling relation for the optimal prepulse intensity. By

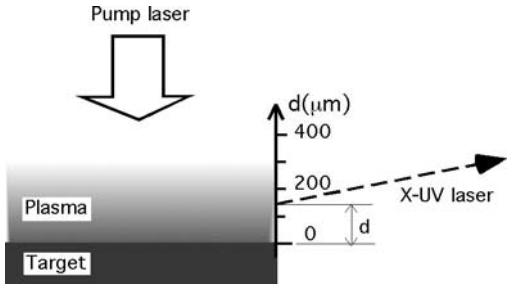

Fig. 7.46. The laser emitting region has a peak at distance d from the target surface. This distance varies with the prepulse contrast and the target material atomic number as shown in Figure 7.37.

estimating the temperature of the prepulsed plasma with the help of a self-similar model (cf. Section 5.1.1) and making the assumption of steady-state populations, the optimal prepulse intensity is found to roughly scale with Z according to [222]

$$\left(I^{\text{prepulse}}\right)_{\text{opt}} \propto \left[\frac{I_{\text{main.pulse}}}{(1-10/Z)\,(Z-9)^{3.5}}\right]^{1.5} \tag{7.9}$$

This relation shows that, at constant main pulse intensity, optimization of lasing in a higher Z target will generally require a smaller prepulse. For instance, from titanium to nickel, the ratio of prepulse–decrease, calculated from the above relation, should be a factor of $\sim$10, which confirms the conclusion of experimental investigations and agrees particularly with the experimental parameters reported in Table 7.7.

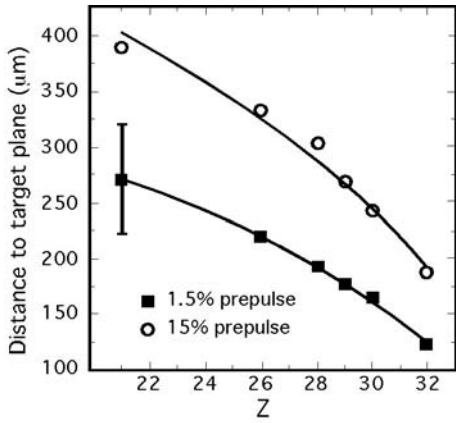

Fig. 7.47. Variation of the distance to the target of the maximum laser intensity as a function of atomic number, for two values of the prepulse contrast.

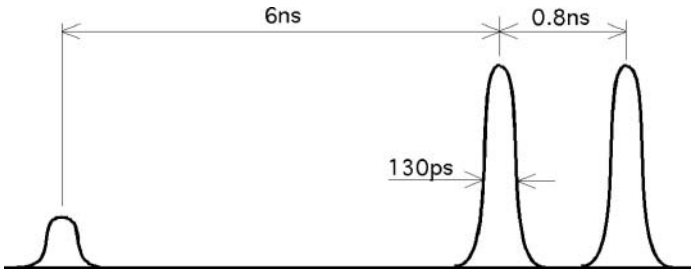

Fig. 7.48. Pulse combination for which the 25.5-nm wavelength laser line of Ne-like iron has been found to increase by a factor 500 when the ratio of prepulse to main pulses decreased by a factor ∼100.

In the case of a neon-like iron target, it has been observed that this effect is much more pronounced still with a structure consisting of one prepulse and two main pulses, illustrated in Figure 7.48 where the pulse width is of 130 ps, the separation of the main pulses, 0.8 ns, the delay between the prepulse and the first main pule, 6 ns, the main pulse intensity $\sim 1.5 \times 10^{13}$ W cm^{-2} [225]. The X-ray laser intensity is found to be more than 500 times larger with a very small 0.01% prepulse than with a much larger 12.5% prepulse level. The output consists of two saturated X-ray flashes separated by 800 ps. The small-signal gain coefficients are 15 ∓ 3 cm^{-1} and 26 ∓ 5 cm^{-1} for the first and the second pulse respectively, the gain–lengths at saturation being found to worth 26 ∓ 5 and 23 ∓ 2.

7.3.5 Prepulsed Ni-Like Lasers: Sn, Sm, Dy, Pd, Ag

The application of the prepulse technique to nickel-like ions made an important development of short wavelength XUV lasers possible. For instance, strong lasing of the 4d–4p, $J = 0-1$ lines of Nd, Sm, Gd, and Dy (cf. the Ni-like level diagram in Fig. 7.1), whose wavelengths are 7.95 nm, 7.36 nm, 6.90 nm, and 6. 43 nm, respectively, was observed for the first time by using two 100 ps pulses separated by 400 ps and a curved target, whose office was to reduce the refraction effect (cf. Fig. 5.13) [226]. Table 7.8 shows the wide extension of the range of XUV laser wavelengths achieved with using various combinations of main pulses and prepulses. An extensive study of the Ni-like 4d to 4p transition wavelengths, which covers the range of atomic number from $Z = 46$ to 22 can be found in Ref. [238].

The energy required to achieve nearly saturated lasing at a given wavelength can be estimated from the diagram represented in Figure 7.49 [239]. The laser irradiance needed to achieve the maximum Ni-like ions population has been determined by the fluid code EHYBRID (cf. Section 5.3.2) [74, 88]. The gain coefficients is calculated under the following assumptions: the ion temperature is fixed at 200 eV, the prepulse fraction amounts to 10% of the main pulse, the delay between the two pulses is 2 ns, the main pulse duration,

Table 7.8. Laser lines observed from Ni-like lasers with prepulse

Element	Z	λ(nm)	References
Nb	41	20.3	[227]
Mo	42	18.9	[227, 228]
Pd	46	14.7	[229]
Ag	47	13.9	[230, 231]
In	49	12.6	[232]
Sn	50	11.9	[233, 234]
Te	52	11.1	[230]
La	57	8.9	[230]
Ce	58	8.6	[230]
Pr	59	8.2	[235]
Nd	60	7.9	[226, 230]
Sm	62	7.3	[226, 230]
Gd	64	6.9	[226, 230]
Dy	68	6.37	[226, 230]
—	—	5.86	[236]
Yb	70	5.03	[235]
Hf	72	4.65	[235, 237]
Ta	73	4.48	[235, 237]
W	74	4.32	[235, 237]

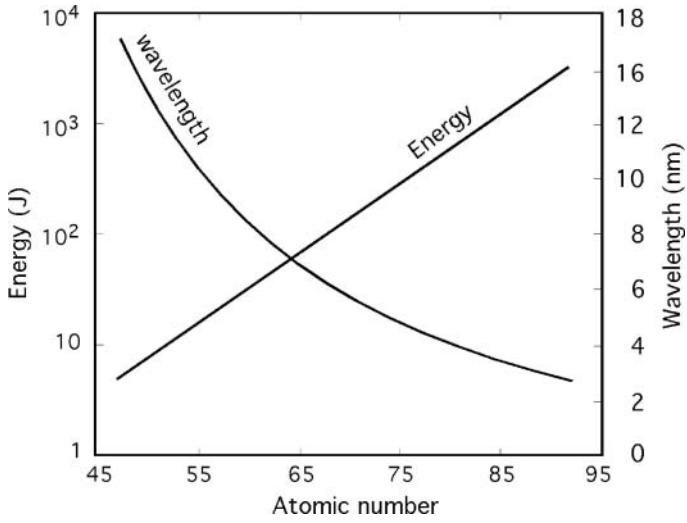

Fig. 7.49. $J = 0-1$ line wavelengths of Ni-like ion lines and pump energy required to obtain laser saturation for these lines (data from Ref. [239]). The main pulse duration is 75 ps, the delay between pulses, 2 ns, the pulse ratio, 10%.

75 ps. The plasma width is 100 μm. The length L of plasma needed to achieve saturation is estimated from a gain–length, gL, of 15. The pump energy calculated under these conditions is reported versus Z on the diagram.

7.3.5.1 Prepulse Optimization

As we saw in Section 7.3.1, computational simulations of the prepulse action account for the general characteristics of the prepulsed plasma behavior, especially for what regards density gradient smoothing and optimization of the main-pulse energy absorption. But many details of the three-dimensional, two-step history of the hydrodynamic plasma evolution escape theoretical predictions. Therefore the efficiency of prepulse optimization remains largely grounded on experimental works.

In the case of neon-like ions, for a long time pumped by long driving pulses (0.5–1 ns), experiments showed that the pump energy could be reduced without significant loss of the laser output by using shorter pulses (∼100 ps). For instance lasing was observed in Ne-like iron, at 25.5 nm, with a pulse duration of 140 ps and a pump energy as low as 11 J. It was also demonstrated that the $J = 0{-}1$ line gain coefficient, which was 5.7 cm^{-1} with a single prepulse, was increased up to 9.2 cm^{-1} with a double prepulse [194].

However for the Ni-like ions long driving pulses never turned out to achieve laser saturation, even with multiple-pulse configuration. This difficulty can be understood from calculation results that show, especially for Ni-like ions, that the zone of strong local gain never merges into the zone of high lasing-particle density when the plasma is long-pulse produced. Thus the gain coefficient integrated over a full amplifying path remains small as compared to the calculated local gain. Therefore the duration of Ni-like laser drive-pulses is systematically chosen to be about 100 ps or less in experiments. Another peculiarity of these lasers is the double prepulse scheme does not present a clear advantage over a single prepulse.

On the other hand, the range of prepulse-to-main pulse delays for achieving strong lasing may be rather narrow, as shown by the curve in Figure 7.50,

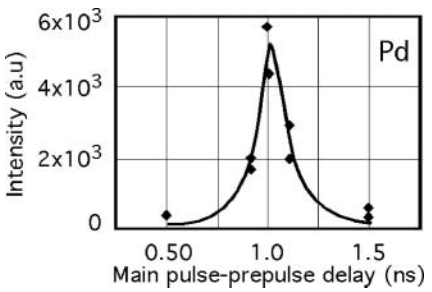

Fig. 7.50. Ni-like palladium laser intensity versus time delay between prepulse and main pulse. These results show a narrow high-efficiency window of time delays (data from Ref. [194]).

which displays a pronounced intensity peak for a 1-ns delay for the 14.7-nm lasing line of palladium. It is important to note that, in this case, the optimum delay was determined using flat targets. In the same experiment, curved targets of various curvature radii did not improve the laser output but reduced it instead [229]. The prepulse-to-main-pulse time interval, on the one hand, and the target curvature, on the other hand, to have probably crossed effects on the beam propagation within the plasma. If it is the case the two parameters cannot be optimized independently from one another (see also [154]).

7.3.5.2 Saturation in Ni-Like Tin

The first demonstration of a saturated Ni-like Sn XUV laser at 11.9 nm was prepared by an investigation of the optimal drive pulse configuration [240]. Figure 7.51 shows the configurations that have been tested. The width (FWHM) of the main pulse is 75 ps, the prepulse energy (10–30)% of the main pulse energy. The XUV laser output is given in units of CCD count on the right of the figure. One sees that the best results were achieved with the single main-pulse–single prepulse configuration. This was the first indication that double pulse or double prepulse configurations were not really suitable for Ni-like ion pumping unlike the case of Ne-like ions (cf. Fig. 7.43).

Not only the total output, but also the beam quality can be lowered if an unsuited pulse configuration is used. This appears from the comparison of the angular beam distributions displayed in Figure 7.52 for three configurations, that are shown in inset. For the configuration constituted of a single prepulse and a single main-pulse [case (a)] the laser peaks at 1.2 mrad from the axis

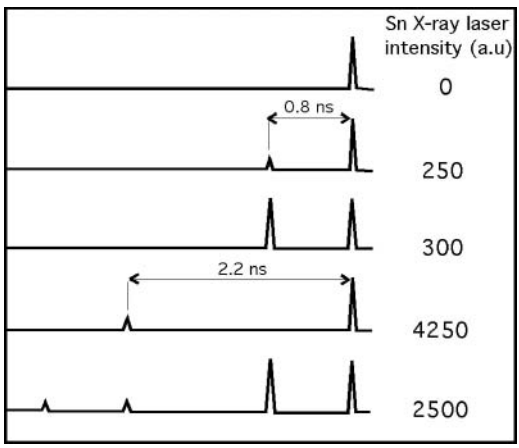

Fig. 7.51. Pulse configurations whose efficiencies were tested in view of reaching saturation of the tin Ni-like laser. Single pulse plus single prepulse give by far the best result.

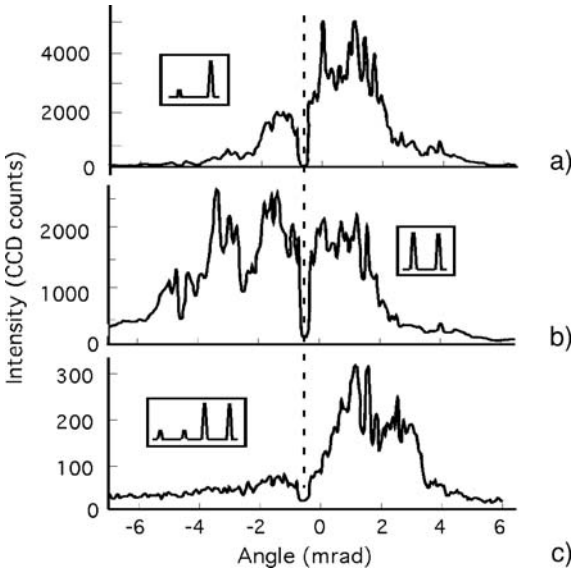

Fig. 7.52. Effect of prepulse configuration on the angular distribution and the peak intensity of the tin laser.

with a divergence of 2.7 mrad. In the case (b), the laser is driven by a double pulse separated by 800 ps and the deflection and divergence angles are seen to be somewhat larger. With a four-pulse configuration [case (c)] the laser spreads over 6.2 mrad, which means that the divergence of the XUV laser is ∼5 times larger than in the case (a).

Saturation has been achieved with the single-pulse, single-prepulse configuration; with a focused intensity of 2×10^{13} Wcm^{-2}. The gain coefficient for the small signal gain was found to be ∼11 cm^{-1}. Saturation appeared for a gain–length product ∼16. The maximum output energy is ∼0.7 mJ, the pulse duration, ∼60 ps. The source size was estimated at 200×60 μm^2. Thus the output intensity was determined to be 9.7×10^{10} Wcm^{-2}.

7.3.5.3 Saturation in Ni-Like Samarium

The same technique, using a 75-ps main pulse preceded by a 2.2-ns prepulse, was to be able to achieve laser saturation for the first time at a wavelength below 10 nm in a samarium plasma. It was achieved at 7.4 nm [232, 241]. The pump laser intensity was $\sim 4.0 \times 10^{13}$ Wcm^{-2}. The experimental setup included the refraction-compensating double-target system represented in Figure 5.10. The flat slab targets measured 18-mm long and the width of the irradiated line was ∼100 μm. Boron and CH filters attenuated the line intensity by a factor of 50 to avoid the saturation of the CCD detectors.

The gain coefficient for the 7.4-nm line was found to be 8.6 ∓ 0.6 cm^{-1}. Saturation occurred for a gain–length product ∼16, as for tin. The maximum

output of the X-ray laser was ∼0.3 mJ distributed over an emission duration of ∼37 ps. The measured beam divergence was found to be 1.2 mrad by 3.5 mrad. The source size was estimated at 50 μm × 60 μm. From these data, the Sm laser intensity could be estimated at $\sim 2 \times 10^{11}$ Wcm^{-2}, which agrees with the calculated value of saturation intensity, 1.3×10^{11} Wcm^{-2}.

7.3.5.4 Saturation in Dysprosium

The shortest saturated-emission wavelength observed in the group of experiments presented here has been achieved by applying the prepulse technique to dysprosium, in experimental conditions similar to those set up for samarium [242]. As indicated in Table 7.8, Ni-like ions of dysprosium exhibit two $J = 0-1$ lasing lines at 6.37-nm and 5.86-nm wavelengths. The main atomic levels involved in the production of the population inversions associated with the two lines are recalled in Figure 7.53. Owing to the small wavelength interval between the two lines, it is necessary to use filters to spectrally isolate the two lines.

The gain coefficients before saturation are found to be 7.5 cm^{-1} and 9 cm^{-1} for the 6.37-nm and the 5.86-nm line, respectively. A noticeable fact is that the saturation processes is not identical for the two lines as follows from Figure 7.54. In the saturation regime, the intensity of the 5.86-nm line, which has the larger gain coefficient, goes on increasing versus the plasma length, whereas the intensity of the 6.37-nm line is dropping off. For a plasma length of 3.5 cm, the intensity of the relatively small gain line is two orders of magnitude smaller than the intensity of the high gain line, while both intensities are similar for 1-cm long plasma.

To understand this behavior, let us remember that Figure 7.53 showed two transitions which share the same upper level and thus compete with one another to depopulate this level. This allows the 5.86-nm wavelength line to take advantage of its higher gain to reduce the transition rate that determines

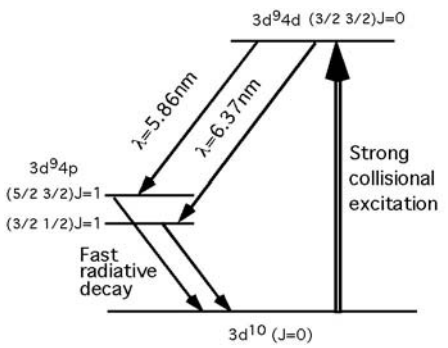

Fig. 7.53. Main transitions involved in the production of population inversion in Ni-like dysprosium. Let us notice the weak wavelength difference between the two lasing lines.

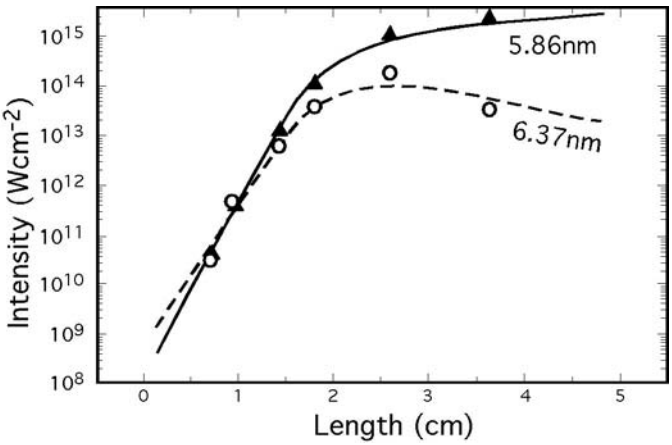

Fig. 7.54. White circles and black triangles represent the measured intensities of the two laser lines of dysprosium versus plasma length. The saturation outset appears when the plasma length reaches about 2 cm. Curves are the results of an ASE intensity calculation model.

the intensity of the second line. An ASE intensity-calculation model, including the steady-state equations of the three levels involved in Ni-like lasing leads to the two curves displayed in Figure 7.54 [242]. The agreement between these curves and the experimental points clearly supports the above interpretation.

7.3.5.5 Saturation in Palladium

Saturated output in a nickel-like Pd laser at 14.7-nm wavelength has been achieved using a 8% prepulse 1 ns before the 100 ps main pulse [229]. In addition to prepulse optimization, great care had been taken to improve the palladium target surface state to reduce the standard deviation from perfect flatness from 0.7 μm to 0.07 μm. This improvement has been achieved by using diamond-machined Pd targets. The comparison between the laser intensities for standard machined or diamond-machined targets definitely shows that the good quality of the target surface is a significant factor of lasing efficiency. Figure 7.55 displays the XUV laser intensity as a function of the driving laser irradiance for the two types of targets. One can see the lasing threshold to decrease from 8.4 to 6.6×10^{12} Wcm^{-2} while the efficiency increase with driving irradiance is four times faster, when the high-quality surface target is used.

With the optimized target and a driving laser irradiance $\sim 1.2 \times 10^{13}$ Wcm^{-2}, provided by a 30-J energy pulse, the measured gain coefficient reaches 8.3 cm^{-1} with a gain–length product near saturation of $\sim$16. The measurement of the laser far-field divergence as a function of plasma length shows that it decreases with increasing length up to laser saturation and exhibits a nearly constant behavior beyond this point (Fig. 7.56). From the 2.2 ∓ 0.2 mrad divergence measured at saturation, the transverse coherence length at the end of the gain medium is found to be $l_c = (2.4 \mp 0.2)$ μm.

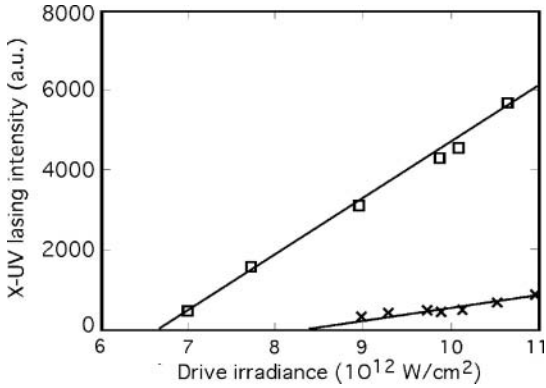

Fig. 7.55. Effect of the target surface state on the palladium laser efficiency for two values of surface roughness: 7 μm (crosses) and 0.7 μm (squares).

7.3.5.6 Ni-Like Silver Lasers

The 13.9-nm wavelength of the 4d–4p ($J = 0-1$) Ni-like Ag laser line (see the diagram in Fig. 7.1) is of a peculiar interest for X-ray laser applications because, owing to the large transparency of silicon at this wavelength, the reflection coefficient of the Mo–Si multilayer mirrors may reach an exceptionally large value $\gtrsim$60%. This is an obvious advantage for the design of XUV optical facilities devoted to scientific and technical investigations, such as X-ray lithography for instance. XUV interferometry based on Ni-like Ag laser is now demonstrated [231].

The saturation of Ni-like Ag laser has been achieved using the prepulse technique and various combinations of the target-irradiation parameters. Information on the pulse–prepulse configurations used and on the corresponding input and output energies, lasing threshold, gain coefficient, and X-ray laser pulse duration are summarized in Tables 7.9, 7.10, and 7.11, respectively.

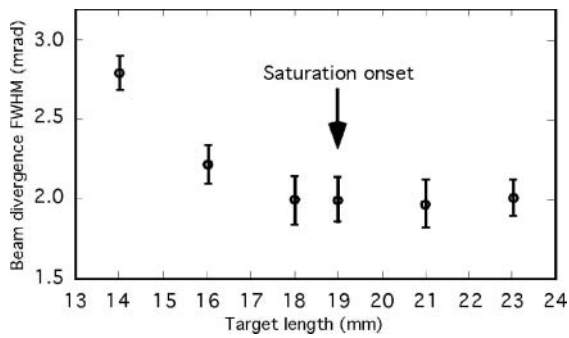

Fig. 7.56. Divergence of the palladium laser beam as a function of the plasma fiber length (data from Ref. [231]).

Table 7.9. Parameters of the pulse configuration (see Fig. 7.57): configuration label (Column 1), main-pulse and prepulse duration (Column 2), time interval between prepulse and main pulse (Column 3), prepulse level as a fraction of the main-pulse energy (Column 4), references (Column 5)

No.	τ_{p} (ps)	τ_{d} (ns)	Prepulse level	Reference
1	75	$\gtrsim$2	10–30%	[243]
2	140	1	8%	[194]
3	100	3	4%	[244]
4	130	5.5	0.7%	[245]

Table 7.10. X-ray laser output for the configurations of Table 7.9: main-pulse energy (Column 2), intensity on target at X-ray laser saturation (Column 3), saturated X-ray laser output (Column 4), energy conversion efficiency (Column 5) (references as in Table 7.9)

No.	E_{target} (J)	$I_{\mathrm{target}}(\mathrm{W/cm^{-2}})$	$E_{\mathrm{XRL}}(\mu\mathrm{J})$	$E_{\mathrm{XRL}}/E_{\mathrm{target}}$
1	75	2.0×10^{13}	90	1.2×10^{-6}
2	30	1.2×10^{13}	—	—
3	140	8.0×10^{13}	300	2.1×10^{-6}
4	60	2.0×10^{13}	50	0.8×10^{-6}

The configuration parameters, viz. pulse duration, prepulse-to-pulse delay and prepulse level are defined in Figure 7.57.

It is to be mentioned that the configuration #4, in Table 7.9, involved a second main pulse, delayed by 800 ps, in order to probe the suitability of a double X-ray pulse for double-passing the plasma with a half-cavity mirror. Double pulses turn out to be necessary in Ni-like lasers because double-pass cannot be achieved with a single short pulses, unlike the case of long-drive pulse Ne-like lasers (see the example of the zinc laser in the present section and Fig. 7.37 in Section 7.3.2). With the parameters of configuration #4, the gain coefficient for the second X-ray pulse was estimated at be 4 $\mathrm{cm^{-1}}$, which

Table 7.11. Lasing threshold (Column 2), gain coefficient (Column 3), X-ray laser pulse duration (Column 4) for the same configurations as in Table 7.9

No.	Threshold $(\mathrm{W/cm^{-2}})$	g $(\mathrm{cm^{-1)}})$	τ_{XRL}(ps)
1	—	7.2	34–55
2	6.6×10^{12}	7.3	—
3	—	19	60
4	1.8×10^{13}	6.0	$\leqq$50

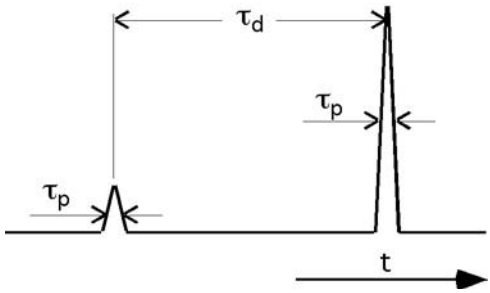

Fig. 7.57. Parameters characterizing the Ni-like laser configurations described in text.

is believed to prove sufficient population inversion for the return pass of the first X-ray radiation pulse to be efficiently amplified.

Tables 7.10 and 7.11 show that configuration #2 requires lesser driving-pulse energy and lesser intensity on target than on the other configuration. Moreover this configuration exhibits a relatively low lasing threshold. This is due to a careful optimization of the time interval between prepulse and main pulse, as well as of the prepulse level. May be more important still, the roughness of the target surface was considerably reduced by special machining [194, 229].

The maximum X-ray laser output energy is provided by configuration #3, for which the input energy was also the largest of the series (Table 7.10). From the gain coefficients displayed in Table 7.11, it is clear that this large X-ray output is associated with an especially large population inversion density. Moreover, taking into account the experimental errors, the energy conversion efficiencies obtained for three of the configurations do not show significant discrepancies around a mean value of 1.4×10^{-6}. This would lead to a value $\sim$40 μJ for the nonmeasured output of configuration #2. These results suggest that, in the range of the pump parameters considered here, the density of population inversion depends nearly linearly on the input energy via the electron plasma temperature.

To complete this survey of experimental results, Table 7.12 displays order-of-magnitude values of X-ray pulse power and intensity corresponding to the

Table 7.12. X-ray laser pulse power (Column 2) and X-ray laser intensity (Column 3) for the same configurations as in Table 7.9

No.	P (MW)	I (GWcm^{-2})
1	1.7	69
2	—	—
3	5	200
4	1	40

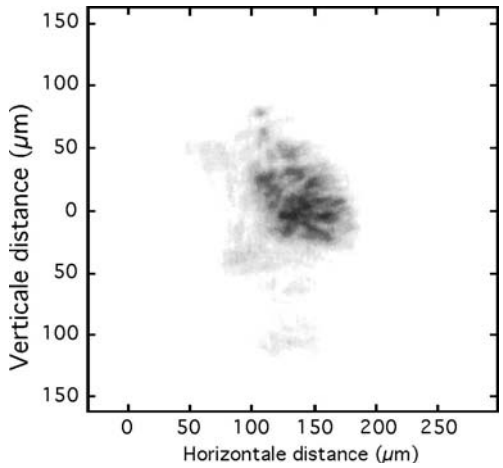

Fig. 7.58. Near-field footprint of the X-ray laser emission of a Ni-like laser (Ref. [241]). This picture reveals a multimode beam structure.

above data. The source size measured in the case of configuration #1 was $\sim 2.5 \times 10^{-5}$ cm^{-2} [241]. In Table 7.12 it is assumed that this value holds approximately for the three other configurations.

In addition Figure 7.58 shows a typical near field image of X-ray laser emission, obtained in a plane perpendicular to the beam axis with the configuration #1 of Table 7.9. The beam intensity irregularities provide a clear indication of the multimode character of the beam. Figure 7.59 displays the decrease of the beam divergence versus plasma length in configuration #2. One sees that the divergence turns out to be minimum near the saturation onset, which occurs in this case for a target length of 21 mm, and then remains nearly constant [229].

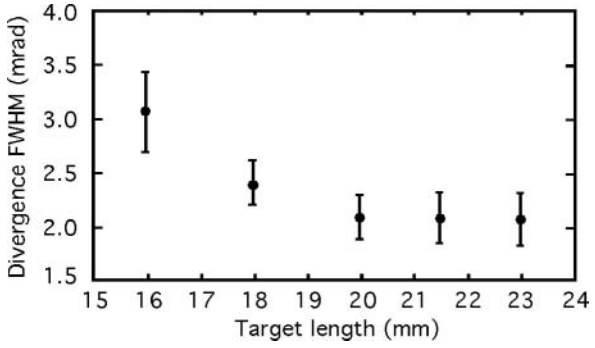

Fig. 7.59. Divergence of the Ni-like laser based on configuration # 2, Table 7.9, as a function of target length (Ref. [231]).

The previous examples show that the Ni-like ion lasing, with the prepulse technique, requires reduced pump–pulse duration, compared to Ne-like ion lasing. Thus, at fixed target irradiation power, the pump energy is also reduced. In other words, less energy than with long-drive pulse, is used for keeping the plasma in a highly ionized state during a time largely exceeding the duration of the gain.

That is why prepulsed Ni-like lasers did open the way to shorter wavelength lasers, down to the "water-window." However, at fixed lasing wavelength, the reduction of the pump energy is followed by a similar reduction of the X-ray laser output. The lasing plasma has been shown to be largely over-ionized in fact [244]. This reduces the Ni-like ion density in the plasma and is a remaining cause of pump energy waste. Thus new improvements in driving the heating of plasma should provide new enhancement of XUV lasers efficiency. The next step on this route is the so-called transient pumping scheme described in the next section.

7.4 Transient Collisional Excitation (TCE) Scheme of Pumping

A new improvement of drive-pulse configuration, illustrated by Figure 7.60, so modifies the kinetics of plasma-heating and the ionization balance that the pump energy can be reduced again [246]. This new pumping scheme is based on the difference between the population inversion lifetime (a few tens of picoseconds) and the ionization time (hundreds of picoseconds). Using a long pulse (100–600 ps) of moderate energy, one can preform a plasma in such a way that lasing ions form its main component. Then an intense short pulse (0.1–10 ps) so rapidly overheats the plasma free-electrons (∼1 KeV) that the abrupt increase of collisional-excitation rate produces a transient population inversion.

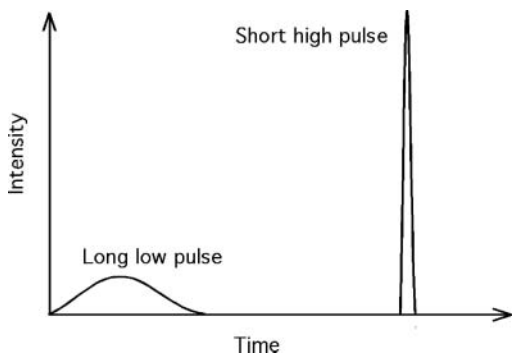

Fig. 7.60. Pump pulse configuration which aims to heat a cold plasma thanks to a short intense pulse, whose energy is deposited onto target by a traveling wave.

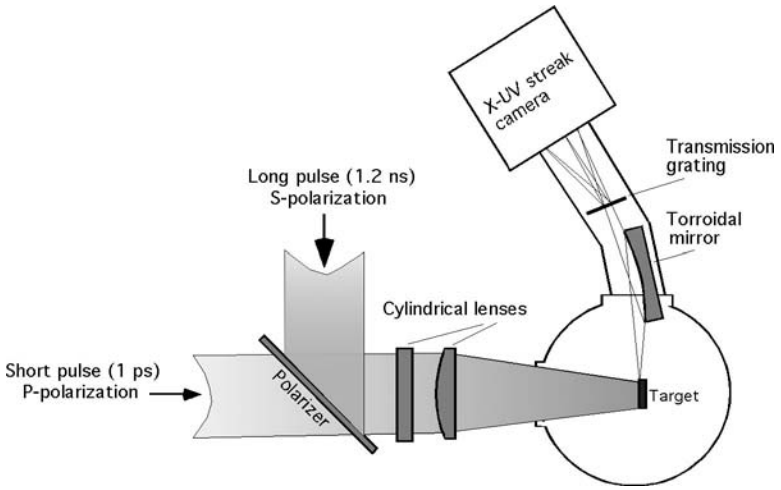

Fig. 7.61. Diagram of the experimental setup used to produce a transient collisionally excited (TCE) Ne-like plasma of titanium (Ref. [163]).

By separating the adjustment of the initial ionization conditions, with the first pulse, from that of the electron temperature, with the second pulse, this system gives the possibility to overcome an otherwise unavoidable mismatch between ionization and temperature dynamics which results in pump energy wasting. The delay between both pulses may be adjusted to optimize the gain generated by the plasma. The duration of the transient population inversion is of the order of a few picoseconds. Gain coefficient can reach much larger values than in the QSS conditions which prevail when long pump pulses are used.

The first experimental results, obtained with the TCE pumping technique, confirmed that very large gain coefficients were achievable with much smaller pump energy than necessary when using the previous techniques. This is illustrated by the performances of the Ne-like titanium laser schematically represented in Figure 7.61 [163]. The figure shows two synchronized beams, one delivering 1-ns and the other 1-ps pulses, entering the vacuum chamber along one and the same axis thanks to a simple polarizer system. The shorter pulses are produced by "compression of amplified chirped pulse" (CPA technique) [247, 248]. A delay of 1 ns separates the short and the long pulse. The XUV radiation is analyzed by a transmission grating spectrograph equipped with a streak-camera of ∼20 ps temporal resolution. Line focus lengths of 2, 3, and 5 mm were used to estimate the gain.

The main lasing line of Ne-like Ti is the $J = 0-1$ one, at 32.6-nm wavelength. The laser emission was observed to start with an energy of 3 J in the long pulse and 2 J in the short pulse. Energies of 4 J in the short pulse and 7 J in the long pulse, viz. approximately hundred times less pump energy than

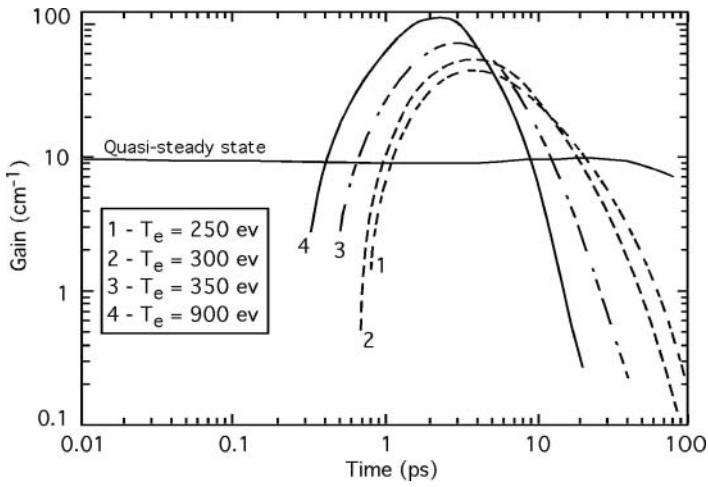

Fig. 7.62. Numerical simulation of gain versus time for various temperatures. The plasma density is fixed at 4×10^{20} cm^{-3}.

in the prepulsed regime, were then used to measure XUV laser intensity as a function of plasma length. The gain coefficient deduced from a fit of experimental data on Lindford formula 1.43 was found to be 19 ∓ 1.4 cm^{-1}, with a gL product of 9.5 ∓ 0.7. The beam divergence was $\sim$15 mrad, which shows that refraction effects remained important.

A computational code, including hydrodynamics and radiative plasma properties (RADEX) has been used to make a numerical model of this new laser [249]. The calculated temporal-evolution of gain for the 32.6-nm line is shown in Figure 7.62 for different values of electron temperature. The temperature rise-time is fixed at 1.5 ps. For comparison, the gain curve calculated for a quasi-steady-state population inversion, at 250-eV temperature, is also plotted in the figure.

Laser saturation was not achieved in the previous experiment, probably because the pump pulse duration was shorter than the propagation time of the XUV beam in the plasma. As a matter of fact, this new pump configuration leaves unsolved the difficulty of fitting a short population-inversion lifetime ($\lesssim$10 ps) to the propagation time of the amplified XUV beam (33 ps/cm). This weak point limits the effective length of the laser because propagation partially occurs in a nonamplifying medium. This obviously affects the behavior of the laser output when the plasma length increases [164, 250, 251]. However, it is possible to remove the discrepancy between gain duration and propagation time if one substitutes a traveling wave to the stationary lighting of the target by the short pulse. This can be achieved by tilting the wave front of the driving laser beam to an angle such that traveling waves move with the velocity of light.

As an example, the 4d–4p ($J = 0-1$) line of Ni-like palladium, at 14.7 nm, was found amplified with a gain coefficient as large as 35.3 cm^{-1} and a gain–length product $\sim 12.5 \mp 0.5$ [252]. The energy values were 0.5–2.2 J for the long (600 ps) pulse and 4.5–5.5 J for the short (1 ps) pulse, delayed by 700 ps from the peak of the long pulse. Laser saturation has been achieved, with a gain–length factor of 18, thanks to traveling wave implementation [253]. It is interesting to mention that the repetition rate was 1 shot/4 min in this experiment, instead of 1 shot/20–120 min for single long-pulse lasers. This strong reduction of the time interval between shots was made possible by the reduced energy required from the pump and the corresponding shorter thermal stabilization time of the laser.

7.4.1 Traveling Wave Implementation

Traveling wave (TW) can be implemented by several methods. For instance a transverse shearing of the wave front can be obtained by reflecting the pump beam on a multi-segment stepped mirror, as shown in Figure 7.63. Let n be the number of mirror steps of height $h = (L \cos i)/n$, where L is the target length. The pump pulse turns out divided in n temporally and spatially separated pulses arriving on target. Under condition that the light propagation time

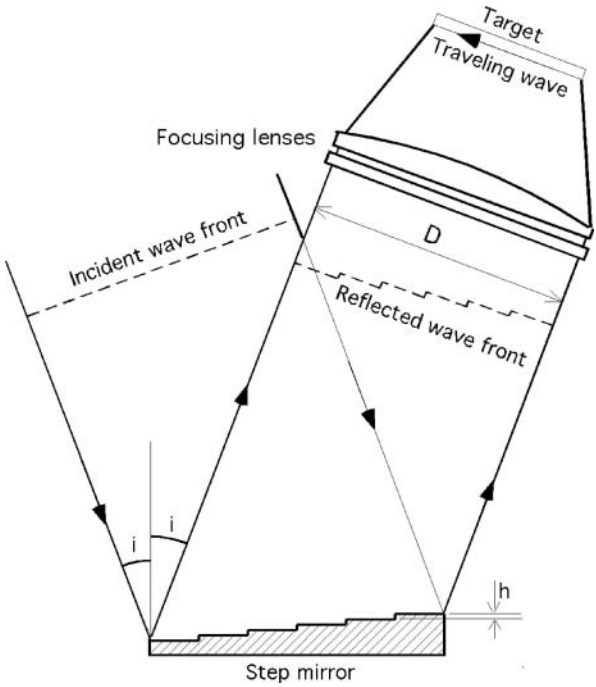

Fig. 7.63. Traveling wave produced by a multi-segment stepped mirror.

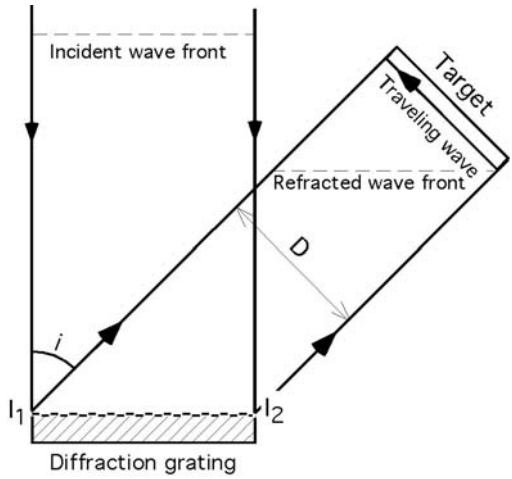

Fig. 7.64. Traveling wave produced by diffraction on plane grating.

over each step is no longer than the pulse duration, τ, the set of n pulses behaves approximately as a continuous traveling wave with the velocity of light. Neglecting the small dephasing due to focusing optics, the condition reads

$$\tau \gtrsim \frac{L}{n}\frac{1}{c} \tag{7.10}$$

For $L = 10$ mm and $n = 5$, for instance, the pulse duration should be $\gtrsim$6 ps. For pulses shorter than L/nc, only a part of the radiation reflected by each segment will be useful for plasma heating. On the other hand, increasing the number of steps, in order to reduce τ, would increase the rate of damage caused to the optics by the beam diffraction by the step edges.

Diffraction gratings offer solutions for a variety of parameters (see for instance [254]). We consider the simple case where the incident beam is normal to the grating surface, as shown in Figure 7.64. Let i be the diffraction angle. The traveling wave velocity is readily found to be

$$V_{\mathrm{tw}} = \frac{c}{\tan i} \tag{7.11}$$

which shows the traveling wave velocity equal to the light velocity when the diffraction angle is 45°. The use of a 1.05-μm wavelength pump laser, for example, requires a 673 grooves/mm grating. A 5% difference from this number leads to ∼10% discrepancy between the light speed and the traveling wave velocity. This leads to a 3.3-ps mismatch between pump action and XUV beam front at the end of a 1-cm long plasma. This difference is acceptable when the population inversion duration exceeds 6–7 ps. For ultrashort pulses and fast atomic kinetics, it may be necessary to calculate the exact angle i, that will give the speed of light to the traveling wave.

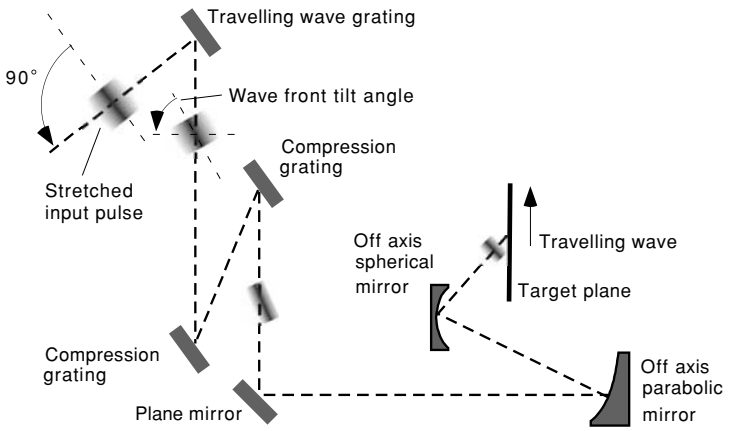

Fig. 7.65. Experimental arrangement which combines the intrinsic wave front tilt resulting from the optics astigmatism with an additional tilt induced by an adjustable grating.

Figure 7.65 shows the diagram of an experimental setup where the astigmatism of the off-axis focusing optics introduces an intrinsic tilt in the wave front [255]. The velocity of the resulting intrinsic traveling wave is estimated at $2.5-2.9 \times c$ [256]. This velocity may be reduced to the light velocity thanks to the addition of a suitable diffraction grating.

Another elegant method consists in slightly tilting the second grating of the compressor used in the "compression of amplified chirped pulse" technique (CPA pulse) to generate the heating short pulse, as shown in Figure 7.66 where ϵ is the grating tilt angle [257]. It is shown that the pair of gratings can be made equivalent to a virtual single grating by simply tilting and translating one of the gratings. The advantages are that (i) no additional optical device

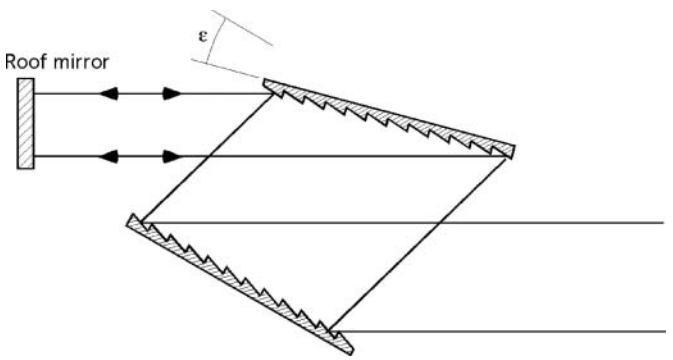

Fig. 7.66. Traveling wave obtained by tilting the second grating of a pulse compressor.

is necessary to implement traveling wave, (ii) traveling wave can be generated in the two amplification directions at any velocity by adjusting the tilt angle of the grating.

However, the question arises if it is or not correct to choose $v_e = c$ as the optimum value of the traveling wave excitation velocity? The familiar radiative transfer equation (1.3) (Section 1.2), corresponds to gain coefficients g, and source function emissivities j, independent of time. In Ref. [258] the time dependence of the *local* values of g and j, which is caused by the change of refractive index induced by the traveling wave excitation, are introduced. Therefore equation (1.3) is replaced by

$$\left(\frac{1}{v_{lg}}\frac{\partial}{\partial t} + \frac{\partial}{\partial z}\right) I(\nu, t) = g(\nu)\, I(\nu, t) + j(\nu, t) \tag{7.12}$$

In this equation, v_{lg} is the *local* group velocity of the traveling wave. In the case of the homogeneous broadening of a Lorentzian line profile, v_{lg} can be approximated at line center by

$$\frac{1}{v_{lg}} = \frac{1}{c} + \left(\frac{g(0)}{2\pi\Delta\nu_{lg}}\right) \tag{7.13}$$

where $g(0)$ is the gain coefficient at the line center and $\Delta\nu_{lg}$ the gain band width. According to equation (6.22), when saturation occurs the small signal-gain $g(\nu)$, should be replaced in equation (7.12) by

$$g_s(\nu) = \frac{g(\nu)}{1 + I_T/I_s}$$

where I_s is the saturation intensity and I_T the line intensity integrated over the line width. Moreover if the local gain moves through the plasma with a constant velocity v_e, the small-signal gain at the line center can be represented as

$$g(z, t, 0) = g(t - z/v_e, 0) \quad \text{for} \quad t \geqq t - z/v_e \tag{7.14}$$

Replacing t by $t - z/v_e$ transforms equation (7.12) to a frame commoving with plasma excitation. This leads to the new equation

$$\left\{\left(\frac{1}{v_{lg}} - \frac{1}{v_e}\right)\frac{\partial}{\partial t} + \frac{1}{\partial z}\right\} I(\nu, t) = g(\nu) I(\nu, t) + j(\nu, t) \tag{7.15}$$

Analytic solutions of this equation can be found if one assumes that the small-signal gain at line center is given by a steep increase followed by an exponential decay of lifetime τ, i.e. $g(t) = g_0 \exp(-t/\tau)$ for $t \geqq 0$. The solutions emphasizes two critical parameters

$$r \equiv \frac{I_0}{I_s} \quad \text{and} \quad k = \frac{1}{2\pi\Delta\nu_{lg}\tau} \tag{7.16}$$

For example, for $g_0 = 50\ \text{cm}^{-1}$ and $k = 0.01$, the peak intensity is found to reach saturation at lengths of $L = 3$, 3.5, and 4 mm when $r = 10^{-5},\ 10^{-6}$, and

10^{-7}, respectively. These results agree with experimental data on germanium (cf. below Section 7.4.5). Furthermore one can deduce from the solutions of equation (7.15) that the conversion efficiency is the greatest when the traveling wave excitation velocity, v_e, is matched to the minimum group velocity, v_{lg}^{min}, determined by the small-signal gain at the peak of the gain coefficient curve. Substituting $g_0 \equiv g(0)_{max}$ in equation (7.13), we find that the optimal traveling wave velocity is given by

$$v_e^{optim} = \frac{c}{1 + (cg_0/2\pi\Delta\nu_{lg})} \tag{7.17}$$

Numerical calculations for germanium show that the optimal excitation velocity is about $0.85 \times c$ before saturation and increases to c when the laser output tends to saturation.

Figure 7.67 gives a very convincing experimental evidence of the crucial part played by the traveling wave in the laser output [259, 260]. The figure shows three CCD images of the Ag-laser spectrum near 13.9 nm. On the right, the TW runs toward the entrance of the transmission grating spectrometer, giving rise to a very intense X-ray laser emission which saturates the detector. Moreover, one sees intense lateral satellites, due to diffraction through the grid used as grating holder. For the central image there is no TW. The lasing line appears clearly but with small intensity. On the left, the TW runs in the direction opposite to the spectrometer and the line intensity vanishes.

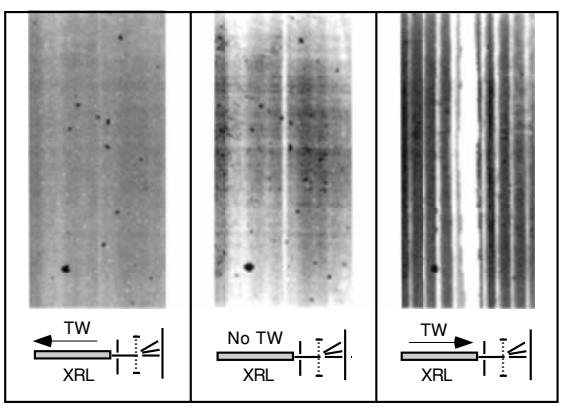

Fig. 7.67. CCD images of the Ni-like silver laser spectrum near 13.9 nm; insets show the propagation direction of the traveling wave (TW) with respect to the X-ray laser beam. On the left, the TW runs in the direction opposite to the spectrometer; the laser line intensity vanishes. For the central image there is no TW; the laser line appears clearly but with small intensity. On the right, the TW runs toward the transmission grating spectrometer; a very intense X-ray laser emission saturates the detector and lateral satellites, due to diffraction through the grating holder grid, appear on both sides of the line.

Quantitatively speaking, the traveling wave is estimated to enhance laser intensity by a factor of 300–400 in this experiment.

7.4.2 TCE Ne-Like Titanium Laser (32.63 nm)

Using the pump laser configuration described in Figure 5.6 (Section 5.2.1), where the focusing optics include tilted mirrors, provides a "natural" traveling wave due to the astigmatism of the system. The focal point moves along the line focus with a phase speed of $\sim 2.5c$ in the direction of the entrance of the XUV analysis system. It is worth looking at the efficiency of this traveling wave, whose front moves continuously ahead of the XUV laser beam wave front. It is clear that the result largely depends on the ratio between gain duration and propagation times.

A very simplified diagram of the overlap of the amplified radiation packet and the heating pulse driven by the traveling wave is displayed in Figure 7.68. For square pulses, one can easily estimate the travel length $L_{\max}$, at which overlap terminates. This length is roughly

$$L_{\max} \sim \frac{\gamma c}{|1-\gamma|}\tau \tag{7.18}$$

where τ is the gain duration and

$$\gamma = \frac{v_{(\text{traveling.wave})}}{c}$$

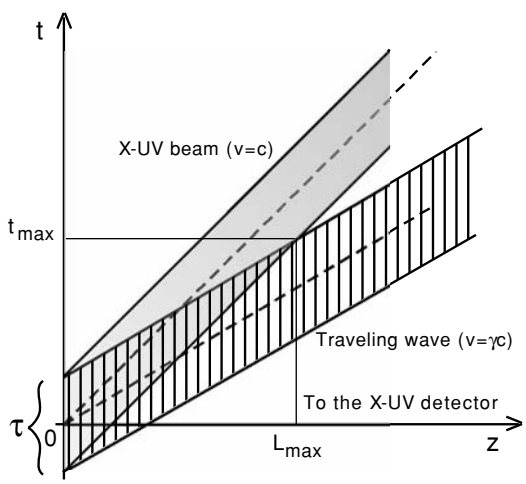

Fig. 7.68. Simplified diagram of partial overlapping of traveling wave and amplified XUV beam, due to the TW being slower than the radiation beam ($\gamma < 1$). τ is the pump pulse duration, $L_{\max}$ the maximum plasma length which can be pumped by a TW of γc velocity. The case where the TW is faster than light ($\gamma > 1$) could be represented by a similar diagram.

The duration of the short-lived population inversion in the Ne-like ions of titanium being estimated at $\tau \sim$10 ps, the largest possible overlapping length for $\gamma = 2.5$ is

$$L_{\max} \sim 5\,\mathrm{mm}$$

which can be sufficient for high gain coefficient experiments.

X-ray laser intensity measurements have been made between 1 mm and 10 mm, with a Nd:glass-laser energy of 1.7 J/mm in the long pulse (1.7×10^{12} W/cm^2 for 1 ns pulse) and of 1.5 J/mm in the short pulse (2.2×10^{14} W/cm^2 in the 7 ps pulse) [256]. Experiments reveal two strong lasing lines which correspond to the 3p–3s ($J = 0{-}1$) transition, at 32.63 nm, and to the 3d–3p ($J = 1{-}1$) transition, at 30.15 nm. Lasing from this transition had not been observed in the QSS regime which prevails in long-pulse pumped lasers. Figure 7.69 displays the measured output of the two lasing lines and the corresponding fitted growth curves.

Data analysis shows that one cannot assign a unique gain coefficient value to either of the two curves, within the limits of target lengths used in this experiment. The largest gain coefficients ($g \sim 46$ cm^{-1} and $g \sim 35$ cm^{-1} for the 32.63-nm and 30.15-nm lines, respectively) are observed for small target lengths, up to 3 mm. Seeing that the overlap with the XUV beam does not stop definitively before ∼5 mm, this value is within the limits of the traveling wave efficiency. Therefore, this plasma segment can generate the large observed transient gain.

X-ray laser modeling helps us to understand the gain evolution for longer plasma columns. Figure 7.70 shows the gain calculated in the transient regime

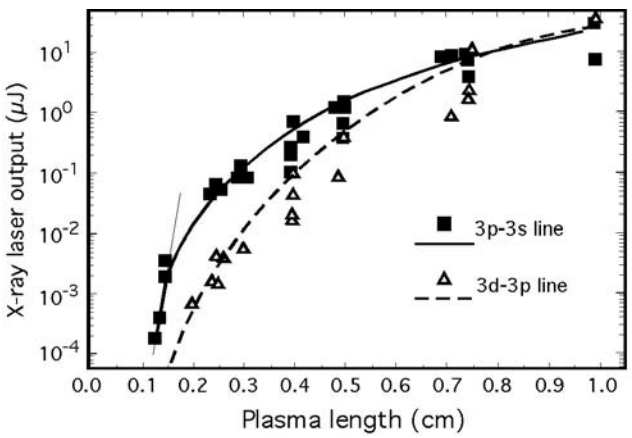

Fig. 7.69. Output of the two lasing lines of the transient Ne-like titanium laser, at 32.63-nm and 30.15-nm wavelength, measured as a function of the plasma length (Ref. [257]). Lasing at these two wavelengths is not observed from long-pulse pumped lasers for which the QSS regime prevails.

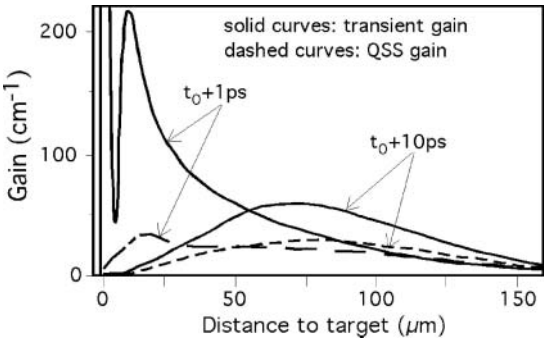

Fig. 7.70. Gain calculated for the 3p-3s line of Ne-like titanium in the transient and in the QSS regime, 1 ps and 10 ps after the arrival of the transient pulse. The first high peak of transient gain, which occurs in the overcritical plasma density region ($n_e > 10^{21}$ cm^{-3}), is quickly driven away from the plasma by the strong refraction ruling this region. The second peak, which contains the main contribution to the experimental gain, decreases and moves away from the target during the 10 ps which are necessary to photons to flight through 3 mm of plasma.

and in the QSS regime at two moments, respectively 1 ps and 10 ps after arrival at the time t_0 of the short pulse. A first high peak of transient gain occurs during a very short time (<1 ps) in the overcritical density region of the plasma ($n_e > 10^{21}$ cm^{-3}). Owing to the strong refraction in this region, the emitted rays rapidly run out the amplifying plasma and did not contribute to the experimentally measured gain. A second peak ($\sim$200 cm^{-1}) occurring in the undercritical region ($n_e \lesssim 10^{21}$cm^{-1}) can be seen in the figure. This peak, which forms the main contribution to the experimental gain, accounts for the fast exponential 3p–3s line intensity increase shown between 1 mm and 3 mm in Figure 7.69. The peak decreases, broadens out, and moves away from the target during the next 10 ps, which is the time necessary for photons to travel through 3 mm of plasma, viz. the plasma length beyond which intensity growth becomes slower, as if laser saturation had started.

The gain–length product, integrated along the intensity growing curve, is about 12 for the 32.6-nm line when the target length reaches the value of 3 mm. Calculation predicts that saturation should occur for $gl \sim 16$. However, saturation is not the only factor in the decreasing rate of the intensity growth above 3 mm. We have seen that the effect of the traveling wave progressively disappears if its phase velocity differs from the speed of light. The main contribution to gain then comes from the QSS regime and is significantly lower than previously with the transient pump pulse (see Fig. 7.70). Nevertheless the major fact is that experiments show that saturation is indeed achieved for a target length of 8.3 mm, for which the value of gl is found to be 16.2.

In addition to the "standard" 3p–3s ($J = 0-1$) transition, Figure 7.71 shows the 3d–3p ($J = 1$–1) transition which provides the second laser line at

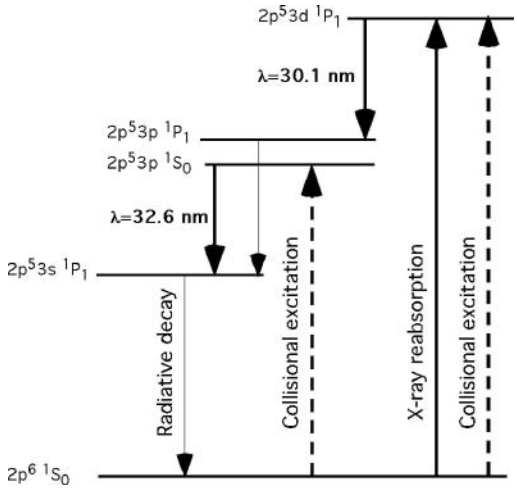

Fig. 7.71. Diagram of the main population inversion mechanisms in a transient collisionally excited Ne-like plasma of titanium.

30.1-nm wavelength. For short plasma lengths Fig. 2.149 showed a smaller intensity for this second line than for the first one but, beyond 8–8.5 mm length, namely in the region where the 32.6-nm line saturates, the intensity ratio tends to be reversed. This agrees with numerical simulations predicting that the saturation intensity is ∼2.8 times larger for the 3d–3p than for the 3p–3s line and this agreement confirms that the saturation is actually achieved for the two lines [256].

A peculiarity of the 3d–3p population inversion is the possible direct contribution, to the 3d level population, of X-ray reabsorption via the 3d–2p resonant line, while the 3p upper level of the standard laser line depends on electronic cascades from the higher lying 3d levels. This may suggest a contribution of photopumping to the 3d–3p population inversion [256, 261]. However a complete characterization of this population inversion requires a quantitative evaluation of the respective parts of photons and electrons in the increase of the 3d population. Moreover, the 3d–3p line is not observed for all lasing materials. The line is clearly visible in the Ne-like chromium laser spectrum [262], but has a very small intensity with iron [263]. No reference has been made to the observation of this line in the TCE pumping results obtained with germanium [264].

As this can be inferred from the measurement of the laser-beam deflection angle at the exit end of the plasma, both 3p–3s and 3d–3p spectral lines are emitted in almost the same plasma region. The deflection angle is found within 8–9 mrad for the both lines. The divergence also has similar values for the two lines, i.e. 2–3 mrad for a 9-mm long plasma with a 0.6-ns long pulse and 6–8 mrad when the duration of the pulse is raised to 1 ns.

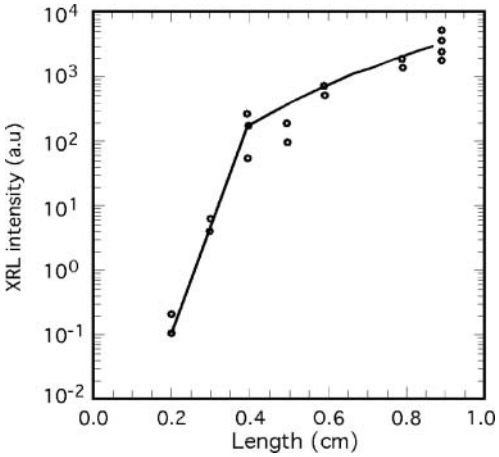

Fig. 7.72. X-ray laser intensity versus plasma length for TCE Ne-like iron. The onset of saturation is immediately visible in the figure for a plasma length ∼4 mm; the small signal gain, in the steep left part, of the curve is measured to be 38.2 cm^{-1}.

Finally, with an output energy of ∼21 μJ, at 32.6 nm, and ∼25 μJ, at 30.1 nm, the energy efficiency of the TCE titanium laser remains near 2×10^{-6}. It is likely that a traveling wave, effective over the entire plasma column length, would increase this value.

7.4.3 TCE Ne-Like Iron Laser (25.5 nm)

The Nd:glass pump laser delivers a long 600 ps pulse followed by a high power 1 ps short pulse, with a peak to peak delay of 1.4 ns [265]. The energy in each beam is ∼5 J and the line focus ∼11 mm. The intensity of the long pulse is about 7×10^{11} W/cm^2, while the intensity of the plasma-heating short pulse is about 5×10^{14} W/cm^2. A traveling wave is implemented by a 5-step mirror which breaks the wave front into so many sections, with temporal delays of 7.7 ps between successive steps (see Figure 7.63). The overall delay is the same as for a wave propagating with the light velocity.

The intensity of the 3s–2p ($J = 0-1$) line, at 25.49-nm wavelength, is shown versus the plasma column length in Figure 7.72. In the portion of exponential intensity increase, up to a length of 0.4 cm, the small-signal gain is found to be 38.2 cm^{-1} and the gain–length product for this length is ∼15.3. Saturation is clearly achieved with a gl product of 18.5 for a 9-mm long target.

7.4.4 TCE Ni-Like Tin Laser (11.9 nm)

The general characteristics of the laser configuration are similar to those of the titanium laser (Section 7.4.2) with the addition of a 300 lines diffraction grating into the CPA beam line to tilt the wave front, with the result that

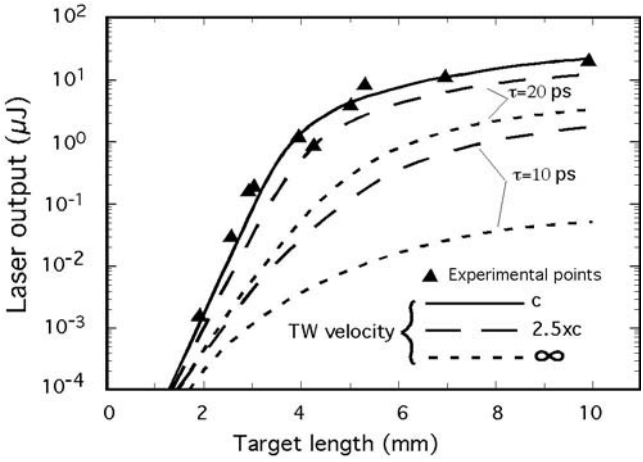

Fig. 7.73. X-ray laser output versus plasma length for TCE Ni-like tin. The figure shows experimentally measured data points compared to numerical simulations for three traveling wave velocities and two time delays between long and short pulse.

the short-pulse intensity spot sweeps across the target at the speed of light (Fig. 7.65). Intensities are 8×10^{12} W/cm^2 for the 300-ps plasma-preforming long pulse and 6×10^{14} W/cm^2 for the 3-ps heating short pulse. A 10% prepulse of 300-ps duration can be sent 3.3 ns ahead of the main pulse but it does not generate significant increase of the laser output. The peak-to-peak time interval between short and long pulse varies between 0 ps and 1000 ps. The maximum output is achieved for a time interval of 550 ps, which proves to be critical to the output value. In Figure 7.73, the experimental data points, corresponding to the 11.9-nm lasing line, show the increase of the XUV radiation output as a function of plasma length. The small-signal gain observed for lengths shorter than ∼4 mm is 42 cm^{-1} [266]. The gain–length product for the full 1-cm long plasma column is estimated at ∼18. Strong amplification is also observed for this line in Ref. [253].

Experimental data are displayed together with a best-fit calculation from an ASE model which includes saturation (solid curve) [101]. The traveling wave is assumed to move forward with the velocity of light. Beyond the plasma length values for which the laser output increased exponentially, the gain coefficient, g, is calculated from the implicit equation

$$g_0 l = \left(1 - \frac{S}{I_\mathrm{s}}\right) gl + \frac{S}{I_\mathrm{s}} \alpha\,(gl) \tag{7.19}$$

where g_0 is the small-signal gain coefficient. Owing to the presence of the traveling wave, the form of this equation corresponds to a unidirectional amplification. S is the source function defined by equations (1.8) and (1.22) (Section 1.2). I_s is the saturation intensity given by equation (6.24) (Section 6.2). The term $\alpha\,(gl)$ accounts for the line narrowing which occurs in homogeneous

profiles for large gl values. In the Lindford's approximation, $\alpha(gl)$ reads [see Eq. (1.43), Section 1.4]

$$\alpha(gl) = \frac{\left(e^{gl} - 1\right)^{3/2}}{\left(gle^{gl}\right)^{1/2}} \tag{7.20}$$

Equation (7.19) is used to calculate laser output increase with plasma length when saturation appears. The fitting procedure shows laser saturation to start once gain–length passes over ∼15, the output being ∼1.2 μJ at this moment. Beyond this limit, the laser output increases approximately linearly with target length up to the 10-mm total length, where the gain–length is estimated at ∼18 and the output at ∼20 μJ. With a source size of 50 × 50 μm at the end of the plasma column and a lasing duration of ∼3 ps, one obtains a saturation intensity of $\sim 1.33 \times 10^{10}$ W/cm^2 and a maximum laser intensity $\sim 2.5 \times 10^{11}$ W/cm^2 for the 10-mm long target.

Calculation can be extended to traveling waves moving faster than light. This requires to take into account the gain duration and to calculate the reduction of the local gain, that is sampled as the laser beam propagates through the gain medium with velocity larger than c ($\gamma > 1$ in Fig. 7.68). Examples for a $2.5c$ velocity and for two-gain FWHM durations can be seen in Figure 7.73. Moreover the case where there is no traveling wave is represented by the curve obtained for an infinite wave velocity.

7.4.5 TCE Ne-Like Germanium Laser (19.6 nm)

The pump laser setup is the same as for the Ti and Sn lasers previously described [255]. The pulse sequence includes a 10% prepulse of 280 ps FWHM duration, the main 280-ps long-pulse separated from the prepulse by 2 ns and the heating short pulse of $\lesssim$3 ps. The intensities are $\sim 5 \times 10^{11}$ W/cm^2, $\sim 5 \times 10^{12}$ W/cm^2, $\sim 1.5 \times 10^{15}$ W/cm^2 for each pulse respectively. The peak-to-peak separation between the long and the short pulse is 80 ps, i.e. the intense short pulse arrives to interact with the preformed plasma in the trailing edge of the main long pulse. The measured signals from targets of length 2–9 mm are shown in Figure 7.74 for the traveling wave and the no-traveling wave cases. The small-signal gain is found to be $\gtrsim$40 cm^{-1} for plasma lengths from 2 mm to 5 mm. Gain duration is estimated at ∼10 ps.

The total output energy for the 9-mm long target is near 100 μJ. The calculated exit pupil aperture is 25 μm × 55 μm (EHYBRID computational code [74, 88, 89]) The corresponding intensity at the exit end of the plasma is $\sim 7 \times 10^{11}$ W/cm^2. The calculated saturation intensity [cf. Eq. (6.24)] is $\sim 2 \times 10^{10}$ W/cm^2 and is reached with a target of 4.5-mm length where the small-signal gain has dropped by a factor 2. Finally, the solid curve in Figure 7.74 shows the good agreement between the output-versus-length variation inferred from simulations and the data provided by experimental measurements.

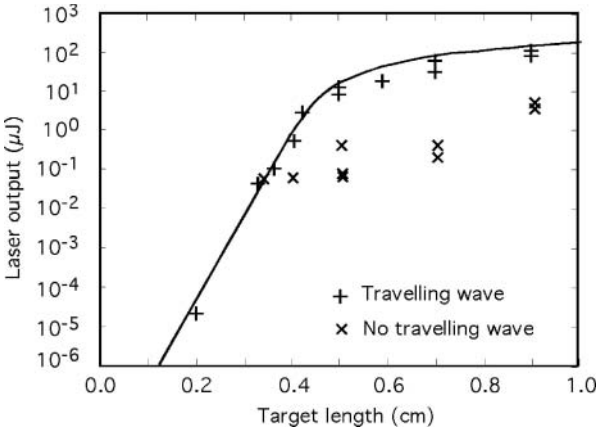

Fig. 7.74. X-ray laser output versus plasma length, with and without using traveling wave, for TCE Ni-like germanium.

7.4.6 TCE Ni-Like Molybdenum Laser (18.9 nm)

The "table-top" pump laser configuration of Ref. [267] yields a long-pulse (∼600 ps) and a short-pulse (∼ps). The time interval between both pulses can be varied. Intensities on the line focus are of the order of 10^{12} W/cm^2 for the plasma-preforming long pulse and 10^{15} W/cm^2 for the heating short pulse. The laser can be fired every 4 min. A five-segment stepped mirror (cf. Fig. 7.63) is used to implement a traveling wave of phase velocity c.

The traveling wave large efficiency is shown by the comparison, in Figure 7.75, of the X-ray laser output of the 4d–4p, $J = 0-1$ lasing line, at 18.9-nm wavelength, with and without traveling wave, for increasing delays between short and long pulse [268]. The output enhancement due to the traveling wave is of 1–2 orders of magnitude for delays of 0.1–0.9 ns.

The variation of the output as a function of target length is displayed in Figure 7.76. The long-pulse and short-pulse energies are 1.13 J and 5.02 J, respectively, with a time interval of 0.7 ns. For short plasma lengths ($l \leq$ 3 mm) the small-signal gain is measured to be 36.5 cm^{-1}. When the plasma length increases, the gain coefficient falls down up to 5.6 cm^{-1}, for 6-mm to 8-mm targets, as a result of the traveling wave fragmentation [cf. Eq. (7.10)] and, possibly too, of refraction effects. The overall gain–length product is estimated at 16.6.

An imaging system, consisting of a quasi-normal incidence spherical mirror and two 45° plane multilayer mirrors, gives images of the near-field beam pattern, with a magnification of ∼14. An example is shown in Figure 7.77. The target surface is at $Z = 0$. The delay between long and short pulses is 0.4 ns and the pulse energies are 2.54 J and 5 J, respectively. From a set of images one could see that increasing the energy of the long pulse increased the size of the lasing aperture in the Z-direction. This effect was likely due to

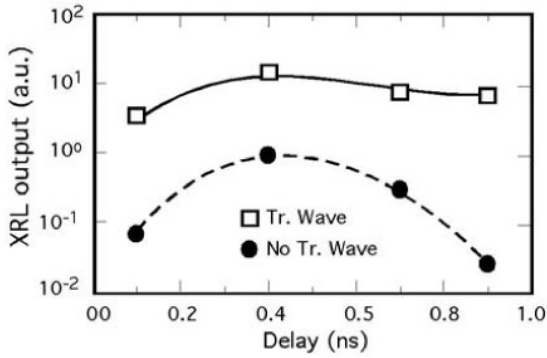

Fig. 7.75. Variation of the laser output of the TCE Ni-like Mo laser at 18.9 nm as a function of the delay between long and short pulse. Moreover, one can see the traveling wave to increase the output by more than one order of magnitude.

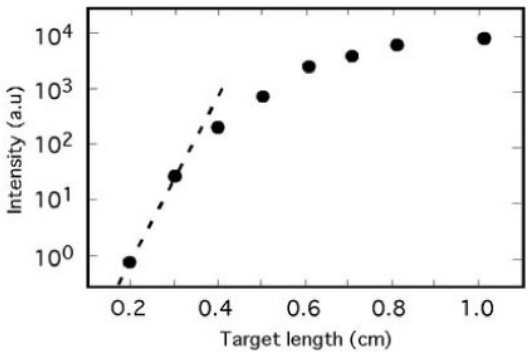

Fig. 7.76. Intensity of the TCE Ni-like molybdenum laser emission as a function of the target length. The gain coefficient measured in the short target length region is 36.5 cm^{-1}.

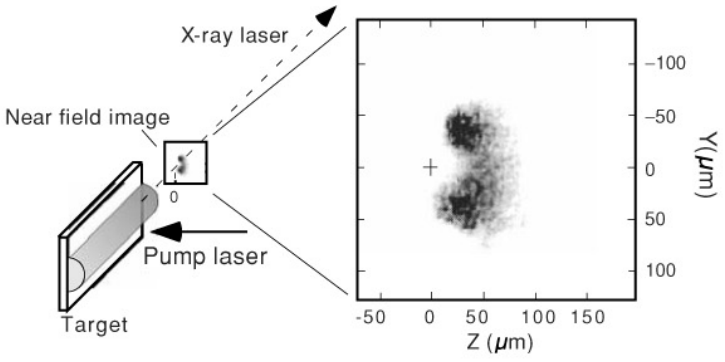

Fig. 7.77. Near-field pattern of the molybdenium X-ray laser beam (from Ref. [266]).

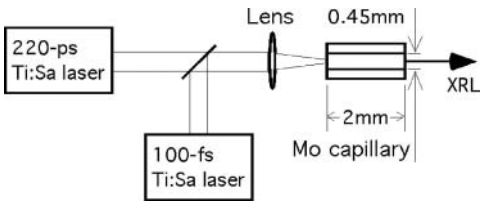

Fig. 7.78. Longitudinally pumped Mo laser using a capillary tube target.

laser action occurring in a larger plasma and in a larger gain region than for lower energies. It is interesting to observe that the beam pattern exhibits also small-scale inhomogeneous structures. Similar inhomogeneities, likely due to the multimode character of the laser emission, often appear in the beams of other XUV lasers.

The total output for a 3.94-J long-pulse, a 4.92-J short-pulse and a 0.7-ns delay between shots has been measured to be $\gtrsim$2.3 μJ. The beam divergence is $\sim 5 \times 10$ mrad^2. The laser brightness is estimated at 10^{22}–10^{23} photons s^{-1}mm^{-2} mrad^{-2} in a $\delta\lambda/\lambda = 0.01\%$ bandwidth.

Interesting examples of longitudinally pumped molybdenum lasers have been reported with either capillaries or slab targets. Longitudinal pumping is expected to improve the matching of the Ni-like ion region to the strongly heated region. Moreover, it spontaneously provides the traveling wave which is essential for TCE pumping.

Figure 7.78 shows a first example where two laser beams of 0.785-μm wavelength are focused on the entrance of a molybdenum capillary tube of 0.45-mm diameter and 2-mm length [269]. A 8-ns delay separates the long pulse (220 ps) from the short one (100 fs). Strong lasing of the 18.9-nm line is observed for a 100-mJ energy in the short pulse. The gain–length product is estimated at ∼12 and the divergence is measured to be 2.6 mrad. The laser operates at the exceptionally large repetition rate of 10 Hz.

The laser configuration used for the second experiment is displayed in Figure 7.79 [270,271]. A 300-ps prepulse is focused along a line on the surface of a 2-mm long Mo slab target with the help of a cylindrical lens. The 475-fs pump pulse is point focused on the preplasma from a direction parallel to the target surface, at a position between 0.1 mm and 0.2 mm from the target surface. The time delay between the two pulses is varied from 1 ns to 10 ns. Typical intensities of the long and short pulses are 1.5×10^{11} W/cm^2 and 3×10^{16} W/cm^2. The measured X-ray laser energy is ∼27 nJ per pulse. The outstanding result of this experiment is the very narrow divergence of the laser, namely 0.34 mrad × 1.2 mrad in the vertical and horizontal directions, respectively. This result is explained in terms of a particularly efficient mode filtering due, in the longitudinal pump beam, to a pedestal of 1×10^{-5} contrast which induces large spatial density and gain gradients.

In a third type of configuration the short pulse beam reaches the plasma column at grazing incidence [272]. This geometry allows refraction to turn the pump beam to the region of electron density below the critical density

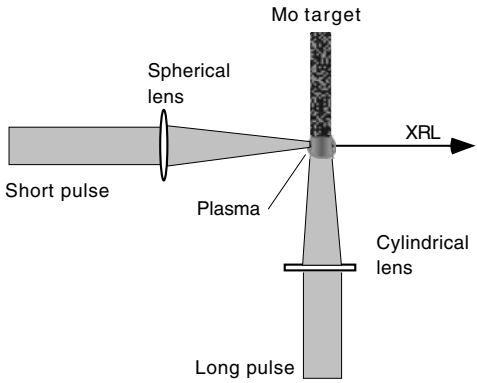

Fig. 7.79. Longitudinally pumped Mo laser using a slab target.

and therefore increases the coupling efficiency between plasma and pumping radiation. With a total energy of 150 mJ only, for both short and long pulses, XUV laser pulses are generated at 10 Hz repetition rate with energy close to saturation.

7.4.7 TCE Ni-Like Silver Laser (13.9 nm)

We have already mentioned that the wavelength of Ni-like silver lasers, 13.9 nm, fits that of the reflection peak of Mo–Si multilayer mirrors. This

Table 7.13. TCE silver-laser experimental data for the 13.9-nm line

	Configuration #						
	1*	2	3	4	5	6	7
Prepulse (J)	0.6	—	0.005	—	—	—	—
Delay (ns)	5.5	—	3	—	—	—	—
Long pulse (ps)	130	750	450	600	600	4	300
Energy (J)	60	3	5	0.4	3	1.5	5
Short pulse (ps)	—	1.5	0.5	0.4	0.3	4	1.3
Energy (J)	—	2	5	2	7.5	10.5	22
Separation (ps)	—	1600	550	200	250	1200	200
Beam frequencies	ω	ω, ω	ω, ω	$\omega,\ \omega$	$2\omega,\ \omega$	$\omega,\ \omega$	$\omega,\ \omega$
Deflection (mrad)	5	14	13	10	10	3	5
Divergence (mrad)	2	20	5	6	3	6	—
Gain (cm^{-1})	5.8	9	14.5	31.9	33.5	35	—
Gain–length	11.6	7.2	10	15	12.7	13.6	—
Output (μJ)	—	0.009	—	3	2	25	10
Duration (ps)	—	50	∼15	7	∼10	—	2
References	[231]	[273]			[259]		[275]

Note. For comparison, long-pulse prepulsed silver-laser data are displayed in column 1*. ω, 2ω are the frequencies of the preforming and heating beam pulses, respectively. The reported divergence values are measured in the horizontal plane.

category of lasers is of special interest for XUV applications that require efficient XUV optical components (cf. Section 7.3.5). That is why these lasers have a large part in the development of TCE X-ray lasers. Table 7.13, which displays the wide range of parameters experimentally investigated till now, illustrates this fact.

Table 7.13 summarizes the gain characteristics observed for the 4d–4p line at 13.9-nm wavelength. Data relative to the standard system which uses a prepulse before the main pulse are shown in column #1* for comparison with TCE lasers. One can see that, notwithstanding a comparatively large energy in the main pulse (60 J), the gain coefficient provided by the standard system (5.8 cm^{-1}) is significantly smaller than all the TCE-gain values reported on the same line.

At the same time, the deflection and the divergence of laser beams are larger for TCE-lasers than for the standard system. In terms of gain building, this suggests that the high transient gain provided by the TCE technique occurs in a rather strongly refractive medium. Configuration #2 is of TCE type, but *without traveling wave*. The gain coefficient obtained in this case (9 cm^{-1}) is larger than the one obtained with the standard system but is smaller than those obtained *with traveling wave,* which are displayed for configurations #3 to #6 in the next columns. Moreover, the absence of traveling wave in configuration #2 results in a relatively small gain–length.

Numerical simulations have been performed to compare the distribution of the energy deposition during plasma heating for configurations #2 and #3 [273]. Figure 7.80 displays, in a plane perpendicular to target surface, the spatial profiles of the energy deposited by the heating pulse in the preformed plasma, at the time of the maximum of the pulse.

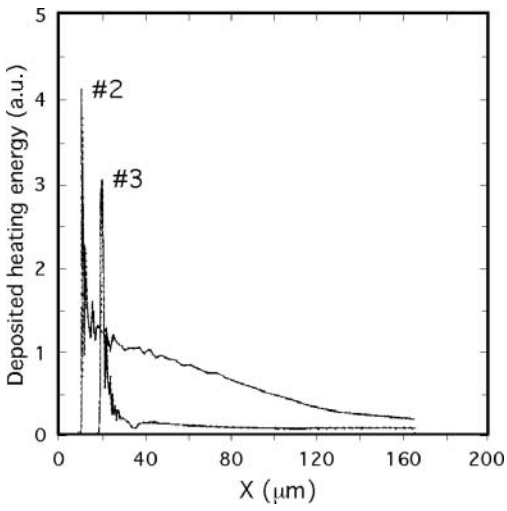

Fig. 7.80. Spatial profile of the energy deposited in the preformed plasma by the heating pulse, for the configurations #2 and #3 in Table 7.13. X is the distance to the target surface.

In configuration #2, plasma heating occurs in a narrow dense region and no gain is produced in the underdense plasma, away from the critical surface (X >20–30 μm). However, in configuration #3, a significant part of energy is absorbed in the underdense plasma thanks to the traveling wave and heats this region up to 250 eV. Thus gain appears in a region of larger volume and of smoother refraction gradients than in configuration #2 and so becomes more observable. This difference originates not only in the traveling wave but also in the shorter time separation between preforming and heating pulse in the case of configuration #3. Now, when peak-to-peak separation is shorter than the preforming pulse half-width, pump-beam absorption by inverse bremsstrahlung may dominate the heating process (cf. Section 5.1.1) and so increase the density of transient population inversion.

Configuration #4 includes both a traveling wave and a short (200 ps) separation between preforming and heating pulse. Showing a large gain coefficient (31.9 cm^{-1}) and a large gain–length ($gl = 15$) obtained with a small pump energy (2 J), the data reported for this configuration confirm the previous analysis.

In configuration #5 the 2ω harmonic of the pump beam ($\lambda = 0.53\,\mu m$) is used, instead of the fundamental frequency ω, to produce the preformed plasma. As before, the fundamental frequency is used to produce the short heating pulse. This two-color pumping system increases the plasma critical electron-density from 10^{21} cm to 4×10^{21} cm^{-3} [cf. equation (2.19), Section 2.1]. Given that the heating pulse wavelength is fixed at 1.06 μm, the energy is deposited in a plasma region of density $\lesssim 10^{21}$ cm^{-3}, which is expected to offer density gradients smoother than those of the critical density region. As a matter of fact, one observes that horizontal divergence is reduced by more than a factor of 2 relatively to the value obtained with configuration # 4. However, gain coefficient, gain–length product and energy output do not show to be significantly changed by the frequency doubling of the long preforming pulse.

The curve of intensity growth versus plasma length, for configuration #5, is shown in Figure 7.81 [259]. An exponential increase, which corresponds to a gain coefficient of 33.5 cm^{-1}, is observed for lengths up to 3.8 mm, which implies a gain–length factor of 12.7. The curve exhibits an abrupt turn to a slow linear increase for larger lengths. This gives the curve a characteristic aspect different from the generally observed saturation pattern.

The intensity at the end of the exponential increase is found to be between 2 and 8.5×10^{10} W/cm^2. From calculation, the saturation intensity should be $\sim 3 \times 10^{10}$ W/cm^2 [274]. The comparison of these values suggests that the X-ray laser operates near to—or at—saturation. On the other hand, the traveling wave velocity fits the velocity of light within a accuracy of ∼5%. Thus, from equation (7.18), the plasma length over which the two waves can overlap, is given by

$$l_{(\mathrm{mm})} \sim 6 \times \tau_{(\mathrm{ps})}$$

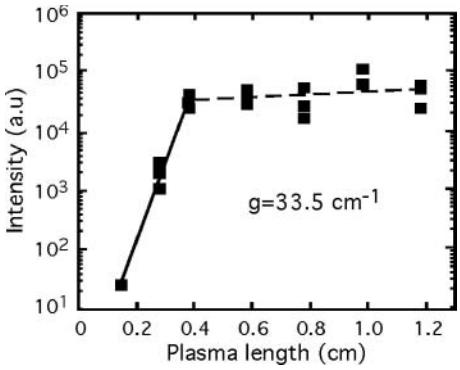

Fig. 7.81. Intensity of the Ni-like Ag TCE laser, at 13.9-nm wavelength, as a function of the plasma length, in the case of configuration # 5 in Table 7.13. The slow linear increase beyond 3.8 mm is believed to result from combined effects of saturation and refraction.

where τ is the gain duration. As the gain duration is estimated to be 10 ps, the sharp turn of the intensity curve at 3.8 mm cannot result from a breaking down of the wave-overlap. One is led thus to consider the peculiar structure appeared in Figure 7.81 as due to the combined effect of saturation and refraction.

Another peculiarity, observed when using the 2ω–ω technique, is the production of two laser lines of similar intensities for a pulse separation $\simeq$250 ps. The wavelength of the new line, identified as a result of $4f^1\ P_1$–$4d\ ^1P_1$ transitions in Ni-like ions, is measured to be 16.05 nm. Its intensity, which is very unstable from shot to shot, depends strongly on the heating pulse energy. Moreover this line appears for plasma lengths greater than 3.8 mm, that is when the 4d–4p line is already saturated. A systematic comparison of the two line intensities suggests a possible correlation between them. It might be interesting also to compare the processes which generates 4d–4p and 3d–3p population inversions in Ni-like silver and Ne-like titanium, respectively (cf. Section 7.4.2).

Comparison of data of configuration #4 and #6 shows that similar values of gain coefficient and gain–length factor are obtained for very different choices of pump parameters. In the first case, the intense short pulse starts heating the plasma before its formation is terminated whereas, in the second case, an 8 times less intense heating pulse reaches the preformed plasma after a long relaxation time. It can be inferred that plasma relaxation, in the second case, allows a deeper penetration of the heating radiation, and so increases the efficiency of the short pulse.

Column 7 shows the result of a direct measurement of the X-ray laser pulse duration with the help of a streak-camera of high temporal resolution [275, 276]. A combination of three effects was used to generate a wave traveling at light speed. As already mentioned in connection with experiments

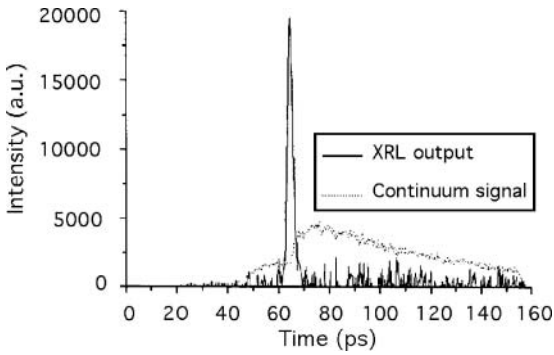

Fig. 7.82. Time profile of the Ni-like silver laser pulse, at 13.9-nm wavelength, measured with a high-resolution streak camera.

using a similar experimental setup, an intrinsic traveling wave of velocity $3c$ is generated by the astigmatism of the focusing optics [255]. A 600 lines/mm grating, inserted into the CPA beam line, brings this velocity near that of light. Furthermore, the second grating of the compressor is lightly tilted for fine tuning.

Figure 7.82 displays the time-resolved profile of the XUV emission at 13.9 nm (solid line). The dotted line represents the continuous spectrum very close to the laser line. It is assumed that the continuous spectrum is dominated by bremsstrahlung emission. Thus the increase of the continuum emission corresponds to the enhancement of the electron temperature due to the short heating pulse. An outstanding fact is that the X-ray laser emission peaks before the temperature has reached its maximum. This suggests that overionization occurs before the maximum of temperature, what causes quenching of gain owing to the destruction of the Ni-like ion population.

The FWHM duration of the X-ray laser pulse shown in Figure 7.82 is measured to be 3.1 ∓ 0.2 ps. The ultimate temporal resolution of the streak-camera is 700 fs. However, experimental limitations occur due to the finite width of the photocathode slit and to the X-ray pulse stretch introduced by the grazing incidence reflection on the spectrometer grating. After deconvolution, the duration of the X-ray laser pulse amounts to 1.9 ∓ 0.7 ps.

As for the spatial coherence of TCE Ni-like silver lasers, it has been measured with both pulses, separated by 1 ns, having the same 1.5-ps duration and an energy ratio of 1:5. Measurements showed a coherence length of 110–140 μm in both horizontal and vertical direction, 1 m away from the source [277].

7.5 Fast Capillary Discharge X-Ray Laser

Amplification of short wavelength radiation in plasmas produced by electric discharges appears as an attractive way to achieve a new class of XUV lasers which could offer a higher repetition rate than laser produced plasmas, for a

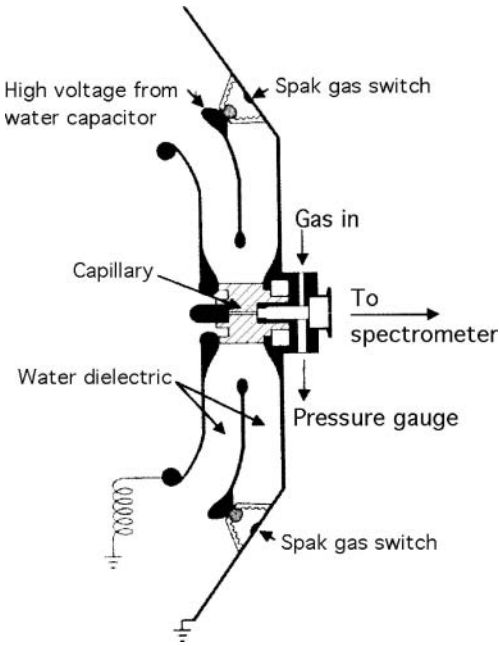

Fig. 7.83. Sketch of the final stage of the fast capillary discharge generator which generates XUV laser emission from ions of the capillary plasma.

relatively low cost [278]. However, the plasma confinement process, necessary to obtain the parameter values of the lasing plasma ($n_e \gtrsim 10^{18}$ cm^{-3}, $T_e \gtrsim 100$ eV) generally goes with turbulences and instabilities, whereas the development of laser action requires plasma characteristic variations to be smooth along the ray paths. Fast capillary discharges proved to be an exception to this rule owing to the coupling which occurs between plasma and capillary wall [56, 279].

7.5.1 Discharge Characteristics

The diagram of Figure 7.83 shows an advanced version of the discharge system, specially designed for very high excitation power [280]. In about 75 ns a conventional Marx generator and a coaxial water capacitor charge the generator final stage represented in Figure 7.83. Two radial water transmission lines, in which water is used as dielectric, and a circular array of pressurized gas spark gaps produce the fast current pulses that excite the plasma in the capillary. The low inductance loop defined by this configuration allows for the generation of current rise-times up to more than 1.5×10^{13} A s^{-1} with peak currents about 200 kA. Capillary channels are preionized with a current pulse of 20–40 A and 10 μs duration. In most experiments described below, the capillary consists of a hole bored through a block of polyacetal.

This generator is aimed at investigating laser emissions provided by Ni-like ions. For the Ne-like ions, which have been the main matter of previous experiments, typical discharge parameters are 20 ns rise-time and 40 kA current peak. This may be obtained from somewhat simplified generators which the diagram of Figure 5.19 (Section 5.2.4) referred to.

In these systems, the magnetic field induced by the current flowing through the preionized gas generates plasma compression, which results in a development comparable to imploding *Z*-pinches (see for instance [281]). For long rise-times of the electric current, the plasma temperature remains relatively low, owing to the heat conduction from plasma to wall, as well as to the wall-ablated material increasing the mass to be heated. But fast rising currents detach the plasma from the wall, which reduces heat losses. Moreover the rapid compression of the preionized gas generates a dense, highly ionized plasma column.

A complex model, which includes magneto hydrodynamic, atomic state population, and radiation transport equations has been developed to numerically investigate the behavior of the capillary discharge plasma [279]. Owing to the crucial role of the boundary conditions, the evaporation of the wall in contact with the high temperature plasma is also included in the model. As a diagnostic of plasma compression, the code calculated the size of an axial pinhole X-ray image of the plasma, for wavelengths below 300 nm, as a function of time. The pulse current peak is 39 kA, the pulse duration 64 ns, and the argon pressure 0.7 Torr. In Figure 7.84, the solid curve shows the temporal

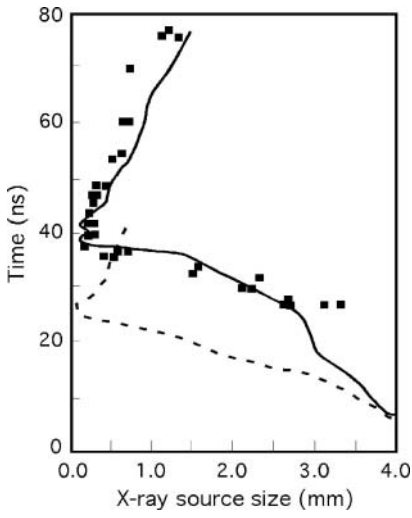

Fig. 7.84. Temporal variation of the plasma diameter. Solid curve: calculation including heat and mass transfer between wall and plasma; the electron density reaches values of 5×10^{18} cm^{-3} to 3×10^{19} cm^{-3}. Solid squares: experimental results. Dashed line: calculation neglecting the wall effects (Ref. [279]).

variation of the image diameter, wall effects being included in calculation. One sees the plasma to contract down to a size of 150–300 μm which is to be compared to the 4 mm initial diameter. The electron density reaches values of 5×10^{18} cm^{-3} to 3×10^{19} cm^{-3}. Experimental results are represented by the solid squares, showing a satisfactory agreement between calculation and experimental measurements. If one assumes that neither heat nor mass is transferred from and to the wall, the result of the calculation model, shown by the dashed line in Figure 7.84, does not coincide with the experimental data. It is possible that not only the symmetry and the small initial radius of the capillary geometry are responsible for the high stability of the fast capillary discharge, but also that wall effects stop instability from growing.

7.5.2 Small-Signal Gain, Saturation, and Output of the Ne-Like Argon Laser

The small-signal gain coefficient of the 3s–3p $J = 0-1$ line of Ne-Like argon, at wavelength of 46.9 nm, is calculated taking into account hundreds of atomic levels. Results for various capillary diameter are displayed in Figure 7.85 versus electron density. It is clear that these gain coefficients are smaller than those calculated for similar Ne-like ion lines in the density and temperature conditions of laser-produced plasmas. We shall see that the length of the capillary plasma, which can reach values larger than the length of laser plasmas by one order of magnitude, compensates this difference as regards the achievement of laser saturation.

Experimental amplification results, first obtained with plasma columns of lengths up to 12 cm, in 4-mm diameter capillary tubes, showed a gain coefficient of 0.6 ∓ 0.04 cm^{-1} and a gain–length product of 7.2 for the 46.9-nm line [57]. The divergence of the laser beam was a of a few milliradians. The capillary channel was situated on the axis of the 3 nF liquid dielectric capacitor. The current pulse amplitude was of 38 ∓ 1 kA, with a ∼60-ns half period.

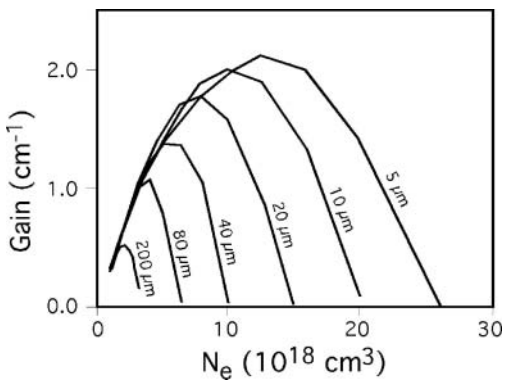

Fig. 7.85. Small-signal gain coefficient of the 3s–3p, $J = 0-1$ line of Ne-like argon ($\lambda = 46.9$ nm), calculated versus electron density, for various capillary diameters.

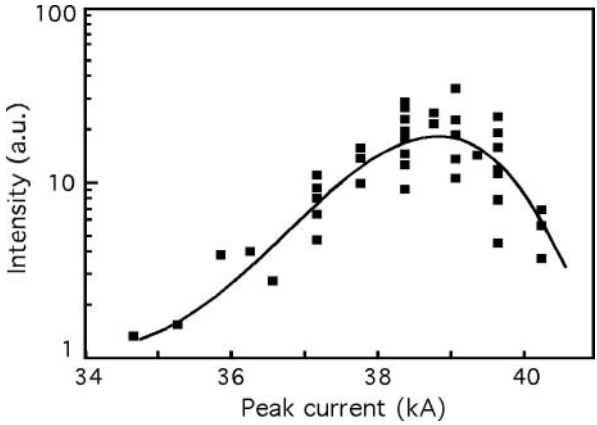

Fig. 7.86. Variation of the 46.9-nm line intensity as a function of the discharge current at a pressure of 700 mTorr (Ref. [278]).

A current of 10 A was used during several microseconds to preionize argon. Argon pressure in the capillary was of 700 mTorr.

The variation of the X-ray laser intensity with the discharge current is shown in Figure 7.86 [282]. The intensity maximum corresponds to a ∼39 kA current. Regarding the dependence of the laser line intensity on argon pressure, Figure 7.87 shows an intensity quasi-plateau between 500 and 750 mTorr.

The fact that the beam divergence is found to be larger than expected from the discharge geometry, and that an annular structure appears for some shots, shows that refraction cannot be neglected [283]. On the other hand, calculation of transverse electron density profiles shows the density gradient

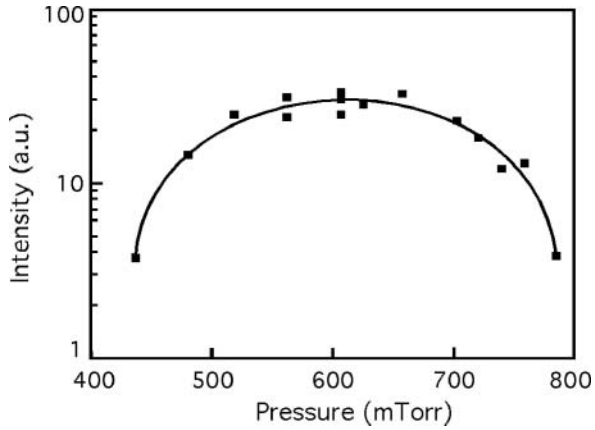

Fig. 7.87. Variation of the 46.9-nm line intensity as a function of the argon pressure at currents ∼39 kA.

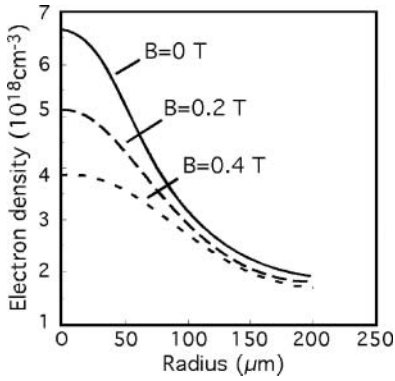

Fig. 7.88. Calculated transverse electron density profiles showing that the density gradient decreases when axial the magnetic field increases (Ref. [283]).

to decrease when the axial magnetic field increases, as it can be seen from examples displayed in Figure 7.88 [284]. Now, the reduction of refraction losses due to the smoothing of the plasma radial profile in a higher magnetic field should increase the laser output.

Computational results and experimental data relative to such an effect are displayed in Figure 7.89. Experimentally measured laser intensities (solid

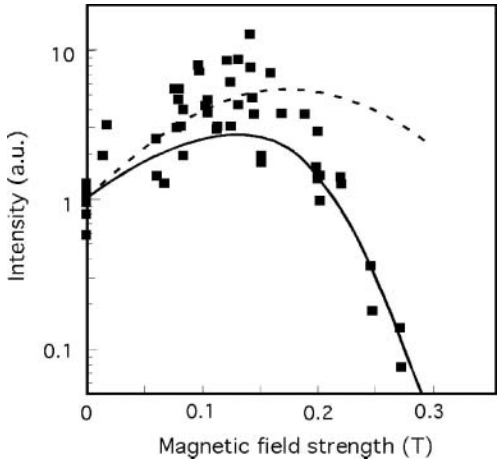

Fig. 7.89. Laser output of 46.9 nm as a function of the axial magnetic strength. Solid squares: measured laser intensities for a 10-cm long, 4-mm diameter capillary filled with 600 mTorr of argon; dashed curve: intensity calculated including the decrease of the electron density when the distance to the capillary axis increases; solid curve: similar calculation including the additional decrease due to line Zeeman splitting.

squares) corresponding to a 10-cm long, 4 mm in diameter capillary filled with 600 mTorr of argon, indeed show the output of the laser to increase for magnetic fields $\lesssim$0.15 T. Beyond this value, the dashed curve shows that the intensity starts decreasing as a result of the electron density lowering observed in the gain region. Modifications of the line profile due to Zeeman splitting produce additional effects which significantly enlarge the line width at large magnetic fields. These effects are included in the calculated intensity represented by the solid curve in Figure 7.89. Calculations are found to be in good agreement with experimental results.

Measuring the output of capillary tubes up to 20 cm in length shows a small-signal gain of 1.16 cm^{-1} and the laser emission saturating for lengths above 15 cm [283]. Furthermore, the results obtained with a half-cavity system (cf. Section 5.2.5), which allows for double-passing a plasma column of 15 cm (corresponding to an effective plasma length of 25 cm) definitely confirm that saturation occurs at gain–length about 14 for an effective length of $\sim$12 cm [285]. For the maximum effective length of 25 cm, the overall gain–length reaches a value of 25. The beam angular profile displays a single central peak without side lobes, which indicates that refraction did not limit the effective gain coefficient in this double-pass experiment. The FWHM of the angular distribution is about 6 mrad.

Experiments showed also that capillary discharge lasers can reach a very high repetition rate compared with the rate presently achievable with laser plasmas. Considering the low repetition rates of 4–0.4 shots per hour achieved by laser pumped X-ray lasers, their interest is focused on their very high peak power (megawatts) and their short pulse duration (1–100 ps). But in the case of capillary discharges, considering a time averaged power of the laser is beginning to make sense. For the experimental works presented above the repetition rate was $\leqq$120 shots per hour. A much larger repetition rate of 10 Hz has been achieved using alumina (Al_2O_3) capillaries filled with preionized argon gas [286]. Alumina produces less capillary-wall-ablated matter than polyacetal. As a consequence, plasma heating necessitates less energy and a $\approx$24 kA peak current proves to be sufficient to achieve lasing. This makes it easier to stabilize the temperature of the experimental setup at high repetition rates.

For experiments with alumina, capillaries had a diameter of 3.2 mm and a length of 18.2 cm. A continuous gas flow and a differential pumping system maintained a nearly optimum gas pressure of 490 mTorr. The pulse rise-time was of 25 ns. The laser has been operating continuously during 30 mn at 5 Hz, with a single capillary withstanding up to 9×10^3 laser shots.

The data presented in Figure 7.90, for which the discharge parameters were optimized at 7 Hz, correspond to 1-min continuous operation. Figure 7.90a displays the laser shot energy distribution which shows a peak at $\sim$135 μJ. Figure 7.90b shows that the average output energy, computed as a running average of 50 contiguous pulses, is $\sim$0.95 mW, namely a photon emission rate of $\sim 2.2 \times 10^{14}$ photons per second.

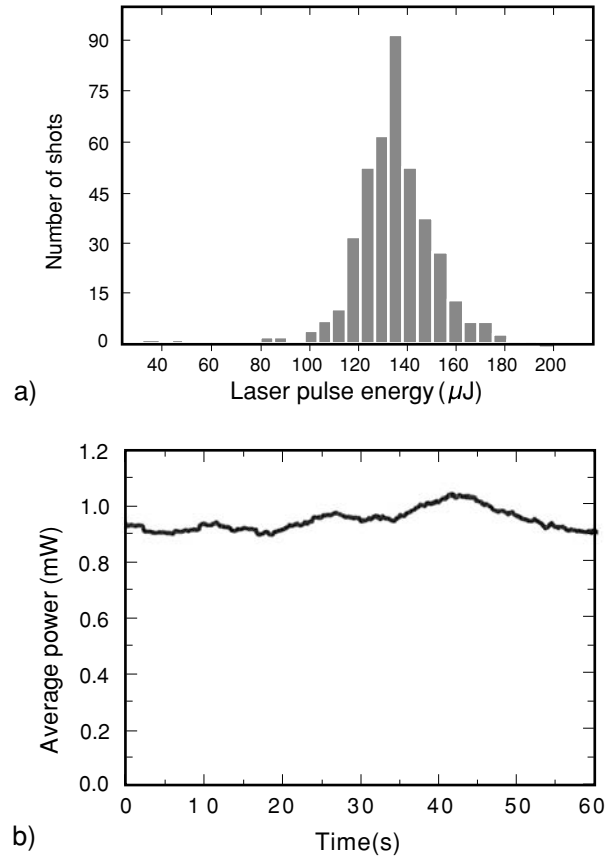

Fig. 7.90. (a) Laser shot energy distribution for one minute continuous operation at 7 Hz; (b) average output energy for 50 contiguous pulses.

7.5.3 Coherence

A remarkable characteristic of capillary discharge lasers is the very high degree of coherence achieved in the XUV beam for long plasma columns [132]. In Section 6.4.2 we showed Young's slit interferograms obtained successively for capillary lengths of 18 cm, 27 cm, and 36 cm (Fig. 6.34). These results were an excellent illustration of the mode-selection mechanism provided by refraction in the plasma column. Regarding the 46.9-n laser, Figure 7.91 displays the experimental values of the degree of coherence $|\mu_{12}|$ obtained for two slit separations together with the $|\mu_{12}|$ profile corresponding to a Gaussian beam profile of 550-μm coherence radius. Considering the small radius of the laser beam, it is estimated that about half the entire laser power is contained in one spatial coherence area (cf. Section 3.2), which shows a unique property of essentially full spatial coherence for a soft X-ray source.

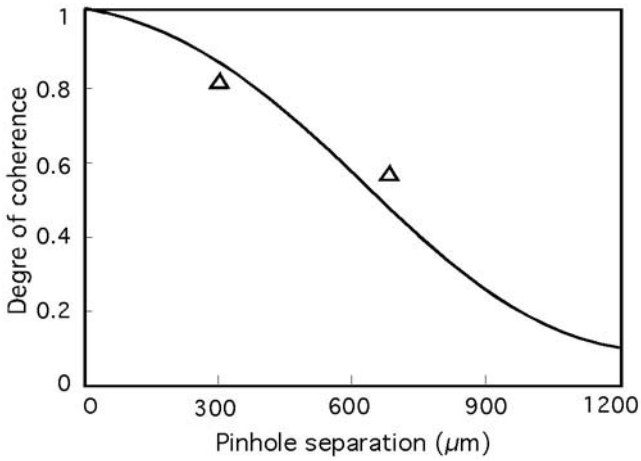

Fig. 7.91. Coherence of the Ne-like argon laser; triangles: experimentally measured degree of coherence for two separation distances in the XUV beam cross-section; solid line: profile of the degree of coherence calculated for a Gaussian beam profile of 550-μm coherence radius.

7.5.4 New Lasing Materials

The results obtained with the capillary discharge in argon, at 46.9 nm, are prompting investigation of new lasing materials, especially in order to produce lasers with high repetition rate at shorter wavelengths. It is clear that the technical issue of the injection of new materials in the capillary will need some effort. A 10-μJ laser has already been demonstrated at 52.9 nm in Ne-like chlorine [287]. To achieve this result chlorine was continuously admitted into the capillary channel through Teflon tubing. A 140-nm thick Al–Si filter was used to separate the laser from the detection system in order to prevent chemical corrosion. Amplification was observed at pressures ranging from 180 mTorr to 330 mTorr. A gain coefficient of 0.45 cm^{-1} and a gain–length product of 7.5 were demonstrated in Ne-like sulfur at 60.84-nm wavelength. To inject sulfur in the capillary channel, sulfur vapor was produced by ablating the wall of a separate 5-mm diameter sulfur channel with a current pulse delivering 200 J in 50 μs [288]. The vapor pressure was approximately 470 mTorr.

Furthermore, a hybrid combination of the transient pumping scheme (cf. Section 7.4) with the capillary discharge laser appears to be promising. The basic idea consists in using the capillary discharge to preform a plasma produced by the long laser pulse in TCE lasers, and rapidly heating this plasma with a short laser pulse [289]. Figure 7.92 shows the diagram of the experimental setup designed to do that [290]. The short-pulse laser beam is seen to be focused at one end of the capillary, within a focal spot of 170 μm in diameter. However, in this configuration pumping operates from an axially focused beam, which makes the pump intensity to vary along the plasma

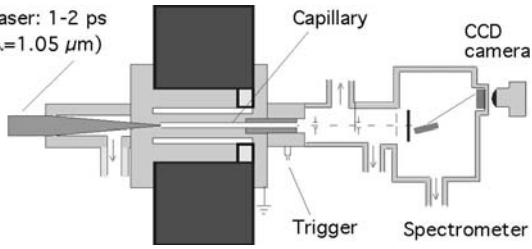

Fig. 7.92. Diagram of the experimental setup designed for longitudinal pumping of a capillary discharge plasma using a short laser pulse.

column owing to the pump energy depletion with the capillary length (cf. Section 7.4.6).

Capillaries of lengths between 1 cm and 3 cm and a diameter of 0.5 cm or 1.0 cm have been investigated. The sulfur vapor was produced by wall ablation, in a separate evacuated channel drilled in a sulfur rod. The preplasma was generated by a small peak discharge current of 2–3 kA. The plasma column exhibited a concave electron density profile in the radial direction, ensuring the guidance of the pumping pulse and of the XUV pulse along the capillary axis. The energy of the 1–2 ps pump laser pulses was 0.3–0.5 J.

An intense Ne-like sulfur line was observed at 60.84 nm wavelength for delays between electric discharges and laser pulses of 25–65 ns. The optimum delay value was found to be 35 ns. A gain coefficient of 4.6 cm^{-1} was observed in the first 1-cm long section of the plasma. The overall gain coefficient was about 2.3 cm^{-1} and the maximum gain–length, 6.8.

Concerning shorter wavelengths, the production of nickel-like ions of cadmium in capillary channels has been demonstrated with a 200 kA current discharge. This opens the way to the possibility of observing laser amplification in Ni-like Cd for the $4d^1S_0$–$4p^1P_1$ line at a wavelength of 13.2 nm [291].

7.6 Optical-Field-Ionization Lasers

This section refers to a new class of XUV lasers, where ionization of the lasing medium is no longer provided by collisions between thermalized particles in the heated plasma, but directly by field effect and multiphoton processes, under the action of a very intense infrared laser beam. In other words, the ions are now created by the optical pulse through tunneling ionization. This results in the simultaneous production of a cold dense collection of ionized atoms surrounded by a very hot electron distribution.

This section deals with the collisionally pumped OFI lasers only. The results obtained in the recombination pumping scheme will be presented in the next section. Let us also mention that we shall again meet such intense field effects in Part III of this book, when describing the generation of coherent

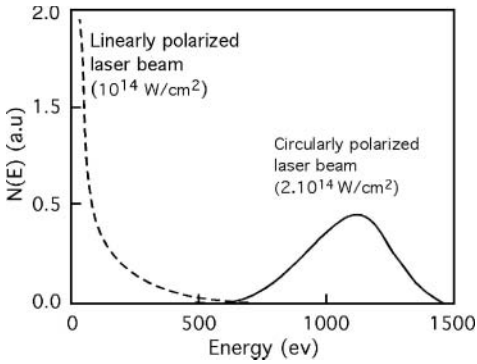

Fig. 7.93. Energy distribution of electrons ejected from atoms for a linearly polarized (dashed line) and a circularly polarized infrared beam (data from Ref. [291]).

high-harmonic XUV radiation. Here we are interested in those electrons that escape from atoms under the field action and then produce population inversions exciting the ions by collisions. In the case of harmonic generation on the other hand, we will have to consider electrons that, during their excursion outside the electronic orbit region of the unperturbed atom, emit radiation at wavelengths which are multiples of the exciting laser wavelength.

It has been shown that the production of high-energy electrons, suitable for XUV laser collisional pumping, requires intense circularly polarized laser radiation [292]. Figure 7.93 illustrates this fact with the calculated energy distribution curves of ejected electrons for linearly (dashed curve) and circularly (solid curve) polarized laser beams. These curves correspond to 10-μm wavelength radiation pulses with intensities $I = 10^{14} \exp[-(t/\tau)^2]$ and $I = 2 \times 10^{14} \exp[-(t/\tau)^2]$, respectively and $\tau = 1.5$ ps. The plasma consists of hydrogen-like ions with an ionization potential of 12.1 eV. It is manifest that the electron ejection mechanisms are not the same for the two polarizations, one leading to a maximum of near-zero energy electrons, the other exhibiting a distribution peak at more than 1000 eV.

This difference appears if we consider an electron released from rest in the laser field. The electron experiences a force proportional to the electric field

$$\overrightarrow{E(t)} = E \cos(\omega t)\, \overrightarrow{e_x} + \alpha E \sin(\omega t)\, \overrightarrow{e_y} \tag{7.21}$$

where $\alpha = 0$ for linear polarization and $\alpha = 1$ for circular polarization. The electron velocity will be given by

$$v_x(t) = \frac{qE}{m\omega} \sin(\omega t) + v_{0x}, \qquad v_y(t) = \alpha \frac{qE}{m\omega} \cos(\omega t) + v_{0y} \tag{7.22}$$

If we assume the initial conditions $v_x(0) = v_y(0) = 0$ at an arbitrarily chosen instant $t = 0$, we obtain

$$v_x(0) = 0,\ v_y(0) = \alpha \frac{qE}{m\omega} \tag{7.23}$$

which means that the electron gains a drift velocity in a direction perpendicular to the field if, and only if, $\alpha \neq 0$. Therefore, after the crossing of an intense laser pulse, the electron kinetic energy depends on the polarization that had the radiation pulse and this effect is maximum for $\alpha = 1$, i.e. for circular polarization.

The average kinetic energy, also called "quiver energy," of an electron oscillating in a field varying as $E\sin(kx - \omega t)$ is $q^2E^2/4m\omega^2$. When a free electron, that initially possesses this oscillatory energy, travels through the light beam from a region of high intensity to a region of lower intensity, its oscillatory energy is converted to a drift kinetic energy [293]. Thus the minimum energy of the ionized electron is not zero but $q^2E^2/4m\omega^2$. For an elliptically polarized beam ($0 < \alpha < 1$) this energy comes to

$$U_{\mathrm{p}} = \left(1 + \alpha^2\right) \frac{q^2E^2}{4m\omega^2} \tag{7.24}$$

The result is that the number of photons associated with the multiphoton ionization process must be higher than expected from the ionization potential considered in the absence of intense field. For this reason U_{p} is considered as a part of the actual ionization potential of an atom submitted to an intense optical field. This part increases proportionally to the intensity of the field and is known as the *ponderomotive potential.* For circularly polarized light the ponderomotive potential is thus $U_{\mathrm{p}} = q^2E^2/2m\omega^2$.

Starting from these observations Lemoff et al. modeled XUV lasers pumped by optical field ionization [294]. Their calculations were performed for the ions Ar^{8+}, Kr^{8+}, and Xe^{8+} that have a closed outer shell, i.e. the $2p^6$, $3d^{10}$, and $4d^{10}$ shells, respectively. The level diagram of each of the three ions is displayed in Figure 7.94, where the atomic energy levels have been obtained by calculation with an uncertainty of less than 10%. The calculated wavelengths of the $J = 0{-}1$ laser lines are 47.8 nm for argon, 31.9 nm for Krypton and 41 nm for xenon.

Figure 7.95 shows the initial energy distribution of the free electrons generated by tunnel ionization for a 30-fs Gaussian pulse with a peak intensity of 10^{17} W/cm^2. It exhibits eight peaks corresponding to the eight bound electrons successively released from the atom during the first stage of the neon-like plasma production. As for the subsequent time evolution of the electron and ion energy distributions, it is controlled by the elastic collisions of the plasma particles. To calculate the gain coefficient, the lasing line shape is assumed to be Lorentzian with a width that is the quadratic sum of three components, the homogenous linewidth, the Doppler linewidth and the electronic Stark width. For an ion density of 10^{17}cm^{-3} the predicted values of gain are 17 cm^{-1}, 94 cm^{-1}, and 107 cm^{-1} for Ar IX, Kr IX, and Xe IX, respectively.

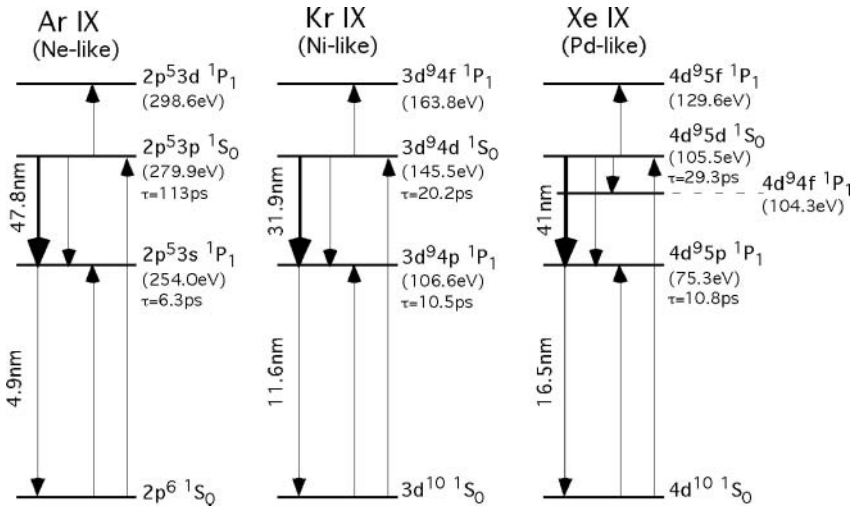

Fig. 7.94. Calculated energy levels of the Ar^{8+}, Kr^{8+}, and Xe^{8+} ions, each of which having a closed outershell ($2p^6$, $3d^{10}$, and $4d^{10}$, respectively). The respective $J = 0-1$ laser line wavelengths are indicated in the diagram (Ref. [294]).

As a matter of fact, experiments definitely establish that lasing occurs, with a high repetition rate, under the action of intense ultrashort optical pulses in palladium-like xenon.

The femtosecond laser system used for this first demonstration of a Pd-like Xe laser [295] was a Ti:Sa chirped-pulse amplification system delivering 40-fs, 800-nm pulses of more than 3×10^{16} W/cm^2 intensity at the focus of the beam, over a length $\geqq$7.4 mm. The diagram of the target cell is shown in Figure 7.96. The pinhole diameter is $\lesssim$500 μm. A mica quarter waveplate generates the circular polarization beam. The pulsed energy reaching the xenon gas with a repetition rate of 10 Hz was of ∼70 mJ. The gain region was

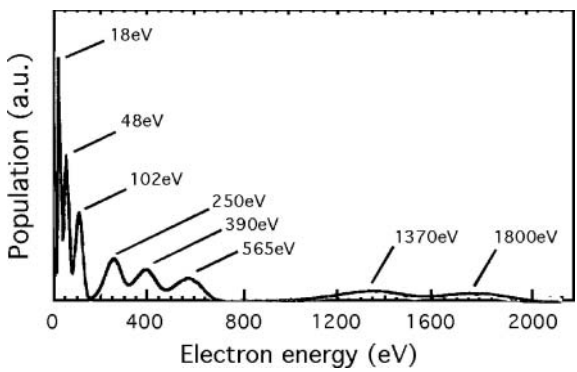

Fig. 7.95. Initial energy distribution of the free electrons generated by tunnel ionization for a 30-fs linearly polarized Gaussian pulse (same Ref. as for Fig. 7.94).

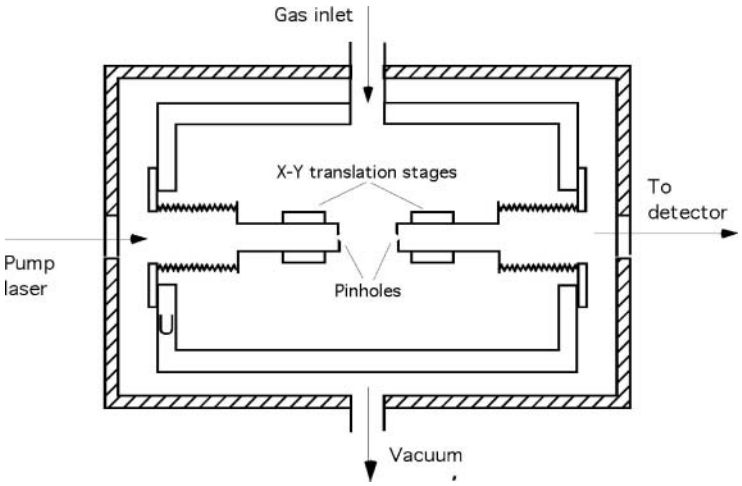

Fig. 7.96. Target cell of a Pd-like xenon OFI laser at 48.81-nm wavelength.

estimated to be between 50 μm and 100 μm in diameter. Translation stages allow accurate adjustment of the pinhole separation.

Figure 7.97 shows the intensity of the 41.81-nm wavelength line to grow exponentially as a function of the xenon pressure and the pinhole separation as well. Each data point in Figure 7.97a and b represents an average of over

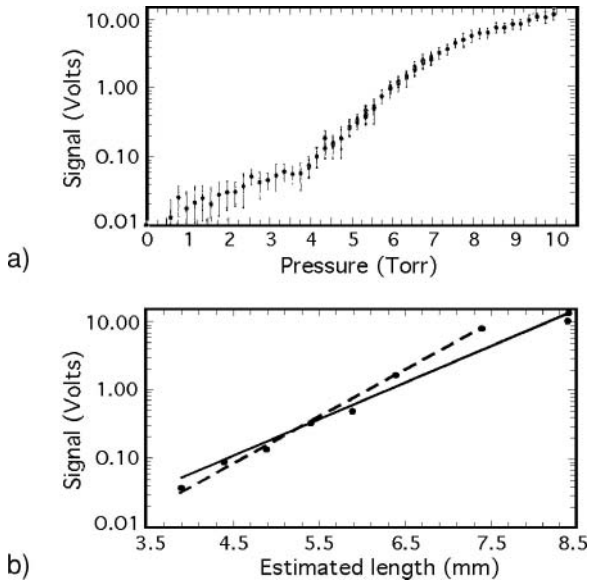

Fig. 7.97. Experimentally observed intensity growth of the $J = 0-1$ xenon laser line versus gas pressure (a) and gas length (b) (data from Ref. [294]).

∼3000 shots. Two Lindford-type fits [cf. Eq. (1.43)], one for the full plasma length (solid line), the other for 3.9 trough 7.4 mm only (dashed curve) have been performed. For the full length the gain is estimated at 13.3 ∓ 0.9 cm^{-1}, with a gain-length product of 11.2. In the reduced portion from 3.9 mm to 7.4 mm one obtains $g = 16.8 \mp 0.5$ cm^{-1} and a gain–length about 12.4. It is to be noticed that, though being very significant, these values are well below those predicted by the model calculation for xenon.

A second step of the development of collisional OFI lasers has been reached with the help of the careful control of gas pressure, driving energy and gas cell length. Moreover, using multipass rather than regenerative amplifiers in the pump laser made it possible to suppress the prepulses which otherwise modify the early stage of plasma formation in an uncheckable way [296–299].

A computational investigation of the optimal conditions for lasing in both Pd-like xenon and Ni-like krypton was performed with the help of detailed calculations [298]. In the case of longitudinal focalization, the limit of the length of the amplifying medium in the focusing region is of the order of the Rayleigh length, z_{R}, for which the beam diameter of a Gaussian beam increases by a factor $\sqrt{2}$. The variable z_{R} is given by [300] (p. 668)

$$z_{\mathrm{R}} = \frac{\pi a^2}{\lambda} \tag{7.25}$$

where a is the beam radius at the focus and λ the wavelength. For a spot size of 20-μm radius and a pump laser wavelength of 800 nm, this length is ∼1.6 mm. Furthermore, the ionization produced at the edge of the light pulse results in electron density gradients that cause refraction of the main part of the pulse radiation, thereby leading to a rapid reduction of the peak intensity and preventing the formation of the lasing ion species. These effects are included in a paraxial wave propagation code. Calculations predict that the Pd-like ions of xenon (Xe^{8+}) occupy 1 mm in length, ∼60 μm radius zone along the laser axis. For krypton the Ni-like lasing ions (Kr^{8+}) are found to be in a ~ 1.6 mm $\times$ 50 μm zone. These ions stages are produced, not exactly at the entrance of the gas cell but after the laser has propagated approximately 1.5 mm into the gas. Calculations also show a region of highly overionized gas up to Xe^{17+} and Kr^{13+}, that can be a source of fast electrons limiting the gain in the lasing region by collisional ionization.

Another important calculation for OFI lasers is that of the electron energy distribution, which is involved in the hydrodynamics and atomic processes leading to population inversions. As an example Figure 7.98 displays the energy distribution curve obtained for xenon in the case of a 3.5×10^{16} Wcm^{-2} laser peak intensity, compared to the equivalent Maxwell distribution of the same mean energy of 350 eV. One sees that the peaks resulting from each ionization stage are not completely separated (cf. Fig. 7.95). This is due to the inverse bremsstrahlung electron heating (see Section 5.1) and to the collisional relaxation processes.

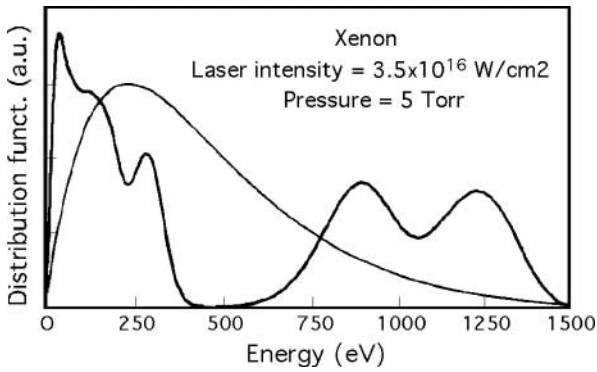

Fig. 7.98. Electron energy distribution calculated for xenon in the case of a 3.5×10^{16} Wcm^{-2} laser peak intensity (thick line) compared to the equivalent Maxwell distribution of the same mean energy of 350 eV (thinner line) from Ref. [297].

Considering the very short time-scale, the quasi-static approximation is not adequate for the collisional–radiative model that is generally used to calculate the gain. The model has to be fully time-dependent instead (Section 1.5). As a an example of calculation results, Figure 7.99 shows the temporal dependance of the gain coefficient of xenon for a pump pule duration of ∼30 ps. The gain is seen to be relatively long-lived with significant gain still being produced at more than 15 ps. The calculation being spatially one-dimensional, refraction of the X-ray laser beam is not included in the results. This contributes to enhance the calculated gain as compared to the experimental results.

Sebban et al. investigated xenon and krypton OFI lasers as a function of gas pressure, driving energy, and plasma length [297, 298]. The diagram of the experimental setup used in these experiments is shown in Figure 7.100. Figure 7.101 displays the variation of output intensities as a function of

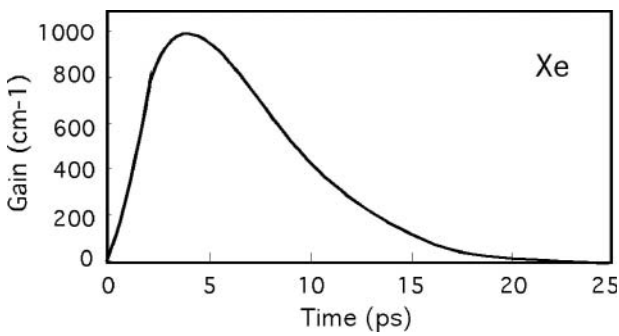

Fig. 7.99. Calculated temporal evolution of the xenon gain coefficient for a pressure of 15 Torr and a pump pulse duration of ∼30 ps (same Ref. as in the previous figure).

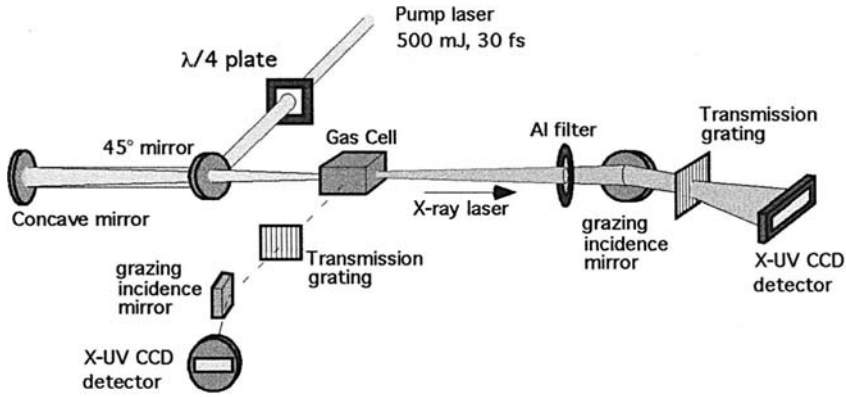

Fig. 7.100. Intensity variation of Xe and Kr OFI lasers as a function of gas pressure. The increase of the number of emitters at first induces the increase of soft X-ray laser intensity. Then the ionization-induced refraction increasingly limits the propagation of the pump laser, which makes the measured intensity to fall down.

pressure. Laser intensity increases at once with pressure, owing to the correlative increase of the emitter number, then comes to be limited and more and more reduced when the driving pulse is increasingly refracted out of the gain region. The intensity maxima occur at 15 Torr for xenon and 20 Torr for krypton. The larger width of the lasing pressure range for krypton denotes that Ni-like ions are more stable regarding further ionization than are Pd-like ions, in accordance with the ionization potential being larger for Ni-like than for Pd-like ions.

Figure 7.102 shows that, for the same reason, the driving energy necessary for the krypton laser to work is larger than for the xenon laser. Moreover indication of laser saturation appears above 500-mJ energy for xenon but not

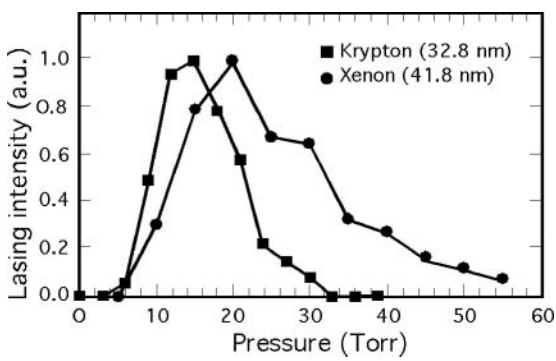

Fig. 7.101. Intensity variation of Pd-like Xe and Ni-like Kr OFI lasers as a function of pump laser energy.

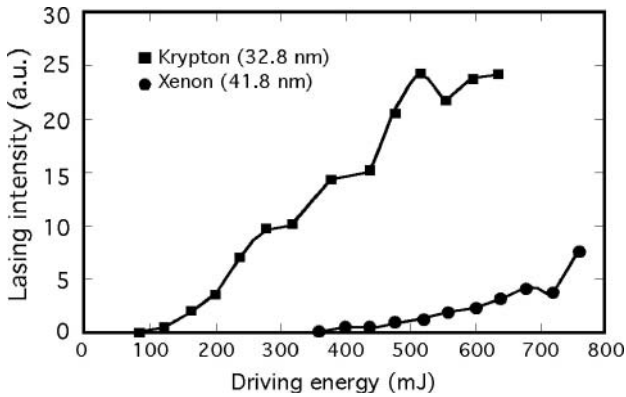

Fig. 7.102. Intensity variation of Xê and KŕF OFI lasers as a function of driving energy.

at all for krypton, even for energies as large as 760-mJ. Additional measurements show that a 760-mJ 60-fs driving laser pulse has an efficiency in terms of XUV lasing similar to that of a 350-mJ 30-fs laser pulse, thereby the critical parameter is the intensity rather than the energy of the driving laser.

Figure 7.103 exhibits lasing intensity curves as a function of plasma length in the range 1.5–5 mm, for xenon and krypton. In the case of xenon the intensity is observed to increase exponentially up to a plasma length of ∼2.2 mm and then begins to saturate. The small-signal gain is estimated at 67 ∓ 3 cm^{-1} and the gain length at saturation at 15 ∓ 7. Due to the longitudinal geometry, the gain is generally not constant over the length of the amplifying medium which is not exactly known itself. This is the cause of a large uncertainty of the laser gain-length estimation.

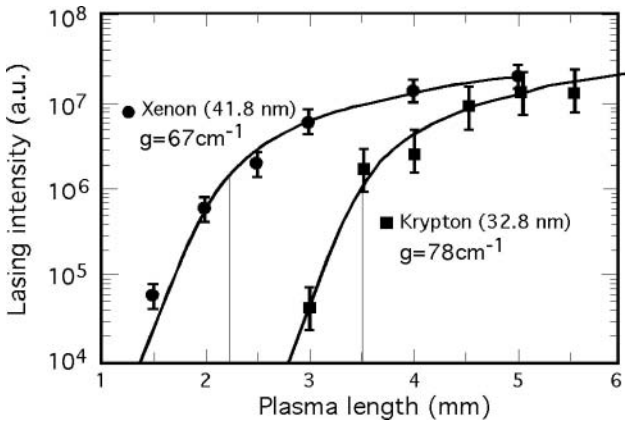

Fig. 7.103. Intensity variation of Xe and Kr OFI lasers versus plasma length.

For krypton, lasing is not observed before the plasma length reaches ∼3 mm. From 3 to 3.5 mm the intensity increase is exponential and the measured gain is found to be 78 ∓ 2 cm^{-1}. A further increase of the cell length results in a new output enhancement by nearly one order of magnitude. This can be understood from the fact that, as shown by Figure 7.102, the krypton laser did not reach saturation in the range of parameters corresponding to this experiment.

The X-ray laser output is measured to be $\sim 5 \times 10^9$ photons/pulse in ∼10 mrad of divergence. The X-ray pulse duration is expected to be 5 ps.

New possibilities, opened by the successful development of OFI soft X-ray lasers, appear with a new technique which combines the krypton laser, at 32.8 *nm* wavelength, with the 25th harmonic of an infrared laser [301]. This harmonic was chosen because its wavelength has close match with the soft X-ray laser line.

The harmonic beam is image-relayed onto the entrance of the soft X-ray amplifier by means of a multilayered toroidal mirror, which ensures high intensity focusing. The Ni-like krypton laser is operated from the small-signal gain up to the saturation regime. One observes a strong enhancement of the harmonic beam when the soft X-ray amplifier is under operation. In nearly saturated conditions, the total intensity is one order of magnitude larger than the sum of the laser and the harmonic line separately emitted. Images of the beam cross-section present strong diffraction structures close to alignment wires, which shows a high degree of coherence.

Several processes may contribute to these results. Given that the harmonic pulse duration is much shorter (20 fs) than the soft X-ray laser gain duration (8 ps), in terms of bandwidth one can expect that the width of the soft X-ray laser line will be much smaller than the width of the harmonic line. Accordingly, while harmonic amplification by the soft X-ray laser is limited at the center of the line by laser saturation, a stronger amplification still occurs in the line wings, so contributing to a total extracted energy well beyond the sum of the laser and the harmonic lines separately. Moreover the transverse distribution of the gain in the soft X-ray laser and the differences of angular geometry between the two combined beams are to be taken into account in a complete discussion of the experimental data.

From these results one can consider the seeding of XUV lasers by high harmonics as a future high-repetition-rate, spatially and temporally coherent, source of subpicosecond XUV-pulses of very large intensity (up to 10^{20} W/cm^2).

8. Recombination Lasers

The principle of pumping using the large cascading stream of electrons resulting from fast plasma recombination has been shortly presented in Section 4.2. The first theoretical approaches date from the early seventies [22, 302] and experimental investigations of recombination techniques applied to XUV lasers have led to a very large number of works, even before the first demonstration of collisional pumping in 1985. One reason for this success is that the production of plasmas suitable for recombination studies requires much less energy than collisional pumping. Thereby laboratories could work on X-ray lasers with nanosecond lasers providing a few tens of Joules per pulse only.

Recombination studies largely contributed to the development of XUV laser beam characterization techniques, especially for gain measurements, before the advent of collisional lasers. However, to this day it has not been possible to reach laser saturation from recombinational pumping, even by using ultrashort pulses. In most cases the gain–length product is found to be between 3 and 6. Notwithstanding recent stimulating works [303, 304]. The way to large output and laser saturation does not clearly appear to be opened yet. In this section we will present a short survey of the achievements of experimental and theoretical research on recombination lasers. We will first consider long pump pulse systems, where "long" is to be understood as involving durations from tens of picoseconds to several nanoseconds. More recent works using picosecond and femtosecond pulses will be presented in a separated section.

8.1 Long Pump Pulses

From the beginning, two main isoelectronic sequences have been explored, those of hydrogen-like [25,44,305] and of lithium-like ions [17,306–310]. In the long pulse regime ($\tau \gtrsim 100$ ps) electrons are heated by inverse bremsstrahlung in the pump laser field (cf. Section 5.1.1). Then ion–electron collisional processes enhance the plasma ionization up to a degree directly depending on the maximum electron temperature. At sufficiently high electronic density,

ionization and recombination mechanisms involving two free electrons, namely the mutually reciprocal processes of ionization by electron impact and three-body recombination, become dominant. When the temperature starts falling as a consequence of plasma expansion, radiative losses and pump intensity diminishing, the three-body recombinations induce a fast increase of those populations high lying below the ionization limit, while lower level populations grow more slowly by cascades from upper levels and radiative recombination. That is why the fast cooling of a dense plasma can generate population inversions between the discrete levels of highly charged ions.

8.1.1 Hydrogen-Like Ions

Hydrogen-like ions, for which accurate transitions rates and energy level data are available, provide the simplest atomic system to investigate the production of population inversions by plasma recombination. The diagram of levels for the ions of this series is recalled in Figure 8.1. The highest level populations, near the ionization limit, are thermalized by ion collisions with free electrons and therefore are in LTE with the plasma free electrons (cf. Section 5.1.2). Below this "thermal band," plasma cooling makes electron cascades to populate lower levels. Population dynamics leads to a time-varying distribution where population inversions may appear.

Inversion is especially promoted between levels 3 and 2 (Balmer α line) because, while recombination increases the population of the $n = 3$ level, the $n = 2$ level is rapidly depleted thanks to its very large radiative decay rate to the ground state. That is why the highest gain generally occurs on the

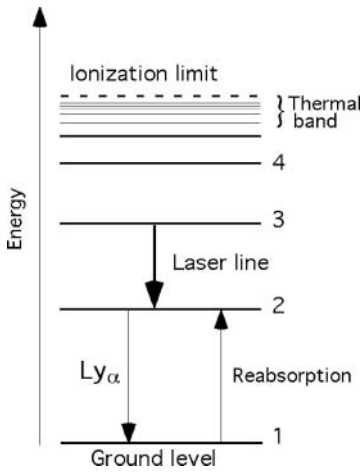

Fig. 8.1. Diagram of the energy levels of H-like ions. The fast radiative decay of the Ly$_\alpha$ line contributes to the creation of a population inversion between the levels 3 and 2.

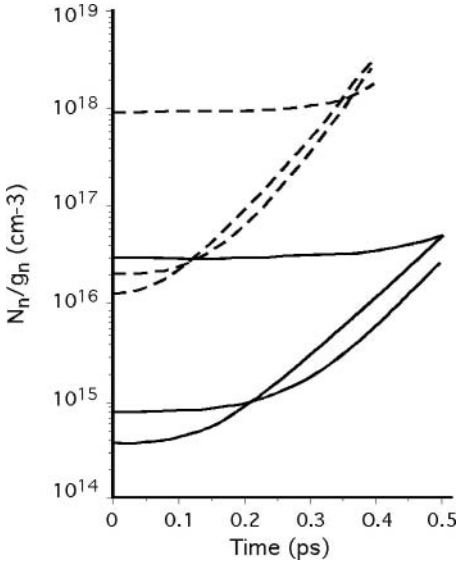

Fig. 8.2. Calculated H-like ion 3–2 population inversions in a recombining plasma [310]. Populations are in steady state at $t = 0$ for 200-eV (dashed lines) and 2000-eV temperatures (solid lines). Temperature decreases exponentially with a half-life of 0.1 ps. The self-absorption in the Ly_α line is fixed at 90%.

3–2 transition, i.e. the first line of the Balmer series (H_α), whose wavelength is given by $\lambda = 656.3/Z^2$ nm, where Z is the ion charge. For plasmas of large volume, reabsorption (also known as "photon trapping" in X-ray lasers physics) of the 2–1 decay radiation can reduce the population inversion.

The calculation of 3–2 population inversions is illustrated in Figure 8.2 for two electron temperatures and a constant self-absorption of Ly_α, arbitrarily fixed at 90% [311]. The plasma was assumed in steady state at time $t = 0$ and electron temperature decreased exponentially with a half-life of 0.1 ps while the electron density remained constant for $t > 0$.

Two types of calculation models, accounting for initial conditions fixed by different laser configurations, have been developed: (1) a cylindrical fiber model [18, 312–317]; (2) a magnetically confined plasma column [25, 44]. Exploding foil targets have also been considered for recombination lasers. However, experiments and calculations performed for H-like magnesium showed difficulties demonstrating gain in this way in the case of long laser pulses [318].

An advantage of starting from a cylindrical thin fiber to produce the amplifying plasma column (cf. Fig. 5.6 in Section 5.2.1) is the means of giving the same simple symmetry to experiments and theoretical models. This makes easier the use of calculated scaling laws to choose the values of the experimental parameters, as well as the comparisons between experimental

results and theoretical predictions. The hydrodynamic expansion of the thin fiber may be described with the help of a self-similarity model (cf. Section 5.1.1 and Ref. [18]). This model, combined with collisional–radiative atomic calculations, has been extensively used in investigating the lasing performances of thin carbon fibers at 18.2 nm, that is the wavelength of the 3–2 line of H-like carbon. Typical information given by these calculations about the conditions for efficient lasing refers to the optimum conditions for gain along the fiber axis. Let R, in cm, be the initial radius of the plasma cylinder, namely its radius after the heating phase, before the plasma starts to cool and recombine, n_e, in cm^{-3}, be the electron density at the same instant. The optimum peak gain scales as [319]

$$g \simeq \frac{6.5 \times 10^7}{n_e^{0.23} R^{1.6}} \text{ cm}^{-1} \tag{8.1}$$

and it is shown to occur for the total initial energy per ion

$$\epsilon \simeq 3.6 \times 10^{-29} n_e^{1.618} R^{2.35} \text{ eV/ion} \tag{8.2}$$

Another example is given in Figure 8.3 which shows two calculated time-dependent gain curves of the 18.2 nm line, the first one taking into account a possibly strong radiation trapping by reabsorption in the 2–3 transition, whereas the second one assumed such reabsorption to be negligible. Calculations are made for a 2.77-mm fiber heated by a 70-ps pulse. The comparison of these curves with the experimental results clearly answers the question of the role of photon trapping in the gain of this laser. One sees that trapping would significantly delay the onset of the gain, which is not observed. Moreover the agreement of the experimentally measured gain values are significantly better with the curve given by the free-from-trapping model.

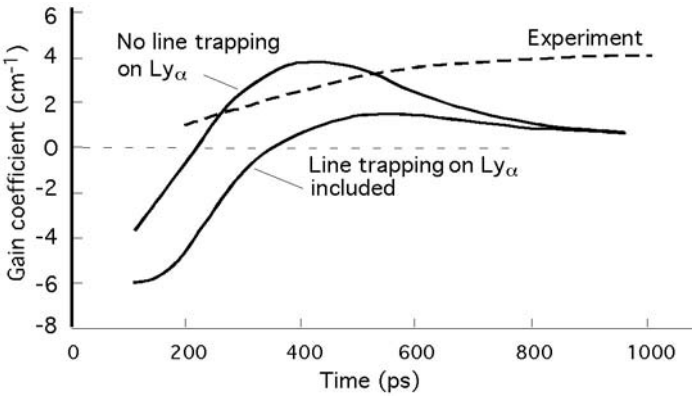

Fig. 8.3. Gain coefficients calculated versus time for the 18.2 nm, 3–2 line of H-like carbon ions, in a recombining plasma (solid lines) compared with experimental results (dashed line) [319]. The agreement is better when no trapping is included in calculation.

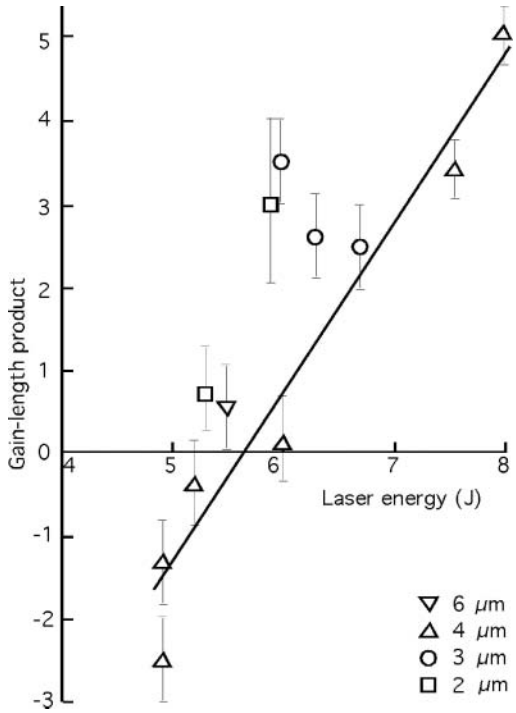

Fig. 8.4. Values of gain–length product, obtained from the comparison of the transverse and the longitudinal intensities of an amplifying plasma column, as a function of the pump laser energy for various carbon fiber diameters.

Significant gain measured at 18.2 nm is shown in Figure 8.4 for various values of the fiber diameter and of the pump laser energy [320]. The Nd pump laser produced pulses of 180 ps up to 10 J energy. A 20% prepulse preceded the main pulse by 200 ps. The fiber was positioned horizontally along the line focus, with its open end directed toward the axial spectrometer. The fiber diameters were ranging from 2 μm to 6 μm.

The intensity of the H_α line was simultaneously measured in the axial and the transverse directions by two grazing incidence spectrographs. In the transverse direction the intensity I_{tran} is proportional to jr, where j is the emissivity function and r the radius of the cooling plasma column. In the axial direction the intensity I_{long} is proportional to $j \times \left(e^{gl} - 1\right)/g$, where l is the plasma column length and g, the gain coefficient (cf. Section 1.2). Comparing these two formulae gives $I_{\text{long}} = I_{\text{tran}} \times Al/r$ with $A \equiv \left(e^{gl} - 1\right)/gl$. Knowing l, r, and measuring I_{long} and I_{tran}, one obtains the "amplification factor" A, from which the gain–length, gl, can be deduced for any value of l. Subject to suitable calibration of the two spectrographs, it is thus possible to obtain the gain–length factor from the comparison of the transverse and the axial intensities. The values of gain–length product, gl, directly deduced from the

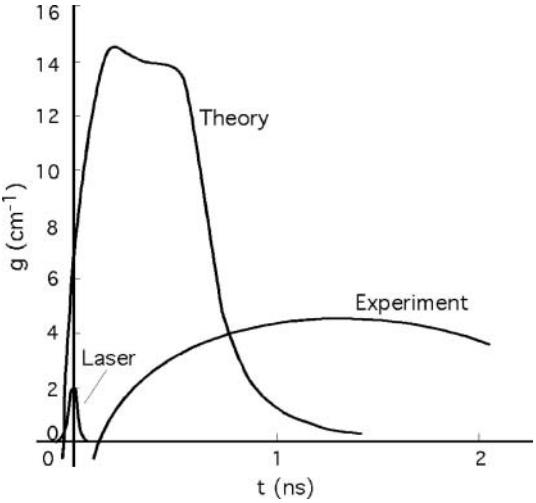

Fig. 8.5. Measured and calculated time dependence of the gain coefficient of the 18.2 nm carbon line. The time profile of the pump laser pulse is shown on the left of the figure. Notwithstanding the large discrepancy between experiments and calculations, the recombining character of the lasing process is evident from gain occurring mostly after the end of the laser pulse.

values obtained for A in various experimental conditions, are those plotted in Figure 8.4.

The six-beam target irradiation facility of Rutherford Appleton Laboratory, previously described in Section 5.2.1 (cf. Fig. 5.6), has given the opportunity to perform accurate gain measurements for carbon fibers of 7-μm diameter and up to 9.5 mm in length. The pump pulse duration was about 70 ps. The absorbed energy of 2.6 ∓ 0.6 J/cm was a tenth of the incident energy. The gain for the 18.2-nm line has been measured from the exponential increase of the line intensity as a function of the fiber illumination length. The gain value has been found to be of 4.1 ∓ 0.6 cm^{-1} at time 1 ns after the peak of the laser pulse [321]. It has been also possible to observe the variation of the gain as a function of time with a 400-ps time resolution. The result is shown in Figure 8.5 together with a calculated curve that exhibits higher peak gain and faster decay than observed in experiments. The discrepancy may result from calculations assuming a perfectly regular medium and returning *local gain* coefficients, whereas experimental results involve ray path integration in a more or less homogeneous medium.

The gain in the H_α line of fluorine at 8.1 nm has been measured using the same target system and coating the carbon fiber with 0.5 μm of LiF [322]. Table 8.1 displays the gain coefficients measured for three values of the absorbed energy. The target length varied from 1.5 mm to 5.8 mm. The results clearly show an optimum pump energy value of 9–10 Jcm^{-1}.

Table 8.1. Gain coefficient for the 8.1-nm line of H-lile fluorine for three different values of the effectively absorbed pump energy Ref [322]

E (Jcm^{-1})	g (cm^{-1})
5 ∓ 0.7	-1.8 ∓ 0.2
9 ∓ 2	4.4 ∓ 1
16 ∓ 1	2 ∓ 1

It is believed that, at low energy, the ground state population of H-like F is relatively high, causing radiation trapping of the Ly$_\alpha$ line radiation, thereby reducing the population inversion (cf. Fig. 8.1). On the other hand, at high energy, the effect of increased temperature results in the reduction the population of the $n = 3$ upper level of the lasing transition which, in turn, reduces gain. Figure 8.6 shows the temporal variation of the measured gain for the optimal absorbed energy of ∼10 Jcm^{-1} and the corresponding calculated curves with and without line-trapping. The results are similar to those previously shown in Figure 8.3 for H-like carbon. This confirms that gain will be observed only under conditions where the Ly$_\alpha$-line trapping is moderate.

At shorter wavelengths, gain has been observed at 5.42 nm for the Balmer $_\alpha$ line of hydrogenlike sodium [323]. One hundred and thirty picoseconds duration pulses of 0.351 μm laser radiation were focused on planar stripe and foil targets, coated with NaF. A time-resolved peak gain of 3.2 ∓ 1 cm^{-1} has been obtained.

We come now to the pumping method that makes use of a strong external magnetic field ($B \sim 100$ kG) to confine the plasma column (cf. Fig. 5.8, Section

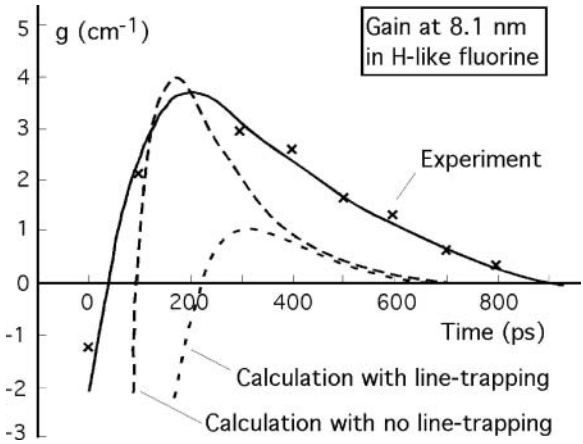

Fig. 8.6. Measured and calculated gain of H-like fluorine ions.

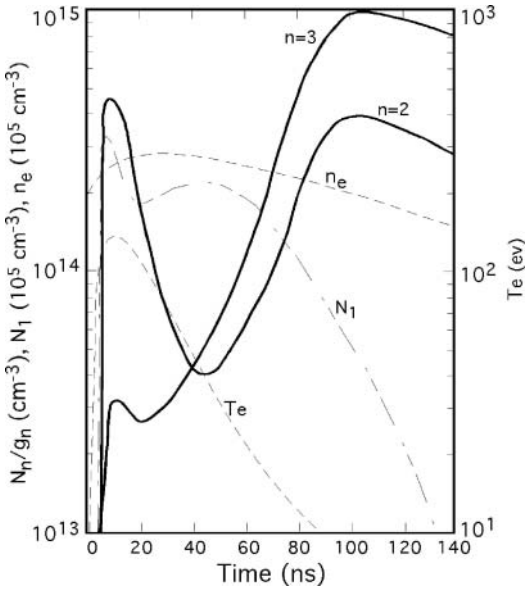

Fig. 8.7. Calculated populations of the lasing line levels of H-like carbon in a magnetically confined plasma as a function of time. Population inversion is found to start 40 ns after confinement onset [25].

5.2.1). The confined plasma is heated by a CO^2 laser, and then cools rapidly by radiation loss [25, 44, 324, 325].

If one assumes the plasma to consist in H-like ions and free electrons only, with electron density n_e and temperature T_e, energy conservation suggests that the radiative decay time amounts to $\tau_{rad} \approx [n_e T_e(t)/n_2 A_{21} h\nu_{21}]$. For a carbon plasma with $n_e = 5 \times 10^{19}$ cm^{-3}, $T_e = 500$ eV, $N_2 \approx 5 \times 10^{14}$ cm^{-3}, $A_{21} = 7 \times 10^{11}$ s^{-1}, $h\nu_{21} = 320$ eV one obtains $\tau_{rad} \approx 4 \times 10^{-8}$ s, from which it appears that typical lasing times will be longer than for other laser-pumped recombination lasers.

Since the three-body recombination, which strongly contributes to the C^{5+}-ion high-lying level populations, is proportional to n_e^2, population inversions will take advantage from the magnetic confinement keeping n_e at a high value for a long time. A model calculation, including ionization, radiative, and three-body recombination gives level populations as a function of time. The results are illustrated by the curves of Figure 8.7, which show the onset of a population inversion of the Balmer$_\alpha$ line levels occurring about 30 ns after the end of plasma heating and then lasting several tens of nanoseconds.

Figure 8.8 shows the carbon target used to produce the plasma in the experiments corresponding to this scheme. The CO_2 laser beam is focused on the surface of the disk by a 3-m focal-length spherical mirror. Carbon blades may be added to create a more uniform plasma in the axial direction and to

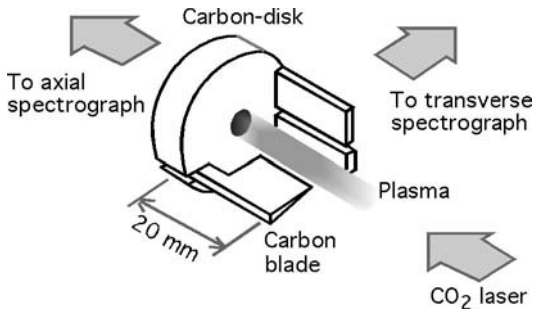

Fig. 8.8. Carbon target used to produce the plasma to be confined in a magnetic field. The solenoid used to produce the axial magnetic field is not represented. The target includes disk and blades of carbon. One or more blades are added to improve uniform plasma uniformity. The CO_2 laser beam is focused onto the disk surface of the by a 3-m focal-length spherical mirror.

provide additional cooling by heat transport from the plasma to the blade. The low inductance solenoid used to produce the axial magnetic field is not represented in the figure.

It can be shown that the electron density profile has an off-axis ring-shaped maximum while the temperature is at a maximum in the center. Therefore the maximum gain should be off axis too, which must be considered when choosing the parameters of the XUV beam detection. Optimum amplification conditions for the 18.2-nm line, leading to a gain–length $gl \sim 6.5$, have been obtained with a magnetic field $B \approx 90$ kG and a pump intensity $\approx 5 \times 10^{12}$ W/cm^2 provided by a 300-J laser pulse of 75-ns FWHM. The XUV laser pulse duration was quite similar. The beam divergence is measured to be 9 mrad for $B = 20$ kG and 5 mrad for $B = 35$ kG, which indicates that the gain region becomes tighter with higher magnetic fields [326]. The XUV pulse energy was estimated at 1–3 mJ and its peak power to 100 kW. The gain–length has been somewhat enhanced to 8 ∓ 2 cm^{-1} by replacing the CO_2 laser by a Nd–glass laser that gives a higher electron density in the center of the plasma. In this case a magnetic field of 50 kG was sufficient to optimize the gain [324, 327].

Quite an original arrangement, whose principle was suggested by observations made in other respects on investigating pumping by ultrashort pulses in microcapillary plasmas, is displayed in Figure 8.9 [327a] (see next section). In the present case a boron plasma is created by longitudinally focusing the beam of a KrF laser at the entrance of a B_2O_3 microcapillary, with a pulse duration of 20 ns. The pulse energy is of 0.2 J. After delay times varying between 1 and 1200 ns a second low energy, 0.45-J, 8-ns Nd:YAG laser is fired on the entrance of the microcapillary through the same focusing lens. The shot repetition rate is of 1 Hz. The rapid intensity increase of the Balmer$_\alpha$ line of H-like boron, at 26.2-nm wavelength, with the length of a 0.35-mm diameter

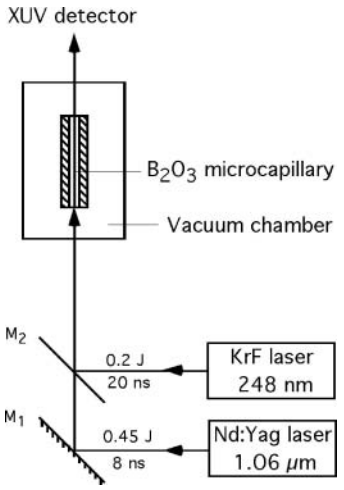

Fig. 8.9. Boron plasma pumped in microcapillary. A KrF laser pulse focused at the entrance of a B_2O_3 microcapillary generates the plasma. A second low energy Nd:YAG laser is fired on the entrance of the microcapillary. The Balmer-α line of H-like boron ($\lambda = 26.2$ nm) shows a gain $\sim$14.3 cm^{-1} with a maximum of gain–length of $\sim$5 for a 3.5-mm length.

capillary denotes amplification. The gain coefficient is measured to be $\sim$14.3 cm^{-1} for a plasma length of 3.5 mm. Thus the gain–length product in this configuration is $\sim$5. Further increase of the plasma length up to 4 mm shows that gl starts to decrease.

8.1.2 Lithium-Like Ions

Figure 8.10 shows the diagram of levels and the radiative transitions of interest for amplification in a recombining Li-like aluminium plasma. Let us assume that the population of the thermal band, composed of all levels of main quantum numbers $n \geq 6$, the population of the ground state $n = 2$, the free electron density n_e, and the electron temperature T_e have constant fixed values in time, and that radiative decay and electron collisions distribute the electrons over the bound levels $n = 3$, $n = 4$, and $n = 5$. The time-dependent populations corresponding to a "pure" atomic relaxation may be obtained from the collisional–radiative model (cf. Section 5.1.2). Figure 8.11 illustrates the results of this calculation [38] and shows that a few tens of picoseconds are sufficient to reach stationary populations involving inversions between levels 4 and 5 and level 3.

A number of theoretical gain studies exploit this effect to investigate lasing conditions in Li-like ion plasmas [328–335]. An early example of gain calculation results is given in Figure 8.12. An aluminium target is supposed to be

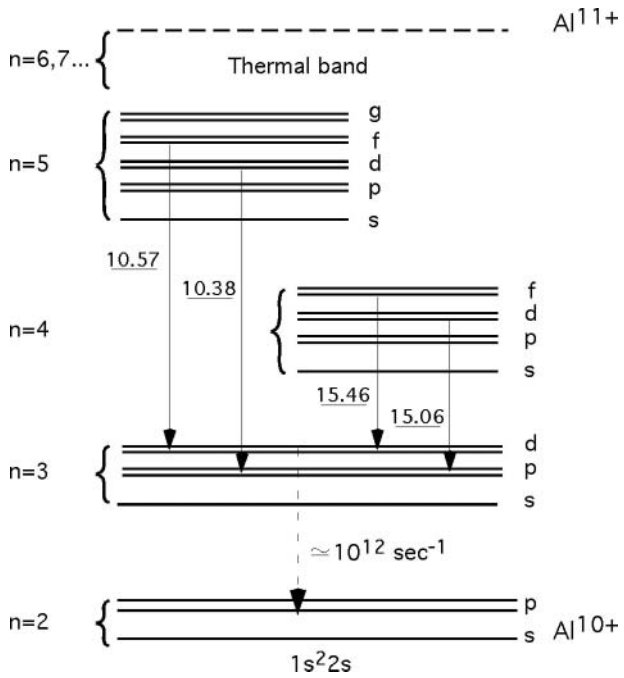

Fig. 8.10. Level diagram of Li-like ions of aluminium. The wavelengths of the four lines subject to amplification are given in nanometers.

irradiated by a 2-ns FWHM Gaussian laser pulse of 1.06-μm wavelength with 1.3×10^{12} W/cm^2. Initial conditions assume a cylindrical plasma of 100-μm radius. The figure displays the population inversions for the 5f–3d and 4f–3d lines as a function of the distance to the target and at several moments between 4 and 6 ns after the top of the laser pulse. Gain clearly occurs during the plasma cooling time, which is easily understandable for recombinational pumping. Furthermore, owing to a larger transition probability, the gain declines more rapidly for the 4f–3d than for the 5f–3d transition.

As in the case the H_α-line of the hydrogen-like carbon, scaling laws can be found to determine the optimum gain conditions for the two 4f–3d and 5f–3d doublet lines of Li-like aluminium [319]. They have forms similar to those obtained for carbon, i.e.

$$g = \alpha n_{\mathrm{e}}^{\beta} R^{\gamma} (\mathrm{cm}^{-1}) \tag{8.3}$$

for a total ion energy

$$\epsilon = A n_{\mathrm{e}}^{B} R^{C} (\mathrm{eV/ion}) \tag{8.4}$$

where n_{e} and R are the initial electronic density (cm^{-3}) and the initial plasma radius (μm,) respectively. The numerical coefficients are displayed in Table 8.2.

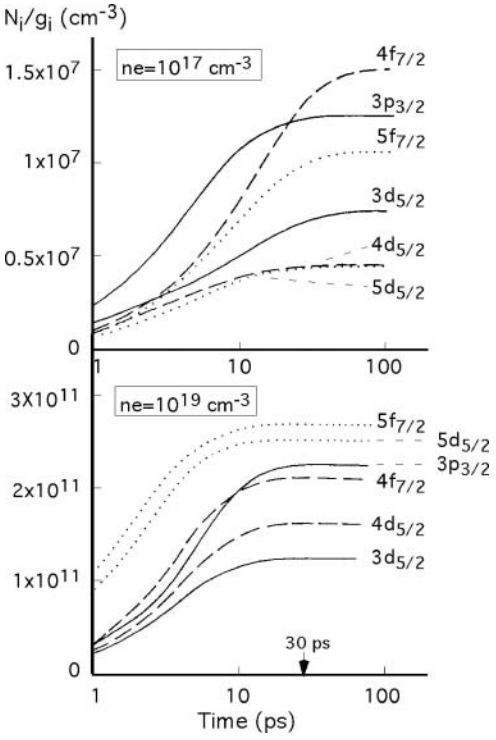

Fig. 8.11. Calculated relaxation of Li-like ion level populations in presence of a gas of free electrons of constant density and temperature. The populations of the thermal band and of the ground level are assumed to be constant as it is approximately the case in plasmas of slowly varying ion populations. Populations inversions appear, especially between the 5f and the 4f level, on the one hand, and the 3d level, on the other hand.

From equation (8.3) it is easy to see that the gain of the 4f–3d line should be larger than that of the 5f–3d line. The calculated curves of Figure 8.13 from Ref. [336] show a similar effect. However they show the gain ratio of the two lines to overturn for small gain and long pulse durations (Fig. 8.13a) as a consequence of the faster decay of the 4f states. This inversion could explain

Table 8.2. Numerical coefficients of the optimum gain scaling law (Ref. [316])

Transition	A	B	C	α	β	γ
$3d_{3/2}$–$4f_{5/2}$	9.1×10^{-27}	1.519	2.444	9.0×10^4	−0.16	−1.22
$3d_{5/2}$–$4f_{7/2}$	9.3×10^{-27}	1.519	2.444	4.6×10^5	−0.16	−1.63
$3d_{3/2}$–$5f_{5/2}$	1×10^{-28}	1.609	2.534	5.6×10^4	−0.16	−1.49
$3d_{5/2}$–$5f_{7/2}$	1×10^{-28}	1.609	2.534	6.2×10^4	−0.16	−1.49

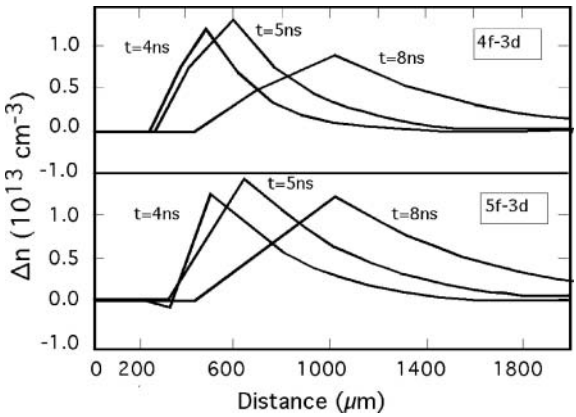

Fig. 8.12. Population inversions calculated as a function of the distance to the target, at three moments after the top of the laser pulse of 2-ns FWHM duration. Inversions are expressed as the difference between the upper and the lower level populations (Ref. [325]).

measurements leading to small gain coefficients apparently inconsistent with each other.

For the gain measurements on Li-like aluminium, whose results are displayed in Figure 8.14, the target was a massive aluminium slab [337]. The 1.06-μm wavelength laser provided pulses of 3.7-ns duration and $\sim 10^{12}$ W/cm^2 intensity. The gain onset for the 5f–3d line at 105.7 nm happened $t \simeq 5$ ns after the top of the laser pulse, which is consistent with the curves of Figure 8.12. For a plasma length of $\sim$1 cm the maximum gain was found at a distance of 0.3 mm from the target surface, between $t = 7.0$ and $t = 7.5$ ns and with a value of 2.7 cm^{-1}. No measurable gain could be observed for the 4f–3d line at 15.4 nm.

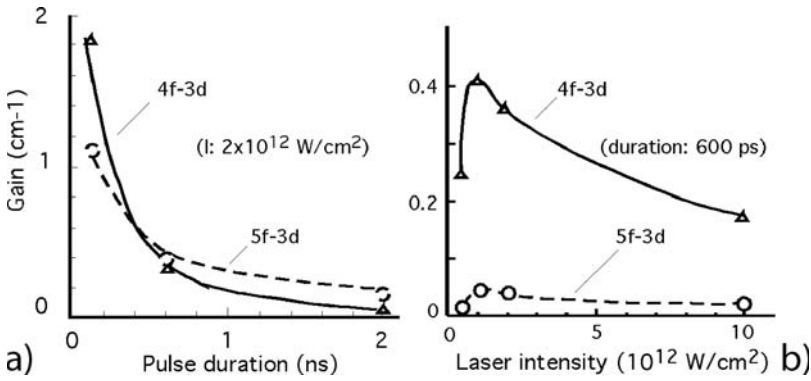

Fig. 8.13. Gain calculated for the Li-like aluminium 4f–3d and 5f–3d transitions as a function of pump pulse duration (a) and laser intensity (b).

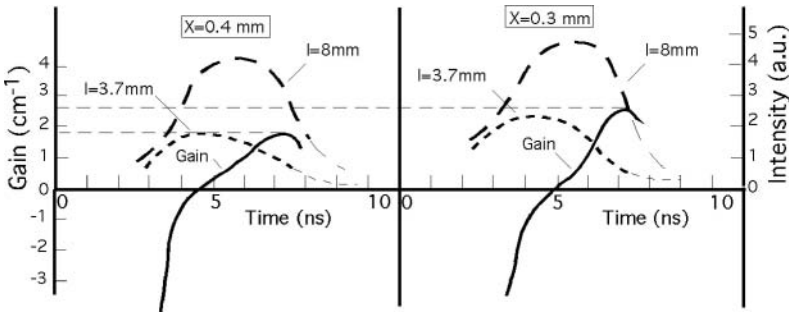

Fig. 8.14. Gain of the Li-like aluminium 5f–3d line ($\lambda = 10.57$ nm) measured as a function of time, at 0.3 and 0.4 mm from the target (solid lines). The dashed lines represent the soft X-ray laser intensity for two different plasma lengths l.

Similar measurements performed during the same experiment with a 2-cm long plasma showed the gain coefficient to be reduced by a factor ∼2. Moreover, with a plasma length of 6 cm and a pump intensity of 2×10^{12} W/cm^2 the gain was measured to be only of 0.5 cm^{-1} [338]. Table 8.3 exemplifies the tendency of the gain coefficient to lessen while the plasma length increases, which will be discussed later on.

A better agreement with theoretical predictions was obtained with a larger laser intensity and a flat target consisting of a 0.5 μm layer of Al and a 0.01μm layer of Au on a 10-μm thick Mylar backing [339]. The 0.351-μm wavelength laser intensity was of 8×10^{13} W/cm^2 with a 650-ps pulse duration. The time-averaged gain coefficients for a 6-mm long plasma were measured to be $g = 4.1 \mp 1.2$.cm^{-1} for the 4f–3d line, $g = 4.5 \mp 1.3$ cm^{-1} for the 4d–3p line, and $g = 3.5 \mp 0.8$ cm^{-1} for the 5f–3d line.

Table 8.3. Experimental data from Li-like Al gain measurements, for plasma lengths from 3mm to 60 mm

	Experiment						
	Facility target	LULI slab	LULI slab	RAL fiber	LULI slab	RAL stripe	LULI slab
l(mm)		3	8	11	18	23	60
Line	λ (nm)	Gain coefficient (cm^{-1})					
5f–3d	10.57	∼3	2–2.5	1.63	0.8–1	1.09	0.5
4f–3d	15.47			2.56		0.61	

Note. The laser facility used for each of the measurements is indicated. The table shows the marqued tendency of the gain coefficient to decrease for increasing plasma length.

Table 8.4. Time-averaged gain of the 4f–3d line of lithium-like Ca (5.77-nm wavelength) as a function of the distance to the target

$x\,(\mu m)$	150	170	210	350
$g\,(cm^{-1})$	4.3	3.8	2.6	0.9

Plasma produced by a CO_2 laser and confined by a strong magnetic field (cf. Fig. 5.8, Section 5.2.1 and Fig. 8.8, previous section) also demonstrated Li-like ion gain [327]. In this case, with a lasing duration of about 20 ns, the 4f–3d gain calculation predicts the aluminium gain peak to occur 87 ns from the beginning of the laser pulse. Experiments demonstrated gain–length products of 3–4 at 15.4 nm in aluminium and of 1–2 at 12.9 nm in silicon.

Li-like laser investigations have been extended to shorter wavelengths by the group of the Shanghai Institute of Optics and Fine Mechanics, using silicon [340], calcium, and fluorine plasmas [341]. For silicon, the targets were thick Si slabs with polished surfaces. The maximum length of the focal line was $\simeq$8 mm. Laser intensity at the target surface was of 1.5×10^{12} W/cm^2. Time-integrated gain coefficients were measured to be 1.5 cm^{-1} and 1.4 cm^{-1} for the 5f–3d line, at 8.89 nm, and the 5d–3p line, at 8.73 nm, respectively. In similar conditions a gain of 3.1 cm^{-1} was observed for the 5f–3d line of aluminium at 105.7 nm.

As for the measurements with Li-like calcium, they have been performed with thick CaF_2 slab targets. The laser intensity was about 4×10^{13} W/cm^2 and the maximum plasma length, 10 mm. Time-integrated measurements were performed at four distances, x, from the target for the 4f–3d line of 5.77-nm wavelength. The results are displayed in Table 8.4. An additional measurement of gain for the Balmer$_\alpha$ line of H-like fluorine returned a value of 1.4 cm^{-1}. The time-resolved intensities of the these two laser lines are shown in Figure 8.15, as also the laser-pulse intensity.

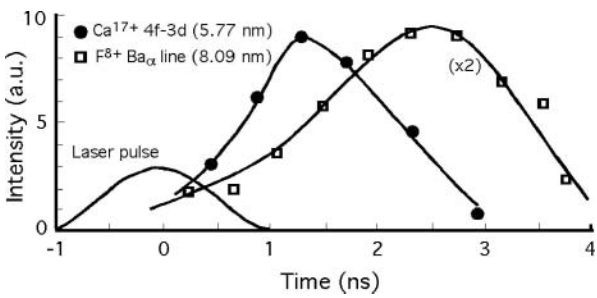

Fig. 8.15. Intensity of the soft X-ray Li-like calcium laser at 5.77-nm wavelength as a function of time, measured using a CaF_2 slab target (Ref. [340]).

To complete this survey of experimental results in recombination pumping, let us also mention that target irradiation by laser pulse-train also showed gain for the 5f–3d lines of lithium-like Al, Si, and Mg [342–345]. The pulse-train consisted in 16 pulses of 100 ps FWHM separated from each other by a 200-ps interval. The total output energy was 4–6 J and the line focus, 23 mm in length and 20 μm in width. The gain coefficients were of 2.8, 2.0, and 1.1 cm^{-1} for 3d–5f transitions of Mg, Al, and Si, respectively. A gain–length product of 5.8 has been obtained with the help of multiple amplification in a cavity [346].

8.1.3 Gain–Length Product Limitation

From the whole of these results one has to accept that, notwithstanding the relatively low energy required to produce lasing action in Li-like ions, it has not yet been possible to achieve large gain–length products and XUV laser saturation in this way. This limitation is unlikely to be merely caused by radiation trapping in the 2p–3d resonance line because detailed calculations show gain coefficients to be reduced by no more than 20% for the 3–4 and 10% for the 3–5 transitions when reabsorption is taken into account [347]. Even stronger radiation trapping could not explain the effect consisting in gain coefficient growing gradually less when plasma length increases, so that the gain–length product remains limited to a small value of the order of 4–5.

On the other hand it has been directly demonstrated that plasma irradiation irregularities can considerably reduce the gain within the plasma column [348]. Therefore let us assume that a plasma column consists of N small elements, $1, 2, \ldots, n-1, n, n+1, \ldots, N$, of length Δl and with gain coefficients, g_n, distributed along the column owing to irradiation irregularity. The output I_n at the exit of the nth element is given by (see Section 1.2)

$$I_n = \frac{j_n}{g_n}\left(e^{g_n \Delta l} - 1\right) + I_{n-1} e^{g_{n-1}\Delta l} \tag{8.5}$$

where j_n is the emissivity given by equation (1.17). The averaged gain at the end of the column is

$$\langle G \rangle = \frac{1}{N}\sum_{i=1}^{N} g_i$$

If we fit an exponential function $I(l)$ to the sequence of the calculated values, I_n, as if we were estimating gain from experimental intensity measurements, we obtain a curve representing the intensity as a function of l

$$I\,(l) = S_{\text{eff}} e^{G_{\text{eff}} \times l}$$

where the effective gain G_{eff} is different from the averaged gain $\langle G \rangle$ and S_{eff} is an effective source function. Calculations performed from experimentally measured irregular irradiation distributions showed that G_{eff} was systematically smaller than $\langle G \rangle$ [348]. Moreover a dilatation of the plasma column, that

increases its length keeping the map of the irregularities unchanged, namely a dilatation that keeps $\langle G \rangle$ constant, was found to generate a decrease of the effective gain G_{eff}. Therefore gain irregularities coming from nonuniform plasma irradiation or possibly from plasma instabilities could, at least partially, account for the drop of gain in longer plasmas. The nonuniformity of the focal line, inherent to the geometrical aberrations of the focusing system, may also contribute to the observed gain decrease at large plasma length [349].

8.2 Short and Ultrashort Pump Pulses

Numerical modeling predicts that saturated output could be achieved for the Balmer$_\alpha$ line of hydrogen-like carbon in less than 1-cm plasma using a driver laser of picosecond duration [350]. As a matter of fact a large gain coefficient of 12.5 ∓ 1.5 cm^{-1} has been achieved at 18.2 nm in a hydrogen-like carbon recombination laser, driven by a 20 J, 2 ps Nd–glass laser line-focused on a 7-μm diameter, 5-mm long carbon fiber, i.e. a gain–length product ∼6 which is exceptionally large for recombination lasers [351]. However the output intensity was estimated at 1.4×10^5 W/cm^2, whereas the saturation intensity is calculated to be 2.5×10^9 W/cm^2, which would require to extend the same lasing conditions to a 8-cm long plasma. Implementing a 1-cm long, very thin fiber target, supported at one end only, positioned with a 1–2 μm spatial accuracy and 1-mrad angular accuracy is extremely difficult. One cannot recommend to try it. Let alone 8 cm! Let us mention though that the scaling laws 8.3 and 8.4 have been extended to short pulses under the form

$$g = 1.1 \times 10^{-12} (\lambda/t)^{1.21} \tag{8.6}$$

$$\epsilon = 2.9 \times 10^6 t^{0.648} \lambda^{-3.7} \tag{8.7}$$

where the laser wavelength λ is in μm, the pulse duration, t in s, g in cm^{-1} and ϵ in eV/ion.

On the other hand, computational simulations of the recombination of initially fully stripped ions surrounded by a dense gas of free electrons show that it is possible to obtain transient population inversions, not only for the Ly$_\alpha$ line but also for the ground state $n = 2$–1 transition of hydrogen-like ions [352]. Furthermore optical field ionization induced by very short laser pulses can produce suitably cold fully stripped ions that are allowed to recombine on a time scale less than picosecond. This led to consider the feasibility of recombination ground-state XUV lasers pumped by very short laser pulses [353]. An interesting property of these lasers would be to lase at wavelengths shorter than using the standard quasi-static recombination scheme.

Detailed calculations performed for Li-like neon ions, involving parametric mechanisms of plasma heating, such as stimulated Raman effect, led to define

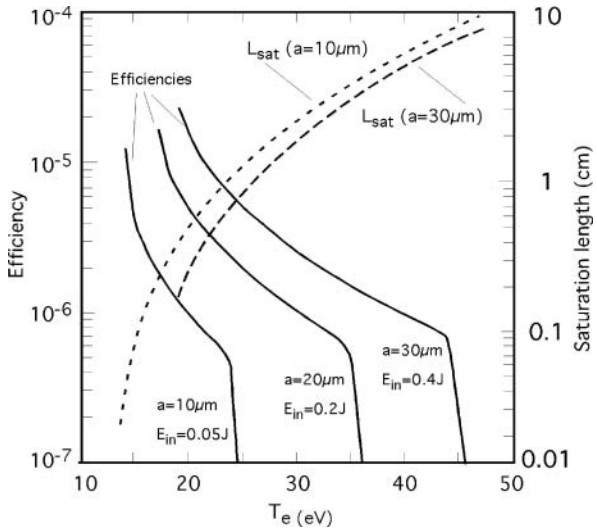

Fig. 8.16. Calculated efficiency of Li-like neon laser as a function of electron temperature for three microcapillary radii (a in the figure). The decrease of efficiency with the temperature increase is found to be very rapid.

the main conditions of laser operation when ultrashort pump pulses are used [354,355]. It is shown that the 3d–2p gain is very sensitive to the initial $n = 2$ population. It requires this population not to exceed 3×10^{-3} times the He-like ion density.

Considering a Gaussian ionizing laser pulse of radius a and wavelength λ, the effective propagation distance, z, is diffraction-limited to two times the Rayleigh length 7.25, i.e.

$$b = \frac{2\pi a^2}{\lambda} \tag{8.8}$$

where b is known by the name of confocal parameter [300 p. 669]. This distance may be reduced to less than 1 mm on account of the refraction in transverse density gradient regions. Ionizing gas within a microcapillary waveguide might be required to overcome this difficulty. An example of calculation results is given in Figure 8.16. One can see that the energy efficiency of the laser, i.e. the ratio of the XUV laser output to the input pump energy strongly decreases with the electron temperature which, therefore, is to be reduced by minimizing electron heating. It is thus clear that, contrary to collisional OFI lasers, recombination lasers rather requires the *linear* polarization of the short pulse radiation (see Section 7.6 and Fig. 7.93).

Amplification has been observed for the 13.5-nm Ly_α-line of hydrogen-like lithium ions by using a subpicosecond KrF laser focused at 10^{17} W/cm^2 [356]. The singly ionized lithium ions were initially prepared by a nanosecond KrF excimer laser and further fully stripped by a 0.5 ps high intensity KrF laser in

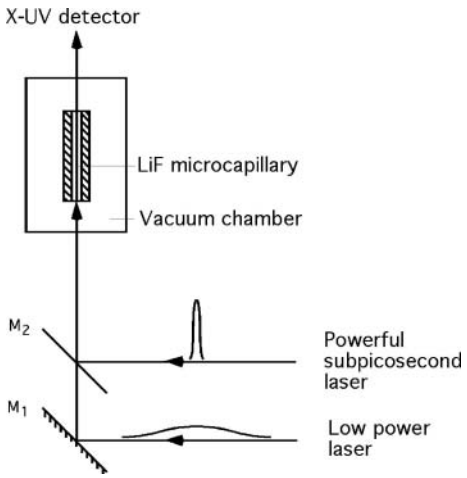

Fig. 8.17. Diagram of a setup designed for lasing on the 2–1 transition of H-like lithium. The Li plasma is produced by capillary wall ablation.

order to improve the definition of the initial conditions. This 20-ns KrF laser was line focused onto a flat solid Li target at an intensity of 10^9 W/cm^2. The estimated electron temperature was of 1.5 eV. The 50-mJ, 500-fs high-power KrF laser pulse was then focused 0.5 mm above the target.

Measuring the intensity of the H-like lithium 13.5-nm line versus the delay between long and short pulse showed that 700 ns was the optimum value of the delay. Gain measurements have been performed for this optimal delay. A strongly nonlinear increase of the line intensity up to a 2-mm long plasma indicated the possibility of gain coefficient $\sim$20 cm^{-1} and $gl \sim 4$. Attempts to increase line intensity with length beyond 2 mm were unsuccessful, indicating the propagation length of the short pulse laser to be likely limited by refraction.

This difficulty encouraged investigating amplification in plasmas produced in wave-guiding microcapillary. An experimental arrangement, in which a lithium plasma is produced by capillary wall ablation, is shown in Figure 8.17 [357]. A low power Nd/Yag laser (1.06 μm, 100 mJ, 5 ns) is focused on the entrance of the microcapillary. The powerful short pulse laser (0.248 nm, 50–60 mJ, 250 fs) is focused onto the lithium plasma at the entrance of the capillary, providing a power density close to 2×10^{17} W/cm^2. The repetition rate of both lasers is 2 Hz. The mirror M_2 is transparent to the 1.06 μm wavelength of the low power laser. Microcapillaries of 1 mm to 5 mm in length and $\sim$300 μm in diameter were made by drilling holes in solid LiF. A delay of a few hundred of nanoseconds separates the two pulses.

In Figure 8.18 the intensity of the 13.5-nm ground state line is plotted versus microcapillary length for a delay of 800 ns. Each point corresponds to an exposure of 20 shots onto a microchannel detector. Fitting the points by a least

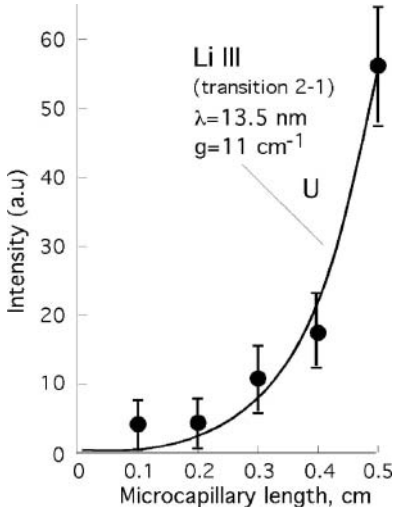

Fig. 8.18. Exponentially increase of the 2–1 (ground state) line of H-like lithium pumped in a microcapillary.

square root method with the Lindford formula [see Eq. (1.43)] indicates gain $g \approx 11$ cm^{-1} and gain–length $gl \approx 5.5$. It has been observed that the 13.5-nm line intensity for a single shot is subject to large fluctuations, indicating possible gain fluctuations due to initial plasma conditions. However the intensity for capillary lengths shorter than 4 mm was too low to allow measurements from a single shot exposure for each length. Attempts to increase the length of the microcapillary up to 8 mm showed that, beyond length of ∼5 mm, one could not create a uniform plasma along the axis of the microcapillary.

In a new development of this work on lasing to the ground state of LiIII ions, the plasma has been produced by electric discharge in the capillary before rapid heating by a short laser pulse [303]. Electric discharge is expected to provide radial distribution of electron density suitable for wave-guiding effect, this allowing for XUV amplification in longer capillaries [304,358]. The principle of the experimental arrangement is similar to that of the hybridly pumped Ne-like sulfur laser described in Section 7.5 (Fig. 7.92) but here it is applied to recombination pumping. The discharge system makes use of three electrodes dividing the length of the 14-mm long capillary in two regions, the trigger gap and the main gap of lengths 4 mm and 10 mm, respectively. The laser delivered 0.5–0.6 J in 500 fs (1.05-μm wavelength) which led to an intensity of 5×10^{17} W/cm^2 in the focal plane of the focusing lens. Optimum gain was obtained in a 600-μm diameter capillary by applying voltages of 10 keV on the trigger gap and 1 keV only on the main gap. The gain–length product was estimated at $gl \sim 7$ though the lack of reproducibility of the discharge conditions did not make it easy to perform regular gl measurement.

9. Schemes for Future Soft X-Ray Lasers

In addition to the lasers presented in the previous chapters, we briefly describe hereafter two schemes of short-wavelength lasers that might contribute in the future to extend laser capabilities to shorter wavelengths, higher intensity, and full coherence.

9.1 Inner Shell Photopumping

A key to shorter wavelengths could be to succeed in pumping neutral atoms by inner shell ionization. The formidable difficulty on the route of inner-shell pumping comes from the very short life-time of the inner-shell vacancies due to the fast radiative decay from upper levels as well as to Auger transitions and other similar processes. The durations of population inversions would lie in the fs range. However the recent progresses in the technique of ultra-fast, high-intensity lasers promote new efforts to realize inner-shell pumped lasers.

For example, Moon et al. investigate a scheme where carbon (10^{18}cm^{-3} foam) is used as the lasant material and gold as the incoherent X-ray pumping source [359, 360]. Photo-ionization of the K shell (286 eV) leaves a hole state $1s2s^22p^2$ in the singly ionized carbon ion, C^+, leading to a possible 1s–2p lasing line at 4.5 nm. On account of the very short pump time, an optical arrangement provides a traveling wave along the 10-mm long line focus, at the carbon target surface. From preliminary experiments, the intensity of the ultrashort pulse laser on target is estimated to be as high than 6.9×10^{17} W/cm^2 in a $\sim$30-μm diameter spot, what is significantly larger than the 1×10^{17} W/cm^2 value used in model calculations. Preliminary X-ray spectra of the back-side emission of the carbon target have been obtained between 2.5- and 5.4-nm wavelength, in various experimental conditions.

Another ambitious project investigates conditions of generating population inversion on an inner-shell transition in cobalt [361, 362]. The laser radiation

of a Ti:sapphire laser is converted into pump X-rays in a thin copper foil placed a short distance before the cobalt foil to be pumped in the K_α-shell. This arrangement realizes a longitudinal configuration, where the radiation emitted by the lasant propagates in the same direction as the X-ray pump radiation.

The cobalt K-edge is at 7.7 k eV, the copper K_α-line at 8 k eV. The cobalt foil can be replaced by a nickel one. The energy of the K-edge of nickel being of 8.3 k eV, the nickel foil cannot be pumped by the cobalt radiation. Hence the comparison between copper and nickel emissions will show the amount of photopumping. Considering only the very first layer of the cobalt foil, the photopumped fraction was measured to be 91% of the total cobalt emission. This was not enough to achieve gain but more sophisticated target designs and higher intensities appear to be able to improve upon this result.

9.2 Free Electron Lasers

Free electron lasers offer quite a different way to achieve short wavelength coherent sources (see for instance [363–366]). When highly relativistic electrons traverse a periodic magnet structure, their transverse oscillations are the source of the emission of "ondulator" radiation. Let us consider an electron bunch, provided by a radio-frequency photocathode electron gun, propagating through the ondulator. If the motions of the various electrons within the bunch are not correlated, the radiated power will increase proportionally to the number of electrons in the bunch, n_e. If the motions become correlated, the fields of the electrons will add in phase. Hence, seeing that the radiated power is proportional to the square of the total electric field, it will rather grow as the square of the electron number, n_e^2, what is characteristic of a coherent emission. This emission process is generally called Self-Amplified Spontaneous Emission (SASE).

In the ondulator, amplification starts from noise and produces intense but wide-band radiation. To reduce the bandwidth and the shot-to-shot variations, the amplifying line of the TESLA Test Facility Free-Electron Laser at DESY includes two successive ondulators [364]. The energy of the electrons at the entrance of the second ondulator is about 240 M eV. An optical system, including a diffraction grating and grazing incidence mirrors, select a narrow band of radiation at the exit of the first ondulator and recombines it with the electron bunch at the entrance of the second ondulator, where it is amplified to saturation.

In the present state of art, the spectral range of tunable radiation at saturated power runs from 95 nm to 105 nm [366]. The pulse energy is of 30–100 μJ with 30–100 fs duration, 1% bandwidth, and 260 μrad angular divergence. Repetition rate is of 1 Hz. Wavelengths down to 30–40 nm are expected to be available at the term of developments presently in progress at the TESLA Test Facility.

References

1. M.A. Dugay, P.M. Rentzepis, Appl. Phys. Lett., **10** (1967) 350.
2. P. Jaeglé, A. Carillon, P. Dhez, G. Jamelot, A. Sureau, M. Cukier, Phys. Lett., **36A** (1971) 345.
3. P. Dhez, P. Jaeglé, S. Leach, M, Velghe, J. Appl. Phys., **40** (1969) 2545.
4. A. Carillon, P. Jaeglé, P. Dhez, Phys. Rev. Lett., **25** (1970) 140(C).
5. A. Carillon, G. Jamelot, A. Sureau, P. Jaeglé, Phys. Lett., **38A** (1972) 91.
6. W.T. Silvfast, J.M. Green, O.R. Wood, Phys Rev. Lett., **35** (1975) 435.
7. P. Jaeglé, G. Jamelot, A. Carillon, A. Sureau, *Laser Interaction and Related Plasma Phenomena*, edited by H.J. Schwarz and H. Hora, Vol. 4A, Plenum, New York, 1976, p. 229; J. Phy., **39** (1978) C4-75.
8. P. Jaeglé, G. Jamelot, A. Carillon, A. Sureau, P. Dhez, Phys. Rev. Lett., **33** (1974) 1070.
9. B. Lax, A.H. Guenther, Appl. Phys. Lett., **21** (1972) 361.
10. A.V. Vinogradov, I.I. Sobelman, Zh. Eksp. Teor. Fiz., **63** (1972) 2113; transl. in JETP **36** (1973) 1115.
11. F.E. Irons, N.J. Peacock, J. Phys. B, **7** (1974) 1109.
12. R.J. Dewhurst, D. Jacoby, G.J. Pert, S.A. Ramsden, Phys. Rev. Lett., **37** (1976) 1265.
13. M. Key, C.L.S. Lewis, M.J. Lamb, Optics Comm., **28** (1979) 331.
14. E.Ya. Kononov, K.N. Koshelev, Yu.A. Levykin, Yu.V. Sidel'nikov, S.S. Churilov, Sov. J. Quant. Electron, **6** (1976) 308.
15. A.N. Zherikhin, K.N. Koshelev, P.G. Kryukov, V.S. Letokhov, S.V. Chelakin, JETP Lett. **25** (1977) 300.
16. V.A. Bhagavatula, B. Yaakobi, Optics Comm., **24** (1978) 331.
17. E.Ya. Kononov, K.N. Koshelev, Sov. J. Quant. Electron. **4** (1974) 1340.
18. G.J. Pert, J. Phys. B: Atom. Mol. Phys., **9** (1976) 3301.
19. R.C. Elton, Appl. Optics, **14** (1975) 97.
20. A.G. Moltchanov, Sov. Phys. Usp., **15** (1972) 124.
21. A.V. Vinogradov, I.I. Sobelman, E.A. Yukov, Sov. J. Quant. Electron., **7** (1977) 32.
22. L.I. Gudzenko, L.A. Shelepin, S.I. Yakovlenko, Sov. Phys. Uspekhi, **17** (1975) 848.
23. G.J. Tallents, J. Phys. B/Atom. Mol. Phys., **10** (1977) 1769.
24. B. Lax, A.H. Guenther, Appl. Phys. Lett., **21** (1972) 361.
25. S. Suckewer, H. Fishman, J. Appl. Phys., **51** (1980) 1922.
26. W.H. Louisell, M.O. Scully, W.B. McKnight, Phys. Rev. A, **11** (1975) 989.
27. J.F. Seely, W.B. McKnight, J. Appl. Phys., **48** (1977) 3691.
28. R.H. Dixon, R.C. Elton, Phys. Rev. Lett., **38** (1977) 1072.
29. S.E. Harris, Optics Lett., **5** (1980) 1.
30. D.L. Matthews, P.L. Hagelstein, M.D. Rosen, M.J. Eckart, N.M. Ceglio, A.U. Hazi, H. Medecki, B.J. MacGowan, J.E. Trebes, B.L. Withen, E.M. Campbell, C.W. Hatcher, A.M. Hawryluk, R.L. Kauffman, L.D. Pleasance, G. Rambach, J.H. Scofield, G. Stone, T.A. Weaver, Phys. Rev. Lett., **54** (1985) 110.
31. A. Carillon, H.Z. Chen, P. Dhez, L. Dwivedi, J. Jacoby, P. Jaeglé, G. Jamelot, J. Zhang, M.H. Key, A. Kidd, A. Klisnick, K. Kodama, J. Krishnan, C.L.S. Lewis, D. Neely, P. Norreys, D.O. Neill, G.J. Pert, S.A. Ramsden, J.P. Raucourt, G.J. Tallents, J. Uhomoibbi, Phys. Rev. Lett., **68** (1992) 2917.

32. (a) T.P. Hughes, *Plasmas and Laser Light*, Adam Hilger, The Institute of Physics, Bristol, England, 1975; (b) An introduction to the absorption of laser light in plasmas, in *Laser–Plasma Interactions*, edited by R.A. Cairns and J.J. Sanderson, Scottish Universities Summer School in Physics Publications, Edinburgh, 1979.
33. J.S.D. Groot, K.G. Estabrook, W.L. Kruer, R.P. Drake, K. Mizuno, S.M. Cameron, Phys. Fluids, **4** (1992) 701.
34. W.L. Kruer, *The Physics of Plasma Laser Interactions, Frontiers in Physics*, Addison-Wesley, Redwood City, CA, 1988.
35. M.H. Key, Energy Transport in Laser-Produced Plasmas, in *Physics of Laser Plasma*, edited by A.M. Rubenchik, S. Witkowski, North-Holland, Amsterdam, 1991.
36. G.J. Pert, *J. Phys. B: Atom. Mol. Phys.*, **9** (1976) 3301; and **12** (1979) 2067.
37. R.W.P. McWhirter, *Plasma Diagnostics Techniques*, Chap. 5, edited by R.H. Huddlestone and S. Leonard, Academic Press, New York, 1965.
38. H. Guennou, A. Sureau, J. Phys. B, **20** (1987) 919.
39. M.D. Rosen, P.L. Hagelstein, D.L. Matthews, E.M. Campbell, A.U. Hazi, B.L. Whitten, B.J. MacGowan, R.E. Turner, R.W. Lee, Phys. Rev. Lett., **54** (1985) 106.
40. D.L. Matthews, P.L. Hagelstein, M.D. Rosen, M.J. Eckart, N.M. Ceglio, A.U. Hazi, H. Medecki, B.J. MacGowan, J.E. Trebes, B.L. Whitten, E.M. Campbell, C.W Hatcher, A.M. Hawryluk, R.L. Kaufman, L.D. Pleasance, G. Rambach, J.H. Scofield, G. Stone, T.A. Weaver, Phys. Rev. Lett., **54** (1985) 110.
41. D. Desenne, L. Berthet, J.L. Bourgade, J. Bruneau, A. Carillon, A. Decoster, A. Dulieu, H. Dumont, S. Jacquemot, P. Jaeglé, G. Jamelot, M. Louis-Jacquet, J.P. Raucourt, C. Reverdin, J.P. Thébault, G. Thiell, *X-Ray Lasers*, Inst. Phys. Conf. Ser. No. 116, IOP Publishing, 1990, p. 351.
42. I.N. Ross , J. Boon, R. Corbett, A.R. Damerell, P. Gottfeldt, C.J Hooker, M.H. Key, G.P. Kiehn, C.L.S. Lewis, O. Willi, Appl. Optics, **26** (1987) 1584.
43. B. Rus, P. Zeitoun, A. Carillon, B. Gauthé, P. Jaeglé, G. Jamelot, A. Klisnick, J.C. Lagron, C. Vinsot, *X-Ray Lasers*, Inst. Phys. Conf. Ser. No. 125, IOP Publishing, 1992, p. 361.
44. S. Suckewer, C.H. Skinner, H.M. Milchberg, C. Keane, D.R. Voorhees, Phys. Rev. Lett., **55** (1985) 1753.
45. A. Klisnick, J. Kuba, D. Ros, R. Smith, P. Fourcade, G. Jamelot, J.L. Miquel, J.F. Wyart, C. Chenais-Popovics, R. Keenan, S.J Topping, C.L.S. Lewis, F. Strati, G.J. Tallents, D. Neely, R. Clarke, J. Collier, A.G. MacPhee, F. Bortolotto, P.V. Nickles, K.A. Janulewicz, *X-Ray Lasers*, 2000, J. Phys. IV (Paris), **11** (2001) Pr2-11.
46. C.L.S. Lewis, D. Neely, J. Uhomoibhi, D.M. O'Neill, S.A. Ramsden, G.J. Tallents, Y.A. Hadithi, M.H. Key, S.J. Rose, G.J. Pert, in *X-Ray Lasers*, Inst. Phys. Conf. Ser. No. 116, IOP Publishing, 1990, p. 231.
47. K. Murai, H. Shiraga, G. Yuan, H. Daido, H. Azuma, E. Miura, R. Kodama, M. Takagi, T. Kanabe, H. Takabe, Y. Kato, D. Neely, D.M. O'Neill, C.L.S. Lewis, J. Opt. Soc. Am. B, **11** (1994) 2287.
48. P. Jaeglé, A. Carillon, H.Z. Chen, P. Dhez, L. Dwivedi, J. Jacoby, G. Jamelot, J. Zhang, M.H. Key, A. Kidd, A. Klisnick, R. Kodama, J. Krishnan,

C.L.S. Lewis, D. Neely, P. Norreys, D.M. O'Neill, G.J. Pert, S.A. Ramsden, J.P. Raucourt, G.J. Tallents, J. Uhomoibhi, *X-Ray Lasers*, Inst. Phys. Conf. Ser. No. 125, IOP Publishing, 1992, p. 1.
49. G.M. Shimkaveg, M.R. Carter, R.S. Walling, J.M. Ticehurst, R.A. London, R.E. Syewart, *X-Ray Lasers*, Inst. Phys. Conf. Ser. No. 125, IOP Publishing, 1992, p. 61.
50. Shiji-Wang, Yuang-Gu, Gualin-Zou, Songyu-Yu, Sizu-Fu, Yuanlong-Ni, Jiang-Wu, Zhengyang-Zhou, Guoqiang-Han, Zucong-Tao, Zunqi-Lin, Shusen-Wang, Wannian-Chen, Dianyuan-Fan, Guoping-Zhang, Jiatian-Sheng, Huimin-Peng, Tanxin-Zjang, Yunfeng-Shao, J. Opt. Soc. Am. B, **9** (1992) 360.
51. J. Krishnan, C. Cairns, L. Dwivedi, M. Holden, M.H. Key, C.L.S. Lewis, A. MacPhee, D. Neely, P. Norreys, G.J. Pert, S.A. Ramsden, C.G. Smith, G.J. Tallents, J. Zhang, *X-Ray Lasers*, 1994; AIP Conf. Proc. **332** (1995) 483.
52. Y. Kato, R. Kodama, H. Daido, K. Murai, G. Yuan, S. Ninomiya, D. Neely, A. MacPhee, C.L.S. Lewis, I.V. Choi, C.H. Nam, T. Kawachi, *X-Ray Laser*, edited by D.C. Eder and D.L. Matthews, 1994; AIP Conf. Proc. **332 (1995)** 35.
53. D.M. Villeneuve, G.D. Enright, H.A. Baldis, Optics Comm., **81** (1991) 54.
54. Z.-Z. Xu, P.-Z. Fan, Z.-Q. Zhang, S.-S. Chen, L.-H. Lin, P.-X. Lu, L. Sun, X.-F. Wang, J.-J. Yu, A.-D. Qian, *X-Ray Lasers*, Inst. Phys. Conf. Ser. No. 116, IOP Publishing, 1990, p. 151.
55. A. Carillon, L.U.L.I. Scientific Report, L.U.L.I., Ecole Polytechnique, 91128 Palaiseau, France, 1993, p. 305.
56. (a) J.J. Rocca, D.C. Beethe, M.C. Marconi, Opt. Lett., **13** (1988) 565; (b) J.J. Rocca, O.D. Cortazar, B. Szapiro, K. Floyd, F.G. Tomasel, Phys. Rev. E, **47** (1993) 1299.
57. J.J. Rocca, V. Shlyaptsev, F.G. Tomasel, O.D. Cortazar, D. Hartshorn, J.L.A. Chilla, Phys. Rev. Lett., **73** (1994) 2192.
58. F.G. Tomasel, J.J. Rocca, V.N. Shlyaptsev, C.D. Macchietto, Phys. Rev. A, **55** (1997) 1437.
59. A.A. Ilyukhin, G.V. Peregudov, E.N. Ragozin, V.A. Chirkov, Sov. J. Quant. Electron., **7** (1977) 519.
60. R.C. Elton, *X-Ray Lasers*, Academic Press, New York, 1990.
61. A.V. Vinogradov, Proceedings of International Colloqium on *X-Ray Lasers*, J. Phys., **47** (1986) C6-287.
62. N.M. Ceglio, D.G. Stearns, A.M. Hawryluk, T.W. Barbee, K. Danzmann, M. Kuhne, P. Mueller, B. Wende, M.B. Stearns, A.K. Petford-Long, C.H. Chang. Proceedings of International Colloqium on *X-Ray Lasers*, J. Phys., **47** (1986) C6-277.
63. P. Dhez, G. Jamelot, A. Carillon, P. Jaeglé, *Laser Techniques in the Extreme Ultraviolet*, edited by S.E. Harris and T.B. Lucatorto; AIP Conf. Proc., **119** (1984) 199.
64. B. Rus, A. Carillon, P. Dhez, P. Jaeglé, G. Jamelot, A. Klisnick, M. Nantel, P. Zeitoun, Phys. Rev. A, **55** (1997) 3858.
65. J.J. Rocca, D.P. Clark, J.L.A. Chilla, V. Shlyaptsev, Phys. Rev. Lett., **77** (1996) 1476.
66. N.M. Ceglio, D.G. Stearns, D.P. Gaines, A.M. Hawryluk, J.E. Trebes, Optics Lett., **13** (1988) 108.

67. A. Dulieu, J.L. Bourgade, J. Bruneau, D. Desenne, H. Dumont, M. Louis-Jacquet, *X-Ray Lasers*, Inst. Phys. Conf. Ser. No. 116, IOP Publishing, 1990, p. 89.
68. A. Glinz, J.E. Balmer, Optics Comm., **111** (1994) 285.
69. J.C. Kieffer, M. Chaker, H. Pepin, J.E. Bernard, H.A. Baldis, Appl. Optics, **28** (1989) 4333.
70. J.C. Kieffer, M. Chaker, H. Pepin, H.A. Baldis, G.D. Enright, B. Lafontaine, D.M. Villeneuve, Phys. Fluids B, **3** (1991) 463.
71. E. Förster, R.J. Hutcheon, O. Renner, I. Uschmann, M. Vollbrecht, M. Nantel, A. Carillon, G. Jamelot, P. Jaeglé, A. Klisnick, *X-Ray Lasers*, 1996, p. 408, Inst. Phys. Conf. Ser. No. 151, IOP Publishing, 1996, p. 408.
72. D. Ress, L.B. Da-Silva, R.A. London, J.E. Trebes, R.A. Lerche, D.K. Bradley, Rev. Sci. Instrum., **66** (1995) 579.
73. E. Keren, O. Kafri, J. Opt. Soc. A, **2** (1985) 111.
74. G.J. Pert, J. Fluid Mech., **131** (1983) 401.
75. A. Demir, G.J. Tallents, Y. Bektöre, C.L.S. Lewis, J. Lin, A. MacPhee, G.J. Pert, *X-Ray Lasers*, Phys. Conf. Ser. No. 159, IOP Publishing, 1998, p. 467.
76. O. Peyrusse, P. Combis, M. Louis-Jacquet, D. Naccache, C.J. Keane, B.J. McGowan, D.L. Matthews, J. Appl. Phys., **65** (1989) 3802.
77. D.M. O'Neill, C.S.L. Lewis, D. Neely, S.J. Davidson, S.J. Rose, R.W. Lee, Phys. Rev. A, **44** (1991) 2641; *X-Ray Lasers*, Inst. Phys. Conf. Ser. No. 116, IOP Publishing, 1990, p. 375.
78. B.K.F. Young, A.L. Osterheld, G.M. Shimkaveg, R.S. Walling, R.L. Shepherd, W.H. Goldstein, L.B. Da Silva, J.L. Portrer, R.E. Stewart, *X-Ray Lasers*, Inst. Phys. Conf. Ser. No. 125, IOP Publishing, 1992, p. 343.
79. C. Chenais-Popovics, J.P. Geindre, J.C. Gauthier, C. Bauche-Arnoult, J. Bauche, J. Bruneau, D. Desenne, M. Louis-Jacquet, D. Naccache, *X-Ray Lasers*, Inst. Phys. Conf. Ser. No. 116, IOP Publishing, 1990, p. 371.
80. C. Bauche-Arnoult, J. Bauche, M. Klapish, Phys. Rev. A, **31 (**1985**)** 2248.
81. J. Dunn, B. La Fontaine, H.A. Baldis, G.D. Enright, D.M. Villeneuve, J.C. Kieffer, M. Nantel, H. Pépin, *X-Ray Lasers*, Inst. Phys. Conf. Ser. No. 125, IOP Publishing, 1992, p. 347.
82. P.D. Gasparyan, F.A. Starikov, A.N. Starostin, Phys. Uspekhi, **41** (1998) 761.
83. R.A. London, M. Strauss, M.D. Rosen, Phys. Rev. Lett., **65** (1990) 563.
84. R.A. London, Phys. Fluids B, **5** (1993) 2707.
85. R. Smith, A. MacPhee, G. Tallents, Ph. Zeitoun, F. Albert, A. Carillon, P. Jaeglé, G. Jamelot, C.L.S. Lewis, A. Klisnick, M. Maillard, D. Ros, S. Sebban, Central Laser Facility, R.A.L. Annual Report, 1996–1997, p. 36.
86. M.H. Key, W. Blyth, G. Cairns, A.R. Damerell, A.E. Dangor, C.N. Danson, J.M. Evans, G.J. Hirst, M. Holden, C.J. Hooker, J. Houliston, J. Krishnan, C.L.S. Lewis, J.M.D. Lister, A.G. McPhee, Z. Najmudin, D. Neely, P.A. Norreys, A.A. Offenberger, K. Osvay, G.J. Pert, S.G. Preston, S.A. Ramsden, I.N. Ross, W. Sibbet, G.J. Tallents, C. Smith, J.S. Wark, J. Zhand, SPIE Proc., **2012** (1993) 22.
87. A. Dulieu, *X-Ray Lasers*, 1992, p. 243, Inst. Phys. Conf. Ser. No. 125, IOP Publishing, 1992, p. 243.
88. P.B. Holden, S.B. Healy, M.T.M. Lightbody, G.J. Pert, J.A. Plowes, A.E. Kingston, E. Robertson, C.L.S. Lewis, D. Neely, J. Phys. B, **27** (1994) 341.

89. J.A. Plowes, G.J. Pert, S.B. Healy, D.T. Toft, Opt. Quant. Electronics, **28** (1996) 219.
90. M. Born, E. Wolf, *Principles of Optics*, 5th edition, Pergamon Press, New York, 1975, Section 3.2.
91. R.A. London, Phys. Fluids, **31** (1988) 184.
92. S. Jacquemot, *X-Ray Lasers*, 1994; AIP Conf. Proc. **332** (1995) 279.
93. R.S. Craxton, LLE Rev., **38** (1989) 88; Laboratory for Laser Energetic, University of Rochester, New York; 19th Annual Anomalous Absorption Conference, Durango, CO, 1989.
94. T. Boehly, R.S. Craxton, R. Epstein, M. Russotto, B. Yaakobi, Optics Comm., **79** (1990) 57.
95. A. Dulieu, S. Jacquemot, *X-Ray Lasers*, Inst. Phys. Conf. Ser. No. 125, IOP Publishing, 1992, p. 239.
96. D. Desenne, L. Berthet, J.L. Bourgade, J. Bruneau, A. Carillon, A. Decoster, A. Dulieu, H. Dumont, S. Jacquemot, P. Jaeglé, G. Jamelot, M. Louis-Jacquet, J.P. Raucourt, C. Reverdin, J.P. Thébault, G. Thiel, *X-Ray Lasers*, Inst. Phys. Conf. Ser. No. 116, IOP Publishing, 1990, p. 351.
97. E.E. Fill, Opt. Comm., **67** (1988) 441; Proceedings of the OSA Topical Meeting on Short Wavelength Coherent Radiation, Optical Society of America, Washington, DC, Vol. 2, 1988, p. 78.
98. J. Nilsen, B.J. MacGowan, L.B. Da Silva, J.C. Moreno, Phys. Rev. A, **48** (1993) 46824.
99. L.W. Casperon, A. Yariv, IEEE J. Selected Topics Quant. Electron., **8** (1972) 8.
100. L.W. Casperon, J. Appl. Phys., **48** (1977) 256.
101. G.J. Pert, J. Opt. Soc. Am. B, **11** (1994) 1425.
102. G.J. Pert, S.B. Healy, S. McCabe, P.A. Simms, *X-Ray Lasers*, Phys. Conf. Ser. No. 159, IOP Publishing, 1998, p. 371.
103. P.B. Holden, B. Rus, G.J. Pert, Phys. Rev. A, **52** (1995) 4107.
104. A. Carillon, H.Z. Chen, P. Dhez, L. Dwivedi, J. Jacoby, P. Jaeglé, G. Jamelot, Z. Zhang, M.H. Key, A. Kidd, A. Klisnick, R. Kodama, J. Krishnan, C.L.S. Lewis, D. Neely, P. Norreys, D. O'Neill, G.J. Pert, S.A. Ramsden, J.P. Raucourt, G.J. Tallents, J. Uhomoibhi, Phys. Rev. Lett., **68** (1992) 2917.
105. P. Jaeglé, A. Carillon, H.Z. Chen, P. Dhez, L. Dwivedi, J. Jacoby, G. Jamelot, Z. Zhang, M.H. Key, A. Kidd, A. Klisnick, R. Kodama, J. Krishnan, C.L.S. Lewis, D. Neely, P. Norreys, D. O'Neill, G.J. Pert, S.A. Ramsden, J.P. Raucourt, G.J. Tallents, J. Uhomoibhi, *X-Ray Lasers*, Inst. Phys. Conf. Ser. No. 125, IOP Publishing, 1992, p. 1.
106. J.A. Koch, B.J. MacGowan, L.B. Da Silva, D.L. Matthews, J.H. Underwood, P.J. Batson, S. Mrowka, Phys. Rev. Lett. **68** (1992) 3291.
107. J.A. Koch, B.J. MacGowan, L.B. Da Silva, D.L. Matthews, J.H. Underwood, P.J. Batson, R.W. Lee, R.A. London, S. Mrowka, Phys. Rev. A, **50** (1994) 1877.
108. C. Garrison, H. Nathel, R.Y. Chiao, J. Opt. Soc. Am. B, **5** (1988) 1528.
109. G. Hazak, A. Bar-Shalom, Phys. Rev. A, **38** (1988) 1300.
110. M. Strauss, Phys. Fluids B, **1** (1989) 907.
111. R.A. London, M. Strauss, M.D. Rosen, Phys. Rev. Lett., **65** (1990) 563.
112. (a) P. Amendt, R.A. London, M. Strauss, Phys. Rev. A, **44** (1991) 7478; (b) P. Amendt, R.A. London, M. Strauss, Phys. Rev. A, **47** (1993) 4348.

113. J.C. Garrison, B. Ritchie, H. Nathel, C.K. Hong, L. Minner, Phys. Rev. A, **43** (1991) 4941.
114. F.A. Starikov, Quant. Electron., **24** (1994) 320.
115. R.A. London, Phys. Fluid B, **5** (1993) 2707.
116. R.P. Ratowsky, R.A. London, Phys. Rev. A, **51** (1995) 2361.
117. E.A. Watson, H.M. Gibbs, F.P. Mattar, M. Cormier, Y. Claude, S.L. McCall, M.S. Feld, Phys. Rev. A, **27** (1983) 345.
118. A. Crubellier, S. Liberman, P. Pillet, J. Phys. B, **19** (1986) 2959.
119. M. Gross, Proceedings of International Colloqium on *X-Ray Lasers*, J. Phys., **47** (1986) C6-223A.
120. A. Sureau, P.B. Holden, Phys. Rev. A, **52** (1995) 3110.
121. O. Larroche, D. Ros, A. Klisnick, A. Sureau, C. Möller, H. Guennou, Phys. Rev. A, **62** (2000) 043815-1.
122. J.A. Koch, B.J. MacGowan, L.B. Da Silva, D.L. Matthews, S. Mrowka, *X-Ray Lasers*, Inst. Phys. Conf. Ser. No. 125, IOP Publishing, 1992, p. 67.
123. Y. Kato, M. Yamanaka, H. Daido, H. Shiraga, H. Azuma, K. Murai, G. Yuan, E. Miura, T. Kanabe, M. Takagi, S. Nakai, C.L.S. Lewis, D.M. O'Neill, D. Neely, M. Niibe, N. Tsukamoto, Y. Fukuda, *X-Ray Lasers*, Inst. Phys. Conf. Ser. No. 125, IOP Publishing, 1992, p. 9.
124. J.W. Goodman, *Statistical Optics*, Chap. 5, Wiley, 1985.
125. L. Mandel, E. Wolf, *Optical Coherence and Quantum Optics*, Chap. 5, Cambridge University Press, Cambridge, UK, 1995.
126. E.E. Fenimore, T.M. Cannon, Appl. Opt., **17** (1978) 337.
127. J.E. Trebes, K.A. Nugent, S. Mwroka, R.A. London, T.W. Barbee, M.R. Carter, J.A. Koch, B.J. MacGowan, D.L. Matthews, L.B. Da Silva, G.F. Stone, M.D. Feit, Phys. Rev. Lett., **68** (1992) 588.
128. J.E. Trebes, *X-Ray Lasers*, Inst. Phys. Conf. Ser. No. 125, IOP Publishing, 1992, p. 265.
129. K.A. Nugent, J. Opt. Soc. Am. A, **8** (1991) 1574.
130. R.E. Burge, G.E. Slark, M.T. Browne, X.-C. Yuan, P. Charalambous, X.-H. Cheng, C.L.S. Lewis, A. MacPhee, D. Neely, J. Opt. Soc. Am. B, **14** (1997) 2742.
131. C.L.S. Lewis, R. Keenan, A. MacPhee, R.M.N. Rourke, G.J. Tallents, G. Eker, J.Y. Lin, S.J. Pestehe, R. Smith, J.S. Wark, E. Wolfrum, J. Zhang, G.J. Pert, S.P. McCabe, P.A. Simms, R.E. Burge, M.T. Browne, P. Charalambous, D. Neely, J. Collier, C.N. Danson, *X-Ray Lasers*, Phys. Conf. Ser. No. 159, IOP Publishing, 1998, p. 1.
132. Y. Liu, M. Seminario, F.G. Tomasel, C. Chang, J.J. Rocca, D.T. Attwood, Phys. Rev. A, **63** (2001) 033802.
133. F. Polack, D. Joyeux, J. Svatos, D. Phalippou, Rev. Sci. Instrum., **66** (1995) 2180.
134. F. Albert, D. Joyeux, P. Jaeglé, A. Carillon, J.P. Chauvineau, G. Jamelot, A. Klisnick, J.C. Lagron, D. Phalippou, D. Ros, S. Sebban, P. Zeitoun, Opt. Comm., **142** (1997) 184.
135. B. Rus, C.L.S. Lewis, G.F. Cairns, P. Dhez, P. Jaeglé, M.H. Key, D. Neely, A.G. MacPhee, S.A. Ramsden, C.G. Smith, A. Sureau, Phys. Rev. A., **51** (1995) 231.
136. F. Albert, B. Rus, Ph. Zeitoun, A. Carillon, P. Jaeglé, G. Jamelot, A. Klisnick, D. Ros, S. Sebban, *X-Ray Lasers*, Inst. Phys. Conf. Ser. No. 151, IOP Publishing, 1996, p. 427.

137. M.C. Marconi, J.L.A. Chila, C.H. Moreno, B.R. Benware, J.J. Rocca, Phys. Rev. Lett., **79** (1997) 2799.
138. J. Nilsen, J.H. Scofield, Phys. Scripta, **49** (1994) 588.
139. B.J. MacGowan, S. Maxon, L.B. Da Silva, D.J. Fields, C.J. Keane, D.L. Matthews, A.L. Osterheld, J.H. Scofield, G Shimkaveg, G.F. Stone, Phys. Rev. Lett., **65** (1990) 420.
140. H. Daido, S. Ninomiya, M. Tagaki, Y. Kato, J. Opt. Soc. Am. B, **16** (1999) 296
141. A.V. Vinogradov, V.N. Shlyaptsev, Sov. J. Quant. Electron., **13** (1983) 1511.
142. U. Feldman, J.F. Seely, A.K. Bathia, J. Appl. Phys, **56** (1984) 2475.
143. M. Cornille, J. Dubau, S. Jacquemot, J. Phys., **47** (1986) C-6 357.
144. B.L. Whitten, A.U. Hazi, M.H. Chen, P.L. Hagelstein, Phys. Rev. A, **33** (1986) 2171.
145. P. Hagelstein, J. Phys. B, **20** (1987) 5785.
146. P.L. Hagelstein, S. Dalhed, Phys. Rev. A, **37** (1988) 1357.
147. P. Beiersdorfer, S. von Goeler, M. Bitter, E. Hinnov, R. Bell, S. Bernabei, J. Felt, K.W. Hill, R. Hulse, J. Stevens, S. Suckewer, J. Timberlake, A. Wouters, M.H. Chen, J.H. Schofield, D.D. Dietrich, M. Gerassimenko, E. Silver, R.S. Walling, P.L. Hagelstein, Phys. Rev. A, **37** (1988) 4153.
148. B.L. Whitten, R.A. London, R.S. Walling, J. Opt. Soc. Am. B, **5** (1988) 2537.
149. M. Cornille, J. Dubau, S. Jacquemot, Atomic Data Nuc. Data Tables, **58** (1994) 1.
150. A.E. Kingston, *X-Ray Lasers*, Inst. Phys. Conf. Ser. No. 116, IOP Publishing, 1990, p. 289.
151. L. Hagelstein, Phys. Rev., **34** (1986) 874.
152. E. Behar, P. Mandelbaum, J.L. Schwob, A. Bar-Shalom, J. Oreg, W.H. Goldstein, Phys. Rev. A, **52** (1995) 3770.
153. H. Daido, S. Ninomiya, T. Imani, Y. Okaichi, M. Takagi, R. Kodama, H. Takabe, Y. Kato, F. Koike, J. Nilsen, K. Murai, Int. J. Modern Phys. B, **11** (1997) 9.
154. Y. Li, G. Pretzler, L. Peixiang, E.E. Fill, Phys. Rev. A, **53** (1996) R652.
155. A. Dasgupta, K.G. Whitney, M. Blaha, M. Buie, Phys. Rev. A, **46** (1992) 5973.
156. M.D. Rosen, R.A. London, P.L. Hagelstein, Phys. Fluids, **31** (1988) 666.
157. S. Maxon, P. Hagelstein, J. Scoffield, Y. Lee, J. Appl. Phys. **59** (1986) 293.
158. S. Maxon, S. Dahled, P.L. Hagelstein, R.A. London, B.J. MacGowan, M.D. Rosen, G. Charatis, G. Bush, Phys. Rev. Lett. **63** (1989) 236.
159. S. Maxon, K.G. Estabrook, M.K. Prasad, A.L. Osterheld, R.A. London, D.C. Eder, Phys. Rev. Lett., **70** (1993) 2285.
160. R.A. London, M.D. Rosen, Phys. Fluids, **29** (1986) 3813.
161. J.H. Hunter, R.A. London, Phys. Fluids, **31** (1988) 3102.
162. M. Nantel, J.C. Kieffer, B. La Fontaine, H. Pépin, Phys. Fluids B, **5** (1993) 1.
163. P.V. Nickles, M. Schnürer, M.P. Kalachnikov, I. Will, W. Sandner, Proc. SPIE, **2520** (1995) 373.
164. P.V. Nickles, V.N. Shlyaptsev, M.P. Kalachnikov, M. Schnürer, W. Sandner, Phys. Rev. Lett., **78** (1997) 2748.
165. D.L. Matthews, M. Eckart, D. Eder, P. Hagelstein, A. Hazi, R.A. London, S. Maxon, D. Nilson, T. Phillips, M. Rosen, J. Scofield, G.M. Shimkaveg, R. Stewart, J. Trebbes, D. Whelan, B. Whitten, J. Woodworth, S. Brown,

Proceedings of International Colloquium on X-Ray Lasers, edited by P. Jaeglé and A. Sureau, J. Phys., **47** (1986) **C6-**1.
166. D.J. Fields, R.S. Walling, A.R. Fry, G.M. Shimkaveg, T.W. Phillips, A.L. Oesterheld, B.J. MacGowan, L.B. Sa Silva, R.E. Stewart, W.H. Goldstein, D.L. Matthews, M.J. Eckart, *X-Ray Lasers*, Inst. Phys. Conf. Ser. No. 116, IOP Publishing, 1990, p. 131.
167. T.N. Lee, E.A. McLean, R.C. Elton, Phys. Rev. Lett. **59** (1987) 1185.
168. R.C. Elton, T.N. Lee, E.A. McLean, J. Phys., **48** (1987) C9-359.
169. G.D. Enright, D.M. Villeneuve, J. Dunn, H.A. Baldis, J.C. Kieffer, H. Pepin, M. Chaker, P.R. Herman, J. Opt. Soc. Am. B, **8** (1991) 2047.
170. D. Naccache, A. Decoster, S. Jacquemot, M. Louis-Jacquet, C. J. Keane, B.J. MacGowan, D.L. Matthews, Phys. Rev. A, **42** (1990) 3027.
171. D. Benredjem, A. Sureau, M. Cornille, J. Dubeau, J. Quant. Spectro. Rad. Transf., **65** (2000) 751.
172. D. Benredjem, C. Mosse, H. Guennou, A. Sureau, A. Demir, B. Talin, C. Moller, J. Phys. B, **33** (2000) 2295.
173. D.M. O'Neill, C.L.S. Lewis, D. Neely, J. Uhomoibhi, M.H. Key, A. MacPhee, G.J. Tallents, S.A. Ramsden, A. Rogoyski, E.A. McLean, G.J. Pert, Opt. Comm., **75** (1990) 406.
174. C.L.S. Lewis, D. Neely, J. Uhomoibhi, D.M. O'Neill, S.A. Ramsden, G.J. Tallents, Y.A. Hadithi, M.H. Key, S.J. Rose, G.J. Pert, *X-Ray Lasers*, Inst. Phys. Conf. Ser. No. 116, IOP Publishing, 1990, p. 231.
175. S. Wang, Y. Gu, G. Zhou, S. Yu, S. Fu, Y. Ni, J. Wu, Z. Zhou, G. Han, Z. Tao, Z. Lin, S. Wang, W. Chen, D. Fan, G. Zhang, J. Zheng, H. Peng, T. Zhang, Y. Shao, J. Opt. Soc. Am. B, **9** (1992) 360.
176. M.K. Inal, J. Dubau, J. Phys. B, **20** (1987) 4221.
177. J.C. Kieffer, J.P. Matte, M. Chaker, Y. Beaudoin, C.Y. Chien, S. Coe, G. Mourou, J. Dubau, M.K. Inal, Phys. Rev. E., **48** (1993) 4648.
178. J. Dubau, M.K. Inal, A.M. Urnov, Phys. Scripta, **T65** (1996) 179.
179. D. Benbredjem, A. Sureau, C. Möller, Phys. Rev. A, **55** (1997) 4576.
180. D. Benbredjem, A. Sureau, B. Rus, C. Möller, Phys. Rev. A, **56** (1997) 5112.
181. L.B. Da Silva, B.J. MacGowan, S. Mrowka, J.A. Koch, R.A. London, D.L. Matthews, J.H. Underwood, Optics Lett., **18** (1993) 1174.
182. P.B. Holden, M. Nantel, B. Rus, A. Sureau, J. Phys. B, **28** (1995) 1369.
183. D.J. Fields, R.S. Walling, G.M. Shimkaveg, B.J. MacGowan, L.B. Da Silva, J.H. Scofield, A.L. Osterheld, T.W. Phillips, M.D. Rosen, D.L. Matthews, W.H. Goldstein, R.E. Stewart, Phys. Rev. A, **46** (1992) 1606S.
184. B.J. MacGowan, S. Maxon, P.L. Hagelstein, C.J. Keane, R.A. London, D.L. Matthews, M.D. Rosen, J.H. Scofield, D.A. Whelan, Phys. Rev. Lett., **59** (1987) 2157.
185. B.J. MacGowan, L.B. Da Silva, D.J. Fields, A.R. Fry, C.J. Keane, J.A. Koch, D.L. Matthews, S. Maxon, S. Mrowka, A.L. Osterheld, J.H. Scofield, G. Shimkaveg, *X-Ray Lasers*, Inst. Phys. Conf. Ser. No. 116, IOP Publishing, 1990, p. 221.
186. D. Naccache, J.L. Bourgade, P. Combis, C.J. Keane, J.P. Le Breton, M. Louis-Jacquet, B.J. MacGowan, D.L. Matthews, J.P. Perrine, G. Thiell, Laser Particle Beams, **9** (1991) 493.
187. G.D. Enright, J. Dunn, D.M. Villeneuve, S. Maxon, H.A. Baldis, A.L. Osterheld, B. La Fontaine, J.C. Kieffer, M. Nantel, H. Pépin, *X-Ray Lasers*, Inst. Conf. Ser. No. 125, IOP Publishing, 1992, p. 45.

188. T. Boehly, M. Russoto, R.S. Craxton, R. Epstein, B. Yaakobi, L.B. Da Silva, J. Nilsen, E.A. Chandler, D.J. Fields, B.J. MacGowan, D.L. Matthews, J.H. Scofield, G. Shimkaveg, Phys. Rev. A, **42** (1990) 692.
189. R. Kodama, D. Neely, Y. Kato, H. Daido, K. Murai, G. Yuan, A. MacPhee, C.L.S. Lewis, Phys. Rev. Lett., **73** (1994) 3215.
190. H. Daido,Y. Kato, K. Murai, S. Ninomiya, R. Kodama, G. Yuan, Y. Oshikane, M. Takagi, H. Takabe, F. Koike, Phys. Rev. Lett., **75** (1995) 1074.
191. L. Yuelin, G. Pretzler, L. Peixiang, E.E. Fill, Phys. Rev. A, **53** (1996) R652.
192. G.F. Cairns, M.J. Lamb, C.L.S. Lewis, A.G. MacPhee, D. Neely, P. Norreys, M.H. Key, C. Smith, S.B. Healy, P.B. Holden, G. Pert, J.A. Plowes, *X-Ray Lasers*, 1994; AIP Conf. Proc., **332** (1995) 289.
193. G.F. Cairns, C.L.S. Lewis, M.J. Lamb, A.G. MacPhee, D. Neely, P. Norreys, M.H. Key, S.B. Healy, P.B. Holden, G. Pert, J.A. Plowes, G.J. Tallents, A. Demir, Opt. Comm., **123** (1996) 777.
194. J.E. Balmer, R. Tommasini, F. Löwenthal, IEEE J. Selected Topics Quant. Electron., **5** (1999) 1435.
195. Z. Zhe, C.L. Yan, W.Y. Gang, Q. Yi, Acta Phys. Sin., **49** (2000) 527.
196. M. Nantel, A. Klisnick, G. Jamelot, P.B. Holden, P. Jaeglé, Ph. Zeitoun, G. Tallents, A.G. MacPhee, C.L.S. Lewis, SPIE Proc., **2520** (1995) 145; Optics Lett., **20** (1995) 2333.
197. M. Nantel, A. Klisnick, G. Jamelot, P.B. Holden, B. Rus, A. Carillon, P. Jaeglé, Ph. Zeitoun, G. Tallents, A.G. MacPhee, C.L.S. Lewis, S. Jacquemot, L. Bonnet, Phys. Rev. E, **54** (1996) 2852.
198. Jacquemot, L. Bonnet, SPIE Proceeding, **2520** (1995) 169.
199. A.G. MacPhee, C.L.S. Lewis, P.J. Warwick, I. Weaver, P. Jaeglé, A. Carillon, G. Jamelot, A. Klisnick, B. Rus, Ph. Zeitoun, M. Nantel, P. Goedkindt, S. Sebban, G.J. Tallents, A. Demir, M. Holden, J. Krishnan, Opt. Comm., **133** (1997) 525.
200. B. Rus, P. Zeitoun, T. Mocek, S. Sebban, M. Kálal, A. Demir, G. Jamelot, A. Klisnick, B. Králiková, J. Skála, G.J. Tallents, Phys. Rev. A, **56** (1997) 4229.
201. E.A. McLean, T.N. Lee, J.A. Stamper, C.K. Manka, H.R. Griem, J. Opt. Soc. Am. B, **9** (1992) 350.
202. P.J. Warwick, C.L.S. Lewis, S. McCabe, A.G. MacPhee, A. Behjat, M. Kurkcuoglu, G.J. Tallents, D. Neely, E. Wolfrum, S.B. Healy, G.J. Pert, Opt. Comm., **144** (1997) 192.
203. P. Jaeglé, A. Carillon, P. Dhez, P. Goedtkindt, G. Jamelot, A. Klisnick, B. Rus, *X-Ray Lasers*, 1994; AIP Conf. Proc. **332** (1995) 25.
204. B. Rus, A. Carillon, P. Dhez, B. Gauthé, P. Goedtkindt, P. Jaeglé, G. Jamelot, A. Klisnick, M. Nantel, A. Sureau, P. Zeitoun, *X-Ray Lasers*, 1994; AIP Conf. Proc., **332** (1995) 152.
205. B. Rus, A. Carillon, P. Dhez, P. Jaeglé, G. Jamelot, A. Klisnick, M. Nantel, P. Zeitoun, Phys. Rev. A, **55** (1997) 3858.
206. B. Rus, T. Mocek, A.R. Präg, M. Kozlova, G. Jamelot, A. Carillon, D. Ros, D. Joyeux, D. Phallipou, Phys. Rev. A, **66** (2002) 63806.
207. P.B. Holden, B. Rus, Opt. Comm., **119** (1995) 424.
208. P. Jaeglé, S. Sebban, A. Carillon, G. Jamelot, A. Klisnick, P. Zeitoun, B. Rus, F. Albert, D. Ros, *X-Ray Lasers*, Inst. Phys. Conf. Ser. No. 151, IOP Publishing, 1996, p. 1.

209. S. Wang, G. Zhou, G. Zhang, J. Zheng, S. Chunyu, *X-Ray Lasers*, 1994; AIP Conf. Proc., **332** (1995) 293.
210. J. Nilsen, Y. Li, P. Lu, J.C. Moreno, E.E. Fill, Opt. Comm., **124** (1996) 287.
211. J. Nilsen, J.C. Moreno, Phys. Rev. Lett., **74** (1995) 3376.
212. J.C. Moreno, R.C. Cauble, P. Celliers, L.B. Da Silva., J. Nilsen, A.S. Wan, Proc. SPIE, **2520** (1995) 97.
213. J. Zhang, P.J. Warwick, E. Wolfrum, M.H. Key, C. Danson, A. Demir, S. Healy, D.H. Kalantar, N.S. Kim, C.L.S. Lewis, J. Lin, A.G. MacPhee, D. Neely, J. Nisen, G.J. Pert, R. Smith, G.J. Tallents, J.S. Wark, Phys. Rev. A, **54** (1996) R4653.
214. A.R. Präg, F. Loewenthal, J.E. Balmer, Phys. Rev. A, **54** (1996) 4585.
215. J. Nilsen, J.C. Moreno, B.J. MacGowan, J.A. Koch, Appl. Phys. B, **57** (1993) 309.
216. E.E. Fill, Y. Li, G. Pretzler, IEEE J. Selected Topics Quant. Electron., **1** (1995) 958.
217. E.E. Fill, Y. Li, D. Schlögl, J. Steingruber, J. Nilsen, Optics Lett., **20** (1995) 374.
218. Y. Li, G. Pretzler, E.E. Fill, Phys. Rev. A, **51** (1995) R4341.
219. Y. Li, G. Pretzler, E.E. Fill, Phys. Rev. A, **52** (1995) R3433.
220. Y. Li, G. Pretzler, E.E. Fill, Optics Lett., **20** (1995) 1026.
221. Y. Li, G. Pretzler, E.E. Fill, Appl. Phys. B, **63** (1996) 125.
222. Y. Li, G. Pretzler, J. Nilsen, E.E. Fill, Optics Commun., **119** (1995) 557.
223. E.E. Fill, Y. Li, G. Pretzler, D. Schlögl, J. Steingruber, J. Nilsen, Proc. SPIE, **2520** (1995) 134.
224. A.R. Präg, F. Loewenthal, R. Tommasini, J.E. Balmer, Appl. Phys. B, **66** (1998) 561; M.D. Rosen, R.A. London, P.L. Hagelstein, Phys. Fluids, **31** (1988) 666.
225. S. Sebban, D. Ros, A.G. MacPhee, F. Albert, A. Carillon, P. Jaeglé, G. Jamelot, A. Klisnick, C.L.S. Lewis, R. Smith, G.J. Tallents, Ph. Zeitoun, Proc. SPIE, **3156** (1997) 11.
226. H. Daido, Y. Kato, R. Kodama, K. Murai, G. Yuan, M. Takagi, H. Takabe, S. Nakai, C.H. Nam, I.W. Choi, D. Neely, A. MacPhee, *X-Ray Lasers*, 1994; AIP Conf. Proc. **332** (1995) 1.
227. J. Zhang, Y.Q. Gu, Y.T. Li, S.T. Chunyu, Y.L. You, W.Z. Huang, S.T. He, Y.L. He, L.Z. Lu, X.D. Yuan, X.F. Wei, C.F. Zhang, Proc. SPIE, **3776** (1999) 103.
228. J. Nilsen, Y. Li, J. Dun, T.W. Barbee Jr., A.L. Osterheld, *X-Ray Lasers*, 2000, J. Phys. IV, **11** (2001) Pr2-67.
229. R. Tommasini, F. Löwenthal, J.E. Balmer, Phys. Rev. A, **59** (1999) 1577.
230. H. Daido, S. Ninomiya, T. Imani, R. Kodama, K. Murai, Y. Kato, F. Koike, J. Nilsen, *X-Ray Lasers*, Inst. Phys. Conf. Ser. No. 151, IOP Publishing, 1996, p. 40.
231. A. Klisnick, D. Ros, P. Zeitoun, F. Albert, A. Carillon, P. Fourcade, S. Hubert, P. Jaeglé, G. Jamelot, C.L.S. Lewis, A. MacPhee, R. O'Rourke, R. Keenan, P. Nickles, K. Janulewicz, M. Kalachnikov, J. Warwick, J.C. Chanteloup, E. Salmon, C. Sauteret, J.P. Zou, D. Joyeux, D. Phalippou, *X-Ray Lasers*, Inst. Phys. Conf. Ser. No. 159, IOP Publishing, 1998, p. 107.

232. J. Zhang, A.G. MacPhee, J. Lin, E. Wolfrum, J. Nilsen, T.W. Barbee Jr., C. Danson, M.H. Key, C.L.S. Lewis, D. Neely, R.M.N. O'Rourke, G.J. Pert, R. Smith, G.J. Tallents, J.S. Wark, Proc. SPIE, **3156** (1997) 53.
233. Y. Li, G. Pretzler, P. Lu, E.E. Fill, Phys. Rev. A, **52** (1996) R652.
234. D. Ros, A. Klisnick, A. Carillon, P. Jaeglé, G. Jamelot, B. Rus, P. Zeitoun, S. Sebban, F. Albert, E. Alfred, *X-Ray Lasers*, Inst. Phys. Conf. Ser. No. 151, IOP Publishing, 1996, p. 50.
235. H. Daido, S. Ninomiya, T. Imani, R. Kodama, M. Takagi, Y. Kato, K. Murai, J. Zhang, Y. You, Y. Gu, Optics Lett., **21** (1996) 1.
236. R. Smith, G.J. Tallents, J. Zhang, G. Eker, S. McCabe, G.J. Pert, E. Wolfrum, *X-Ray Lasers*, 1998, p. 71, Phys. Conf. Ser. No. 159, IOP Publishing, 1998, p. 71; Phys. Rev. A, **59** (1999) R47.
237. H. Daido, S. Sebban, H. Tang, N. Sakaya, Y. Tohyama, T. Norimatsu, K. Mima, Y. Kato, S. Wang, Y. Gu, G. Huang, K. Murai, R. Butzbach, I. Uschmann, M. Vollbrecht, E. Förster, Proc. SPIE, **3776** (1999) 54.
238. J.H. Scofield, B.J. MacGowan, Phys. Scripta, **46** (1992) 361.
239. G.J. Tallents, G. Eker, F. Strati, S.J. Pestehe, J. Lin, R. Smith, S. Dobosz, A.G. MacPhee, C.L.S. Lewis, R.M.N. O'Rourke, R. Keenan, G.J. Pert, S. McCabe, D. Neely, R. Allot, Proc. SPIE, **3776** (1999) 75.
240. J. Zhang, A.G. MacPhee, J. Lin, E. Wolfrum, R. Smith, C. Danson, M.H. Key, C.L.S. Lewis, D. Neely, J. Nilsen, G.J. Pert, G.J. Tallents, J.S. Wark, P.J. Warwick, Phys. Lett. A, **234** (1997) 410.
241. J. Zhang, A.G. MacPhee, J. Lin, E. Wolfrum, R. Smith, C. Danson, M.H. Key, C.L.S. Lewis, D. Neely, J. Nilsen, G.J. Pert, G.J. Tallents, J.S. Wark, Science, **276** (1997) 1097.
242. R. Smith, G.J. Tallents, J. Zhang, G. Eker, S. McCabe, G.J. Pert, E. Wolfrum, Phys. Rev. A, **59** (1999) R47.
243. J. Zhang, A.G. MacPhee, J. Nilsen, J. Lin, T.W. Barbee Jr., C. Danson, M.H. Key, C.L.S. Lewis, D. Neely, R.M.N. O'Rourke, G.J. Pert, R. Smith, G.J. Tallents, J.S. Wark, E. Wolfrum, Phys. Rev. Lett., **78** (1997) 3856.
244. S. Sebban, H. Daido, N. Sakaya, Y. Kato, K. Murai, H. Tang, Y. Gu, G. Huang, S. Wang, A. Klisnick, Ph. Zeitoun, F. Koike, H. Takenaka, Phys. Rev. A, **61** (2000) 043810.
245. D. Ros, A. Klisnick, P. Fourcade, A. Carillon, G. Jamelot, P. Jaeglé, Ph. Zeitoun, S. Hubrt, S. Jacquemot, L. Bonnet, D. Joyeux, D. Phallipou, J. Phys. IV, France, **Pr2-11** (2001) 143.
246. V.N. Shlyaptsev, P.V. Nickles, T. Schlegel, M.P. Kalachnikov, A.L. Osterheld, Proc. SPIE, **2012** (1993) 111.
247. D. Strickland, G. Mourou, Opt. Comm., **56** (1985) 219.
248. M.P. Kalachnikov, P.V. Nickles, I. Will, F. Billhardt, M. Schnürer, Laser Particle Beams, **12** (1994) 463.
249. Yu.V. Afanasiev, V.N. Shlyaptsev, Sov. J. Quant. Electron., **19** (1989) 1606.
250. C.N. Danson, L.J. Barzanti, Z. Chang, A.E. Damerell, C.B. Edwards, S. Hancock, M.H.R. Hutchinson, M.H. Key, S. Luan, R.R. Mahadeo, I.P. Mercer, P. Norreys, D.A. Pepler, D.A. Rodkiss, I.N. Ross, M.A. Smith, R.A. Smith, P. Taday, W.T. Toner, K.W.M. Wigmore, T.B. Winston, R.W.W. Wyatt, F. Zhou, Opt. Comm., **103** (1993) 392.
251. J. Dunn, A.L. Osterheld, Y. Li, J. Nilsen, V.N. Shlyaptsev, IEEE J. Selected Topics Quant. Electron., **5** (1999) 1441.

252. J. Dunn, A.L. Osterheld, R. Shepherd, W.E. White, V.N. Shlyaptsev, R.E. Stewart, Phys. Rev. Lett., **80** (1998) 2825.
253. J. Dunn, Y. Li, A.L Osterheld, J. Nilsen, S.J. Moon, K.B. Fournier, J.R. Hunter, A.Ya. Faenov, T.A. Pikuz, V.N. Shlyaptsev, SPIE Proc., **3776** (1999) 2.
254. J.L. Collier, C.N. Danson, R.M. Allot, M.H.R. Hutchinson, C.L.S. Lewis, D. Neely, D.A. Pepler, T.B. Winstone, J. Zhang, *X-ray Lasers*, Inst. Phys. Conf. Ser. No. 159, IOP Publishing, 1998, p. 649.
255. C.L.S. Lewis, R. Keenan, A.G. MacPhee, B. Moore, R.M.N. O'Rourke, G.J. Tallents, S. Dobosz, J. Peschete, F. Strati, J.S. Wark, E. Wolfrum, G.J. Pert, S.P. MacCabe, P.A. Simms, R. Allot, J. Collier, C.N. Danson, A. Djaoui, D. Neely, Proc. SPIE, **3776** (1999) 293.
256. M.P. Kalachnikov, P.V. Nickles, M. Schnürer, W. Sandner, V.N. Shlyaptsev, C. Danson, D. Neely, E. Wolfrum, J. Zhang, A. Behjat, A. Demir, G.J. Tallents, P.J. Warwick, C.L.S. Lewis, Phys. Rev. A, **57** (1998) 4778.
257. J.C. Chanteloup, E. Salmon, C. Sauteret, A. Migus, P. Zeitoun, A. Klisnick, A. Carillon, S. Hubert, D. Ros, P. Nickles, M. Kalachnikov, J. Opt. Soc. Am. B, **17** (2000) 151.
258. F. Strati, G.J. Tallents, Phys. Rev. A, **64** (2001) 013807.
259. J. Kuba, A. Klisnick, D. Ros, P. Fourcade, G. Jamelot, J.L. Miquel, N. Blanchot, F. Wyart, Phys. Rev. A, **62** (2000) 043808.
260. A. Klisnick, J. Kuba, D. Ros, R. Smith, P. Fourcade, G. Jamelot, J.L. Miquel, J.F. Wyart, C. Chenais-Popovics, R. Keenan, S.J. Topping, C.L.S. Lewis, F. Strati, G.J. Tallents, D. Neely, R. Clarke, J. Collier, A.G. MacPhee, F. Bortolotto, P.V. Nickles, K.A. Janulewicz, *X-Ray Lasers*, 2000; J. Phys. IV (Paris), **11 Pr2** (2001) 11.
261. J. Nilsen, Y. Li, J. Dunn, J. Opt. Soc. Am. B, **17** (2000) 1084.
262. J. Dunn, A.L. Osterheld, Y. Li, J. Nilsen, J.R. Hunter, Y. Li, A.Ya. Faenov, V.N. Shlyaptsev, T.A. Pikuz, V.N. Shlyaptsev, *X-Ray Lasers*, 2000, J. Phys. IV (Paris), **11 Pr2** (2001) 19.
263. S.J. Moon, J. Dunn, A. Faenov, T. Pikuz, K.B. Fournier, A.L. Osterheld, V.N. Shlyaptsev, Y. Li, J. Nilsen, Proc. SPIE, **3776** (1999) 9.
264. P.J. Warwick, C.L.S. Lewis, M.P. Kalachnikov, P.V. Nickles, M. Schnürer, A. Behjat, A. Demir, G.J. Tallents, D. Neely, E. Wolfrum, J. Zhang, G.J. Pert, J. Opt. Soc. Am. B, **15** (1998) 1808.
265. J. Dunn, A.L. Osterheld, V.N. Shlyaptsev, Y. Li, J. Nilsen, R. Shepherd, L.B. Da Silva, *X-Ray Lasers*, Inst. Phys. Conf. Ser. No. 159, IOP Publishing, 1998, p. 51.
266. J.Y. Lin, G.J. Tallents, A.G. MacPhee, A. Demir, C.L.S. Lewis, R.M.N. O'Rourke, G.J. Pert, D. Ros, P. Zeitoun, Opt. Comm., **166** (1999) 211.
267. L. Yuelin, J. Nilsen, J. Dunn, A.L. Osterheld, A. Ryabtsev, S. Churilov, Phys. Rev. A, **58** (1998) R2-668P.
268. Y. Li, J. Dunn, J. Nilsen, T.W. Barbee Jr., A.L Osterheld, V. N. Shlyaptsev, J. Opt. Soc. Am. B, **17** (2000) 1098; SPIE Proc. **3776** (1999) 45.
269. R. Li, Z.Z. Xu, *X-Ray Lasers*, 2000; J. Phys. IV (Paris), **11 Pr2** (2001) 27.
270. T. Ozaki, H. Kuroda, R.A. Ganeev, A. Ishizawa, T. Kanai, *X-Ray Lasers*, AIP Conf. Proc., **641** (2002) 65.

271. T. Ozaki, R.A. Ganeev, A. Ishizawa, T. Kanai, H. Kuroda, Phys. Rev. Lett., **89** (2002) 253902.
272. R. Keenan, J. Dunn, P.K. Patel, D.F. Price, R.F. Smith, V.N. Shkyaptsev, Phys. Rev. Letters, **94** (2005) 103901.
273. S. Jacquemot, L. Bonnet, J.L. Miquel, S. Hulin, *X-Ray Lasers*, Inst. Phys. Conf. Ser. No. 159, IOP Publishing, 1998, p. 363.
274. A. Klisnick, J. Kuba, D. Ros, R. Smith, G. Jamelot, A. Carillon, Meas. Sci. Technol., **12** (2001) 1813.
275. A. Klisnick, J. Kuba, D. Ros, R. Smith, G. Jamelot, C. Chenais-Popovics, R. Keenan, S.J. Topping, C.L.S. Lewis, F. Strati, G.J. Tallents, D. Neely, R. Clarke, J. Collier, A.G. MacPhee, F. Bortolotto, P.V. Nickles, K.A. Janulewicz, Phys. Rev. A, **66** (2002) 033810.
276. Y. Abou-Ali, G.J. Tallents, M. Edwards, R.E. King, G.J. Pert, S.J. Pestehe, F. Strati, R. Keenan, C.L.S. Lewis, S. Topping, O. Guilbaud, A. Klisnick, D. Ros, R. Clarke, D. Neely, M. Notley, A. Demir, Optics Commun., **215** (2003) 397.
277. H. Tang, H. Daido, M. Kishimoto, K. Sukegawa, R. Tai, S. Mosesson, M. Tanaka, P. Lu, T. Kawachi, K. Nagashima, K. Nagai, T. Norimatsu, K. Murai, H. Takenaka, Y. Kato, K. Mima, K. Nishihara, Jpn. J. Appl. Phys., **42** (2003) 443.
278. J.J. Rocca, Rev. Sci. Instrum., **70** (1999) 3799.
279. V.N. Shlyaptsev, J.J. Rocca, A.L. Osterheld, SPIE Proc. **2520** (1995) 365.
280. J.J. Gonzalez, M. Frati, J.J. Rocca, V.N. Shlyaptsev, A.L. Osterheld, Phys. Rev. E, **65** (2002) 026404.
281. N.R. Pereira, J. Davis, J. Appl. Phys., **64** (1988) R1.
282. J.J. Rocca, M.C. Marconi, F.G. Tomasel, V.N. Shlyaptsev, J.L.A. Chilla, P.D. Clark, SPIE Proc. **2520** (1995) 201.
283. J.J. Rocca, M.C. Marconi, J.L.A. Chilla, P.D. Clark, F.G. Tomasel, V.N. Shlyaptsev, IEEE J. Select. Topics Quant. Electron., **1** (1995) 945.
284. F.G. Tomasel, V.N. Shlyaptsev, J.J. Rocca, Phys. Rev. A, **54** (1996) 2474.
285. J.J. Rocca, D.P. Clark, L.L.A. Chilla, V.N. Shlyaptsev, Phys. Rev. Lett., **77** (1996) 1476.
286. B.R. Benware, C.D. Machietto, C.H. Moreno, J.J. Roccan Phys. Rev. Lett., **81** (1998) 5804.
287. M. Frati, M. Seminario, J.J. Rocca, Opt. Lett., **25** (2000) 1022.
288. F.G. Tomasel, J.J. Rocca, V.N. Shlyaptsev, C.D. Macchietto, Phys. Rev. A, **55** (1997) 1437.
289. V.N. Shlyaptsev, J.J. Rocca, M.P. Kalachnikov, P.V. Nickles, W. Sandner, A.L. Osterheld, J. Dunn, D.C. Eder, SPIE Proc. **3156** (1997) 193.
290. K.A. Janulewicz, J.J. Rocca, F. Bortolotto, M.P. Kalachnikov, V.N. Shlyaptsev, W. Sandner, P.V. Nickles, Phys. Rev. A, **63** (2001) 33803.
291. S. Sakadzic, A. Rahman, M. Frati, F.G. Tomasel, J.J. Rocca, V.N. Shlyaptsev, A.L. Osterheld, SPIE Proc., **4505** (2001) 35.
292. P.B. Corkum, N.H. Burnett, F. Brunel, Phys. Rev. Lett., **62** (1989) 1259.
293. T.J. McIlrath, P.H. Bucksbaum, R.R. Freeman, M. Bashkansky, Phys. Rev. A, **35** (1987) 4611.

294. B.E. Lemoff, C.P.J. Barty, S.E. Harris, Optics Lett., **19** (1994) 569.
295. B.E. Lemoff, C.Y. Yin, C.L. Gordon III, C.P.J. Barty, S.E. Harris, Phys. Rev. Lett., **74** (1995) 1574.
296. S. Sebban, R. Haroutunian, Ph. Balcou, G. Grillon, A. Rousse, S. Kazamias, T. Marin, J.Ph. Rousseau, L. Notebaert, M. Pittman, J.P. Chambaret, A. Antonetti, D. Hulin, D. Ros, A. Klisnick, A. Carillon, P. Jaeglé, G. Jamelot, J.F. Wyart, Phys. Rev. Lett., **86** (2001) 3004.
297. S. Sebban, T. Mocek, D. Ros, L. Upcraft, P.H. Balcou, R. Haroutunian, G. Grillon, B. Rus, A. Klisnick, A. Carillon, G. Jamelot, C. Valentin, A. Rousse, J.Ph. Rousseau, L. Notebaert, M. Pittman, D. Hulin, Phys. Rev. Lett., **89** (2002) 253901.
298. S. Sebban, L. Upcraft, P.H. Balcou, M. Pittman, R. Haroutunian, G. Grillon, C. Valentin, A. Rousse, J.Ph. Rousseau, L. Notebaert, D. Hulin, J. Opt. Soc. Am. B, **20** (2003) 195.
299. P.H. Balcou, S. Sebban, R. Haroutunian, G. Grillon, J.Ph. Rousseau, A. Rousse, L. Notebaert, M. Pittman, J.P. Chambaret, D. Hulin, A. Klisnick, D. Ros, P. Jaeglé, A. Carillon, G. Jamelot, J.F. Wyart, *X-Ray Lasers*, 2000; J. Phys. IV (Paris), **11 Pr2** (2001) 175.
300. A.E. Siegman, *Lasers*, University of Science Books, Mill Valley, CA, 1986, p. 668.
301. Ph. Zeitoun, G. Faivre, S. Sebban, T. Mocek, A. Hallou, M. Fajardo, D. Aubert, Ph. Balcou, F. Burgy, D. Douillet, S. Kazamias, G. de Lachèze-Murel, T. Lefrou, S. le Pape, P. Mercère, H. Merdj, A.S. Morlens, J.P. Rousseau, C. Valentin. Nature, **431** (2004) 426.
302. J. Peyraud, N. Peyraud, J. Appl. Phys. **43** (1972) 2993.
303. A. Goltsov, A. Morozov, Y. Ping, I. Geltner, S. Suckewer, U. Feldman, T. Jones, C. Moore, J. Seely, P. Sprangle, A. Ting, R. Elton, K. Krushelnick, A. Zigler, *X-Ray Lasers*, 2000; J. Phys. IV (Paris), **11 Pr2** (2001) 165.
304. I. Geltner, Y. Ping, A. Morozov, S. Suckewer, *X-Ray Lasers*, AIP Conf. Proc. **6**41 (2002) 199.
305. D. Jacoby, G.J. Pert, S.A. Ramsden, L.D. Shorrock, G.J. Tallents, Opt. Comm., **37** (1981) 193.
306. P. Jaeglé, G. Jamelot, A. Carillon, C. Wehenkel, Jpn. J. Appl. Phys. **17** (1978) 483 (abstract).
307. G. Jamelot, P. Jaeglé, A. Carillon, A. Bideau, C. Möller, H. Guennou, A. Sureau, Proc. Int. Conf. Lasers, **81** (1982) 178.
308. P. Jaegle, G. Jamelot, A. Klisnick, A., Sureau, H. Guennou, AIP Conf. Proc., **119** (1984) 468.
309. G. Jamelot, A. Klisnick, A. Carillon, H. Guennou, A. Sureau, P. Jaeglé, J. Phys. B: At. Mol. Phys., **18** (1985) 4747.
310. C.L.S. Lewis, R. Corbett, D. O'Neill, C. Regan, S. Saadat, C. Chenais-Popovics, T. Tomie, J. Edwards, G.P. Kiehn, R. Smith, O. Willi, A. Carillon, H. Guennou, P. Jaegle, G. Jamelot, A. Klisnick, A. Sureau, M. Grande, C. Hooker, M.H. Key, S.J. Rose, I.N. Ross, P.T. Rumsby, G.J. Pert, S.A. Ramsden, Plasma Phys. Controlled Fusion, **30** (1988) 35.
311. G.J. Tallents, J. Phys. B: Atom. Mol. Phys., **10** (1977) 1769.
312. G.J. Pert, J. Phys. B: Atom. Mol. Phys., **12** (1979) 2067.
313. G.J. Pert, G.J. Tallents, J. Phys. B: Atom. Mol. Phys., **14** (1981) 1525.

314. G.J. Tallents, Plasma Phys., **27** (1985) 1427.
315. W. Brunner, R. John, Th. Schlegel, Lasers Particles Beams, **6** (1988) 621.
316. G.J. Pert, S.J. Rose, Appl. Phys. B, **50**(1990) 307.
317. D.C. Eder, Phys. Rev. A, **1** (1989) 24.
318. D.C. Eder, M.D. Rosen, R.W. Lee, J.E. Trebes, N.M. Ceglio, M.J. Eckart, R.L. Kauffman, B.J. MacGowan, D.L. Matthwes, J. Opt. Am. Soc. B, **4** (1987) 1949.
319. P.B. Holden, G.J. Pert, J. Phys. B, **25** (1992) 3085.
320. D. Jacoby, G.J. Pert, L.D. Shorrock, G.J. Tallents, J. Phys. B: Atom. Mol. Phys., **15** (1982) 3557.
321. C. Chenais-Popovics, R. Corbett, C.J. Hooker, M.H. Key, G.P. Kiehn, C.L.S. Lewis, G.J. Pert, C. Regan, S.J. Rose, S. Sadaat, R. Smith, T. Tomie, O. Willi, Phys. Rev. Lett., **59** (1987) 2161.
322. M. Grande, M.H. Key, G. Kiehn, C.L.S. Lewis, G.J. Pert, S.A. Ramsden, G. Regan, S.J. Rose, R. Smith, T. Tomie, O. Willi, Opt. Comm., **74** (1990) 309.
323. Y. Kato, E. Miura, T. Tachi, H. Shigara, H. Nishimura, H. Daido, M. Yamanaka, T. Jitsuno, M. Takagi, P.R. Herman, H. Takabe, S. Nakai, C. Yamanaka, M.H. Key, G.J. Tallents, S.J. Rose, P.T. Rumsby, Appl. Phys. B, **50** (1990) 247.
324. D. Kim, C.H. Skinner, G. Umesh, S. Suckewer, Opt. Lett., **14** (1989) 665.
325. D. Kim, C.H. Skinner, A. Wouters, E. Valeo, D. Voorhees, S. Suckewer, J. Opt. Soc. Am. B, **6** (1989) 115.
326. S. Suckewer, C.H. Skinner, D. Kim, E. Valeo, D. Voorhees, A. Wouters, Phys. Rev. Lett., **57** (1986) 1004.
327. D. Kim, C.H. Skinner, A. Wouters, E. Valeo, D. Voorhees, S. Suckewer, Proceedings of the OSA Topical Meeting on Short Wavelength Coherent Radiation, OSA, 1988, p. 116.
327a. D.V. Korobkin, A. Goltsov, A. Morosov, S. Suckewer, Phys. Rev. Lett., **81** (1998) 1607.
328. A. Klisnick, H. Guennou, J. Viremont, J. Phys., **47** (1986) C6-345.
329. A. Sureau, H. Guennou, C. Möller, Europhysics. Lett., **5** (1988) 19.
330. D. Kim, C.H. Skinner, A. Wouters, E. Valeo, D. Voorhees, S. Suckewer, SPIE Proc., **875** (1988) 20.
331. H. Guennou, A. Klisnick, C. Möller, A. Sureau, J. Phys. (Paris), **50** (1989) C1-609.
332. M.H. Key, N. Tragin, S.J. Rose,
333. A. Klisnick, A. Sureau, H. Guennou, C. Möller, J. Viremont, Appl. Phys. B, **50** (1990) 153.
334. A. Klisnick, J. Viremont, N. Grandjouan, H. Guennou, A. Sureau, *X-Ray Lasers*, 1994; AIP Conf. Proc., **332** (1995) 137.
335. D. Benredjem, A. Calisti, A. Sureau, B. Talin, J. Quant. Radiat. Transfer, **55** (1996) 149.
336. A. Klisnik, A. Sureau, H. Guennou, C. Möller, J. Virmont, Appl. Phys. B, **50** (1990) 153; *X-Ray Lasers*, Inst. Phys. Conf. Ser. No. 116, IOP Publishing, 1990, p. 17.
337. P. Jaeglé, G. Jamelot, A. Carillon, A. Klisnick, A. Sureau, H. Gennou, J. Opt. Soc. Am. B, **4** (1987) 563.

338. P. Jaeglé, A. Carillon, P. Dhez, B. Gauthé, F. Gadi, G. Jamelot, A. Klisnick, Europhys. Lett., **7** (1988) 337.
339. J.C. Moreno, H.R. Griem, S. Goldsmidth, J. Knauer, Phys. Rev. A, **39** (1989) 6033.
340. Z.Z. Xu, Z.Q. Zhang, P.Z. Fan, S.S. Chen, L.H. Lin, P.X. Lu, X.P. Feng, X.F. Wang, J.Z. Zhou, A.D. Qian, Appl. Phys. B, **50** (1990) 147.
341. Z.Z. Xu, P.Z. Fan, L.H. Lin, Y.L. Li, X.F. Wang, R.X. Li, P.X. Lu, S.S. Han, L. Sun, A.D. Qian, Z.Q. Zhang, J.Z. Zhou, Phys. Rev. A, **49** (1994) 485.
342. H. Yashiro, T. Hara, K. Ando, F. Negishi, S. Ido, Y. Aoyagi, *X-Ray Lasers*, Inst. Phys. Conf. Ser. No. 116, IOP Publishing, 1990, p. 111.
343. T. Hara, H. Hirose, K. Ando, F. Negishi, Y. Aoyagi, *X-Ray Lasers*, Inst. Phys. Conf. Ser. No. 125, IOP Publishing, 1992, p. 97.
344. N. Yamaguchi, A. Ogata, C. Fujikawa, T. Ohchi, K. Okasaka, T. Hara, J. Electron Spectrosc., **101–103** (1999) 907.
345. N. Yamaguchi, Y. Okamoto, H. Yamagushi, T. Hara, *X-Ray Lasers*, AIP Conf. Proc. **641** (2002) 623.
346. T. Hara, N. Yamagushi, C. Fujikawa, K. Okasaka, T. Ohchi, *X-Ray Lasers*, Inst. Phys. Conf. Ser. No. 159, IOP Publishing, 1998, p. 203.
347. D. Benredjem, A. Sureau, P. Zeitoun, A. Klisnick, C. Möller, J. Quant. Spectrosc. Radiat. Tranfer., **56** (1996) 167.
348. G. Jamelot, A. Carillon, P. Dhez, B. Gauthé, P. Jaeglé, A. Klisnick, J.P. Raucourt, *X-Ray Lasers*, 1992, Inst. Phys. Conf. Ser. No. 125, IOP Publishing, 1992, p. 89; SPIE Proc., **1551** (1992) 65.
349. R. Li, Z. Zhang, Y. Liu, Z. Xu, Y. Cheng, Phys. Scripta, **56** (1997) 472.
350. J. Zhang, M.H. Key, Appl. Phys. B, **XX**, **58** (1994) 13.
351. J. Zhang, M.H. Key, P.A. Norreys, G.J. Tallents, A. Behjat, C. Danson, A. Demir, L. Dwivedi, M. Holden, P.B. Holden, C.L.S. Lewis, A.G. MacPhee, D. Neely, G.J. Pert, S.A. Ramsden, S.J. Rose, Y.F. Shao, O. Thomas, F. Walsh, Y.L. You, Phys. Rev. Lett., **74** (1995) 1335.
352. W.W. Jones, A.W. Ali, Appl. Phys. Lett., **26** (1975) 450; J. Appl. Phys. **48**, (1977) 3118; J. Phys. B, **11** (1978) 187.
353. N.H. Burnett, P.B. Corkum, J. Opt. Soc. Am. B, **6** (1989) 1195.
354. P. Amendt, D.C. Eder, S.C. Wilks, Phys. Rev. Lett., **66** (1991) 2589.
355. D.C. Eder, P. Amendt, S.C. Wilks, Phys. Rev. A, **45** (1992) 6761.
356. Y. Nagata, K. Midorikawa, S. Kubodera, M. Obara, H. Tashiro, K. Toyoda, Phys. Rev. Lett., **71** (1993) 3774.
357. D.V. Korobkin, C.H. Nam, S. Suckewer, A. Goltsov, Phys. Rev. Lett., **77** (1996) 5206.
358. Y. Avitzour, I. Geltner, A. Morosov, Y. Ping, S. Suckewer, *X-Ray Lasers*, AIP Conf. Proc., **641** (2002) 212.
359. S.J. Moon, D.C. Eder, Phys. Rev. A, **57** (1998) 1391.
360. S.J. Moon, F.A. Weber, P.M. Celliers, D.C. Eder, *X-Ray Lasers*, AIP Conf. Proc., **641** (2002) 342.
361. E.E. Fill, G. Pretzler, T. Shlegel, *X-Ray Laser*, 2000; J. Phys. IV, **11** (2001) Pr2-217.
362. G. Pretzler, T. Schlegel, E.E. Fill, D.C. Eder, Phys. Rev. E, **62** (2000) 5618.

363. D. Attwood, *Soft X-Rays and Extreme Ultraviolet Radiation*, Chapter 5, Cambridge University Press, Cambridge, UK, 1999.
364. J. Feldhaus, J. Krzywinski, E.L. Saldin, E.A. Schneidmiller, M.V. Yurkov, *X-Ray Lasers*, Inst. Phys. Conf. Ser. No. 159, IOP Publishing, 1998, p. 553.
365. K. Tiedtke, *X-Ray Lasers*, AIP Conf. Proc., **641** (2002) 379.
366. V. Ayvazyan, et al., Phys. Rev. Lett., **88** (2002) 104802/1-4.

Part III. High Harmonic Generation

10. Introduction

When the radiation pulse of an intense laser propagates in gas, the atoms of the gas emit odd harmonics of incident radiation. If λ is the incident wavelength, the outgoing radiation consists in a superposition of λ, $\lambda/3$, $\lambda/5, \ldots$, components. The experimental environment of high harmonic generation is similar to that described for OFI soft X-ray lasers in Section 7.6. The only important difference is that OFI lasers requires circularly polarized pump in order to strongly heat the free electrons produced by interaction with laser field, while high harmonic generation (HHG) is produced by linearly (or elliptically) polarized radiation which generates a low electron energy distribution (cf. Fig. 7.93, Section 7.6). Whereas OFI laser emission is a collective nonlinear response of gas to an intense pump beam, harmonic emission is a coherent nonlinear response of individual atoms [1]. The possibility to go from OFI laser to harmonic emission by a simple $\pi/2$ rotation of a $\lambda/4$ thin plate has been experimentally demonstrated [2].

The diagram of Figure 10.1 schematically depicts the experimental setup used to generate high order harmonics. The beam of a short-pulsed laser of frequency ω_{L} is focused across an atomic jet of rare gas. Harmonics of frequency $q\omega_{\mathrm{L}}$, generated in the direction of the incident beam, are spatially separated by an optical grating. A photon detector performs intensity measurements. An example of experimental spectrum obtained in Ne, at a pressure of 40 Torr, is displayed in Figure 10.2. Laser intensity at the beam focus was of 1.5×10^{15} W/cm^2 [3].

Figure 10.3 illustrates the main characteristics of high harmonic spectra, namely the harmonic odd parity, the rapid intensity decrease of the lowest order harmonics, followed by a long horizontal *plateau* and an abrupt cutoff to higher energies [4]. Odd parity is inherent to photon absorption in dipolar interaction because absorption of two (or any even number) photons cannot provide the simultaneous conservation of global energy and of global momentum, whereas absorption of three (or any odd photon number) can do it. The reader may find a number of high harmonic spectra obtained from atoms ([5–11]) and atomic ions ([12–19]) in published papers.

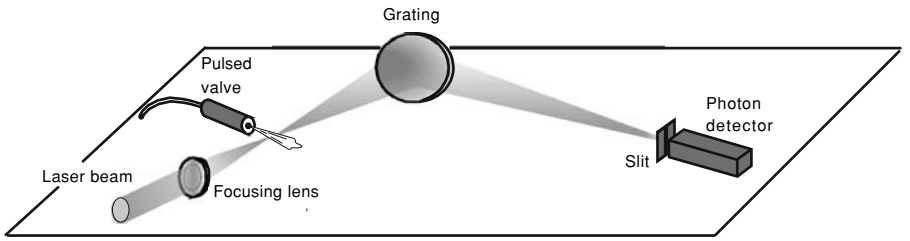

Fig. 10.1. Principle of an experimental for high harmonic generation. An intense pulsed laser beam is focused near a gas puf. The harmonic spectrum is analyzed and detected thanks to a diffraction grating and a photon detector.

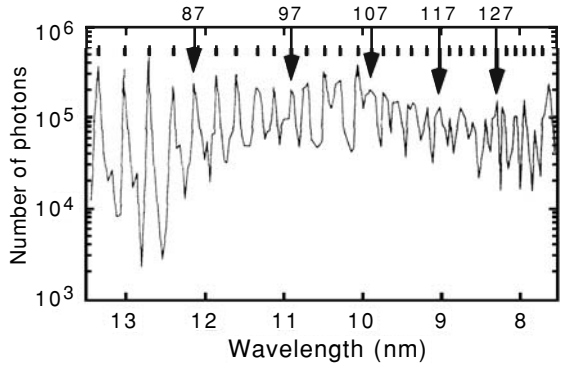

Fig. 10.2. Experimentally observed harmonic spectrum produced in Ne (from. [Ref. 3]).

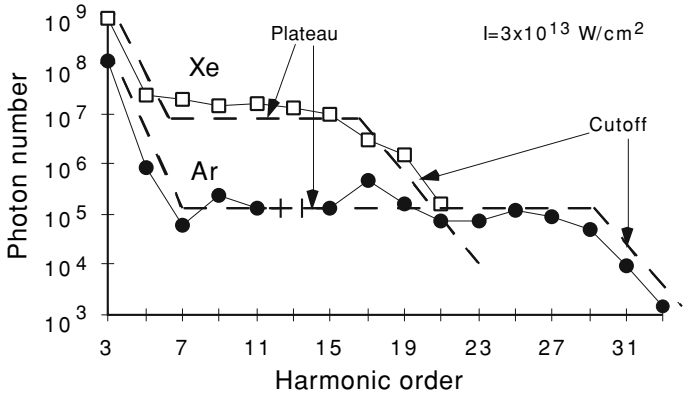

Fig. 10.3. Harmonic spectra obtained from Ar and Xe (Ref. [4]). Four general characteristics of harmonic spectra appear in the figure: the *odd parity* of harmonics, a fast intensity decrease for the lowest order harmonics, the presence of a region of approximately constant harmonic intensity, called *plateau,* and the spectral *cutoff* at higher energy.

For the position of the cutoff at plateau end, it is determined by the atom ionization potential, I_p, and by the additional ponderomotive potential, U_p. We have seen in Section 7.6 that U_p as form [Eq. (7.24)]

$$U_\mathrm{p} = \frac{e^2 E^2}{4m\omega^2} \tag{10.1}$$

for a linearly polarized oscillating field, $E \sin \omega t$. Replacing E and ω by laser intensity, I_L, and wavelength, λ, equation (10.1) reads

$$U_\mathrm{p} \simeq 9.33 \times 10^{-14} I_\mathrm{L} \lambda^2 \tag{10.2}$$

Now the initial velocity of an ionized electron varies, with the same frequency ω as above, as a function of the time t_0 at which this electron has been released in the electric field. Therefore the time-averaged kinetic energy of electrons must be a function of the phase ωt_0 of the field at time t_0. This energy is calculated to be [20]

$$\left\langle \frac{1}{2} m v^2 \right\rangle = \frac{e^2 E^2}{4m\omega^2} \left(1 + 2\cos^2 \omega t_0\right) \tag{10.3}$$

from which one sees that the energy gained by electrons oscillating in the field should be distributed between U_p and $3U_\mathrm{p}$. Consequently the maximum energy of harmonic photons is expected near a value E_max given by

$$E_\mathrm{max} = I_\mathrm{p} + \alpha U_\mathrm{p} \tag{10.4}$$

where

$$\alpha = 3$$

in the present classical model. Quantum calculation will confirm the linear scaling of the cutoff energy with both ionization potential and laser intensity and provide a better accuracy of the value of α. Single-atom calculations lead to [21, 22]

$$\alpha = 3.17 \tag{10.5}$$

which agrees with a large number of experimental observations. Nevertheless propagation effects for very high laser intensity have been shown to possibly reduce α up to a value of ~ 2 [23].

Another important parameter is the Keldish parameter

$$\gamma = \left(\frac{I_\mathrm{p}}{2U_\mathrm{p}}\right)^{1/2} \tag{10.6}$$

which limits the tunneling ionization regime to experimental conditions where $\gamma \ll 1$. Subject to this condition, the ionization rate is essentially determined by the instantaneous field strength.

11. Survey of the Theoretical Background

High harmonic generation is a process in which an atom absorbs q photons of energy ω_{L} and emits one photon of energy $q\omega_L$. Harmonics are emitted by electrons which (i) tunnel through the atomic potential barrier, (ii) are accelerated by the laser field toward the nucleus and recombine. The theory of the whole process involves a microscopic level, relative to the nonlinear behavior of single atoms in strong fields, and a macroscopic level which deals with the coherent propagation of harmonic radiation in the excited medium. It is clear that the HHG study is an appealing topic for improving the understanding of strong radiation–matter interaction. Neverthless, the goal of this section is no more than a brief introduction to both microscopic and macroscopic aspects of HHG considered as a coherent source of XUV radiation. The reader can access original works (see for instance [4, 24–28]).

11.1 Atoms in Strong Field

Calculation of classical trajectories of one electron in the field of a proton, on which superposes an oscillating laser field, provides a simplified but easily understandable description of the physics involved in HHG (see for instance [29]). An intense laser field increases considerably the eccentricity of an initial periodic Kepler orbit. Moreover electron trajectories involve oscillations at the laser frequency which modify the time-dependence of the dipole moment. Then several types of orbits appear according to initial conditions. Some trajectories rapidly lead to atom ionization while others remain bound during a long time. Calculation of time-dependent dipole for a number of trajectories (e.g. 10000), followed by time averaging their squared Fourrier transform, provides the spectrum of emission frequencies. Applied to a classical hydrogen atom, this model remarkably predicts the *plateau* where photon yield is roughly constant between the harmonics n°. 7–27 [30].

In terms of quantum mechanics, the description of the same process discerns three stages: tunneling ionization, electron propagation according

to discrete above-threshold ionization (ATI) channels, possibly terminated by laser-induced recombination with emission of harmonic radiation (see for instance [31]). In addition, the existence of macroscopic fields, one driving the above-threshold ionization, others being produced by electron recombination, requires that there be proper phase matching between these fields.

Let us start with the calculation of quantitative conversion efficiencies for each component of harmonic spectrum, which calls on quantum approach. In the case of weak fields ($I_{\mathrm{L}} \lessapprox 10^{13}$ W/cm^2) where the lowest order perturbation theory can be used, harmonic spectrum is described by an expansion of induced polarization in odd powers of electric field. The term corresponding to the qth harmonic is [24]

$$P_q = 2^{1-q} \chi_q E^q \tag{11.1}$$

where χ_q is the qth order nonlinear susceptibility (or atomic polarizability). Using the right term of equation (11.1), multiplied by N for a collection of atoms of density N, as source term in propagation equations shows that the harmonic intensity I_q follows the variation of the driving laser intensity I_{L}, according to relation

$$I_q \propto |F_q|^2 \, |N \chi_q|^2 \, I_{\mathrm{L}}^q \tag{11.2}$$

Equation (11.2) involves the nonlinearity of single atoms and of macroscopic medium as well. F_q is the so-called *phase-matching* factor which introduces the difference with the case of N independent atoms in this equation. Elements of phase matching theory shall be presented in the next section.

Weak field calculations shows that $|F_q|^2$ decreases rapidly with q. This can be observed in the left part of the curves in Figure 11.1, where intensities, calculated by L. Krause et al. for helium [32], are plotted versus harmonic order for two values of the excitation intensity I_{L}. A steep intensity decrease occurs before the plateau.

The N^2 factor in equation (11.2) accounts for the coherent character of harmonic emission. This N^2 dependence of harmonic intensities has been

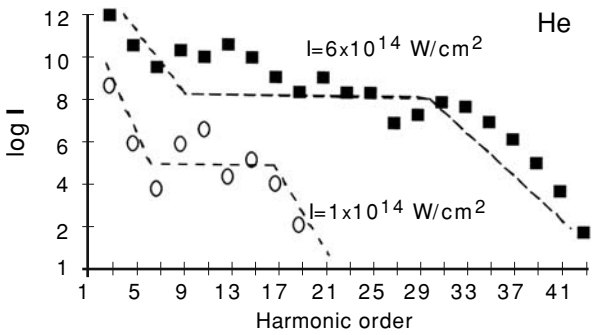

Fig. 11.1. Calculated intensity of harmonics produced in He (Ref. [32]).

experimentally confirmed measuring the number of photons in the 17th harmonic emitted by krypton as a function of gas pressure [33]. However, the lowest order perturbation theory does not predict the experimentally observed plateau of conversion efficiency. The main reason for this failure is that, under strong field, electrical susceptibilities acquire a laser intensity dependence, which perturbation calculations does not account for.

At very large laser intensity, a relevant method of HHG calculation is the direct integration of the time-dependent Schrödinger equation [34,35]. In the case of single-electron atomic calculations this equation can be written as

$$i\frac{\partial}{\partial t}\Psi\left(r,t\right)=\left(-\frac{1}{2}\frac{d^2}{dr^2}+\frac{l(l+1)}{2r^2}-\frac{1}{r}-E_0f(t)z\ \sin(\omega_Lt)\right)\Psi(rt) \tag{11.3}$$

where E_0 is the laser peak-amplitude. The field is polarized in z direction and $f(t)$ is the laser pulse envelope. For many-electron atoms, this equation allows separate calculations of l-dependent effective potentials as functions of the radial coordinate [4]. Time-dependent calculations treat the excitation of a single electron in the mean field of nucleus plus remaining electrons assumed to be frozen in their ground state. Let

$$P(t)=\langle\Psi^*(r.t)\left|z\right|\Psi\left(r.t\right)\rangle \tag{11.4}$$

be the time-varying induced dipole. The intensity of the harmonic spectrum is obtained by Fourier transform of $P(t)$, i.e.

$$P(\omega)=\frac{1}{T_1-T_2}\int_{T_1}^{T_2}dte^{-i\omega t}\left\langle\Psi^*(r.t)\left|z\right|\Psi\left(r.t\right)\right\rangle \tag{11.5}$$

where the $\mathrm{T}_1-\mathrm{T}_2$ interval covers a few cycles of laser pulse, and calculating

$$I(\omega)\propto\left|P\left(\omega\right)\right|^2 \tag{11.6}$$

Figure 11.1 shows that the spectral characteristics summarized in the introductory section (Chapter 10) are well reproduced by this theoretical approach, though propagation effects are not yet included in calculations. As expected the height of the plateau and the energy of the cutoff increase strongly with excitation intensity.

Another effect of excitation intensity increase is to ionize more neutral atoms, whose population thus decreases. Therefore higher intensities make to appear a *saturation* regime in which the fast increase of harmonic intensity comes to its end. For an example of detailed experimental study of saturation effects, in the case of Xe, the reader may refer to [36].

Results of calculations performed for the 13th harmonic produced in Xe, focusing the Gaussian beam of a 1064-nm wavelength laser into a 15-Torr jet, are shown in Figure 11.2 [45]. For the dashed curve, only single-atom effects, i.e. the dependence of atom polarizability on laser field intensity, and the phase mismatch between the 13th harmonic and the fundamental field, are considered. The solid curve is obtained by adding the ionization of the medium to other effects. The comparison of the two curves clearly shows

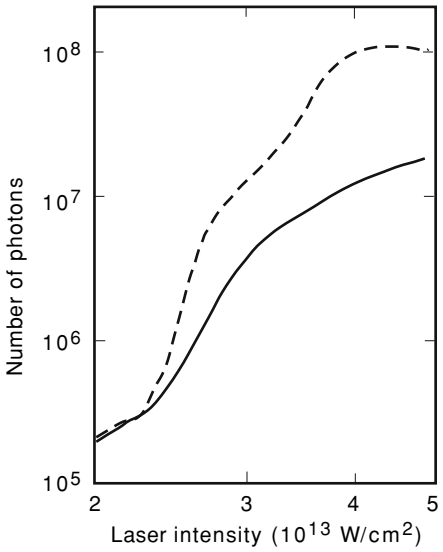

Fig. 11.2. Output of the 13th harmonic produced by Xe, as a function of the laser intensity, calculated including single atom effects and the phase mismatch between the harmonic and the fundamental field (dashed line) and adding the ionization of the medium (solid line).

that ionization, which results in the production of free electrons and in the corresponding depletion of the neutral atom population, originates the most part of saturation effect.

The path-integral approach recently developed [37–39], describes many interaction processes of strong-field with atoms in terms of "quantum orbits," i.e. space–time trajectories of participating electrons. In the first step of HHG, a bound electron undergoes tunnel ionization. In a second step it is accelerated by the laser field. The last step may be either electron recombination or rescattering. Therefore the probability amplitude of HHG (or ATI) can be represented as the sum of three terms corresponding to (1) the bound electron up to ionization at time t_i, (2) the ionized free electron between the times t_i and t_f, (3) the final process (recombination or rescattering) at time t_f. For each harmonic (or each high-order ATI), the total action S, which determines the phase of the amplitude probability, $a \exp[iS\mathbf{r}(\mathbf{t})/h]$, is represented by the sum

$$S\mathbf{r}(\mathbf{t}) = S_{\text{bound}}(t_i) + S_{\text{free}}(t_f, t_i) + S_{\text{final}}(t_f) \tag{11.7}$$

By requiring the action (11.7) to be stationary, one obtains equations which describe the dynamics of HHG.

A somewhat surrealist representation of HHG may help us to picture the second steps. In the space–time reference system of an electron freely

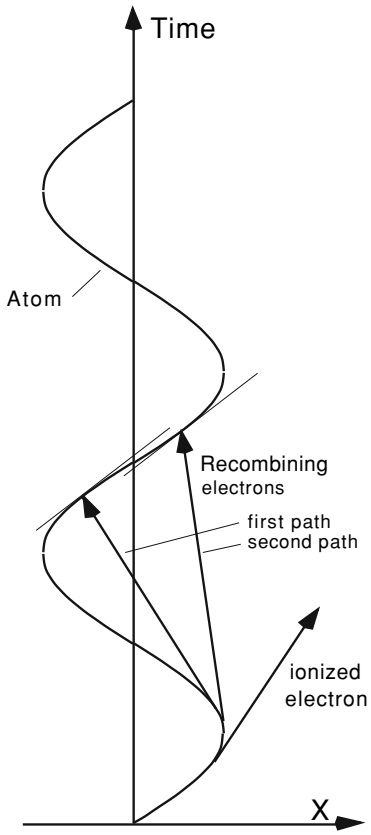

Fig. 11.3. Representation of the electron main quantum paths in the space–time reference system of an electron freely oscillating in the laser field. The trajectory of the emitting atom is the sine curve.

oscillating in laser field, the emitting atom has a sinusoidal trajectory along the vertical t axis. This is represented in Figure 11.3. Free electrons follow straight lines whose slopes correspond to electron drift-velocity. Ionized electrons appear in this space with a zero absolute velocity, which implies that the electron straight line is tangential to the atom sine trajectory at the moment of ionization.

One observes from this graph that an electron ionized before the maximum of the laser electric field during optical cycle will not re-encounter its parent ion. In contrast, an electron ionized after the top of the cycle will collide with ion, what involves a finite probability of radiative recombination. The repetition of this process every half-cycle results in a high-harmonic spectrum [40]. Moreover, one can observe that two trajectories will result in identical velocities at the moment of the collision. These trajectories are known as the two "main quantum paths" which contribute to harmonic generation. The

quantum interference between both paths induces laser-intensity-dependent oscillations in the field strength as well as in the phase of the harmonic.

HHG theory can be extended to an elliptically polarized laser field (see for instance [41] – [44]). It is not surprising that the harmonic strength may be found to decrease rapidly with ellipticity. The macroscopic fields generated by beam propagation are polarized with polarization degree close to unity. Numerical calculation of the rotation angle of the ellipse with respect to laser light gives an angle of $\sim 30^\circ$ in the case of neon [42].

11.2 Phase-Matching

Single-atom calculations are not sufficient to interpret all experimental data such as angular distributions, temporal and spectral profiles, and coherence, nor are they sufficient to optimize the generation of high harmonics. The coherence of the driving laser in a way is transferred to harmonics. However, far from being simple, this transfer has intermediary agents as the phases of the excited dipoles, which are laser-intensity-dependent, and the macroscopic properties of the emitting medium, in which harmonic beams will be built by a coherent addition process of the fields produced by the different atoms.

It has been established that, for each harmonic, both dipole and propagation effect can be accounted for by a field propagation equation in which the dipole is taken as source term [45]. In the paraxial approximation, namely assuming that fields propagate close to the laser axis oz, the equation corresponding to the qth harmonic has the form

$$\nabla_\perp^2 E_q + 2ik_q \frac{\partial E_q}{\partial z} = -4\pi \left(q\omega/c\right)^2 P_q \exp\left[-i \int_{-\infty}^{z} \Delta k_q \left(z'\right) dz'\right] \tag{11.8}$$

where $\Delta_\perp^2$ operates on the transverse coordinates. In this equation P_q is the induced polarization [Eq. (11.1)] and $k_q(z) = n_q(z) q\omega_q/c$ where $n_q(z)$ is the refractive index for the qth harmonic. Let us recall that a constant difference Δk between the wave vectors induces a phase difference

$$\Delta\phi = z\Delta k \tag{11.9}$$

after propagation along distance z. Therefore the term

$$\Delta k_q = k_q - qk_1 \tag{11.10}$$

in equation (11.8) characterizes the phase mismatch at a given point.

By replacing ω by $2\pi c/\lambda$ in the expression of k equation (11.10) becomes

$$\Delta k_q = 2\pi \left[\frac{n_q(z)}{\lambda_q} - q\frac{n(z)}{\lambda}\right] \tag{11.11}$$

where λ is the wavelength of the driving laser and n is the refractive index

for this wavelength. In the weak field limit $n_q(z)$ is defined by

$$n_q(z) = 1 + 2\pi N_{\mathrm{a}}(z)\chi_q(q\omega) \tag{11.12}$$

where $N_{\mathrm{a}}(z)$ is the atom density. From equation (11.1), the atomic dipole polarizability $\chi_q(q\omega)$ in the last term of equation (11.12) is given by

$$\chi_q(q\omega) = 2^{q-1}P_q(q\omega)/E^q \tag{11.13}$$

where $P_q(q\omega)$ is the Fourier coefficient of the qth term of the $P(\omega)$ expansion (11.5).

An important fact is that, for strong fields, the polarizability becomes dependent on the field intensity. Then $\chi_q(q\omega)$ is to be replaced by $\chi_q(q\omega, |E_1|^2)$ in equation (11.12), what means that phase mismatch becomes a function of the laser intensity. Furthermore, at very large intensity, atoms start to ionize and free electrons appear in gas. Corresponding terms are to be added to the atomic contribution in the second member of equation (11.12).

Intensity and phase calculations performed versus laser intensity by using the time-dependent Schrödinger equation (11.3) are illustrated in Figure 11.4 for the 45th harmonic of the 825-nm radiation generated by neon atoms [46]. For laser intensities $\lesssim 2 \times 10^{14}$ W/cm^2 the harmonic intensity collapses. This is the cutoff region. One sees the dipole phase, also called atomic phase ϕ_{at}, to vary more rapidly in the plateau than in the cutoff region. Intensity oscillations, which appear for $I \gtrsim 2 \times 10^{14}$ W/cm^2, i.e. in the plateau region, are quantum interference effects. When the beam propagation effects are included in intensity calculation, by using Equation (11.8) and (11.11), these oscillations are greatly reduced, what results in smoothing the intensity curve.

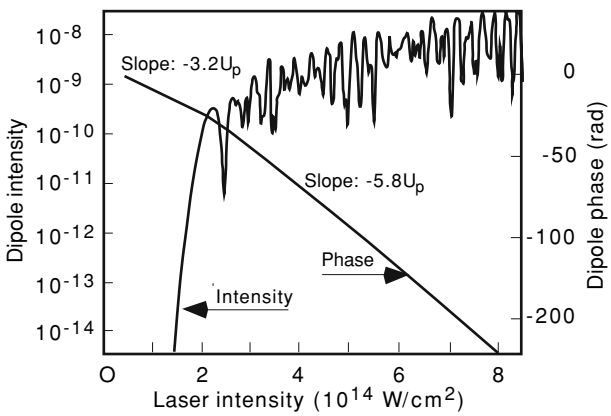

Fig. 11.4. Intensity and phase of the dipole emitting the 45th harmonic in neon, represented versus laser intensity ($\lambda_{\mathrm{L}} = 825$ nm). The cutoff occurs at an intensity of $\sim 2 \times 10^{14}$ W/cm^2. Note the change of the phase variation slope near the cutoff (Ref. [46]).

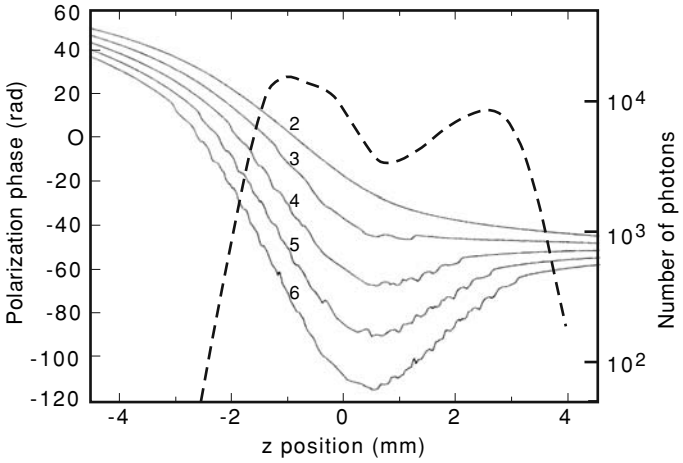

Fig. 11.5. Total polarization phase in the region of the laser focus ($z = 0$) for five laser intensities between 2 and 6×10^{14} W/cm^2 (thin continuous lines) *and* total number of photons for the 45th harmonic (dashed line); data from (Ref. [46]).

By showing the behavior of phase and intensity in the region of the beam focus, Figure 11.5 lets anticipate the great practical importance of phase calculations for the optimization of harmonic emission. In this figure, one can see the 45th harmonic-phase variation over 8 mm along the z-axis, for values of laser intensity standing from 2×10^{14} to 6×10^{14} W/cm^2. The laser is focused at $z = 0$. One observes that, for the largest intensity, the phase variation reaches the very large value of $\sim$180 rad. The dashed curve represents the conversion efficiency for the same harmonic as a function of the position of the center of the nonlinear medium relative to the laser focus.

A generalization of the study of phase-matching conditions leads to characterize the spatial dependence of the atomic phase $\phi_{\rm at}$ by means of the gradient $\nabla\phi_{at}$ and to define an effective wave vector such that [47]

$$\mathbf{K}(r,z) = \nabla\phi_{\rm at}(r,z) \tag{11.14}$$

where r is the radial coordinate. The gradient $\nabla\phi_{\rm at}(r,z)$ is shown to represent the momentum gained by the electron in the continuum due to the ponderomotive force and others field gradient effects. The condition for optimum phase matching reads

$$\mathbf{k}_q = q\mathbf{k}_1 + \mathbf{K} \tag{11.15}$$

Spatial maps of the beam wave vector $\mathbf{k}_1(r,z)$ and of the effective atomic wave vector $\mathbf{K}(r,z)$ may be obtained by calculation. Searching how the wave vectors and the electron momentum gain combine shows two geometries for which good phase matching are achieved. One of them, that corresponds to a

collinear phase-matching, results in a Gaussian-like beam and the second one, corresponding to a noncollinear phase-matching, yields an annular beam.

It is also shown that the phase-matching diagrams depend on the quantum paths defined in Section 11.1 (see Fig. 11.3). Since the return time of the electron—i.e. the timespan between the time where the electron is released in the continuum and the time of recombination—depends on the trajectory which is followed, the gain of momentum differs from a path to another one. This time is smaller along the trajectory with a small return time. The phase-matching condition (11.15) may thus turn out to be fulfilled for one quantum path only, which will dominate the propagation effects.

12. General Characteristics of High-Order Harmonic Emission

Radiation provided by high harmonics generation results from the addition of fields emitted by individual atoms, among which the propagation of the driving laser beam introduces phase relations. Therefore coherence is an original property of high harmonics (see for instance [48]). This has been brilliantly illustrated by the demonstration that two harmonic sources, generated independently in a gas jet using the same picosecond infrared laser, are locked in phase [49]. Nevertheless, as we saw in Section 11.2, the phase transfer from the laser to the emitting atoms occurs via a medium of space–time varying refraction index where, in addition, the phase-matching conditions strongly depend on the laser intensity. Therefore phase-matching optimization has a great part in the ultimate harmonic properties, especially coherence, angular distribution, intensity, and energy cutoff.

12.1 Coherence

12.1.1 Coherence Control

To optimize the coherent addition of atom emissions it is necessary to reduce the phase mismatch Δk_q [Eqs. (11.10) and (11.11)] where the refractive index $n_q(z)$ is a fast-varying function of the laser intensity. As the intensity variation along the propagation axis is particularly large in a small region on each side of the laser focus, it is clear that phase-matching optimization will considerably depend on the focusing conditions [50].

In the framework of Gaussian beams theory, the sharpness of the focalization is characterized by the confocal parameter 8.8 (Section 8.2)

$$b = \frac{2\pi a^2}{\lambda}$$

where a is the radius of the focal spot. Let L be the length of the portion of excited gas. If $b > L$ the experimental conditions are those of a "weak focusing." Oppositely, for $b < L$, they are those of a "tight focusing."

Table 12.1. Phases yielded by Gaussian beam focusing; b is the confocal parameter; a is the associated beam radius at the focus position; 0 mm is the position of the focus

b (**mm**)	a (μ**m**)	ϕ_{geo} (3 mm)	ϕ_{geo} (2 mm)	ϕ_{geo} (1 mm)	ϕ_{geo} (0 mm)
10	36	31.0 rad	21.8 rad	11.3 rad	0
5	26	50.2 rad	38.7 rad	21.8 rad	0
1	11	80.5 rad	76.0 rad	63.4 rad	0

Let us recall that the surface of the beam transverse section increases by a factor 2 from the focus to points placed at distance $b/2$ on each side of the focus. For geometrical reasons, the phase of the beam, ϕ_{geo}, also known as the Gouy phase, is a function of the position along the z axis. This function reads [51]

$$\phi_{\text{geo}}(z) = -\arctan\left(\frac{2z}{b}\right) \tag{12.1}$$

where the focus position is $z = 0$. For a point situated at distance r from the axis the function is complex and takes the form

$$\phi_{\text{geo}}(r, z) = \arg\left[\frac{1}{b + 2iz}\exp\left(-\frac{k_1 r^2}{b + 2iz}\right)\right]$$

When the interaction length L between laser and nonlinear medium is much larger than b, the system is said to operate in weak (or loose) focusing conditions. The opposite geometry is that of tight-focusing. Table 12.1 illustrates the magnitude of the laser-beam phases yielded by this effect as a function of the distance z, for three different focalizations. The laser wavelength is 0.825 μm.

In Figure 12.1 the phase distribution corresponding to the confocal parameter $b = 5$ is represented by the short dashed curve, that is symmetrical about the origin. This phase is to be added to the dipole phase represented, for a peak intensity of 6×10^{14} W/cm^2, by the long dashed curve. The excited gas is neon and the atomic density profile along the z-axis is a Lorentzian function with a 0.8-mm FWHM, truncated at $z \mp 0.8$ mm. The total phase is represented by the solid curve. The best phase-matching conditions are such as the polarization phase variation over the medium length is minimal. Figure 12.1 shows a region of the total phase curve where the phase varies slowly, namely the portion of the curve running from 3 mm to 4 mm from the focus. In all other regions the variation is significantly faster. The conclusion is that phase-matching on axis will be optimum for ∼1 mm long generating medium, the laser focus being situated ∼3 mm before the medium. Thus one sees that both the medium length and its distance to the focus are important for an efficient generation of coherent high harmonics. As for off-axis propagation, it reveals favored directions which lead to the formation of relatively intense

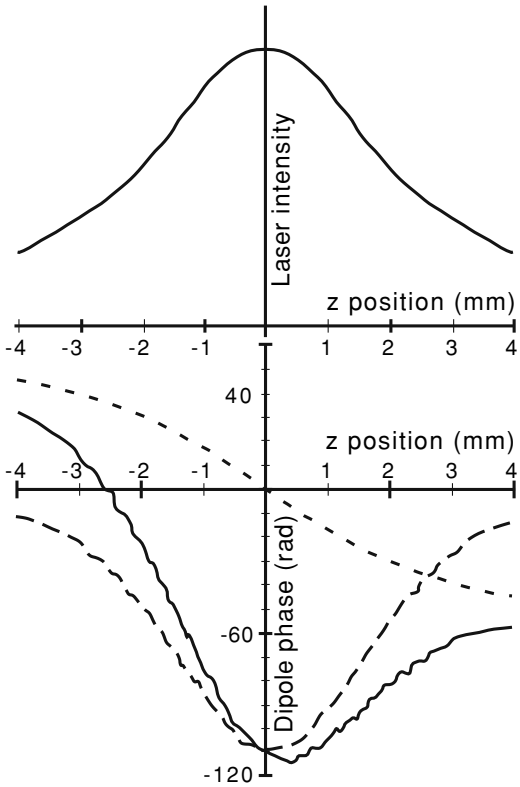

Fig. 12.1. Polarization phase in Ne on the propagation axis. Short dashed line: geometric (Gouy) phase of the fundamental; long dashed line: dipole phase; solid line: total polarization phase (data from Ref. [50]). The laser intensity is represented in the upper part of the figure. The laser propagates from the left to the right.

annular beams. For a more detailed discussion of coherence effects, the reader is recommended to refer to Ref. [50].

Figure 12.2 shows the transverse harmonic intensity profile for two distances of the laser focus, $z = 3$ mm (solid line) and $z = -1$ (dashed line). The frame (a) corresponds to the near field, at the very exit of the generating gas ($z + 0.8$ mm), and the frame (b) to the far field, at the output of the experimental device for instance. One sees that, when the laser is focused 3 mm before the medium, the harmonic profile is very regular. The half-width of the near-field profile is calculated to be 18 μm compared to 45 μm for the fundamental. When the laser is focused 1 mm after the medium, the spatial profiles become annular with an external radius of about 25 μm, which is as large as the fundamental one in the same conditions. Comparison of the curves of frames (c) and (d) shows the temporal emission profiles to be regular and very similar for both $z = -1$ mm and $z = 3$ mm while the spectral profile is

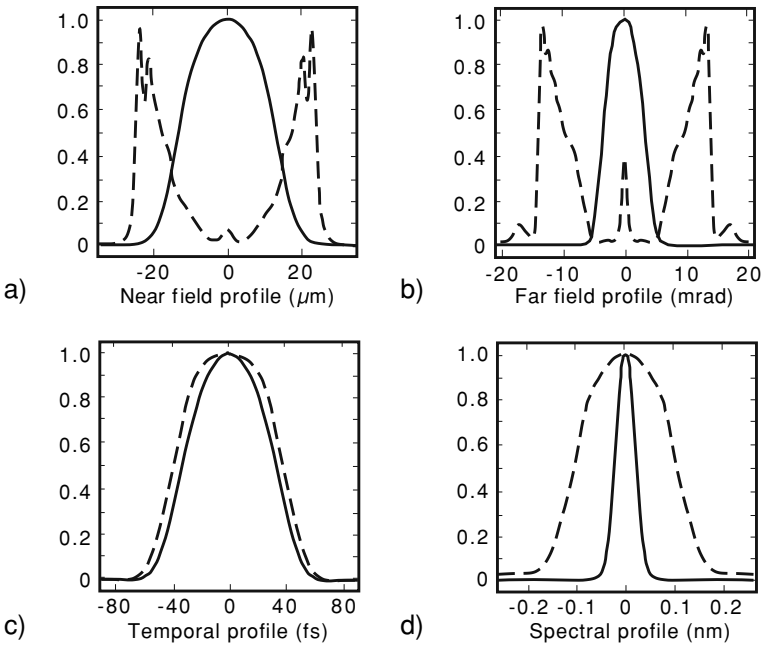

Fig. 12.2. Spatial, angular, temporal, and spectral profiles of the 45th harmonic for the positions $z = 3$ mm (solid line) and $z = -1$ mm (dashed line).

largely broadened for $z = -1$ mm compared to its width for $z = 3$ mm. This is shown to be an effect of the phase modulation induced by the phase dipole dependence on the fundamental intensity. For $z = 3$ mm the FWHM of the profile is 0.04 nm, which corresponds to about four times the Fourier limit.

12.1.2 Spatial Coherence Measurements

Whatever convincing predictions are provided about harmonic coherence by the phase-matching theory, experimental measurements remain necessary to determine up to which point the coherence of the fundamental laser radiation is preserved in HHG. Two methods have been used.

12.1.2.1 Young's Slit Method

The experimental arrangement is similar to the one represented in Figure 10.1 with the addition of a pair of thin slits 4 cm away from the gas jet plume, before diffraction of the harmonic radiation by the grating. The spatial-coherence length determination from Young's fringe visibility needs to vary the slit separation. Slit pairs of 28, 50, 75, and 100 μm separation have been used. The width of the slits was of 8 ∓ 1 μm.

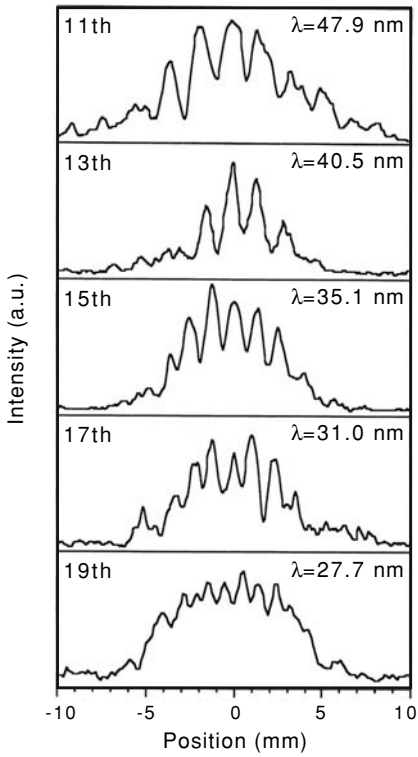

Fig. 12.3. Interference fringes obtained near the focus of the laser by the Young's slit method for 11th to 19th harmonics (Ref. [52]).

Harmonics were generated with a frequency doubled Nd:glass laser yielding 2-ps, 0.5-J radiation pulse of 1.054-μm wavelength. The focusing optics aperture was reduced in order to produce a uniform, near flattop profile in the focal area. The Gaussian beam was focused into a helium gas plume produced by a pulsed jet backed with 50 bars of pressure. The estimate density in the gas plume was of 5×10^{18} cm^{-3}. The spatial profiles of harmonics, observed between 27 and 48 nm wavelength, were found to be roughly Gaussian with an FWHM about 200 μm at a laser intensity of 4×10^{15} W/cm^2.

Typical interference patterns obtained on the 11th to the 19th harmonic with a pair of 50 μm spaced slits are shown in Figure 12.3, i.e. quite close to the focus [52]. One sees that the fringe visibility, defined from the maximum intensity at the top of fringes and the minimum intensity between two successive fringes by using equation (3.6) (Section 3.1), decreases with increasing harmonic order. In addition, for the same 50-μm slit spacing, Figure 12.4 shows the fringe visibility for the 15th harmonic ($\lambda = 35.1$ nm), chosen as an example, to decrease with laser peak intensity. This visibility is seen to be pretty good (0.7–0.8) before that the intensity reaches the saturation value,

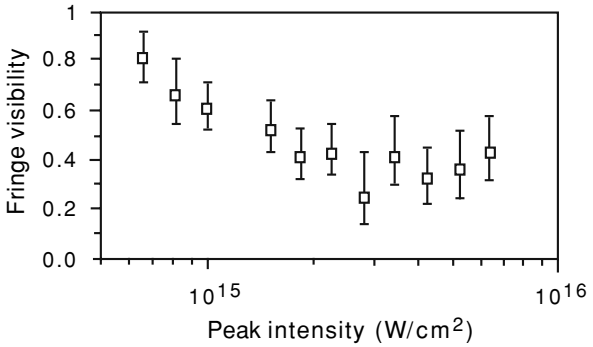

Fig. 12.4. Fringe visibility for the 15th harmonic as a function of the laser intensity.

for which gas ionization becomes significant, and falls down to ∼0.4 above this value.

For the same harmonic and the same spacing, the equivalent incoherent source diameter, calculated by using the van Cittert–Zernike theorem [cf. Section 3.1 and Eq. (6.56) in Section 6.4.1], should be of 16 μm. On the other hand, the actual harmonic source size is roughly equal to the laser spot size, i.e. about 70 μm, what would lead to an almost zero fringe visibility for a 50-μm slit spacing. Therefore the observed harmonic coherence is much better than that yielded by radiation propagation from an incoherent source of the same diameter.

12.1.2.2 Fresnel Bi-Mirror Interferometry

A diagram of the Fresnel bi-mirror interferometer has been shown previously in Figure 6.35 (Section 6.4.2). Here we recall the principle of this device so as to show how it supplies a direct access to the spatial coherence of a XUV beam. Figure 12.5 shows the bi-mirror separating the incident beam into two reflected beams, which then recombine thanks to a suitable choice of the angle between the mirrors. Interference fringes are formed in the recombination space of the ray-pairs.

A very interesting feature of the bi-mirror system is that only these pairs of rays, which are separated by a constant distance d in the transverse section of the incident beam, will interfere. As examples, three interfering ray pairs, respectively generated on points (P_0, P_2), (P_1, P_3), and (P_2, P_4), such as $P_0P_2 = P_1P_3 = P_2P_4 = d$, are displayed in Figure 12.5. Looking at Figure 12.6, one can see that the size of the investigated field increases with the distance d, which can be thus easily changed by varying the distance between the detector and the interferometer.

So long as d remains smaller than the coherence length, the fringe visibility is kept essentially constant. The fringe contrast is weaker on both sides of the fringe pattern because the electric field along asymmetric rays interfere

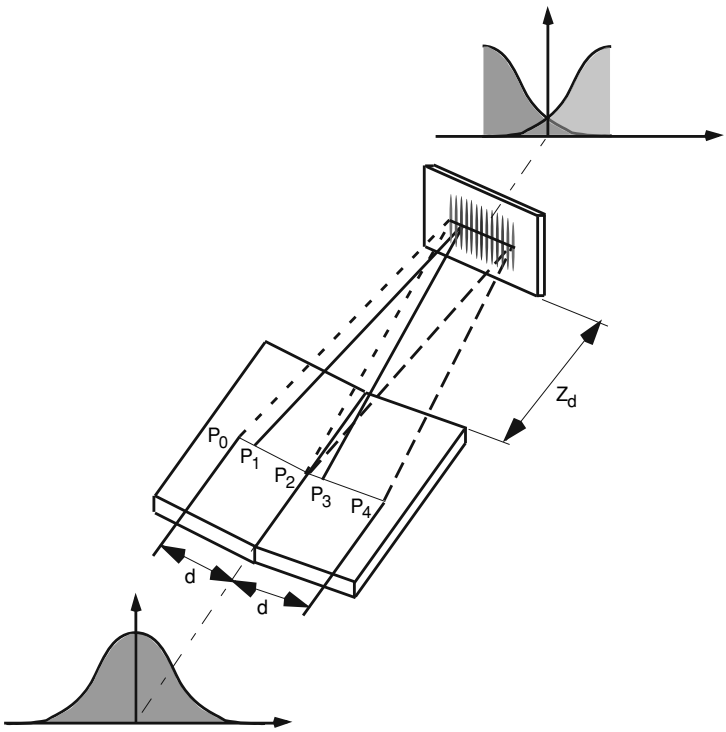

Fig. 12.5. This diagram of the bi-mirror interferometer shows three pairs of rays, originating from P_0 and P_2, P_1 and P_3, P_2 and P_4, respectively, and recombining in the observation plane.

with different amplitudes, one of which decreasing to zero on each side of the fringe pattern. When d becomes longer than the coherence length, the fringe visibility decreases and the fringes may finally disappear. Therefore the interference pattern can be read as a *single-shot mapping of the spatial coherence* throughout the beam. In contrast, the Young's slit system needs as many shots as necessary to map the coherence and requires the slits to be moved throughout the beam section after each shot.

A sketch of the experimental setup is displayed in Figure 12.7 [53]. Harmonics are generated in a xenon gas jet from the 60-fs, 800-nm radiation pulses of a Ti:sapphire laser. The intensity focused into the gas is 10^{13}–10^{14} W/cm^2. Harmonic selection is achieved by reflection on a Mo/Si multilayer mirror and a 100-nm thick aluminium filter. The harmonic profile is close to Gaussian, with a full width of about 3 mm at $1/e^2$. The two-dimensional detector is placed at a distance Z_d from the exit of the interferometer. Changing Z_d between 1 and 3 m, the transverse coherence can be probed for transverse distances $d \simeq \alpha Z_d$, i.e. $d \simeq 1$–3 mm in the present case. As the spatial resolution of the two-stage microchannel plate (MCP) detector, coupled to a phosphor

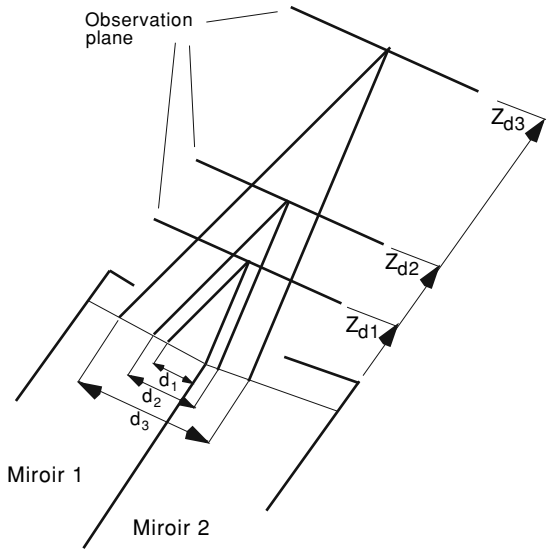

Fig. 12.6. This diagram of the recombining rays shows that the ray separation distance d before reflection varies proportionally to the distance Z_d, between the interferometer and the observation plane. Therefore, changing the distance of the detector to the interferometer produces a proportional change of the coherence length probed in the beam.

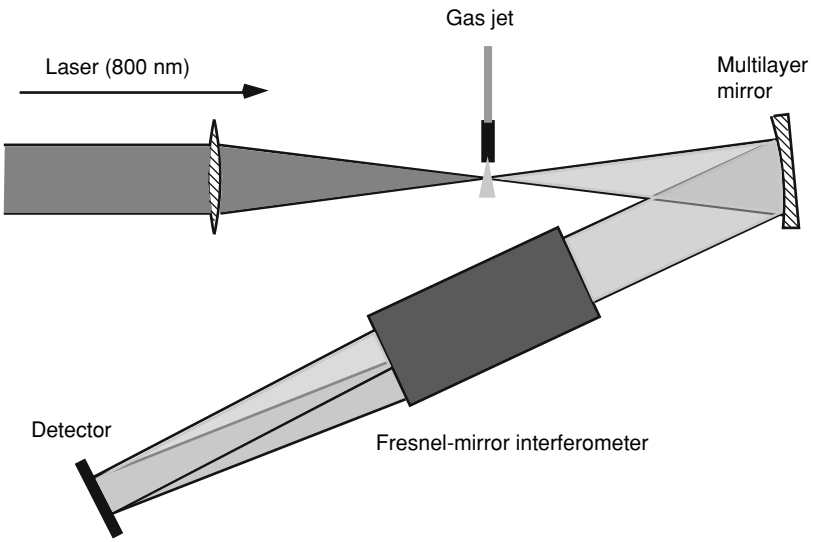

Fig. 12.7. Experimental setup for spatial coherence measurements of high-order harmonics using a Fresnel bi-mirror interferometer.

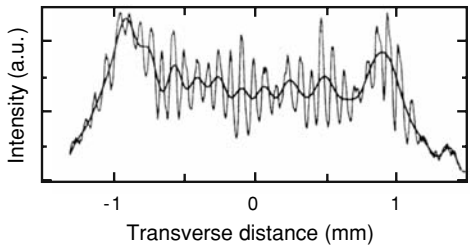

Fig. 12.8. Transverse section of the interference pattern obtained in the observation plane with the bi-mirror interferometer. Thin line: fringe spatial profile in the observation plane; thick line: contribution of the diffraction by the bi-mirror edge to the observed spatial fringe profile.

screen, is about 90 μm, it is necessary to tilt the screen up to a grazing angle of 8° in order to magnify the fringe spacing by a factor 7, which provides a ∼450-μm spacing on the detector.

Figure 12.8 displays a transverse section of the well-contrasted fringe pattern recorded by the detector in the observation plane. This pattern involves the contributions of two components, the 13th and the 15th harmonics, called H13 and H15, of wavelengths $\lambda_{13} = 61.53$ nm and $\lambda_{15} = 53.33$ nm and a contribution from the diffraction by the edge of the bi-mirror.

Fourrier analysis allows to subtract unwanted components which otherwise induce fringe modulations. The contribution from the edge diffraction, obtained by spectral rebuilding after substraction of harmonic contributions is shown by the thick line curve in Figure 12.8. The superposition of two fringe patterns, which have slightly different spacings, namely ∼0.06 for H13 and 0.05 nm for H15 induces a beat modulation of the fringe contrast. However, for the three spacings, $d = 1, 2$, and 3 mm, well-contrasted fringes have been obtained in the full investigated space, indicating a good spatial coherence throughout the full beam diameter. After calculation, the degree of coherence $\gamma_d(x, y)$, at a point of coordinates x, y, is found fluctuating slightly around an average value of 0.6, with a standard deviation of 0.06, throughout the full 2-mm × 2.5-mm coherence map achieved in the transverse section of the harmonic beam.

To investigate the influence of the harmonic generation parameters, the 2D-averaged degree of coherence γ_d has been determined for H13 as function of the position of the laser focus before the gas jet (cf. Section 10.2) at fixed backing pressure and as a function of the backing pressure at fixed jet/focus position. We recall that the pressure in the gas jet is about 10 times lower than the backing pressure. Calculations have been made for pairs of rays separated in the incident beam by $d = 1$ mm and 2 mm, respectively. The results are displayed in Figure 12.9. For $d = 1$ mm the degree of coherence is found $\gtrsim 0.7$ in the whole rang of parameters. In Figure 12.9a one can see that γ_d reaches 1 for $P = 1000$ Torr, $d = 1$ mm, the focus being placed at 40 mm before the jet.

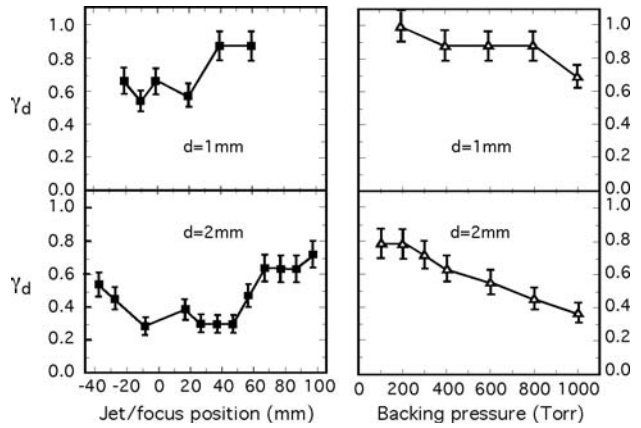

Fig. 12.9. (a) and (b) Degree of coherence as a function of the jet/focus position z, for a backing pressure $P =$ 1000 Torr and two separation distances between the rays, $d = 1$ mm and $d =$ 2 mm; (c) and (d) Degree of coherence as a function of the backing pressure P, for a jet/focus position $z = 23$ mm and for the same d values as in (a) and (b) (data from Ref. [53]).

For $d = 2$ mm (Fig. 12.9b), γ_d increases from 0.3, when the beam is focused in the jet, up to 0.7 when the laser is focused at 100 mm before the jet. These results clearly illustrate the importance of the choice of the focus-to-jet distance, in agreement with the calculations performed in phase matching theory (cf. Section 11.2). Figure 12.9d shows γ_d decreasing almost linearly as the pressure increases from 200 Torr to 1000 Torr. This effect is imputed to gas ionization which increases with pressure: the enhancement of the free electron density induces more decorrelation of the time dependent fields which propagate in the gas (see for instance [54, 55]).

In Figure 12.10, the values of γ_d, measured with the beam focus placed 60 mm before the jet, are plotted as a function of the diameter d of the cell in which the coherence of the H13 harmonic is probed. The degree of coherence obtained from an incoherent source placed at the same distance (1.30 m) and of the same radius (100 μm) is plotted for comparison in the same figure. This comparison shows that the diameter of the cell in which $\gamma_d \sim 0.4$ is ∼10 times larger for the harmonic beam than for the incoherent source.

12.1.3 Temporal Coherence

The temporal coherence of high-order harmonics has been investigated using an artful method, in which a Michelson interferometer yields two spatially separated sources, close to each other, with a small time interval. Each source interacts with the gas jet and generate an harmonic beam. After reflection

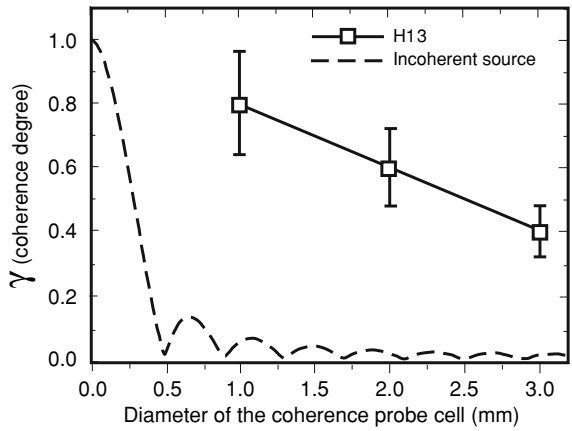

Fig. 12.10. Experimental values of the degree of coherence γ_d (squares) as a function of the diameter d, of the coherence probe cell. For comparison the dashed line shows the degree of coherence provided by the propagation of radiation from an incoherent source of same diameter and situated at the same distance.

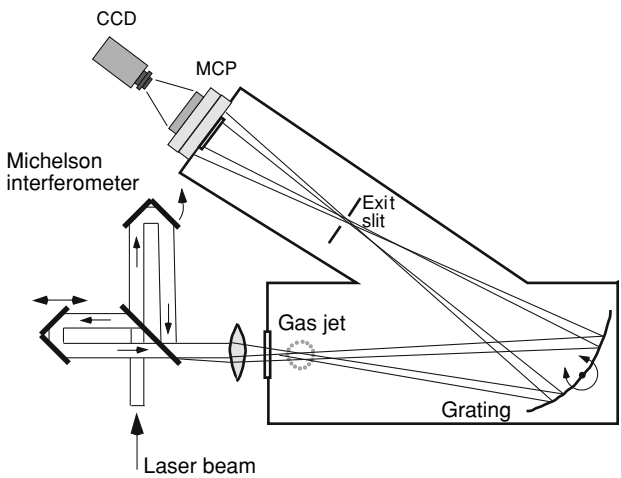

Fig. 12.11. A Michelson interferometer introduces a well-defined delay between two pump pulses. A small misalignment of the second arm allows to focus the beams into two separate positions of the argon jet. The gas jet transfers the time delay between the infrared pulses to two harmonic beams whose interferences reflect the properties of the harmonic beam temporal coherence (Ref. [38]).

on a concave grating, the two beams recombine and far field fringes can be observed in the space where the two beams converge beyond the focal zone.

Figure 12.11 shows the principle of the experimental arrangement. The laser is an amplified Ti:sapphire system delivering 100 fs pulses in a 14-nm

bandwidth around 790 nm. The Michelson interferometer produces pairs of pump pulses whose relative delay can be accurately adjusted by means of a computer-controlled stepping motor which slightly modifies the length of one the arms of the interferometer. A small misalignment of the second arm allows to focus the beams into two separate positions of the argon jet. In this way one obtains two sources separated from each other by $\sim$50 μm and temporally separated by a well-defined time interval. The jet is placed near the entrance slit of a 1-m vacuum UV monochromator. The fringes of the spatially overlapped beams are detected 50 cm after the exit slit of the monochromator, on a Micro Channel Plate detector (MCP) coupled to a phosphor screen which is read by a CCD camera.

The whole system works primarily with the harmonics as the Michelson interferometer does it with the infrared laser. The gas jet is like an interface between infrared and harmonic beams, which transfers the time delay between the infrared pulses to two harmonic beams. The last step is the detector recording the fringe pattern, which appears in the far field, as a function of the time delay. Therefore, what is probed by this setup is the correlation time between the same spatial areas in the two beams, i.e. the temporal coherence of the harmonic radiation.

The result is that, when the two pulses overlap in time, interference fringes appear for all the observed harmonics, from the 7th to the 21st, with a contrast up to 0.6. The fringe visibility $V(\tau) = (I_{\max} - I_{\min}) / (I_{\max} + I_{\min})$ is measured as a function of the time delay, τ. At the center of the spatial profile, the coherence time is obtained as the half-width at half-maximum of the curve $V(\tau)$. These coherence times vary from 20fs to 40 fs, which is of the same order as the duration of the harmonic pulses. The corresponding bandwidths are comprised between 0.1 and 0.2 nm.

A remarkable feature of the fringe patterns consists in the presence of two well spatially separated region according to the radial coordinate r, around the center of the interferogram. For the 15th harmonic for instance, one observes intense fringes for $\tau = 0$ fs and $r < 2$ mm, viz. in the central interferogram region. In the outer region (2 mm $< r <$ 8 mm) the fringes are much less intense although their contrast is practically unchanged. However, for a time delay $\tau = 15$ fs, the fringes completely disappear in the outer region while the loss of contrast remains moderate in the central region. Figure 12.12, which shows the fringe visibility around $r = 0$ mm and around $r = 5$ mm as a function of the time delay, clearly shows a temporally coherent region observable with a contrast decreasing up to $\tau \sim 50$ fs (full circles) and an almost incoherent outer region (open circles).

Calculation of the fringe patterns well accounts for this difference between the central and outer regions. The difference is shown to originate from the presence of two "main quantum paths" for the harmonic emission (Section 11.2, Figure 11.3). Two main trajectories of recombining electrons contribute with different phase properties to the dipole moment of any given harmonic. A consequence of this difference is the "short" trajectory to emit well-collimated

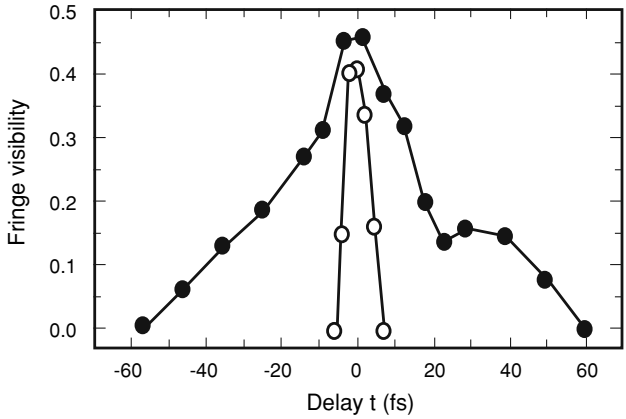

Fig. 12.12. Fringe visibility versus the temporal delay between the two pump pulses. In the center of the beam, the fringe visibility decreases slowly when the time delay increases. Conversely, in the outer part of the beam, the fringe visibility falls in even for very short delays.

radiation with a long coherence time, whereas the "long" trajectory gives rise to a strongly divergent emission with a short coherence time.

12.2 Conversion Efficiency

The conversion efficiency for a given harmonic is the ratio of the absolute energy yielded by this harmonic to the pump laser energy focused into the nonlinear medium. Thus the determination of harmonic generation efficiencies requires an absolutely calibrated detection device as, for instance, an X-ray CCD (charge-coupled device) preliminarily calibrated with the help of synchrotron radiation.

Examples of output energy measurements performed with the CCD detector are shown in Figure 12.13 [56]. Pump pulses of 650-fs duration were produced by a Nd:glass laser, on the one hand, and by its frequency doubled harmonic, on the other hand, in a neon gas-jet. The confocal parameter was of 2.5 cm and the interaction length, 0.8 mm. Fifty milli Joules of the 526-nm light were focused within a 140-μm spot size and 90 mJ of the 1053-nm light, in a 180-μm spot size. The measurements were conducted with an atom density of 2×10^{19} atoms $\mathrm{cm}^{-3} \mp 30\%$ and a peak intensity of 1×10^{15} cm^{-3}.

The conversion efficiencies of the plateau harmonics, deduced from the energies reported in Figure 12.13 for the 526-nm pump light, are $(2\text{–}5)\times 10^{-8}$. Efficiencies decrease by almost three orders of magnitude on using the 1053-nm pump light. This collapse can be ascribed to the deterioration of the phase-matching factor resulting from the wavelength doubling (cf. Section 11.2). However, the cutoff of the 1053-nm harmonics occurs at much shorter

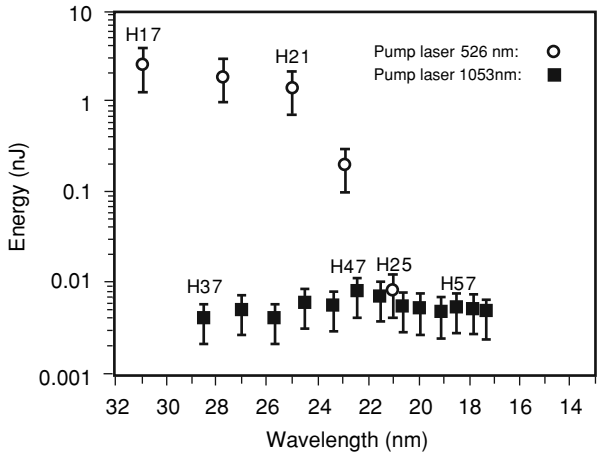

Fig. 12.13. Harmonic output energy measurements performed for two exciting laser wavelengths. These measurements show that the cutoff is at a much shorter wavelength for the long-wavelength driving laser (1053 nm) but that the conversion efficiencies are much larger for the short-wavelength driving laser (526 nm).

wavelength than in the case of the 526-nm harmonics because, according to equations (10.2) and (10.4), the decrease of the exciting wavelength reduces the ponderomotive energy and consequently the maximum energy of the harmonic radiation also.

Recent experiments with long focal length (2 m) and high pump energy raised the conversion efficiency to 10^{-5} for the 15th harmonic in xenon ($\lambda \simeq 53$ nm) with a number of photons per pulse about 5×10^{11}, i.e. a pulse energy of $\sim$1 μJ [57]. Energies about 6 μJ per pulse at 73.6 nm , 0.7 μJ per pulse at 42.6 nm and 0.3 μJ at 29.6 nm have been obtained in similar experiments [58, 59].

12.2.1 Scaling Law in the Plateau Region

The plateau region of the high-order harmonic spectrum is characterized by a nearly constant conversion efficiency up to an abrupt cutoff to the shorter wavelengths. As previously mentioned the width of the plateau varies, in the single atom response, as $I_\mathrm{p} + 3.17U_\mathrm{p}$ where I_p is the field-free ionization potential of the atom and U_p, the ponderomotive energy which is proportional to the intensity and to the squared wavelength of the laser (cf. Chapter 10).

In most experimental situations, where the interaction length is smaller than the length of the medium, harmonic intensities in the plateau region are observed to scale as

$$I_\mathrm{q} \propto b^3 \times \tau \tag{12.2}$$

where $b = 2\pi a^2/\lambda$ is the confocal parameter and τ the driving laser pulse

duration [36, 60]. The relative harmonic intensities and the position of the cutoff are unchanged over a large variation of the parameter b.

It is shown that the b^3 dependence results from the proportionality of the harmonic field strength to the length over which the field can be coherently built up. This length is proportional to b. Thus the harmonic intensity is proportional to b^2. The total number of photons is proportional to the spatially integrated intensity, i.e. to b^3. Oppositely, in the case of weak focusing, the harmonic field would remain in phase with the driving polarization term over the full length of the medium and the integrated intensity would be then proportional to b. As for the τ dependence, it simply results from the temporal integration of intensity.

To extend harmonic emission to shorter wavelengths, i.e. to increase the conversion efficiency in the cutoff region, it is necessary to choose light atoms for the target gas, in order to increase I_p, and high-intensity, low-frequency driving lasers, in order to increase U_p. Let us recall that the ionization potentials for Xe, Kr, Ar, Ne, and He are 12.13, 13.99, 15. 76, 21.6, and 24.6 eV, respectively. This has led to chose helium to investigate HHG in the "water window," i.e. the 2.28–4.47 nm wavelength interval. Discrete harmonics peaks have been observed up to order 221 ($\lambda = 3.6$ nm) with using the 26 fs pulses of a 800-nm wavelength laser [61].

At higher intensities, gas ionization depletes neutral atoms which induces harmonic emission saturation. However, shorter duration of the driver pulses increase the critical intensity for saturation [62, 63]. This is why the high-energy end of the unresolved coherent continuum spectrum could be extended up to 2.5 nm using a helium gas jet irradiated by sub-10-fs laser pulses [64, 65].

12.2.2 Influence of Atomic Density

The coherent character of harmonic emission let expect harmonic intensity to vary as the square of the atomic density of the gas jet (cf. equation (11.2) in Section 11.1). Nevertheless, the fall of the harmonic coherence observed at high gas pressure (cf. Fig. 12.9) shows that, due to the increasing ionization, the higher the pressure, the more perturbed the building of a squared-density dependence of harmonics.

Measurements of harmonic intensity, as a function of the pressure in the gas jet, require to characterize the atomic density in the interaction region, for various backing pressures and various focus-to-nozzle distances, with sufficient time resolution. Let us recall that the backing pressure is the gas pressure applied to the valve before its opening and jet emission. First of all we need to know the pressure distribution and the peak pressure within the jet. For the results presented below the jet diagnostic method is based on optical interferometry [66]. The gas was flowing through a 6-mm long tube of 0.9-mm diameter and the valve was opened 750 μs before the laser pulse.

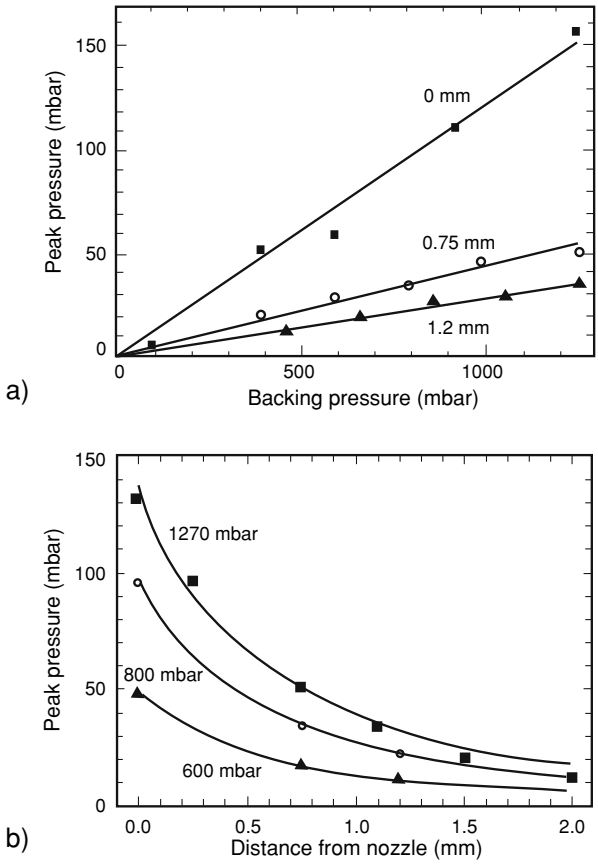

Fig. 12.14. Pressure in the gas jet: (a) peak pressure as a function of the backing pressure for a fixed distance from nozzle; (b) peak pressure as a function of the distance from nozzle for a fixed backing pressure (Ref. [66]).

It has been found that

(a) the spatial profile of the gas distribution has a Lorentzian-like shape, except in the wings and there is no significant profile dependence on gas species, Ar or Ne, at the same backing pressure.
(b) at fixed backing pressure, the width (FWHM) of the profile increases approximately linearly as a function of the laser-to-nozzle distance within an experimental range of 0–1.2 mm.
(c) at fixed distance from the nozzle orifice, the shape of the normalized spatial profile is almost independent of the backing pressure within the experimental range of 3–80 mbar.
(d) as shown in Figure 12.14a, peak pressure increases almost linearly versus backing pressure.

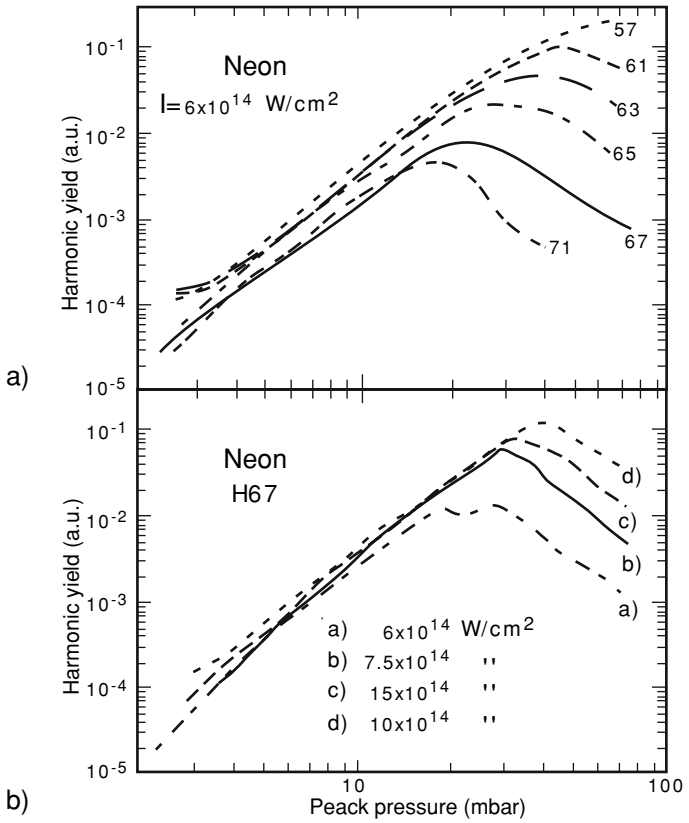

Fig. 12.15. Harmonic yield in neon versus peak pressure: (a) for harmonics 57–71 for a fixed laser intensity; (b) for harmonic 67 and four laser intensities from 6 to 10^{14} W/cm^2.

Furthermore, Figure 12.14b shows the behavior of the peak pressure when the distance from the nozzle varies, for three fixed values of the backing pressure.

Experimental results show that the cutoff region is considerably affected by the gas pressure. This appears clearly in Figure 12.15a, which shows the harmonic yield as a function of the peak pressure for H57, H61, H63, H65, H67, and H71 at a laser intensity of 6×10^{14} W/cm^2. Each measured point is an average of 100 shots. While in the plateau region (harmonics below the 55th) the photon yield had been found increasing as the square of the atomic density in the whole pressure range (3–80 mbar), for harmonics of the cutoff region, the photon yield goes through a maximum and then decreases. Moreover the optimum yield occurs at decreasing pressure when the harmonic order increases, which means that the extent of the plateau falls off at high pressure.

Figure 12.15b, which displays the variation of the photon yield of the 67th harmonic for several laser intensities from 6×10^{14} to $\times 10^{15}$ W/cm^2, shows the optimum pressure to increase with the laser intensity. Therefore, to keep constant the extension of the plateau to higher harmonic orders when the pressure increases, it should be necessary to make a corresponding enhancement of the laser intensity. Similar effects are observed with argon.

From numerical simulations performed in the framework of atomic dipole calculation and propagation equations (cf. Sections 11.1 and 11.2), the main effect responsible for the observed effects is the laser field defocusing, due to the presence of an increasing number of free electrons in the partially ionized gas at high pressure. Plotting the map of the laser electric field at fixed time shows that the maximum intensity occurs near the entrance of the medium, viz. in a region of a rather low atomic density, and falls down quickly moving off because the beam immediately started to defocus. Thus the harmonics in the cutoff region, which are produced at the highest intensity only, are strongly reduced, while the harmonics in the plateau, which are produced even at lower intensities, i.e. when the defocusing of the laser beam is not as important, increase with the atomic density in a larger pressure range.

12.2.3 Influence of the Length of the Pumped Medium

Harmonic signal measurement versus the length of the nonlinear medium, at a constant pressure, is necessary to investigate the effects limiting the efficiency which are not pressure dependent.

A windowless gas cell, shaped like an arrowhead, as represented in Figure 12.16, makes it possible to vary the medium length, keeping the pressure constant [67]. The gas is injected, with a backing pressure of 0.5 bar, through a 1-mm diameter hole thanks to a pulsed piezoelectric valve. The entrance and exit holes of the laser beam are made by letting the laser burn them in the 50-μm thin copper foil which constitutes the sides of the cell. They

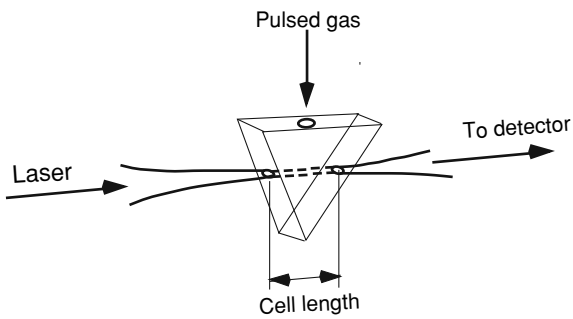

Fig. 12.16. Gas cell, shaped like an arrowhead, used to vary the medium length by vertical translations, keeping the pressure constant.

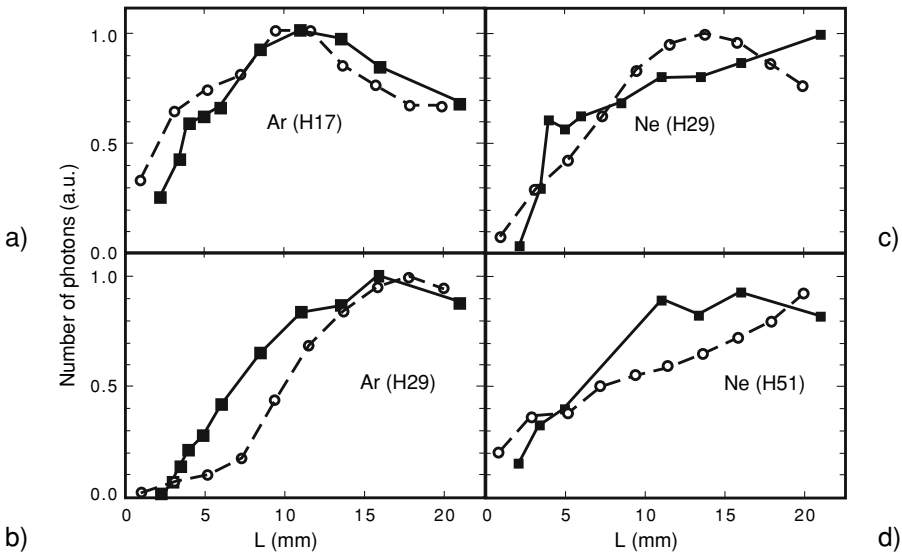

Fig. 12.17. Harmonic yield as a function of the nonlinear medium length. Solid curves: experimental results: broken curves: numerical simulations. Absorption has no significant part to the observed fall of the conversion efficiency for longer medium length. The efficiency maxima are due to good phase-matching conditions for the corresponding length (Ref. [67]).

have a diameter of ∼0.5 mm. The pressure in the gas is estimated at ∼5 mbar. Vertical translations of the gas cell allows the medium length to vary according to the experimental process. Holes are sealed after each operated position, and new ones are made, so that the pressure in the cell may be kept constant.

For the results presented here, the fundamental beam was provided by a 10-Hz terawatt Ti:sapphire laser operating at a wavelength of 800 nm. The pulse duration was 110 fs. A small optical aperture was obtained limiting the beam diameter to 20 mm and choosing a lens of 2-m focal length, placed into the vacuum chamber. With an energy per pulse of ∼9 mJ, the laser peak intensity was estimated $\sim 4 \times 10^{14}$ W/cm^2.

The experimental results for argon and neon harmonics are summarized in the solid curves of Figure 12.17. Harmonics H17 of argon and H29 of neon belong to the plateau region whereas H29 of argon and H51 of neon are close to the cutoff region. On the other hand, for the two argon harmonics, the pump intensity was above the saturation threshold, which did imply gas ionization and presence of free electrons. Conversely, for the neon harmonics, the measured intensities were significantly weaker than the saturation intensity and one did not expect large phase mismatch coming from free electrons.

The curves show the number of photons obtained for each harmonic to increase with increasing length up to 10–15 mm for argon and somewhat

Table 12.2. Calculated longitudinal coherence length (mm) for the geometrical phase, dispersion due to neutral atoms, and dispersion due to free electrons

	Ar H17	Ar H29	Ne H29	Ne H51
L_{geo}	−3.8	−2.2	−2.2	−1.3
L_{disp}	−23	−17	−40	−22
L_{e}	1.3	0.8	13	7.3

more for neon. These results are compared with numerical simulations (broken curves in Fig. 12.17) making use of atomic dipole calculations and numerical solution of the propagation equations. Simulations show a similar trend to the experiments except for medium lengths around 20 mm in the case of neon.

To discuss the different contributions to the phase mismatch along the z axis, $\delta\phi(z)$, between the polarization due to the laser field and the harmonic field, it is useful to define a coherence length L_{c} by relation

$$L_{\text{c}} = \pi / \frac{d\delta\phi(z)}{dz} \tag{12.3}$$

The value of L_{c} is an indicator of the growth velocity of the phase mismatch $\delta\phi(z)$. For large L_{c} the phase mismatch grows only slowly along the axis. Processes that generate the highest values of L_{c} have thus the largest contribution to the harmonic photon yield. Therefore L_{c} can be considered as a local *coherence length* in the propagation direction.

In the present case L_{c} has been calculated including three processes: (1) the variation of the geometrical phase of a Gaussian beam in the region of the focus [Eq. (12.1)] L_{geo}, (2) the dispersion due to refraction in the neutral atom gas, L_{disp}, (3) the dispersion due to free electrons, L_{e}. Table 12.2 gives the values of L_{c} for the four harmonics experimentally investigated.

In addition, one has to consider the change of the dipole phase (or atomic phase) with the laser intensity $\delta\phi_{\text{at}}(z) = -\alpha I(z)$ (see Fig. 11.4 in Section 11.2). Phase addition for the four processes gives the total coherence length

$$L_{\text{tot}} = \left[L_{\text{geo}}^{-1} + L_{\text{at}}^{-1} + L_{\text{disp}}^{-1} + L_{\text{e}}^{-1} \right]^{-1} \tag{12.4}$$

where

$$L_{\text{at}}^{-1} = -\frac{\alpha}{\pi} \frac{dI\,(z)}{dz} \tag{12.5}$$

The absolute value of L_{tot} is represented for the harmonic H29 of neon in Figure 12.18. The figure shows that a region of good phase-matching, with a coherence length larger than 10 mm (hatched area), appears not far from the focus, over a length of at least 5 mm. Examination of the different contributions to the coherence length shows that the good phase matching in this

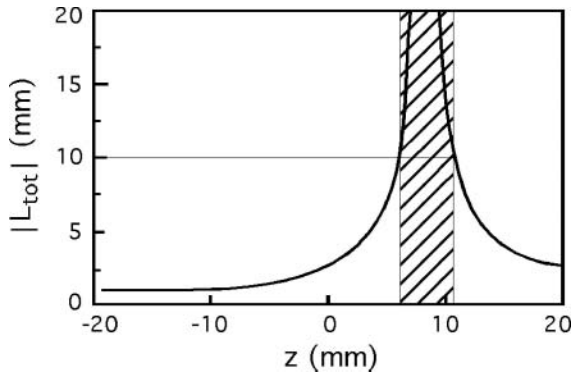

Fig. 12.18. Variation of the length L_c, which defines the growth velocity of the phase mismatch, with the increase of the medium length.

region is due to the large values of $\left|L_{at}^{-1}\right|$, namely to the strong variation of the dipole phase across the focus in this region.

Finally estimation of the e^{-1} absorption length of the investigated harmonics, at a pressure of 5 mbar, shows that absorption has no significant part to the conversion efficiency variations experimentally observed.

12.2.4 Influence of the Diameter of Apertured Beam

Aperturing the laser beam proves to be a simple and efficient way to optimize the production of harmonics. As an example Figure 12.19 shows the measured and the calculated variation of the harmonic n°21 of Argon as a function of the aperture diameter [68]. Both curves show a sharp rise for narrow diaphragms followed by a slower decrease when the aperture diameter tends to the value of the full aperture. Calculation shows that the effects of the truncated aperture are multiple and their combination is complex. The increase of the aperture carries an increase of the laser flux, but this dependence is altered by the variation of the aperture transmission according to the waist of the laser beam. Moreover the Gouy phase length and the wave front are also modified. Comparison between the calculated and measured curves in Figure 12.19 shows that the introduction of these effects in calculations well accounts for the main characteristics of the role of the aperture.

12.2.5 Phase-Matching by Wave Guiding

Generally speaking, phase-matching consists in minimizing the difference of phase between driving polarization and induced harmonics fields over the interaction length. Exact phase-matching would correspond to

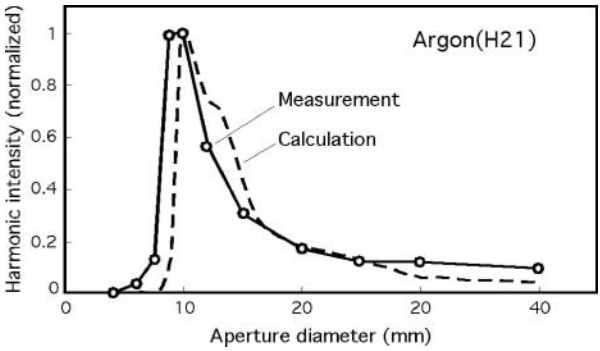

Fig. 12.19. Effect of the increase of the aperture diameter d on the harmonic intensity. Solid line: experimental measurements; broken line: calculated curve (Ref. [68]).

$\Delta k = k_q - qk_{\text{laser}} = 0$, where q is the harmonic order [see. Eq. (11.10)]. Now the divergence of the laser beam implies the decrease of the driving intensity in the propagation direction. This intensity decrease results in a corresponding dipole phase change and is thereby a cause of phase mismatch. A reduction of the beam divergence beyond the focus ought to enhance the conversion efficiency and the beam quality. Wave guiding techniques have been thus investigated theoretically and experimentally in many works with a view to achieve efficient phase-matching in the interaction region (see for instance [69–78]).

One can use two methods to obtain nearly uniform intensity distributions in the interaction region. One of them applies to the self-channeling induced by self-focusing of Gaussian beams of high peak intensity due the nonlinearity of refractive indexes [cf. Eq. (11.12)] [79]. The other one is wave guiding in hollow fibers [70]. Hollow fibers confine the beam by repeated grazing incidence reflections of the coherent radiation on the inside walls of the fiber. The phase velocity of the laser light can be adjusted by changing the inside diameter of the fiber or by changing the gas pressure.

For both methods the gas jet is replaced by a gas cell in which the atom density distribution is uniform. Figure 12.20 shows experimental arrangements corresponding to the two techniques. Self-channeling is obtained by simply focusing the laser in the cell. Regarding a hollow fiber, it must be placed within the cell so that the pressure in the fiber may be the same as in the cell. In both cases one uses short laser pulses which reduce the gas ionization as well as the resulting dispersion.

Midorikawa et al. compared the high-order harmonic generation obtained with argon in hollow fiber and with neon in self-guided channel [71, 72, 75, 80]. The results are displayed in Figure 12.21.

Argon was excited by a 80-fs duration pulse with 4-mJ energy, generated by a Ti:sapphire laser ($\lambda = 800$ nm) at 10-Hz repetition rate. Laser pulses

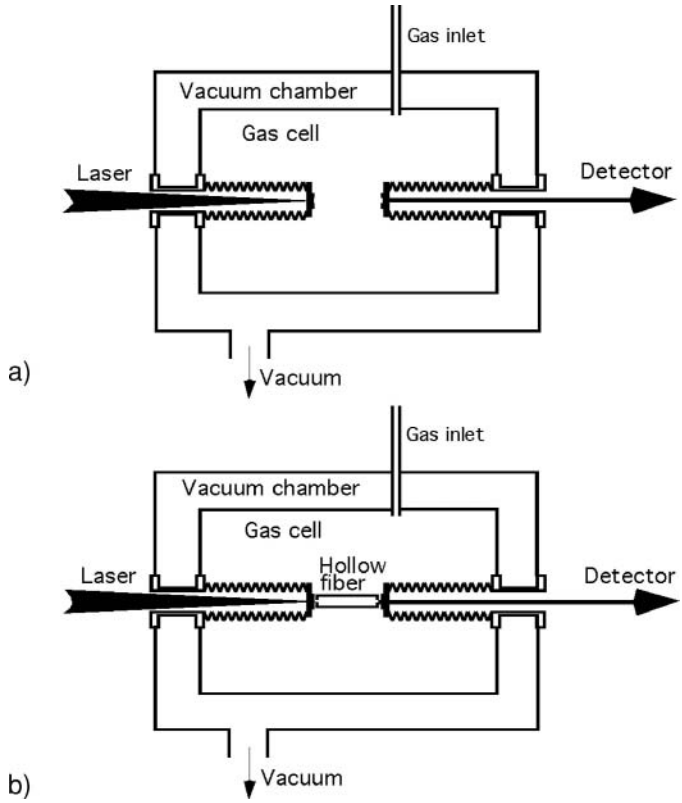

Fig. 12.20. Wave guiding harmonic sources using (a) hollow fiber and (b) self-channeling.

were focused in front of the fiber. The focal length was 50 cm, the diameter of the focal spot 90 μm, and the confocal parameter 0.4 cm. The hollow fiber had a bore diameter of 126 μm in fused silica with a length of 3 cm.

For the results presented in Figure 12.21a, argon pressure in the gas cell was 5 Torr. The laser intensity in the interaction region was estimated at 5×10^{14} W/cm^2. The harmonic spectrum was time integrated over 10 s. The spectral lines appearing in the region around the 11th to the 13th harmonic are the second-order diffraction of the 21st to the 27th harmonics. The comparison of the spectrum presented in Figure 12.21a with that obtained in the same conditions, but without wave-guide, confirmed that the intensity enhancement around the 25th harmonic was a marked effect of the hollow fiber.

The measured enhancement factors are plotted in Figure 12.22. One can see a rapid increase of the intensity enhancement from the 21st to the 25th harmonic where it reaches a factor ∼100. For comparison, calculations of the

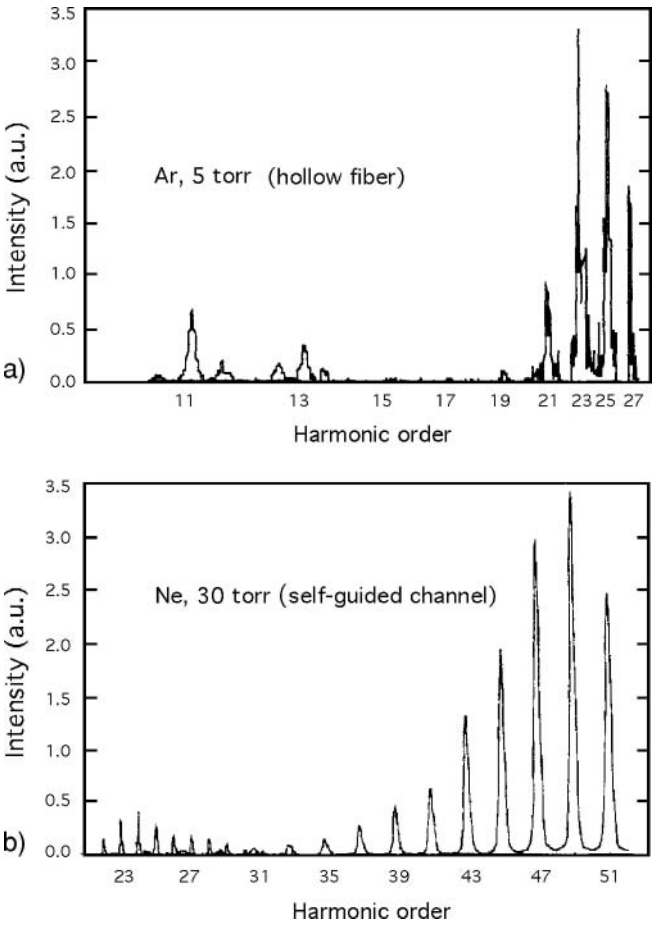

Fig. 12.21. Comparison of high-order harmonic generation obtained in hollow fiber, with argon, and in self-guided channel, with neon. The lines appearing in the region of the 11th to the 13th harmonic in Ar are the second-order diffraction of the 21st to the 27th harmonics.

phase mismatch $\Delta k_{\mathrm{q}} = 2\pi\,(n_{\mathrm{q}}/\lambda_{\mathrm{q}} - qn/\lambda)$ [(Eq. (11.11)], for argon in the microfiber, provides the enhancement distribution represented by the solid curve. There is a good agreement between calculations and experimental measurements.

Removing the hollow fiber from the gas cell, self-channeling could be experimented in neon in order to extend the phase matched harmonics to shorter wavelengths. As shown in Figure 12.20b, the experimental geometry is nearly the same as in the previous experiment, except for the removal of the fiber. The focused laser beam diameter was measured to be 40 μm instead 90 μm in the hollow fiber experiment. Transverse observation of the laser pulse propagation

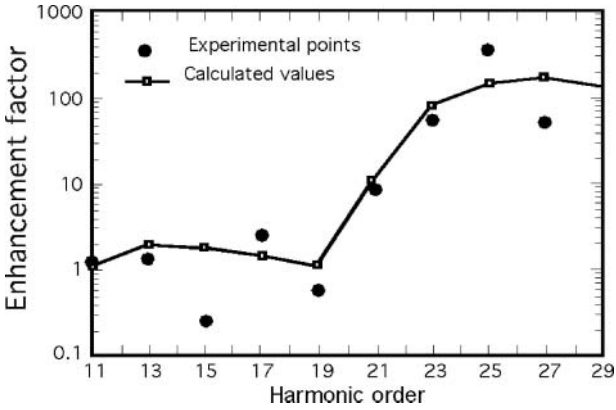

Fig. 12.22. Harmonic intensity enhancement factor provided by wave guiding in a hollow fiber. Argon pressure: 5 Torr; laser intensity: 5×10^{14} W/cm^2. Circles: experimental points; solid curve: calculation results.

showed a column of orange light, which denoted a plasma channel of length ∼8 mm. Self-guiding effect was deduced from the observation of a decrease of the beam divergence when the pressure increased above 10 Torr. The distance between the two 300-μm diameter pinholes, mounted at the ends of two bellow arms, determined the propagation length. The interaction intensity had been estimated at 1.5×10^{14} W/cm^2 and the value of pulse duration at 100 fs.

For a 1-mm interaction length, on pressurizing the gas cell from 10 Torr to 40 Torr, the observed high-order harmonic spectra exhibited a plateau type. Moreover, at a pressure of 30 Torr, all the harmonics from the 23rd to the 51st were equally magnified when the interaction length increased from 1 mm to 4 mm. Changes in the harmonic intensity distribution emerged after the interaction length has been increased beyond 4 mm. Harmonics near the cutoff order still increased, whereas the harmonics in the plateau region started to diminish. From 4 mm to 7 mm length, harmonics near the cutoff increased by a factor of 4 whereas the plateau harmonics decreased by a factor of 10. The harmonic spectrum obtained with a 30 Torr neon pressure and an interaction length of 7 mm is shown in Figure 12.21b.

From equations (11.1) and (11.2) the intensity of the qth harmonic varies according to relation $I_\mathrm{q} \propto N^2 \chi_\mathrm{q}^2 F_\mathrm{q}^2$ where N is the atom density, χ_q is the qth-order nonlinear susceptibility (11.1). F_q is the z-dependent phase-matching integral between the fundamental and the qth-harmonic field, which results from the exponential term in the second member of equation (11.8). Therefore, one can estimate the phase-mismatch by fitting I_q to the experimentally intensities measured for 30-Torr neon as a function of the interaction length. The values of Δk obtained for the harmonic spectrum of Figure 12.21b were 8, 6, 4, and 0.1 cm^{-1} for the 25th, 37th, 43rd, and 49th harmonics, respectively. Thus phase-matching was almost complete for the 49th harmonic. As

a result the conversion efficiency around the 49th harmonic was found to be $\sim 10^{-6}$, which is significantly larger than that obtained from standard gas jet experiments.

12.2.6 Emitters of Complex Structure: Molecules, Clusters, Solid–Vacuum Interfaces

12.2.6.1 Molecules

There are significant potential differences expected for harmonic generation between atoms and molecules on account of the additional complexity introduced by the molecular structure. The geometry of the molecule can be linear of variable chain length, bent or cyclic. According to the character of molecular orbitals, the initial electronic state may show nonatomic features. Therefore, there are many possible causes of change in harmonic conversion efficiency in comparison with atomic gases. Harmonic generation in molecular systems has been studied in a number of works to answer questions about harmonics produced in molecules as also in the fragments following molecule dissociation, or about particular electronic structures potentially able to produce larger harmonic yield [81–93]. However experiments did not yet reveal any significant improvement of the general characteristics of harmonic emission compared with noble gases.

Figure 12.23 shows harmonic spectra for two groups of molecules (ionization potentials from 10.9 to 12.9 eV and from 13.8 to 15.8 eV, respectively) obtained with a 150-ps pulse of 800-nm laser radiation [83]. Xe and Ar spectra obtained in the same experimental conditions are represented for comparison. The backing pressure was kept constant at 1300 mbar. The number density in the jet was found of the order of 10^{18} atoms/cm^3. The laser focus was placed at the centre of the gas jet. The focused intensity was 2×10^{14} W/cm^2 with an uncertainty of about 50%.

Spectra exhibit the characteristic plateau and cutoff behavior for both atomic and molecular gases. It also shows that the plateau is wider for the gases with a high ionization potential (Fig. 12.23b) than for those with a low ionization potential (Fig. 12.23a). On the other hand one does not observe any significant difference between the behaviors of diatomic and more complex molecules and, regarding the conversion efficiency in the plateau region, molecules do not show advantage over the atomic gases. Measurements performed with 400-nm wavelength laser radiation lead to results which present the same characteristics as those of the spectra obtained at 800 nm. It is also observed that, in the case of the SF_6 molecule, which is not represented in the figure, dissociation taking place at an early stage might contribute to harmonic generation.

Insight into the role of fragmentation in the case of complex molecules has been obtained using of two different pulse lengths to produce harmonics [86]. With short pulses (70 fs) the variation of harmonic intensity in benzene

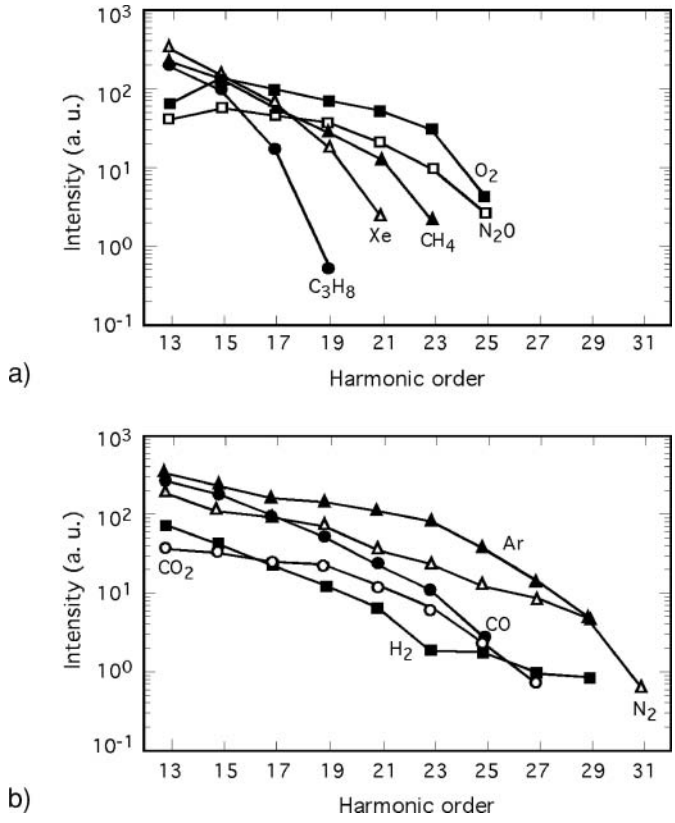

Fig. 12.23. Harmonic spectra of two groups of molecules. Ionization potentials are comprised between 10.9 and 12.9 eV for the group (a) and between 13.8 and 15.8 eV for the group (b). Xe and Ar spectra obtained in the same experimental conditions are represented for comparison (Ref. [83]).

(C_6H_6) and cyclohexane (C_6H_{12}), as a function of the laser intensity, had exactly the character expected from atoms, i.e. a rapid initial increase and then saturation for all the orders observed ($q = 7$–13). The intensity range for these observations was 5×10^{13}–2×10^{15} W/cm^2. Saturation is ascribed to the depletion of neutral species following ionization at high intensity.

With longer pulses (240 fs) the intensity curves do not show any trace of saturation up to the laser intensity upper limit of 5×10^{15} W/cm^2. This result suggests that the dissociation of benzene and cyclohexane molecules, which occurs at an increasing rate during the laser pulse, is accompanied by the transfer of harmonic generation from molecules to fragments.

Investigating harmonic generation efficiency with a direct control of molecule dissociation confirms clearly that dissociation enhances the harmonic conversion efficiency [91]. To perform such a control, the experimental arrangement used consisted of two laser pulses separated in time, both focused

into the gas, one to generate the photodissociation of iodine molecules, the other to excite harmonic generation. The duration of the preparation pulse (molecule dissociation) was 300 ps with 60-mJ energy, while the harmonic excitation pulse duration was only 70 fs with 40-mJ energy. The relative delay Δt between the two pulses varied over a range of 700 ps, with a resolution <100 fs. The focused intensities in the interaction region could vary in the range of 5×10^{13}–5×10^{14} W/cm^2 for the 70 fs pump pulse and of 1×10^{11}–2×10^{12} W/cm^2 for the 300 ps preparation pulse (below the threshold for HHG).

Conversion efficiency measurements have been performed for the 9th harmonic from $\Delta t = -200$ ps (pump pulse preceding the preparation pulse) to $\Delta t = 500$ ps (preparation pulse preceding the pump pulse). The efficiency was found to increase nearly linearly in the interval -150 ps $\lesssim \Delta t \lesssim 150$ ps, i.e. as long as the pump pulse reaches the gas during the dissociation induced by the 300-ps pulse. The maximum enhancement factor was ∼1.8. For $\Delta t > 150$ ps harmonics were generated entirely from atomic iodine and their intensities remained approximately constant. A final measurement point obtained for $\Delta t = 9$ ns showed the same behavior to continue.

Very interesting are the observations of change of harmonic intensity as a function of pump intensity, with and without dissociating pulse. For the results presented in Figure 12.24, the dissociating pulse interacted with the I_2 molecules 170 ps before excitation pulse coming. The figure shows a practically constant enhancement factor due to molecule dissociation, through the excitation intensity range, with an averaged value of 2.6. This result suggests that the observed enhancement has its origin in a fundamental difference between the responses of single atoms compared to molecules. Considering that the dipole phase depends upon the angle between the molecular axis and the pump laser polarization, an additional dephasing mechanism would exist between the emitters in randomly aligned molecular media, which induces a worse phase-matching compared with the atomic case [91]. This explanation could account for the general observation of a less efficient harmonic generation from molecular species than from atoms. Further works in harmonic generation in laser-aligned molecules support this interpretation [92].

12.2.6.2 Clusters

At a certain critical value of the backing pressure above the gas jet, atoms begin bunching together owing to cooling and fast expansion. They form Van der Waal bonded clusters of a few nanometers in diameter. Clusters under consideration in this section hold several hundreds to several thousands atoms.

Since clusters are smaller than the laser wavelength, the individual atomic electrons may oscillate coherently in the laser field so that they contribute to a global cluster electric dipole, which will modify the nonlinearity of the medium. The impact of a short laser pulse on clusters produces microplasmas which remain compact by inertia for time scales of the order of the laser pulse

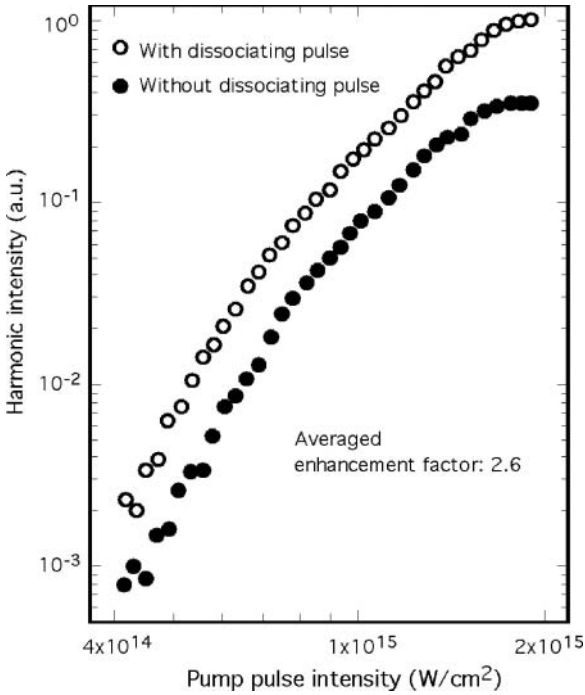

Fig. 12.24. Enhancement factor due to molecule dissociation, through the 4×10^{14}–2×10^{15} W/cm^2 excitation intensity range. The dissociating pulse precedes the exciting pulse by 170 ps. The enhancement, of 2.6 mean-value, proves to be independent of the excitation intensity (Ref. [90]).

($\lesssim$100 fs). Therefore, investigation of high harmonics generated from clusters will show properties that will differ from those of atoms in gas [94–98].

Experimental conditions of harmonic generation from argon clusters illustrate this difference. The experimental arrangement comprises a pulsed-gas jet fed under 7.3-bar Ar backing-pressure, with a 600-μm diameter aperture, which produces clusters containing approximately 500 atoms (radius ∼2 nm), and alternatively a static gas cell (∼30 mbar) which contains only monomer atoms [94]. The average atom density is about $10^{18}\,\mathrm{cm}^{-3}$ in both monomer and cluster gas.

Figure 12.25 shows the yield of the 23rd harmonic from (a) monomers and (b) clusters as a function of pump intensity (140-fs pulse duration, 825-nm wavelength laser pulses). One sees that the harmonic emission outset needs much higher pump intensity for clusters than for monomers.

To explain this observation, one considers clusters as dielectric spheres in which the laser electric field is shielded by a factor depending on a dielectric constant which reflects both contributions of bound and free electrons. Calculation shows that shielding results in a time-averaged decrease in the

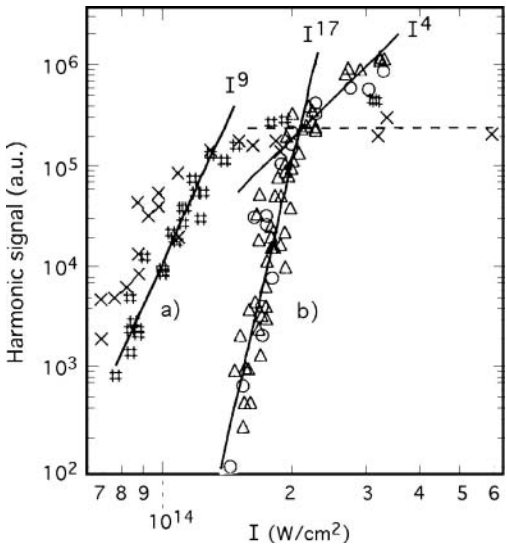

Fig. 12.25. Measured harmonic signal for Ar gas (right line a) and for Ar clusters (right line b). For clusters the harmonic appearance intensity is larger and the slope is stiffer than for atoms. Static gas cell pressure, 70 and 40 Torr; backing pressure of sonic jet, 115 and 135 psi.

laser intensity within clusters. This may explain that the laser intensity ought to be enhanced in clusters, compared with monomers, in order to reach the harmonic emission intensity threshold.

Moreover the power law of yield increase versus laser intensity is calculated to be I^{17} for clusters while it is I^9 only for monomers. The stiffer slope in the case of clusters is assigned to the difference of the atomic potential experienced by a bound electron in a cluster, where it is modified by the nearest neighbors (three-well potential), compared to an isolated atom (single-well potential). Though subject to some noise, calculations performed by using a semiclassical model for the 19th through the 23rd harmonics, indicate a power law I^{20} for the three-well potential versus I^{15} for the single-well one.

Figure 12.25 also shows differences in harmonic intensity saturation, strongly marked in the case of monomer atoms, especially at a pressure of $\sim$53 mbar, but much less manifest in the case of clusters where the power law reduces from I^{17} to I^4 above 2×10^{14} W/cm^2. Besides the cutoff in harmonic spectra obtained from clusters is observed to somewhat shift to higher energy with respect to the cutoff in monomer atom spectra [94]. It is suggested that both these experimental facts should be attributed to the increase of the effective binding energy, i.e. of the ionization potential I_{P} in the cutoff law 10.4 in clusters compared with isolated atoms.

At this point remains the question of the comparison of harmonic yields between clusters and monomers. A direct comparison has been made possible

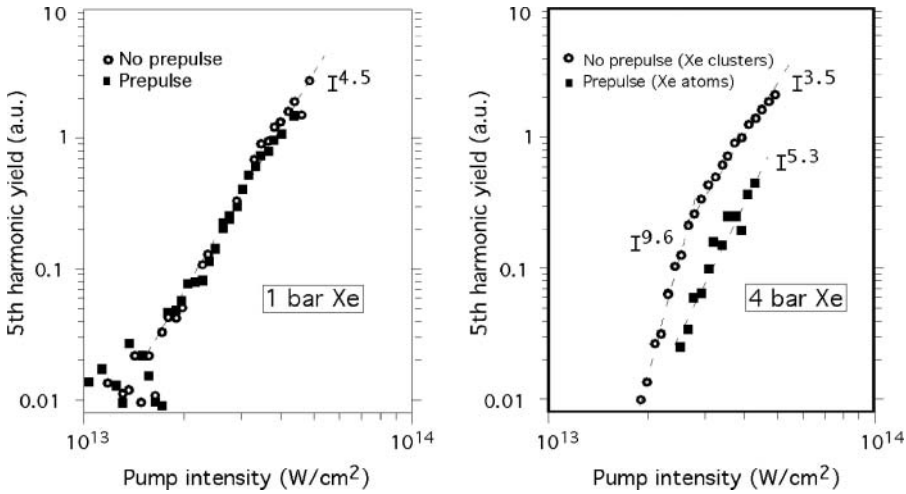

Fig. 12.26. Intensity comparison of harmonics produced with clusters (white circles) and with atomic gas (black squares) and for two backing pressures.

by using an Xe gas-jet with high backing pressure (1–4 bar) yielding clusters, and UV prepulse (266-nm wavelength, 7-ns duration) that disassemble the weakly bounded clusters at will [95]. A Raylegh scattering diagnostic is applied to the gas-jet to ensure that no cluster remain in the interaction region. Comparison of harmonic intensity is made for the fifth harmonic of 390 nm light ($\lambda_5 = 78$ nm) in Xe with prepulse (no clusters) and without prepulse (clusters). Figure 12.26 shows the results for two values of the backing pressure, 1 bar, near the threshold of cluster formation, and 4 bar. For the lower pressure (Figure 12.26a), the harmonic yields with and without prepulse are almost identical. However for a 4-bar backing pressure one observes in Figure 12.26b a three- to five-fold intensity enhancement without the prepulse, i.e. when the 160-fs, 780-nm laser is interacting with clusters of ∼2500 atoms. This gives the magnitude of the increase of conversion efficiency from isolated Xe atoms to clusters in the 2.5×10^{14} to 5×10^{14} W/cm^2 laser intensity range.

12.2.6.3 Harmonic Generation from Solid–Vacuum Plasma Interface

The mechanism of HHG by strong laser interaction with solid targets is physically different from that based on the nonlinear dipole interaction with single atoms. However here we give a general outline of investigations about this new HHG mechanism because it is a part of the effort to increase harmonic generation efficiency, especially to shorter wavelengths.

We recall that the impact of an intense laser-pulse on a solid target surface in vacuum generates a thin plasma layer, whose density varies from vacuum to solid density over a short length of a few microns (cf. Fig. 5.2 in Section 5.1.1). Without going into the details of the processes that determine the steep

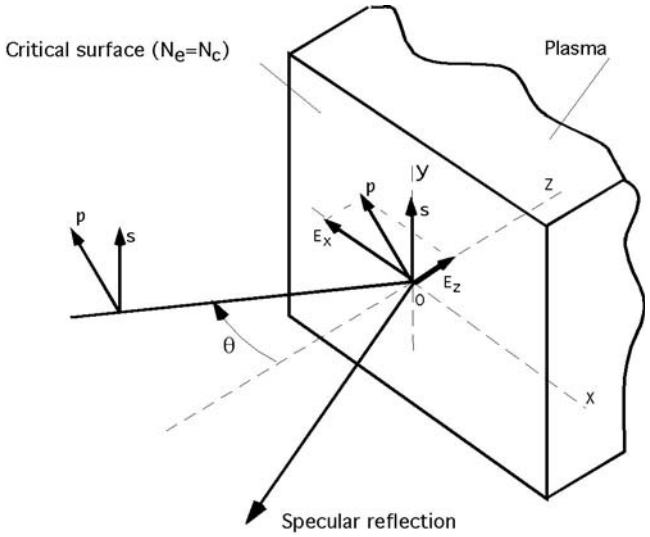

Fig. 12.27. Oblique incidence reflection at the critical surface of the plasma. s-Polarized radiation is specularly reflected. p-Polarized radiation has a longitudinal E_z component which induces resonant absorption and plasma oscillations in regions where the electron density increases above the critical value.

density gradient at the boundary of laser light absorption, we will show the origin of the nonlinear response of the plasma to excitation by laser radiation. For detailed presentations of theoretical investigations on this subject the reader is recommended to refer to original papers [99–106].

A process which plays an important role in laser-plasma interaction is the so-called *resonant absorption*. Lets us consider the plasma surface for which the free electron density N_e equals the critical density (Eqs. 2.19, 2.20)

$$N_\mathrm{c} = \frac{4\pi^2 c^2 \varepsilon_0 m_\mathrm{e}}{e^2 \lambda_\mathrm{L}^2} \simeq \frac{1.1 \times 10^{21}}{\lambda_{\mathrm{L}[\mu\mathrm{m}]}^2} \left[\mathrm{cm}^{-3}\right]$$

where λ_L is the laser light wavelength. Laser light does not penetrate into the plasma beyond the surface of critical density. Figure 12.27 shows, for p and s polarizations, the sketch of the electric field components corresponding to a beam arriving under oblique-incidence onto the critical surface, where specular reflection occurs. For s-polarization, the field vector is parallel to the critical surface. There is obviously no field component in the direction of the propagation axis, *OZ*. Conversely, for the p-polarized field, the oblique incidence induces two components, E_x and E_z, the second of which penetrating the plasma beyond the critical surface.

Therefore, the interaction of a linearly polarized oblique beam with a plasma depends strongly on the direction of the incident light polarization. This remains partially true for a beam focalized in normal incidence since, in

this case; the ray paths are oblique excepted near the axis of the focal cone. If the critical surface is perfectly plane, a s-polarized beam is specularly reflected, without excitation transfer to plasma electrons. If the critical surface is rippled by plasma instabilities, as for instance Rayleigh–Taylor instabilities, multiple local penetrations of a s-polarized wave become possible. This may contribute harmonics to the generated spectrum.

Concerning the E_z component of the electric field, it induces oscillations of plasma free electrons (plasmons) perpendicularly to the critical surface. The source of the nonlinear response to plasmon excitation is the longitudinal variation of the restoring forces acting upon the charge perturbation, which results from the density gradient along the OZ axis. A first consequence of this dissymetry of electron oscillations is an effect of laser–matter interaction, well known in inertial confinement fusion research, that is the ejection of fast electrons and of accompanying ions from plasma toward vacuum. The second consequence is that these electrons that keep their periodic motion across the interface give rise to radiation at harmonic frequencies of the driving fundamental laser frequency [99].

Following P. Gibbon (Ref. [102]) the harmonic generation in solid–vacuum interface plasma can be described via a linear mode coupling occurring in the steep density gradient region, beyond the critical density, N_c. The incident laser electromagnetic wave $(\omega_L, \mathbf{k}_L)$ creates plasmons $(\omega_p, \mathbf{k}_p)$, with $\omega_p = \omega_L$. As illustrated in Figure 12.28, the laser photon and the plasmon mix to produce a second harmonic $\omega_2 = 2\omega_L$. A nonreflected part of the ω_2 wave propagate to the $4N_c$ surface, that is to the critical density for ω_2, creating a plasmon of frequency $2\omega_L$. This generates in turn a third harmonic at $3\omega_L$, which is resonant at $9N_c$ and so on. It is clear that, to extend this process to higher harmonics, the laser field must be strong enough to allow its E_z component to reach denser plasma regions.

One sees that both odd and even harmonics can be generated by this mechanism. Furthermore, calculations predict a flat harmonic spectrum with a cutoff fixed by the plasma frequency corresponding to the upper level density, N_u, of the steeply rising density profile. Substituting $\lambda = 2\pi c/\omega$ in Eq. 2.20, Figure 12.28 shows that the maximum harmonic order should be

$$q_{\max} \lesssim \sqrt{\frac{N_u}{N_c}} \tag{12.6}$$

where numerical simulations of the pressure balance between laser light and cold dense plasma lead to the approximative relation

$$N_u \sim \frac{E_0^2}{8\pi T_c} \tag{12.7}$$

In this equation, E_0 is the incident laser electric field and T_c, the background temperature [107].

For very high laser intensities, the relativistic electron velocity, $\mathbf{v}$, makes it necessary to take into account not only the force $e{\cdot}E_Z$ but also the force

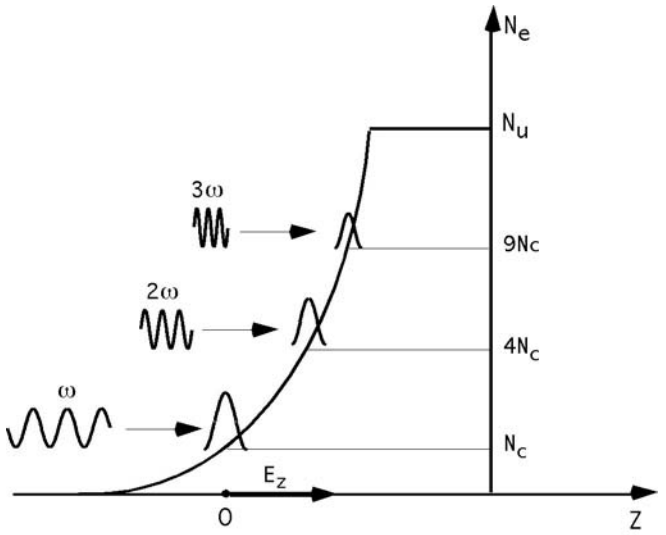

Fig. 12.28. Generation of harmonics near the plasma critical surface. N_e is the rapidly varying electron density in the region of the plasma critical density N_c. E_z is the longitudinal component of the laser electric field reaching the plasma in oblique incidence. Successive mixings of E_z-excited plasmons and laser photons generate harmonics. N_c, $4N_\mathrm{c}$, $9N_\mathrm{c}$, ... are the successive critical densities corresponding to the fundamental and the 2nd, 3rd, ... harmonics. The upper density N_u is fixed by the pressure balance between light and cold dense plasma.

$(e/c) \cdot \mathbf{v} \times \mathbf{B}$ where $\mathbf{B}$ is the magnetic field [108]. Harmonics may thus be generated by nonlinear mixing of transverse and longitudinal oscillations. This opens the way to the generation of even harmonics from s-polarized incident radiation. As for p-polarized radiation at 45° incidence, numerical simulations predict the conversion efficiency for high orders ($q \gg 1$) to vary according to relation [102]

$$\eta_\mathrm{q} \simeq 9 \times \left[I\lambda_\mathrm{L}^2 \left(10^{18}\ \mathrm{W/cm^2\,\mu m^2} \right) \right]^2 q^{-5} \tag{12.8}$$

An important fact is that the maximum observable harmonic order, q_max, is shown to scale as $\left(I\lambda_\mathrm{L}^2 / T_\mathrm{e}^{1/2} \right)$, where T_e is the electron temperature, without any effective harmonic cutoff. In other words, at a given laser wavelength, there would be no other limit to the extension of harmonic to shorter wavelengths than the available laser intensity. Whatever it may be, calculation predicts that, for $I\lambda_\mathrm{L}^2 > 10^{19}\ \mathrm{W/cm^{-2}/\mu m^2}$ and $N_u/N_\mathrm{c} = 10$, at least 60 harmonics can be generated with power efficiency $>10^{-6}$ (see for instance [110, 112]).

The investigation of harmonic properties emitted by solid–vacuum interface has been made easier by the demonstration that harmonic generation can be interpreted as a reflection of the driving beam on a relativistic

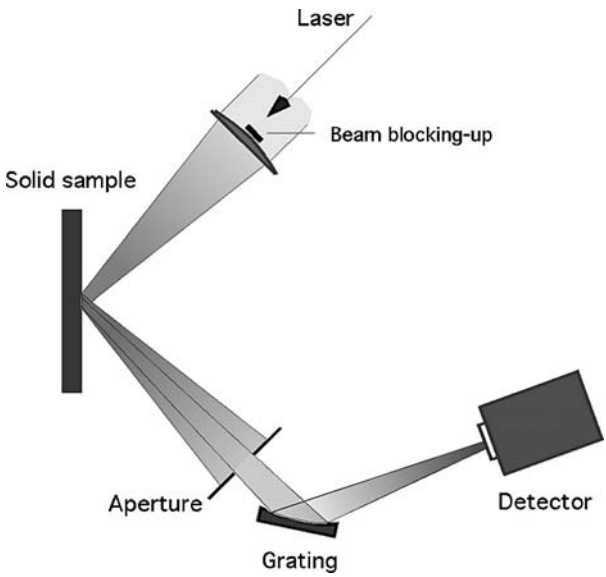

Fig. 12.29. Diagram of an experimental setup generating high harmonics in the thin plasma layer produced by laser impact at the surface of a solid material.

oscillating mirror [104]. It is assumed that the duration of the light pulse is sufficiently short for the motion of the ions to be neglected. Then the collective oscillating motion of the electrons is represented by the motion of the critical surface (cf. Fig. 12.27), which behaves as an effective reflecting surface. The periodic change of electron density associated to this motion induces a phase modulation of the reflected wave. Let $s(t) = s_0 \sin \omega_{\mathrm{m}} t$ be the displacement of the reflecting surface in the z-direction. The phase shift of the reflected wave resulting from this displacement is given by

$$\phi(t) = \frac{2\omega_{\mathrm{L}} s_0}{c} \cos\theta \sin \omega_{\mathrm{m}} t \tag{12.9}$$

and the electric field , E_{R}, of the reflected wave satisfies

$$E_{\mathrm{R}} \propto e^{-i\varpi_{\mathrm{L}} t} e^{i\phi(t)} = e^{-i\varpi_{\mathrm{L}} t} \sum_{n=-\infty}^{n=\infty} J_n \left(\frac{2\omega_{\mathrm{L}} s_0}{c} \cos\theta \right) e^{-in\omega_{\mathrm{m}} t} \tag{12.10}$$

where J is the Bessel function. Now it is shown that the periodic motion of the reflecting surface is produced at frequency $2\omega_{\mathrm{L}}$, or at a superposition of ω_{L} and $2\omega_{\mathrm{L}}$, depending on the polarization and on the angle θ. Therefore the second member of equation (12.10) represents even and odd harmonics of the incident laser light. This model is very useful when discussing harmonic selection rules.

The diagram of a typical experimental setup for the investigation of HHG by solid–vacuum interface is shown in Figure 12.29. It is similar to the

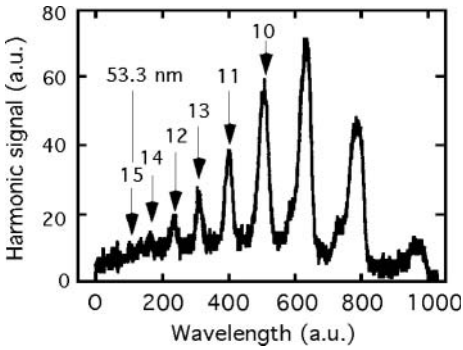

Fig. 12.30. Harmonic of 800-nm laser radiation produced from a 200-nm aluminium layer. Odd and even harmonics are observed (Ref. [109]).

standard setup (see for instance Fig. 10.1), excepted for the obliquity of the incidence angle on the solid target surface. A small disk blocks the center of the incident laser beam in order to suppress the specularly reflected fundamental radiation. An aperture is used to block the reflected laser beam while passing harmonics in the center of the beam. All the elements displayed in the figure are enclosed in a nonrepresented vacuum chamber.

Figure 12.30 shows a harmonic spectrum obtained from the 800-nm wavelength light of a titan sapphire laser of 130 fs duration [109]. Targets were optical flats coated with a 200 nm aluminium layer. The available energy was 30 mJ and the peak intensity was estimated at $\sim 10^{17}$ W/cm^2. The pressure in the vacuum chamber was 10^{-3} mbar. The spectrum extends between 40 nm and 100 nm. Both odd and even harmonics are observed. The highest order is the 15th harmonic at a wavelength of 53.3 nm. An order of magnitude estimate of the photon yield gives $\sim 2 \times 10^9$ and $\sim 10^8$ photons per pulse for the 10th and the 15th harmonic, respectively. This corresponds to photon conversion efficiencies of $\sim 2 \times 10^{-8}$ and $\sim 10^{-9}$ respectively. Experimental conditions do not allow one to decide wether the shortest wavelength of observed harmonics corresponds to the cutoff law of equation (12.6) or to a limit simply fixed by the laser intensity according to the $I\lambda^2$ scaling.

A number of experimental investigations have been performed with picosecond instead of femtosecond pulses [110–113]. Norreys et al. observed up to the 75th harmonic of the p-polarized 1052-nm infrared light of a Nd-laser yielding 2.5 ps pulses, without any evidence of a clearly defined cutoff [110]. The angle of incidence on the target was 54°. Target consisted of a 2 μm CH plastic coated on 200-nm thick 15-μm wide Al cross wires on optically polished glass slabs. The intensity on target was estimated at $\sim 9 \times 10^{18}$ W/cm^2.

The harmonic emission exhibits a significantly larger angular distribution than the cone angle of the laser beam. Detailed investigation of the third harmonic angular distribution, over a 103° angle, did not show any intensity change. The assumption of isotropic harmonic emission was thus made.

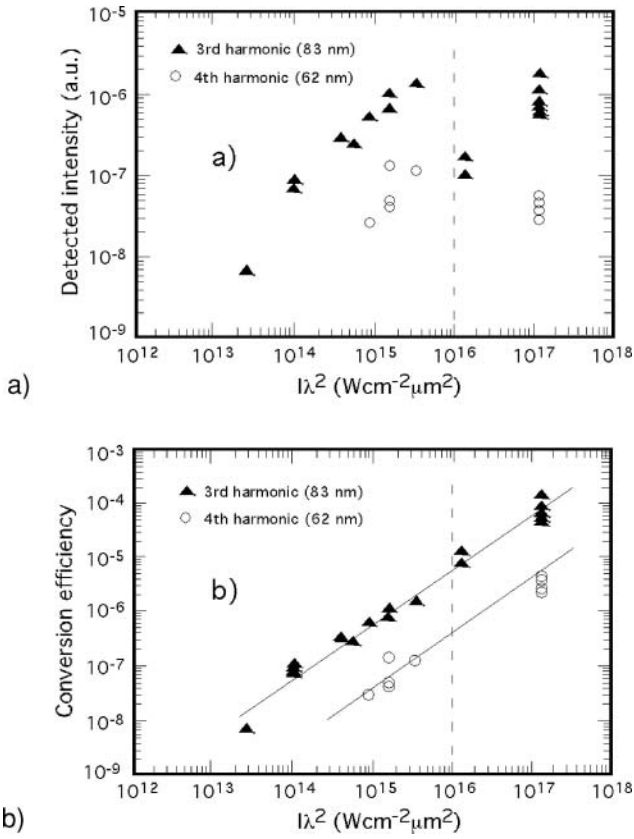

Fig. 12.31. (a) Third and fourth harmonic intensities plotted versus $I\lambda_{\mathrm{L}}^2$. A drop occurs at $I\lambda_{\mathrm{L}}^2 \sim 10^{16}$ W/cm^{2}μm^2. (b) Conversion efficiency deduced from the measured $I\lambda_{\mathrm{L}}^2$ values after intensity integration in 2π sterad when $I\lambda_{\mathrm{L}}^2 > 10^{16}$ W/cm^{2}μm^2. The results are consistent with the assumption of an essential change of reflection processes when $I\lambda_{\mathrm{L}}^2$ is above the limit of 10^{16} W/cm^{2}μm^2.

Similar observations were made also with s-polarized light. The lack of difference between s- and p-polarization relatively to harmonic emission suggested that the critical surface was rippled, likely by instabilities of the Rayleigh–Taylor type. Owing to the isotropic angular distribution, the radiated powers for single harmonics were calculated assuming a constant yield into 2π steradian. Energy conversion efficiencies $\geq 10^{-6}$ were so obtained into each harmonic up to the 68TH. Nevertheless it would be hazardous to compare these values to those obtained when the emitted beam divergence is a few mrads only.

Insight in harmonic angular distribution in various experimental conditions has been provided by the systematic study of the $I\lambda^2$ scaling of the conversion

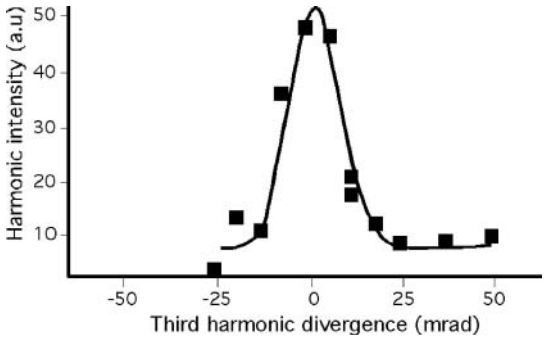

Fig. 12.32. Angular profile of the third harmonic for $I\lambda_L^2 \sim 6.10^{14}$ W/cm^{2}μm^2. The emission of the same harmonic is found nearly isotropic for $I\lambda_L^2 \sim 2.10^{17}$ W/cm^{2}μm^2 (Ref. [113]).

efficiency [cf. Eq. (12.8)] [112] . Experiments were performed using a KrF laser providing 1-ps pulses at 248.6 nm. Targets consisted in optically polished slabs of fused silica. The incident radiation was p-polarized. A first result of this choice was the harmonic intensity to exhibit an extremely strong dependence on laser radiation incidence angle, with a peak occurring around 30°.

Harmonic intensities measured as a function of $I\lambda_L^2$ are displayed in Figure 12.31 for the third (83 nm) and the fourth (62 nm) harmonics. One can see in Figure 12.31a that the harmonic intensity increases till $I\lambda_L^2$ reaches a value $\sim 10^{16}$ Wcm^{-2} μm^2 and drops significantly near this point. The authors suspected that this feature was due to a transition from specular to diffuse emission of harmonic radiation. Therefore they deduce the conversion efficiencies from the measured intensities, assuming that the corresponding emission was confined in the $f/3.3$ cone angle of the reflected laser pulse for $I\lambda_L^2 < 10^{16}$ W/cm^{2}μm^2 but that, for $I\lambda_L^2 \geq 10^{16}$ W/cm^{2}μm^2, emission was distributed into 2π steradian. Figure 12.31b shows that this assumption leads the linear $I\lambda_L^2$-scaling of the efficiency to cover the full investigated range of intensities, what is consistent with numerical simulations for low harmonics orders [101]. This result clearly supports the interpretation of the observed drop of the intensity in terms of a transition from specular to diffuse reflection between 4×10^{15} and 2×10^{16} W/cm^{2}μm^2, likely owing to surface rippling at higher irradiance.

The direct observation of the transverse profiles of harmonic emission confirms the strong increase of the beam divergence for increasing laser intensity [113]. Angular profile measurements have been performed with the p-polarized radiation of a 2.2 ps, 1024 nm Nd-laser. Figure 12.32 shows the rather narrow profile measured for the third harmonic with $I\lambda_L^2 \sim 6 \times 10^{14}$ W/cm^{2}μm^2. Similar profiles, of FWHM ∼20 mrad, are also obtained for the second, fourth, and fifth harmonics, showing the harmonic divergence to be similar to that of the laser at this level of irradiance (Ref. [113a]). In contrast

Table 12.3. Experimental parameters for the three sets of measurements presented in Figure 12.33. Contrast ratios have been evaluated 1 ps before the peak pulse

	I	II	III
λ (nm)	395	790	790
Contrast	10^{-6}	$\sim 5 \times 10^{-3}$	10^{-3}
L/λ_L	~ 0.2	$\gtrsim 0.4$	$\gtrsim 0.8$

with these results, the divergence increases considerably for the same harmonics as $I\lambda_L^2$ is between 1×10^{15} and 1×10^{16} W/cm^{2}µm^2. Furthermore, at 2×10^{17} W/cm^{2}µm^2, the harmonic emission is found nearly isotropic ([113b]).

Face to the limit assigned, by critical surface instabilities, to the increase of irradiance in the case of long laser pulses, the remedy appears being to turn again to femtosecond pulses in order to shorten the time for instabilities to develop. However it is not sufficient that, strictly considered, the pulse is short. A possible pedestal before the pulse, as well as poor contrast ratio, may have a detrimental effect on harmonic emission by creating plasma before the onset of the short pulse, what modifies plasma conditions at the onset of the pulse.

To investigate these effects, Zepf et al. [114] realized three experimental cases differing from each other by the contrast ratio of a 150-fs driving pulse. The contrast ratio at 1 ps before peak was deduced from autocorrelation measurements of the pulse temporal profiles. Moreover, using the temporal profile data to feed a hydrodynamical code allowed for estimating the density scale length L/λ_L, where L defined by equation

$$\frac{dn_e(z)}{dz} = \frac{n_c}{L} \tag{12.11}$$

determines the slope of the $n_e(z)$ curve near the critical density n_c, namely the steepness of the density profile. The Ti:sapphire laser produced 150-fs, 200-mJ pulses at 790 nm with a contrast ratio I_{foot}/I_{peak} of 10^{-3}. The laser light was incident onto an optically polished glass target at 45°. A slight change in the grating setting of the pulse compressor unit provided an enhancement of the contrast ratio to $\sim 5 \times 10^{-3}$. Frequency doubling of the pulses in a KDP crystal resulted in 60-mJ, 395-nm pulses with a contrast of 10^{-6}, 1 ps before peak pulse. Table 12.3 summarizes the experimental characteristics for the three experimental cases. The density scale length has been estimated for $I\lambda_L^2 = 1.6 \times 10^{18}$ W/cm^{2}µm^2.

The only observable harmonic with s-polarized light was the third harmonic of the 790 nm radiation and the efficiency was three orders of magnitude lower than with p-polarization. Its angular distribution was concentrated in the specular direction.

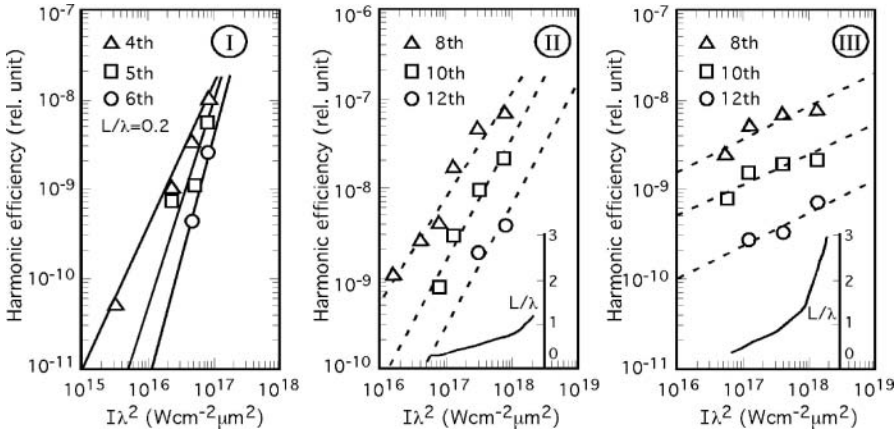

Fig. 12.33. Scaling of harmonic efficiency as a function of $I\lambda_{\mathrm{L}}^2$ for the experimental parameters described in Table 12.3. For low contrasts (frames II and III) the long time between the onset and the peak of the pulse prevents the density length scale L/λ, to be represented by a constant value. These results show that high efficiencies need ultrashort clean pulses.

Harmonic efficiencies presented in Figure 12.33 have been measured for p-polarized laser light. In the high contrast case (Fig. 12.33-I) the figure shows the $I\lambda_{\mathrm{L}}^2$ scaling of the efficiency for a fixed value of the density length scale, $L/\lambda_{\mathrm{L}} = 0.2$. Numerical calculations show this value to correspond to the range of the optimum of conversion efficiency. The white symbols are the experimental points for the 4th, 5th, and 6th harmonics. The solid lines give the slope of the scaling predicted by the numerical code. The slopes are 1.5, 2.2, and 2.6 for the 4th, 5th, and 6th harmonics, respectively. One observes an excellent agreement between simulations and experiments over a large range of intensities. A single density scale length ($L/\lambda_{\mathrm{L}} = 0.2$) is sufficient to obtain this result because, at high contrast, the peak intensity only has an influence on the onset of plasma formation and consequently on the density scale length.

For lower contrasts (Fig. 12.33 II and III), one cannot fit the experimental data with the $I\lambda_{\mathrm{L}}^2$ intensity scaling, using a single value of L/λ_{L}, because the scale length itself strongly depends on the time interval between the onset of the plasma formation and the peak pulse. In this case the scale length of the plasma increases with increasing intensity. The dashed lines are thus simply power law fits to the experimental points. The solid lines, at the bottom of each frame, represent the set of the values that L/λ_{L} should have in order that the experimentally observed slopes might be reproduced by the numerical simulations. The increase of the density scale length to higher irradiance results from the plasma formation onset occurring earlier in time, what gives more time before the peak pulse for a longer density gradient to develop via hydrodynamical expansion.

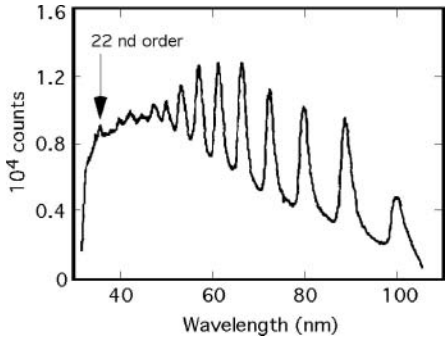

Fig. 12.34. Harmonic spectrum obtained by focusing a 35-fs p-polarized laser pulse onto polished optical glass. The pulse contrast ratio is 10^{-6}.

A clear conclusion of this study is that the lower the contrast of the laser pulse, the weaker the I/λ^2 scaling of the harmonic conversion efficiency. Therefore the pulse "cleanness," i.e. no pedestal and high contrast ratio, is a very important factor of progress toward high efficiencies of short wavelength harmonics. This is illustrated by the example of the harmonic emission obtained with an ultrashort 35-fs pulse of 10^{-6} contrast ratio 1 ps before peak, displayed in Figure 12.34 [40]. The intensity of the ∼800-nm incident laser beam, focused onto an optically polished glass target, reached 5×10^{17} W/cm^2, close to the relativistic regime. Harmonics are clearly observed from 8th to 22nd orders, i.e. from 100 nm to 36 nm. A signal was observed to shorter wavelengths down to ∼18 nm. Measurement of the reflected beam angular distribution through an aluminium filter showed the divergence to be between 50 and 100 mrad, that is slightly smaller than that of the laser.

12.2.7 Two-Color High Harmonic Generation

New important capabilities of operating the conditions of high harmonic generation are provided by replacing the driving field

$$E(t) = E_0 \sin \omega t$$

by a bichromatic driving field, which reads

$$E(t) = E_1 \sin \omega_1 t + E_2 \sin(\omega_2 t + \varphi) \tag{12.12}$$

when both fields are linearly polarized in the same direction. φ is the relative phase between the two fields. Experiments and calculations show that the relative field intensity E_2/E_1, and the phase term φ, are efficient parameters, actually relevant to the control of harmonic spectra.

Calculation of the single atom interaction with the bichromatic field is performed solving the time-dependent Schrödinger equation (11.3), where the usual monochromatic laser field is replaced by the new expression (12.12) of

the field (see, e.g. [115–121]). According to Ref. [118], the expression of the time-dependent dipole moment of an atom in a field of arbitrary temporal shape reads

$$x(t) = i \int_0^t dt' \int d^3p d_x^* \left[\mathbf{p} - \mathbf{A}(t)\right] \exp\left[-iS\left(\vec{p}, t, t'\right)\right] \tag{12.13}$$

$$\times E(t') d_x \left[\mathbf{p} - \mathbf{A}(t')\right] + c.c. \tag{12.14}$$

where $\mathbf{d}(p,t)$ is the field-free atomic dipole moment, $E(t)$, the bichromatic field (12.12) and

$$A(t) = \left[-(E_1/\omega_1)\sin(\omega_1 t) - (E_2/\omega_2)\mathrm{Si}\, n(\omega_2 t + \varphi), 0, 0\right] \tag{12.15}$$

is the corresponding vector potential.

In this equation $E(t')d_x\left[\mathbf{p} - \mathbf{A}(t')\right]$ represents the probability for an atomic electron to carry out a transition, at time t', from the ground state to a continuum state with momentum $\mathbf{p}$. The term $\exp\left[-iS\left(\mathbf{p}, t, t'\right)\right]$ where

$$S(p,t,t') = \int_{t'}^{t} dt'' \left(\frac{\left[\mathbf{p} - \mathbf{A}(t'')\right]^2}{2} + I_\mathrm{p} \right) \tag{12.16}$$

is the phase factor acquired by the electronic wave function propagating from time t' until time t [cf. Eq. (11.7)]. The term $d_x^*\left[\mathbf{p} - \mathbf{A}(t)\right]$ described the electron–ion recombination at time t.

Concerning the propagation equations, for each harmonic they ought to include the polarization induced by each of the frequencies contained in the incident field. Let ω_i be the frequency of a given harmonic, defined as

$$\omega_i = q_1\omega_1 + q_2\omega_2 \tag{12.17}$$

where the integers q_1 and q_2 denote the total number of photons absorbed or emitted. Note that this expression includes the case of incommensurate incident frequencies. The nonlinear polarization induced at the frequency ω_i by the two-colors field has the form

$$\mathbf{P}_i(\mathbf{r},t) = \frac{1}{2} \sum_{q_1,q_2} \mathbf{P}_{q_1,q_2}(\mathbf{r},t) e^{i(q_1 k_1 z - q_1\omega_1 t + q_2 k_2 z - q_2\omega_2 t)} + c.c. \tag{12.18}$$

The propagation equation takes a form similar to equation (11.8) established in the case of a monochromatic incident laser field. According to Ref. [118] this equation reads

$$\nabla_\perp^2 \mathbf{E}_i(\mathbf{r},t) + 2ik_i \frac{\partial \mathbf{E}_i(\mathbf{r},t)}{\partial z} = -\frac{1}{\epsilon_0}\left(\frac{\omega_i}{c}\right)^2 \sum_{q_1,q_2} \mathbf{P}_{q_1,q_2}(\mathbf{r},t) e^{-i\Delta k_{q_1,q_2} z} \tag{12.19}$$

where $E_i(r,t)$ be the envelop function of the field and

$$\Delta k_{q_1 q_2} = k_i - q_1 k_1 - q_2 k_2 \tag{12.20}$$

is the phase mismatch.

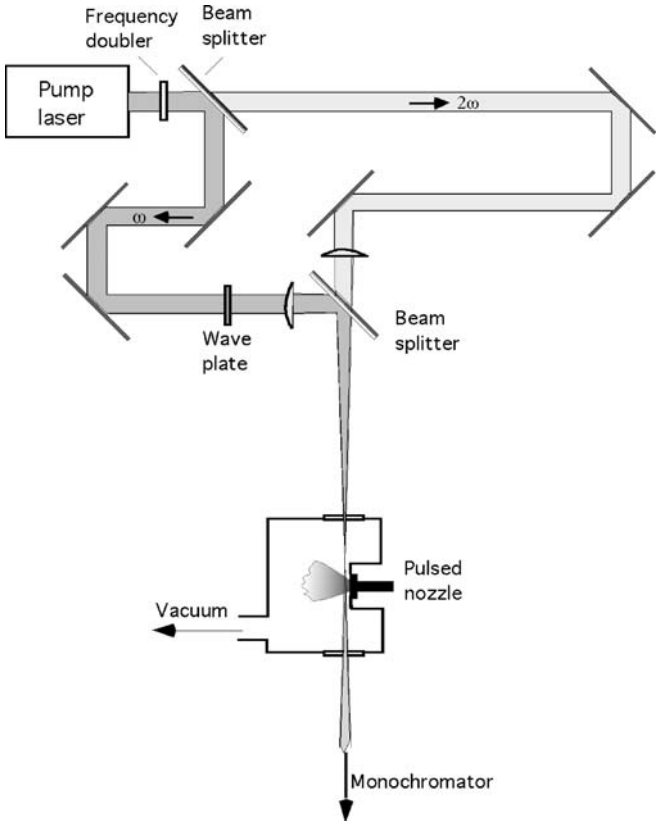

Fig. 12.35. Experimental setup used to generate harmonics from $\omega - 2\omega$ mixing. The wave plate is used to match the beam polarizations.

The diagram of Figure 12.35 shows the principle of an experimental setup for two-color harmonic generation, corresponding to the $\omega - 2\omega$ mixing. A portion of the laser light is frequency doubled when flying across a KDP crystal. The beam is then spited into two beams of frequencies ω and 2ω respectively. A wave plate in inserted across one or two of the beams to match polarizations. The delay between beams is adjustable. The fundamental and the second harmonic are recombined by a second beamsplitter and then focused close to the gas jet. For incommensurate frequency mixing, the second beam is produced by an optical parametric generator—or amplifier—(OPG or OPA) consisting in a laser-pumped nonlinear material which produces a tunable coherent light beam (see for instance [122, 123]).

Figure 12.36 shows partial harmonic spectra obtained from the fundamental (ω) and the second harmonic (2ω) of a Nd glass laser (1053-nm wavelength) [124]. The spectrum of the 2ω field (526-nm wavelength) is shown in the upper frame. The $\omega + 2\omega$ mixing, with orthogonal polarizations, provides

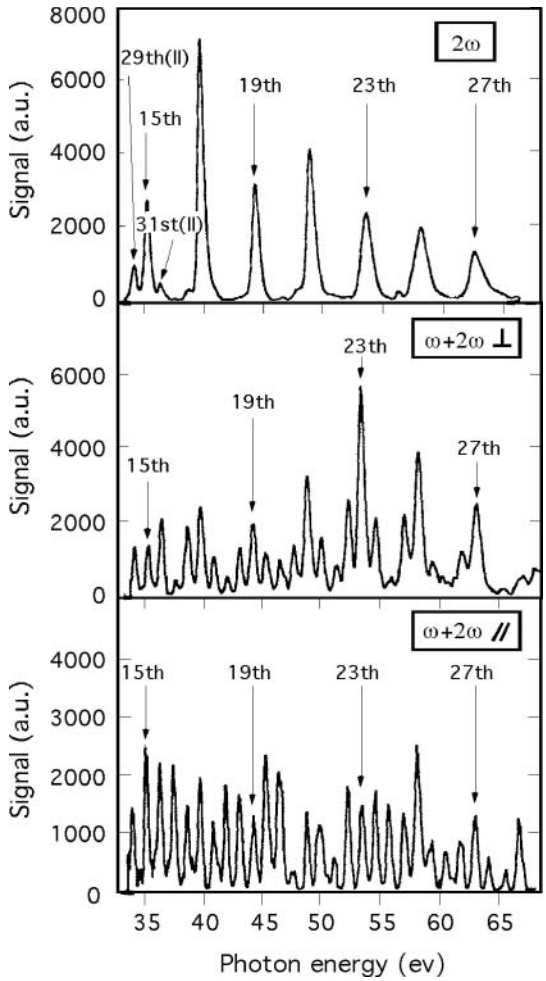

Fig. 12.36. $\omega + 2\omega$ harmonic spectra of Nd-laser radiation focused in helium for parallel and perpendicular polarizations, compared with the 2ω spectrum in the same energy range.

the spectrum of the middle frame and the one with parallel polarization provides the spectrum of the bottom frame. Spectra were obtained with a strong 2ω-field (1×10^{16} W/cm^2) and a much weaker ω-field (2×10^{13} W/cm^2). This large difference was due to fundamental and second harmonics not being spatially separated. The two fields were thus focused in the helium jet by one and the same optical lens of very different chromatic dispersions for each of the two frequencies.

Comparison of upper and middle spectra shows the injection of the ω - field to introduce three additional peaks between pairs of the odd harmonics of the 2ω-field. The peaks which are immediately on either side of these odd

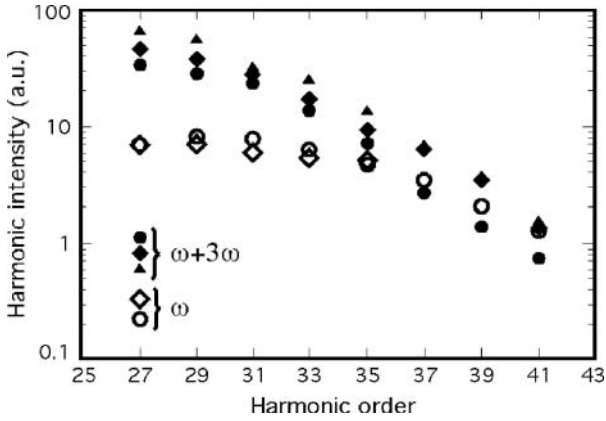

Fig. 12.37. Demonstration of strong harmonic intensity enhancement by interference of ω and 3ω fields (Ref. [125]).

harmonics have an energy equal to the odd multiples of the ω-field. However they are not considered as simple harmonics of this field because they appear only when both fields are present. They are rather attributed to sum- and difference-frequency processes where $(q-1) \times 2\omega$-photons plus $1 \times \omega$-photon, or $(q+1) \times 2\omega$-photons minus $1 \times \omega$-photon, are absorbed, leading to the $2q-1$ and $2q+1$ odd frequency signals.

In addition, the figure shows peaks in between the odd harmonics of the 2ω-field, which appear at energies corresponding to even multiples of the fundamental frequency. For parallel polarization, the generation efficiency of these peaks is far above that of the ordinary odd harmonics of the 2ω-field. They may appear owing to the ω-field breaking the symmetry of the Hamiltonian of the 2ω-field interaction with atom. Alternatively they can result from the sum of an odd number of $1 \times 2\omega$-photons plus $2 \times \omega$-photons. More details on these processes may be found in Ref. [124].

Figure 12.37 shows the harmonic distribution of an $\omega + 3\omega$ field obtained in Ne, compared with that given by the ω field [125]. In this experiment, focusing is achieved with the help of an off-axis parabolic mirror so that the chromatic aberration is eliminated. The confocal parameter is of 0.5 mm, which gives rise to a tight focusing. The fundamental radiation is provided by a 100-fs Ti:sapphire laser (745 nm) with an intensity of 5×10^{14} W/cm^2. The amplitude ratio $E_{3\omega}/E_{1\omega}$ is estimated at 0.4. The relative phase between the two fields can be adjusted by a delay line with the help of a piezoelectric transducer. In the distribution obtained for the ω-field, the usual plateau is clearly observed (open symbols) from 27th to ∼35th orders. However the cutoff is out the observation range. For the $\omega + 3\omega$ mixed field the figure shows three experimentally measured points (filled symbols) for each harmonic intensity. The outstanding result, in the plateau region, is the one-order-of-magnitude enhancement of the harmonic intensity due to the two-color interference.

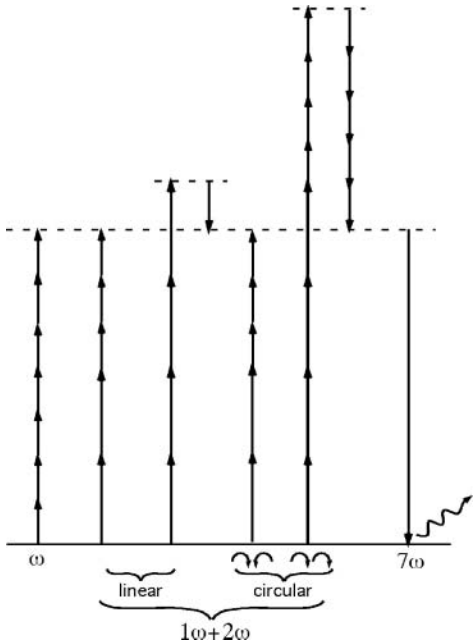

Fig. 12.38. Possible ways to generate a given harmonic (7ω) by mixing 1ω and 2ω fields with linear and circular polarizations.

More generally, when both pump fields act simultaneously with parallel or perpendicular polarization, a number of nonlinear processes may contribute radiation at a given harmonic wavelength. This is illustrated in Figure 12.38 which shows the generation of 7ω harmonic photons by mixing 1ω and 2ω fields with different polarizations [116]. Experiments confirm the efficiency of polarization combinations made available by frequency mixing.

Figure 12.39 displays the measured intensities of harmonic signals produced in argon by combining linear or circular polarizations. The experimental setup is similar to that displayed in Figure 12.35, but two MgF_2 wave plates are now inserted into the beams, one for each color, to manipulate polarizations. The birefringent axis are perpendicular to the plate surfaces. By tilting the plates, the phase difference between the ordinary and the extraordinary polarization can be changed continuously from zero to $\lambda/2$. The driving laser is a 150-fs Ti:sapphire operating at 773 nm. The focused intensities are nearly the same for the 773-nm and the 386.5-nm colors. Argon is injected into the vacuum chamber with a backing pressure of 2 bar. The atom density in the interaction region is of 10^{17}–10^{18} W/cm^2.

Figure 12.39a shows the spectra separately provided by 1ω and 2ω linearly polarized pumps. For the 1ω-field the harmonic spectrum has a clear plateau structure from the argon ionization energy (15.76 eV corresponding to the

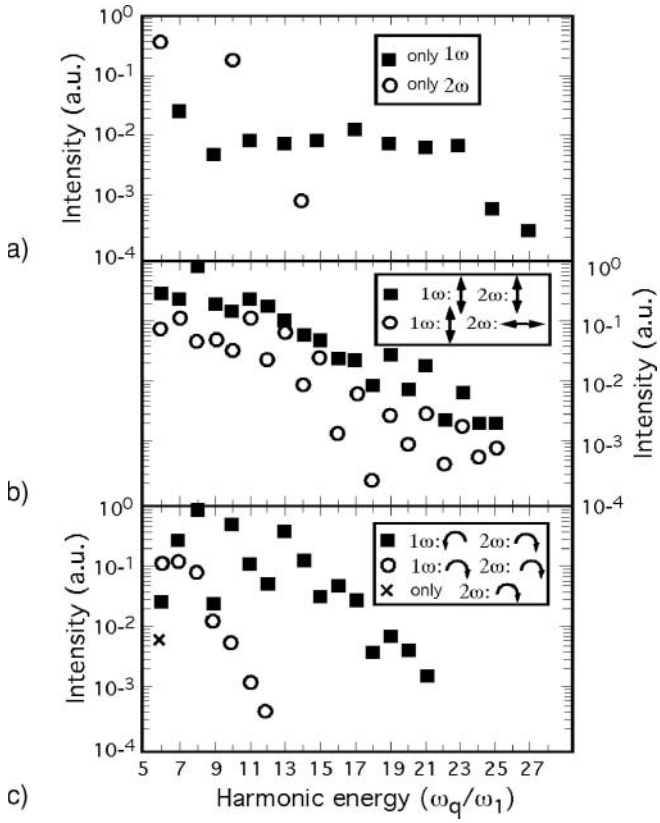

Fig. 12.39. $1\omega + 2\omega$ frequency mixing signals for different polarizations of the fields. ω_1 is the laser frequency (data from Ref. [115]).

value 9.75 on the ω_q/ω_1 scale) up to a cutoff energy of ∼40 eV, i.e. $\omega_q/\omega_1 \simeq 25$. For the 2ω field, harmonics up to the seventh order (14ω) were observed with no plateau structure as the seventh harmonic is already at the cutoff energy. It should be noted that neither field generates $2p2\omega$ even harmonics but only $(2p+1)\omega$ and $(2p+1)2\omega$ harmonics. Focused intensities were about 3×10^{15} W/cm^2.

In Figure 12.39b, 1ω-field odd harmonic intensities are seen to be enhanced by up to two orders of magnitude in comparison with Figure 12.39a. As a matter of fact, these harmonics can be now generated by different nonlinear processes such as $2(2\omega) + 3(1\omega)$ or $4(2\omega) - 1(1\omega)$ mixing represented in Figure 12.38 for the case of the 7th harmonic. Besides, harmonics generated by two perpendicular fields prove to be less intense than those generated by the parallel fields. According to the semiclassical model, this property should be ascribed to the smaller probability that an ionized electron returns to the ion and thus emits harmonic photons in the case of perpendicular fields.

For corotating circularly polarized beams, all $p\omega$-frequencies can be generated but the number of participating processes is limited by the requirement $(p \mp 1)(2\omega) - (p \mp 2)((1\omega) = p\omega$, as indicated in Figure 12.38. This restriction reduces the harmonic intensity compared with harmonic generation by counterrotating fields. The location of the white-circle marks in Figure 12.38c illustrates this effect very clearly. In this case a given frequency can be generated by the sum-mixing process $p(2\omega) + (p \mp 1)\omega$ giving $(3p \mp 1)\omega$ frequencies. This excludes the frequencies $p\omega$.

As for the cross ($\times$) mark in Figure 12.39c, it indicates a low intensity $3(2\omega)$ harmonic. This anomaly is reasonably ascribed to the incomplete circularly polarization of the beams. An ellipticity of 0.9 would be sufficient to explain the appearance of this nonallowed harmonic. Most of experimental data reported above agree with the theoretical results of a model calculation of the single atom interaction with field (see [116]).

An interesting challenge consists in using the additional parameters resulting from bichromatic excitation to realize phase matching to the benefit of an unique harmonic of large intensity [126]. The experimental setup is similar to the one of Figure 12.35. The pump is a 150-fs, 770-nm laser. The energy of the ω beam is 25 mJ, which provides an intensity of $\sim 10^{16}$ W/cm^2 in the 40-μm diameter focus. The energy of the 2ω beam is 5.5 mJ only. The two beams are parallel polarized. The nozzle is equipped with three aligned holes so that the length of the nonlinear medium can be approximately tripled.

Examination of the different components of the phase mismatch shows that the case of difference-frequency mixing is much more favorable than the case of sum-frequency mixing process for which both the geometric and the dispersive terms of the phase mismatch are generally positive. In the case of a difference-frequency mixing processes

$$\omega_q = q\omega = m(2\omega) - l\omega \tag{12.21}$$

favorable conditions occurs when $m = 2l$ because the dispersive phase mismatch is negative and is given by

$$\Delta k_q^d = -\frac{1}{q}\frac{\omega_p^2}{2\omega c} = -\frac{e^2}{m_e c^2} N_{\mathrm{e}} \frac{\lambda}{q} \tag{12.22}$$

On the other hand, the value of the geometrical phase mismatch for the case of weak focusing can be estimated from equation

$$\Delta k_q^{\mathrm{geo}} = 2(m - l - 1)/b \tag{12.23}$$

Thus the total phase mismatch

$$\Delta k_q = \Delta k_q^{\mathrm{geo}} + \Delta k_q^d \tag{12.24}$$

depends on the free electron density. Free electrons appear because, due to the high intensity of the fundamental beam (10^{16} W/cm^2), a plasma is formed at the front of the laser pulse and serves as the nonlinear medium. Thus there exists an optimum electron density, depending on the harmonic order, where

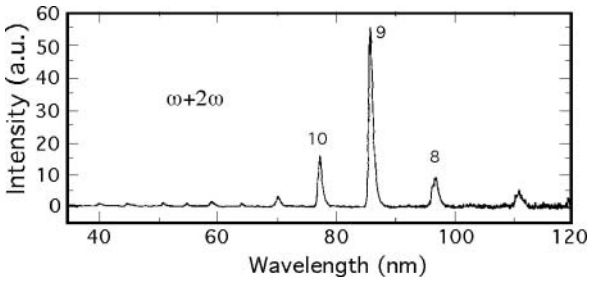

Fig. 12.40. Demonstration of phase-matching for a unique harmonic by frequency-difference mixing (Ref. [125]).

the mismatch is equal to zero. The corresponding harmonic signal is expected to dominate the spectrum.

This occurs indeed for the 9th harmonic at 85.5 nm, as shown in Figure 12.40 where the 9th harmonic is orders of magnitude stronger than in case (not represented in the figure) where it is directly produced by the fundamental radiation. This behavior provides evidence for phase-matched difference frequency-matching mixing, $9\omega = 6(2\omega) - 3\omega$, in the two-color field. Moreover, it is observed that the intensity of the 9th harmonic has a sharp maximum as a function of the backing pressure, as this can be expected from equations (12.22) and (12.24).

12.2.8 Tunability

12.2.8.1 Tunability Using Frequency Mixing

Intense tunable XUV radiation sources are desirable for many applications. In the case of harmonics, the tunability might be directly obtained from the pump laser since titan–sapphire lasers are tunable by themselves. However the adjustment of the chirping and pulse-compression unit, which is an essential part of an ultrashort terawatt pulse system, is uneasy and difficult to achieve for continuously varying wavelengths. Therefore it is more practical to mix the radiation frequency (ω_{L}) of the pump laser with the easily tunable frequency (ω_{OPG}) of an OPG.

The diagram of an experimental setup for producing tunable XUV pulses is shown in Figure 12.41 from Ref. [127]. In the OPG, a baryum borate crystal (BB0) is pumped by the 2nd harmonic of the Ti:sapphire laser, a small change of the incidence angle allowing for the variation of the secondary radiation wavelength between 520 and 650 nm. A description of the OPG can be found in [128]. The Ti:sapphire pump laser provided 150-fs laser pulses with an energy up to 100 mJ. Sum and difference mixing signals, $n\omega_{\mathrm{L}} \mp \omega_{\mathrm{OPG}}$ (n pair), appeared in argon, krypton, and xenon, with the strongest signals down to 40 nm in xenon. Figure 12.42 shows as an example the tuning, between 85.6

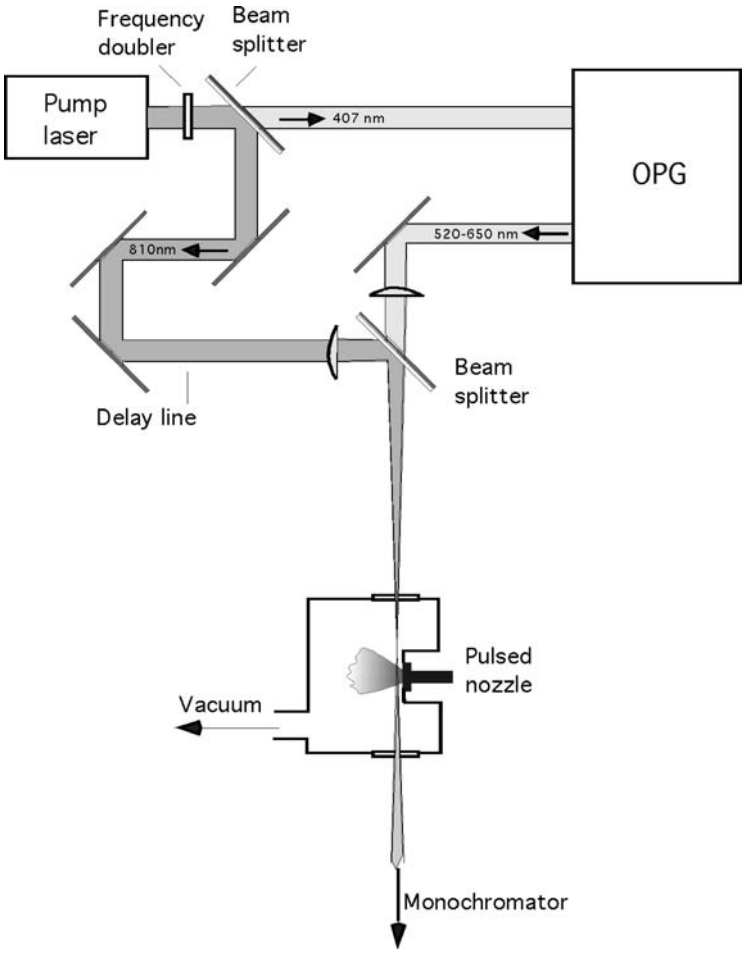

Fig. 12.41. Experimental arrangement for the generation of tunable harmonics. The OPG generates tunable radiation in the 520–650 nm wavelength interval from the 2nd harmonic of the pump laser. Frequency mixing with the fundamental (810 nm) provides tunable EUV harmonics.

and 88 nm, of a sum-frequency mixing signal near the 9th harmonic. Moreover, sum mixing signals were observed to increase linearly with OPG energy from 100 μJ to 350 μJ, which is the maximum OPG energy. About one third of the spectral range between two harmonics was covered.

Tunability has been extended to 70% of the spectrum between two subsequent harmonics and up to 70 eV ($\lambda \simeq 15$ nm), thanks to a larger tuning range of the OPG and to the inclusion of $\mp 2\omega_{\mathrm{L}}$ and $\mp\omega_{\mathrm{OPG}}$ into the mixing process [117,129]. Further extension to shorter wavelengths, in neon or argon, seems to be possible with a higher OPG energy.

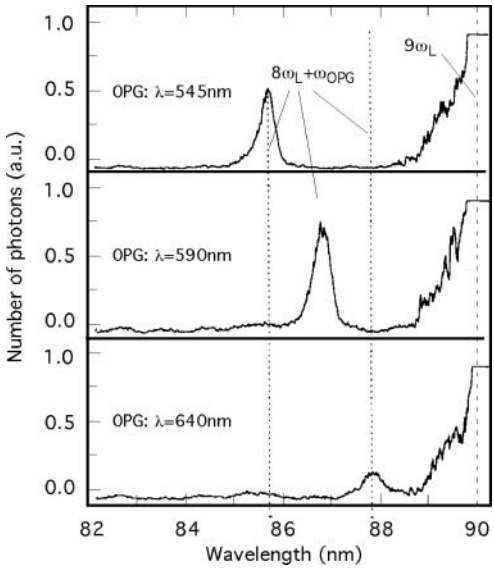

Fig. 12.42. Example of tunable harmonic provided by laser-OPG radiation frequency mixing (Ref. [127]).

The curves of Figure 12.43 represent the number of photons emitted, in neon, argon, and xenon, at the wavelengths of the harmonic processes and of the nearest sum and difference mixing processes. $2N$+1 is the label the laser harmonic order. The peak just to the right (respectively left) of the harmonic signal corresponds to a frequency of $2N\omega_{\mathrm{L}} + \omega_{\mathrm{OPG}}$ [respectively $(2N + 2)$ $\omega_{\mathrm{L}} - \omega_{\mathrm{OPG}}$] and is referred to as $(2N) + 1$ [respectively $(2N + 2) - 1$], where + (respectively −) denote sum (respectively difference) frequency process. For each of the gas, the figure displays the curve corresponding to the $2N$+1 harmonics and those corresponding to sum and difference processes, labeled $(2N) + 1$ and $(2N) - 1$. It is worth noticing that the curves present the same general features as the harmonics, namely plateau and cutoff. On the other hand, the comparison of the efficiency of sum and difference processes shows the relative strengths of the +1 and −1 processes to change from xenon to neon, that is to say for increasing energy of the emitted photons in each case. While $(2N + 1)$ processes dominate in xenon (between 15 and 30 eV), they are dominated by the $2N - 1$ processes in neon (between 40 and 70 eV). No conclusive explanation of this behavior appears from phase-matching considerations. It is thus expected to originate in the single atom dynamics.

A different route to a fully tunable XUV source is opened by the demonstration of HHG directly produced using a high intensity OPG, without mixing with fundamental radiation, up to about 80 eV in xenon [130]. This result has been achieved thanks to the increase of the OPG intensity in the focus up to $\sim 3 \times 10^{14}$ W/cm^2. However, an issue in the development of this

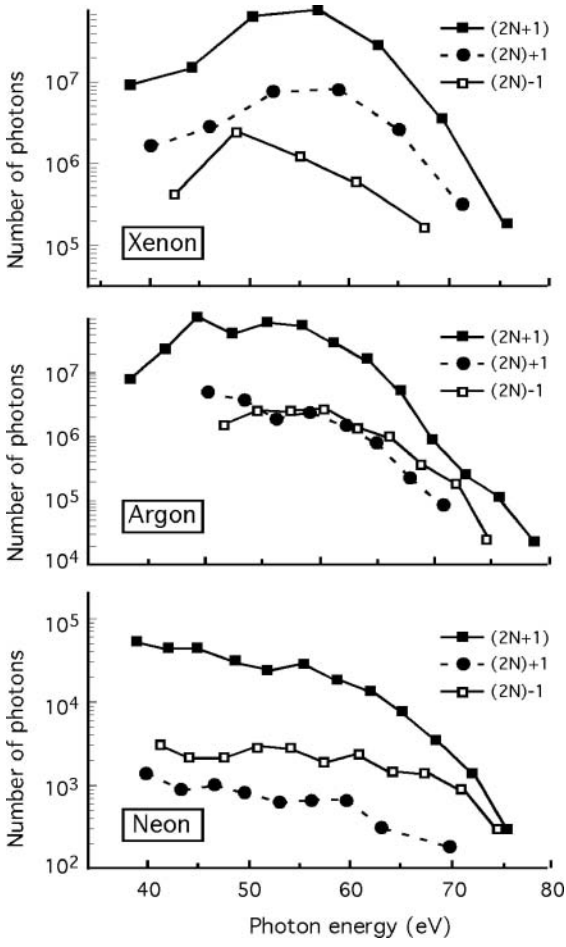

Fig. 12.43. Number of photons for the different processes in xenon, argon, and neon as a function of photon energy. $(2N+1)$ refers to the harmonic with frequency $(2N+1)\omega_{\mathrm{L}}$; $(2N)\mp 1$ refer to signals of frequencies $2N\omega_{\mathrm{L}} \mp \omega_{\mathrm{OPG}}$ (data from Ref. [129]).

technique may appear because of the spectral bandwidth of the OPG which is significantly larger than that of the fundamental and dominates the width of the harmonic lines.

12.2.8.2 Tunability Using the Blueshift of Harmonic Lines

It is well established that a short-pulse laser focused into a gas medium is shifted toward the short wavelengths [15, 131–133]. The shift originates from free electrons created by the laser pulse ionizing the gas. A free-electron density $N_{\mathrm{e}}(\mathbf{r}, z, t)$, where $\mathbf{r}$ and z are the usual transverse and longitudinal

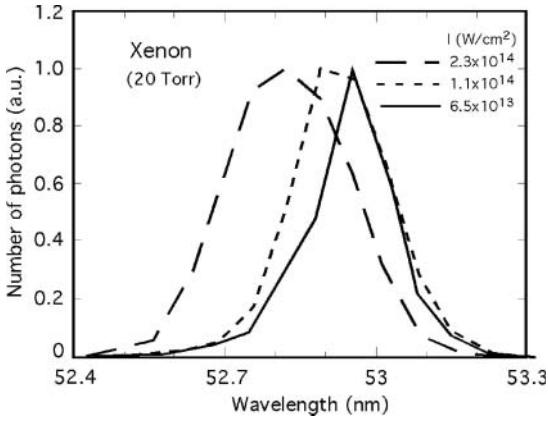

Fig. 12.44. Blueshifts of the 15th harmonic of a 800-nm laser for three laser intensities.

variables, induces a variation of the refractive index [15]

$$\delta n_1(\mathbf{r}, z, t) = -\frac{2\pi e^2}{m\omega^2} N_e(\mathbf{r}, z, t) \tag{12.25}$$

where ω is the laser frequency. The temporal variation of the index, i.e. of the phase of the radiation field, is responsible for the production of the spectral blueshift which can be estimated by the simple expression (CGS units)

$$\delta\lambda_1 = -\frac{\lambda^3 e^2}{2\pi m c^3} \frac{dN_\mathrm{e}}{dt} L \tag{12.26}$$

where L is the interaction length previously defined (see Section 12.1.1). The shift of the fundamental induces a shift of harmonics, which, for the qth harmonic, is

$$\delta\lambda_q = \frac{\delta\lambda_1}{q} \tag{12.27}$$

Another shift can be induced by the propagation of the harmonic in the medium. However, for harmonics of high orders, this shift is negligible compared to that of the fundamental field. As N_e in equation (12.26) is a function of gas pressure and of pump intensity, through the tunneling ionization rate, $\delta\lambda_q$ will vary with these experimental parameters. Figure 12.44 shows for example the shift of the 15th harmonic of the 800-nm radiation of a Ti:sapphire laser in xenon, at 20-Torr pressure, for three laser intensities [15].

A method to vary the effective pump intensity in the gas consists in varying the position of the gas jet relative to the laser focus along the z-axis. Altucci et al. [134,135] investigated the dependence of the blueshift of the harmonic spectral peaks upon the distance z, from the laser focus to the gas jet. Figure 12.45

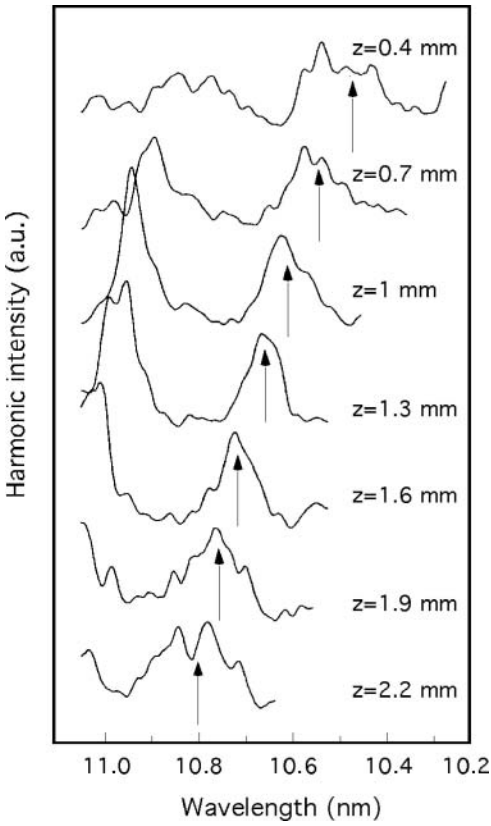

Fig. 12.45. Tunability of the 73rd harmonic obtained by varying the distance z, from the laser focus to the gas jet.

shows the detail of the spectral region around the 73rd harmonic of the 793-nm Ti:sapphire laser in neon. The total shift measured in the interval 0.4 mm $\leq z \leq$ 2.2 mm was $\gtrsim$0.3 nm, that is approximately the wavelength separation between the 71st and the 73rd harmonics. The pump intensity variation for the 0.4–0.2 mm interval was estimated at $\approx 2.14 \times 10^{14}$–$4.9 \times 10^{14}$ W/cm^2. It has been observed that the blue shift is only weakly dependent on the harmonic order in the far plateau region ($q > 39$ in the present case).

Therefore, a blueshift-based tunability of high-order harmonics between $\sim$20 and $\sim$8 nm may be obtained by simply adjusting the gas-jet position relative to the laser focus.

References

1. See, for instance, A. McPherson, G. Gibson, H. Jara, U. Johann, T.S. Luk, I.A. McIntyre, K. Boyer, C.K. Rhodes, J. Opt. Soc. Am. B., **4** (1987) 595.

2. S. Sebban, R. Haroutunian, Ph. Balcou, G. Grillon, A. Rousse, S. Kazamias, T. Marin, J.Ph. Rousseau, L. Notebaert, M. Pittman, J.P. Chambaret, A. Antonetti, D. Hulin, D. Ros, A. Klisnick, A. Carillon, P. Jaeglé, G. Jamelot, J.F. Wyart, Phys. Rev. Lett., **86** (2001) 3004.
3. A. L'Huillier, Ph. Balcou, Phys. Rev. Lett., **70** (1993) 774.
4. A. L'Huillier, K.J. Shafer, K.C. Kulander, J. Phys. B, **24** (1991) 3315.
5. K. Kondo, N. Sarukura, K. Sajiki, S. Watanabe, Phys. Rev. A, **47** (1993) R2480.
6. K Miyazaki, H Takada, Phys. Rev. A, **52** (1995) 3007.
7. Y. Nagata, K. Midorikawa,M. Obara, K. Toyoda, Optics Lett., **21** (1996) 15.
8. F. Le-Kien, K. Midorikawa, A. Suda, Japanese J. Appl. Phys., Part-2 Lett., **37** (1998) L733.
9. K. Miyazaki, H. Sakai, G.U. Kim, H. Takada, Phys. Rev. A, **49** (1994) 548.
10. J. Peatross, D.-D. Meyerhofer, Phys. Rev. A, **52** (1995) 3976.
11. G. Sommerer, H. Rottke W., Sandner, Laser Phys., **9** (1999) 430.
12. K.J. Schafer, J.L. Krause, K. Kulander, SPIE Proc., **1860** (1993) 190.
13. K. Midorikawa, S. Kubodera, H. Tashiro, K. Toyoda, Modern Phys. Lett. B, **7** (1993) 1533.
14. S. Kubodera, Y. Nagata, T. Akiyama, T.K. Midorikawa, M.Obara, H. Tashiro, K. Toyoda, Phys. Rev. A, **48** (1993) 4576.
15. C.G. Wahlstrom, J. Larsson, A. Persson, T. Starczewski, S. Svanberg, P. Salieres, Ph. Balcou, A. L'Huillier, Phys. Rev. A, **48** (1993) 4709.
16. K. Kondo, T. Tamida, Y. Nabekawa, S. Watanabe, Phys. Rev. A, 49 (1994) 3881.
17. C.G. Wahlstrom, S. Borgstrom, J. Larsson, S.G. Pettersson, Phys. Rev. A, **51** (1995) 585.
18. S.G. Preston, A. Sanpera, M. Zepf, W.J. Blyth, C.-G. Smith, J.-S. Wark, M.-H. Key, K. Burnett, M. Nakai, D. Neely, A.A.Offenberger, Phys. Rev. A, **53** (1996) R31.
19. K. Krushelnick, W. Tighe, S. Suckewer, J. Opt. Soc. Am. B, **14** (1997) 1687.
20. T.F. Gallagher, Phys. Rev. Lett., **61** (1988) 2304.
21. P.B. Corkum, Phys. Rev. Lett., **71** (1993) 1994.
22. M. Lewenstein, Ph. Balcou, M.Yu. Ivanov, A. L'Huillier, P.B. Corkum, Phys. Rev. A, **49** (1994) 2117.
23. A. L'Huillier, M. Lewenstein, P. Salières, Ph. Balcou, M. Yu. Ivanov, J. Larsson, C.G. Wahlström, Phys. Rev. A, **48** (1993) R3433.
24. B. Gao, A.F. Starace, Phys. Rev. A, **39** (1989) 4550.
25. M.B. Gaarde, P. Antoine, A. L'Huillier, K.J. Schafer, K.C. Kulander, Phys Rev. A, **57** (1998) 4553.
26. J. Gao, F. Shen, J.G. Eden, Phys. Rev. A, **61** (2000) 043812.
27. X.M. Tong, S.I. Chu, Phys Rev. A, **64** (2001) 013417.
28. P. Salières, A. L'Huillier, P. Antoine, M. Lewenstein, Adv. At. Mol. Phys., **41** (1999) 83.
29. J.G. Leopold, I.C. Percival, J. Phys. B, **12** (1979) 709.
30. G. Bandarage, A. Maquet, J. Cooper, Phys. Rev. A, **41** (1990) 1744.
31. M.Yu. Kuchiev, V.N. Ostrovsky, L. Phys. B, **32** (1999) L-189.
32. J.L. Krause, K.J. Schafer, K.C. Kulander, Phys. Rev. A, **45** (1992) 4998.
33. F. Li, A. L'Huillier, M. Ferray, L.A. Lompré, G. Mainfray, Phys Rev. A **39** (1989) 5751.

34. L. Krause, K.J. Schafer, K.C. Kulander, Phys. Rev. Lett., **68** (1992) 3535.
35. K.C. Kulander, B.W. Shore, Phys. Rev. Lett., **62** (1989) 524; J. Opt. Soc. Am. B, **7** (1990) 502.
36. L.A. Lompré, A. L'Huillier, M. Ferray, P. Monot, G. Mainfray, C. Manus, J. Opt. Soc. Am. B, **7** (1990) 754.
37. P. Salières, B. Carré, L. Le Déroff, F. Grasbon, G.G. Paulus, H. Walther, R. Kopold, W. Becker, D.B. Milosevic, A. Sanpera, M. Lewenstein, Science, **292** (2001) 902.
38. M. Bellini, C. Lynga, A. Tozzi, M.B. Gaarde, T.W. Hansch, A. L'Huillier, C.G. Wahlstrom, Phys. Rev. Lett., **81** (1998) 29.
39. G.G. Paulus, F. Grasbon, A. Dreischuh, H. Walther, R. Kopold, W. Becker, Phys. Rev. Lett., **84** (2000) 3791.
40. Ph. Balcou, R. Haroutunian, S. Sebban, G. Grillon, A. Rousse, G. Mullot, J.P. Chambaret, G. Rey, A. Antonetti, D. Hulin, L. Roos, D. Descamps, M.G. Gaarde, A. l'Huillier, E. Constant, E. Mevel, D. von der Linde, A. Orisch, A. Tarasevitch, U. Teubner, D. Klöpfel, W. Theobald, Appl. Phys. B, **74** (2002) 509.
41. W. Becker, S. Long, J.K. McIver, Phys. Rev. A, **50** (1994) 1540.
42. Ph. Antoine, A. L'Huillier, M. Lewenstein, P. Salières, B. Carré, Phys. Rev. A, **53** (1996) 1725.
43. J. Gao, F. Shen, J.G. Eden, J. Phys. B, **32** (1999) 41539.
44. D.B. Milosevic, J. Phys. B, **33** (2000) 247.
45. A. L'Huillier, Ph. Balcou, S. Candel, K.J. Schafer, K.C. Kulander, Phys. Rev. A, **46** (1992) 2778.
46. M. Lewenstein, P. Salières, A. L'Huillier, Phys. Rev. A, **52** (1995) 4747.
47. Ph. Balcou, P. Salières, A. L'Huillier, M. Lewenstein, Phys. Rev. A, **55** (1997) 3204.
48. B. Carré, P. Salières, L. Le Déroff, H. Merdji, J.F. Hergott, T. Auguste, P. Monot, P. D'Oliveira, D. Joyeux, J. Phys. IV, **11** (2001) Pr2-355.
49. R. Zerne, C. Altucci, M. Bellini, .M.B. Gaarde, T.W. Hänsh, A. L'Huillier, C. Lynga, C.G. Wahlström, Phys. Rev. Lett., **79** (1997) 1006.
50. P. Salières, A. L'Huillier, M. Lewenstein, Phys. Rev. Lett., **74** (1995) 3776.
51. A.E. Siegman, *Lasers*, University of Science Books, Mill Valley, CA, 1986, p. 682.
52. T. Ditmire, E.T. Gumbrell, R.A. Smith, J.W.G. Tish, D.D. Meyerhofer, M.H.R. Hutchinson, Phys. Rev. Lett., 77 (1996) 4756.
53. L. Le Déroff, P. Salières, B. Carré, D. Joyeux, D. Phallipou, Phys. Rev. A, **61** (2000) 043802.
54. S.C. Rae, K. Burnett, Phys. Rev. A, **48** (1993) 2490.
55. S.C. Rae, K. Burnett, J. Cooper, Phys. Rev. A, **50** (1994) 34387.
56. T. Ditmire, J.K. Crane, H. Nguyen, L.B. DaSilva, M.D. Perry, Phy. Rev. A., **51** (1995) R902.
57. J.F. Hergott, M. Kovacev, H. Merdji, C. Hubert, Y. Mairesse, E. Jean, P. Breger, P. Agostini, B. Carré, P. Salières, Phys. Rev. A, **66** (2002) 021801(R).
58. E. Takahashi, Y. Nabekawa, K. Midorikawa, Optics Lett., **22** (2002) 1920.
59. E. Takahashi, Y. Nabekawa, M. Nurhuda, K. Midorikawa, J. Opt. Soc. Am. B, **20** (2003) 158.

60. Ph. Balcou, C. Cornaggia, A.S.L. Gomes, L.A. Lompré, A. L'Huillier, J. Phys. B, **25** (1992) 4467.
61. Z. Chang, A. Rundquist, H. Wang, M.M. Murname, H.C. Kapteyn, Phys. Rev. Lett., **79** (1997) 2967.
62. J. Zhou, J. Peatross, M.M. Murnane, H.C. Kepteyn, I.P. Christov, Phys. Rev. Lett., **76** (1996) 752.
63. K.J. Schafer, K.C. Kulander, Phys. Rev. Lett., **78** (1997) 638.
64. C. Spielmann, N.H. Burnett, S. Sartania, R. Koppitsch, M. Schnürer, C. Kan, M. Lenzner, P. Wobraushek, F. Krausz, Science, **278** (1997) 661.
65. M. Schnürer, C. Spielmann, P. Wobrauschek, C. Streli, N.H. Burnett, C. Kan, F. Ferencz, R. Koppitsch, Z. Cheng, T. Brabec, F. Krausz, Phys. Rev. Lett., **80** (1998) 3236.
66. C. Altucci, T. Starczewski, E. Mevel, C.G. Wahlström, B. Carré, A. L'Huillier, J. Opt. Soc. Am. B, **13** (1996) 148.
67. C. Delfin, C. Altucci, F. De Fillipo, C. de Lisio, M.B. Gaarde, A. L'Huillier, L. Roos, C.G. Wahlström, J. Phys. B, **32** (1999) 5397.
68. S. Kazamias, F. Weihe, D. Douillet, C. Valentin, T. Planchon, S. Sebban, G. Grillon, F. Augé, D. Hulin, Ph. Balcou, Eur. Phys. J. D, **21** (2002) 353.
69. H.M. Milchberg, C.G. Durfee, T.J. McIlrath, Phys. Rev. Lett., **75** (1995) 2494.
70. A. Rundquist, C.G. Durfee, Z. Chang, C. Herne, S. Backus, M.M. Murnane, H.C. Kapteyn, Science, **280** (1998) 1412.
71. K. Midorikawa, Y. Tamaki, J. Itatani, Y. Nagata, M. Obara, IEEE J. Selected Topics Quant. Electron., **5** (1999) 1475.
72. Y. Tamaki, Y. Nagata, M. Obara, K. Midorikawa, Phys. Rev. A, **59** (1999) 4041.
73. K. Midorikawa, Y. Tamaki, J. Itatani, M. Obara, SPIE Proc., **3776** (1999) 135.
74. J.F. Holzman, A.Y. Elezzabi, F.E. Vermeulen, C.E. Capjack, SPIE Proc., **3771** (1999) 22.
75. Y. Tamaki, J. Itatani, M. Obara, K. Midorikawa, Phys. Rev. A, **62** (2000) 063802.
76. K. Midorikawa, E. Takahashi, Y. Tamaki, Y. Nagata, Y. Nabekawa, SPIE Proc., **4505** (2001) 189.
77. A.N. Naoumov, A.M. Zheltikov, A.B. Fedotov, D.A. Sidorov-Biryukov, J. Opt. Soc. Am. B, **18** (2001) 811.
78. M. Nisoli, E. Priori, G. Sansone, S. Stragira, G. Cerullo, S. De Silvestri, C. Altucci, R. Bruzzese, C. De Lisio, P. Villoresi, L. Poletto, M. Pascolini, G. Tondello, Appl. Phys. B, **74** (2002) S11.
79. A. Braun, G. Korn, X. Liu, D. Du, J. Squier, G. Mourou, Opt. Lett., **20** (1995) 73.
80. Y. Tamaki, J. Itatani, Y. Nagata, M. Obara, K. Midorikawa, Phys. Rev. Lett., **82** (1999) 1422.
81. Y. Liang, S. Augst, S.L. Chin, Y. Beaudoin, M. Chaker, J. Phys. B, **27** (1994) 5119.
82. D.J. Fraser, M.H.R. Hutchinson, J.P. Marangos, Y.L. Shao, J.W.G. Tisch, M. Castillejo, J. Phys. B, **28** (1995) L739.
83. C. Lynga, A. L'Huillier, C.G. Wahlström, J. Phys. B, **29** (1996) 3293.
84. O.G. Calderon, R. Gutierrez-Castrejon, J.M. Guerra, IEEE J. Quant. Electron., **35** (1999) 47.

85. A.D. Bandrauk, H. Yu, Phys. Rev. A, **59** (1999) 539.
86. N. Hay, R. de Nalda, T. Halfmann, K.J. Mendham, M.B. Mason, M. Castillejo, J.P. Marangos, Phys. Rev. A, **62** (2000) 041803.
87. V.P. Gavrilenko, E. Oks, J. Phys. B, **33** (2000) 1629.
88. N. Hay, M. Castillejo, R. de Nalda, E. Springate, K.J. Mendham, J.P. Marangos, Phys. Rev. A, **61** (2000) 053810.
89. N. Hay, R. de Nalda, T. Halfmann, K.J. Mendham, M.B. Mason, M. Castillejo, J.P. Marangos, Eur. Phys. J., **14** (2001) 231.
90. R. Vellota, N. Hay, M.B. Mason, M. Castillejo, J.P. Marangos, Phys. Rev. Lett., **87** (2001) 183901.
91. N. Hay, R. Vellota, M.B. Mason, M. Castillejo, J.P. Marangos, J. Phys. B, **35** (2002) 1051.
92. N. Hay, R. Vellota, M. Lein, R. de Nalda, E. Heesel, M. Castillejo, J.P. Marangos, Phys. Rev. A, **65** (2002) 053805.
93. M. Lein, N. Hay, R. Vellota, J.P. Marangos, P.L. Knight, Phys. Rev. Lett., **88** (2002) 183903, and Phys. Rev. A, **66** (2002) 023805.
94. T.D. Donnelly, T.K. Neuman, M.D. Perry, R.W. Falcone, Phys. Rev. Lett., **76** (1996) 2472.
95. J.W. Tisch, T. Ditmire, D.J. Fraser, N. Hay, M.B. Mason, E. Springate, J.P. Marangos, M.H.R. Hutchinson, J. Phys. B, **30** (1997) L709.
96. J.W.G. Tisch, Phys. Rev. A, **62** (2000) 041802.
97. J.R.V. de Aldana, L. Roso, J. Opt. Soc. Am. B, **18** (2001) 325.
98. V. Veniard, R. Taieb, A. Maquet, Phys. Rev. A, **65** (2002) 013202.
99. B. Bezzerides, R.D. Jones, D.W. Forslund, Phys. Rev. Lett., **49** (1982) 202.
100. S.V. Bulanov, N.M. Naumova, F. Pegoraro, Phys. Plasma, **1** (1994) 745.
101. P. Gibbon, Phys. Rev. Lett., **76** (1996) 50.
102. P. Gibbon, IEEE J. Quant. Electron., **33** (1997) 1915.
103. D. von der Linde, K. Rzàzewsky, Appl. Phys. B, **63** (1996) 499.
104. R. Lichters, J. Meyer-ter-Vehn, A. Pukhov, Phys. Plasmas, **3** (1996) 3425.
105. S. Nuzzo, M. Zarcone, G. Ferrante, S. Basile, Laser Particle Beams, **18** (2000) 483.
106. B. Shuai, B. Shen, R. Li, Z. Xu, Phys. Scripta, **65** (2002) 438.
107. R.L. Carman, D.W. Forslund, J.M. Kindel, Phys. Rev. Lett., **46** (1981) 29.
108. S.C. Wilks, W.L. Kruer, W.B. Mori, IEEE Trans. Plasma Sci., **21** (1993) 120; SPIE Proc., **1860** (1993) 70.
109. D. von der Linde, T. Engers, G. Enke, P. Agostini, G. Grillon, E. Nibbering, A. Mysyrowicz, A. Antonetti, Phys. Rev. A, **52** (1995) R25.
110. P.A. Norreys, M. Zepf, S. Moustaizis, A.P. Fews, J. Zhang, P. Lee, M. Bakarezos, C.N. Danson, A. Dyson, P. Gibbon, P. Loukakos, D. Neely, F.N. Walsh, J.S. Wark, A.E. Dangor, Phys. Rev. Lett., **76** (1996) 1832.
111. J. Zhang, M. Zepf, P.A. Norreys, A.E. Dangor, M. Bakarezos, C.N. Danson, A. Dyson, A.P. Fews, P. Gibbon, M.H. Key, P. Lee, P. Loukakos, S. Moustaizis, D. Neely, F.N. Walsh, J.S. Wark, Phys. Rev. A, **54** (1996) 1597.
112. D.M. Chambers, P.A. Norreys, A.E. Dangor, R.S. Marjoribanks, S. Moustaizis, D. Neely, S.G. Preston, J.S. Wark, I. Watts, M. Zepf, Opt. Com., **148** (1998) 289.
113. A. Ishisawa, K. Inaba, T. Kanai, T. Ozaki, H. Kuroda, (a) IEEE J. Quant. Electron., **35** (1999) 60; (b) SPIE Proc., **3886** (2000) 573; (c) IEEE J. Quant. Electron., **37** (2001) 384.

114. M. Zepf, G.D. Tsakiris, G. Pretzler, I. Watts, D.M. Chambers, P.A. Norreys, U. Andiel, A.E. Dangor, K. Eidmann, C. Gahn, A. Machacek, J.S. Wark, K. Witte, Phys. Rev. E, **58** (1998) R5253.
115. M. Protopapas, P.L. Knight, K. Burnett, Phys. Rev. A, **49** (1994) 1945.
116. H. Eichmann, A. Egbert, S. Nolte, C. Momma, B. Welleghausen, W. Becker, S. Long, J.K. McIver, Phys. Rev. A, **51** (1995) R3414.
117. M.B. Gaarde, A. L'Huillier, M. Lewenstein, Phys. Rev. A, **54** (1996) 4236.
118. Ph. Balcou, A.S. Dederichs,, M.B. Gaarde, A. L'Huillier, J. Phys. B, **32** (1999) 2973.
119. S.-Q. Gong, Z.-Y. Wang, S.-D. Du, Z.-Z. Xu, J. Modern Optics, **46** (1999) 1669.
120. C. Figueira de Morisson Faria, M. Dörr, W. Becker, W. Sandner, Phys. Rev. A, **60** (1999) 1377.
121. D.B. Milosevic, W. Becker, R. Kopold, Phys. Rev. A, **61** (2000) 063403.
122. W. Joosen, P. Agostini, G. Petite, J.P. Chambaret, A. Antonetti, Opt. Lett., **17** (1992) 133.
123. R. Danielius, A. Piskarskas, A. Stabinis, G.P. Banfi, P. Di Trapani, R. Righini, J. Opt. Soc. Am. B, **10** (1993) 2222.
124. M.D. Perry, J.K. Crane, Phys. Rev. A, **48** (1993) R4051.
125. S. Watanabe, K. Kondo, Y. Nabekawa, A. Sagisaka, Y. Kobayashi, Phys. Rev. Lett., **73** (1994) 2692.
126. S. Meyer, H. Eichmann, T. Menzel, S. Nolte, B. Wellegehausen, B.N. Chichkov, C. Momma, Phys. Rev. Lett., **76** (1996) 3336.
127. H. Eichmann, S. Meyer, K. Riepl, C. Momma, B. Welleghausen, Phys. Rev. A, **50** (1994) R2834.
128. B. Welleghausen, H. Welling, C. Momma, M. Feuerhake, K. Mossavi, H. Eichmann, Optical Quant. Electron., **28** (1996) 267.
129. M.B. Gaarde, P. Antoine, A. Persson, B. Carré, A. L'Huillier, C.G. Wahlström, J. Phys. B, **29** (1996) L163.
130. B. Shan, A. Cavalieri, Z. Chang, Appl. Phys. B, 74 (2002) S23.
131. M.C. Downer, W.M. Wood, J.L. Trisnadi, Phys. Rev. Lett., **65** (1990) 2832.
132. J.J. Macklin, J.D. Kmetec, C.L.Gordon III, Phys. Rev. Lett., **70** (1993) 766.
133. K. Miyazaki, H. Takada, Phys. Rev. A, **52** (1995) 3007.
134. C. Altucci, R. Bruzzese, C. de Lisio, M. Nisoli, S. Stagira, S. de Silvestri, O. Svelto, A. Boscolo, P. Ceccherini, L. Poletto, G. Tondello, P. Villoresi, Phys. Rev. A, **61** (1999) 021801.
135. P. Ceccherini, A. Boscolo, L. Poletto, G. Tondello, P. Villoresi, C. Altucci, R. Bruzzese, C. de Lisio, M. Nisoli, S. Stagira, S. de Silvestri, O. Svelto, Laser Particle Beams, **18** (2000) 477.

Part IV. A Survey of Coherent XUV Sources Applications

13. Introduction

The use of intense coherent sources of XUV radiation is diversified in a large field of scientific and technical applications: plasma physics, atomic physics, surface state studies, XUV optics, nonlinear optics, production of ultrashort (attoseconds) XUV light pulses, physics of ultrafast phenomena, biology and others. A large number of applications of soft X-ray lasers and high-order harmonics are already demonstrated. The original properties of coherent sources that application requirements have to fit, separately or together, concern radiation wavelength, coherence and monochromaticity of the beam, pulse energy, pulse duration and repetition rate. In addition, the size of the source facility should be of a usual laboratory scale.

Table 13.1 recalls the magnitude of the main emission parameter values of X-ray lasers and high-order harmonics. Harmonics exhibit higher repetition rate, shorter pulse duration but faster decrease of emission intensity toward short wavelengths than X-ray lasers which, in turn, provide much higher intensities at shorter wavelength, but with a much lower repetition rate than harmonics. The energy per pulse is larger by several orders of magnitude for X-ray lasers than for harmonics but the pulse duration is longer, what reduces the difference between peak powers. Concerning radiation coherence, harmonic radiation is fully spatially coherent, while the transverse coherence length of X-ray lasers is about 100 μm at 1 m from the laser exit. However, thanks to the longer pulse duration of the laser, the number of "coherent photons" per pulse is similar in both sources. Therefore, for interferometry and holography experiments which do not require temporal resolution shorter than ∼50 ps, both sources may provide similar quality of interferograms, with the advantage of a better beam monochromaticity in the case of XUV lasers. In addition, harmonic wavelengths can be made tunable, either by a two color mixing technique or using the blue shift induced by the presence of free electrons in the gas. Let us note that the parameter values that appear in Table 13.1 are subject to change with future source developments. This will be probably the case of the repetition rate of X-ray lasers, whose potential

Table 13.1. Emission characteristics of far UV and XUV coherent sources: 1. Ne-like collisionally pumped lasers with prepule; 2. Capillary discharge lasers in argon; 3. Transient Ni-like collisional excitation pumped laser; 4. HHG from 1053 nm; 5. 526 nm radiation in neon; 6. 2N+1 sum-frequency process in xenon; 7. Optimized focal length in xenon; 8. DESY VUV free electron laser

	Output	Duration	λ	$\Delta\lambda/\lambda$	Repetition
X-ray lasers					
1	0.1−10 mJ	50−100 ps	$\gtrsim$15 nm	$\sim 10^{-4}$	8×10^{-4} Hz
2	0.1−0.9 mJ	∼1 ns	46.9 nm	”	1−10 Hz
3	25−100 μJ	2−7 ps	$\gtrsim$12 nm	”	4×10^{-3} Hz
HHG					
4	0.01 nJ	*Sub*−ps	$\gtrsim$25 nm	$\sim 10^{-3}$	10 Hz
5	1 nJ	”	”	”	”
6	0.1 nJ	”	$\gtrsim$20 nm	”	”
7	1 μJ	”	$\gtrsim$40 nm	”	”
FEL					
8	30−100 μJ	30−100 fs	$\gtrsim$95 nm	$\sim 10^{-2}$	10 Hz

enhancement is up to 10 Hz with the help of diode-pumped lasers [1]. In the near future FEL will operate at shorter wavelengths.

Seeing that the time-scale required for each particular utilization of pulsed coherent XUV radiation is of chief physical importance, we choose this characteristic to sort out a number of already demonstrated applications, at the cost of other titles in which they could be involved.

13.1 Interferometry of Laser-Created Plasma

Optical interferometry is used long since to investigate electron density profiles in high-density plasmas. Experimental measurements of electrondensity distributions are excellent sources of data for the control of numerical plasma codes and for the identification plasma instabilities. However, a density limit, given by equation. 2.20

$$n_{\mathrm{c}} \simeq \frac{1.1 \times 10^{21}}{\lambda^2_{[\mu\mathrm{m}]}} \left[\mathrm{cm}^{-3}\right]$$

exists for the propagation of radiation of any wavelength λ. Soft X-ray wavelengths will obviously penetrate much deeper in dense plasmas that infrared or visible light can do. That is why XUV laser interferometry generates interest as a tool for dense plasma investigation.

DaSilva et al. [2] calculated the parameter space accessible for plasma probing using the wavelength of the collisionally pumped yttrium laser, namely 15.5 nm. In addition to the critical density, they assume two constraints, which are the free–free absorption and the limited number of recordable fringes. For

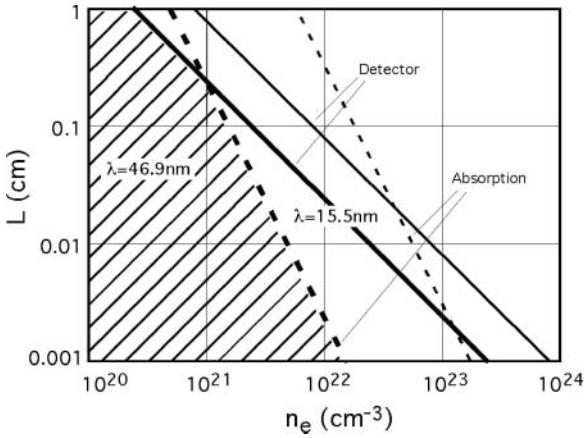

Fig. 13.1. Limits of plasma electron density reachable by interferometry for two XUV wavelengths. Dashed lines: XUV absorption in plasma; solid lines: fringe resolution by detector.

a 1-KeV plasma temperature and an average ionization 30, the free–free absorption coefficient is found to be $\alpha \simeq 2.6 \times 10^{-43} n_{\mathrm{e}}^2$. If one allows for one optical depth of absorption over a length L (i.e. $\alpha L = 1$), n_{e} and L must satisfy the condition

$$n_{\mathrm{e}}^2 L \leqq 3.8 \times 10^{42}$$

where the length unit is cm. On the other hand, the number of fringes for a propagation length L is given by

$$N_{\mathrm{fringe}} = \frac{\delta\phi}{2\pi} = \frac{1}{\lambda}\int_0^L (1-n)dL \approx \frac{n_{\mathrm{e}}}{2n_{\mathrm{c}}}\frac{L}{\lambda}$$

where n is the refractive index, given by relation $n = \sqrt{1 - n_{\mathrm{e}}/n_{\mathrm{c}}}$ [see Eq. (5.2)]. The number of fringes is bounded by the resolution and the size of the detector. Assuming 50 fringes as a realistic number in the present state of art for the soft X-ray range, one obtains the space of accessible density and plasma length limited by the tin lines represented in Figure 13.1.

A similar calculation performed for the 46.9-nm wavelength of the argon fast capillary discharge laser (cf. Section 7.5) shows an important reduction of the available space of parameters. Absorption increase is now the main cause of the lowering of accessible densities. However, below densities about 10^{21} cm^{-3} the increase of the number of fringes makes detector resolution to become the main limit to the investigation of large size plasmas.

Interferograms of a laser-produced plasma presented hereafter have been obtained using the capillary discharge argon laser [3,4]. The XUV interferometer consists in Mach–Zehnder configuration modified to use only grazing incidence optical components (Fig. 13.2). A first grating diffracts the soft

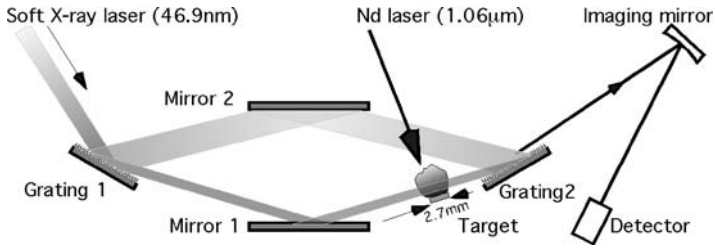

Fig. 13.2. Grazing incidence Mach–Zehnder interferometer designed for the investigation of plasma electron-density distribution.

X-ray laser beam into the two arms of the interferometer. The incidence angle is selected to evenly split most of the radiation between the zero and the first diffraction orders. Two grazing incidence mirrors redirect the beams toward the second grating. The investigated plasma is produced on the path of one of the beams by focusing the 1.06-μm light of a Nd–Yag laser onto a slab target. The focal spot at the target surface is ∼30 μm wide and ∼2.7 mm in length. The recombination of the beams, produced thanks to the second grating, generates the interference pattern. A multilayer mirror yields plasma interferogram images with 25× magnification onto the detector plane.

The examples of interferograms displayed in Figure 13.3 have been obtained from a Cu target irradiated by pulses of ∼13 ns FWHM duration. As for the duration of the 46.9-nm probe pulse, it is 1.2 ns. Interferograms correspond to times 0, 3.9, and 16.8 ns, respectively, 0 ns being the starting time of the 1.06 μm laser pulse. One sees fringes to shift with plasma expansion. Electron density maps can be computed from the fringe shifts at each location. Electron densities are found to be measurable at distances as short as 25–30 μm from the target, where they are about 5×10^{19} cm^{-3}. Another series of measurements, for a 18-mm-long line-plasma, probed electron densities up to

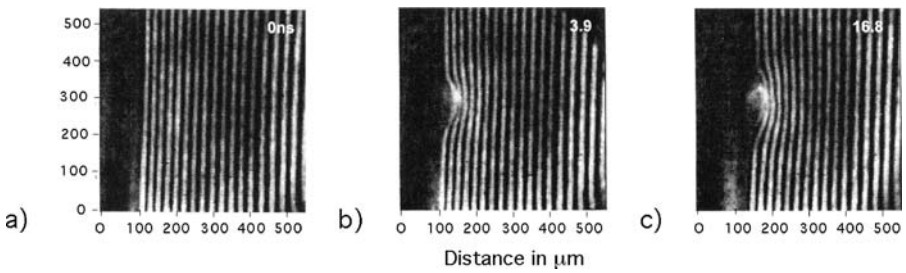

Fig. 13.3. Interferograms of plasma produced by focusing a ∼13-ns duration infrared pulse on a copper target. The duration of the 46.9-nm probe pulse is 1.2 ns. The recording times for (a), (b), and (c) are 0, 3.9, and 16.8 ns, respectively. 0 ns is the starting time of the infrared pulse (Ref. [3]).

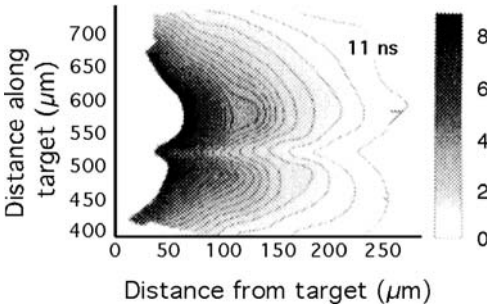

Fig. 13.4. Example of density map obtained from a line focus plasma, 11 ns after the start of the infrared pulse. A density depression is observed along plasma axis.

1×10^{20} cm^{-3}. For a point-focus plasma with ∼300 μm dimension, the spatial density distribution has been measured for densities up to $\sim 6.5 \times 10^{20}$ cm^{-3}.

An interesting example of physical finding provided by plasma interferometry is illustrated in Figure 13.4. This figure shows one of the density maps obtained from interferograms depicting the evolution of a 30-μm × 1.8-mm line focus plasma, with the same 13-ns pulse duration as in the previous experiment. The focused intensity is about 10^{11} Wcm^{-2} [5]. The map displayed in Figure 13.4 is computed from an interferogram obtained 11 ns after the beginning of the 1.06-μm pulse. This map shows that the density distribution presents a concave shape with a density minimum on axis, the observed asymmetry being due to a slight target misalignment. Bidimensional hydrodynamic simulations show that the side-lobes are created outside the laser-irradiated target region owing to cold material evaporation under the action of XUV plasma radiation. The lobes have a slower expansion than the hotter central region. Pressure balances in the lateral direction require a density depression on axis. Because the evaporation of the off-spot material and the cold plasma expansion take a relatively long time ∼4–10 ns, such an effect cannot be clearly identified in shorter pulse experiments.

13.2 Interferometry and Shadography of Exploding Wire Plasma

Thin exploding metal wires are used to form plasmas capable of generating extremely high intensity of X-ray radiation (see for instance [6]). Optical interferometry provides mapping of exploding wire in the corona region with plasma density values of 10^{17}–10^{18} cm^{-3}. Soft X-ray lasers are required to probe the plasma at the higher densities that occur on the early stages of the evolution. Interferograms obtained by Jankowska et al. [7] to this end, shown in this section, illustrate this capability of X-ray lasers.

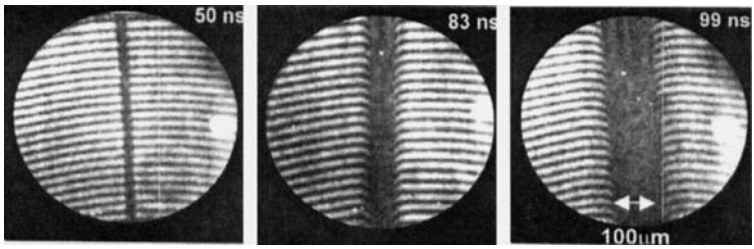

Fig. 13.5. Interferograms corresponding to the early stages of the explosion of a 25-μm aluminium wire. The times indicated are relative to the initiation of the current pulse which has a 4.7 kA peak amplitude at 155 ns.

The experimental setup is similar to the one of Figure 13.2, the wire assembly replacing the slab target and the Nd laser. The plasma is generated by heating Al wires, 15 or 25 μm in diameter, with current pulses of 4.7 or 6.0 kA peak intensity, with an increase rate of the averaged current of 30 $\mathrm{A\,ns^{-1}}$ and 42 $\mathrm{A\,ns^{-1}}$ respectively. Measurements are conducted under vacuum pressure $< 2 \times 10^{-5}$ Torr.

Figure 13.5 shows examples of interferograms corresponding to the early stages of the explosion of a 25-μm aluminium wire. The times indicated are relative to the initiation of the current pulse which has a 4.7 kA peak amplitude at 155 ns. The central part of the vaporized wire completely absorbs the probe beam. The images can be then treated as shadowgrams from which the wire-core expansion is observed to reach an asymptotic velocity of 3.4×10^5 $\mathrm{cm\,s^{-1}}$. Near the edge of the expanding wire, interferograms exhibit a fringe shift which increases with time. For the interferogram corresponding to a 83-ns delay, the shift can be measured up to a distance of 80 μm from the wire axis. Thus the refractive index of the plasma can be mapped in the shell around the colder central matter. However both free electrons and neutral atoms contribute to the refraction with relative parts which vary with the distance to

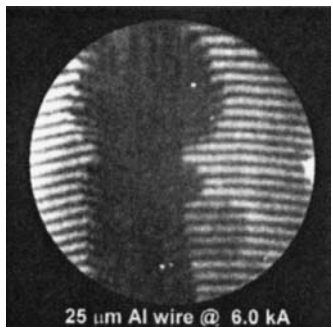

Fig. 13.6. Image nonuniformity denoting plasma instability produced by a 6 kA, 42 $\mathrm{A\,ns^{-1}}$ current.

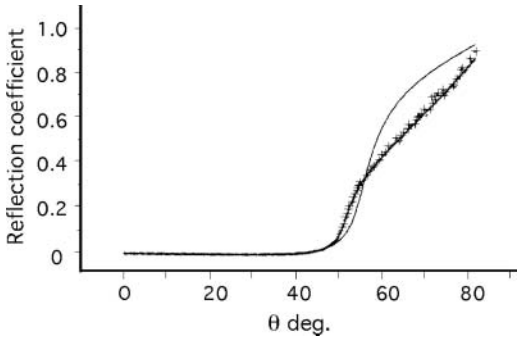

Fig. 13.7. Si reflection coefficient versus incidence angle. Cross symbols: experimental data; thin line: calculated for a clean surface with Fresnel formula; thick line: calculated for a transition contamination layer.

the wire axis. Thus the treatment of experimental data is more complex than for the case of highly ionized plasmas.

Experiments conducted for different excitation currents and wire diameter show that, for a given wire diameter, the increase of deposited energy generates expansion instabilities. This perturbed state is obvious from the nonuniformities observed along the wire axis, as shown for example in Figure 13.6 which corresponds to a 25-μm diameter wire and a 6 kA, 42 A ns^{-1} current instead of the 4.7 kA, 30 A ns^{-1} current previously used (Fig. 13.5).

13.3 Reflectometry of Solid Materials

The relatively high repetition rate of the fast capillary discharge laser makes it an efficient tool for measuring the optical constants of solid materials at 46.9-nm wavelength. The reflection coefficients of a set of materials involving Si, GaP, InP, GaAs,GaAsP, and Ir have been obtained as a function of incidence angle [8]. For example Figure 13.7 shows the measured reflectivity data for Si (cross symbols) compared with the curves calculated from Fresnel formula for a clean silicon surface (thin line) and for a transition contamination layer (thick line) [9]. The fitting of theoretical curves on experimental data provides the optical constants α and β for pure Si [cf. Eqs. (2.8) and (2.9)].

14. Time-Resolution About 100 Picoseconds

About 100 ps is a typical pulse duration for most of the (nontransient) collisionally pumped lasers. Developed since the middle of the nineties, these lasers already proved to be novel tools in various fields of research. Their main advantage is to provide a very large amount of monochromatic photons, from $\sim$25 eV to less than 100 eV energy, in a well-collimated beam. The XUV laser beam has a good spatial coherence which enables to carry out instantaneous interferograms from rapidly evolving physical objects. Furthermore, used in grazing incidence reflection, XUV radiation is a nondestructive surface probe thanks to the peculiar properties of optical constants in this spectral range.

The only serious limit to the full efficiency of contemporary X-ray lasers comes from their low repetition rate (cf. Table 12.4). It should be recalled that the origin of this limit does not rest in the physics of X-ray lasers but in the time necessary to cool the amplifiers of the infrared pump laser after each shot. As we mentioned previously, new designs of pump lasers will reduce this time in the future.

14.1 Characterization of Dense Plasmas

14.1.1 Density Measurements Up To $\gtrsim 10^{21}$ Electrons cm^{-3}

Figure 14.1 shows the principle of the experimental arrangement for density measurements used at LLNL (USA) [10]. The plasma to be probed is produced by focusing the beam of a 0.53-μm wavelength laser on a silicon wafer, overcoated with 10 μm of CH. The target is in the shape of a triangle to allow a range of plasma lengths to be probed simultaneously. The probe beam, of 15.5-nm wavelength, is provided by a neon-like yttrium laser (cf. Section 7.2.3). The laser has an output energy of $\sim$3 mJ, a divergence of 10–15 mrad (FWHM) and an output pulse width of 350 ps. The high brightness of this laser allows for obtaining single shot exposures. A spherical multilayer mirror is used to collimate the beam and inject it into the interferometer. The plasma

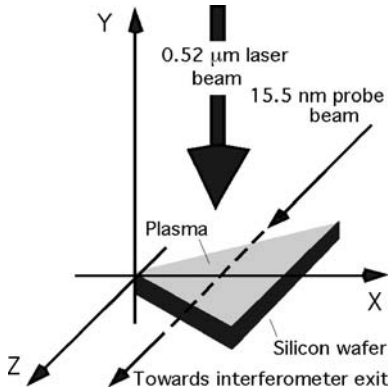

Fig. 14.1. Diagram of the plasma production arrangement used with the 15.5-nm yttrium laser (LLNL, USA) for plasma density measurements. The target is coated with 10 μm of CH. With the triangular plasma shape, a range of plasma lengths can be probed simultaneously with a single laser shot.

is placed on one of the arms of the Mach–Zehnder interferometer (nonrepresented in the figure). Each of the two normal-incidence beam splitters of the interferometer involves 8–12 Mo/Si layer pairs.

For the results presented as example in Figure 14.2, the plasma length covered by the probe beam was 0.7 mm, that is the width of the triangle at a distance of 0.35 mm from the tip of the target. The figure shows the fringe intensity as a function of the distance to the target surface. Similar curves can be obtained from the same interferogram for distances to the tip of target comprised between 0.025 and ∼1 mm. The thick solid line shows the values of the electronic density deduced from the measured fringe shifts. The dashed line shows the electron density profile which has been calculated by

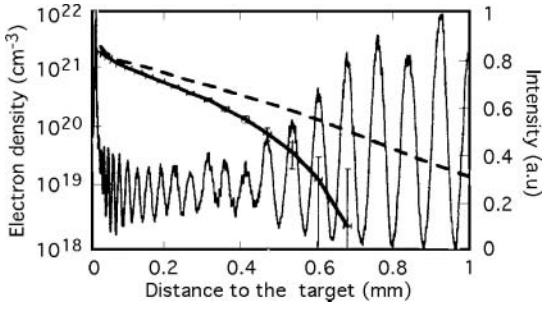

Fig. 14.2. Fringe intensity as a function of the distance to the target surface for a 0.7 mm in length plasma. Thick solid line: electronic density deduced from the measured fringe shifts; dashed line: result of one-dimensional numerical simulation of electron-density profile.

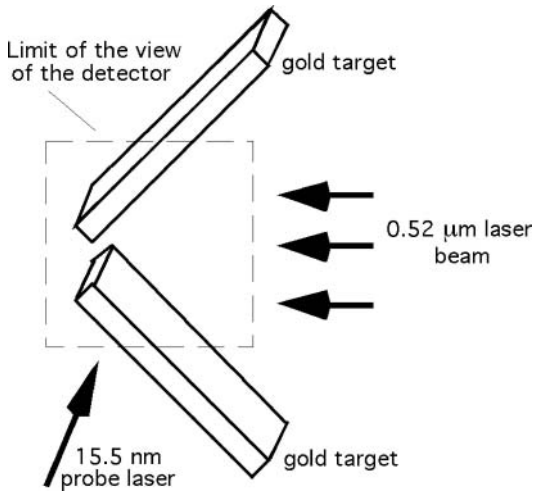

Fig. 14.3. Diagram of a plasma collision experiment. Under laser impact the gold slabs generate two counterstreaming plasmas which collide at late time.

one-dimensional numerical simulation. The discrepancy between the measured and the calculated density values is observed to increase as one moves away from the surface. This discrepancy is ascribed to the lateral expansion of the plasma, which cannot be accounted for by a one-dimensional calculation.

14.1.2 Colliding Plasmas

The understanding of collision of high-density plasmas is important for the design of the hohlraums used in indirectly driven inertial confinement fusion (ICF) research. Figure 14.3 shows the diagram of a plasma collision experiment intended to study the part of plasma interpenetration in the development of the collision [11]. Two gold slabs are aligned at 45° with respect to the symmetry axis, with a gap width $\geqq 500\,\mu m$ between the tips of the slabs. A line-focused 0.53-μm driving laser incident to the slabs generates two counterstreaming plasmas which collide later. The pulse duration is of 1 ns. The 15.5-nm X-ray laser probe-beam, which is perpendicular to the axis of the driving laser, allows to obtain interferograms in sub-200 ps exposures.

Accurate measurements of electron-density profiles can be obtained from interferograms such as the one presented in Figure 14.4 [12], which shows the evolution of the counterstreaming plasmas from interpenetration at early time to stagnation, where significant stable structures of the electronic distribution are observed in the region of the symmetry axis.

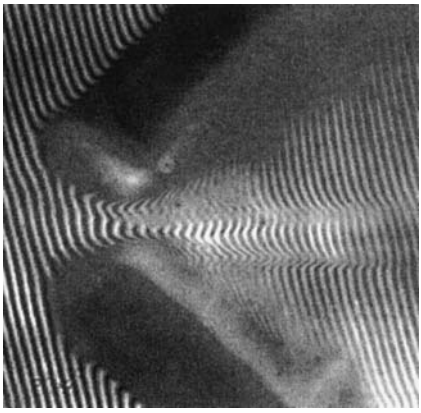

Fig. 14.4. Interfrogram of colliding plasmas. Electron-density profiles, obtained from such interferograms, show the plasma evolution from interpenetration to stagnation.

14.1.3 Soft X-Ray Radiographic Probing of Laser-Irradiated Thin Si Foils

In directly driven ICF experiments, high-intensity laser radiation ablates the surface of a capsule containing the fusionable D–T mixing. This generates a high pressure on the capsule wall, which is expected to lead to a spherical implosion. In case of initial roughness of the capsule surface or of nonuniformities in the laser-driven intensity, Rayleigh–Taylor instabilities develop during the process, which impedes the material pressure to arrive at the level where fusion might start. Nonuniformities in the laser intensities are generated by diffraction of the coherent beam at the edge of apertures in the focusing optics for instance.

One way to smooth intensity thus consists in destroying the beam coherence before focusing. This can be partially made with the help of random phase plates (RPP) that introduce randomly distributed phase changes in the beam. This system generates irradiation speckles. Furthermore the static speckle pattern can be made rapidly fluctuating by spectral dispersion using a broad band laser (SSD). With this technique the spatial irradiance profile undergoes large random fluctuations on picosecond time-scale but is smooth on long time scales [13].

Soft X-ray laser is used to perform and compare radiographic images of Si thin foils irradiated through RPP only and RPP–SSD smoothed speckle pattern [14, 15].

Figure 14.5 shows the X-ray laser system for measuring the density modulations imprinted on a 3-μm thick Si foil by an intense incident laser beam of 0.35-μm wavelength and 400-ps duration. Density modulations are detected as optical depth modulations thanks to a 15.5 nm X-ray laser beam which

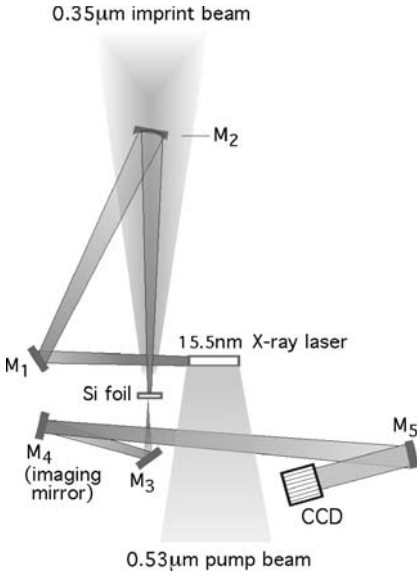

Fig. 14.5. The beam of a 0.35-μm laser imprints modulations at the surface of a silicon foil. Foil radiography with the 15.5-nm X-ray laser beam detects the optical depth changes induced in the foil by density modulations.

traverses the foil perpendicularly to its surface. A thickness variation of only 50 nm results in a 10% change in the transmitted intensity.

Radiography images, at $t = 260$ ps, of the imprinted modulations of optical depth in a 100 μm square region of the Si foil are displayed in Figure 14.6. Figure 14.6a shows the modulations due to static speckle pattern. Translated in terms of foil thickness, the rms modulation is found to be of 115 nm only at shock breakout. Figure 14.6b corresponds to the foil imprinted with the SSD smoothed beam. The rms modulation deduced from the image is reduced to

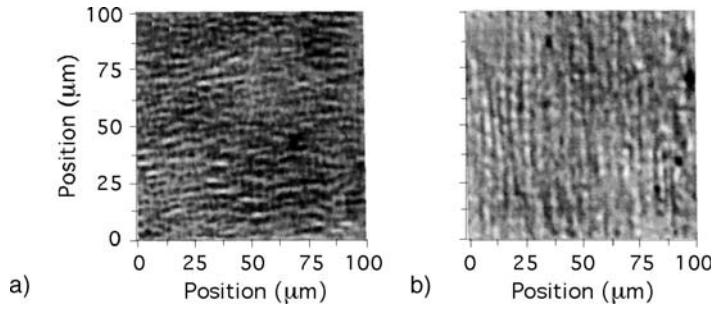

Fig. 14.6. Radiography images, at $t = 260$ ps, of the imprinted modulations of optical depth in a 100-μm square region of the Si foil. (a) The modulations due to static speckle pattern. (b) The foil imprinted with the SSD smoothed beam.

72 nm by the rapid fluctuation of the speckles pattern, what assesses the effectiveness of SSD bandwidth for the suppression of modulation imprint.

14.2 Atomic Physics

14.2.1 Lifetime Measurement of Excited He-States

The emergence of intense pulsed sources of XUV radiation promotes pump/probe techniques as a tool for atomic and molecular process studies, including transitions between levels separated by energies of tens of eV. Let us recall that a pump/probe technique consists in using a first photon pulse—the pump—to induce a given excited state of the physical system, followed by a second pulse—the probe—to characterize the evolution of the state after chosen time intervals.

This technique is illustrated here by the 13th harmonic of a 760-nm beam used as a pump of 21-eV energy to excite helium in the 1s 2p ^{1}P state and, subsequently, the 3rd harmonic of a 1.06-μm beam used as a probe of 3.5-eV energy to ionize the excited He atoms at given times after excitation [16]. The ionization rate decrease with the pump-to-probe delay increase provides the lifetime of the excited state.

Figure 14.7 shows the principle of the experimental setup. The second harmonic of a Nd:YAG laser pumps a dye laser, which generates 80 ps pulses tunable between 715 and 900 nm. At the same time the third harmonic of the Nd laser at 355 nm is used as the probe pulse via an adjustable delay line. The system repetition rate is 10 khz. The 13th harmonic at 58.4 nm of the rare gas of a pulsed jet is selected thanks to a near normal incidence spherical grating.

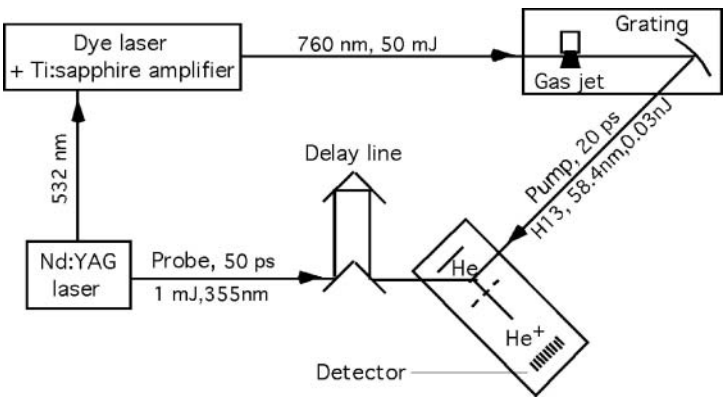

Fig. 14.7. Pump-probe experiment for the measurement of the He 1s 2p ^{1}P state life-time. The pump is the 13th harmonic, at 58.4 nm, emitted by a gas jet. The probe is the third harmonic of a Nd laser, at 355 nm. The time interval between pump and probe is adjusted by a delay line. The ions generated by the probe are separated in a time-of-flight tube.

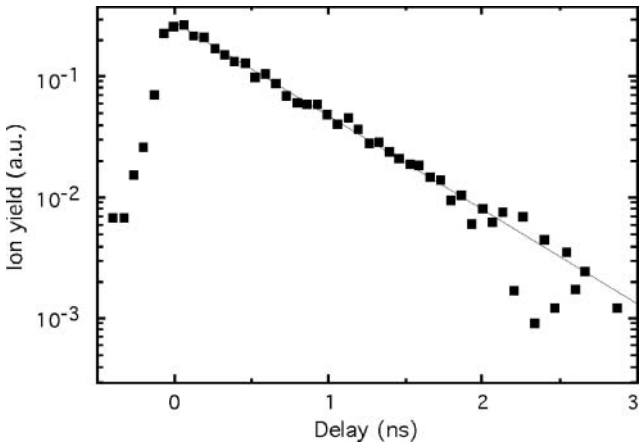

Fig. 14.8. Number of detected ions as a function of the delay time. The slope of the straight line fit to the data determines the lifetime of the 1s 2p ^{1}P excited state.

The 13th harmonic beam and the 335-nm probe light pulse are approximately focused at the crossing point of the two beams over a $\sim$0.5–1 mm diameter. The generated He ions are separated in a time-of-flight tube and detected by a Micro Channel Plate. Figure 14.8 shows the number of He^+ ions as a function of the delay time between the pump and the probe. Each point is an average of 200 shots. The helium pressure was 7×10^{-6} mbar, corresponding to an atomic density of 1.4×10^{11} W/cm^2. One sees the logarithm of the signal to vary linearly with the delay time over more than 2 ns, that is about four times the exponential decreasing time. This allows lifetime to be measured with a good accuracy. Measurements have been performed for seven different pressures between 2×10^{-7} mbar (4×10^9 atoms/cm^3) and 6×10^{-5} mbar (1.2×10^{12} W/cm^3). From the mean value of this ensemble of measurements, the lifetime of the 1s 2p ^{1}P state is found to be 0.57 ∓ 0.03 ns. This value is in good agreement with those deduced from experimental measurements of the 1s^2–1s 2p transition oscillator strength.

14.2.2 Absolute Photo-Ionization Cross-Section of Excited He-States

A somewhat more complex variant of the same experimental setup was carried out in order to allow for the measurement of the absolute ionization cross-sections of the 1s 2p and 1s 3p helium level as a function of the photon energy. A diagram of the excitation–ionization processes under consideration is shown in Figure 14.9. [17].

Using the second, third, and fourth harmonics of the Nd:YAG laser, at 532, 355, and 266 nm, provides 70-ps probe pulses with 2.3, 3, 5, and 4.7 eV photon energy respectively to ionize He excited states. A wavelength of 752 nm obtained by tuning the Dye laser gives a 1.6 eV probe pulse. The photon

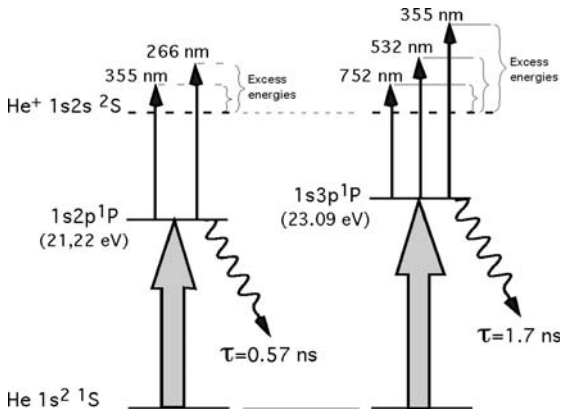

Fig. 14.9. Diagram of the excitation–ionization processes via the 1s 2p and 1s 3p states. The photon energy necessary to pump He into the 1s 2p ^{1}P state (21.22 eV) is obtained with the 13th harmonic of a 760-nm laser beam. The seventh harmonic of a doubled 752-nm beam provides the 23.09-eV energy pulse to pump He into the 1s 2p ^{3}P state. The second, third, and fourth harmonics of the Nd:YAG laser provides 70-ps probe pulses to ionize He excited states.

energy necessary to pump He into the 1s 2p^{1}P state (21.22 eV) is obtained with the 13th harmonic of the 760-nm beam. Doubling the 752-nm beam and selecting the seventh harmonic of the resulting radiation provides the 23.09-eV energy pump pulse for the 1s 2p ^{3}P. Both probe and pump beams are linearly polarized, with the same polarization, set to be perpendicular to the horizontal plane. The pump pulse duration is $\sim$30 ps. The delay between pump and probe pulses is set to 250 ps in order to separate excitation and ionization steps.

Helium is introduced in the experimental chamber by a synchronized pulsed gas nozzle. The ions produced by photo-ionization of the preliminary excited He atoms are collected by a high extraction field and analyzed by time-of-flight spectrometry. A calibrated photodiode allows for the determination of the probe energy with an uncertainty estimated at $\mp$15%. With the help of a beam splitter, the spatial profile of probe beam is reproduced on a CCD camera. Measuring the number of produced ions for various positions of the lens used to focus the probe beam provides the pump beam spatial profile. Beam radii are estimated about 100 and 500 μm for the probe and the pump, respectively.

The number of ions produced in the interaction volume V is equal to

$$N_{\mathrm{He}^+} = \int \rho_{H_e^+} dV \tag{14.1}$$

where the ion density ρ_{He^+}, reads

$$\rho_{\mathrm{H_e^+}} = \rho_{\mathrm{H_e}} \sigma_{\mathrm{excit}} N_{\mathrm{pump/S}} \times e^{-\Delta\tau/\tau} \left(1 - e^{-\sigma_{\mathrm{ioniz}} N_{\mathrm{probe/S}}}\right) \tag{14.2}$$

where $N_{\mathrm{pump/S}}$ ($N_{\mathrm{probe/S}}$) represents the number of photon per cm^2 for the

Table 14.1. Experimentally determined absolute photo-ionization cross-section in megabarn for helium excited states 1s2p (3p), as a function of the photon energy above the ionization energy of the excited state

	λ_{probe} (nm)	$\mathbf{E}_{\text{excess}}$ (eV)	$\sigma_{\text{ionization}}$ (Mb)
He $1s2p\,^1P_1$	355	0.12	16.6
	266	1.29	6.6
He $1s3p\,^1P_1$	752	0.15	24.4
	532	0.83	10.5
	355	1.99	4.2

pump (probe) beam, σ_{excit} (σ_{ioniz}), the excitation (ionization) cross-section. The variable $\Delta\tau$ is the time delay between pump and probe pulses, τ the lifetime of the intermediate excited state.

The values obtained for the absolute photo-ionization cross-section of excited helium are summarized in Table 14.1. The total uncertainty is $\sim$25%. The agreement of the experimentally measured cross-sections with theoretical calculations is found excellent. In particular these experimental data confirms the theoretical prediction of a cross-section energy dependence stronger for ionization from the 3p than from the 2p state.

14.3 Material Properties

14.3.1 Snapshots of Intense Electric Field Effects on Metal Surface

Contemporary microscopy techniques make visible nanometer-scale structures of matter. To obtain images of so small structures it is generally necessary to spatially scan the investigated surface. However scanning techniques can be used only with surface structures remaining unchanged all the time necessary to perform a scan, i.e. a long time compared to the time scale of microscopic defects evolution.

Therefore a great interest is attached to the development of techniques allowing for the observation of rapidly evolving microscopic surface structures. The use of intense visible or ultraviolet laser beam as surface probe comes up against damages occasioned to the material through the well known effect of surface-ripple formation (see, e.g. [18]). This effect is a consequence of interferences between the light diffracted by the residual surface roughness and the penetrating wave. In the case of X-ray lasers, the reader remembers that the real part of the refractive index, $n = 1 - \delta$ [Eq. (2.7)] is close to but less than unity. Therefore a beam reflected under sufficiently large incidence is submitted to total reflection, which makes negligible energy penetration into solid material, as well as subsequent damages. The pulses of XUV lasers are thus well suited for solid surface probing, more especially as they have the

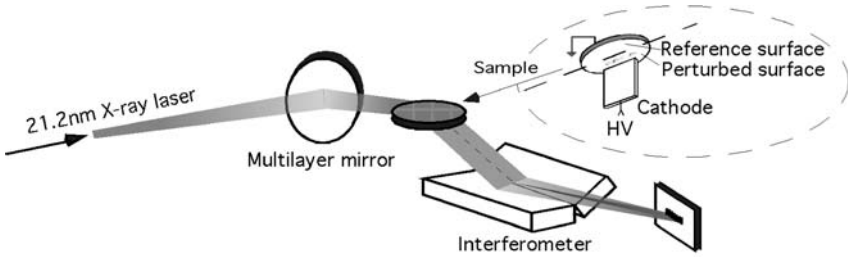

Fig. 14.10. Experimental arrangement for the study of nano-defects produced on solid surfaces by high electric field. The sample is a planar 1-cm diameter polished metal disk. The electric arrangement is shown in inset.

high spatial resolution, the short duration and the high intensity required to obtain snapshot data via holography or holographic interferometry.

As a matter of fact, soft X-ray laser interferometry has been successful used to investigate the microscopic response to a strong electric field applied on a metallic surface [19, 20]. The metal and the field values were chosen to roughly reproduce the conditions of a resonant cavity of superconducting accelerator. The anode metal was niobium and the electric field could vary from 0 to more than 50 MV/m.

Figure 14.10 shows the experimental arrangement. The 21-nm wavelength, $\sim$80 ps pulse duration probe beam is produced by a collisionally pumped Zn laser. After reflection at 45° incidence on a flat multilayer mirror, the laser beam reaches the Nb polished sample surface at 6.5° grazing angle. The sample is a planar, 1-cm diameter, 0.4-nm rms polished, metal disk. The electric arrangement is shown in inset. The E field is produced by supplying high voltage between a steel cathode and the niobium sample. The cathode presents a 0.2×6 mm rectangular surface in front of the Nb anode. This surface is situated below one of the halves of the Nb disk, in order to keep the second half—the reference surface in the figure—outside the strong field action area. The distance between the two surfaces is $\sim$750 μm. The vacuum in the chamber is of 5×10^{-6} Torr, which is much higher than the residual pressure in accelerator cavity. A possible field emission current was dispatched to a picoamperemeter.

The interferometer is of the Fresnel bi-mirror type, previously described in Section 6.4.2 (see also Section 12.1.2). The advantage of a wave-front division interferometer, like the bi-mirror system, is to provide the coherent reference beam which is necessary to obtain holographic data after beam recombination. The reference beam makes the phase of the incident wave on reflection on the unperturbed metal to be the common phase origin of the wave interferences when the beams recombine. This beam is the half-part of the incident beam which is reflected by the reference surface (see figure). Each laser shot provides an interference pattern corresponding to a sample area of 450 μm transverse size.

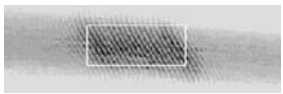

Fig. 14.11. Interferogram corresponding to the unperturbed surface. Data are saved within the limits of the white rectangle.

Figure 14.11 displays an interferogram corresponding to the unperturbed surface. The small fringe curvature near the ends is due to a remnant surface convexity. It should be noted that the grazing incidence of the detector geometry introduces a large difference between vertical and horizontal scales. The white frame in the figure represents a 0.3×9 mm rectangle on the surface sample. Owing to the 6.5° grazing incidence, the corresponding detector resolutions are $\sim$2.5 and $\sim$170 μm in width and in length, respectively. The resolution in the direction perpendicular to the metal surface only is obtained on a nanometer scale.

A succession of laser shots, without E field being applied to electrode surface, gave interferograms very similar to the example given in Figure 14.11, which confirms that there was no damage caused to the surface by the X-ray laser. Then the E field has been increased after each shot, the time interval between shots being of 20 min, that is the cooling time of the Nd pump laser. Figure 14.12 shows the changes appearing in interferogram under increasing E-field application. To make them easily visible, each interferogram has been pixel-by-pixel subtracted from one and the same unperturbed zero-field interferogram. The remnant unshifted fringes are due to a 1–2 pixel uncertainty on positioning interferograms before subtraction. An observed 1-pixel fringe shifts correspond to 6-nm resolution for vertical metal surface shifts. Hologram reconstruction, which increases the signal-to-noise, then carries the resolution limit to 2 nm.

Figure 14.12a, obtained when applying an E field of 12 MV/m does not reveal any significant perturbation on the surface. In Figure 14.12b, E field increase to 14 MV/m makes to appear a large perturbed zone though no electric breakdown had yet been detected. In Figure 14.12c a new increase of the E field to 27 MV/m enlarges and somewhat shifts the visible limit of the perturbed area. After a spontaneous microdischarge had occurred, the 37 MV/m image exhibit diffraction structures which show the surface perturbation to extend far beyond the interference fringe domain. Later interferograms, obtained without increasing the field after the first shot at 37 MV/m, showed a new extension of the perturbed zone toward the right side of Figure 14.12, followed by a stationary period which did not stop after switching off the E field.

The hologram reconstruction program returns the phase shifts at the metal surface from the fringe pattern. On the other hand, for pure morphologic surface perturbations, the phase shifts are proportional to the vertical surface shift on each point. Then holographic reconstruction allows one to draw 3D maps of the surface from the interferometric data.

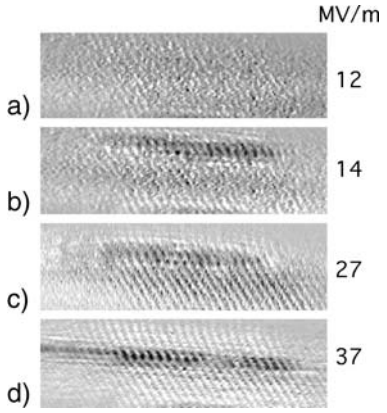

Fig. 14.12. Effect of increasing electric field application to the metal surface. (a) does not reveal surface perturbation for $E \simeq 12$ MV/m. (b) A large perturbed zone to appear at $E = 14$ MV/m. (c) A new E field increase enlarges the perturbed area. (d) Diffraction structures showing surface perturbation to extend far beyond the interference fringe domain.

Examples of surface maps are shown in Figure 14.13. The vertical resolution limit is $\sim$2 nm. Figure 14.13a–c shows fold-like structures roughly arranged parallel to the direction of constant applied field. This character is conserved from shot to shot as long as a large fields were applied. White color points out the largest altitudes, while black color points to the deepest "valleys". The largest vertical distance between white and black areas is found to be $\sim$10 nm in Figure 14.13a, $\sim$13 nm in Figure 14.13b and $\sim$16 nm in Figure 14.13c. The amplitude of local surface shifts from a shot to the next one can be larger if, for example, the bottom of a valley turned into the top of a peak. The largest amplitude of vertical shift observed through the whole experimental run was 19 nm, just after the breakdown at 37 MV/m. The evolving structures observed in this experiment are believed to mainly occur in a thin surface layer of niobium oxide and adsorbed gas.

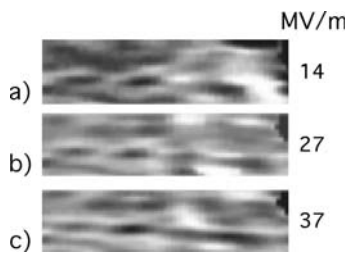

Fig. 14.13. Surface maps obtained by holographic reconstruction. White color points out the largest altitudes above the sample surface, while black color points to the deepest "valleys." The maximum vertical distance between white and black areas is $\sim$10 nm. The smallest perceptible vertical shift is 2 nm.

Similar experiments performed with the soft X-ray laser of PALS fully confirm the suitability of XUV laser interferometry for the study of nanometer defects on metal surfaces [21, 22].

14.3.2 CsI Crystal Luminescence Induced by Very Intense XUV Flux

CsI is an insulating crystal into which low energy photons do not create defects which would be the sources of crystal luminescence. The UV luminescence band at 300 nm ($E = 4.1$ eV) does not start at the fundamental absorption edge (6 eV) but only at the threshold of the 4d transition of the iodine. On the other hand the spectrum of the photostimulated desorption of Cs^+ has a maximum at the absorption energy of the 4d level of cesium. These two effects could be related to the *collective relaxation* of electronic excitation created by the hole at the 4d level. Hence the hypothesis was made that the emission at 300 nm is due to the recombination of the exciton localized at a site perturbed by a short-lived defect and created by the relaxation of the 4d hole. Observation of the defect creation in the region of the 4d level was thus important to support this hypothesis [23–25].

The photon energy of the collisionally pumped zinc X-ray laser is 58.5 eV. This energy is suitable to the selective excitation of the 4d level of iodine ions. Therefore the high intensity of the XUV laser makes it possible for the first time to investigate the effect of a high density of secondary electronic excitations on relaxation process. The principle of the experimental setup is shown in Figure 14.14.

The luminescence spectrum excited by high energy X-rays consists of two emission bands peaking at 300 and 400 nm, noted as A_1 and A_2, clearly visible in Figure 14.15c which shows a spectrum obtained with synchrotron radiation. When the spectrum is excited by synchrotron radiation in the XUV wavelength range, at 58 eV (Fig. 14.15b), the same bands are observed but with a reversed intensity ratio. This high sensitivity to the excitation

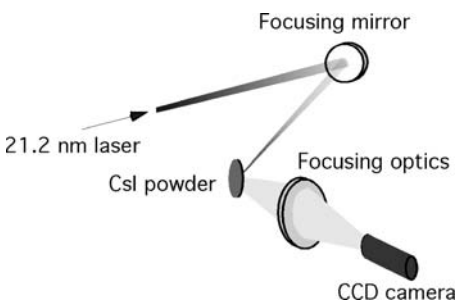

Fig. 14.14. Experimental arrangement for the study of crystal luminescence excited by very high XUV photon density.

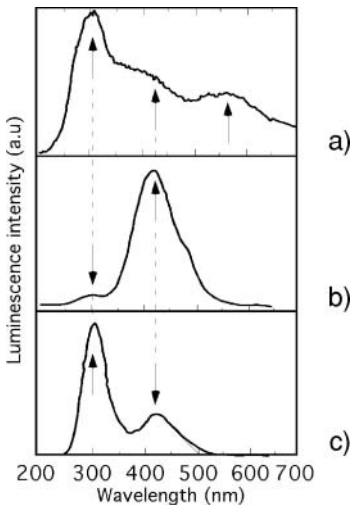

Fig. 14.15. CsI luminescence spectra excited by soft X-ray laser at 58 eV (a), by synchrotron radiation at the same photon energy (b), and by synchrotron radiation at high X-ray energy (c).

energy can be accounted for by the different origins of the two emissions bands (cf. [23]).

The luminescence spectrum of CsI excited by the soft X-ray laser beam at 58 eV is noticeably different from those obtained with synchrotron radiation. First of all, a new emission band, A_3 in Figure 14.15a, appears with a maximum at $\sim$550 nm. Moreover the intensity ratio A_1/A_2 is significantly larger as compared to the spectrum obtained at lower flux with synchrotron radiation. These changes are to be attributed to a substantial increase of the photon density in the crystal when excitation is provided by soft X-ray laser.

It is a fact that 90% of the incident 58-eV photons are absorbed within the first 600 nm of the crystal. Hence the incident photon flux can be estimated at 8×10^{10} photons/cm^2 in the case of X-ray laser excitation (Fig. 14.15a). Then the distances between the primary electronic excitations are within the range of 20–200 nm. These values are comparable with the migration lengths of the defects in the crystal. Therefore the A_3 band can been ascribed to complex defects which occur only if elementary defects are created at small distances so that they can meet during migration. A similar observation has been made in the case of γ-excitation of mechanically deformed CsI crystal. These results demonstrate the novelty of the results that can be provided by X-ray lasers in this field.

14.4 Production of Highly Focused XUV Beams

Several potential utilizations of XUV radiation, as the study of laser–matter interaction, the generation of nonlinear optical processes in gas and solids or,

in another aspect, X-ray microlithography, necessitate sources of very high brightness. Soft X-ray lasers such as the TCE Ni-like silver laser, for example, could produce coherent intensity as high as $\sim 10^{14}$ W/cm^2, at 13.9-nm wavelength, in a diffraction-limited focal spot of diameter $\lesssim 1$ μm. This requires XUV beams of very high quality. One is thus led to develop beam quality control methods.

14.4.1 Method of Wave Front Characterization

If we consider a coherent beam, the wave vector at a given point of the wave front is the gradient of the phase of the wave at this point. Given that the wave vectors are supposed to converge toward the focus, the control of focusing characteristics can be performed through a close examination of the form of the wave front. That is why the Shack–Hartmann technique, consisting in sampling the beam by the way of a lens array, is commonly used to investigate the defaults of large astronomical mirrors in visible light.

This technique can be extended to soft X-rays where the usual optical lenses are replaced by Bragg–Fresnel lenses (cf. Section 2.4). A small part of a Bragg–Fresnel lens array is shown in Figure 14.16 [26]. The lenses are typically of 1-mm diameter for a 0.5 m focal length. The array, which is supported on a

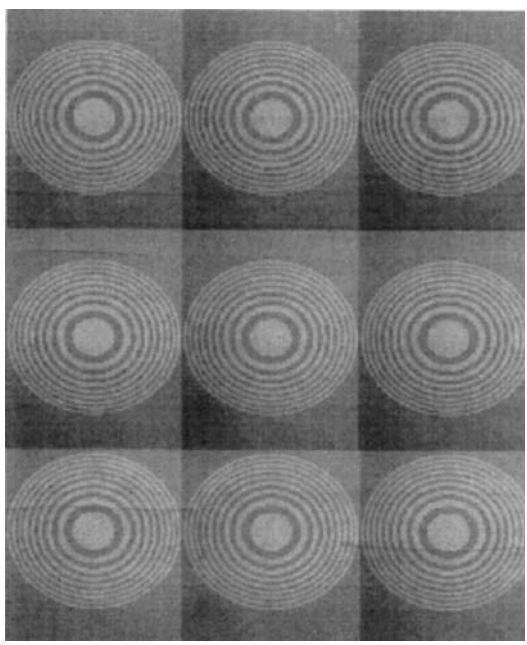

Fig. 14.16. Small part of a Bragg–Fresnel lens array used to closely examine the wavefront of an XUV beam. The lens diameter is 1 mm. The full array consists of $\sim$400 diffractive lenses [24].

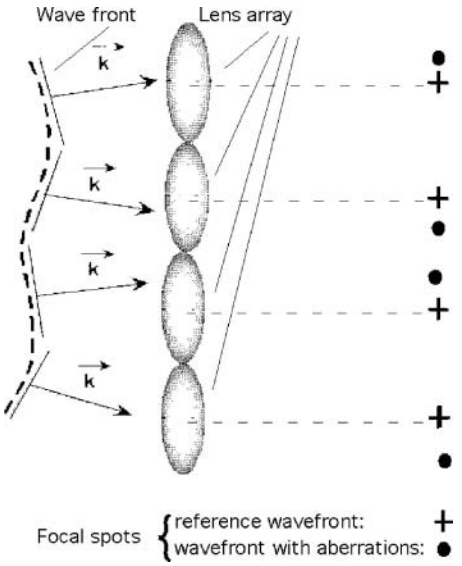

Fig. 14.17. Principle of wave-front characterization. The measured distance between reference spot and actual spot gives the angle of the wave vector with the reference direction.

SiO_2 substrate of 25 mm in diameter, is composed typically of $\sim$400 diffractive lenses [28].

Each lens of the array selects a beamlet from the incident radiation. Each beamlet is focused on a point whose transverse position depends on the direction of the wave vector **k** corresponding to the plane wave tangent to the local part of the beam selected by the lens. Comparing the position of the focal spots with those provided by a reference wave front, one has access to the aberrations of the investigated wave front. The principle of this method is illustrated in Figure 14.17. The accuracy and the sensitivity of the method have been characterized by using the radiation of an ondulator in the 7–25 nm wavelength range. Accuracy measurement better than $\lambda/120$ has been achieved at a wavelength of 13.4 nm [27].

14.4.2 Measurement of the Spatial Intensity Distribution of a Soft X-Ray Laser Beam

A complete characterization of a soft X-ray laser beam [29] has been made in the case of the capillary discharge argon laser, which gives a spatially fully coherent beam at $\lambda = 46.9$ nm (cf. Section 7.5). For a laser-pumped soft X-ray laser, the total beam should be diaphragmed down in order that the investigated beam may be coherent.

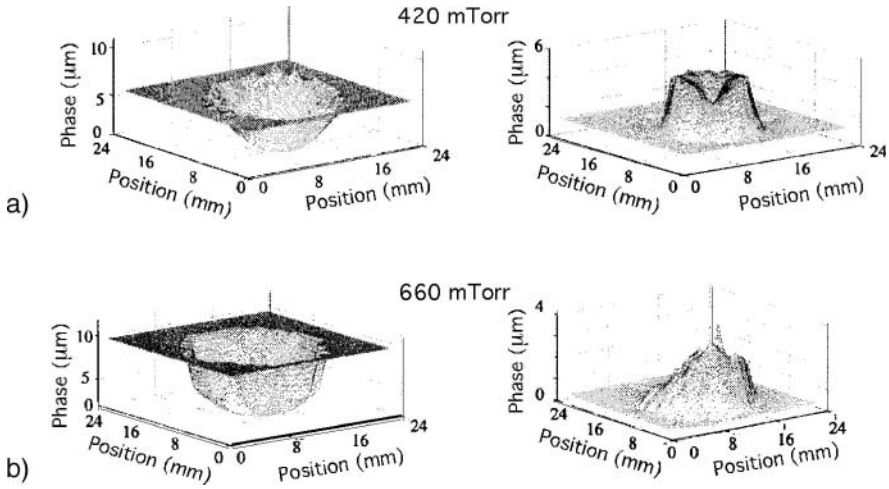

Fig. 14.18. Wave front calculated from the Bragg–Fresnel lens array data for two gas pressures in capillary: (a) 420 mTorr; (b) 660 mTorr (left-hand side: phase front shape; right-hand side: intensity distribution).

The capillary length was 35 cm. The Shark–Hartmann array involved 200 diffractive lenses working in reflection at an incidence angle of 22.5°. The lenses, of 700-μm radius, were etched on an 1-in. diameter flat silicate substrate. The focal length was 50 cm, which ensures a resolution of 0.1 μrad on the wave vector angle. The corresponding accuracy on the wave front characterization is $\lambda/300 \simeq 0.16$ nm. The wave front was obtained by the method described in the previous paragraph. The intensity of the laser beam was sufficient to record the focal spots in a single shot.

Examples of results are displayed, for two argon pressures in capillary tube, in Figure 14.18. The wave front was found to be nearly a divergent spherical

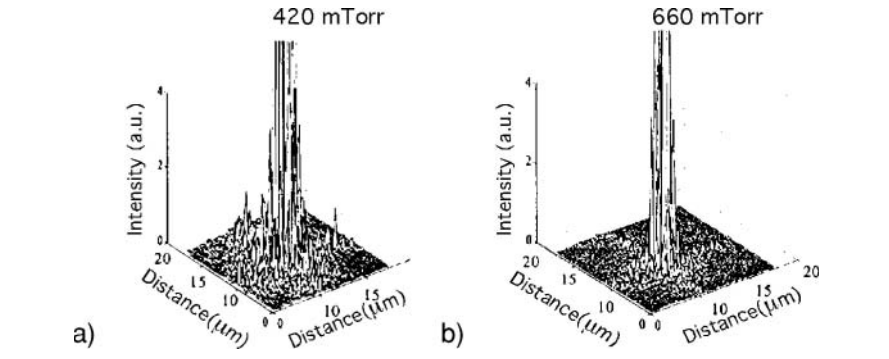

Fig. 14.19. Intensity distribution at the focus of the soft-X-ray laser obtained from experimental data by numerical simulation.

wave of curvature radius ∼13 m for all pressures. This divergence mainly results from beam refraction induced by the radial electron density gradient in the capillary plasma column. Refraction is also responsible for the annular intensity distribution shown in Figure 14.18a. More generally it was observed that the amplitude wave front defects decreased as the pressure was increased from 200 to 660 mTorr. This effect is ascribed to the smoother electron density gradients resulting from a reduced plasma column compression at higher discharge pressure.

The experimental data collected by the lens array technique have been used to obtain the intensity distribution at the focus of the soft X-ray laser by numerical simulation. Examples of results are shown in Figure 14.19 for the same pressures as in Figure 14.18. Figure 4.19b exhibits the strong peak corresponding to the nearly optimum laser operating pressure of 420 mTorr. This peak includes 70% of the total energy in a 0.5 μm focal spot.

15. Time-Resolution About One Picosecond

15.1 Picosecond X-Ray Laser Interferometry

A first spatial mapping of plasma electron density with temporal resolution in the picosecond range has been achieved thanks to the COMET laser, pumped by transient collisional excitation of Ni-like ions of palladium,with a laser line at 14.7-nm wavelength [30]. This laser provides an energy of $\sim$25 μJ per shot (i.e. $\sim 2 \times 10^{12}$ photons) with a spectral resolution $\Delta\lambda/\lambda \lesssim 10^{-4}$. The time interval separating the shots is 4–5 min.

A diagram of the interferometry experiment is displayed in Figure 15.1. The Mach–Zehnder type interferometer represented in the figure is quite similar to that previously shown in Figure 13.2. The investigated line-plasma is focused on one of the interferometer arms. The second arm conveys the reference beam. An example of interferogram for a 0.5-cm long plasma is shown in Figure 15.2. The plasma was produced by a 600-ps,1054-nm laser pulse. The spatial resolution of the CCD detector limited the resolution of the fringe structure and consequently the maximum measured density which was $\sim 3 \times 10^{20}$ cm^{-3}.

Picosecond snapshots of the transverse density distribution of a plasma column, produced on an aluminum slab target by the 1.2 *ns* pulse of an infrared laser, have also been obtained by using an imaging Fresnel bi-mirror interferometer [31]. Interferograms were recoreded in a plane perpendicular to the plasma column axis [32].

The probe beam is the 13.9 *nm* beam of the Ni-like Ag laser. A variable delay is introduced between the probe and the heating beam in order to obtain snapshots of the interferogram separated by 1 *ns*. The spatial resolution is about 1.75 mm in both directions of the plasma transverse plane.

1 *ns* after the heating pulse, a weak curvature of the fringes in the direction of the probed plasma was observed. In agreement with the simulated fringe shift produced by the plasma in the same interferometry configuration. However for the plasma probed 2 and 3 *ns* later, regions appear where a marked fringe bending in the opposite direction occurs.

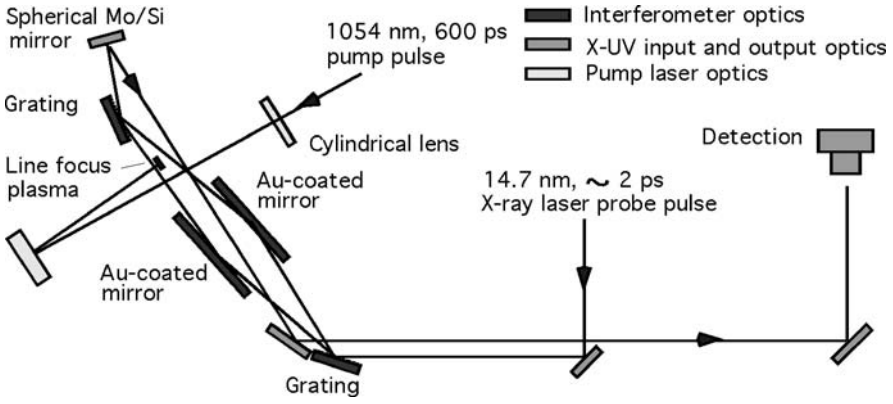

Fig. 15.1. Experimental arrangement used to investigate laser-produced plasma evolution with ∼1-ps time resolution.

This inversion is what one can expect if the refractive index in these regions is greater than the unity while it remains lower than one in other regions. From Eq. 2.18 (Sec. 2.1), we know that an index lower than one corresponds to the interaction of the radiation with the free electrons of the plasma. Inversely Eq. 2.7 and 2.8 show that the contribution of bound electrons to the index may be positive or negative according to the respective values of the radiation frequency and the atomic level frequency. This effect is important only if the two frequencies are very close to each other.

As a matter of fact, Tang et al. notice that a 2p-2d transition of Al^{2+} ions has an energy very close to the one of soft X-ray laser photons. Moreover calculations by Nilsen et al. [33] show that bound electrons can dominate

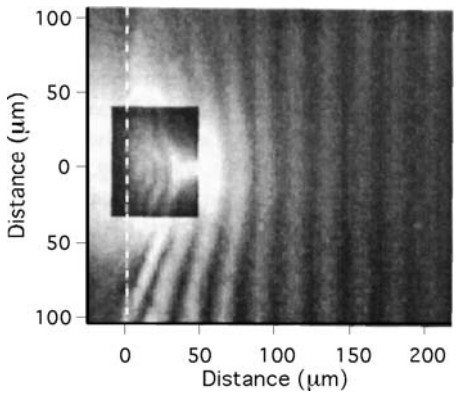

Fig. 15.2. One-picosecond time-scale interferogram of a line focus plasma obtained with 14.7-nm radiation. The inset shows the higher density plasma interferogram with an improved contrast.

the plasma refraction index. Then the index may be made greater than one, or it may be sufficiently enhanced to retun overestimated values of the free electron density. Therefore detailed calculations will be necessary to obtain reliable information from interferometric data.

Regarding the development of new spectrometry techniques, a first approach of Fourier-transform spectrometry has been achieved by Zeitoun et al. with the help of a XUV Michelson interferometer [34].

15.2 Material Probe at the Picosecond Scale

15.2.1 Study of the Surface Domain–Structure of Ferroelectric $BaTiO_3$

Let us recall that ferroelectricity is the property of some crystals that present spontaneous electric polarization. Ferroelectric polarization decreases with temperature increase and cancels as the Curie temperature is reached. Likewise ferromagnetic materials, ferroelectric crystals present regions of constant polarization, the so-called ferroelectic domains, whose size varies with the temperature.

The dynamic of the process, that leads from the ferroelectric to the paraelectric phase beyond Curie temperature, is not yet fully understood because detailed experimental data about the variations of the domain surface-structure are still missing. Techniques based on scanning probe microscopy, for example, give only long-time averaged observation results. Polarizing microscopy in visible light provides relatively low resolution because of the long radiation wavelength. However, seeing that the electric polarization of the surface domains directly affects the amplitude and the phase of the reflected XUV radiation, the intense short pulses of coherent photons provided by X-ray lasers may be used to probe the domain surface–structure of such materials. As a matter of fact the formation of speckles is a general feature of coherent beams, when they are transmitted through a medium (or reflected by an interface) which generates randomly distributed phase shifts into the wave front. Therefore R.Z. Tai et al. [35] developed a technique based on the detection of the speckles diffracted by the sample surface as the beam of an X-ray laser was reflected on this surface.

The experimental setup is schematically shown in Figure 15.3. The laser beam at 13.9 nm is provided by a TCE silver laser (cf. Section 7.4.7). It carries about 10^{12} photons per pulse, with a number of coherent photons estimated to be about 10^8 per pulse. Pulse duration is estimated at $\sim$7 ps. A Mo/Si multilayer mirror at 45° incidence produces a vertically polarized probe beam. An 80-μm (horizontal) × 200-μm (vertical) slit, significantly narrower than the transverse coherence length, is used to produce a fully coherent beam. Hence the free pattern of the probing beam is the Fresnel diffraction pattern of the slit. The total number of photons contributing in this pattern is estimated at 2×10^6 per shot.

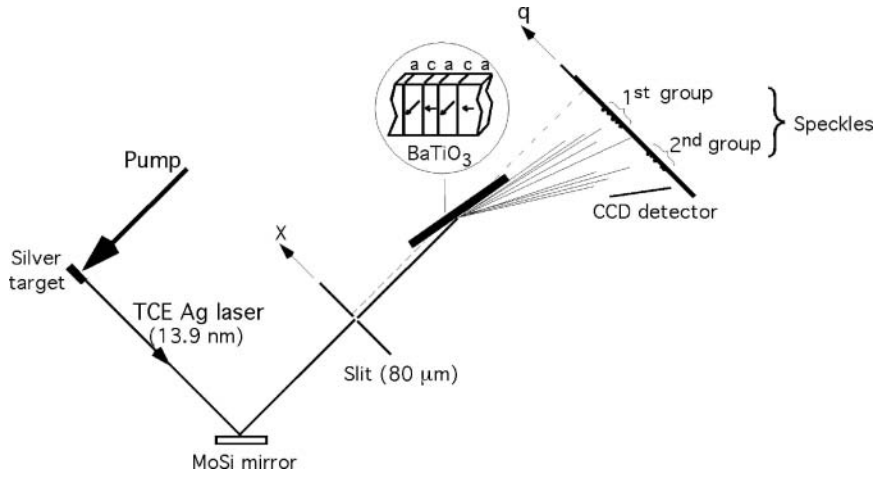

Fig. 15.3. Principle of the experimental setup designed to probe the domain structure of $BaTiO_3$ as a function of temperature at the picosecond time-scale.

The chosen material for the probed sample is $BaTiO_3$ single crystal with alternative a/c domains aligned in parallel (see the inset in Figure 15.3). The Curie temperature is 122°C. The grazing angle is 10°. The diffracted speckles, as the beam is reflected under a 10° grazing angle on the $BaTiO_3$ surface, are detected by a CCD camera 0.5 m from the slit.

The sketch of the CCD-detector surface in Figure 15.3 suggests that speckles are separated into two groups. This is effectively observed for a temperature of the diffracting crystal of 24°C. Each group mainly involves photons scattered by the same type of domains (for instance, a domains). As the temperature increases toward the Curie temperature, the speckle patterns progressively evolve into one group. Above the Curie temperature, the structure in speckles disappears and turns into an only spot that corresponds to specular reflection of the beam on the crystal surface.

If one assumes the crystal surface to be projected on the slit plane, the ferroelectric domains can be included in the description of the crystal optical properties by using a complex transmittance, whose value along the X axis has the form

$$T(x) = T_0(x) \exp\left[i\phi(x)\right] \tag{15.1}$$

where $T_0(x)$ stands for the amplitude transmittance and $\phi(x)$ represents the phase retardation in the sample. The authors define a correlation function accounting for a domain distribution in the matter as

$$\gamma(x) = \frac{\int_{-\infty}^{+\infty} T^*(x'+x)T(x')dx'}{\int_{-\infty}^{+\infty} T^*(x')T(x')dx'} \tag{15.2}$$

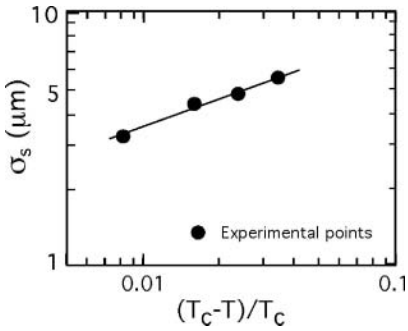

Fig. 15.4. Measured $BaTiO_3$ surface domain size as a function of the reduced temperature $\mu = (T_c - T)/T_c$ near the Curie temperature T_c.

Let us assume $I(q)$ to be the domain-structure diffracted intensity distribution along the q direction and $I_{sp}(q)$ be the intensity measured for the free pattern obtained in specular reflection. The correlation function $\gamma(x)$ may be obtained from I_q and $I_{sp}(q)$ as the ratio of the Fourier transforms $F[(I_q)]$ and $F[I_{sp}(q)]$, i.e.

$$\gamma(x) = \frac{F[(I_q)]}{F[I_{sp}(q)]} \tag{15.3}$$

The Fourier transform of the matter correlation function, $\gamma(x)$, leads to the power spectrum of I_q which gives a statistical description of the domain distribution in the spatial frequency space.

This analysis has shown that, at a temperature of 24°C, the average distance of the nearest two domains of a given type, a or c, was 1.17 μm. This distance was reduced to 0.32 μm at 118°C. Above the Curie temperature, the whole of the speckles turned into a pure slit diffraction pattern, indicating a complete annihilation of the a/c domain structure. Moreover a correlation length, σ_s, that is the average domain size at given temperature, may be defined from the autocorrelation part of $\gamma(x)$. Figure 15.4 shows σ_s as a function of the reduced temperature $\mu = (T_c - T)/T_c$ near the Curie temperature. The least-square fitting of the experimental points leads to an exponential law, $\sigma_s \sim \mu^k$, with $k = 0.37 \mp 0.02$. This law is considered to imply strong fluctuations of the polarization near the critical point.

15.2.2 Time-Resolved Measurement of Material Scintillation

Luminescence of barium fluoride, BaF^2, is used in particle scintillation detectors. Two types of emissions compose the BaF^2 luminescence excited by photons of the XUV region. The first one which consists in excitonic luminescence, is centered at 290 nm. The second one, induced by radiative transition of a valence electron to a Ba 5p core-level, is of the type of Auger free luminescence. It is centered at 220 nm. The decay time of the BaF^2 exciton by photoabsorption in the excitonic band is known to be about 600 ns, while free

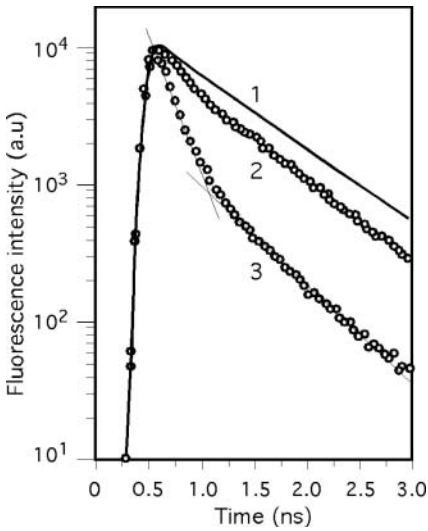

Fig. 15.5. Luminescence decay of BaF^2. (1) Excitation by synchrotron radiation at 40 eV; (2) excitation by low-intensity harmonic pulses at the same photon energy; (3) excitation by high-intensity harmonic pulses at the same photon energy.

Auger luminescence, with a decay time $\sim$0.9 ns, is much faster. Moreover, luminescence yield and decay time are observed to decrease when excitation is produced by heavy ions or alpha particles rather than by synchrotron radiation. Luminescence excitation by intense ultrashort XUV pulses produced by high harmonic generation (HHG) is expected to give more insight into the mechanisms implied in the whole of the luminescence observed in standard experimental conditions.

Therefore the fast part of the luminescence decay has been investigated on using the 2-ps pulses of the 27th harmonic of a Ti:sapphire laser ($\lambda \sim 31$ nm) operating at a repetition rate of 1-kHz [36]. The results for free Auger luminescence are shown in Figure 15.5. Curve 1 shows the intensity decay obtained with synchrotron radiation at 31 nm. For excitation by harmonic pulses of low intensity (curve 2) the decay is close to that measured with synchrotron radiation ($\sim$0.8 nm). Then we can see that the increase of harmonic intensity induces a nonexponential decay (curve 3) which exhibits two characteristic times of $\sim$0.3 ns and $\sim$0.7 ns. The intensity and the decay of excitonic emission are also affected by the excitation intensity. These changes in luminescence characteristics at a certain wavelength are to be ascribed to the interaction of closely spaced electronic excitation when the excitation intensity increases.

15.2.3 Single-Shot Probe of Photoelectron Emission

The 14.7-nm XUV laser, shortly described in Section 15.1, has been used to demonstrate the capability for this type of laser to perform electronic structure

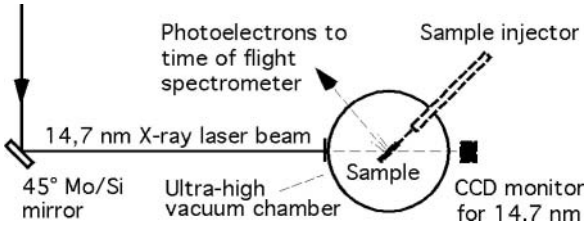

Fig. 15.6. Diagram of the experimental setup used to observe single shot electron-band structures.

measurements on a single laser shot [30]. Figure 15.6 shows the experimental setup. A 45° Mo/Si mirror is used as a filter to select the X-ray laser wavelength and minimize the thermal radiation of the palladium plasma. The pressure in the vacuum chamber is 5×10^{-7} mbar. The 2-ps XUV laser pulse irradiate a solid tantalum sample. Photoelectrons of binding energy less than the laser photon energy (84.5 eV) are ejected from the sample and collected into the drift tube of a time-of-flight spectrometer. Electrons of lower binding energy in the solid arrive first on the microchannel plate detector. The next electrons are detected with a delay which is an increasing function of the binding energy.

Figure 15.7 displays, as an example, a preliminary photoelectron spectrum recorded for an *in situ* sputter-cleaned Ta reference sample, illuminated with 10^9–10^{10} XUV photons. Electrons coming from the valence band and from two shallow core levels ($4f_{7/2}$ and $4f_{5/2}$ with binding energy of 22 eV and 24 eV, respectively) are expected to arrive between 100 ns and 150 ns. Peaks corresponding to these features are observed in the spectrum on a background of secondary emission. Electrical noise, associated to the tantalum plasma, is registrated with the photoelectron spectrum on the detector.

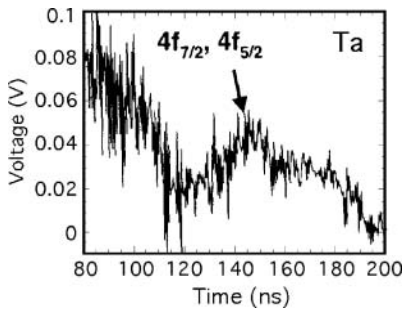

Fig. 15.7. Preliminary photoelectron spectrum obtained from an *in situ* sputter-cleaned tantalum reference sample, irradiated by a picosecond pulse of 10^9–10^{10} XUV photons.

16. Subfemtosecond Time-Resolution

16.1 Frequency-Domain Interferometry Applied to Electron-Density Measurements

The advent of light pulse stretching and recompression techniques has opened the way to the generation of intense laser pulses of extremely short duration ($\lesssim$0.1 ps). Thus, completely new techniques, as frequency-domain XUV interferometry, can be now implemented to gain access to the study of ultrafast processes [37, 38].

Frequency-domain interferometry is a temporal counterpart of the Young-slit interference experiment. Let us assume that we know how to generate two temporally separated phase-locked pulsed sources, i.e. two pulsed sources of field that maintain a constant phase relation between them. Using pulse stretching by reflection at the surface of a diffraction grating, which takes the place (in time) of diffraction through Young's slits (in space), we can generate fringes by recombining the two fields.

Two phase-locked pulses can be produced from a single laser pulse with a system, like that represented in Figure 16.1, which includes a birefringent plate and a linear polarizer [37]. A Ti:sapphire laser provides 60-ps pulses of linearly polarized light. The beam passes through the birefringent plate, which is rotated at 45° from laser polarization. The difference of group velocity on the two axes of the plate generates two temporally separated pulses, with fields oscillating in two orthogonal directions. A polarizer placed after the plate projects both components on the same axis. The delay between the pulses depends directly on the birefringent plate thickness.

The principle of the experimental setup used for frequency-domain interferometry is shown in Figure 16.2. The beam of a Ti:sapphire laser is divided into two parts. The one, of low energy, provides the twin phase-locked pulses. The second one, of higher energy, is used to produce a plasma in the experimental chamber. A rare gas jet, irradiated by the twin laser pulses, generates two phase-locked harmonic pulses which are then focused at the plasma. After passing the grating of a XUV flat-field spectrometer, beam recombination

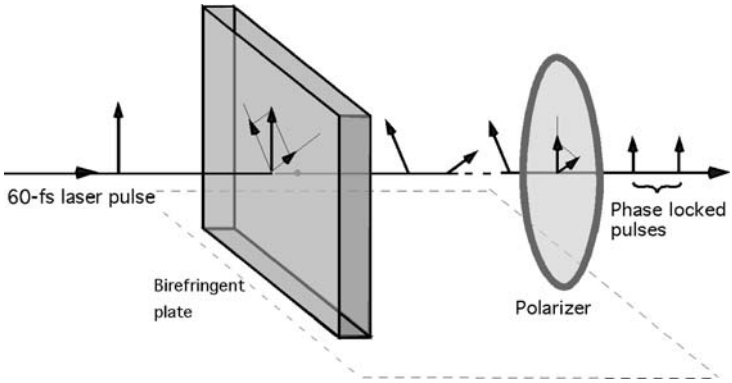

Fig. 16.1. Birefringent plate and polarizer association which produces two phase-locked pulses from a single ultrashort laser pulse.

generate fringes which are detected either as a step-by-step scan, with a photomultiplier placed behind a slit, or in a single shot, on a microchannel plate.

In the absence of gas in the experimental chamber, this setup allows for a direct study of phase-locking between two harmonic pulses. As an example,

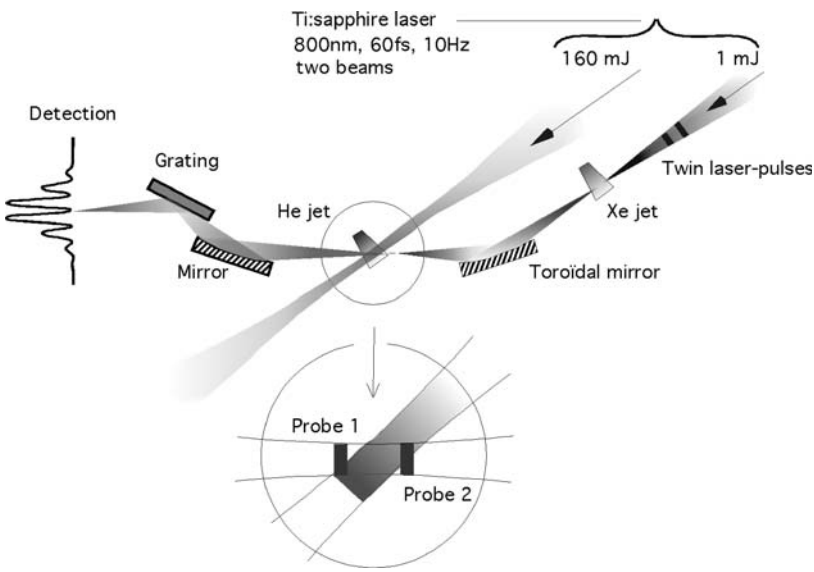

Fig. 16.2. Experimental setup for frequency-domain interferometry. Harmonics produced in xenon by two temporally separated mode-locked pulses, interfere after stretching on the surface of a diffraction grating. When helium plasma is introduced on the path of the harmonic beams, the fringes are shifted. Measuring the time-dependent phase shifts leads to the time-dependent electronic density of the plasma.

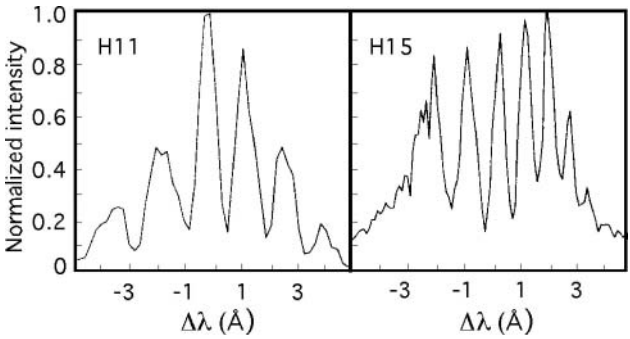

Fig. 16.3. Fringes obtained for the 11th and the 15th harmonics when harmonics propagate freely.

Figure 16.3 displays the experimental fringe patterns of H11 (a) and H15 (b), generated in argon by two pulses delayed by 120 fs. One sees the fringe period to be shorter for the higher harmonic. This result illustrates a scale rule according to which the fringe space period is proportional to the square of the harmonic wavelength. It is worth noticing that a consequence of this rule is that interferometry with higher order harmonics requires higher detector resolution.

Introducing helium, for example, in the experimental chamber, frequency-domain interferometry can be applied to plasma diagnostic. A focused laser intensity of 10^{18} W/cm^2 creates the plasma by optical field ionization. Preliminary examination shows the plasma atomic density profile, determined with a Mach–Zehnder interferometer, to be approximately Gaussian. The maximum density is 2.4×10^{19} cm^{-3} for a backing pressure of 18 bars. Completely stripped ions are produced on the full length of the jet along the pump beam axis. The time delay between the two phase-locked harmonic pulses is fixed at 300 fs. The pump-probe delay is varied in order to probe ionization dynamics.

The fringes are shifted proportionally to the relative phase change, $\phi_{1,2}(t)$, between the two phase-locked pulses. The phase shift obeys equation

$$\phi_{1,2}(t) = 2\pi \frac{[n\,(t) - 1]\,L}{\lambda} \approx -2\pi \frac{N_{\mathrm{e}}(t)L}{2\lambda N_{\mathrm{c}}} \tag{16.1}$$

where $n(t)$ is the time-varying refractive index. N_{e} is to be understood as space-averaged electron density. L is the plasma length and N_{c} is the critical density corresponding to the harmonic wavelength.

Let $\delta\lambda$ to be the measured phase shift in the wavelength domain, τ the delay between the two phase-locked harmonic pulses, and Δt the pump-probe delay. The normalized shift is defined by relation

$$\frac{\delta\lambda}{\Delta\lambda}\,(\Delta t) = \frac{\phi_2(\Delta t + \tau/2) - \phi_1(\Delta t - \tau/2)}{2\pi} \tag{16.2}$$

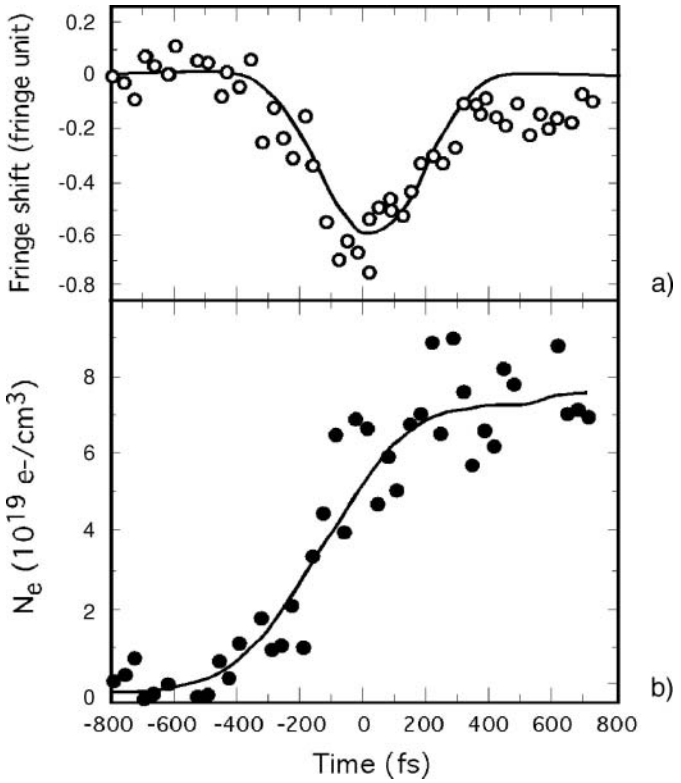

Fig. 16.4. (a) Fringe shifts measured as a function of time during helium plasma evolution; (b) time-dependent plasma density deduced from measured fringe shifts.

where $\Delta\lambda$ is the shift which would correspond to a 2π phase difference. Using this equation, the space-averaged electron density, $N_e(t) = -(2\lambda N_c/L)\,\phi_{1,2}(t)/2\pi$, can be rewritten as

$$N_e(\Delta t + \tau/2) = N_e(\Delta t - \tau/2) - \frac{2\lambda N_c}{L}\frac{\delta\lambda}{\Delta\lambda}(\Delta t) \tag{16.3}$$

Figure 16.4a shows the experimentally measured normalized fringe shift as a function of the pump-probe delay. For large negative delays ($\Delta t < -800$ fs) the plasma is not still created, which implies $N_e(\Delta t - \tau/2) \approx 0$. From this initial value and the measured fringe shifts represented in Figure 16.4a, equation (16.3) provides the electron density as a function of time.

The experimentally measured values of N_e are displayed in Figure 16.4b, where the solid curve represents the results of three-point averaging. One can see that the full density variation spreads out 0.8-ps duration only.

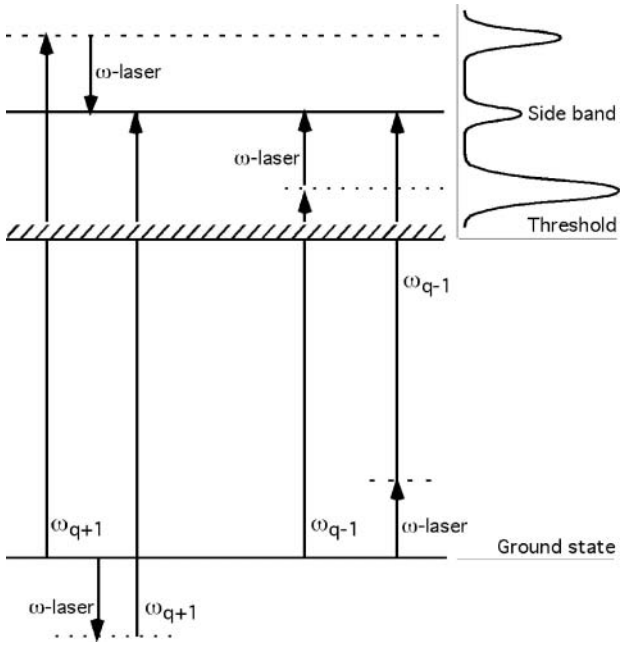

Fig. 16.5. Quantum paths contributing to the photoelectron generation in argon jet by mixed-color two-photon ionization (Ref. [29]).

16.2 Generation of Attosecond Pulses

An exciting potentiality of high-order harmonics consists in the generation of intense coherent pulses of duration in the attosecond (as $= 10^{-18}$ s) domain. With such few-cycle strong-field pulses it will be possible to find access to a new approach of atomic and molecular processes restoring the role of the field phase in electron dynamics [39–48].

In the previous sections, the center of interest was the frequency spectrum of harmonics, i.e. the generation and the propagation of the individual harmonics of pump radiation. An important characteristic of harmonic radiation was the existence of a plateau of approximately constant intensity lines, ranging along an energy interval of about 20 eV (cf. Fig. 10.3, Chapter 10). Harmonics were spatially separated with using diffraction gratings.

Here the point of view is modified. We consider the beam of the spatially mingled harmonics and we wonder about the phases within this pack of fields involving so much frequencies. On account of the coherence of the primary excitation by the pump laser, the harmonic phases are expected not to be independent from each other. In the ideal case of mode-locked harmonics one should observe beatings between harmonic waves. Seeing that the period of

the pump field is $\simeq$2.7 fs, phase relations between harmonics might thus generate the propagation of subfemtosecond pulse trains (cf. e.g. [46]).

Phase relations between individual harmonics depend on several factors among which pump intensity and beam focusing have a large part (cf. Section 11.2). To examine the detailed temporal behavior of the plateau harmonics, taken as a whole, it is necessary to Fourier transform a global harmonic beam. In other words, one has to change from the frequency domain to the time domain. This transformation makes to appear the train of attosecond pulses, that is nothing but the global temporal beam structure due to the phase relations between the individual harmonic fields. However, there is no known experimental method to directly resolve such sharp temporal structures.

P.M. Paul et al. [47] succeeded in demonstrating the generation of attosecond pulses by retrieving the harmonic phases from the spectrum of photoelectrons yielded by multiphoton bicolor ionization. Let us consider the diagram of photoionizing processes shown in Figure 16.5. The variable ω is the infrared frequency of the pump laser and $\omega_{q+1} = (q+1)\omega$ (conversely $q-1$), the frequency of the harmonic of order $q+1$ (conversely $q-1$). Each of these two harmonics causes ionization only by single-photon process. The two corresponding bands are represented in the inset of Figure 16.5. Simultaneously the high intensity of the infrared pump field induces additional multiphoton ionizing transitions with absorption or emission of infrared photons. As a result of the bicolor transitions, side bands appear in the photoelectron spectrum. Limiting the infrared intensity allows two-photon transitions only to occur. In this case, the modification of the initial one-photon spectrum is reduced to a single side band on each side of each harmonic. Moreover, at low IR intensity, only the two nearest harmonics will contribute to each side band peak. These peaks appear at energies that are even multiples of ω, i.e. they are inserted between two successive odd harmonics peaks.

Let us assume that the infrared field is delayed by a time τ with respect to the harmonic field. The total transition probability for photoelectron emission for a given side band has the form [48]

$$P_{\text{photoelectron}} = A^2 + B^2 + 2AB\cos(2\omega_{\text{IR}}\tau + \phi_{q-1} - \phi_{q+1} + \Delta\phi_{\text{atomic}}) \tag{16.4}$$

In this expression there is no absolute phase origin. $\omega_{\text{IR}}\tau = \phi_{\text{IR}}$ is the phase of the infrared radiation field relative to that of a chosen harmonic, e.g. the $(q-1)$th harmonic. The terms A and B are directly related to the transition matrix elements for the harmonics $q-1$ and $q+1$, respectively. $\Delta\phi_{\text{atomic}}$ is a small term which can be calculated with high precision within the framework of second-order perturbation theory. Thus experimentally measuring the magnitude of the side band peak as a function of the adjustable delay τ will give access to the phase difference $\phi_{q-1} - \phi_{q+1}$ between the $(q-1)$th and the $(q+1)$th harmonics. Therefore the low intensity IR beam is to be considered as the probe which reveals the temporal structure of the harmonic pack.

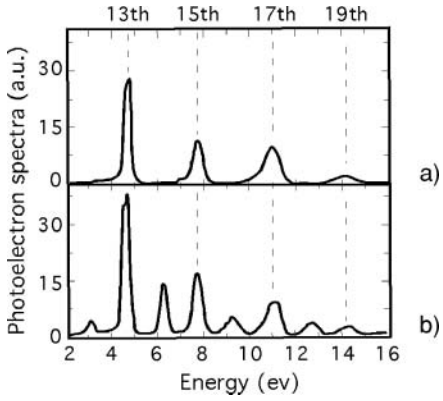

Fig. 16.6. Photoelectron spectrum generated by (a) the global field of the IR laser harmonics, (b) the addition of copropagating IR radiation to the global harmonic field, with a 1.7-fs time delay between both fields.

In the experimental setup, the beam of a Ti:sapphire laser (800 nm, 40 fs, 1 kHz) is split into two colinear parts of unequal intensities. The most intense of the two beams focuses $\sim 10^{14}$ W/cm^2 into an argon jet which generates harmonics. The second one, delayed by the adjustable time interval τ, propagates along the same axis as the harmonics. Both beams are then focused into a second argon jet which is located in an electron time-of-flight spectrometer. The IR probe intensity at this focus is $\lesssim 10^{12}$ W/cm^2, that is far below the threshold for multiphoton ionization by infrared radiation.

An example of the photoelectron spectra obtained at the output of the spectrometer is displayed in Figure 16.6. Figure 16.6a shows the spectrum of Ar photoionized by the XUV harmonic superposition only. In Figure 16.6b

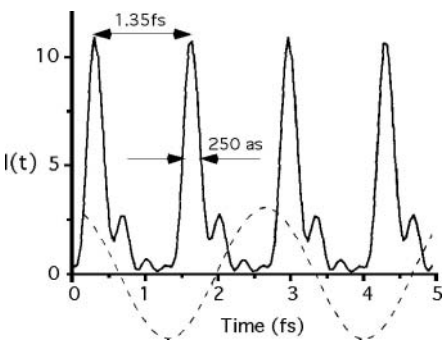

Fig. 16.7. Reconstructed temporal profile of the sum of the 11th, 13th, 15th, 17th, and 19th harmonics. The profile consists of a sequence of 250-as peaks, spaced by 1.35 fs. The dashed line shows the IR probe profile.

copropagating IR radiation is added to the harmonics with a delay $\tau = -1.7$ fs, causing side bands to appear between the harmonic peaks.

The magnitude of four side bands have been measured as a function of the time delay τ. The plot of experimental data shows curves oscillating in phase with a periodicity of 1.35 fs, that is with the expected frequency of $2\omega_{\mathrm{IR}}$. As the atomic phase $\Delta\phi_{\mathrm{atomic}}$ can be known from calculation, each measured side band leads to the value of the phase difference $\phi_{q-1} - \phi_{q+1}$ between two consecutive harmonics. Choosing one of the phases as the origin, the four others harmonic phases can be determined. Together with the relative harmonic amplitudes of the associated photoelectron peaks, obtained from the data of Figure 16.6 and similar experimental results, the measured harmonic phases determine the temporal intensity profile of the total field. Figure 16.7 shows the temporal profile obtained for the sum of the 11th, 13th, 15th, 17th, and 19th harmonics. It consists of a sequence of 250-as peaks, spaced by 1.35 fs.

In view of future developments of atto-sciences, it would be useful to generate single attosecond pulses. A possible approach could consist in taking advantage from the high sensitivity of harmonics to the pump laser degree of polarization ellipticity to realize a temporal gate. However, the laser pulse duration should be previously reduced to 15–20 fs compared with the 40 fs of the above experiment [49].

17. Future Prospects

Only already demonstrated applications of coherent XUV sources have been described in the previous sections. We conclude this chapter by a short review of fields in which laboratory research already opens the way to new developments.

17.1 Nonlinear XUV Optics

Nonlinear XUV optics is a very interesting challenge for X-ray lasers. Nonlinear absorption, third harmonic generation, four-wave mixing and stimulated Raman scattering are considered to be feasible in plasma and gases irradiated by X-ray lasers. A detailed review of theoretical researches can be found in [50].

Preliminary experiments have been carried out on four-wave mixing with using the 23.1-nm line of the Ne-like nickel soft X-ray laser [51–53]. The objective of these experiments is to induce processes like $2\omega_{\mathrm{XRL}}{-}\omega_{\mathrm{opt}}$ soft X-ray emission which nearly double the laser frequency. The initial X-ray laser beam was split into two beamlets which then recombined at the focus of the optical field. An only limited parameter scan, for which no nonlinear signal was detected, could be made till now. It showed that the optimization of experimental parameters needed to improve the knowledge of the beam coherence.

17.2 Microlithography

Lithography is a process used to pattern the nanoelectronics computer chips. The number of transistors per chip, the chip frequency, and the correlate microprocessor performances increase with the reduction of the printable line width. Using an ultraviolet KrF laser operating at 248-nm wavelength as a light source, patterns are printed with 180 nm in line width as in space between lines. A transition to ArF laser at 193 nm reduces the line width to 130 nm,

with a corresponding increase of a factor 2 for the number of transistors per chip and one third for the chip frequency. The present challenge is to reduce the line width to 65 nm (45 nm for isolated lines). Two techniques, XUV lithography and electron beam projection, are candidate (cf. [54] and inserted references).

XUV lithography is based on multilayer coated reflective optics operating near 13-nm wavelength. The reason of this choice is the relatively high reflectivity (70%) of Mo/Si and Mo/Be mirrors at ∼100 eV, immediately below the photoabsorption threshold of the L- and the K-shell respectively. This choice fits well to the 13.9-nm wavelength of the TCE Ni-like laser (see for instance [55]).Owing to their currently low repetition rate, most of X-ray lasers could not be considered appropriate for large-scale chip production. Nevertheless they have the qualities required for being efficient tools for interferometry testing of optical components, scattering studies, metrology, and defect inspection. The fast capillary discharge laser (cf. Section 7.5) is worth of a special examination on account of his higher repetition rate (see for instance [56]). In the future, the development of diode-laser pumped X-ray lasers may provide new capabilities of X-ray lasers in this field. Concerning high-order harmonic-based XUV sources, new progress in phase matching could provide an enhancement of the time-averaged power sufficient to be used for lithography [57].

17.3 Biological Applications

Large attention is payed to biological applications. Contact microscopy with an X-ray laser source successfully demonstrated biological specimen imaging [58–62]. However this technique is not suitable for imaging three-dimensional objects as those corresponding to the complex functional strucures of chromosomes.

Soft X-ray holographic microscopy is considered a promising technique for high resolution, three-dimensional images of wet biological objects. As a matter of fact, a high-image contrast could be obtained by using a highly coherent, intense soft X-ray source of suitable wavelength. It is commonly admitted that the wavelengths between the absorption K-edges of carbon and oxygen (4.37–2.32 nm), i.e. the so-called "water window," would be the best for holography. For a more detailed examination, London et al. [63] calculated the scattering cross-section for a 15-nm radius protein sphere, both in vacuum and in water. They concluded that wavelength slightly longer than 4.37 nm would be better for protein in water, because it minimizes the necessary source power and maximizes the penetrability of X-rays through wet samples. Assuming a focal spot diameter of 10-μm diameter, the total energy requirement for imaging the specimen, with a resolution of 30 nm at $\lambda = 4.4$ nm, was found to be ∼330 μJ. Hitherto one of the best performances at short wavelength for an X-ray laser is emission of 300-μJ pulses at 13.9-nm

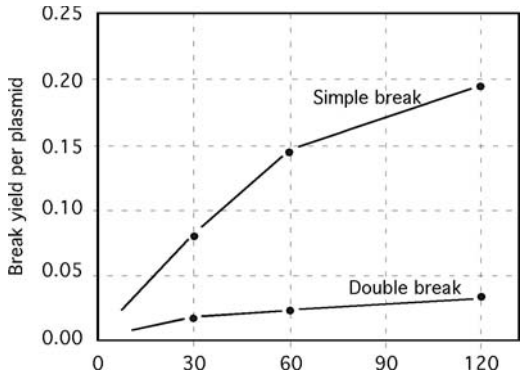

Fig. 17.1. DNA damages against XUV laser radiation density.

wave-length (cf. Table 7.10). The way to fill the gap between the requirements of holographic methods near 4 nm and the capabilities of present X-ray lasers is not clear yet. Progress in short pulse, high repetition rate XUV lasers are still necessary.

A very different direction of research appears with using soft X-ray lasers to irradiate biological specimens. The role of inner-shell ionization of the constituting atoms in the cell lethality has been investigated by synchrotron X-ray radiation above the carbon and oxygen K-shell ionization limits or using heavy ion beams [64]. Theoretical models suggest the radiation action on the cell to be related to such preferential localizations of ionizations on DNA. To improve the understanding of the cell lethality process, it is also important to assess the damages created by soft X-rays of energy smaller than those of the K-shells. This requires a high-intensity monochromatic flux so that exposure time may be consistent with the lifetime of the biological sample under vacuum. Two experiments, in which X-ray laser is chosen as irradiation source, are in progress. One, described in [65], uses a TCE silver laser at 13.9-nm wavelength (cf. Section 7.4.7). The other is similar but the soft X-ray source is the PALS zinc laser at 21.2 nn, described in [66]. It has recently given preliminary results showing L-shell ionizations to induce a number of damages to DNA which exhibits a roughly linear growth against the dose of soft X-rays (Fig. 17.1). [67]. These works are expected to contribute in a better qualitative and quantitative knowledge of DNA damages, as well as DNA repair mechanisms.

References

1. C. Orth, R. Beach, C. Bibeau, E. Honea, K. Jancaitis, J. Lawson, C. Marshall, R. Sacks, K. Schaffers, J. Skidmore, S. Sutton, SPIE Proceedings, **3265** (1998) 114.

2. L.B. DaSilva, T.W. Barbee Jr., R. Cauble, P. Celliers, D. Ciarlo, S. Libby, R.A. London, D. Matthews, S. Mrowka, J.C. Moreno, D. Ress, J.E. Trebes, A.S. Wan, F. Weber, Phys. Rev. Lett., **74** (1995) 3991.
3. J. Filevitch, M.C. Marconi, K. Kanizay, J.L.A. Chilla, J.J. Rocca, *X-Ray Lasers*, 2000; J. Phys. IV France, **11** (2001) Pr2-483.
4. E. Jankowska, E.C. Hammarsten, J. Filevitch, M.C. Marconi, J.J. Rocca, IEEE Trans. Plasma Sci., **30** (2002) 46.
5. J. Filevitch, J.J. Rocca, E. Jankowska, E.C. Hammarsten, M.C. Marconi, S.J. Moon, V.N. Shlyaptsev, *X-Ray Lasers*, 2002; AIP Conf. Proc. **641** (2002) 489.
6. T.W.L. Sanford, R.C. Mock, R.B. Spielman, M.G. Haines, J.P. Chittenden, K.G. Whitney, J.P. Apruzese, D.L. Peterson, J.B. Greenly, D.B. Sinars, D.B. Reisman, D. Mosher, Phys. Plasmas, **6** (1999) 2030.
7. E. Jankowska, E.C. Hammarsten, B. Szapiro, J. Filevitch, M.C. Marconi, J.J. Rocca, *X-Ray Lasers,* 2002 AIP Conf. Proc., **641** (2002) 498.
8. I.A. Artioukov, B.R. Benware, J.J. Rocca, M. Forsythe, Yu.A. Uspenskii, A.V. Vinogradov, SPIE Proc., **3776** (1999) 224.
9. I.A. Artioukov, B.R. Benware, R.M. Fechtchenko, J.J. Rocca, M. Seminario, A.V. Vinogradov, M. Yamamoto, *X-Ray Lasers,* 2000; J. Phys. IV France, **11** (2001) Pr2-451.
10. L.B. DaSilva, T.W. Barbee Jr., R. Cauble, P. Celliers, C.D. Decker, D.H. Kalantar, M.H. Key, R.A. London, J.C. Moreno, J.E. Trebes, A.S. Wan, F. Weber, *X-Ray Lasers,* Inst Phys. Conf. Ser. No. 151, IOP Publishing, 1996, p. 496.
11. A.S. Wan, C.A. Back, T.W. Barbee Jr., R. Cauble, P. Celliers, L.B. DaSilva, C. Decker, S. Glenzer, J.C. Moreno, R.A. London, P.W. Rambo, G.F. Stone, J.E. Trebes, F. Weber, *X-Ray Lasers,* Inst Phys. Conf. Ser. No. 151, IOP Publishing, 1996, p. 504.
12. A.S. Wan, T.W. Barbee Jr., R. Cauble, P. Celliers, L.B. DaSilva, J.C. Moreno, P.W. Rambo, G.F. Stone, J.E. Trebes, F. Weber, IEEE Trans. Plasma Sci., **27** (1999) 120.
13. M.H. Emery, J.H. Gardner, R.H. Lehmberg, S.P. Obenschain, Pys. Fluids B, **3** (1991) 2640.
14. D.H. Kalantar, M.H. Key, L.B. DaSilva, S.G. Glendinning, J.P. Knauer, B.A. Remington, F. Weber, S.V. Weber, Phys. Rev. Lett., **76** (1996) 3574.
15. P.J. Warwick, A. Demir, D.H. Kalantar, M.H. Key, N.S. Kim, C.L.S. Lewis, J. Lin, A.G. MacPhee, D. Neely, B.A. Remington, S. Rose, R. Smith, G.J. Tallents, J.S. Wark, S.V. Weber, E. Wolfrum, J. Zhang, *X-Ray Lasers,* Inst Phys. Conf. Ser. No. 151, IOP Publishing, 1996, p. 509.
16. J. Larsson, E. Mevel, R. Zerne, A. L'Huillier, G.G. Wahlström, S. Svanberg, J. Phys. B, **28** (1995) L53.
17. M. Gisselbrecht, D. Descamps, C. Lynga, A. L'Huillier, C.-G. Wahlström, M. Meyer, Phys. Rev. Lett., **82** (1999) 4607.
18. J.F. Young, J.S. Preston, H.M. van Driel, J.E. Sipe, Phys. Rev. B, **27** (1983) 1155.
19. P. Zeitoun, F. Albert, P. Jaegle, D. Joyeux, M. Boussoukaya, A. Carillon, S. Hubert, G. Jamelot, A. Klisnick, D. Phallipou, J.C. Lagron, D. Ros, S. Sebban, A. Zeitoun-Fakiris, Nucl. Instrum. Methods Phys. Res. A, **416** (1998) 189.

20. F. Albert, P. Zeitoun, P. Jaegle, D. Joyeux, M. Boussoukaya, A. Carillon, S. Hubert, G. Jamelot, A. Klisnick, D. Phallipou, J.C. Lagron, D. Ros, A. Zeitoun-Fakiris, Phys. Rev. B, **60** (1999) 11089.
21. B. Rus, T. Mocek, A.R. Präg, M. Kozlova, M. Hudecek, G. Jamelot, A. Carillon, D. Ros, J.C. Lagron, D. Joyeux, D. Phallipou, Plasma Physi. Controlled Fusion, **44** (2002) B207.
22. T. Mocek, D. Ros, B. Rus, D. Joyeux, A.R. Präg, M. Kozlova, A. Carillon, D. Phalippou, F. Ballester, E. Jacques, M. Boussoukaya, G. Jamelot, *X-Ray Lasers,* 2002; AIP Conf. Proc., **641** (2002) 518.
23. A.N. Belsky, I.A. Kamenskiskh, S. Sebban, P. Jaeglé, G. Jamelot, A. Carillon, A. Klisnick, Ph. Zeitoun, F. Albert, D. Ros, B. Rus, P. Martin, C. Pedrini, *X-Ray Lasers,* 2000; J. Phys. IV France, **11** (2001) Pr2-495.
24. S. Sebban, P. Jaeglé, G. Jamelot, A. Carillon, A. Klisnick, Ph. Zeitoun, F. Albert, D. Ros, *X-Ray Lasers,* Inst Phys. Conf. Ser. No. 151, IOP Publishing, 1996, p. 528.
25. P. Jaeglé, S. Sebban, A. Carillon, G. Jamelot, A. Klisnick, Ph. Zeitoun, B. Rus, M. Nantel F. Albert, D. Ros, J. Appl. Phys., **81** (1997) 2406.
26. S. Le Pape, Ph. Zeitoun, P. Dhez, M. François, M. Idir, D. Ros, A. Carillon, Laser Particle Beams, **19** (2001) 55.
27. P. Mercere, Ph. Zeitoun, M. Idir, S. Le Pape, D. Douillet, X. Levecq, G. Dovillaire, S. Bucourt, K.A. Goldberg, P.P. Naulleau, S. Rekawa, Optics Lett., **28** (2003) 1354.
28. S. Le Pape, Ph. Zeitoun, M. Idir, P. Dhez, D. Ros, A. Carillon, J.J. Rocca, M. François, Eur. Phys. J. AP, **20** (2002) 197.
29. S. Le Pape, Ph. Zeitoun, M. Idir, P. Dhez, J.J. Rocca, M. François, Phys. Rev. Lett., **88** (2002) 183901.
30. J. Dunn, R.F. Smith, J. Nilsen, A.J. Nelson, T.W. Van Buuren, S.J. Moon, J.R. Hunter, J. Filevich, J.J. Rocca, M.C. Marconi; V.N. Shlyaptsev, *X-Ray Lasers,* 2002; AIP Conf. Proc., **641** (2002) 481.
31. D. Joyeux, R. Mercier, D. Phalippou, M. Mullot, M. Lamare, in X-ray Lasers 2000, ed. by G. Jamelot, C. Möller, A. Klisnick, Journal de Physique IV, **11** (2001), Pr2-511.
32. H. Tang, O. Guilbaud, G. Jamelot, D. Ros, A. Klisnick, D. Joyeux, D. Phalippou, M. Kado, M. Nishikino, M. Kishimoto, K. Sukegawa, M. Ishino, K. Nagashima, H. Daido, Applied Physics B, **78** (2004) 97.
33. Nilsen,-J.; Scofield,-J.-H., Opt. Letters., **29** (2004) 2677.
34. Zeitoun P., Balcou P., Bucourt S., Delmotte F., Dovillaire G., Douillet D., Dunn J., Faivre G., Fajardo M., Goldberg K.A., Hubert S., Hunter J.R., Idir M., Jacquemot S., Kazamias S., Pape S.L., Levecq X., Lewis C.L.S., Marmoret R., Mercere P., Morlens A.S., Naulleau P.P., Ravet M.F., Remond C., Rocca J.J., Smith R.F., Troussel P., Valentin C., Vanbostal L., Applied Physics B, **78** (2004) 983.
35. R.Z. Tai, K. Namikawa, M. Kishimoto, M. Tanaka, K. Sukegawa, N. Hasegawa, T. Kawachi, M. Kado, P. Lu, K. Nagashima, H. Daido, H. Maruyama, A. Sawada, M. Ando, Y. Kato, Phys. Rev. Lett., **89** (2002) 257602.
36. P. Martin, A.N. Belsky, E. Constant, E. Mevel, F. Salin, *X-Ray Lasers,* 2000; J. Phys. IV France **11** (2001) Pr2-503; IEEE Trans. Nucl. Sci., **48** (2001) pt.1:1137.

37. P. Salières, L. Le Déroff, T. Auguste, P. Monot, P. d'Oliveira, D. Campo, J.-F. Hergott, H. Merdji, B. Carré, Phys. Rev. Lett., **83** (1999) 5483.
38. J.-F. Hergott, T. Auguste, P. Salières, L. Le Déroff, P. Monot, P. D'Oliveira, D. Campo, H. Merdji, B. Carré, J. Opt. Soc. Am. B, **20** (2003) 171.
39. T. Brabec, F. Krausz, Rev. Mod. Phys., **72** (2000) 545.
40. Gy. Farkas, Cs. Tóth, Phys. Lett. A, **169** (1992) 447.
41. S.E. Harris, J.J. Macklin, T.W. Hänsch, Opt. Commun. **100** (1993) 487.
42. M. Ivanov, P.B. Corkum, T. Zuo, A. Bandrauk, Phys. Rev. Lett., **74** (1995) 2933.
43. Ph. Antoine, A. L'Huillier, M. Lewenstein, Phys. Rev. Lett., **77** (1996) 1234.
44. V. Veniard, R. Taieb, A. Maquet, Phys. Rev. A, **54** (1996) 721.
45. N.A. Papadogiannis, B. Witzel, C. Kalpouzos, D. Charalambidis, Phys. Rev. Lett., **83** (1999) 4289.
46. P.M. Paul, E.S. Toma, P. Breger, G. Mullot, F. Augé, Ph. Balcou, H.G. Muller, P. Agostini, Science, **292** (2001) 1689.
47. P.M. Paul, E.S. Toma, P. Breger, G. Mullot, F. Augé, Ph. Balcou, H.G. Muller, P. Agostini, Science, **292** (2001) 1689.
48. P. Agostini, P.M. Paul, P. Breger, E.S. Toma, H.G. Muller, G. Mullot, F. Augé, Ph. Balcou, Acta Phys. Polo., **101** (2002) 313.
49. H. Merdji, Y. Mairesse, E. Priori, K. Kovacev, P. Agostini, P. Breger, P. Montchicourt, P. Salières, B. Carré, O. Tcherbakoff, E. Mével, E. Constant, *X-Ray Lasers,* 2002; AIP Conf. Proc., **641** (2002) 406.
50. P.L. Shkolnikov, A.E. Kaplan, *X-Ray Lasers,* Inst. Phys. Conf. Ser. No. 151, IOP Publishing, 1996, p. 4512.
51. R.M.N. O'Rourke, C.L.S. Lewis, A. Hibbert, *X-Ray Lasers,* Phys. Conf. Ser. No. 159, IOP Publishing, 1998, p. 687.
52. S.J. Topping, R. Keenan, C.L.S. Lewis, R.M.N. O'Rourke, A.G. MacPhee, S. Dobosz, G.J. Tallents, M. Notely, D. Neely, *X-Ray Lasers,* 2000; J. Phys. IV (Paris), **11** (2001) Pr2-487.
53. S.J. Topping, R. Keenan, C.L.S. Lewis, A.M. McEvoy, S. Hubert, *X-Ray Lasers*, 2002; AIP Conf. Proc., **641** (2002) 544.
54. D.T. Attwood, *X-Ray Lasers,* 2000; J. Phys. IV (Paris), **11** (2001) Pr2-443.
55. O.R. Wood II, D.L. White, J.E. Bjotkohlm, L.E. Fetter, D.M. Tennant, A.A. MacDowel, B. LaFontaine, G.D. Kubiak, J. Vacuum Sci. Technol. B, **15** (1997) 2448.
56. A.V. Vinogradov, Quant. Electron., **32** (2002) 1113.
57. A. Paul, R.A. Bartels, R. Tobey, H. Green, S. Weiman, I.-P. Christov, M.M. Murnane, H.-C. Kapteyn, S. Backus, Nature **421** (6918) 51.
58. C.H. Skinner, S.D. DiCicco, D. Kim, R.J. Rosser, S. Suckewer, A.P. Gupta, J.G. Hirschberg, J. Microsc., **159** (pt. 1) (1990) 51.
59. L.B. Da Silva, J.E. Trebes, R. Balhorn, S. Mwroka, E. Anderson, D.T. Atwood, T.W. Barbee, J. Brase, M. Corzett, J. Gray, J.A. Koch, C. Lee, D. Kern, R.A. London, B.J. MacGowan, D.L. Matthews, G. Stone, Science, **258** (1992) 269.
60. B.J. MacGowan, SPIE Proc., **1741** (1992) 2.
61. S.D. DiCicco, D. Kim, L. Polonsky, C. Skinner, S. Suckewer, SPIE Proc., **1741** (1992) 160.
62. K. Shinohara, *X-Ray Lasers,* Inst. Phys. Conf. Ser. No. 151, IOP Publishing, 1996 p. 533.

63. R.A. London, M.D. Rosen, J.E. Trebes, Appl. Opt., **28** (1989) 3397.
64. A. Touati, A.M. Herve du Penhoat, B. Fayard, C. Champion, F. Abel, F. Gobert, M. Lamoureux, M.F. Politis, L. Martins, M. Ricoul, L. Sabatier, E. Sage, A. Chetioui, Radiat. Protec. Dosimetry, **99** (2002) 83.
65. A. Klisnick, G. Jamelot, D. Ros, A. Carillon, P. Jaeglé, M. Boussoukaya, O. Guilbaud, J. Kuba, R. Smith, J.C. Lagron, L. Vanbostal, D. Joyeux, D. Phalippou, S. Sebban, A. Touati, M.A.H. du Penhoat, F. Ballester, E.-J. Petit, B. Rus, T. Mocek, F. Strati, M. Edwards, G.J. Tallents, R. Keenan, S. Topping, C.L.S. Lewis, P. Neumeyer, D. Ursescu, T. Kühl, H. Tang, H. Daido, *X-Ray Lasers,* 2002; AIP Conf. Proc., **641** (2002) 166.
66. B. Rus, T. Mocek, A.R. Präg, M. Kozlova, M. Hudeček, G. Jamelot, J.C. Lagron, A. Carillon, D. Ros, D. Joyeux, D. Phalippou, *X-Ray Lasers,* 2002; AIP Conf. Proc., **641** (2002) 182.
67. D. Ros, B. Rus, (private communication, 2005).

Index